NASA Technical Memorandum 106303

N94-20497
--THRU--
N94-20519
Unclas

G3/32 0191320

(NASA-TM-106303) SOLID STATE
TECHNOLOGY BRANCH OF NASA LEWIS
RESEARCH CENTER: FIFTH ANNUAL
DIGEST (NASA) 273 p

Solid State Technology Branch of NASA Lewis Research Center Fifth Annual Digest

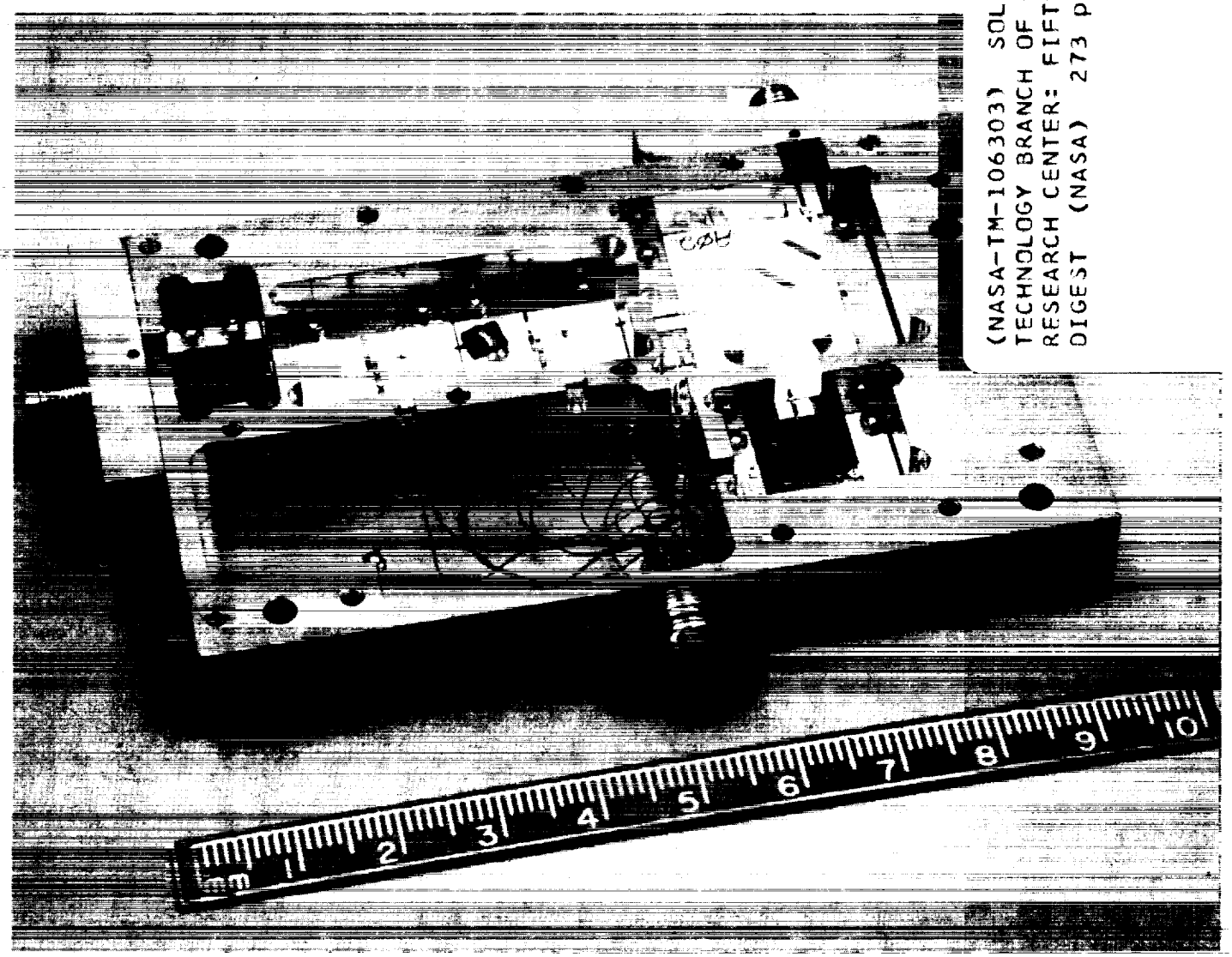

NASA

June 1992—June 1993
Lewis Research Center

Preface

This year, 1993, was the year of "changing the paradigm," "empowering the staff," "satisfying the customer," "considering the stakeholders," and "transferring the technology," for "times are changing." However, customers are never satisfied with a substandard product. Salesmanship (transfer mechanisms) does not substitute for a good product. In fact, if one has trouble "transferring technology," there's a fair chance that the problem lies with the quality of the technology, since invariably the ease of technology transfer is proportional to its quality. These parts of the paradigm have not changed and will not change. What has changed, particularly for industrial research, is that the link to applications must be extremely short. As a result, most industrial labs have, in fact, become development labs or even product improvement labs. It falls, therefore, to the government laboratories to fill the void and supply the more long-range, high-risk research that feeds those development labs. Such research then is the "product" of the government laboratory. And the industrial development lab is its "customer," albeit a nonpaying one, to whom the technology must be transferred. This is not a new philosophy for the Solid State Technology Branch and the list of coauthors on the papers here illustrates that clearly.

The 49 papers in this volume include coauthors from Texas Instruments, Spire Corporation, Hughes Research Laboratories, IBM R&D Labs, TRW, Ball Aerospace, and Johnson Space Center—all "customers" for our technology and our expertise—all papers in which our in-house team has made a genuine contribution. In addition they include collaborators from 14 major universities, such as the University of Michigan, University of Texas, UCLA, Ohio State University, and the University of Nebraska—strong evidence that our work provides, quite properly in my opinion, a bridge between the truly basic research of the university and the focused shorter term development programs of industry.

The technical content of the papers presented here represents much the same mix as in previous years. In spite of the erosion of budgets, however, the number of papers presented or published in the year ending June 30, 1993 has increased dramatically. The digest which appeared in June 1991 contained reprints of just 25 papers; the June 1992 edition comprised 35; this year's volume contains a record high 49 papers which have been either published in journals or presented at conferences. Most of these latter are also available in the proceedings of those conferences.

Principal thrusts for this year include, in the circuits area, development of new transmission media, including analytical models, and techniques for coupling them to antennas; work on the use of silicon as a microwave substrate; methods to remove active devices or circuits from the substrate on which they were fabricated; and the development of pseudomorphic devices based on indium phosphide with an active layer of high indium content InGaAs.

Materials characterization work focused heavily on MODFET structures, such as InGaAs/InP, as well as on the evaluation of SiGe/Si materials from a multitude of sources. This last activity, as well as the work on transmission lines on silicon, is related to an attempt to evaluate the SiGe/Si structure for use in either FET or HBT-based microwave circuits, and possibly hybrid microwave/digital circuits.

Finally, work in superconductivity is still focused primarily on part 2 of the Naval Research Laboratory's (NRL) High Temperature Superconducting Space Experiment (HTSSE-II). During the year, a prototype superconducting X-band receiver, developed in collaboration with the Jet Propulsion Laboratory, was delivered to NRL. Work was also undertaken this year on the deposition of BKBO superconducting films, primarily for use in mixers at THz frequencies.

Facilities augmentations this year were relatively modest, but included an automated noise figure measurement set up which permits us to measure device noise figures both at room temperature and at cryogenic temperatures.

Finally, we would like to acknowledge the contributions of Dr. Richard Q. Lee of the Antenna and RF Systems Technology branch. The collaboration between Dr. Lee and personnel of the Solid State Branch has been exceptionally fruitful.

Regis F. Leonard
Chief, Solid State Technology Branch
NASA Lewis Research Center
August 1993

SOLID STATE TECHNOLOGY BRANCH OF NASA LEWIS RESEARCH CENTER FIFTH ANNUAL DIGEST June 1992 – June 1993

Contents

Section One
Microwave Circuit and Antenna Development

A 10-GHz Amplifier Using an Epitaxial Lift-Off Pseudomorphic HEMT Device
by Paul G. Young, Robert R. Romanofsky, Samuel A. Alterovitz, Rafael A. Mena, and Edwyn D. Smith 3

An X-Band "Peeled" HEMT Amplifier
by Paul G. Young, Robert R. Romanofsky, Samuel A. Alterovitz, and Edwyn D. Smith 7

Characteristics of 0.8- and 0.2-μm Gate Length $In_xGa_{1-x}As/In_{0.52}Al_{0.48}As/InP$ ($0.53 \leq x \leq 0.70$) Modulation-Doped Field-Effect Transistors at Cryogenic Temperatures
by Richard Lai, Pallab K. Bhattacharya, David Yang, Timothy L. Brock, Samuel A. Alterovitz, and Alan N. Downey 15

Performance of a Wideband GaAs Low-Noise Amplifier at Cryogenic Temperatures
by S.S. Toncich, K.B. Bhasin, T.K. Chen, and P.C. Claspy 23

Full Wave Characterization of Microstrip Open End Discontinuities Patterned on Anisotropic Substrates Using Potential Theory
by S.S. Toncich, R.E. Collin, and K.B. Bhasin 27

A Comprehensive Theoretical and Experimental Study of Coplanar Waveguide Shunt Stubs
by Nihad I. Dib, George E. Ponchak, and Linda P.B. Katehi 31

A Comparative Study Between Shielded and Open Coplanar Waveguide Discontinuities
by N.I. Dib, W.P. Harokopus, Jr., G.E. Ponchak, and L.P.B. Katehi 35

A Theoretical and Experimental Study of Coplanar Waveguide Shunt Stubs
by Nihad I. Dib, George E. Ponchak, and Linda P.B. Katehi 47

Coplanar Waveguide Radial Line Stub
by R.N. Simons and S.R. Taub 55

Attenuation and ε_{EFF} of Coplanar Waveguide Transmission Lines on Silicon Substrates
by Susan R. Taub and Paul G. Young 57

Novel Coplanar Waveguide to Slotline Transition on High Resistivity Silicon
by R.N. Simons, S.R. Taub, and P.G. Young 61

Microwave Characterization of Slotline on High Resistivity Silicon for Antenna Feed Network
by Rainee N. Simons, Susan R. Taub, Richard Q. Lee, and Paul G. Young 63

New Coplanar Waveguide Feed Network for 22 Linearly Tapered Slot Antenna Subarray
by Rainee N. Simons, Thomas D. Perl, and Richard Q. Lee 71

Linearly Tapered Slot Antenna With Dielectric Superstrate
by Rainee N. Simons and Richard Q. Lee 73

Effect of a Dielectric Overlay on a Linearly Tapered Slot Antenna Excited By a Coplanar Waveguide
by Rainee N. Simons, Richard Q. Lee, Thomas D. Perl, and John Silvestro 77

Characteristics of Linearly Tapered Slot Antenna With CPW Feed on High Resistivity Silicon
by Rainee N. Simons, Susan R. Taub, and Richard Q. Lee 81

Nonplanar Linearly Tapered Slot Antenna With Balanced Microstrip Feed
by Rainee N. Simons, Richard Q. Lee, and Thomas D. Perl 85

Slot-Coupled Patch Antenna With Coplanar Waveguide Feed
by Richard Q. Lee and Rainee N. Simons 89

Bandwidth Enhancement of Dielectric Resonator Antennas
by Richard Q. Lee and Rainee N. Simons 93

Space Power Amplification With Active Linearly Tapered Slot Antenna Array
by Rainee N. Simons and Richard Q. Lee 97

An Analysis of the Frequency Limitations of an $Al_xGa_{1-x}As/GaAs$ Optical Modulator
by M. Tabib-Azar, P.C. Claspy, C. Chorey, and K.B. Bhasin 101

Section Two
Semiconductor Material Characterization

Ellipsometric Characterization of $In_{0.52}Al_{0.48}As$ and of Modulation Doped Field Effect Transistor Structures on InP Substrates
by S.A. Alterovitz, R.M. Sieg, J. Pamulapati, and P.K. Bhattacharya 109

Ellipsometric Study of Metal-Organic Chemically Vapor Deposited III-V Semiconductor Structures
by Samuel A. Alterovitz, Patricia A. Sekula-Moise, Robert M. Sieg, Mark N. Drotos, and Nancy A. Bogner 113

Enhancement of Shubnikov-de Haas Oscillations by Carrier Modulation
by S.E. Schacham, E.J. Haugland, and S.A. Alterovitz 119

Temperature Independent Quantum Well FET With Delta Channel Doping
by P.G. Young, R.A. Mena, S.A. Alterovitz, S.E. Schacham, and E.J. Haugland 123

Room-Temperature Determination of Two-Dimensional Electron Gas Concentration and Mobility in Heterostructures
by S.E. Schacham, R.A. Mena, E.J. Haugland, and S.A. Alterovitz 125

Spectroscopic Ellipsometry Studies of HF Treated Si (100) Surfaces
by Huade Yao, John A. Woollam, and Samuel A. Alterovitz 129

High Frequency Performance of $Si_{1-x}Ge_x/Si_{1-y}Ge_y/Si_{1-x}Ge_x$HBTs
by D. Rosenfeld and S.A. Alterovitz 133

Ellipsometric Study of $Si_{0.5}Ge_{0.5}$/Si Strained-Layer Superlattices
by R.M. Sieg, S.A. Alterovitz, E.T. Croke, and M.J. Harrell 135

Spectroscopic Ellipsometric Characterization of $Si/Si_{1-x}Ge_x$ Strained-Layer Superlattices
by H. Yao, J.A. Woollam, P.J. Wang, M.J. Tejwani, and S.A. Alterovitz 139

Development of $Si_{1-x}Ge_x$ Technology for Microwave Sensing Applications
by Rafael A. Mena, Susan R. Taub, Samuel A. Alterovitz, Paul E. Young, Rainee N. Simons, and David Rosenfeld 145

New Technique for Oil Backstreaming Contamination Measurements
by S.A. Alterovitz, H.J. Speier, R.M. Sieg, M.N. Drotos, and J.E. Dunning 157

The Quantum Efficiency of HgCdTe Photodiodes in Relation to the Direction of Illumination and to Their Geometry
by D. Rosenfeld and G. Bahir 163

Section Three
High Temperature Superconductivity

Space Applications of Superconducting Microwave Electronics at NASA Lewis Research Center
by R.F. Leonard, K.B. Bhasin, R.R. Romanofsky, C.D. Cubbage, and C.Z. Chorey 173

Y-Ba-Cu-O Superconducting/GaAs Semiconducting Hybrid Circuits for Microwave Applications
by K.B. Bhasin, S.S. Toncich, C.M. Chorey, N.J. Rohrer, and G.J. Valco 181

A High Temperature Superconductivity Communications Flight Experiment
by P. Ngo, K. Krishen, D. Arndt, G. Raffoul, V. Karasak, K. Bhasin, and R. Leonard 185

C-Band Superconductor/Semiconductor Hybrid Field-Effect Transistor Amplifier on a $LaAlO_3$ Substrate
by J.J. Nahra, K.B. Bhasin, S.S. Toncich, G. Subramanyam, and V.J. Kapoor 199

10 GHz $YBa_2Cu_3O_{7-\delta}$ Superconducting Ring Resonators on $NdGaO_3$ Substrates
by H.Y. Tot, G.J. Valco, and K.B. Bhasin 203

TlCaBaCuO High Tc Superconducting Microstrip Ring Resonators Designed for 12 GHZ
by G. Subramanyam, V.J. Kapoor, C.M. Chorey, and K.B. Bhasin 209

Conductor-Backed Coplanar Waveguide Resonators of $YBa_2Cu_3O_{7-\delta}$ on $LaAlO_3$
by Felix A. Miranda, Kul B. Bhasin, Keon-Shik Kong, Tatsuo Itoh, and Mark A. Stan 219

Conductor-Backed Coplanar Waveguide Resonators of Y-Ba-Cu-O and Tl-Ba-Ca-Cu-O on $LaAlO_3$
by F.A. Miranda, K.B. Bhasin, M.A. Stan, K.S. Kong, and T. Itoh 221

A 10 GHz Y-Ba-Cu-O/GaAs Hybrid Oscillator Proximity Coupled to a Circular Microstrip Patch Antenna
by Norman J. Rohrer, M.A. Richard, George J. Valco, and Kul B. Bhasin 225

Performance of TlCaBaCuO 30 GHZ 64 Element Antenna Array
by L.L. Lewis, G. Koepf, K.B. Bhasin, and M.A. Richard 231

Microwave Properties and Characterization of Co-Evaporated BSCCO Thin Films
by F.A. Miranda, C.M. Chorey, M.A. Stan, C.E. Nordgren, R.Y. Kwor, and T.S. Kalkur 235

Processing, Electrical and Microwave Properties of Sputtered Tl-Ca-Ba-Cu-O Superconducting Thin Films
by G. Subramanyam, V.J. Kapoor, C.M. Chorey, and K.B. Bhasin 243

Electrical-Transport Properties and Microwave Device Performance of Sputtered TlCaBaCuO Superconducting Thin Films
by G. Subramanyam, V.J. Kapoor, C.M. Chorey, and K.B. Bhasin 247

The Effect of Fluctuations on the Electrical Transport Behaviour in $YBa_2Cu_3O_{7-x}$
by Satish Vitta, S.A. Alterovitz, and M.A. Stan 255

Ellipsometric Study of Ambient-Produced Overlayer Growth Rate on $YBa_2Cu_3O_{7-x}$ Films
by Robert M. Sieg, Samuel A. Alterovitz, and Joseph D. Warner 263

Magnetic Flux Relaxation in $YBa_2Cu_3O_{7-x}$ Thin Film: Thermal or Athermal
by Satish Vitta, M.A. Stan, J.D. Warner, and S.A. Alterovitz 269

Biographies

Samuel A. Alterovitz 277
Christopher M. Chorey 277
Alan N. Downey 278
Edward J. Haugland 278
Thomas J. Kascak 279
Regis F. Leonard 279
Rafael A. Mena 280
Felix A. Miranda 280
Carlos R. Morrison 281
George E. Ponchak 281
John J. Pouch 282
Robert R. Romanofsky 282
David Rosenfeld 283
Samuel E. Schacham 283
Ajit K. Sil 284
Rainee N. Simons 284
Mark A. Stan 285
Stephan Stecura 285
Susan R. Taub 286
Joseph D. Warner 286
Paul G. Young 287
Solid State Technology Branch Members 288

SECTION ONE

MICROWAVE CIRCUIT AND ANTENNA DEVELOPMENT

A 10-GHz Amplifier Using an Epitaxial Lift-Off Pseudomorphic HEMT Device

Paul G. Young, Robert R. Romanofsky, *Member, IEEE*, Samuel A. Alterovitz, Rafael A. Mena, and Edwyn D. Smith, *Senior Member, IEEE*

***Abstract*—A process to integrate epitaxial lift-off devices and microstrip circuits has been demonstrated using a pseudomorphic HEMT on an alumina substrate. The circuit was a 10 GHz amplifier with the interconnection between the device and the microstrip circuit being made with photolithographically patterned metal. The measured and modeled response correlated extremely well with a maximum gain of 6.8 dB and a return loss of –14 dB at 10.4 GHz.**

I. Introduction

In 1978, Konagai *et al.* [1] demonstrated that a thin film of GaAs based material could be removed from it's growth substrate using a preferential etch of a buried AlAs layer. It is well known [2] that AlAs etches in HF:DI (1:10) at a rate 10^7 times faster than $Al_xGa_{1-x}As$ when x is less than 0.4. Also, because of the unique relationship between the lattice constant of AlAs–GaAs based materials, a structure can be made on GaAs that has a thin layer of AlAs grown between the substrate and the active device layer. The active layer is then later easily removed from the substrate via a HF etch of the AlAs sacrificial layer and the thin active layer can be attached to a limitless number of host substrates.

Work on epitaxial lift-off (ELO) techniques has progressed from optoelectronical devices [3], [4], to active circuits [5], and to microwave applications [6]–[8]. Shah *et al.* [6] demonstrated a MESFET device that had been fabricated after ELO which resulted in a f_{max} of 14 GHz. Van Hoof [7] demonstrated a MESFET that had been fabricated before ELO. They compared device properties to see the effects of the ELO step and found some degradation in the extrinsic transconductance due to ELO. The focus of our research has been in the area of microwave applications with a distinct focus on active devices. Recently, we fabricated high-electron mobility transistors (HEMT) and estimate the effects of the ELO step on HEMT device characteristics [9], [10]. We found no degradation in the performance of the devices, but rather an enhancement of f_T and the low-frequency gain. It was shown by Mena *et al.* [11] that an enhancement in the 2-D carrier confinement was detected after ELO, which would, in turn, explains the improvement in the gain of the HEMT device.

Manuscript received November 19, 1992. The work at the University of Toledo was funded under NASA Grant NAG3–1226.

P. G. Young and E. D. Smith are with the Department of Electrical Engineering, University of Toledo, 2801 West Bancroft, Toledo, OH 43606.

R. R. Romanofsky, A. A. Alterovitz, and R. A. Mena are with the NASA Lewis Research Center, 21000 Brookpark Road, MS 54/5, Cleveland, OH 44135.

IEEE Log Number 9207950.

The purpose of making ELO devices is to independently optimize device and substrate properties in microwave circuit design. Here, for the first time, we present the integration of an ELO pseudomorphic HEMT (P-HEMT) device on a microwave substrate to fabricate a 10-GHz amplifier. The design will use a discrete ELO transistor attached to an alumina substrate. A classical, narrow band amplifier was designed using open circuit stub match and the typical scattering parameters of an ELO PHEMT device. Contact between the circuit and the PHEMT ELO device was made via photolithographically patterned metal lines. These interconnect lines step from the alumina substrate to the device, without the need of bondwires.

II. Fabrication

The P-HEMT structure was MBE grown material, provided by QED Corporation, consisting of a $Al_{0.23}Ga_{0.77}As$–$In_{0.2}Ga_{0.8}As$–GaAs quantum-well structure with silicon pulse doping in the wide-band $Al_{0.23}Ga_{0.77}As$ region. A 500-Å AlAs release layer was grown between the GaAs substrate and the superlattice to enable the ELO step. Varied thicknesses of the AlAs sacrificial layer from 50 to 1000 Å were evaluated and no significant difference in the ELO capability was detected.

Device fabrication started with a mesa isolation process that etched approximately 1500 Å of material to insure isolation while avoiding the AlAs layer. Ohmic contacts were formed using Au–Ge–Au–Ni–Au alloyed for 15 seconds at 400° C. Contact composition and alloying parameters are critical in maintaining good contact resistivities after ELO. Because of the extreme flexing of the thin film after ELO, the contacts must be able to withstand large angles of flexing without damage. Ti–Au gates were used to form 0.8-, 1.0-, and 1.2-μm gate lengths. The structure uses a dual 100-μm gate finger design to form a 200-μm gate width with a source to drain separation of 4 μm.

The ELO step was done using an apiezon wax coating of approximately 30-μm thick on the front side of the sample and cured at 150°C for 30 minutes. This gives the wax a compressive force to help facilitate the ELO step and protects the active device. The sample edges were cleaned and subjected to a preferential etch of hydrogen peroxide:ammonia hydroxide to remove the exposed active edge layer, leaving the AlAs release layer exposed [12]. The samples were then allowed to etch in a diluted HF solution overnight at room temperature to release the active layer from the GaAs substrate. Samples were attached to the alumina substrates and adhesion

© 1993 IEEE. Reprinted, with permission, from IEEE Microwave and Guided Wave Letters, vol. 3, no. 4, Apr. 1993, pp. 107-109.

PRECEDING PAGE BLANK NOT FILMED

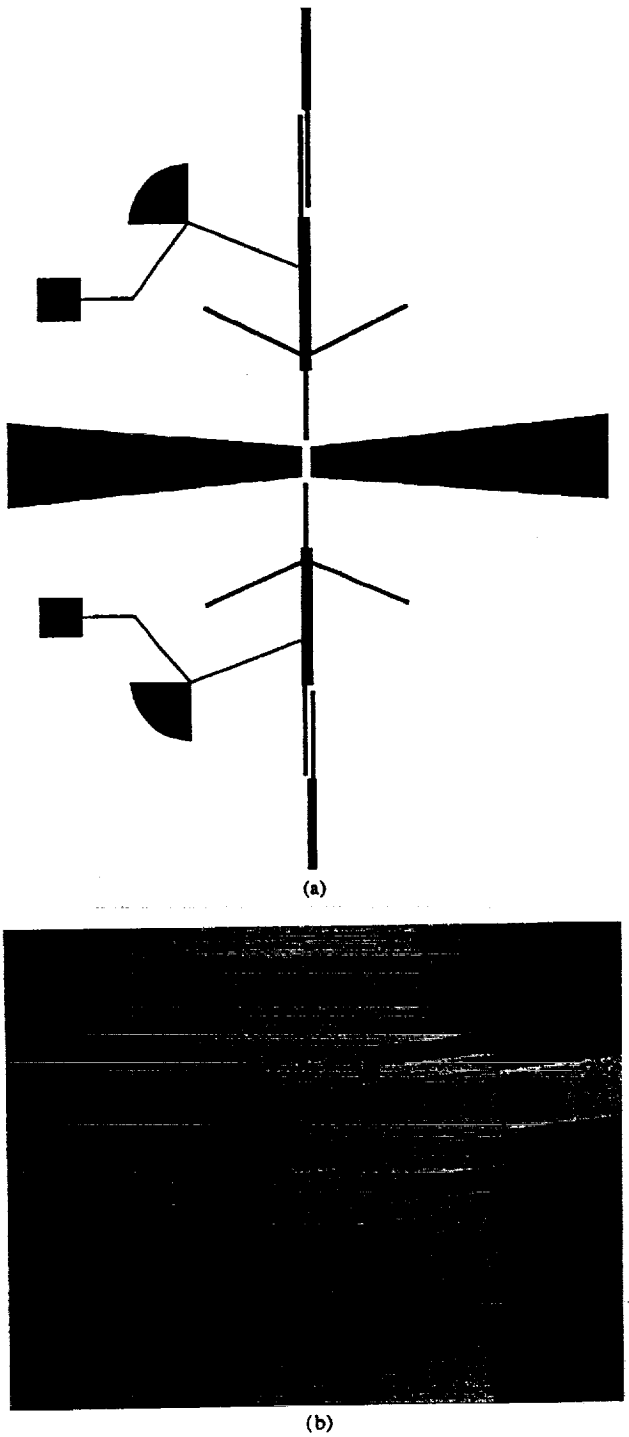

(a)

(b)

Fig. 1. (a) Microstrip amplifier design on alumina. (b) Actual ELO device with microstrip contacts.

of the device was achieved via Van der Waals forces. To improve adhesion for further circuit processing and to allow for more stable device measurements, the devices were coated with a spin-on glass (SOG) and cured at 250°C for 4 hours. The SOG also improves the metal step coverage over the 8000-Å step generated by the ELO film and the alumina substrate [10]. A classical narrow-band, high-gain amplifier

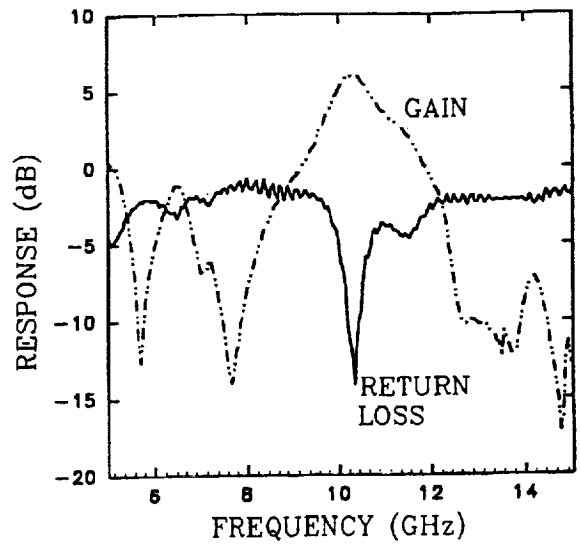

Fig. 2. Gain and return loss response of the amplifier circuit at −10-dBm input power.

was designed using EESOF™ with a center frequency of 10 GHz and optimized for a 10 mil alumina substrate. The microstrip circuit consist of one quarter wavelength coupled line dc blocks, series/shunt microstrip matching networks and bias networks that use a 1/4 wavelength high-impedance line cascaded with a 1/4 wavelength radial stub to provide RF isolation. The amplifier transmission lines were formed with a metal lift-off process after the ELO device was attached using 1.6 μm of gold. Contact between the transmission lines and the finished amplifier were made by opening contacts through the SOG. The amplifier design and finished active device are shown in Fig. 1(a) and (b), respectively.

III. Results and Discussion

The circuit was mounted into a custom designed package utilizing coaxial connectors. Measurement of the device was done on a HP8510B based automatic network analyzer and the bias of the circuit was adjusted for optimum output performance.

The gain and return loss are shown in Fig. 2 for the finished circuit. A small signal gain maximum of 6.8 dB was measured at 10.4 GHz at a gate bias of −1.8 volts and drain bias of 3 volts. This compares with the modeled gain maximum of 9.2 dB with a design bandwidth of 1 GHz. However, the modeled response did not take into account such parameters as connector loss, radiation losses or an imperfect ground plane. The grounding used for this design was a front side ground plane created via a tapered 1/2 wavelength line to physical ground. Experimentally it was shown that the ground plane was sensitive to the slight variations in shape and imperfections that tended to degrade the amplifier gain. The return loss for the amplifier is a much narrower bandwidth than the gain response with a minimum of −14 dB at 10.4

™ EESOF is a registered trademark of EESOF, 5601 Lindero Canyon Road, Westlake Village, CA 91362.

GHz and a −2 dB out of band response. The data was taken at a −10 dBm input rf power level.

There was a strong correlation between the shape and frequency tracking of the modeled and measured data. In a circuit that utilizes standard discrete HEMT devices, it is difficult to predict the effect of bondwire length at the input, output and ground plane of the device. With ELO devices, the effect of bondwires are eliminated and the interconnecting lines between the circuit and the discrete device can be modeled accurately. The SOG was also investigated to determine its effect on RF device performance and it was determined to be negligible.

IV. Conclusion

An ELO P-HEMT discrete device was used in a narrow band amplifier design on an alumina substrate. The interconnection between the discrete device and the transmission lines of the alumina substrate were photolithographically defined eliminating the need for bondwires. The gain of the circuit was 6.8 dB and the return loss minimum was −14 dB at 10.4 GHz. This is the first reported use of a ELO P-HEMT device in a microwave circuit and demonstrates the feasibility of such a process for microwave applications.

Some of the advantages of using ELO devices and optimized substrates in microwave circuit design are: reduced substrate losses of the transmission lines; smaller transmission lines by using substrates with a smaller effective wavelength (λ_{eff}), i.e., 20% reduction in λ_{eff} when the substrate ϵ_r is increased from 13.1 to 20 at 10 GHz; better substrate power dissipation; lower engineering cost associated with circuit tuning and redesigns; and the integration of devices with dissimilar profiles such as diodes, FET's, optoelectronic, and passive components.

Acknowledgment

The authors wish to thank N. Varaljay for his technical assistance throughout this research.

References

[1] M. Konagai, M. Sugimoto, and K. Takaashi, "High efficiency GaAs thin film solar cells by peeled film technology," *J. Cryst. Growth* (Netherlands), vol. 45, pp. 277–280, 1978.

[2] E. Yabonovitch, D. Hwang, T. Gmitter, L. Florez, and J. Harbison," Van der Waals bonding of GaAs epitaxial liftoff films onto arbitrary substrates," *Appl. Phys. Lett.*, vol. 56, pp. 2419–2421, 1990.

[3] E. Yablonovitch, E. Kapon, T. Gmitter, C. Yun, and R. Bhat, "Double heterostructure GaAs/AlGaAs thin film diode lasers on glass substrates," *IEEE Photonics Technol. Lett.*, vol. 1, no. 2, pp. 41–42, 1989.

[4] W.K. Cahn, A. Yi-Yan, and T.J. Gmitter, "Grafted semiconductor optoelectronics," *IEEE J. Quantum Electron.*, vol. 27, no. 3, pp. 717–725, Mar. 1991.

[5] I. Pollentier, P. Demeester, P. Van Daele, D. Rondi, G. Glastre, A. Enared, and R. Blondeau, "Fabrication of long wavelength OEIC's using GaAs on InP Epitaxial Lift-off technology," *Third Int. Conf. Indium Phosphide and Related Materials*, Cardiff, Wales, April 8–11, 1991, pp. 268–271.

[6] D. Shah, W. Chan, T. Gmitter, L. Florez, H. Schumacher, and B. Van der Gaag, "DC and RF performance of GaAs MESFET fabrication on silicon substrate using epitaxial lift-off technique," *Electron. Lett.*, vol. 26, no. 22, pp. 1865–1866, 1990.

[7] C. Van Hoof, W. De Raedt, M. Van Rossum, and G. Borghs, "MESFET lift-off from GaAs substrate to glass host," *Electron. Lett.*, vol. 25, no. 2, pp. 136–137, 1989.

[8] P. Young, R. Romanofsky, S. Alterovitz, and E. Smith, "X-band 'peeled' HEMT amplifier," in *SPIE 1992 Symp. Compound Semiconductor Phys. and Develop.*, Somerset, NJ, vol. 1680, pp. 127–138, Feb 1992.

[9] P. Young, S. Alterovitz, R. Mena, and E. Smith, "Microwave properties of 'peeled' HEMT device on sapphire substrates," in *Int. Semiconductor Device Res. Symp. Proc.*, pp. 689–692, 1991.

[10] P. Young, R. Mena, S. Alterovitz, and E. Smith, "Device characterization of 'peeled' HEMT devices on insulating substrates," accepted for publication, *IEEE Trans. Electron. Devices.*

[11] R. Mena, S. Schachm, P. Young, S. Alterovitz, and E. Haugland, "Transport properties of epitaxial lift-off films," accepted for publication in *J. Appl. Phys.*

[12] D. Wilt, F. DeAngelo, R. Thomas, S. Bailey, G. Landis, D. Brinker, and N. Fatemi, "Peeled film GaAs solar cells for space power," NASA Tech. Memo. 103125, 1990.

N94-20498

AN X-BAND "PEELED" HEMT AMPLIFIER

Paul G. Young*, Robert R. Romanofsky**, Samuel A. Alterovitz**, Edwyn D. Smith*

*University of Toledo
Electrical Engineering Department
Toledo, Ohio 43606

**NASA Lewis Research Center
Space Electronics Division
Cleveland, Ohio 44135

ABSTRACT

A discrete peeled high electron mobility transistor (HEMT) device was integrated into a 10 GHz amplifier. The discrete HEMT device interconnects were made using photo patterned metal, stepping from the 10 mil alumina host substrate onto the 1.3 um thick peeled GaAs HEMT layer, eliminating the need for bond wires and creating a fully integrated circuit. Testing of devices indicate that the peeled device is not degraded by the peel off step but rather there is an improvement in the quantum well carrier confinement. Circuit testing resulted in a maximum gain of 8.5 dB and a return loss minimum of -12 dB.

INTRODUCTION

Epitaxial lift off of GaAs based layers allows for the removal of the active layer from the growth substrate and reattachment of the thin film discrete device to various host substrates. The thin film layers are of the order of microns thick and allow for the integration of a thin film active GaAs layer into normally incompatible device technologies such as indium phosphide, silicon or sapphire.

Various discrete devices have been peeled off and attached to host substrates. As examples, solar cell [1][2] and laser structures [3] were first demonstrated using the peel off technology. FET [4] devices were also peeled and tested on host substrates with a reported F_{max} of 14 GHz for a 1.3 um GaAs MESFET.

To determine the effects of the peel off step on HEMT devices, data was presented by this author [5],[6] and the devices showed a quantum well electron carrier confinement improvement of the order of 10% after peel off. When designing a HEMT based circuit the effects of the peel off step are required to predictably design and fabricate a microwave circuit.

To date, there has been no reported integration of a peeled HEMT device into a microwave circuit due to processing problems and the lack of

© 1992 SPIE. Reprinted, with permission, from High-Speed Electronics and Optoelectronics; 1992, vol. 1680, pp. 72-78.

PRECEDING PAGE BLANK NOT FILMED

device characterization. This paper will demonstrate an integrated X-band amplifier on alumina utilizing a peeled HEMT discrete device. The microwave circuit uses microstrip lines optimized for the alumina substrate and the peeled device is connected to the microstrip lines via photo patterned metal stepping over the thin film active device, thus eliminating the need for bond wires.

FABRICATION

The HEMT structure was MBE grown material, provided by QED Corporation, consisting of a $Al_{0.3}Ga_{0.7}As/GaAs/Al_{0.3}Ga_{0.7}As$ square quantum well structure with silicon pulse doping in the wideband $Al_{0.3}Ga_{0.7}As$ region. A 500A AlAs release layer was grown between the GaAs substrate and the superlattice to facilitate the "peel off" (See figure 1.)

Devices were fabricated using a mesa etch procedure for device isolation. Ohmic contacts were formed using a standard metal liftoff process and sequentially e-beam evaporated Au/Ge/Au/Ni/Au contacts. Alloying of the contacts was done in a RTA system for 15 seconds at 400C. Gate photo patterning was followed by gate recessing to reduce exposure of the undoped wide bandgap AlGaAs material. Ti/Au was used to form 1.0, 1.2, and 1.4 um gate lengths. The structure uses a dual 100 um gate finger design to form a 200 um gate width with a source to drain separation of 4 um.

The peel off process was done using an apiezon wax coating of approximately 30 um thickness. The wax was cured at 150 C for 30 minutes to give a compressive force to the wax to help facilitate the peel off step. The sample edges were cleaned and subjected to a hydrogen peroxide:ammonia hydroxide etch to remove the exposed active edge layer, leaving to AlAs release layer exposed. The samples were then allowed to etch in a diluted HF solution overnight at room temperature to release the active layer from the GaAs substrate.

Samples were attached to the alumina substrates and adhesion of the device was achieved via Van der Waals forces. To improve adhesion for further circuit processing and to allow for more stable device measurements, the devices are coated with a spin on glass and cured at 250 C for 4 hours (see figure 2(a)). Contacts were then opened using standard photo processing and metal pattering was complete as shown in figure 2(b).

A classical narrowband, high gain amplifier was designed with a center frequency of 10 GHz and optimized on a 10 mil thick alumina substrate. The microstrip circuit consists of quarter-wavelength coupled line DC blocks, series/shunt microstrip matching networks and bias networks which use a 1/4 wavelength high impedance line cascaded with a 1/4 wavelength radial stub to provide rf isolation. The finished amplifier is shown in figure 3.

RESULTS AND DISCUSSION

To do the circuit design, an analysis of the discrete device performance is required to evaluate the rf response after peel off. Figure 4 illustrates the measured gain response before and after peel off for a discrete HEMT device. As can be seen, the device experiences an improvement in the low frequency gain of approximately 2 dB but F_{max} doesn't appear to be improved in this devices structure. An analysis of H_{21} before and after peel off indicate F_T values of 26 and 30 GHz, respectively, with H_{21} showing a positive shift of 2 dB for the peeled sample.

Analysis of the S-parameters before and after peel off show a 5 dB decrease in S_{12} and an increase of .5 dB for S_{21} after peel off. Based on a lumped element equivalent circuit model of the peeled and unpeeled device, it was concluded that the intrinsic transconductance increased from the before peeled value of 194 mS/mm to 204 mS/mm. The most significant parametric change was a decrease in the drain-source resistance from 725 to 557 ohms before and after peel off.

Hall measurements were also conducted on peeled and non peeled Hall bars and the increase in the device performance for the peeled device is attributed to an improvement of the quantum well electron carrier confinement [5] resulting in an increased intrinsic transconductance.. While there was an improvement in the transconductance, it's effect on F_{max} was offset by the decrease in the source-drain resistance. Consequently, F_{max} remained the same while F_T experienced a 4 GHz enhancement after peel off.

DC characteristics of the amplifier circuit is shown in figure 5 for a device using one of the two 100 um gate fingers. As is illustrated by the DC performance, metal step coverage was achieved from the alumina substrate onto the 1.5 um thick GaAs HEMT device resulting in a fully integrated circuit.

Circuit performance of the X-band circuit was measured and is compared to modeled results (see figure 6). The design indicates a gain maximum response of 12 dB at 9.2 GHz while the measured gain was found be 8.5 dB at 9.3 GHz for the peeled HEMT amplifier. Further deviations from the designed response are seen in the measured circuit at frequencies greater than 9.3 GHz. Best return loss for the peeled circuit at 10.3 GHz was -12 dB as compared to the modeled value return loss at 10.3 GHz of -18 dB.

Based on the circuit model, the origin of the gain curve spike is attributed to source to ground inductance. Additionally, losses of the circuit can also be traced to connector losses and a imperfect rf ground scheme. The grounding used in this design utilizes low impedance, 1/2 wavelength stubs to ground rather than industry standard via holes to ground.

CONCLUSION

This paper presents the first reported use of a peeled HEMT device in a microwave integrated circuit. A X-band amplifier was modeled and fabricated using a discrete HEMT device on an alumina substrate. A fully integrated circuit was achieved eliminating the need for bond wires.

The discrete device performance was evaluated for a GaAs square channel structure and the discrete device response did experience a parametric change. An increase in the intrinsic transconductance and decrease of source-drain resistance after peel off was seen.

Amplifier performance was evaluated and the maximum gain was 8.5 dB at 9.3 GHz. Amplifier performance did follow the modeled trend but there was circuit loss which decreased the overall amplifier gain.

ACKNOWLEDGMENTS

This work was funded under NASA grant NAG3-1226. The author wishes to thank Raphael Mena and Nicholas Varaljay for their assistance and guidance throughout this research.

REFERENCES

1. M.Konagai,M.Sugimoto,K.Takaashi,"High Efficiency GaAs Thin Film Solar Cells by Peeled Film Technology",J.Cryst.Growth(Netherlands), 45,pp.277-280,1978
2. D.Wilt,F.DeAngelo,R.Thomas,S.Bailey,G.Landis,D.Brinker,N.Fatemi, "Peeled Film GaAs Solar Cells for Space Power",NASA Tech. Memo.,103125,1990
3. E.Yablonovitch,E.Kapon,T.Gmitter,C.Yun,R.Bhat,"Double Heterostructure GaAs/AlGaAs Thin Film Diode Lasers on Glass Substrates",IEEE Photonics Technol. Lett.,vol.1,no.2,pp.41-42,1989
4. D.Shah,W.Chan,T.Gmitter,L.Florez,H.Schumacher,B.Van der Gaag,"DC and RF Performance of GaAs MESFET Fabrication on Silicon Substrate using Epitaxial Lift-off Technique",Electron.Lett.,vol.26, no.22,pp.1865-1866,1990
5. P.Young,S.Alterovitz,R.Mena,E.Smith,"Microwave Properties of 'Peeled' HEMT Device on Sapphire Substrates",International Semiconductor Device Research Symposium Proc.,pp.689-692,1991
6. P.Young,R.Mena,S.Alterovitz,E.Smith,"Device Characterization of 'Peeled' HEMT Devices on Insulating Substrates",to be published.

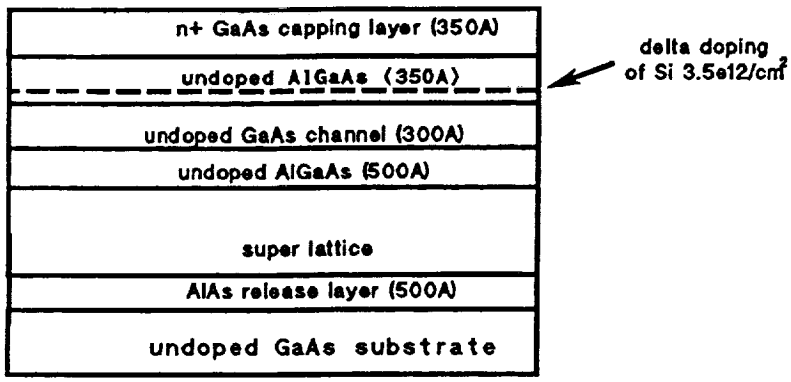

Figure 1. Square well, GaAs channel peel HEMT structure.

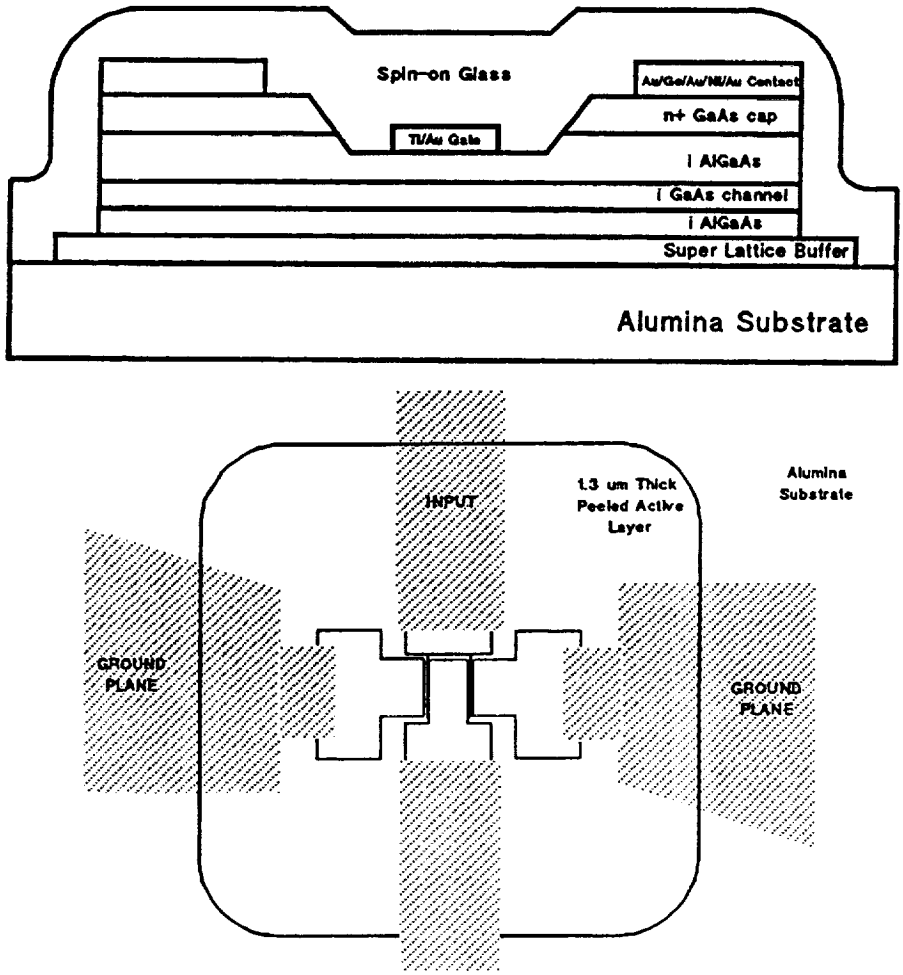

Figure 2. a.) Finished device structure with spin-on glass,
b.) Discrete device structure showing metal contact method.

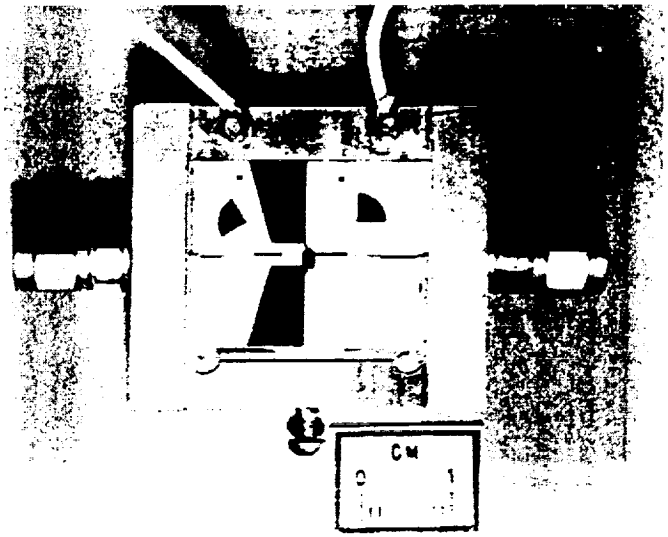

Figure 3. Finished X-band amplifier.

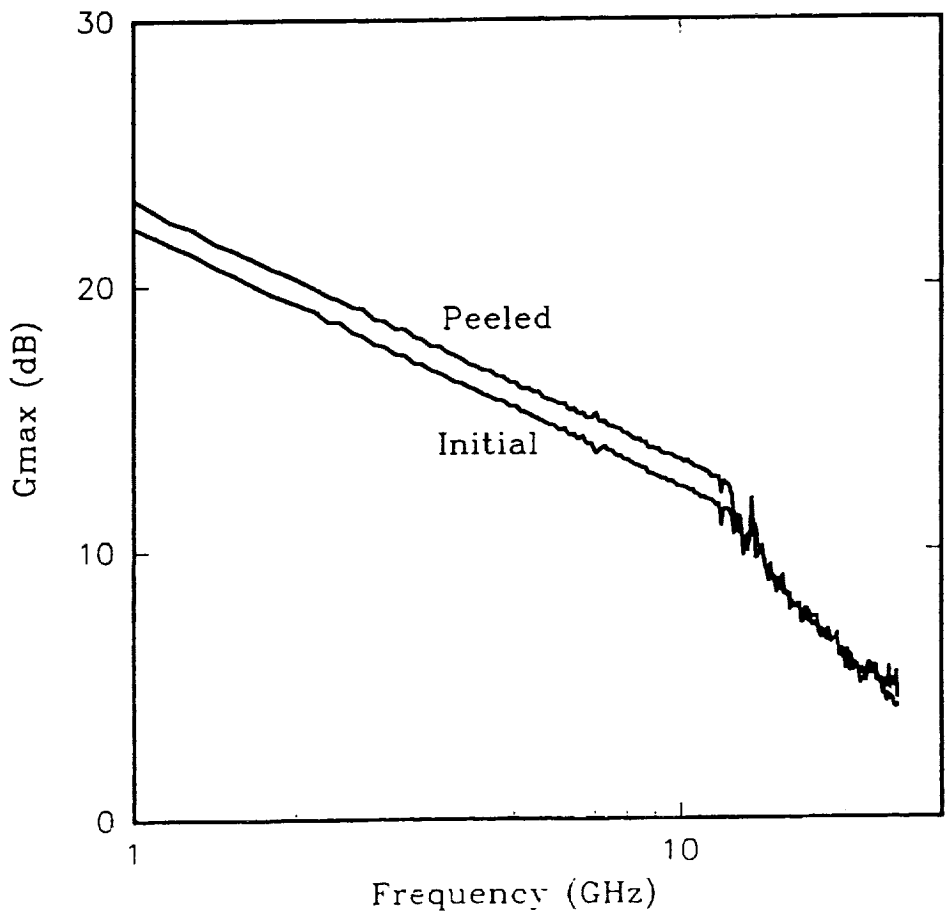

Figure 4. Measured G_{max} before and after peel off for a discrete square well HEMT device.

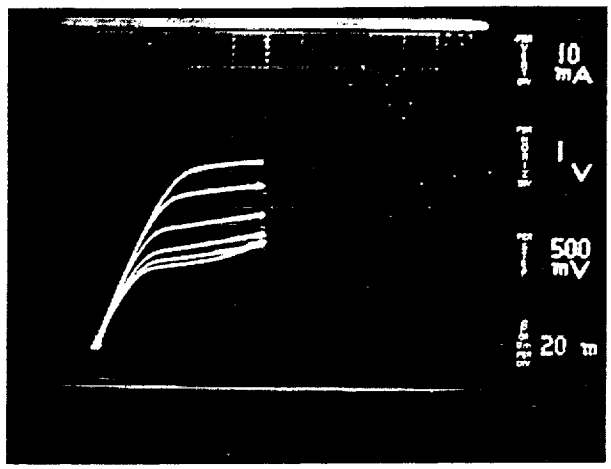

Figure 5. Measured DC characteristics of Amplifier for a one of the two 100 um gate fingers.

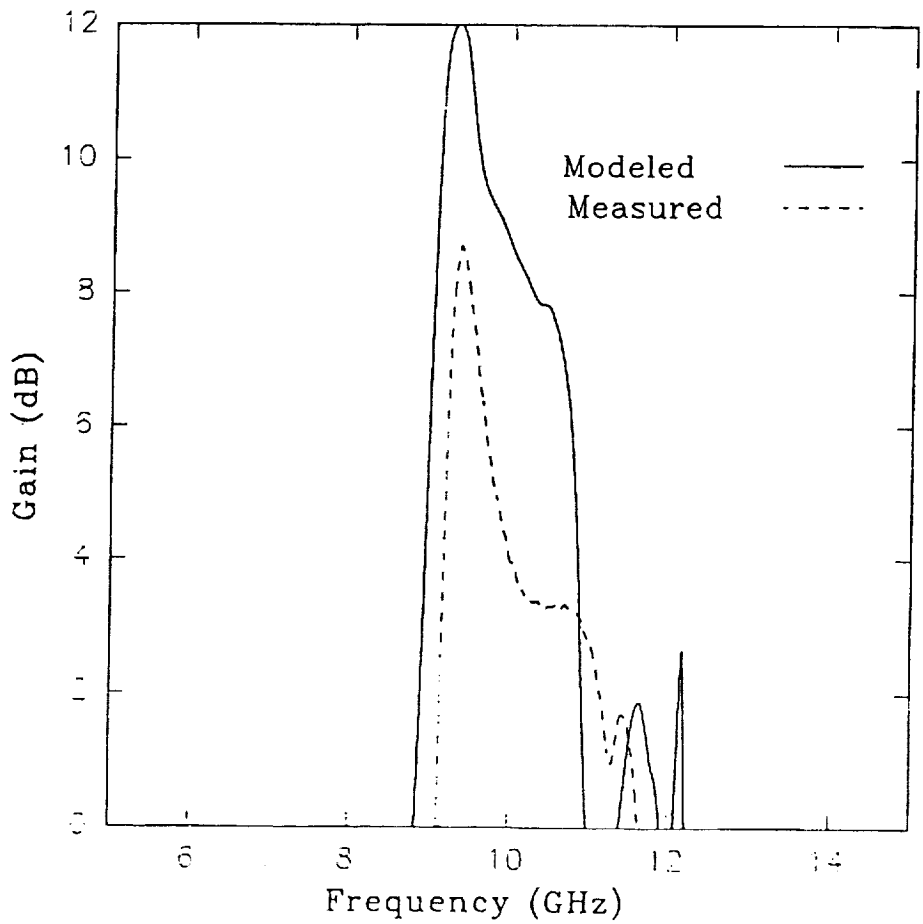

Figure 6. Measured and modeled gain response for the X-Band amplifier.

N94-20499

Characteristics of 0.8- and 0.2-μm Gate Length $In_xGa_{1-x}As/In_{0.52}Al_{0.48}As/InP$ ($0.53 \leq x \leq 0.70$) Modulation-Doped Field-Effect Transistors at Cryogenic Temperatures

Richard Lai, Pallab K. Bhattacharya, *Fellow, IEEE,* David Yang, Timothy L. Brock, Samuel A. Alterovitz, and Alan N. Downey

***Abstract*—We have investigated analytically and experimentally the performance characteristics of InP-based $In_xGa_{1-x}As/In_{0.52}Al_{0.48}As$ ($0.53 \leq x \leq 0.70$) pseudomorphic modulation-doped field-effect transistors (MODFET's) as a function of strain in the channel, gate, length, and temperature. The strain in the channel was varied by varying the In composition x. The temperature was varied in the range of 40–300 K and the devices have gate lengths L_g of 0.8 and 0.2 μm. Analysis of the device was done using a one-dimensional self-consistent solution of the Poisson and Schrödinger equations in the channel, a two-dimensional Poisson solver to obtain the channel electric field, and a Monte Carlo simulation to estimate the carrier transit times in the channel. An increase in the value of the cutoff frequency is predicted for an increase in In composition, a decrease in temperature, and a decrease in gate length. The improvements seen with decreasing temperature, decreasing gate length, and increased In composition were smaller than those predicted by analysis. The experimental results on pseudomorphic InGaAs/InAlAs MODFET's have shown that there is a 15–30% improvement in cutoff frequency in both the 0.8- and 0.2-μm gate length devices when the temperature is lowered from 300 to 40 K.**

I. Introduction

INDIUM PHOSPHATE-based pseudomorphic modulation-doped field-effect transistors (MODFET's) have demonstrated high-frequency and low-noise performance superior to that of any other field-effect transistors [1], [2]. In exploring the properties of high-performance pseudomorphic MODFET's, there are several important and critical issues. The transport properties of the channel and ultimately the device performance depend on the nature of the heterointerface across which electron transfer takes place. This, in turn, depends on the amount of strain in the channel, the growth parameters, and the growth modes. The question is, how much strain should be accommodated in the channel before the advantages listed above are outweighed by growth-related factors which ultimately degrade the transistor performance? Another important issue is the improvement in the performance of pseudomorphic MODFET's as the gate length is reduced. In other words, it is important to determine if the performance of submicrometer-gate pseudomorphic MODFET's is significantly better than that of lattice-matched submicrometer devices. Finally, cryogenic operation of MODFET receivers and amplifiers has shown improved gain characteristics and lower noise figures compared to operation at room temperature [3], [4]. Other potential benefits such as greater reliability, lower metal resistance, and integration with high-temperature superconductors have further increased the interest in MODFET operation at cryogenic temperatures [5].

In the work reported here, we have investigated some of these issues in the context of understanding the performance characteristics of 0.8- and 0.2-μm gate length $In_xGa_{1-x}As/In_{0.52}Al_{0.48}As$ heterostructure ($x = 0.53, 0.60$, and 0.70) pseudomorphic MODFET's at cryogenic temperatures.

II. Numerical Analysis of Device Performance

We have analyzed the microwave performance of both the 0.8- and 0.2-μm devices in order to understand the characteristics of pseudomorphic InGaAs/InAlAs MODFET's. The schematic of a typical structure is shown in Fig. 1. The source-to-drain spacing is 3.5 and 2.0 μm for the 0.8- and 0.2-μm gate-length devices, respectively. The unintentional background doping for the InGaAs and InAlAs layers is assumed to be 2.0×10^{15} cm^{-3}. The simulation was carried out as follows: first, the charge distribution in the growth direction (z direction) was obtained by self-consistently solving one-dimensional Poisson's equation and Schrödinger equation; next the two-dimensional Poisson's equation was solved for the device by a finite difference technique and the electric field along

Manuscript received March 4, 1991; revised February 11, 1992. This work was supported by the National Aeronautic and Space Administration (Lewis Research Center) under Grant NAG-3-988 and the Army Research Office (URI Program) under Contract DAAL03-87-K0007. The review of this paper was arranged by Associate Editor M. Shur.

R. Lai, P. K. Bhattacharya, D. Yang, and T. L. Brock are with the Center for High-Frequency Microelectronics and Solid State Electronics Laboratory, The University of Michigan, Ann Arbor, MI 48109-2213.

S. A. Alterovitz and A. N. Downey are with Space Electronics Division, NASA Lewis Research Center, Cleveland, OH 44135.

IEEE Log Number 9202291.

© 1992 IEEE. Reprinted, with permission, from IEEE Transactions on Electron Devices, vol. 39, no. 10, Oct. 1992, pp. 2206-2213.

PRECEDING PAGE BLANK NOT FILMED

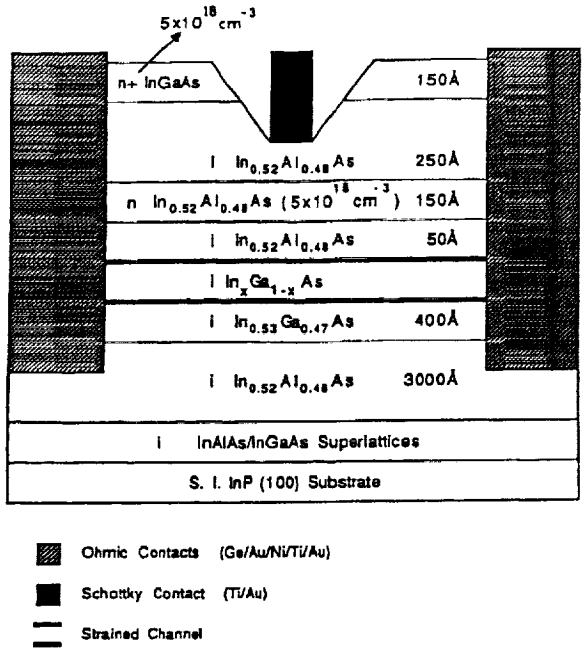

Fig. 1. Layer schematic of pseudomorphic $In_xGa_{1-x}As/In_{0.52}Al_{0.48}As$ (x = 0.53, 0.60, and 0.70) channel MODFET's on InP substrates.

the channel (x direction) was found; finally, the Monte Carlo technique [6], [7] was used for transient analysis of electron transport in the pseudomorphic InGaAs channel. A typical calculated band profile is shown in Fig. 2. The electric field profiles for a 0.2-μm device with In composition x = 0.70 are shown in Fig. 3(a) and (b). The gate is located in the middle of the plot, i.e., from 0.9 to 1.1 μm in position.

Self-consistent solutions of Poisson and Schrödinger equations show that as the In content in the pseudomorphic channel increases, the sheet charge carrier density n_s also increases. This is expected and has been also observed experimentally. It arises mainly due to the increase in the band offset at the heterointerface ΔE_c with increasing indium in the channel. Note that in order to improve the quality of the active heterojunction, a 400-Å smoothing layer of lattice-matched InGaAs is incorporated below the channel layer. The electron wave function actually extends into this buffer layer, which can lead to inferior charge control with gate bias. Higher indium composition in the channel layer can lead to better charge confinement so that most of the conduction electrons will have smaller effective mass.

The electric field obtained from the solution of two-dimensional Poisson equation shows that most of the channel, except the region below the gate, is under low electric field. At the drain side of the gate, the electric field increases due to a pinch-off effect. As the gate length decreases from 0.8 to 0.2 μm, the electric field under the gate changes abruptly (Figs. 3(a) and (b)) due to the small dimension of the Schottky gate.

The Monte Carlo analysis gives insight to the electron transport properties in the channel. For both 0.8- and 0.2-

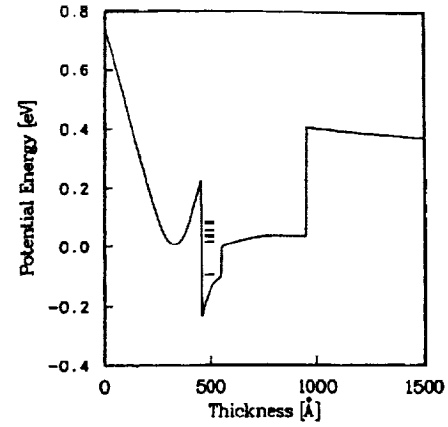

Fig. 2. Calculated conduction band profile and subband energies of strained-channel $In_{0.6}Ga_{0.4}As/In_{0.52}Al_{0.48}As/InGaAs$ MODFET (V_{gs} = V_{ds} = 0 V, T = 300 K).

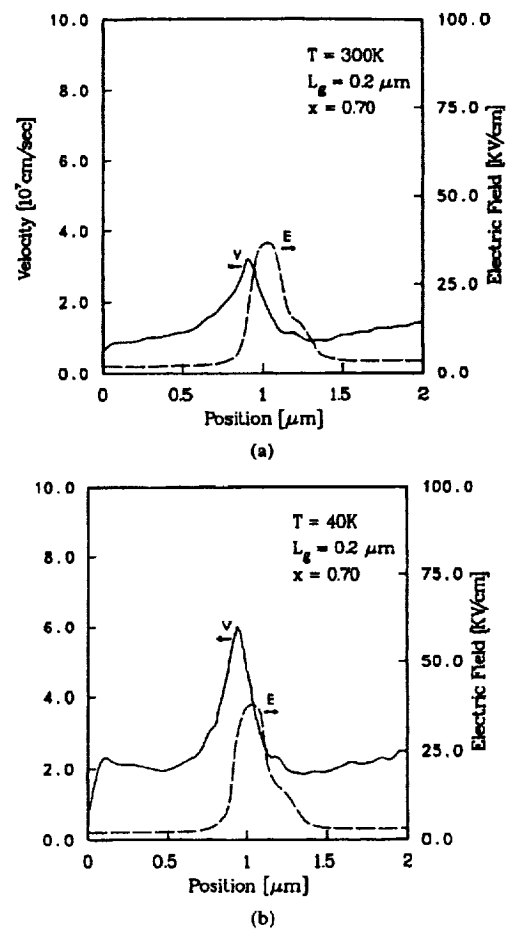

Fig. 3. Calculated electron velocity and electric field versus position in the source–drain region of an $In_{0.70}Ga_{0.30}As/In_{0.52}Al_{0.48}As$ MODFET having a 0.2-μm gate-length and 2.0-μm source–drain spacing with V_{gs} = 0.2 V and V_{ds} = 1.5 V at a temperature of (a) 300 K and (b) 40 K.

μm gate-length devices, a small fraction of the electrons traveling in the high-field region of the channel are scattered into the L valley. They gradually relax back into the Γ valley as they travel through the gate–drain section. This is shown, as an example, in Fig. 4 for a 0.2-μm gate-

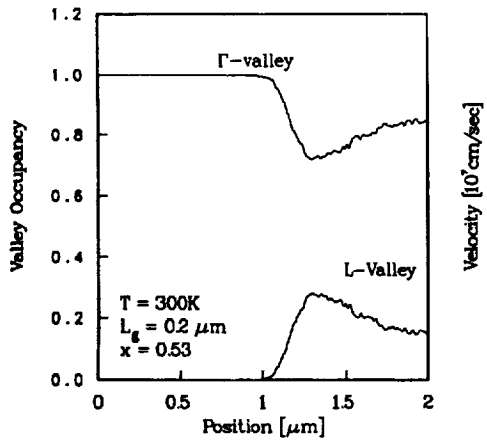

Fig. 4. Calculated Γ- and L-valley occupancy versus position in the source-drain region of an $In_{0.53}Ga_{0.47}As/In_{0.52}Al_{0.48}As$ MODFET with 0.2-μm gate-length and 2.0-μm source-drain spacing. V_{gs} = 0.2 V and V_{ds} = 1.5 V for this calculation.

length device with the In composition in the channel x = 0.53. As x increases, the transfer to the L valleys decreases due to the larger Γ–L separation.

For the 0.8-μm gate-length device, the electron velocity in the channel increases with increasing In composition and decreasing temperature. For the 0.2-μm gate-length device, the abrupt change of the electric field under the gate leads to nonstationary transport [8]. Electron transport under the gate in these devices is dominated by velocity overshoot effects. Calculated 300 K velocities and electric fields in the channel for a 0.2-μm gate-length device with x = 0.7 are shown in Fig. 3(a). As the temperature is reduced to 40 K, phonon scattering is greatly reduced and the overshoot increases as seen in Fig. 3(b). The average channel velocities for the different samples at 300 and 40 K are listed in Table I.

The time required for electrons to transit the channel under the gate is obtained from a transient Monte Carlo analysis. The intrinsic cutoff frequency without considering the gate–drain transit time is then obtained from

$$f_{T,\,\mathrm{int}} = \frac{1}{2\pi\tau} \tag{1}$$

where τ is the gate delay time. The calculated delay times for 0.8- and 0.2-μm gate-length device with channels of different composition and at temperatures of 40 and 300 K are shown in Fig. 5(a) and (b). The values of $f_{T,\,\mathrm{int}}$ obtained from (1) are listed in Table II.

The trends in the calculated cutoff frequency values show the general improvement in values when increasing the In composition in the channel, decreasing the temperature, and decreasing the gate length. Indeed, we have observed experimentally the improvement in the average velocity for $In_xGa_{1-x}As/In_{0.52}Al_{0.48}As$ ($0.53 \le x \le 0.65$) MODFET structures both with increasing In composition and decreasing temperature [9]. The improvement with increasing In composition can be attributed mainly to a smaller effective mass, a larger ΔE_c, and a decrease in alloy scattering. The improvement with decreasing temperature can be mainly attributed to a decrease in phonon scattering as well as other scattering rates. At the lower temperatures, polar optical phonon emission, ionized im-

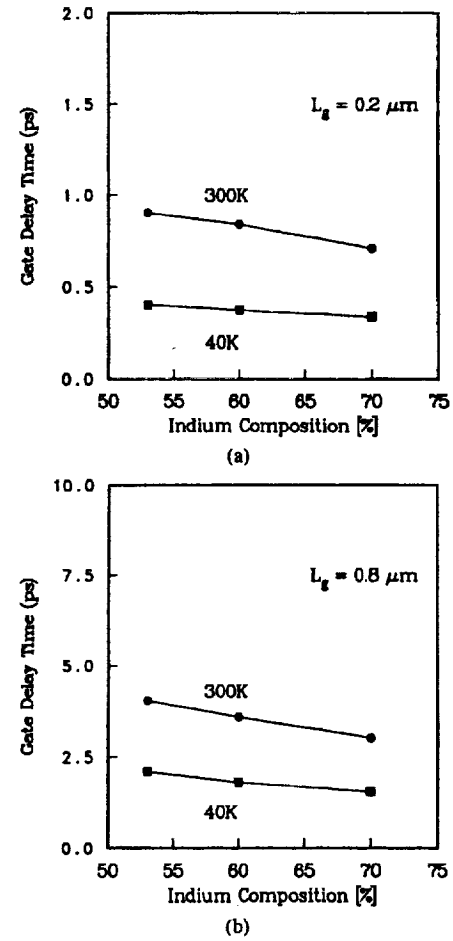

Fig. 5. Calculated gate delay times versus In composition at 300 and 40 K in pseudomorphic $In_xGa_{1-x}As/In_{0.52}Al_{0.48}As$ (x = 0.53, 0.60, and 0.70) channel MODFET's with (a) a 0.2-μm gate-length device and (b) a 0.8-μm gate-length device with V_{gs} = 0.2 V and V_{ds} = 1.5 V.

TABLE I
AVERAGE CALCULATED CHANNEL VELOCITIES (10^7 cm/s) IN 0.2- AND 0.8-μm GATE PSEUDOMORPHIC $In_xGa_{1-x}As/In_{0.52}Al_{0.48}As$ MODFET'S

V_{av} x/L_g	300 K 0.8 μm	40 K 0.8 μm	300 K 0.2 μm	40 K 0.2 μm
0.53	0.98	1.96	1.08	2.13
0.60	1.06	2.17	1.17	2.20
0.70	1.20	2.42	1.35	2.50

TABLE II
ROOM AND LOW-TEMPERATURE INTRINSIC CUTOFF FREQUENCIES $f_{T,\,\mathrm{int}}$ (GHz), OF 0.8- AND 0.2-μm GATE MODFET'S WITH PSEUDOMORPHIC $In_xGa_{1-x}As/In_{0.52}Al_{0.48}As$ QUANTUM WELLS CALCULATED BY USING (1)

$f_{T,\,\mathrm{int}}$ x/L_g	300 K 0.8 μm	40 K 0.8 μm	300 K 0.2 μm	40 K 0.2 μm
0.53	39.5	75.7	176.2	396.1
0.60	44.4	87.7	189.2	426.1
0.70	52.7	102.4	223.9	474.4

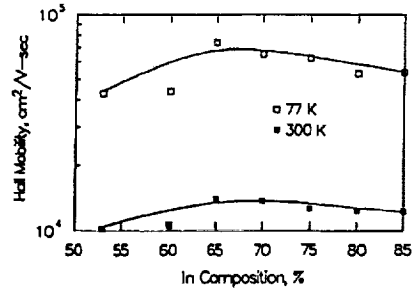

Fig. 6. Hall mobility versus In composition in pseudomorphic $In_xGa_{1-x}As/In_{0.52}Al_{0.48}As$ ($0.53 \leq x \leq 0.85$) channel MODFET structures.

TABLE III
MEASURED MICROWAVE ROOM-TEMPERATURE CHARACTERISTICS OF 0.8- AND 0.2-μm GATE MODFET'S WITH PSEUDOMORPHIC $In_xGa_{1-x}As/In_{0.52}Al_{0.48}As$ QUANTUM WELLS

L_g (μm)/x		0.53	0.60	0.65	0.70	0.75	0.80	0.85
0.8	f_T (GHz)	22-35	29-40	40-45	35-50	30-40	40-45	30-35
0.8	f_{max} (GHz)	40-55	40-60	45-55	60-70	40-50	40-55	45-50
0.2	f_T (GHz)	80-115	100-155		121-180			

purity scattering, piezoelectric scattering, and alloy scattering become the dominant scattering mechanisms. With decreasing gate length from 0.8 to 0.2 μm, velocity overshoot of the electrons increases the average velocity in the channel which leads to higher values of cutoff frequency. When combining the improvements seen with two or more of the variables (In composition, temperature, and gate length) interesting trends can be seen. The improvement seen with decreasing temperature is smaller as the In composition is increased in the channel. Also, the improvement seen with decreasing temperature is smaller with decreasing gate length. It should be noted that the data obtained from the analysis represent the theoretical uppermost limit in cutoff frequency obtainable for these devices. Due to nonideal device characteristics, such as interface roughness and interface traps in the layers, it is expected that any experimental data would show lower values for cutoff frequency compared to the theoretical ones, as will be evident in Section VI.

III. MOLECULAR BEAM EPITAXIAL GROWTH AND TRANSPORT PROPERTIES

The next step was to attempt to verify experimentally some of the results and their trends derived from the theoretical analysis. Schematic of the typical MODFET structure grown by MBE is shown in Fig. 1. Hall measurements were first made on van der Pauw samples to determine the transport properties. The Hall samples were recessed so that the InGaAs cap layers were removed to reduce parallel conduction. The sheet electron density in all the samples varied in the range of $2.0\text{-}3.2 \times 10^{12}$ cm^{-2}. In Fig. 6, we show a plot of the 300 and 77 K mobilities versus In content in the channel. It may be noted that as excess In is added, initially the mobility increases as expected. However, upon further increase of In, the mobility starts to saturate and even decrease. We have recently analyzed this transport behavior in detail and have found that the turnaround in mobility occurs at large misfits (>1.5%) due to the onset of a three-dimensional island growth mode [10]. In other words, the minimum free energy for a strained system for misfits >1.5% favors a three-dimensional surface. It is interesting and important to note that the dc and microwave characteristics of the MODFET's made with channels of increasing In content also exhibit the same behavior. In other words, the performance peaks at about $x = 0.70$ beyond which there is an observed degradation. The measured microwave characteristics of 0.8- and 0.2-μm gate pseudomorphic MODFET's at room temperature are listed in Table III.

IV. DEVICE FABRICATION

The heterostructures, shown in Fig. 1, were used to fabricate both 0.8- and 0.2-μm gate-length pseudomorphic $In_xGa_{1-x}As/In_{0.52}Al_{0.48}As$ ($x = 0.53$, 0.60, and 0.70) MODFET's. Standard lithography was used to fabricate the devices. The source-to-drain separation for the 0.8- and 0.2-μm gate length devices were 3.5 and 2.0 μm, respectively. For the 0.8-μm gate devices, optical lithography was used while for the 0.2-μm gate devices, electron-beam lithography using a P(MMA-MAA)/PMMA bilayer resist system was used. With the bilayer resist, T-shaped gates consisting of Ti/Pt/Au were realized and the gate length was measured using Scanning Electron Microscopy (SEM) to be 0.15-0.2 μm. The gate widths on the devices ranged between 50 and 150 μm.

V. DC CHARACTERISTICS

The 0.8-μm gate device showed a peak transconductance of 510 mS/mm at 300 K with a channel current of

200 mA/mm while the 0.2-μm gate device showed a peak transconductance of 705 mS/mm with a channel current of 300 mA/mm. Both devices were biased at a drain voltage of 1.5 V. The devices also showed low gate leakage (110 μA at $V_g = -0.5$ V for a 0.2×45 μm^2 device) and good pinchoff characteristics although in the submicrometer devices, output conductance increased dramatically. This increase in the output conductance may be attributed to an increase in leakage in the buffer layer, an increase in the background impurities (we observed a significant increase in the background impurities in our system when the wafers used for 0.2-μm gate devices were grown), and short-channel effects. 77 K dc measurements on the 0.8-μm gate device showed an increase in peak transconductance to 680 mS/mm, a decrease in output conductance from 40 to 20 mS/mm, and a decrease in gate leakage from 9 to less than 1.0 μA measured at a drain bias of 1.5 V and a gate bias of 0 V.

VI. Microwave Characteristics at Room and Cryogenic Temperatures

Room-temperature microwave characteristics were measured for both 0.8- and 0.2-μm gate devices and for each In channel composition. The scattering parameters were measured using an HP8510 automatic network analyzer and a CASCADE wafer probe station from 0.5 to 26.5 GHz at various gate and drain bias voltages. Table III shows some of the results of the pseudomorphic $In_xGa_{1-x}As/In_{0.52}Al_{0.48}As$ MODFET's ($0.53 \leq x \leq 0.85$) that have been fabricated in our laboratory. Estimation of the maximum available gain cutoff frequency f_{max} for the submicrometer devices were not made because the stability factor k was smaller than 1.0 over the entire measured frequency range. The current-gain cutoff frequency f_T was extrapolated from the measured current gain (H_{21}) versus frequency dependence with a -6-dB/octave slope. The best result achieved was an extrapolated f_T value of 180 GHz for an $In_{0.70}Ga_{0.30}As/In_{0.52}Al_{0.48}As$ MODFET with a gate dimension of 0.15×150 μm^2 with a maximum stable gain (MSG) of 17.5 dB at 26.5 GHz.

For cryogenic microwave characterization, the devices were diced, mounted, and bonded to coplanar chip carriers. The devices were measured in a coplanar waveguide test fixture (DESIGN TECHNIQUES). A spring loading capability was added to the test fixture to ensure repeatable contacts between the device carrier and the coaxial connectors especially during cooling. The cryogenic system included a helium closed-cycle refrigerator, a temperature controller, a silicon diode thermometer, and the test fixture attached to the refrigerator cold finger in a vaccum environment. The cryogenic system is capable of achieving and stabilizing temperature down to 40 K. The microwave measurements were again done using an HP8510 automatic network analyzer. Prior to cooling the device, the measurement setup was calibrated at room temperature using a set of open, short, and through standards. Then, a short-circuit standard was

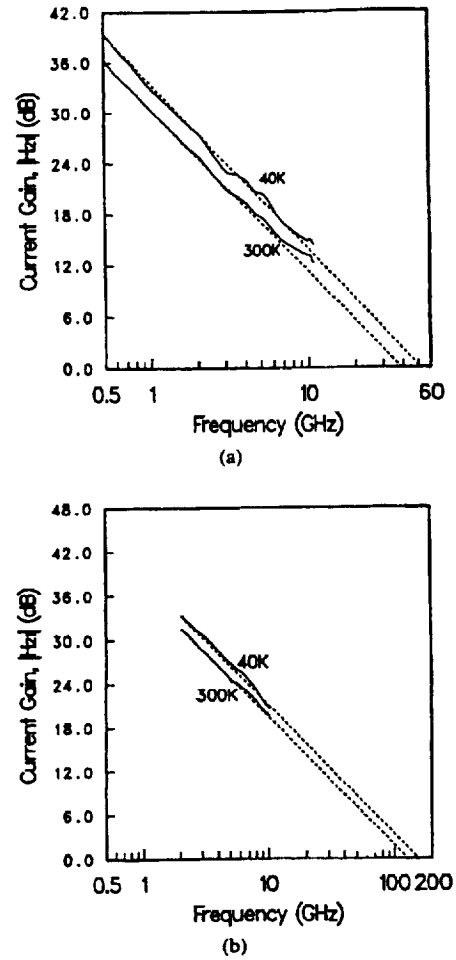

Fig. 7. Current gain H_{21} versus frequency for a pseudomorphic $In_{0.70}Ga_{0.30}As/In_{0.52}Al_{0.48}As$ channel MODFET at 40 and 300 K for (a) a 0.8-μm gate-length device and (b) a 0.2-μm gate-length device.

cooled to the desired temperatures to account for any shifts in the reference plane caused by the contraction of the cables, connectors, and the coplanar lines due to the lowering of temperature. This calibration method was found to be valid up to a frequency of 10–11 GHz. The problems at higher frequencies seem to be due to the fact that accounting for shifts in the reference plane is not sufficient to correct for the differences between room temperature and cryogenic temperatures. For example, the return loss for a through line measured at cryogenic temperatures after using the calibration routine becomes significantly degraded at higher frequencies.

The microwave characteristics of each device were measured at 300, 200, 120, 77, and 40 K from 0.5 to 11.0 GHz. The devices were measured over a range of V_{ds} from 1.2 to 1.8 V and at various values of V_{gs} near the peak g_m point. For both the 0.8- and the 0.2-μm gate devices, there was an observed increase in the measured magnitude of S_{21} of up to 3 dB and commensurate increase in the current gain H_{21} with decreasing temperature (shown in Fig. 7(a), (b) for the 0.8- and 0.2-μm gate devices with an $In_{0.70}Ga_{0.30}As$ channel) with decreasing temperature. The

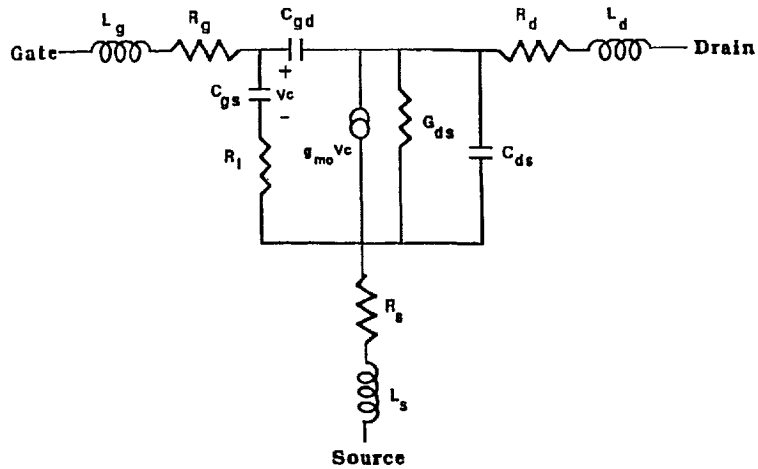

Fig. 8. Standard equivalent circuit model for a MODFET.

TABLE IV
EXTRAPOLATED VALUES FOR CUTOFF FREQUENCY f_T (GHz) FROM CRYOGENIC MICROWAVE CHARACTERISTICS OF 0.2- AND 0.8-μm GATE MODFET'S WITH PSEUDOMORPHIC $In_xGa_{1-x}As/In_{0.52}Al_{0.48}As$ QUANTUM WELLS (V_d = 1.5 V)

f_T x/L_g	300 K 0.8 μm	40 K 0.8 μm	300 K 0.2 μm	40 K 0.2 μm
0.53	22	29	92	105
0.60	29	38	105	130
0.70	38	51	121	145

TABLE V
EQUIVALENT CIRCUIT PARAMETERS OF 0.8-μm (V_d = 1.5 V, V_g = 0.0 V) AND 0.2-μm (V_d = 1.4 V, V_g = 0.15 V) GATE-LENGTH MODFET'S WITH PSEUDOMORPHIC $In_{0.70}Ga_{0.30}As/In_{0.52}Al_{0.48}As$ QUANTUM WELLS

	0.8 μm 300 K	0.8 μm 40 K	0.2 μm 300 K	0.2 μm 40 K
L_g (nH)	0.63	0.64	0.28	0.30
L_s (nH)	0.05	0.05	0.07	0.07
L_d (nH)	0.51	0.53	0.07	0.10
R_g (Ω)	5.61	4.27	8.14	7.78
R_s (Ω)	3.79	3.46	3.33	2.50
R_d (Ω)	3.78	3.37	3.64	3.08
R_i (Ω)	12.16	9.08	9.30	8.30
C_gs (pF)	0.265	0.286	0.15	0.17
C_gd (pF)	0.012	0.010	0.020	0.019
C_ds (pF)	0.052	0.054	0.060	0.065
τ_c (ps)	5.95	5.81	1.5	1.5
g_{mo} (mS)	75.0	97.9	133	184
G_ds (mS)	4.08	3.65	18.8	19.0

data are summarized in Table IV, which gives the characteristics of specific devices measured at 300 and 40 K. The improvement in cutoff frequency with lowering of temperature from 300 to 40 K was generally found to be between 15 and 30% for all the devices.

VII. Device Analysis and Discussion

The measured microwave data were modeled to a standard equivalent circuit model for a MODFET (Fig. 8). The fitting of the microwave data had a maximum error of 5-10% over the frequency range of 0.5 to 11.0 GHz primarily due to noise in the measured data. Table V shows the equivalent circuit parameters that were extracted for the pseudomorphic $In_{0.70}Ga_{0.30}As/In_{0.52}Al_{0.48}As$ MODFETs at 40 and 300 K. The parasitic gate-to-source capacitance C_{gs} is decreased as the gate length decreased from 0.8 to 0.2 μm, which will lead to an increase in cutoff frequency and hence the maximum oscillation frequency. The intrinsic f_T values showed approximately the same improvement in performance with lowering of temperature as the extrinsic f_T. The improvement in microwave performance for both the 0.8- and 0.2-μm gate-length devices is approximately 15-30% when the temperature is lowered from 300 to 40 K and the relative improvement is found to be approximately the same as In composition in the channel is increased. The experimental results indicate a smaller improvement of cutoff frequency as In composition is increased and temperature is decreased than the values predicted in the analysis. More experiments need to be done to further investigate this point. However, the improvement with decreasing temperature was found to be slightly higher in the 0.8-μm device (25-30%) compared to the 0.2-μm (15-20%) device. This is consistent with the trend predicted by the analysis. Also, the values for cutoff frequency measured experimentally are significantly less than those predicted in the analysis section. Part of the reason may be due to the fact that effective gate length of a MODFET is larger than the metallurgical gate length [11]. The extra effective gate length can add up to an increase of 0.08 μm to the gate length of the device and can explain part of the difference between the calculated and measured data. Note that the transconductance delay time τ_c, which is obtained from a fit of the measured microwave data with the equivalent circuit, is different from τ in (1).

The extracted output conductance G_{ds} decreases with lowering of temperature, as shown in Fig. 9 for a 0.8-μm gate device with an $In_xGa_{1-x}As$ channel (x = 0.53, 0.60, and 0.70), and this trend is the same as that for the dc

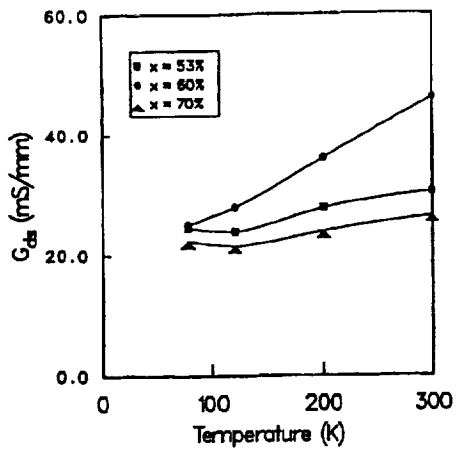

Fig. 9. Output conductance G_{ds} versus temperature for pseudomorphic $In_xGa_{1-x}As/In_{0.52}Al_{0.48}As$ (x = 0.53, 0.60, and 0.70) channel MODFET's with V_{ds} = 1.5 V and V_{gs} biased for peak gain.

measured output conductance. The main reason for this is the improved confinement of the carriers in the 2DEG channel at lower temperatures. A slight increase in the extracted gate to source capacitance C_{gs} was also observed (10%). This has been previously observed and modeled in GaAs/AlGaAs MODFET's [12]. It should be noted that the trends in G_{ds} and C_{gs} with temperature were observed for both the 0.2- and 0.8-μm gate-length devices.

Another observation that was made during these measurements was the absence of significant effects due to deep-level traps such as the collapse of I–V characteristics which have been seen in AlGaAs/GaAs MODFET structures at low temperatures [13]. It should be noted that since the chamber was completely enclosed, the measurements were carried out in the dark. A small threshold shift of up to +0.21 V was observed in the dc characteristics for both the 0.2- and 0.8-μm gate-length devices. This value is smaller compared to the threshold shifts observed in AlGaAs/GaAs MODFET devices which typically range from +0.2 to +0.4 V [13]. The threshold shift in AlGaAs/GaAs MODFET's were mainly due to DX centers in the AlGaAs layers. Meanwhile, the threshold voltage shift in InAlAs/InGaAs MODFET's were due to interface traps in the InAlAs/InGaAs interface.

VIII. Conclusion

In conclusion, we have investigated the performance characteristics of InP-based pseudomorphic MODFET's with varying the In composition ($0.53 \leq x \leq 0.70$) which changes the strain in the channel. The temperature is varied in the range of 40–300 K and the devices have gate lengths L_g of 0.8 and 0.2 μm. The analytical analysis predicts an increase in the intrinsic cutoff frequency with increasing In composition and decreasing temperature and gate length. Also, the analysis predicts that the increase in cutoff frequency with decreasing temperature is less significant with increasing In composition and decreasing gate length. Preliminary experimental results show that as In composition increase from 0.53 to 0.70, f_T increase by 30–40%, and as the temperature decrease from 300 to 40 K, f_T improves by 15–30%, both for 0.8- to 0.2-μm devices. These are among the first reported microwave measured data of pseudomorphic $In_xGa_{1-x}As/In_{0.52}Al_{0.48}As$ MODFET's at cryogenic temperatures.

Acknowledgment

The authors wish to thank C. Chorey, K. B. Bhasin, B. T. Ebihara, and R. Simons for helpful contributions on the cryogenic system, J. Pamulapati and W. Li for MBE growth of the samples, and G. I. Ng, M. N. Tutt, and D. Pavlidis for helpful discussions and contributions.

References

[1] G. I. Ng, W. P. Hong, D. Pavlidis, M. Tutt, and P. K. Bhattacharya, "Characteristics of strained $In_{0.65}Ga_{0.35}As/In_{0.52}Al_{0.48}As$ HEMT with optimized transport parameters," *IEEE Electron Device Lett.*, vol. 9, pp. 439–441, Sept. 1988.

[2] U. K. Mishra, A. S. Brown, and S. E. Rosenbaum, "DC and RF performance of 0.1 μm gate length $Al_{0.48}In_{0.52}As/Ga_{0.38}In_{0.62}As$ pseudomorphic HEMTs," in *IEDM Tech. Dig.*, 1988, pp. 180–183.

[3] K. H. Duh, W. F. Kopp, P. Ho, P. Chao, M. Ko, P. M. Smith, J. M. Ballingall, J. J. Bautista, and G. G. Ortiz, "32-GHz cryogenically cooled HEMT low-noise amplifiers," *IEEE Trans. Electron Devices*, vol. 36, pp. 1528–1534, Aug. 1989.

[4] S. Weinreb, M. W. Pospieszalski, and R. Norrod, "Cryogenic HEMT low-noise receivers for 1.3 to 43 GHz range," in *IEEE MTT-S Dig.*, 1988, pp. 945–948.

[5] R. K. Kirshman, "Low-temperature electronics," *IEEE Circuits and Devices Mag.*, pp. 12–24, Mar. 1990.

[6] S. Adachi, "Material parameters of $In_{1-x}Ga_xAs_yP_{1-y}$ and related binaries," *J. Appl. Phys.*, vol. 53, p. 8775, 1986.

[7] M. Jaffe and J. Singh, "Band structure and charge control studies of n- and p-type pseudomorphic modulation-doped field-effect transistors," *J. Appl. Phys.*, vol. 65, pp. 329–338, 1989.

[8] T. Wang and C. H. Hsieh, "Numerical analysis of nonequilibrium electron transport in AlGaAs/InGaAs/GaAs pseudomorphic MODFET's," *IEEE Trans. Electron Devices*, vol. 37, pp. 1930–1938, Sept. 1990.

[9] P. R. Berger, P. K. Bhattacharya, J. Singh, and K. K. Bajaj, "Role of strain and growth conditions on the growth front profile of on GaAs during the pseudomorphic growth regime," *Appl. Phys. Lett.*, vol. 53, pp. 684–686, 1988.

[10] W. P. Hong, G. I. Ng, P. K. Bhattacharya, D. Pavlidis, and S. Willing, "Low- and high-field transport properties of pseudomorphic $In_xGa_{1-x}As/In_{0.52}Al_{0.48}As$ ($0.53 \leq x \leq 0.65$) modulation-doped heterostructures," *J. Appl. Phys.*, vol. 64, pp. 1945–1949, Aug. 1988.

[11] P-C Chao, M. S. Shur, R. C. Tiberio, K. H. G. Duh, P. M. Smith, J. M. Ballingall, P. Ho, and A. A. Jabra, "DC and microwave characteristics of sub-0.1 μm gate-length planar-doped pseudomorphic HEMT's," *IEEE Trans. Electron Devices*, vol. 36, pp. 461–463, Mar. 1989.

[12] L. P. Sadwick and K. L. Wang, "A treatise on the capacitance-voltage relation of high electron mobility transistors," *IEEE Trans. Electron Devices*, vol. ED-33, pp. 651–656, May 1986.

[13] A. Kastalsky and R. A. Kiehl, "On the low-temperature degradation of AlGaAs/GaAs modulation-doped field-effect transistors," *IEEE Trans. Electron Devices*, vol. ED-33, pp. 414–423, Mar. 1986.

Richard Lai received the B.S. degree in electrical engineering at the University of Illinois, Urbana, in 1986 and the M.S.E.E. degree from the University of Michigan, Ann Arbor, in 1988.

Currently he is working towards the Ph.D. degree in electrical engineering at the University of Michigan. His research involves studying InP-based MODFET's for applications in InP-based MMIC and OEIC circuits.

Pallab K. Bhattacharya (M'78-SM'83-F'89) received the B.Sc. degree with honors in physics in 1968, and the B.Tech. and M.Tech. degrees in radio physics and electronics in 1970 and 1971, respectively, all from the University of Calcutta, India. He received the M.Eng. and Ph.D. degrees in 1976 and 1978, respectively, from the University of Sheffield, England.

From 1975 to 1978, he was with the Electronics and Electrical Engineering Department, University of Sheffield, where his doctoral research dealt with the investigation of deep-level defects in GaAs and (Al, Ga)As. From 1978 to 1983, he was a member of the Electrical Engineering faculty at Oregon State University, Corvallis, where he established facilities for epitaxial growth and characterization of III-V semiconductors. There he worked on phase equilibria and LPE growth of high-purity InGaAs and InGaAsP, their low- and high-field transport properties and detailed electrical and optical characterization of MOCVD-grown AlGaAs. He also demonstrated extremely low noise performance in InGaAs:Fe photoconductive detectors. He spent the 1981-1982 academic year as an Invited Professor of the Swiss Federal Institute of Technology, Lausanne, where he worked on molecular beam epitaxy and the fabrication of high-speed detectors. He is currently Professor of Electrical Engineering and Computer Science at the University of Michigan, Ann Arbor, and Director of the Solid-State Electronics Laboratory. His research interests include LPE and MBE growth of III-V semiconductors and their electrical and optical properties, photodetectors, quantum-well devices, and integrated-optical devices.

Dr. Bhattacharya is a member of the American Physical Society and Sigma Xi. He received the Alexander von Humboldt Award in 1980.

David Yang was born in Hsinchu, Taiwan, in 1963. He received the B.S. degree in physics and the M.S. degree in electrical engineering from the National Tsing Hua University in 1985 and 1987, respectively. He is currently working towards the Ph.D. degree in electrical engineering and computer science at the University of Michigan at Ann Arbor.

Since 1989 he has been working as a Research Assistant in the Solid-State Electronics Laboratory, Department of Electrical Engineering and Computer Science, University of Michigan. His research interests include device modeling, fabrication, and characterization of submicrometer-gate FET's, and monolithic microwave integrated circuit applications.

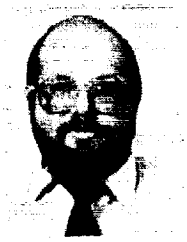

Timothy L. Brock has been a Research Engineer at the University of Michigan, Ann Arbor, since October 1989. His primary responsibilities involve electron-beam lithography relating to submicrometer circuit and device fabrication. Prior to this he held a research position at the University of Illinois, Urbana, and has been involved with several publications involving electron beam applications.

Samuel A. Alterovitz received the Ph.D. degree in solid state physics in 1971 from Tel Aviv University, Tel Aviv, Israel.

After a two-year postdoctoral appointment at the University of Illinois, Urbana, he joined the staff of the Physics Department at Tel Aviv University where he achieved the rank of Tenured Associated Professor. In both places he worked on properties of superconducting materials, especially critical currents and critical fields. In 1981, he accepted a position in the Electrical Engineering Department at the University of Nebraska, Lincoln, as Senior Engineering Research Scientist. In 1983, he transferred to NASA Lewis Research Center, Cleveland, OH, where he in now a Senior Research Scientist. He played an important role in developing new materials (e.g., InGaAs) for high-speed, low-noise, high-efficiency electronic devices. He also developed ellipsometry for novel and multilayer structures. He is now working on epitaxial liftoff techniques development, materials and devices for cryogenic electronics applications, and on further applications of the ellipsometric technique. He has authored over 100 papers in referred journals and over 100 meeting presentations and has edited two books. He is an active National Research Council postdoctoral adviser.

Dr. Alterovitz is a member of the American Physical Society, the Materials Research Society, and the American Vacuum Society.

Alan N. Downey received the B.E.E. degree from Cleveland State University, Cleveland, OH, in 1979, and the M.S.E.E. degree from the University of Toledo, Toledo, OH, in 1983.

He joined NASA Lewis Research Center, Cleveland, OH, in 1977 and joined the Space Communications Division in 1979. From 1979 to 1985 he was engaged in microwave measurement and solid-state technology research, followed by a three-year hiatus in the Communications Projects Branch, acting as Experiments Manager for the Applications Technology Satellites Program. He returned to the Solid State Technology Branch in July of 1989, and his current research interests include the RF characterization of novel HEMT structures at cryogenic temperatures, MMIC applications, and micromachined passive electronic components for submillimeter wave radiometry.

PERFORMANCE OF A WIDEBAND GaAs LOW-NOISE AMPLIFIER AT CRYOGENIC TEMPERATURES

S. S. Toncich and K. B. Bhasin
National Aeronautics and Space Administration
Lewis Research Center
Cleveland, Ohio

T. K. Chen and P. C. Claspy
Department of Electrical Engineering and Applied Physics
Case Western Reserve University
Cleveland, Ohio

KEY TERMS

GaAs low-noise amplifier, cryogenic temperatures, microwave measurements

ABSTRACT

The gain, noise figure, and 1-dB compression point of a commercially available GaAs amplifier were measured at cryogenic temperatures. The gain and noise figure characteristics were improved by decreasing temperature, while the 1-dB compression point remained unchanged. Repeated temperature cycling had no adverse effect on amplifier performance. © *1992 John Wiley & Sons, Inc.*

I. INTRODUCTION

It is well known that semiconductor devices and circuits exhibit lower noise figures and higher gains at cryogenic temperatures [1–3]. The lower noise figure is due to reduced lattice vibrations in the device and the fact that external, additive noise varies directly with the absolute temperature. Gallium arsenide (GaAs) devices have better low-temperature characteristics than silicon devices, since they do not suffer from carrier freeze out when the doping is insufficient to form impurity bands. As a result, GaAs conductivity remains high even at very low temperatures, where Si conductivity is decreasing. The higher conductivity of GaAs makes it the key semiconductor in microwave devices and circuits. GaAs and heterostructure FETs have been extensively investigated at cryogenic temperatures [1–3]; however, GaAs monolithic microwave integrated circuits (MMIC) only recently have been evaluated. It was found that cryogenic operation would result in an increase in gain and a reduction in noise figure of MMICs, as is observed for discrete GaAs FET amplifiers [4, 5].

While important parameters for determining the cryogenic gain of an FET circuit, such as the transconductance at cryogenic temperatures, can sometimes be inferred from room-temperature data, this is not uniformly true. The same holds for cryogenic temperature values of minimum noise temperature. The spread in values is smaller for FETs from the same lot than for FETs from different lots. This means that before any amplifier design with stringent specifications can be carried out, extensive testing of the devices to be used will have to be performed. For devices such as distributed amplifiers, an additional problem is one of maintaining the integrity of bonds, traces, and/or solder joints. This is especially true if the device is repeatedly cycled over temperature.

II. EXPERIMENTAL DESIGN

For our experiment we used an AVANTEK low-noise amplifier (LNA), the PGM 11421. The amplifier is specified with a frequency response from 4 to 11 GHz, a minimum gain of 8.0 dB, a typical noise figure of 2.5 dB, and a minimum power output for 1-dB gain compression of +5 dBm. The dc bias for the package was 8 V at 60 mA (max.) The amplifier was mounted in a brass test fixture between 50-Ω input/output microstrip lines which were fabricated on a 10-mil Duroid ($\epsilon_r = 2.3$) substrate, designed to be 1-λ_g long at 8 GHz. This length as chosen so as to minimize the interaction between the launcher pins and the amplifier. The coax to microstrip connection was accomplished by using SMA female flange connectors. A small amount of silver paint was used to improve the contact between the center conductor of the launcher and the microstrip line, and 0.010-in. diameter gold bond wire was used to connect the microstrip line to the amplifier package.

To measure the performance of amplifiers at low temperatures, a cryogenic system was used. It consists of a test chamber which can be evacuated by a vacuum pump, a cold finger on which the sample is mounted, an electrical feedline which supplies dc bias to the amplifier, and two electrical temperature sensors. With no thermal load, the cold finger is capable of achieving a temperature of 10 K. The sensors were connected to a temperature controller which could maintain a desired temperature by controlling a heater element wrapped around the cold finger via a feedback system. Two semirigid copper coaxial cables which extend beyond the cryocooler are used as input and output lines for the RF signals. Each semirigid cable is 12 in. long to minimize the thermal load on the circuit in the cryostat as well as the thermal gradient between the inside and outside environments. A piece of indium foil was put between the cold finger and the test fixture to help increase the thermal conductivity.

One of the temperature sensors was mounted on the cold finger; the other one was alternately mounted on the top surface of the test fixture, or on the side of the fixture as close as possible to the amplifier. There is a temperature difference between the two locations of the sensor on the test fixture of nearly 4 K. This temperature difference would vary with different types of amplifiers that had different dc bias levels. This is due to the fact that the amplifier is dissipating heat into the test fixture. While the sensor near the amplifier may indicate a temperature of 77 K, clearly the amplifier package is at a higher internal temperature. This is not considered a problem since the purpose of the experiment is to see whether or not commercially packaged devices could function in the cryogenic environment which is required to exploit the advantages of high-temperature superconducting passive (HTS) devices that must operate at cryogenic temperatures. Whatever advantages may be obtained by cooling the package amplifier to its actual internal temperature is an added bonus to the primary advantage of using these packaged devices in the same cryogenic environment along with HTS passive devices.

The *S* parameters were measured on a HP 8510B automatic network analyzer. A full two-port calibration was performed at the ends of the semirigid coax inside the cryostat so as to establish the reference planes at the terminals of the amplifier test fixture. The calibration performed at 300 K was used to make the measurements at 77 K, since no practical method exists at the present to perform this calibration at 77 K inside the cryostat. A two-port calibration was chosen over a TRL calibration since the amplifier test fixture was one piece, so that separate TRL fixtures would be required to perform the calibration. Using separate test fixtures would introduce errors due to physical differences in the test fixtures used to perform the TRL. As is the case for two port calibration, no

© Microwave and Optical Technology Letters/vol. 5, no. 8, 1992. Reprinted by permission of John Wiley & Sons, Inc.

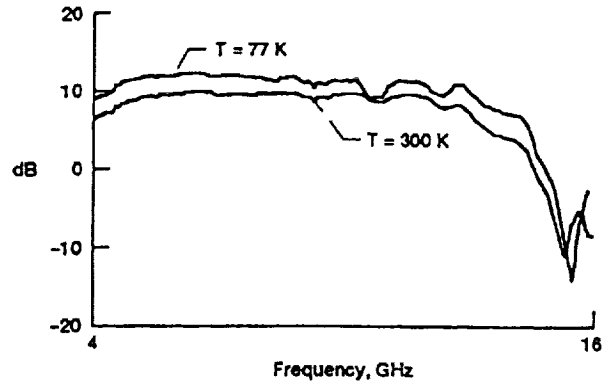

Figure 1 Gain of the LNA at T = 300 K and T = 77 K

technique exists at present to perform a TRL calibration at low temperature that does not involve repeated temperature cycling. Since the purpose of this experiment was to determine whether or not commerical amplifier packages can operate reliably at cryogenic temperatures, it was determined that a two-port calibration would suffice for this experiment. Future work will focus on optimum measurements and characterization of these devices, at which time a text fixture suitable for accurate TRL calibration will be used.

III. RESULTS

Figure 1 displays the measured S_{21} values for the PGM 11421 GaAs FET amplifier at room temperature and 77 K. The useful frequency range of this amplifier is specified as 4–11 GHz. These figures show that the gain increased about 2 dB with decreasing temperature from 300 to 77 K. As expected, the bandwidth increased at low temperature since the transconductance increases and output capacitance decreases with decreasing temperature, and these parameters determine the high-frequency cutoff for an FET [7].

Noise-figure measurements were made on a HP 8970A noise figure meter. Figure 2 shows the values for the noise figure at 300 and at 77 K. These results show that the noise figure was about 2.5 dB at room temperature, and dropped to about 1 dB at 77 K.

To obtain accurate noise figure measurements, the LNA was replaced by a 50-Ω thru line supplied by Avantek, and the insertion loss for the test fixture, along with the two semirigid cables of the cryostat were measured on the ANA at 300 and at 77 K. This loss was measured to be nearly 2 dB at 300 K, and 1 dB at 77 K, over the frequency range of 4.0–11.0 GHz. One half of this loss, representing the loss of the test setup up to the input to the LNA, was subtracted away

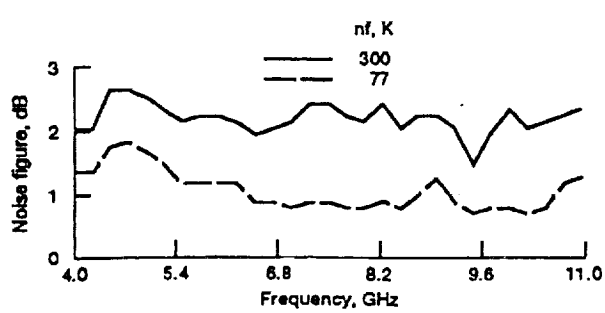

Figure 2 Noise figure of the LNA at T = 300 and 77 K

TABLE 1 Measured Input 1-dB Gain Compression Points at Selected Frequencies for the PGM 11421 Low-Noise Amplifier at 300 and at 70 K. These Values have an Accuracy of ±0.5 dB.

	P_{in-1} (dBm)	
Frequency (GHz)	300 K	70 K
4.0	3.0	2.5
4.5	3.0	2.5
5.0	4.0	3.5
5.5	4.0	4.0
6.0	3.5	3.5
6.5	4.0	3.5
7.0	3.5	3.5
7.5	4.5	4.5
8.0	4.5	5.0
8.5	4.5	4.0
9.0	5.0	4.5
9.5	5.0	4.5
10.0	5.5	5.0
10.5	6.0	6.0
11.0	6.5	6.0

from the noise figure values obtained for the LNA. The other half of this insertion loss acts as a second stage contribution to the measured noise figure, and this was entered into the 8970A as a correction factor to the calibration that was performed. The effects of the bond wires are included in this measurement. The total insertion loss of the test fixture alone can be used to determine the actual gain of the LNA as well.

Table 1 shows the result obtained for the input 1-dB compression point at 300 and at 77 K. As may be seen from this table, the change in compression point with temperature is negligible. In order to perform this measurement, the loss in the cables used was measured in the HP 8510B at 300 and at 77 K. This information was used to accurately determine the input 1-dB compression point (P_{in-1}) for the amplifier.

To obtain these measurements, the LNA was cycled down to 77 K five times. It was used in other experiments as well, and has been cycled down to 35 K 30 times to date, and there has been no loss of performance noticed so far. The only low-temperature failures noticed in this experiment involved broken bond wires between the amplifier and the input/output microstrip lines. For reliable performance, it was found that the amplifier bonding pads should be located at the same height as the microstrip lines, and that there should be some slack introduced into the bond wire to allow for vibration from the compressor pump in the cold head assembly and thermal contraction in the Duroid substrate. The Duroid substrate had to be firmly bonded to the test fixture near the amplifier to ensure against warping in the substrate as the fixture is cycled over temperature.

IV. CONCLUSION

This article has presented gain and noise figure performance of the commercial packaged GaAs amplifier at different temperatures. As expected, a lower noise figure and a higher gain were induced by decreasing the temperature. No significant change in the input 1-dB compression point was observed.

The results obtained in this experiment would indicate that commercially packaged devices can be used at cryogenic temperatures. This would be a significant help in developing cryogenic microwave sytems where packaged devices can be used in conjunction with high-temperature superconducting (HTS)

passive components [8], all at the same temperature. While this experiment does not establish the long-term reliability of commercial MMIC packages that are repeatedly cycled over temperature, it shows that there is potential for reliable operation in circumstances where the MMIC package is cooled only once, and kept at cryogenic temperatures for an extended length of time.

ACKNOWLEDGMENT

The authors wish to thank Mr. Ed Rylander, Sr., Test Engineer at Avantek Inc., Folsom, CA, for his generous advice on noise figure measurements and for supplying Avantek thru lines for calibration purposes.

REFERENCES

1. M. W. Pospieszalski, S. Weinreb, R. D. Norrod, and R. Harris, "FETs and HEMT's at Cryogenic Temperatures—Their Properties and Use in Low-Noise Amplifiers," *IEEE Trans. Microwave Theory Tech.*, Vol. MTT-36, 1988, pp. 552–560.
2. S. Weinreb, D. Fenstermacher, and R. Harris, "Ultra Low-Noise, 1.2–1.7 GHz, Cooled GASFET Amplifiers," *IEEE Trans. Microwave Theory Tech.*, Vol. MTT-30, 1982, pp. 849–853.
3. S. Weinreb and M. W. Pospieszalski, "X-Band Noise Parameters of HEMT Devices at 300° K and 12.5° K," in *Proc. 1985 Int. Microwave Symp.*, 1985, pp. 539–542.
4. C. R. Moore, W. C. Trimble, M. L. Edwards, and T. R. Sanderson, "Cryogenic Performance of a GaAs MMIC Distributed Amplifier," *IEEE Trans. Microwave Theory Tech.*, Vol. MTT-39, 1991, pp. 567–571.
5. S. Weinreb, "Low-Noise, Cooled GASFET Amplifiers," *IEEE Trans. Microwave Theory Tech.*, Vol. MTT-28, 1980, pp. 1041–1054.
6. S. M. Sze, *Physics of Semiconductor Devices*, Wiley, New York, 1981.
7. T. Van Duzer, "Superconductor-Semiconductor Hybrid Devices, Circuits, and Systems," *Cryogenics*, Vol. 28, Aug. 1988, pp. 527–531.
8. K. B. Bhasin et al., "High-Temperature Superconducting Thin Film Microwave Circuits: Fabrication, Characterization, and Applications," *Proc. SPIE*, Vol. 1292, April 1990, pp. 71–82.

Received 1-16-92; revised 2-13-92

FULL WAVE CHARACTERIZATION OF MICROSTRIP OPEN END DISCONTINUITIES PATTERNED ON ANISOTROPIC SUBSTRATES USING POTENTIAL THEORY

S.S. Toncich*
National Aeronautics and Space Administration
Lewis Research Center
Cleveland, Ohio 44135

R.E. Collin
Department of Electrical Engineering & Applied Physics
Case Western Reserve University
Cleveland, Ohio 44106

and

K.B. Bhasin
National Aeronautics and Space Administration
Lewis Research Center
Cleveland, Ohio 44135

Abstract

A technique for the full wave characterization of microstrip open end discontinuities fabricated on uniaxial anisotropic substrates using potential theory is presented. The substrate to be analyzed is enclosed in a cut-off waveguide, with the anisotropic axis aligned perpendicular to the air-dielectric interface. A full description of the sources on the microstrip line is included with edge conditions built in. Extention to other discontinuities is discussed.

Introduction

While there is extensive data available on the microwave characterization of a variety of microstrip discontinuities using both quasi-static [1-3] and full wave techniques [4-6], the characterization has been restricted to isotropic substrates. To date, there is no published data regarding microstrip discontinuities patterned on anisotropic substrates. Some very useful microwave substrates however, like sapphire, are anisotropic and so any discontinuity structures fabricated on them can not be properly characterized by the techniques that have been developed for isotropic dielectric substrates.

A technique for the full wave characterization of microstrip open ends fabricated on lossless uniaxial anisotropic substrates has been developed and is presented here. It is based on a dynamic source reversal technique that uses potential theory [7], which is a generalization of the charge resversal technique introduced several years ago [1]. The discontinuity is enclosed in a waveguide of infinite extent whose dimensions are such that the guide is cut-off for the propagating frequency on the microstrip. All sources on the microstrip are represented, and the technique does not require a model for the source exitation.

Dynamic Source Reversal Technique

The anisotropic axis of the substrate is aligned perpendicular to the air-dielectric interface as shown in Fig. 1. The anisotropic dielectric may be represented as a tensor quantity given by

$$\boldsymbol{\kappa}(y) = \kappa(y)\mathbf{I} + [\kappa_y(y) - \kappa(y)]\mathbf{a}_y\mathbf{a}_y \tag{1}$$

where I is the unit dyad and $\kappa(y) = \kappa_y(y) = 1$ for $y > h$. The microstrip line is assumed to be infinitely thin and located at a height $y = h^+$. In terms of the sources on the microstrip line, the scalar and vector potentials, Φ and $\mathbf{A}$ respectively, for the dielectric loaded waveguide may be determined from

$$(\nabla^2 + \kappa k_0^2)A_x = -\mu_0 J_x \tag{2}$$

$$(\nabla^2 + \kappa k_0^2)A_z = -\mu_0 J_z \tag{3}$$

$$(\nabla^2 + \kappa_y k_0^2)A_y = j\omega\mu_0\epsilon_0(\kappa - 1)\Phi(h)\delta(y - h) + j\omega\mu_0\epsilon_0(\kappa_y - \kappa)\partial\Phi/\partial y \tag{4}$$

$$[\kappa(\partial^2/\partial x^2 + \partial^2/\partial z^2) + \partial(\kappa(y)\partial/\partial y)/\partial y + \kappa^2(y)k_0^2]\Phi = -\rho/\epsilon_0 + j\omega(\kappa_y - 1)A_y(h)\delta(y - h) - j\omega(\kappa_y - \kappa)\partial A_y/\partial y \tag{5}$$

The potentials appearing in Eqs. (2) to (5) are obtained from the appropriate Green's functions and the corresponding sources using

$$A_{x,z}(x,h,z) = \mu_0 \int_{x'}\int_{z'} G_{x,z}(x,h,z;x',h,z')J_{x,z}(x',h,z')dx'dz' \tag{6}$$

*National Research Council—NASA Research Associate at Lewis Research Center.

© 1993 IEEE. Reprinted, with permission, from IEEE MTT-S Digest, pp. 1527-1530.

PRECEDING PAGE BLANK NOT FILMED

$$\epsilon_0\Phi(x,h,z) = \int_{x'}\int_{z'} G_\Phi(x,h,z;x',h,z')\rho(x',h,z')dx'dz' \tag{7}$$

From these potentials the electric field components are found using

$$E_x = -j\omega A_x - \partial\Phi/\partial x$$

$$E_y = -j\omega A_y - \partial\Phi/\partial y$$

$$E_z = -j\omega A_z - \partial\Phi/\partial z \tag{8}$$

where it is required that for this particular geometry E_x and E_z vanish on the microstrip. The fields thus obtained are expressed in terms of LSE and LSM modes of the dielectric loaded waveguide. The anisotropic effect appears only in the LSM mode terms, which are present in A_y and Φ. The LSE modes are unchanged from those obtained for the isotropic case.

A complete set of dominant mode sources on the microstrip are represented; the longitudinal and transverse currents, as well as the charge on the microstrip line, with appropriate edge conditions built in. For a wide range of practical open end discontinuities, a valid approximation is that $J_x = 0$, so therefore $A_x = 0$. As a result, only the boundary condition $E_z = 0$ is required for this problem.

A line terminated at $z = 0$, thus forming an open end, would create reflected dominant mode sources on the line, along with perturbed sources localized near the discontinuity. The total source distribution on an open end may be written as

$$J_z(x',h,z') = J_{0\,z}(x')(e^{-j\beta z'} - Re^{+j\beta z'}) + J_{1\,z}(x',z') \tag{9}$$

$$\rho(x',h,z') = \rho_0(x')(e^{-j\beta z'} + Re^{+j\beta z'}) + \rho_1(x',z') \tag{10}$$

for $z' \leq 0$, where $J_{0\,z}$, ρ_0 and β are the yet to be determined amplitudes and propagation constant, respectively of the dominant microstrip mode, R is an unknown reflection coefficient, and $J_{1\,z}$ and ρ_1 represent the perturbed source amplitudes near the open end. Weighted Chebychev polynomials are used to represent the sources in x for both dominant and perturbed sources, while triangle and pulse functions are used to represent the perturbed sources in z.

Equations (9) and (10) may be written as

$$J_z(x',h,z') = [j(1+R)J_{0\,z}(x')(B_{in}\cos(\beta z') - \sin(\beta z')) + jJ_{1\,z}(x',z')] \cdot [1 - U(z')] \tag{11}$$

$$\rho(x',h,z') = [(1+R)\rho_0(x')(B_{in}\sin(\beta z') + \cos(\beta z')) + \rho_1(x',z')] \cdot [1 - U(z')] \tag{12}$$

where $U(z')$ is the Heavyside unit step function which is 0 for $z' < 0$ or 1 for $z' > 0$, and $jB_{in} = (1 - R)/(1 + R)$ is the normalized input susceptance for the open end. In Eqs. (11) and (12) the dominant mode sources are assumed to exist for $-\infty \leq z' \leq \infty$. Then dominant mode sources for $z' > 0$ are subtracted away to create the terms that multiply the $(1 + R)$ coefficient in (11) and (12). Since the amplitudes of $J_{1\,z}$ and ρ_1 are arbitrary at this point, they may be defined so as to include the $(1 + R)$ term. Now the $(1 + R)$ term is common to all of the source terms, so it may be normalized to 1.0. Using Eqs. (11) and (12) in Eqs. (6) and (7) and substituting into Eq. (8) gives the electric field in terms of the sources on the open end microstrip line. When the requirement that $E_z = 0$ on the microstrip is enforced, the terms corresponding to the dominant mode on the infinite line already satisfy the boundary condition on the strip, so they drop out. The sources existing for $z' > 0$ may be considered "source reversed" terms which produce an impressed field in the reigon $z \leq 0$ but localized near the discontinuity. The factor $(1 + R)$ can be included into the arbitrary amplitude of the dominant mode sources. Thus, apart from the unknown parameter B_{in}, the dominant mode sources in $z' > 0$ produce a known forcing function in the strip for $z' < 0$. The electric field produced by the perturbed sources $J_{1\,z}$ and ρ_1, must cancel the tangential component of the applied field for $z \leq 0$. A modified perturbation technique [8] is used to determine the unknown dominant mode amplitudes and propagation constant for an infinite line. The method of moments is then used to reduce the resulting integral equation to a matrix equation which can be solved for the unknown input admittance B_{in}, as well as for $J_{1\,z}$ and ρ_1. Only one matrix inversion is required to find B_{in}.

Results

The pulse width, Δ, of the expansion functions was chosen to be 0.32 mm at f = 2.0 GHz (or $\Delta \simeq 0.0053\lambda_g$ for sapphire). This pulse width guaranteed a converged value for B_{in} [7] for all of the examples presented. To verify the accuracy of the theory as well as the resulting program, the program was checked for the isotropic case, and was able to duplicate data obtained in [1] and [7].

Table I shows the results obtained using this technique for several different anisotropic substrates as a function of microstrip line width. The open circuit capacitance, C_{oc} is found using $C_{oc} = B_{in}/\omega Z_0$, where the characteristic impedance Z_0 is obtained from a computer program developed on the basis of the theory presented in [8] for the characterization of infinite microstrip lines with sidewalls, but no top cover. To justify using values of Z_0 thus obtained, calculations performed for a microstrip line with an air dielectric showed less than 2% difference in Z_0 values obtained with and without a top cover. Table II shows the variation of C_{oc} as a function of line width for sapphire, and compares the results obtained for a substrate with an isotropic dielectric constant of 9.4, as well as for an isotropic dielectric constant of 11.6. Table III shows the effects of fixed waveguide dimensions on B_{in} and C_{oc} as a function of frequency of the propagating microstrip mode. For low frequencies, B_{in} varies linearly with frequency, starting to deviate as the frequency increases, this effect becomes more pronounced until the cut off frequency of the E_{11} waveguide mode is reached. This effect may be overcome by either frequency scaling the input parameters or by adjusting the waveguide dimensions accordingly.

The BASIC computer program developed to implement this technique can be executed on a personal computer with as little as 640K of RAM. Other discontinuity structures can be characterized in a similar manner. The technique is computationally efficient, there is no need to model the source excitation, and the admittance can be solved for directly in the case of a one port network. All integrals involving the expansion and testing functions are performed analytically so no numerical integrations are necessary, and the dominant portions of slowly converging series can be extracted and summed into closed form.

This technique can be extended to rapidly and accurately characterize a number of other commonly used discontinuity structures, especially "coaxial" two port structures such as asymmetrical gaps and steps in width. To characterize a two port structure in terms of an equivalent "Tee" or "Pi" network, the Tangent Plane method [9] can be used to extract parameter values.

References

1. P. Silvester, and P. Benedek, "Equivalent capacitance of microstrip open circuits," IEEE Trans. Microwave Theory Tech., vol. MTT-20, pp. 511-516, 1972.

2. P. Silvester, and P. Benedek, "Equivalent capacitance of microstrip gaps and steps," IEEE Trans. Microwave Theory Tech., vol. MTT-20, pp. 729-733, 1972.

3. P. Anders, and F. Arndt, "Microstrip discontinuity capacitances and inductances for double steps, mitered bends with arbitrary angle, and asymmetric right angle bends," IEEE Trans. Microwave Theory Tech., vol. MTT-28, pp. 1213-1217, 1980.

4. R.H. Jansen, "Hybrid mode analysis of end effects of planar microwave and millimeter wave transmission lines," IEEE proc. Pt. H: Microwaves, Optics, Antennas, vol. MTT-128, no. 2, pp. 77-86, 1981.

5. J.C. Rautio, and R.F. Harrington, "An electromagnetic time-harmonic analysis of shielded microstrip circuits," IEEE Trans. Microwave Theory Tech., vol. MTT-35, pp. 726-731, 1987.

6. R.W. Jackson, "Full wave, finite element analysis of irregular microstrip discontinuities," IEEE Trans. Microwave Theory Tech., vol. MTT-37, pp. 81-89, 1989.

7. S.S. Toncich, and R.E. Collin, "Characterization of microstrip discontinuities by a dynamic source reversal technique using potential theory," in 14th. Triennial URSI International Symposium on Electromagnetic Theory, pp. 520-523 (Sydney, Australia), 1992.

8. B.E. Kretch, and R.E. Collin, "Microstrip dispersion including anisotropic substrates," IEEE Trans. on Microwave Theory Tech., vol. MTT-35, pp. 710-718, 1987.

9. R.E. Collin, Field theory of guided waves. New York: McGraw Hill. Ch. 5, 1960.

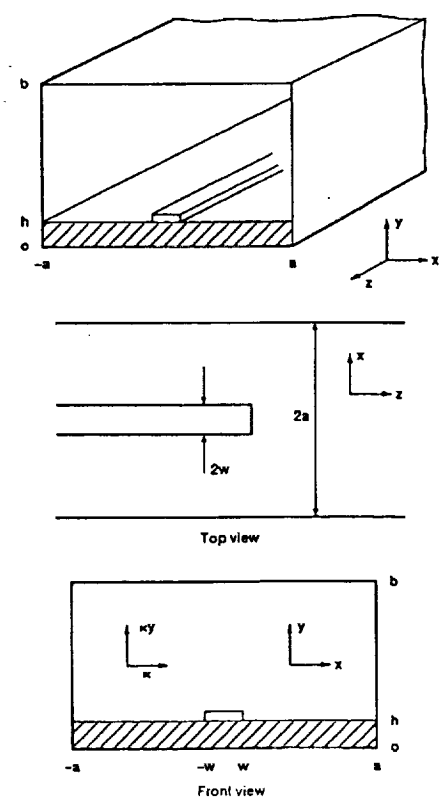

Figure 1.—Shielded microstrip geometry.

TABLE I.—OPEN CIRCUIT CAPACITANCE, C_{OC}, FOR SEVERAL ANISOTROPIC DIELECTRIC MATERIALS. FREQUENCY = 2.0 GHz, h = 1.0 mm, b = 11 mm, 2a = 20 mm FOR W/h < 4.0 ELSE 2a = 10(W/h). Z_0 VALUES OBTAINED FROM REF. 8. UNITS ARE pF/METER FOR C_{OC}.

		W/h					
		0.25	0.5	1.0	2.0	4.0	6.0
PTFE/Woven glass	κ_e	1.914	1.941	1.981	2.042	2.129	2.182
$\kappa = 2.84$	Z_0	150.5	119.9	90.02	62.46	39.82	29.50
$\kappa_y = 2.45$	C_{oc}/W	29.85	23.71	19.90	17.66	16.29	15.60
Boron nitride	κ_e	2.676	2.699	2.738	2.808	2.922	2.999
$\kappa = 5.12$	Z_0	127.4	101.7	76.68	53.38	34.09	25.25
$\kappa_y = 3.4$	C_{oc}/W	43.04	33.95	28.27	24.84	22.72	21.66
Sapphire	κ_e	6.724	7.012	7.647	8.145	9.007	9.514
$\kappa = 9.4$	Z_0	80.90	63.65	46.94	31.82	19.80	14.52
$\kappa_y = 11.6$	C_{oc}/W	80.36	65.56	56.38	50.95	47.43	45.35
Epsilam 10	κ_e	6.885	7.047	7.306	7.721	8.308	8.679
$\kappa = 13$	Z_0	79.90	63.44	47.39	32.61	20.55	15.14
$\kappa_y = 10.3$	C_{oc}/W	95.28	76.26	64.44	57.35	52.93	50.49

TABLE II.—VARIATION OF C_{OC} AS A FUNCTION OF LINE WIDTH FOR SAPPHIRE, $k = 9.4$, $k_y = 11.6$ COMPARED TO THAT OF AN ISOTROPIC DIELECTRIC. FREQUENCY = 2.0 GHz, h = 1.0 mm, b = 11 mm, 2a = 20 mm FOR W/h < 4.0, ELSE 2a = 10(W/h). UNITS ARE pF/METER FOR C_{OC}.

		W/h					
		0.25	0.5	1.0	2.0	4.0	6.0
Sapphire $\kappa = 9.4$ $\kappa_y = 11.6$	C_{oc}/W	80.36	65.56	56.38	50.95	47.43	45.35
$\kappa = 9.4$ $\kappa_y = 9.4$	C_{oc}/W	75.56	61.06	52.10	46.80	43.42	41.52
$\kappa = 11.6$ $\kappa_y = 11.6$	C_{oc}/W	90.18	73.27	62.58	56.21	52.13	49.77

TABLE III.—VARIATION OF THE NORMALIZED INPUT SUSCEPTANCE, B_{in}, AND OPEN CIRCUIT CAPACITANCE, C_{OC}, WITH FREQUENCY. WAVEGUIDE DIMENSIONS ARE 2a = 20 mm, b = 11 mm AND h = 1 mm.

Frequency, GHz	B_{in}	C_{oc}(pF/m)
0.5	0.008388	56.26
1.0	.016776	56.26
2.0	.033256	56.38
4.0	.068373	56.85
6.0	.167738	90.81

N94-20500

A COMPREHENSIVE THEORETICAL AND EXPERIMENTAL STUDY OF COPLANAR WAVEGUIDE SHUNT STUBS

Nihad I. Dib[†], George E. Ponchak[*] and Linda P. B. Katehi[†]

[†] *Radiation Lab., University of Michigan, 3228 EECS Building, Ann Arbor, MI 48109-2122*
[*] *NASA, Lewis Research Center, 21000 Brookpark Rd, MS 54-5, Cleveland, OH 44135*

ABSTRACT

A comprehensive theoretical and experimental study of straight and bent CPW shunt stubs is presented. In the theoretical analysis, the CPW is assumed to be inside a cavity, while, the experiments are performed on open structures. A hybrid technique has been developed to analyze the CPW discontinuities which has been proven to be accurate since the theoretical and experimental results agree very well. Throughout this study, the effect of the cavity resonances on the behavior of the stubs with and without air-bridges is investigated. In addition, the encountered radiation loss due to the discontinuities is evaluated experimentally.

INTRODUCTION

Recently, with the push to high frequencies and monolithic technology, coplanar waveguides (CPWs) have experienced a growing interest due to their appealing properties. While there is no need for via holes in CPW circuits, air-bridges are fundamental components required to connect the ground planes for suppression of the coupled slotline mode. In the past few years, there has been several attempts to characterize, theoretically and/or experimentally, CPW discontinuities with air-bridges or bond wires [1-5]. The Finite Difference Frequency Domain method was used in [6] to treat two common types of CPW air-bridges where it was found that the reflection coefficient (or S_{11}) varies linearly with frequency. This fact suggests that a typical air-bridge can be modeled as a frequency dependent lumped element [1, 2]. With this fact in mind, a hybrid technique has been developed by the authors [2] to analyze CPW discontinuities with air-bridges. In this technique, at first, the frequency dependent equivalent circuit of the discontinuity, with the air-bridges removed, is derived using a full wave analysis which is based on the Space Domain Integral Equation (SDIE) method [7]. Then, this equivalent circuit is modified by incorporating the air-bridge parasitic inductance and capacitance which are evaluated using a quasi-static model.

In this paper, the above mentioned hybrid technique is used to study a variety CPW shunt stub geometries (Fig.2) and the validity of the model is verified by performing extensive measurements. The scattering parameters of the stubs with and without air-bridges are presented and a very good agreement is found between theoretical and experimental data. In addition, the effect of cavity resonances (since a shielded structure is assumed in the theory) on the behavior of these stubs is shown. Moreover, the encountered radiation loss due to the discontinuities is investigated experimentally.

THEORY

In the theoretical analysis, the CPW under consideration (Fig.1) is assumed to be inside a rectangular cavity of perfectly conducting walls. As pointed out in the introduction, the hybrid technique developed in [2] is used to analyze the shunt CPW stubs shown in Fig.2. First, the frequency dependent equivalent circuit of the discontinuity, with the air-bridges removed, is derived using the Space Domain Integral Equation (SDIE) method [7]. Then, this equivalent circuit is modified by incorporating the parasitic reactances introduced by the air-bridges. These reactances, a series inductance and a shunt capacitance, are evaluated by modeling the air-bridges as sections of an air filled microstrip line or parallel plate waveguide. The SDIE method will not be discussed here since it has been presented in detail in [7]. However, a slight modification on the equivalent circuit presented in [2] is needed as discussed below.

After applying the method of moments, the electric field in the slot apertures, which forms standing waves of the fundamental coplanar waveguide mode away from the discontinuity, is obtained. Notice that the slotline mode will not be excited in the CPW feed lines since the discontinuities considered here (Fig.2) are symmetric with respect to the center axis of the feeding lines. Consequently, an ideal transmission line method can be used to determine the scattering parameters and evaluate the elements of the equivalent circuit shown in Fig.3a. It should be noticed that in the case of straight stubs, the two reactances X_1 and X_2 are equal due to the symmetry of the circuit. Fig.3b shows the new equivalent circuit after taking the air-bridges into consideration. The air-bridges can be modeled as sections of an air-filled microstrip line [1], and simple design formulas can be used to evaluate the parasitic capacitance C_a and inductance L_a. Alternatively, a parallel plate waveguide model can be employed to evaluate the same parasitic effects. It is found that the difference in the values of the parasitic reactances as predicted by the two models has a

© 1993 IEEE. Reprinted, with permission, from 1992 IEEE MTT-S Digest, CH3141-9/92/0000-0947, pp. 947-950.

negligible effect on the preformance of the circuit. Finally, new scattering parameters are evaluated from the modified equivalent circuit.

RESULTS AND DISCUSSION

In the numerical results shown here, the considered CPW discontinuities are suspended inside a rectangular cavity , as shown in Fig.1, with $h = 400\mu m$, $\epsilon_{r1} = 13$, $\epsilon_{r2} = 1$, $S = 75\,\mu m$, $W = 50\,\mu m$, and $h_1 = h_2 = 1.2\,mm$. On the other hand, the slots and center conductor of the CPW stubs have equal widths of $25\,\mu m$. In addition, in the case of the open-end stubs, the width of the open-end is $25\,\mu m$. In all examples presented here, the stubs are placed symmetrically at the center of the cavity.

The experiments were performed in an open environment with the CPW circuits fabricated on $400\,\mu m$ thick GaAs using lift-off processing. The CPW center strip and ground planes consist of $200A$ of Cr and $1.5\,\mu m$ of Au. The air-bridges have $10\,\mu m$ square posts and are $14\,\mu m$ wide. The air-bridge thickness and height are $1.0\,\mu m$ and $3.0\,\mu m$ respectively. The GaAs circuit was placed on a piece of $3.175\,mm$ 5880 RT/duroid which has a dielectric constant of 2.2.

The circuits were tested with HP 8510 network analyzer and a Cascade probe station. The calibration standards for a TRL calibration were fabricated on the wafer to allow calibration to the reference planes of the CPW stubs. To cover the 5-40 GHz bandwidth, three delay lines were used. The probe positioning on the wafer was determined to be repeatable to within $3\,\mu m$ which creates a maximum error in the phase of S_{21} of 0.76° at 40 GHz.

Fig.4 shows the S-parameters of the straight open-end stub (Fig.2a) of length $L = 1100\,\mu m$ and with the air-bridges removed as a function of frequency. It is noticed that the theoretical and experimental results agree very well up to the first resonance, after which, discrepancy in noticeable. This is attributed to the radiation loss encountered in the measurements which is mainly due to the excitation of the slotline mode in the CPW stubs in the absence of the air-bridges. It is found that the anomalous behavior seen between 41 and 45 GHz is due to a cavity resonance at 43 GHz which corresponds to the LSM_{121} mode excited in the partially filled lower cavity (the cavity width was chosen to be $3.425\,mm$). It is interesting to note that the LSM_{111} and LSM_{131} modes which have resonant frequencies of 38 and 48 GHz, respectively, do not show any effect on the stub. This may be attributed to the fact that the longitudinal electric field component of the LSM_{111} and LSM_{131} is an odd function with respect to a symmetry plane placed at the center of the cavity, as opposed to the LSM_{121} mode whose longitudinal component is an even function around the same plane. Thus, cavity modes, which have an even variation with respect to this plane, interact with the slotline mode in the stubs, which in turn affects the value of the series reactance in the equivalent circuit. It is expected that if the CPW structure is placed asymmetrically inside the cavity, other cavity resonances will also have an effect on the circuit performance.

Fig.5 shows the S-parameters of the same straight open-end stub with air-bridges. As it can be seen, the stub resonates at nearly 24.5 GHz where the length of the stub is approximately quarter of a coplanar mode wavelength. It can be noticed that the agreement between the theoretical and experimental data in Fig.5 is much better than the one seen in Fig.4. This can be attributed to the fact that the air-bridges tend to prevent the slotline mode from being excited in the CPW stubs which effectively reduces radiation losses. In addition, it can be seen that the resonance effect noticed in Fig.4 has disappeared since X_3 is shorted by the relatively small air-bridge inductance L_a. Alternatively, the air-bridges short out the slotline mode, thus, eliminating interaction with the cavity resonances. As a result, with the presence of air-bridges, cavity resonances have no effect on the characteristics of a straight stub as long as it is placed symmetrically inside the cavity. One can also notice an anomalous effect at 40 GHz existing in Fig.5. A similar effect has been found in [4] for the case of a bent open-end stub. This effect may be due to a resonating slotline mode excited in the stubs beyond the air-bridge.

Fig.6 shows $Mag(S_{12})$ for the bent open-end CPW stub (Fig.2b) of mean length $1100\,\mu m$ with and without air-bridges. In this case, the width of the cavity is taken to be $2\,mm$. It can be seen that for the bent stub without air-bridges, the agreement between theory and experiment is better than that seen in fig.4 for the straight stub without air-bridges. The same behavior, observed in the straight open-end stubs with air-bridges at 40 GHz, can be seen more clearly in Fig.6 for the bent stubs with air-bridges. Moreover, the resonant frequency of this bent stub with air-bridges is approximately the same as the one for the straight stub of the same mean length.

From the measured scattering parameters, the loss factor due to the stubs can be calculated. This loss factor includes radiation, conductor, and dielectric losses. Since the stubs are all the same length, a comparison of the loss factor can provide a measure of the radiation loss. Fig.7a shows the loss factor of the open-end stubs without air-bridges. It is noticed that loss is maximum at the resonant frequency of the stubs, which is similar to what has been found in microstrip stubs [8]. Furthermore, the loss factor for the straight stub is larger than that for the bent stub. Lower loss is due to the fact that in the case of bent stubs, the fields radiated by the slotline modes in the two opposing stubs partially cancel. This explains why the agreement between the theoretical and experimental results for the bent stubs without air-bridges (Fig.6) is better than that for the straight stubs without air-bridges (Fig.4). The loss factor for the open-end stubs with air-bridges is shown in Fig.7b. The air-bridges reduce radiation loss by shorting out the coupled slotline mode, but it is still noted that the straight stub have increasing radiation loss after the first resonant frequency.

Numerical and experimental results for the short-end stubs (Figures 2c and 2d) will be presented in the symposium.

CONCLUSIONS

A comprehensive theoretical and experimental study of CPW shunt stubs has been presented. In the theoretical analysis, the CPW was assumed to be inside a cavity, while, the experiments were performed in an open environment. A hybrid technique has been developed to analyze the CPW discontinuities which proved valid since the results obtained theoretically and experimentally agreed very well. In addition, the effect of the cavity resonances on the behavior of the stubs has been studied. It was found that air-bridges suppress the slotline mode and cancel the effect of the cavity resonances on the characteristics of the stub. Moreover, It has been shown through experiments that bent CPW stubs should be used whenever the circuit layout permits to reduce the radiation loss caused by the parasitic coupled slotline mode.

ACKNOWLEDGMENT

The theoretical work was supported by the National Science Foundation under contract ECS-8657951.

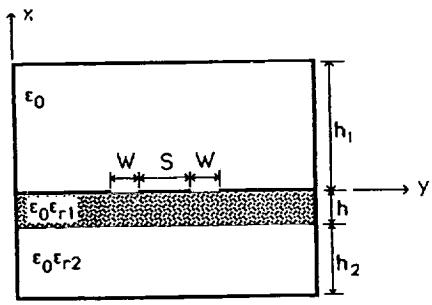

Figure 1: A cross section of a CPW inside a cavity.

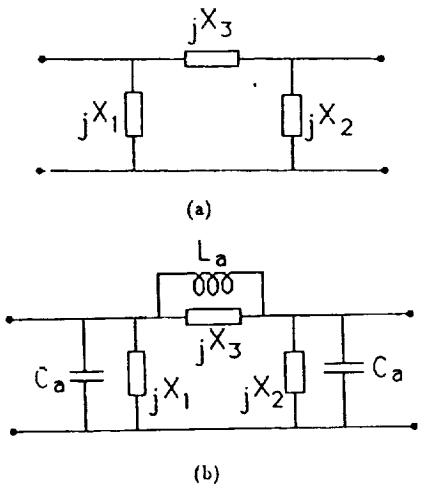

Figure 3: (a) Equivalent circuit of the CPW discontinuities shown in Fig.2 without the air-bridges. (b) The modified equivalent circuit after taking the air-bridges into consideration. (The reference planes are taken at the end of the uniform feeding lines)

REFERENCES

[1] N. Koster, *et al*, " Investigation of Air Bridges Used for MMICs in CPW Technique, " *Proc. of 19th European Microwave Conference* , pp. 666-671, Sep. 1989.

[2] N. Dib, P. Katehi and G. Ponchak, "Analysis of Shielded CPW Discontinuities with Air Bridges, " *in 1991 IEEE MTT-S Digest*, Boston, pp. 469-472.

[3] T. Becks and I. Wolff, " Calculation of Three-Dimensional Passive Structures including Bond-Wires, Via-Holes and Air-Bridges Using the Spectral Domain Analysis Method," *Proc. of 21st European Microwave Conference* , pp. 571-576, Sep. 1991.

[4] M. Rittweger, M. abdo and I. Wolff, " Full-Wave analysis of Coplanar Discontinuities Considering Three-Dimensional Bond Wires, " *in 1991 IEEE MTT-S Digest*, Boston, pp. 465-468.

[5] M. Rittweger, *et al*, "Full-Wave Analysis of a Modified Coplanar Air Bridge T-Junction, " *Proc. of 21st European Microwave Conference* , pp. 993-998, Sep. 1991.

[6] K. Beilenhoff, W. Heinrich and H. Hartnagel, " The Scattering behavior of Air Bridges in Coplanar MMIC's, " *Proc. of 21st European Microwave Conference* , pp. 1131-1135, Sep. 1991.

[7] N. Dib and P. Katehi, "Modeling of Shielded CPW Discontinuities Using the Space Domain Integral Equation Method (SDIE), " *Journal of Electromagnetic Waves and Applications*, pp. 503-523, April 1991.

[8] W. Harokopus and P. Katehi, "Characterization of Microstrip Discontinuities on Multilayer Dielectric Substrates Including Radiation Losses," *IEEE Trans. on MTT*, pp.2058-2065, Dec. 1989.

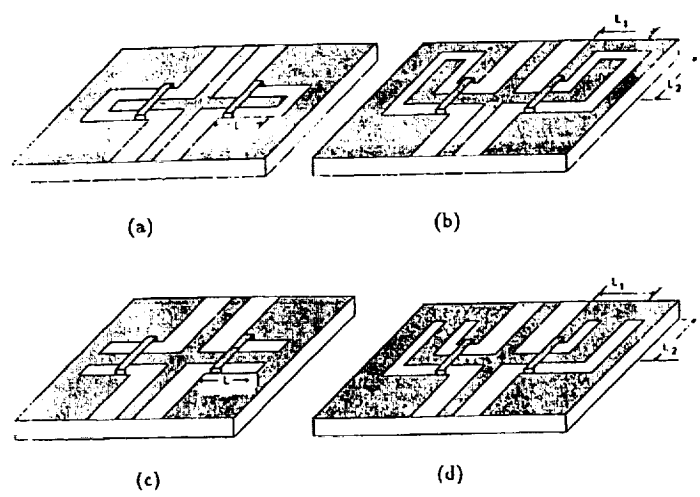

Figure 2: Different CPW shunt stubs. (a) Straight open-end CPW stub. (b) Bent open-end CPW stub. (c) Straight short-end CPW stub. (d) Bent short-end CPW stub.

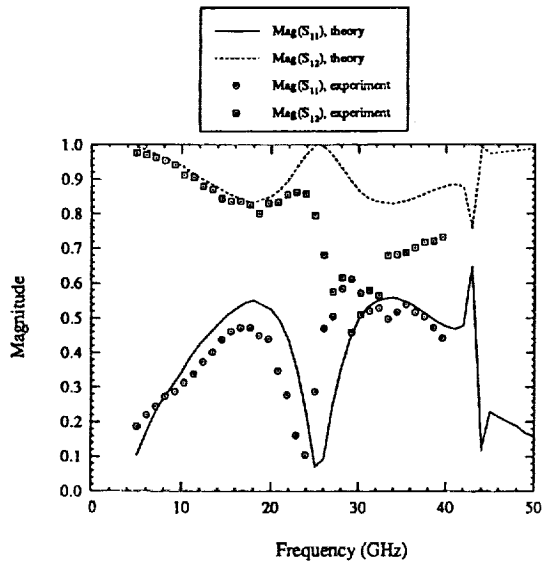

Figure 4: Scattering parameters of the straight open-end stub without air-bridges with $L = 1100\mu m$.

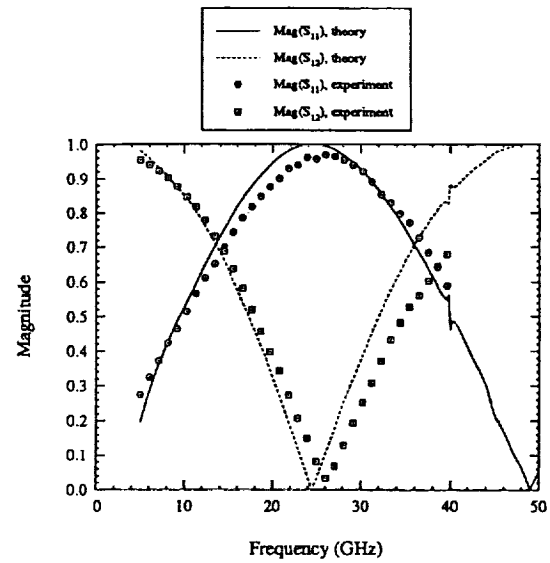

Figure 5: Scattering parameters of the straight open-end stub with air-bridges with $L = 1100\mu m$.

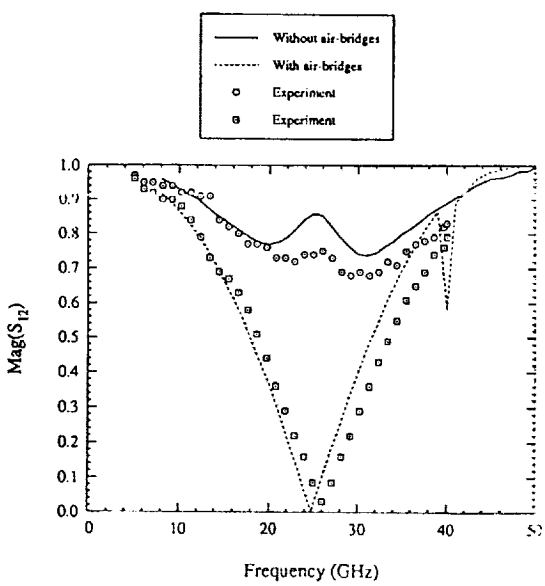

Figure 6: $Mag(S_{12})$ of the bent open-end stub with and without air-bridges with mean length of $1100\mu m$ ($L_1 = 100\mu m$, $L_2 = 1025\mu m$)

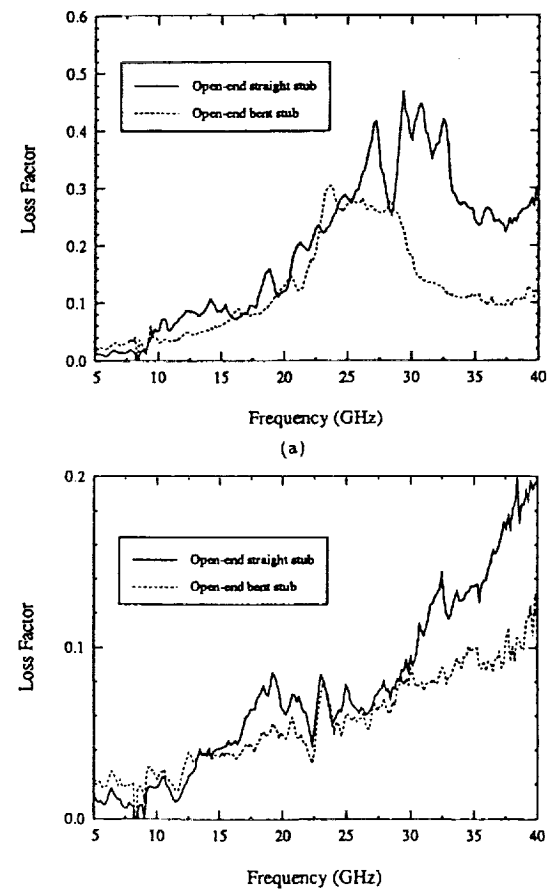

Figure 7: The measured loss factor of the open-end CPW stubs (a) without air-bridges. (b) with air-bridges.

N94-20501

A Comparative Study between Shielded and Open Coplanar Waveguide Discontinuities

N. I. Dib[1], W. P. Harokopus, Jr.[2], G. E. Ponchak[3], and L. P. B. Katehi[1]

[1]Department of EECS, University of Michigan, Ann Arbor, Michigan 48109

[2]Texas Instruments, Dallas, Texas 75070

[3]NASA Lewis Research Center, Cleveland, Ohio 44135

Received January 17, 1992; revised April 14, 1992.

ABSTRACT

A comparative study between open and shielded coplanar waveguide (CPW) discontinuities is presented. In this study, the space domain integral equation method is used to characterize several discontinuities such as the open-end CPW and CPW series stubs. Two different geometries of CPW series stubs (straight and bent stubs) are compared with respect to resonant frequency and radiation loss. In addition, the encountered radiation loss due to different CPW shunt stubs is evaluated experimentally. The notion of *forced radiation* simulation is presented, and the results of such a simulation are compared to the *actual* radiation loss obtained rigorously. It is shown that such a simulation cannot give reliable results concerning radiation loss from printed circuits. © 1992 John Wiley & Sons, Inc.

INTRODUCTION

Coplanar waveguide (CPW) is rapidly becoming the transmission line of choice in high-frequency applications and is successfully competing against the microstrip which has been the primary structure for hybrid and monolithic circuits. Due to many years of microstrip use, a large body of published data and CAD software pertaining to low- and high-frequency microstrip circuit and antenna design has been widely available. In contrast, models for shielded or open coplanar waveguide circuit design are still under development [1–21]. In addition, there is little data available concerning the radiation loss from CPW discontinuities [7,12,19]; therefore, there are no guidelines for low-loss, high-frequency CPW design. Nevertheless, despite this scarcity of reliable circuit models, CPW has provided an attractive alternative to conventional microstrip lines at high frequencies due to many appealing properties [22–27]. These include the ability to wafer probe, and the ease in connecting shunt lumped elements or devices without using via holes. Such advantages arise because both conducting surfaces (the center conductor and the ground plane) are on the same side of the dielectric substrate.

Another important characteristic of coplanar waveguides is that the line impedance and phase velocity are less dependent on the substrate height than on the aspect ratio (slot width/center conductor width). Since the conducting surfaces of a CPW structure are all printed on the same interface, careful design could efficiently confine the fields to this interface. This characteristic benefits both shielded and open CPW lines as it provides control over leakage and unwanted parasitic coupling. Printed lines which are not enclosed in a metallic package, such as the feed network of a monolithic array, tend to radiate power in the

© International Journal of Microwave and Millimeter-Wave Computer-Aided Engineering, vol. 2, no. 4, 1992. Reprinted by permission of John Wiley & Sons, Inc.

form of space and surface waves. In conventional monolithic lines, the level of parasitic radiation is strongly affected by the electric thickness of the substrate, which complicates high-frequency design due to little flexibility in choosing appropriate substrate structures. Since mechanical considerations put a lower limit on the physical thickness of integrated circuit substrates, it is difficult to avoid excessive loss when operating above 100 GHz in lines such as the microstrip where the field penetrates the whole substrate. In contrast, in coplanar waveguides the substrate thickness plays a lesser role; the fields are concentrated in the slots and are better confined on narrow apertures. Since the dimensions of the slots are limited only by photolithographic techniques, coplanar waveguides have more flexibility in design and, therefore, greater potential for low radiation loss and low dispersion.

However, even if coplanar waveguides radiate much less than a microstrip operating at the same frequency, as this frequency enters the submillimeter-wave region, the radiation loss increases and complicates the design. As a result, further reduction of parasitic radiation is required. A way to achieve this and be able to extend the operation of a coplanar waveguide into the submillimeter-wave region is to generate a surface-wave–free environment. This is possible with the use of a matched dielectric lens which has been exploited effectively to excite aperture-type radiating elements [28,29]. In such a structure, as in almost all CPW circuits, air-bridges (or bond wires) are used to connect the ground planes in order to suppress the coupled slotline mode. These air-bridges can be characterized by either using a rigorous full wave analysis [10,16,17,20] or a hybrid technique [11,14].

In this article, shielded and open CPW discontinuities will be analyzed using the space domain integral equation (SDIE) technique [8,9,12,30]. This method has shown excellent versatility in the study of a wide range of planar elements, and its accuracy has been demonstrated by comparison to measurements performed on a variety of open and shielded structures. The integral equation is formulated in terms of equivalent magnetic currents flowing on the slot apertures, as opposed to the full-wave technique presented in refs. [1,6,19], where an integral equation in terms of the electric current on the conducting surfaces is formed. The former technique is more appropriate for CPW problems where the ground planes approach the boundary surfaces, while the latter better fits

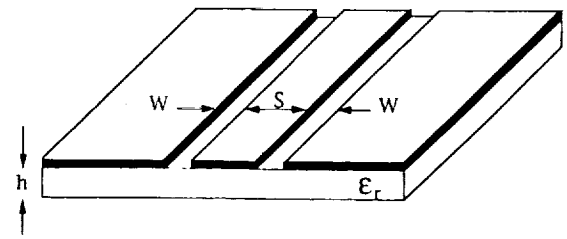

Figure 1. A generic geometry of a conventional coplanar waveguide structure.

problems having finite size conductors. The SDIE technique, as presented here, accurately takes into account all loss mechanisms by employing the appropriate Green's functions. Specifically, in the case of open coplanar waveguide discontinuities, the open space Green's function is expressed in terms of Sommerfield integrals so that radiation in the form of space and surface waves is accurately evaluated. This is in contrast to techniques used elsewhere [31,32], which simulate open space by setting the cover resistance to 377 Ω (forced radiation). Resonant properties and radiation losses for a number of shielded and open CPW stub discontinuities will be presented and guidelines for design will be given.

2. THEORY

A generic geometry for a conventional coplanar waveguide structure is shown in Figure 1. The dielectric layers supporting the coplanar structure are considered lossless and the conducting surfaces have zero ohmic loss. The two-slot apertures have width W and are separated by a distance S. With the application of the equivalence principle, the two slots can be replaced by equivalent magnetic currents ($\vec{M}_s^+$, $\vec{M}_s^-$) flowing on a perfectly conducting surface which covers the slot apertures (see Fig. 2). These magnetic currents radiate electric fields, which are continuous across the surface

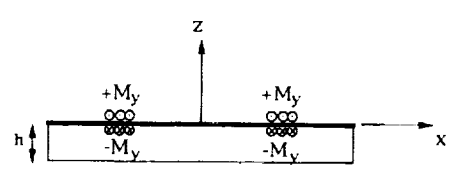

Figure 2. The equivalent problem obtained after the application of the Equivalence Principle. Only the longitudinal component of the surface magnetic current density is shown here.

of the slot apertures, as shown by the following equations:

$$\vec{M}_s^+ = -\vec{M}_s^- = \vec{M}_s \tag{1}$$

with

$$\vec{M}_s^+ = \vec{E}_s \times \hat{a}_z \qquad z \geq 0 \tag{2}$$

$$\vec{M}_s^- = \vec{E}_s \times (-\hat{a}_z) \qquad z \leq 0 \tag{3}$$

where $\vec{E}_s$ is the electric field in the slot apertures. Furthermore, continuity of the magnetic fields on the slot apertures results in the expression

$$\hat{a}_z \times [\vec{H}^+(\vec{M}^+) - \vec{H}^-(\vec{M}^-)] = \hat{a}_z \times \vec{H}^{\text{inc}} \tag{4}$$

where $\vec{H}^+(\vec{M}^+)$ and $\vec{H}^-(\vec{M}^-)$ are the magnetic fields radiated above and below the slots, respectively, and $\vec{H}^{\text{inc}}$ is the incident magnetic field exciting the CPW line. The magnetic fields may be expressed in terms of the unknown equivalent magnetic currents through a first-order Fredholm integral equation:

$$\vec{H}^{\pm} = \int\int_{S_{\text{CPW}}} [k_{\pm}^2 \bar{I} + \vec{\nabla}\vec{\nabla}] \cdot \bar{F}_m^{\pm}(\vec{r}/\vec{r}\,') \cdot \vec{M}_s^{\pm}(\vec{r}\,')\, ds'. \tag{5}$$

In eq. (5), S_{CPW} is the surface of the slot apertures and $k_{\pm}^2$ and $\bar{F}_m^{\pm}$ are the wavenumbers and magnetic field dyadic Green's functions in the regions above and below the CPW slots, respectively. The space domain integral eq. (4) is solved numerically using the Method of Moments [33]. In this solution scheme, the equivalent magnetic currents flowing on the slot apertures are expanded into a summation of piecewise sinusoidal basis functions, as shown:

$$\vec{M}(x', y') = \sum_{i=x,y} \hat{a}_i \sum_{n_i=1}^{N_i+1} \sum_{m_i=1}^{M_i+1} [V_{n_i m_i}]^T [\phi_{n_i m_i}(x', y')] \tag{6}$$

where $[V_{n_i m_i}]^T$ is the transposition of the vector of unknown current coefficients, and $[\phi_{n_i m_i}(x', y')]$ is the vector of the known basis functions. These functions are considered to be separable with respect to x' and y' parameters and have the following form:

$$\phi_{n_x m_x}(x', y') = f_{n_x}(x') g_{m_x}(y') \tag{7}$$

$$\phi_{n_y m_y}(x', y') = f_{n_y}(y') g_{m_y}(x') \tag{8}$$

with

$$f_{n_x}(x') = \begin{cases} \dfrac{\sin[\xi(x' - x_{n_x-1})]}{\sin(\xi \ell_x)} & x_{n_x-1} \leq x' \leq x_{n_x} \\ \dfrac{\sin[\xi(x_{n_x+1} - x')]}{\sin(\xi \ell_x)} & x_{n_x} \leq x' \leq x_{n_x+1} \\ 0 & \text{elsewhere} \end{cases} \tag{9}$$

$$g_{m_x}(y') = \begin{Bmatrix} 1 & y_{m_x} \leq y' \leq y_{m_x+1} \\ 0 & \text{elsewhere} \end{Bmatrix} \tag{10}$$

where ℓ_x is the subsection length and ξ the wave number in the dielectric. The functions $f_{n_y}(y')$ and $g_{m_y}(x')$ are given by eqs. (9) and (10) with x, x', y, and y' replaced by y, y', x, and x', respectively.

In view of eqs. (6) and (7), and with the application of Galerkin's method, equation (4) takes the matrix form:

$$[Y_{mn}^{\nu\mu}][V_{nm}^{\nu\mu}] = [I_{\nu\mu}] \tag{11}$$

with $Y_{mn}^{\nu\mu}$ the elements of the admittance matrix, $I_{\nu\mu}$ the elements of the excitation vector, and V_{nm} the amplitude coefficients for the magnetic current expansion functions. The excitation of the CPW structures is provided by ideal current sources appropriately placed on the slot apertures [8,9]. The solution of the matrix eq. (11) results in the evaluation of the equivalent magnetic currents and, consequently, the electric fields in the slots. From the field distribution, the network parameters may be computed by transmission line theory assuming that a single mode (the coplanar mode) is excited along the feeding lines [8,9]. For example, the input impedance of a one port CPW discontinuity can be evaluated from the positions of the minima and maxima of the electric field standing wave in the feeding lines. These minima and maxima positions may be obtained accurately by applying cubic spline fit on the field distribution derived through the method of moments. Such a technique has been successfully used previously, and has shown very good accuracy in characterizing multiport planar discontinuities [8,9,30,34].

The integral equation method, as it has been outlined above, applies to open and shielded problems in exactly the same way. What makes the solution of these two problems different is the form of the Green's function and the computational considerations required for its numerical

evaluation. Issues associated with the accurate evaluation of the Green's function and the complexities introduced by its form in the open and shielded CPW structures will be discussed in detail in following sections. The Green's function included in the integral eq. (5) is the electric vector potential produced by a unit magnetic current source and, as such, satisfies all the appropriate conditions on the boundary surfaces surrounding the volume of interest. Specifically, in *open* CPW problems, the magnetic field satisfies the radiation condition:

$$\lim_{\vec{r}\to\infty} \vec{r}\left(\frac{\partial \vec{H}}{\partial \vec{r}} - jk\vec{H}\right) = 0 \qquad (12)$$

while, in the case of *shielded* CPW, the spatial spectral components of the magnetic field given by eq. (5) satisfy the following equation on the cavity walls:

$$\hat{n}_w \times (\vec{\nabla} \times \vec{H}_k) = \overline{Z}^k_{sw} \cdot \vec{H}_k \qquad (13)$$

where k indicates the order of the spatial spectral field components, $\hat{n}_w$ is the vector normal to the walls toward the interior of the cavity, and $\overline{Z}^k_{sw}$ is the surface impedance dyad [35] for the kth spatial spectral component. In the case of perfectly conducting walls this dyad becomes identical to zero, while for resistive walls it becomes complex. The surface impedance spectral dyad is uniquely specified by the boundary conditions of the problem under study, and for this reason is restricted in form. This implies a very limited choice of values which could simulate physically realizable boundaries. Furthermore, there are no values for these spectral dyads, which could accurately simulate free space. Attempts to force radiation in shielded problems by arbitrarily choosing the spectral dyads can lead to quite inaccurate and inconclusive results, specifically with respect to radiation loss for circuit elements and radiation resistance for antenna elements. In the following sections, we discuss issues associated with the Green's function in shielded and open CPW and will also address the approach of *forced radiation*.

2.1. Shielded Coplanar Waveguides

When the CPW structure under study is shielded by a cavity (see Fig. 3), the excited electromagnetic field can be decomposed into a discrete infinite set of spectral solutions, each one satisfying the appropriate boundary conditions on the cavity walls. Similarly, the modified Green's function pertinent to the corresponding boundary value problem is a dyad

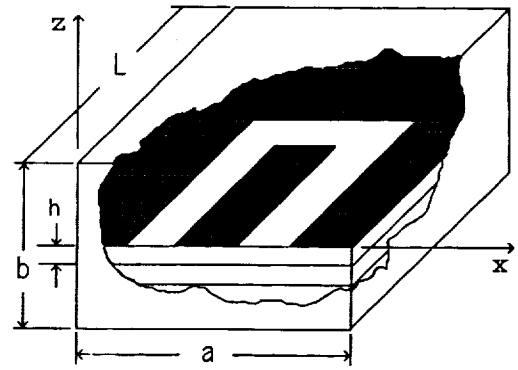

Figure 3. A coplanar waveguide shielded by a cavity filled with several dielectric layers.

$$\overline{G}^{\pm}_m = G^{\pm}_{xx}\,\hat{x}\hat{x} + G^{\pm}_{yx}\,\hat{y}\hat{x} + G^{\pm}_{yy}\,\hat{y}\hat{y} + G^{\pm}_{xy}\,\hat{x}\hat{y} \qquad (14)$$

which is defined as

$$\overline{G}^{\pm}_m = [k^2_{\pm}\overline{I} + \vec{\nabla}\vec{\nabla}] \cdot \overline{F}^{\pm}_m(\vec{r}/\vec{r}\,'). \qquad (15)$$

Each component of $G^{\pm}_m$ is a superposition of infinitely many discrete solutions and, consequently, can be written into the form of a double infinite sum of PG (Pincherle–Goursat) type, as shown below [8,9]

$$G^{+}_{xx}(\vec{r}/\vec{r}\,') = \sum_{m=0}^{\infty}\sum_{n=0}^{\infty} \frac{2e_n}{aL}\frac{1}{k^2_{z+} - k^2_{+}}[k^2_x P_+ + k^2_y Q_+] \sin(k_x x')\cos(k_y y')\sin(k_x x)\cos(k_y y) \qquad (16)$$

$$G^{+}_{yx}(\vec{r}/\vec{r}\,') = \sum_{m=1}^{\infty}\sum_{n=1}^{\infty} \frac{4}{aL}\frac{k_x k_y}{k^2_{z+} - k^2_{+}} \cdot [P_+ - Q_+] \sin(k_x x')\cos(k_y y')\cos(k_x x)\sin(k_y y) \qquad (17)$$

$$G^{+}_{xy}(\vec{r}/\vec{r}\,') = \sum_{m=1}^{\infty}\sum_{n=1}^{\infty} \frac{4}{aL}\frac{k_x k_y}{k^2_{z+} - k^2_{+}}[P_+ - Q_+] \cos(k_x x')\sin(k_y y')\sin(k_x x)\cos(k_y y) \qquad (18)$$

$$G_{yy}^{+}(\bar{r}/\bar{r}') = \sum_{m=0}^{\infty}\sum_{n=0}^{\infty} \frac{2e_m}{aL}\frac{1}{k_{z+}^2 - k_+^2}[k_y^2 P_+ + k_x^2 Q_1] \cos(k_x x')\sin(k_y y')\cos(k_x x)\sin(k_y y) \quad (19)$$

where

$$P_+ = \left(\frac{k_{z+}}{\omega\mu_+}\right)\frac{\omega\mu_+ + jk_{z+} Z_+^{\mathrm{LSE}} \tan(k_{z+} d_+)}{k_{z+} Z_+^{\mathrm{LSE}} + j\omega\mu_+ \tan(k_{z+} d_+)} \quad (20)$$

$$Q_+ = \left(\frac{\omega\epsilon_+}{k_{z+}}\right)\frac{k_{z+} + j\omega\epsilon_+ Z_+^{\mathrm{LSM}} \tan(k_{z+} d_+)}{\omega\epsilon_+ Z_+^{\mathrm{LSM}} + jk_{z+} \tan(k_{z+} d_+)} \quad (21)$$

$$e_n = 1 \quad n = 0$$
$$= 2 \quad n \neq 0 \quad (22)$$

$$e_m = 1 \quad m = 0$$
$$= 2 \quad m \neq 0 \quad (23)$$

$$k_x = \frac{m\pi}{a} \quad (24)$$

$$k_y = \frac{n\pi}{L} \quad (25)$$

$$k_+^2 = \omega^2\mu_+\epsilon_+ \quad (26)$$

$$k_+^2 = k_{z+}^2 + k_x^2 + k_y^2 \quad (27)$$

where d_+, μ_+, and ϵ_+ are the thickness, permeability, and permittivity of the dielectric layer directly above the slot aperture. In the above expressions, G_{ij}^+ denotes H_i^+ at $z = 0$ due to an infinitesimal M_j at $z' = 0$, where $i, j = x, y$. In addition, Z_+^{LSE} and Z_+^{LSM} are the LSE and LSM input impedances seen at $z = d_+$, which can be computed using transmission line theory. That is, each layer (except the ones surrounding the slot aperture) is replaced by an ideal transmission line with a characteristic impedance (Z_0^{LSE} or Z_0^{LSM}) and an eigenvalue, k_{z_i}, where

$$k_{z_i}^2 + k_y^2 + k_x^2 = \omega^2\mu_i\epsilon_i$$

$$(Z_0^{\mathrm{LSE}})^i = \frac{\omega\mu_i}{k_{z_i}}$$

$$(Z_0^{\mathrm{LSM}})^i = \frac{k_{z_i}}{\omega\epsilon_i}$$

The components of G_m^- are given by equations similar to eqs. (16)–(27) [8,9].

In the expressions for the modified Green's function, as given by (16)–(27), the summations over m and n are theoretically infinite. For the numerical solution of the integral equation, these summations are truncated, and the number of terms kept depends on the convergence behavior of the admittance matrix. Due to the nature of the problem solved here, the above summations have a convergence behavior similar to summations described elsewhere [34]. In the present work, the number of terms in the summations and the number of basis functions are chosen so that convergence of the scattering parameters of the coplanar waveguide discontinuity is achieved [8,9].

2.2. Open Coplanar Waveguides

When the cavity of a shielded CPW is moved to infinite, the environment surrounding the structure becomes open permitting real power to leak to free-space in the form of radiation modes (*space waves*) or guided modes (*surface and leaky waves*). From these two types of generated electromagnetic waves, the former have a continuous spectrum, while the latter a discrete one. As a result, the infinite summations in the shielded CPW case, which are characteristic of the Green's functions and the corresponding excited fields, turn into infinite integrals of Sommerfeld type. In the simplest case of an open CPW printed on a dielectric substrate of thickness h and with a dielectric constant, ϵ_r (see Fig. 1), the components of the magnetic-field dyadic Green's function, $\bar{F}_m^-$, are in the form [36]:

$$F_{xx}^- = F_{yy}^- = \frac{1}{j\omega\, 2\pi\mu_0}\int_0^\infty J_0(\lambda\rho)\frac{\lambda}{u} \frac{u\cosh[u(h+z)] + \epsilon_r\mu_0 \sinh[u(h+z)]}{f_1(\lambda, \epsilon_r, h)}\, d\lambda \quad (28)$$

$$F_{zx}^- = \cot(\phi)\, F_{zy}^- = -\frac{1 - \epsilon_0\epsilon_r}{j\omega\, 2\pi\mu_0}\cos(\phi) \int_0^\infty J_1(\lambda\rho)\frac{\sinh(uz)}{\lambda^2 f_1(\lambda, \epsilon_r, h)\, f_2(\lambda, \epsilon_r, h)}\, d\lambda. \quad (29)$$

The functions, $f_1(\lambda, \epsilon_r, h)$ and $f_2(\lambda, \epsilon_r, h)$, are the characteristic equations for the surface waves, TE

and TM, to the dielectric interface, and are given by:

$$f_1(\lambda, \epsilon_r, h) = \epsilon_r u_0 \cosh(uh) + u \sinh(uh) \quad (30)$$

$$f_2(\lambda, \epsilon_r, h) = u_0 \sinh(uh) + u \cosh(uh) \quad (31)$$

$$u_0^2 = \lambda^2 - \omega^2 \mu_0 \epsilon_0 \quad (32)$$

$$u^2 = \lambda^2 - \omega^2 \mu_0 \epsilon_0 \epsilon_r. \quad (33)$$

This formulation allows for a dielectric substrate or half space of any dielectric constant, thus, the components of $\overline{F}_m^+$ can also be obtained from the same equations.

For the solution of eq. (11), most of the computation effort is spent on the evaluation of the elements of the admittance matrix. The complexity in these computations comes from the Sommerfeld integration as it is combined with multiple space integrals. As a result, these integrals are computed using a special treatment, which consists of numerical and analytical techniques as described elsewhere [36,37].

2.3. Forced Radiation

There has been an attempt to model radiation loss from printed circuits by setting the resistance of the top wall of the shielding box to 377 Ω [31,32]. As noted above, such an attempt can lead to quite inaccurate and inconclusive results. In fact, forced radiation simulations may predict a loss factor much larger than the "actual" one, which can only be obtained through a rigorous analysis of the open structure [32]. This is due to the fact that there are no values for the surface impedance dyad in eq. (13) which could accurately simulate free-space environment. In the next section, a CPW series stub inside a box with the resistance of the lower and bottom walls set to 377 Ω will be analyzed. Radiation loss predicted from such a simulation will be compared to the "actual" radiation loss. In addition, it will be shown that the distance at which these walls are positioned is a critical parameter that affects the derived results considerably.

3. NUMERICAL EXAMPLES

Figure 4 shows the normalized capacitive reactance for an open-end CPW discontinuity of shielded and open type. The results for the two

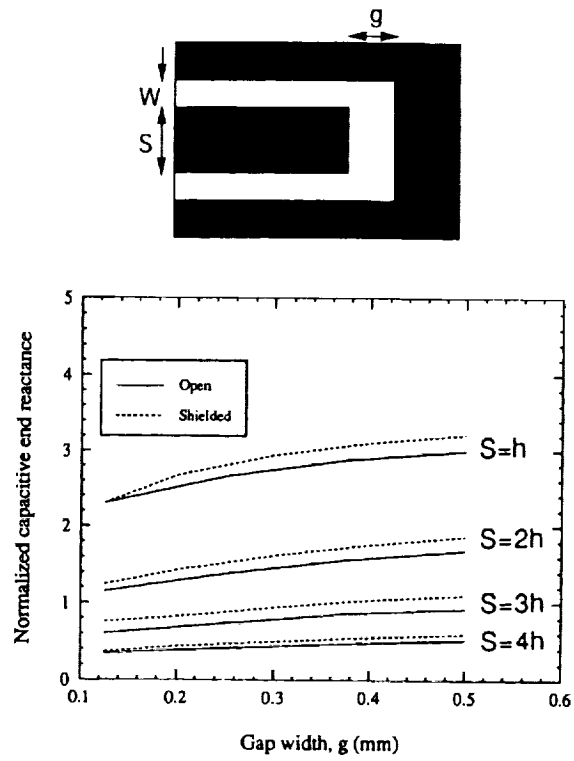

Figure 4. Normalized capacitive end reactance of an open-end CPW; W = 0.25 mm, h = 0.5 mm, and ϵ_r = 13.1

cases are in good agreement, differing only by the amount of power radiated into the substrate and free space. The radiation loss from this one-port discontinuity (Fig. 5) increases with the gap width and the center conductor width.

Two series stub geometries are shown in Figure 6, and the magnitude of S_{12} of both stubs with a mean length of 1.35 mm is given in Figure 7. This

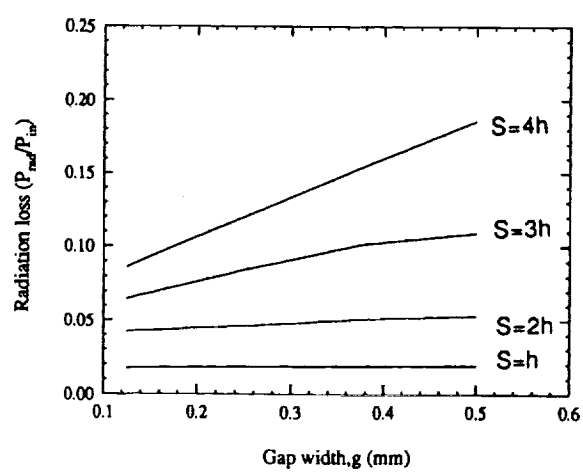

Figure 5. Radiation loss of a CPW open-end discontinuity. Dimensions are the same as in Figure 4.

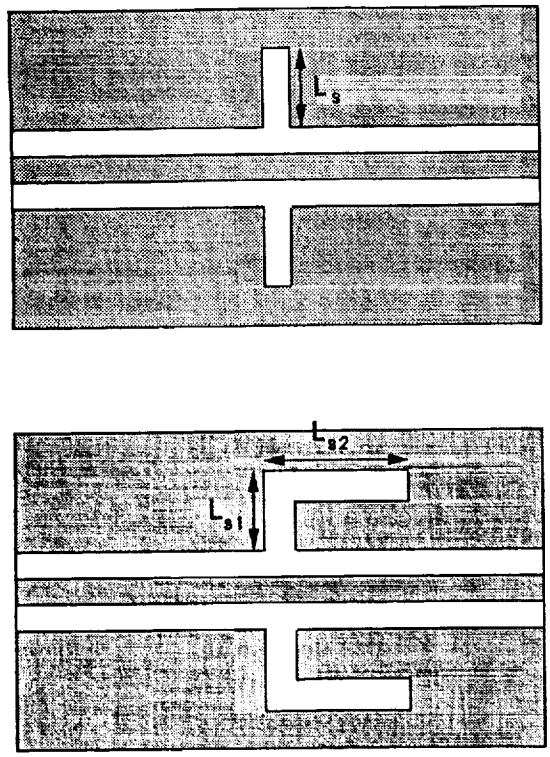

Figure 6. Two different CPW series stub geometries.

plot indicates that the stub geometry may affect the resonant frequency by as much as 7%. Specifically, the straight stub has a resonance at about 22 GHz, while for the bent geometry the resonance is 1.5 GHz higher. The sharper resonance of the nonshielded bent stub indicates lower radiation loss than the straight stub. As shown in Figure 8, the straight stub experiences severe loss which exceeds 25% of the input power. The parasitic radiation is high in this example because the electric fields in the two-stub slots are in phase, and thus they radiate constructively. In contrast, the electric fields in the bent geometry are 180° out of phase.

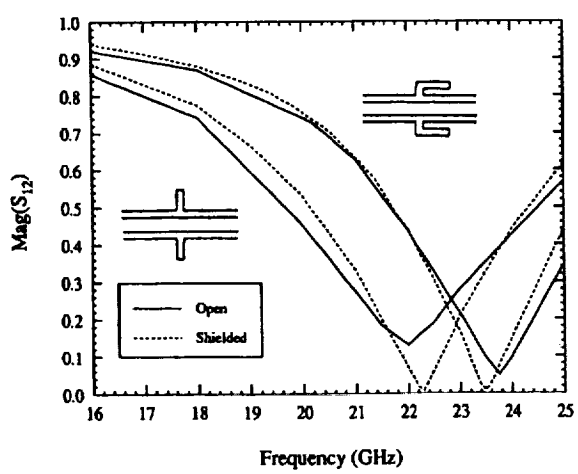

Figure 7. Mag(S_{12}) of the CPW series stub geometries with mean length of 1.35 mm, W = 0.225 mm, S = 0.45 mm, h = 0.635 mm, ϵ_r = 9.9, L_s = 1.35 mm, L_{s1} = 0.45 mm, and L_{s2} = 1.125mm.

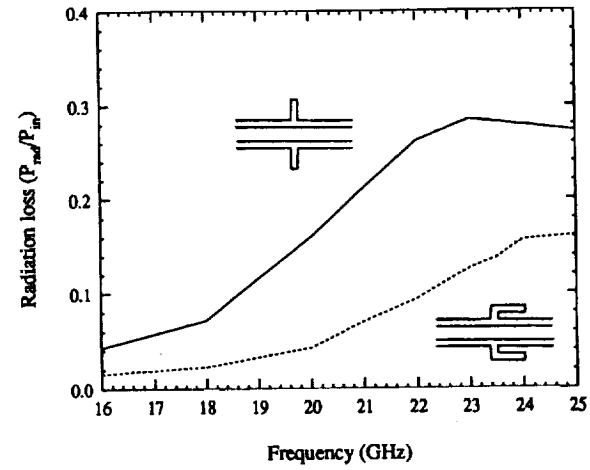

Figure 8. Radiation loss, $1 - |S_{11}|^2 - |S_{12}|^2$, of the CPW series stub geometries. Dimensions are the same as in Figure 7.

Four different CPW shunt stubs are shown in Figure 9, where air-bridges are used to connect the ground planes of the CPW stub in order to prevent the excitation of the coupled slotline mode. A comprehensive theoretical and experimental study of these stubs has been performed [11,38]; however, for illustration purposes, only the measured radiation loss of the open-end stubs will be presented here. Figure 10 shows the measured loss factor of these stubs, which includes radiation, conductor, and dielectric losses. Since the stubs are all of the same length, a comparison of the loss factor can provide a measure of the radiation loss. It can be noticed that loss is maximum at the resonant frequency for all stubs, which agrees with the radiation behavior of microstrip stubs above resonance [30]. Furthermore, the loss factor for straight stubs is larger than that for bent stubs. This is due to the fact that, in the case of bent stubs, the fields radiated by the coupled slotline modes in the two opposing stubs partially cancel. It can be seen also that the air-bridges reduce radiation loss by shorting out the coupled slotline model in the CPW stubs. But, it is still noted that the straight stubs have increasing radiation loss after the first resonant frequency.

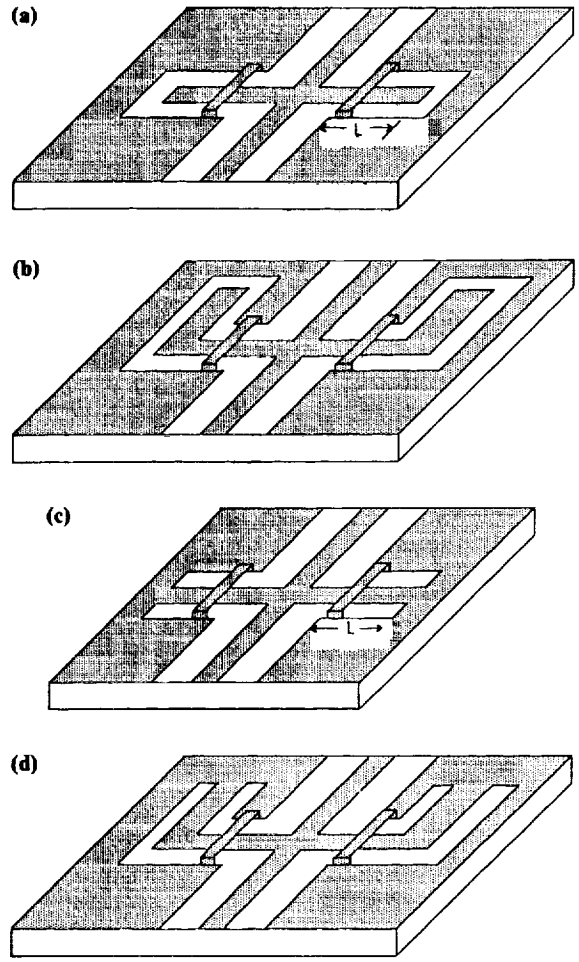

Figure 9. Different CPW shunt stubs. (a) Straight open-end CPW stub. (b) Bent open-end CPW stub. (c) Straight short-end CPW stub. (d) Bent short-end CPW stub.

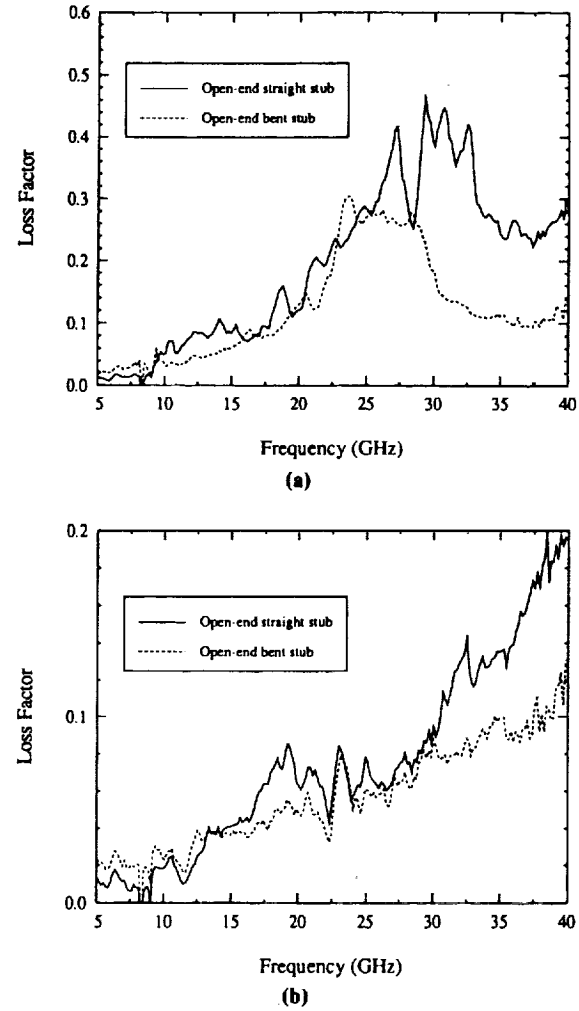

Figure 10. The measured loss factor ($1 - |S_{11}|^2 - |S_{12}|^2$) of the open-end shunt stubs (a) without air-bridges and (b) with air-bridges. S = 75 μm, W = 50 μm, h = 400 μm, ϵ_r = 13, mean stub length = 1100 μm; the slots and center conductor of the stubs have equal widths of 25 μm.

Figure 11 compares the radiation loss of a straight series stub, as predicted by setting the resistance of the top and bottom walls of the rectangular box to 377 Ω, to the "actual" radiation loss. The top and bottom walls are at a distance D from the slot aperture and the lower interface of the dielectric substrate, respectively. In addition, the parameter "a" indicates the cavity width. It can be noticed that the parameter D undoubtedly affects the final result. Furthermore, there is no specific D at which one can be sure that the predicted radiation loss is the closest to the actual one. Thus, such a simulation cannot provide any consistent results with respect to the radiation loss in printed circuits or radiation resistance in printed antennas. Nonetheless, such a simulation can still predict the resonant frequency of the circuit or antenna element.

4. CONCLUSIONS

A comparative study between open and shielded CPW discontinuities has been presented. In this study, the space domain integral equation method was used to characterize several discontinuities such as the open-end CPW and CPW series stubs. It has been found that bent CPW stubs tend to radiate less than straight ones, which makes them more appropriate for use in microwave circuits. The notion of "forced radiation" simulation has been presented in which an open structure is simulated by setting the resistances of the top and bottom walls of the shielding box to 377 Ω. The results of such a simulation have been compared

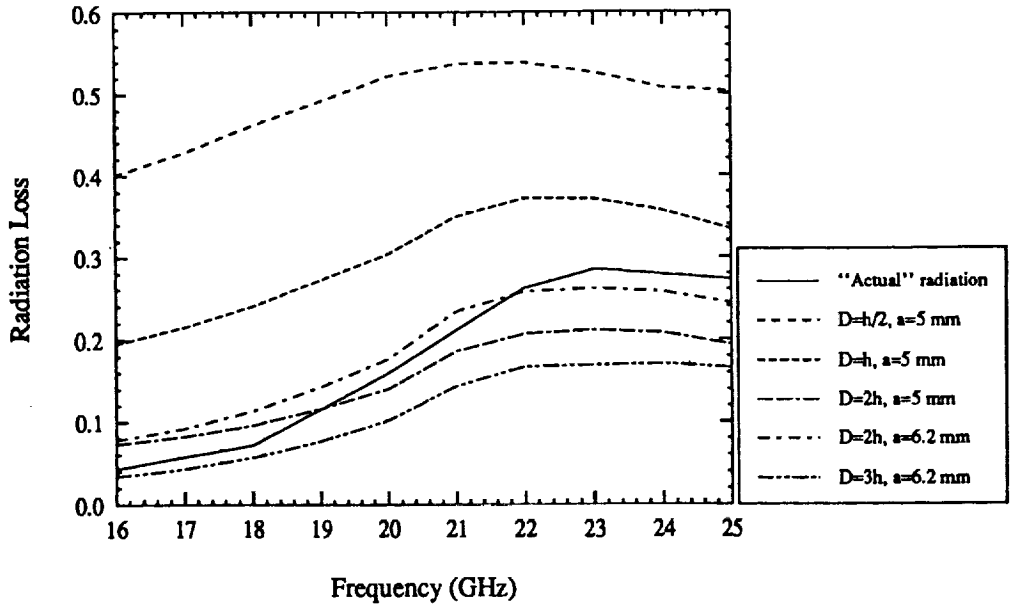

Figure 11. Forced radiation loss from a straight series stub as compared to "actual" loss. Dimensions are the same as in Figure 7.

to the "actual" radiation loss obtained rigorously. It has been found that these results are not reliable since they are considerably affected by the size of the cavity.

ACKNOWLEDGMENTS

This work was partially supported by the National Science Foundation under contract ECS-8657951 and partially by Texas Instruments and Hughes Research Laboratories, Malibu, CA.

REFERENCES

1. R. W. Jackson, "Considerations in the use of coplanar waveguide for millimeter wave integrated circuits," *IEEE Trans. Microwave Theory Tech.*, Vol. 34, Dec. 1986, pp. 1450–1456.
2. R. N. Simons and G. E. Ponchak, "Modeling of some coplanar waveguide discontinuities," *IEEE Trans. Microwave Theory Tech.*, Vol. 36, Dec. 1988, pp. 1796–1803.
3. G. Kibuuka, R. Bertenburg, M. Naghed, and I. Wolff, "Coplanar lumped elements and their application in filters on ceramic and gallium arsenide substrates," *Proc. 19th Eur. Microwave Conf.*, London, Sept. 1989, pp. 656–661.
4. C. W. Kuo and T. Itoh, "Characterization of the coplanar waveguide step discontinuity using the transverse resonance method," *Proc. 19th Eur. Microwave Conf.*, London, Sept. 1989, pp. 662–665.
5. N. Koster, S. Koblowski, R. Bertenburg, S. Heinen, and I. Wolff, "Investigation of air bridges used for MMICs in CPW technique," *Proc. 19th Eur. Microwave Conf.*, London, Sept. 1989, pp. 666–671.
6. R. W. Jackson, "Mode conversion at discontinuities in finite-width conductor-backed coplanar waveguide," *IEEE Trans. Microwave Theory Tech.*, Vol. 37, Oct. 1989, pp. 1582–1589.
7. M. Drissi, V. Fouad Hanna, and J. Citerne, "Analysis of coplanar waveguide radiating end effects using the integral equation technique," *IEEE Trans. Microwave Theory Tech.*, Vol. 39, Jan. 1991, pp. 112–116.
8. N. Dib and P. Katehi, "Modeling of shielded CPW discontinuities using the space domain integral equation method (SDIE)," *J. Electromag. Waves Appl.*, April 1991, pp. 503–523.
9. N. Dib, P. Katehi, G. Ponchak, and R. Simons, "Theoretical and experimental characterization of coplanar waveguide discontinuities for filter applications," *IEEE Trans. Microwave Theory Tech.*, May 1991, pp. 873–882.
10. M. Rittweger, M. Abdo, and I. Wolff, "Full-wave analysis of coplanar discontinuities considering three-dimensional bond wires," *1991 IEEE MTT-S Int. Microwave Symp. Dig.*, pp. 465–468.
11. N. Dib, P. Katehi, and G. Ponchak, "Analysis of shielded CPW discontinuities with air bridges," *1991 IEEE MTT-S Int. Microwave Symp. Dig.*, pp. 469–472.
12. W. Harokopus and P. Katehi, "Radiation loss from open CPW discontinuities," *1991 IEEE MTT-S Int. Microwave Symp. Dig.*, pp. 743–746.

13. M. Naghed, M. Rittweger, and I. Wolff, "A new method for the calculation of the equivalent inductances of coplanar waveguide discontinuities," *1991 IEEE MTT-S Int. Microwave Symp. Dig.*, pp. 747–750.
14. R. Bromme and R. Jansen, "Systematic investigation of CPW MIC/MMIC structures using strip/slot 3D electromagnetic simulator," *1991 IEEE MTT-S Int. Microwave Symp. Dig.*, pp. 1081–1084.
15. N. Dib and P. Katehi, "The effect of mitering on CPW discontinuities," *Proc. 21st Eur. Microwave Conf.*, Sept. 1991, pp. 223–228.
16. T. Becks and I. Wolff, "Calculation of three-dimensional passive structures including bond-wires, via-holes and air-bridges using the spectral domain analysis method," *Proc. 21st Eur. Microwave Conf.*, Sept. 1991, pp. 571–576.
17. M. Rittweger, N. Koster, S. Koblowski, R. Bertenburg, S. Heinen, and I. Wolff, "Full-wave analysis of a modified coplanar air bridge T-junction," *Proc. 21st Eur. Microwave Conf.*, Sept. 1991, pp. 993–998.
18. U. Mueller, M. Rittweger, and A. Beyer, "Coplanar short considered by the TLM-method with symmetrical condensed nodes," *Proc. 21st Eur. Microwave Conf.*, Sept. 1991, pp. 999–1003.
19. J. McClean, A. Wieck, K. Ploog, and T. Itoh, "Fullwave analysis of open-end discontinuities in coplanar stripline and finite ground plane coplanar waveguide in open environments using a deterministic spectral domain approach," *Proc. 21st Eur. Microwave Conf.*, Sept. 1991, pp. 1004–1007.
20. K. Beilenhoff, W. Heinrich, and H. Hartnagel, "The scattering behavior of air bridges in coplanar MMICs," *Proc. 21st Eur. Microwave Conf.*, Sept. 1991, pp. 1131–1135.
21. M. Naghed and I. Wolff, "Equivalent capacitances of coplanar waveguide discontinuities and interdigitated capacitors using a three dimensional finite difference method," *IEEE Trans. Microwave Theory Tech.*, Vol. 38, Dec. 1991, pp. 1808–1815.
22. C. P. Wen, "Coplanar waveguide: A surface strip transmission line suitable for nonreciprocal gyromagnetic device applications," *IEEE Trans. Microwave Theory Tech.*, Vol. 17, Dec. 1969, pp. 1087–1090.
23. M. Houdart, "Coplanar lines: Application to broadband microwave integrated circuits," *Proc. 6th Eur. Microwave Conf.*, Rome, 1976, pp. 49–53.
24. P. A. Holder, "X-band microwave integrated circuits using slotlines and coplanar waveguide," *Radio Electronics Engineering*, Vol. 48, Jan./Feb. 1978, pp. 38–42.
25. R. N. Simons, "Propagation characteristics of some novel coplanar waveguide transmission lines on GaAs at mm-wave frequencies," *1986 Conf. on Millimeter Wave/Microwave Measurements and Standards for Miniaturized Systems*, pp. 79–92.
26. G. Ghione and C. U. Naldi, "Coplanar waveguides for MMIC applications: effect of upper shielding, conductor backing, finite-extent ground planes, and line-to-line coupling," *IEEE Trans. Microwave Theory Tech.*, Vol. 35, March 1987, pp. 260–267.
27. T. Hirota, Y. Tarusawa, and H. Ogawa, "Uniplanar MMIC hybrids—a proposal of a new MMIC structure," *IEEE Trans. Microwave Theory Tech.*, Vol. 35, June 1987, pp. 576–581.
28. L. P. B. Katehi, "Novel transmission lines for the submillimeter-wave region," *IEEE Proc.* (to appear).
29. W. P. Harokopus, B. Cormanyos, L. P. B. Katehi, and G. M. Rebeiz, "Theoretical and experimental study of lens-supported aperture antennas," *IEEE Trans. Ant. Propagat.* (to appear).
30. W. P. Harokopus and P. B. Katehi, "Characterization of microstrip discontinuities on multilayer dielectric substrates including radiation losses," *IEEE Trans. Microwave Theory Tech.*, Dec. 1989, pp. 2058–2065.
31. *Sonnet Software User's Manual*, Release 2.2, Nov. 1991.
32. U. Rohde, "Improved noise modeling of GaAs FETs, Part 1: Using an enhanced equivalent circuit technique," *Microwave J.*, Nov. 1991, pp. 87–101.
33. R. F. Harrington, *Field Computation by Moment Methods*, Macmillan, New York, 1968.
34. L. P. Dunleavy and P. B. Katehi, "Generalized method for analyzing shielded thin microstrip discontinuities," *IEEE Trans. Microwave Theory Tech.*, Vol. 36, Dec. 1988, pp. 1758–1766.
35. T. E. van Deventer, P. B. Katehi, and A. C. Cangellaris, "An integral equation method for the evaluation of conductor and dielectric losses in high frequency interconnects," *IEEE Trans. Microwave Theory Tech.*, Dec. 1989, pp. 1964–1971.
36. P. B. Katehi, "A space domain integral equation approach in the analysis of dielectric-covered slots," *Radio Sci.*, Vol. 24, March/April 1989, pp. 253–260.
37. P. B. Katehi and N. G. Alexopoulos, "Real axis integration of Sommerfeld integrals with applications to printed circuit antennas," *J. Math. Phys.*, Vol. 24(3), March 1983, pp. 527–533.
38. N. Dib, G. Ponchak and L. P. Katehi, "A comprehensive theoretical and experimental study of coplanar waveguide shunt stubs," *1992 IEEE MTT-S Int. Microwave Symp.*, New Mexico, June 1992, pp. 947–950.

BIOGRAPHY

Nihad Dib received the BSc and MSc degrees in Electrical Engineering from Kuwait University in 1985 and 1987, respectively. He worked as a Laboratory Engineer in the ECE Department at Kuwait University for two years. He has been with the Radiation Laboratory, University of Michigan, since September of 1988, where he is currently working toward his PhD degree. He is a recipient of a predoctoral Rackham Fellowship, University of Michigan, during the 1991–92 academic year. His research deals mainly with the construction of CAD programs for the analysis of coplanar waveguide structures.

William P. Harokopus, Jr. was born in Detroit, Michigan, in 1963. He received his BSEE, MSEE, and PhD degrees from the University of Michigan in 1985, 1986, and 1991, respectively. From 1987–1991 he worked as a research assistant in the Radiation Lab at the University of Michigan. Duties consisted of the development of numerical techniques to study the behavior of microstrip and coplanar waveguide discontinuities and circuits. In 1991 he joined the Advanced Technology and Components Division of Texas Instruments in Mckinney, Texas. He is currently working as an antenna engineer in the Antenna/Non-Metallics Department.

George Ponchak received his BEE from Cleveland State University, Cleveland, Ohio, in 1983 and the MSEE from Case Western Reserve University, Cleveland, in 1987. He joined the NASA Lewis Research Center, Cleveland, in July of 1983 as a member of the Space Communications Division. Since joining NASA he has been engaged in research in solid-state technology development, transmission lines, and monolithic microwave integrated circuits (MMICs). He is currently pur- his PhD degree at the University of Michigan.

Linda P. B. Katehi received the BSEE degree from the National Technical University of Athens, Greece, in 1977 and the MSEE and PhD degrees from the University of California, Los Angeles, in 1981 and 1984, respectively. In September 1984, she joined the faculty of the EECS Department of the University of Michigan, Ann Arbor. Since then, she has been involved in the modeling and computer-aided design of millimeter and near-millimeter wave monolithic circuits and antennas. In 1984 she received the W. P. King Award and, in 1985, the S. A. Schelkunoff Award from the Antennas and Propagation Society. In 1987, she received an NSF Presidential Young Investigator Award and an URSI Young Scientist Fellowship. She is a senior member of IEEE AP-S, MTT-S, and a member of Sigma Xi and URSI Commission D.

N94-20502

A Theoretical and Experimental Study of Coplanar Waveguide Shunt Stubs

Nihad I. Dib, *Member, IEEE*, George E. Ponchak, *Member, IEEE*, and Linda P. B. Katehi, *Senior Member, IEEE*

***Abstract*—A comprehensive theoretical and experimental study of straight and bent coplanar waveguide (CPW) shunt stubs is presented. In the theoretical analysis, the CPW is assumed to be inside a cavity, while, the experiments are performed on open structures. For the analysis of CPW discontinuities with air-bridges, a hybrid technique has been developed which has been validated through extensive theoretical and experimental comparisons. Throughout this study, the effect of the cavity resonances on the behavior of the stubs with and without air-bridges is investigated. In addition, the encountered radiation loss due to the discontinuities is evaluated experimentally.**

I. Introduction

COPLANAR WAVEGUIDE (CPW) is rapidly becoming the transmission line of choice in high frequency applications and is successfully competing against the microstrip which has been the primary structure for hybrid and monolithic circuits. Due to many years of microstrip use, a large body of published data and CAD software pertaining to low- and high-frequency microstrip circuit and antenna design has been widely available. On the contrary, models for shielded or open coplanar waveguide circuit design are still under development [1]–[22]. Nevertheless, despite this scarcity of reliable circuit models, CPW has provided an attractive alternative to conventional microstrip lines at high frequencies due to many appealing properties [23]–[31].

While there is no need for via holes in CPW circuits, air-bridges are fundamental components required to connect the ground planes for suppression of the coupled slotline mode. In the past few years, there has been several attempts to characterize, theoretically and/or experimentally, CPW discontinuities with air-bridges or bond wires [16]–[22]. The full wave computationally intensive Finite Difference Time Domain technique was used in [17], [21] to analyze a CPW shunt stub with bond wires and a modified CPW air-bridge T-junction. On the other hand, the Finite Difference Frequency Domain method was used in [22] to treat two common types of CPW air-bridges where it was found that the reflection coefficient (or S_{11}) varies linearly with frequency. This fact suggests that a typical air-bridge can be modeled as a freuency dependent lumped element [16], [18], [19], [28], [32]. With this in mind, a hybrid technique has been developed to analyze CPW discontinuities with air-bridges. In this technique, the frequency dependent equivalent circuit of the discontinuity, with the air-bridges removed, is derived using the Space Domain Integral Equation (SDIE) method [8], [9]. Then, this equivalent circuit is modified by incorporating the air-bridge parasitic inductance and capacitance which are evaluated using a quasistatic model.

Manuscript received Feb. 4, 1992; revised Apr. 27, 1992. This work was supported by the National Science Foundation under contract ECS-8657951.

N. I. Dib and L. P. B. Katehi are with the Radiation Lab. University of Michigan, 3228 EECS Building, Ann Arbor, MI 48 109-2122.

G. E. Ponchak is with the NASA Lewis Research Center, 21 000 Brookpark Road, MS-54-5, Cleveland, OH 44135.

IEEE Log Number 9204032.

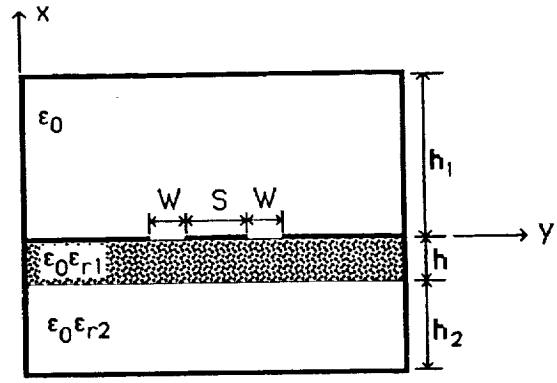

Fig. 1. A cross section of a CPW inside a cavity.

In this paper, the above mentioned hybrid technique is used to study a variety of CPW shunt stub geometries (Fig. 2) and the validity of the model is verified by performing extensive measurements. The scattering parameters of the stubs with and without air-bridges are presented and a very good agreement is found between theoretical and experimental data. In addition, since a shielded structure is assumed in the formulation of the theory, the effect of cavity resonances on the behavior of these stubs is shown. Moreover, the encountered radiation loss in open discontinuities is investigated experimentally.

II. Theory

In the theoretical analysis, the CPW under consideration is assumed to be shielded by a rectangular cavity with perfectly conducting walls as shown in Fig. 1. As pointed out in the introduction, a hybrid technique is used to analyze coplanar waveguide discontinuities with air-bridges. First, the frequency dependent equivalent circuit of the discontinuity, with the air-bridges removed, is derived using the Space Domain Integral Equation (SDIE) method [8], [9]. Then, this equivalent circuit is modified by incorporating the parasitic reactances introduced by the air-bridges. Only the main steps of the SDIE method are given here, since the details can be found in [8], [9].

© 1993 IEEE. Reprinted, with permission, from IEEE Transactions on Microwave Theory and Techniques, vol. 41, no. 1, Jan. 1993, pp. 38-44.

PRECEDING PAGE BLANK NOT FILMED

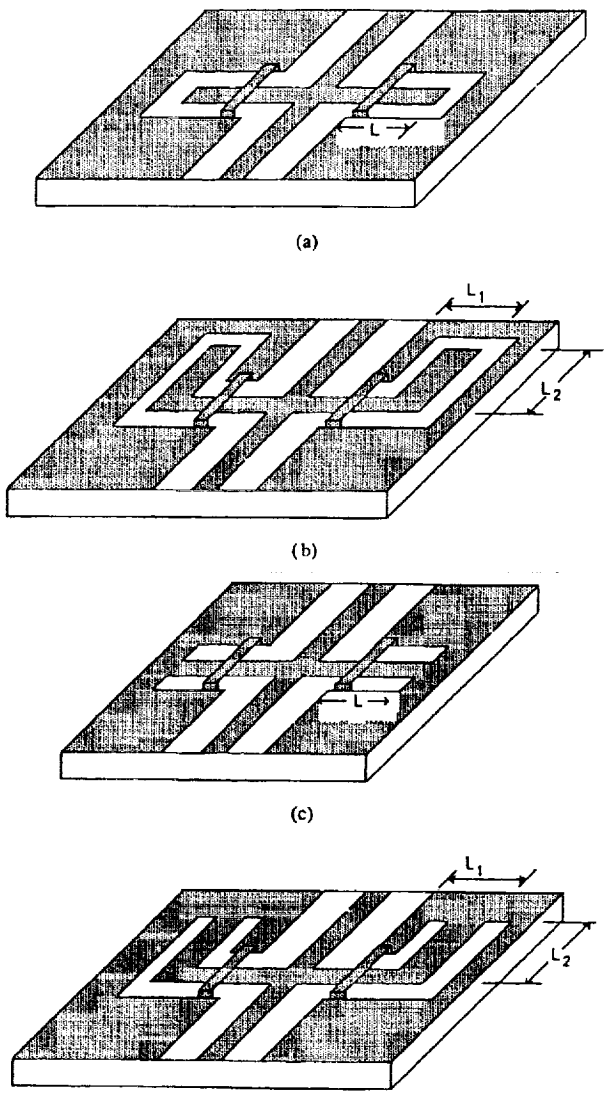

Fig. 2. Different CPW shunt stubs. (a) Straight open-end CPW stub. (b) Bent open-end CPW stub. (c) Straight short-end CPW stub. (d) Bent short-end CPW stub.

A. SDIE Method

The boundary problem pertinent to any CPW discontinuity may be split into two simpler ones by applying the equivalence principle which introduces an equivalent magnetic current $\overline{M}_s$ on the slot apertures [8]–[10]. This surface magnetic current radiates an electromagnetic field in the two waveguide regions (above and below the slots) so that the continuity of the tangential electric field on the surface of the slots is satisfied. The remaining boundary condition to be applied is the continuity of the tangential magnetic field on the surface of the slot apertures which leads to the following integral equation

$$\hat{x} \times \int_S \int [\overline{\overline{G}}_0^h(\vec{r}/\vec{r}') + \overline{\overline{G}}_1^h(\vec{r}/\vec{r}')] \cdot \overline{M}_s(\vec{r}')ds' = \overline{J}_s \qquad (1)$$

with $\overline{\overline{G}}_{0,1}^h$ the magnetic field dyadic Green's functions in the two waveguide regions [8], [9] and $\overline{J}_s$ an assumed ideal electric current source exciting the coplanar waveguide mode. The integral equation which is formulated here in terms of equivalent magnetic currents flowing on the slot apertures is different from the fullwave technique presented in [1], [5], [14], where an integral equation in terms of the electric current on the conducting surfaces is formed. The former technique is more appropriate for CPW problems where the ground planes approach the boundary surfaces (open or shielded), while the latter better fits problems with finite size ground conductors.

The integral equation (1) is solved using the Method of Moments [33] where the unknown magnetic current is expanded in terms of rooftop basis functions. Then, Galerkin's method is applied to reduce the above equation to a linear system of equations

$$\begin{pmatrix} Y_{yy} & Y_{yz} \\ Y_{zy} & Y_{zz} \end{pmatrix} \begin{pmatrix} V_y \\ V_z \end{pmatrix} = \begin{pmatrix} I_z \\ I_y \end{pmatrix}. \qquad (2)$$

In the above, $Y_{ij}(i = y, z; j = y, z)$ represent blocks of the admittance matrix, V_i is the vector of unknown y and z magnetic current amplitudes, and I_j is the excitation vector which is identically zero everywhere except at the position of the sources. The solution of the matrix equation (2) results in the evaluation of the equivalent magnetic currents and consequently the electric fields on the slots.

In case of isolated CPW structures which are symmetric with respect to the center line, the coupled slotline mode is not excited, and hence, the aperture fields in the feeding lines form standing waves of the fundamental coplanar waveguide mode. Consequently, using the derived electric field, transmission line theory can be utilized to determine the scattering parameters and derive a lumped element equivalent circuit for the discontinuity. In case of asymmetric CPW discontinuities, the derived field in the feeding lines is the sum of the fundamental coplanar and slotline modes each one having its own spatial parameters, and consequently, a special treatment is needed to separate the two modes and derive the scattering parameters of the discontinuity [35].

B. Modeling the Air-Bridges

Fig. 3(a) shows the equivalent circuit (π-model) for the CPW discontinuities shown in Fig. 2 with the air-bridges removed. X_1 and X_2 represent the reactances due to the coplanar waveguide mode excited in the CPW stub, while X_3 is due to the coupled slotline mode [34]. The reference planes at which these reactances are evaluated are at the ends of the uniform feeding lines. It should be noted that in the case of straight stubs, the two reactances X_1 and X_2 are equal due to the symmetry of the circuit. Thus, only two independent excitations are needed to evaluate the elements of the equivalent circuit, as opposed to three required in the case of the bent stubs ($X_1 \neq X_2$) [9].

Fig. 3(b) shows the new equivalent circuit after taking the air-bridges into consideration. The air-bridges can be modeled as sections of an air-filled microstrip line [16], [28], and simple formulas can be used to evaluate the parasitic capacitance

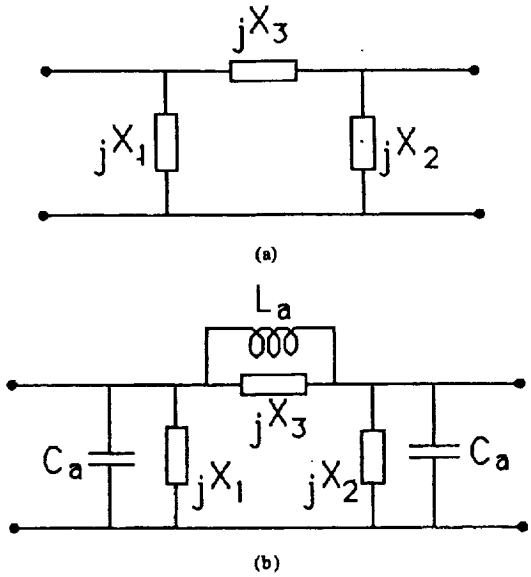

Fig. 3. (a)Equivalent circuit of the CPW discontinuities shown in Fig. 2 without air-bridges. (b) The modified equivalent circuit after taking the air-bridges into consideration.

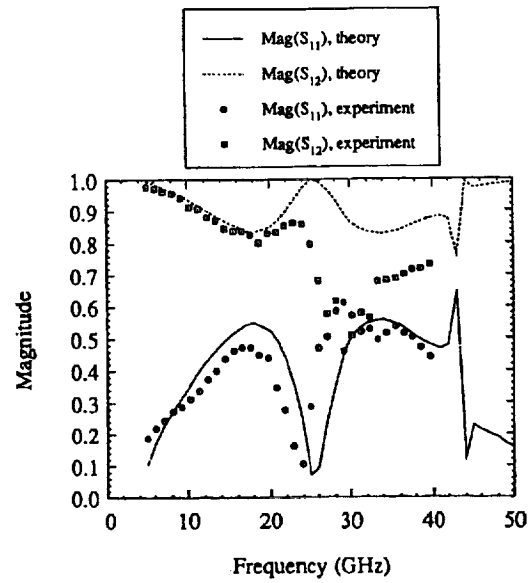

Fig. 4. Scattering parameters of the straight open-end stub without air-bridges ($L = 1100\,\mu$m).

C_a and inductance L_a [34]. Alternatively, a parallel plate waveguide model can be employed to evaluate the same parasitic effects. It has been found that the difference in the values of the parasitic reactances as predicted by the two models has a negligible effect on the performance of the circuit. Finally, new scattering parameters are evaluated from the modified equivalent circuit. It should be emphasized that such a hybrid technique assumes that the air-bridges are positioned as close to the cross junction as possible, which is always the case in practice. Moreover, it is worth mentioning that the CPU time required for the evaluation of the scattering parameters (taking into account all the existing physical symmetries) ranges from one to three minutes for each frequency on Apollo Domain 10 000.

III. Results and Discussion

In the numerical results shown here, the considered CPW discontinuities are suspended inside a rectangular cavity, as shown in Fig. 1, with $h = 400\,\mu$m, $\epsilon_{r1} = 13$, $\epsilon_{r2} = 1$, $S = 75\,\mu$m, $W = 50\,\mu$m, and $h_1 = h_2 = 1.2$ mm. The characteristic impedance of such a line is approximately 50Ω. On the other hand, the slots and center conductor of the CPW stubs have equal widths of $25\,\mu$m. In addition, in the case of the open-end stubs, the width of the open-end is $25\,\mu$m. In all examples presented here, the stubs are placed symmetrically at the center of the cavity with length approximately equal to $3\lambda_g$.

The experiments were performed in an open environment with the CPW circuits fabricated on $400\,\mu$m thick GaAs using lift-off processing. The CPW center strip and ground planes consist of 200 \AA of Cr and $1.5\,\mu$m of Au. The air-bridges have $10\,\mu$m square posts and are $14\,\mu$m wide. The air-bridge thickness and height are $1.0\,\mu$m and $3.0\,\mu$m, respectively. The GaAs circuit rests on a piece of 3.175 mm 5880 RT/duroid which has a dielectric constant of 2.2.

It will be shown that the theoretical and experimental data agree despite the difference in ϵ_{r2} of the substrate ($\epsilon_{r2} = 1$ versus 2.2). This is due to the relatively large thickness of the GaAs substrate layer as compared to S + 2W. The choice of $\epsilon_{r2} = 1$ in the theoretical calculations is intended in order to avoid some of the unwanted cavity resonances.

The circuits were tested with an HP 8510 network analyzer and a Cascade probe station. The calibration standards for a TRL calibration were fabricated on the wafer to allow calibration to the reference planes of the CPW stubs. To cover the 5–40 GHz bandwidth, three delay lines were used. The probe positioning on the wafer was determined to be repeatable to within $3\,\mu$m which creates a maximum error in the phase of S_{21} of 0.76° at 40 GHz.

A. Open-End Shunt Stubs

Fig. 4 shows the magnitude of the scattering parameters of the straight open-end stub (Fig. 2(a)) of length $L = 1100\mu$m with the air-bridges removed as a function of frequency. It is noticed that the theoretical and experimental results agree very well up to the first resonance, after which, discrepancy is noticeable. This is attributed to the fact that no loss is assumed in the theoretical formulation, while, experiments were performed on CPW structures in an open environment. The loss encountered in the measurements is mainly due to radiation by the slotline mode excited in the CPW stubs in the absence of the air-bridges. To understand the unexpected behavior seen between 41 and 45 GHz, the reactances X_1 and X_3 of the equivalent circuit are plotted in Fig. 5. It can be seen that X_1, which corresponds to the coplanar mode in the CPW stub, behaves as a real open-end shunt stub. On the other hand, X_3, which is due to the slotline mode in the CPW stubs, behaves somewhat anomalously between 41

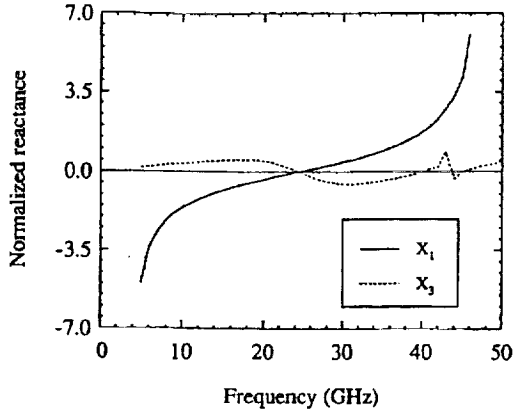

Fig. 5. The normalized reactances of the equivalent circuit for the straight open-end stub of length $L = 1100\,\mu$m. The second resonance of X_1 occurs at approximately 48.2 GHz which is difficult to show on this plot.

and 45 GHz. It is found that this behavior is due to a cavity resonance at 43 GHz which corresponds to the LSM_{121} mode excited in the partially filled lower cavity (the cavity width was chosen to be 3.425 mm). It is interesting to note that the LSM_{111} cavity mode, which has a resonant frequency of 38 GHz, does not show an observable effect on the stub under consideration. Also, the shunt reactances seem to be unaffected by the LSM_{121} cavity mode.

Fig. 6 shows the scattering parameters (magnitude and phase) of the same straight open-end stub with air-bridges. The good agreement between the theoretical and experimental results validates the developed hybrid technique. As it can be seen, the stub resonates at nearly 24.5 GHz where the length of the stub is approximately quarter of a coplanar mode wavelength. It can be noticed that the agreement between the theoretical and experimental data in Fig. 6(a) is much better than the one seen in Fig. 4. This is due to the fact that the air-bridges tend to prevent the slotline mode from being excited in the CPW stubs which effectively reduces radiation losses encountered in the measurements. In addition, it can be seen that the resonance effect noticed in Fig. 4 has disappeared since X_3 is shorted by the relatively small air-bridge inductance L_a. As a result, with the presence of air-bridges, cavity resonances have no effect on the characteristics of a straight stub as long as it is placed symmetrically inside the cavity. One can also notice an anomalous effect at 40 GHz existing in Fig. 6. A similar effect has been found in [17] for the case of a bent open-end stub. This effect may be due to a resonating slotline mode excited in the stubs beyond the air-bridge.

Fig. 7 shows the magnitude of the scattering parameters for the bent open-end CPW stub (Fig. 2(b)) of mean length $1100\,\mu$m without air-bridges. In this case, the width of the cavity is taken to be 2 mm. It can be seen that the agreement between theory and experiment is better than that seen in Fig. 4 for the straight stub without air-bridges. Moreover, it has been found that the parallel combination of X_1 and X_2 behaves as expected for a real shunt open-end stub (i.e. similar to the variation of X_1 in Fig. 5). Fig. 8 shows the magnitude of the scattering parameters of the same bent open-end stub with air-bridges. It can be seen that the anomalous effect at 40 GHz is

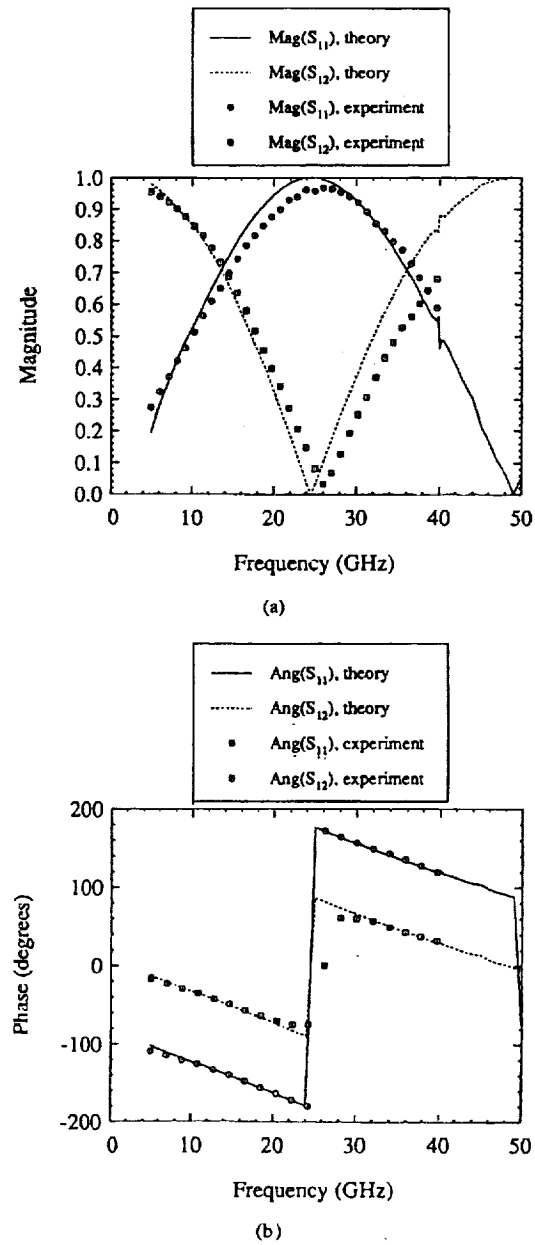

Fig. 6. Scattering parameters of the straight open-end stub with air-bridges. ($L = 1100\,\mu$m).

more pronounced in this case than that in Fig. 6. In addition, the resonant frequency of this bent stub with air-bridges is approximately the same as the one for the straight stub of the same mean length.

B. Short-End Shunt Stubs

Figs. 9 and 10 show $Mag(S_{11})$ for the straight and bent short-end CPW stubs, respectively, of mean length $L = 1100\,\mu$m with and without air-bridges. It can be noticed that both stubs resonate at approximately 25.5 GHz. The same arguments presented above for the open-end stub hold here too.

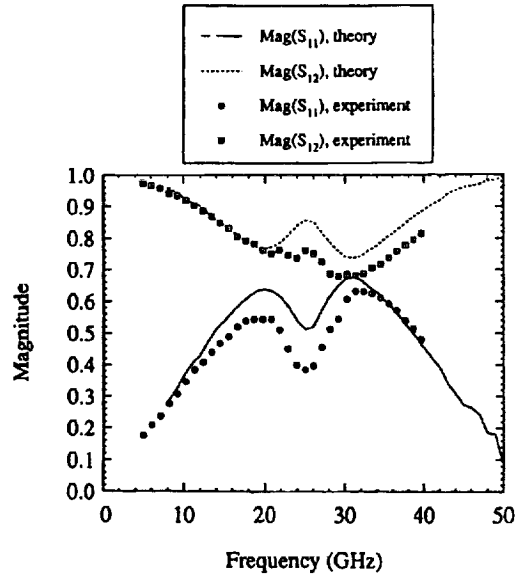

Fig. 7. Scattering parameters of the bent open-end stub without air-bridges. ($L_1 = 100\,\mu$m, $L_2 = 1025\,\mu$m).

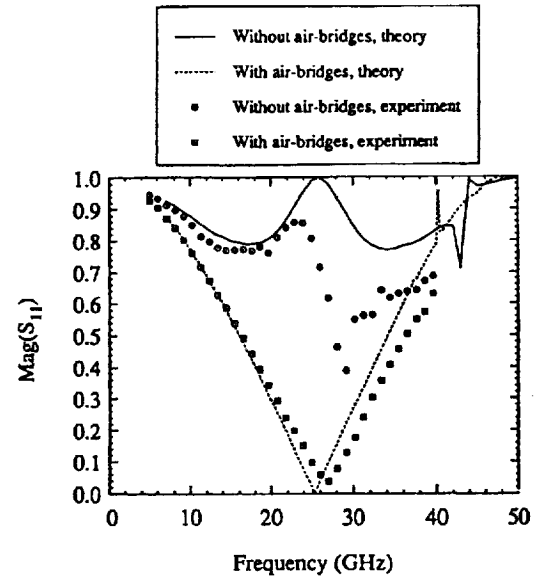

Fig. 9. Mag(S_{11}) of the straight short-end stub with and without air-bridges. ($L = 1100\,\mu$m).

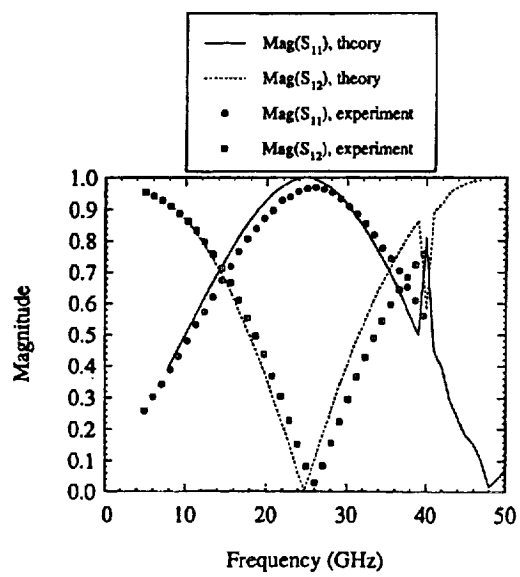

Fig. 8. Scattering parameters of the bent open-end stub with air-bridges. ($L_1 = 100\,\mu$m, $L_2 = 1025\,\mu$m).

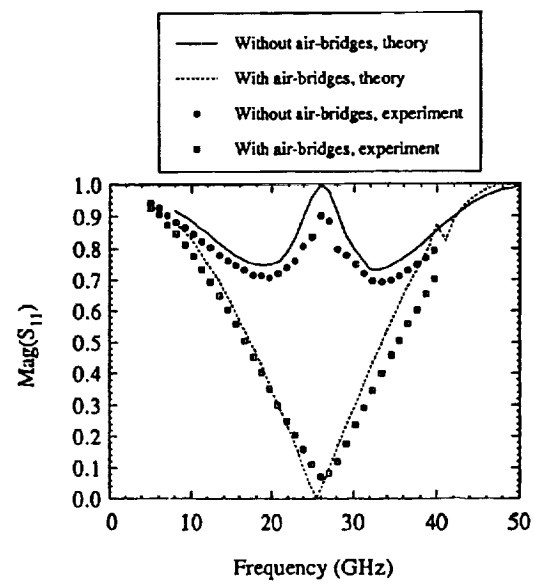

Fig. 10. Mag(S_{11}) of the bent short-end stub with and without air-bridges. ($L_1 = 100\,\mu$m, $L_2 = 1025\,\mu$m).

It is interesting to note that for all structures containing air-bridges, the measured resonant frequency is larger than the theoretically predicted one. This systematic deviation may be due to the effect of finite metallization thickness (1.5 μm) which is neglected in the theoretical analysis. The finite metallization thickness reduces the phase constant [36] and thus increases the stub resonant frequency. EEsof Touchstone has predicted an increase of approximately 1.2% in the resonant frequency of a section of CPW of length 1100 μm due to the finite conductor thickness.

Since the experiments were performed on open CPW discontinuities, the measured scattering parameters can provide the loss factor. This loss factor includes radiation, conductor and dielectric losses. However, since the stubs are all of the same length and printed on the same substrate, a comparison of the loss factor can provide a measure of the radiation loss. Figs. 11(a) and 12(a) show the loss factor of the short-end and open-end stubs without air-bridges, respectively. It is noticed that loss is maximum at the resonant frequency for all stubs, which is similar to what has been found in microstrip stubs [37]. Furthermore, the loss factor for straight stubs is larger than that for bent stubs especially after resonance. This behavior is due to the fact that in the case of bent stubs, the fields radiated by the coupled slotline mode in the two opposing stubs

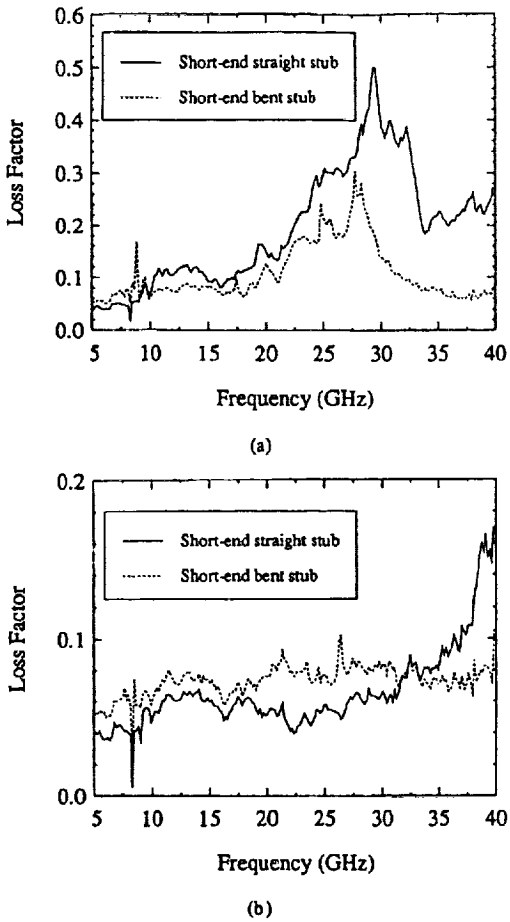

Fig. 11. The measured loss factor $(1 - |S_{11}|^2 - |S_{12}|^2)$ of the short-end CPW stubs. (a) Without air-bridges. (b) With air-bridges.

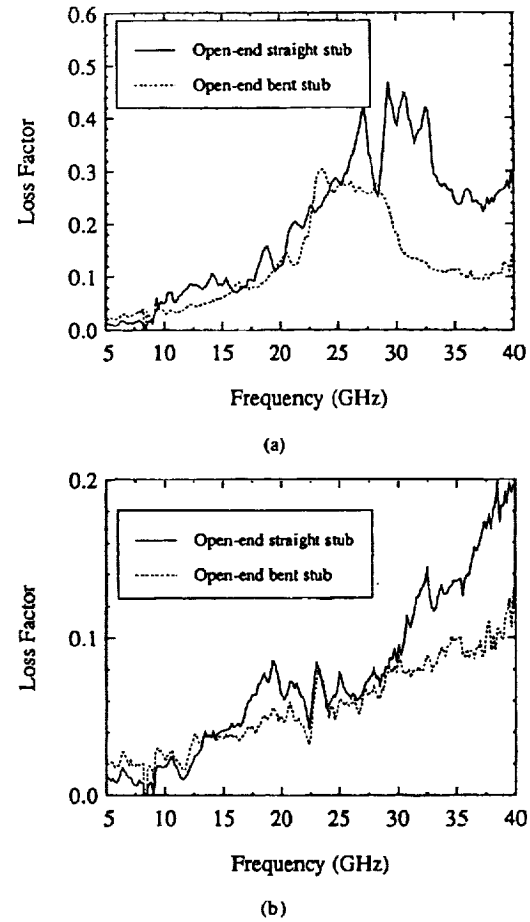

Fig. 12. The measured loss factor of the open-end CPW stubs. (a) Without air-bridges. (b) With air-bridges.

partially cancel. This explains why the agreement between the theoretical and experimental results for the bent stubs without air-bridges (Fig. 7 and Fig. 10) is better than that for the straight stubs without air-bridges (Figs. 4 and 9). The loss factor for the stubs with air-bridges is shown in Figs. 11(b) and 12(b). It can be seen that the presence of air-bridges reduces the loss factor appreciably since they short out the radiating coupled slotline mode. However, it is still noted that the straight stubs have increasing radiation loss after the first resonant frequency. Finally, it can be noticed that the difference between the loss factor of the straight and bent stubs (with or without air-bridges) below the resonant frequency is within the experimental error. Thus, no concluding remarks can be made concerning the loss from the two stubs in this region.

IV. Conclusions

A comprehensive theoretical and experimental study of CPW shunt stubs has been presented. In the theoretical analysis, the CPW was assumed to be inside a cavity, while, the experiments were performed in an open environment. A hybrid technique has been developed to analyze the CPW discontinuities which proved valid since the results obtained theoretically and experimentally agreed very well. It was found that bent stubs without air-bridges tend to radiate less than straight stubs of the same length. In addition, the effect of the cavity resonances on the behavior of the stubs has been studied. It has been shown through experiments that bent CPW stubs should be used whenever the circuit layout permits to reduce the radiation loss caused by the parasitic coupled slotline mode.

References

[1] R. W. Jackson, "Considerations in the use of coplanar waveguide for millimeter wave integrated circuits," *IEEE Trans. Microwave Theory Tech.*, vol. MTT-34, pp. 1450–1456, Dec. 1986.

[2] R. N. Simons and G. E. Ponchak, "Modeling of some coplanar waveguide discontinuities," *IEEE Trans. Microwave Theory and Tech.*, vol. 36, pp. 1796–1803, Dec. 1988.

[3] G. Kibuuka, R. Bertenburg, M. Naghed, and I. Wolff, "Coplanar lumped elements and their application in filters on ceramic and gallium arsenide substrates," in *Proc. 19th European Microwave Conf.*, London, Sept. 1989, pp. 656–661.

[4] C. W. Kuo and T. Itoh, "Characterization of the coplanar waveguide step discontinuity using the transverse resonance method," in *Proc. 19th European Microwave Conf.*, London, Sept. 1989, pp. 662–665.

[5] R. W. Jackson, "Mode conversion at discontinuities in finite-width conductor-backed coplanar waveguide," *IEEE Trans. Microwave Theory Tech.*, vol. 37, pp. 1582–1589, Oct. 1989.

[6] M. Naghed and I. Wolff, "Equivalent capacitances of coplanar waveguide discontinuities and interdigitated capacitors using a three dimensional finite difference method," *IEEE Trans. Microwave Theory Tech.*, vol. 38, pp. 1808–1815, Dec. 1990.

[7] M. Drissi, V. Fouad Hanna, and J. Citerne, "Analysis of coplanar waveguide radiating end effects of using the integral equation technique," *IEEE Trans. Microwave Theory Tech.*, vol. 39, pp. 112–116, Jan. 1991.
[8] N. Dib and P. Katehi, "Modeling of shielded CPW discontinuities using the space domain integral equation method (SDIE)," *J. Electromagnetic Waves and Applications*, pp. 503–523, Apr. 1991.
[9] N. Dib, P. Katehi, G. Ponchak, and R. Simons, "Theoretical and experimental characterization of coplanar waveguide discontinuities for filter applications," *IEEE Trans. Microwave Theory Tech.*, vol. 39, pp. 873–882, May 1991.
[10] W. Harokopus and P. Katehi, "Radiation loss from open CPW discontinuities," in *1991 IEEE MTT-S Int. Microwave Symp. Dig.*, Boston, pp. 743–746.
[11] M. Naghed, M. Rittweger, and I. Wolff, "A new method for the calculation of the equivalent inductances of coplanar waveguide discontinuities," in *1991 IEEE MTT-S Int. Microwave Symp. Dig.*, Boston, pp. 747–750.
[12] N. Dib and P. Katehi, "The effect of mitering on CPW discontinuities," in *Proc. 21st European Microwave Conf.*, Sept. 1991, pp. 223–228.
[13] U. Mueller, M. Rittweger, and A. Beyer, "Coplanar short considered by the TLM-method with symmetrical condensed nodes," in *Proc. 21st European Microwave Conf.*, Sept. 1991, pp. 999–1003.
[14] J. McLean, A. Wieck, K. Ploog, and T. Itoh, "Fullwave analysis of open-end discontinuities in coplanar stripline and finite ground plane coplanar waveguide in open environments using a deterministic spectral domain approach," in *Proc. 21st European Microwave Conf.*, Sept. 1991, pp. 1004–1007.
[15] C. Kuo and T. Itoh, "Characterization of shielded coplanar type transmission line junction discontinuities incorporating the finite metallization thickness effect," *IEEE Trans. Microwave Theory Tech.*, vol. 40, pp. 73–80, Jan. 1992.
[16] N. Koster *et al.*, "Investigation of air bridges used for MMIC's in CPW technique," in *Proc. 19th European Microwave Conf.*, Sept. 1989, pp. 666–671.
[17] M. Rittweger, M. Abdo, and I. Wolff, "Full-Wave analysis of coplanar discontinuities considering three-dimensional bond wires," in *1991 IEEE MTT-S Int. Microwave Symp. Dig.*, Boston, pp. 465–468.
[18] N. Dib, P. Katehi, and G. Ponchak, "Analysis of shielded CPW discontinuities with air bridges," in *1991 IEEE MTT-S Int. Microwave Symp. Dig.*, Boston, pp. 469–472.
[19] R. Bromme and R. Jansen, "Systematic investigation of CPW MIC/MMIC structures using strip/slot 3D electromagnetic simultor," in *1991 IEEE MTT-S Int. Microwave Symp. Dig.*, Boston, pp. 1081–1084.
[20] T. Becks and I. Wolff, "Calculation of three-dimensional passive structures including bond-wires, via-holes and air-bridges using the spectral domain analysis method," in *Proc. 21st European Microwave Conf.*, Sept. 1991, pp. 571–576.
[21] M. Rittweger, N. Koster, S. Koblowski, R. Bertenburg, S. Heinen, and I. Wolff, "Full-wave analysis of a modified coplanar air bridge T-junction," in *Proc. 21st European Microwave Conf.*, Sept. 1991, pp. 993–998.
[22] K. Beilenhoff, W. Heinrich, and H. Hartnagel, "The scattering behavior of air bridges in coplanar MMIC's," in *Proc. of 21st European Microwave Conf.*, Sept. 1991, pp. 1131–1135.
[23] C. P. Wen, "Coplanar waveguide: A surface strip transmission line suitable for nonreciprocal gyromagnetic device applications," *IEEE Trans. Microwave Theory Tech.*, vol. MTT-17, pp. 1087–1090, Dec. 1969.
[24] M. Houdart, "Coplanar lines: Application to broadband microwave integrated circuits," in *Proc. 6th European Microwave Conf.*, Rome, 1976, pp. 49–53.
[25] P. A. Holder, "X-band microwave integrated circuits using slotlines and coplanar waveguide," *Radio Electronics Engineering*, vol. 48, pp. 38–42, Jan./Feb. 1978.
[26] R. N. Simons, "Propagation characteristics of some novel coplanar waveguide transmission lines on GaAs at MM-wave frequencies," in *Proc. 1986 Conf. Millimeter Wave/Microwave Measurements and Standards for Miniaturized Systems*, Alabama, Nov. 6–7, 1986.
[27] G. Ghione and C. U. Naldi, "Coplanar waveguides for MMIC applications: Effect of upper shielding, conductor backing, finite-extent ground planes, and line-to-line coupling," *IEEE Trans. Microwave Theory Tech.*, vol. MTT-35, pp. 260–267, Mar. 1987.
[28] T. Hirota, Y. Tarusawa, and H. Ogawa, "Uniplanar MMIC hybrids—A proposed new MMIC structure," *IEEE Trans. of Microwave Theory Tech.*, vol. MTT-35, pp. 576–581, June 1987.
[29] M. Muraguchi *et al.*, "Uniplanar MMIC's and their applications," *IEEE Trans. of Microwave Theory Tech.*, vol. MTT-36, pp. 1896–1990, Dec. 1988.
[30] M. Riaziat, E. Par, G. Zdasiuk, S. Bandy, and M. Glenn, "Monolithic millimeter wave CPW circuits," in *1989 IEEE MTT-S Int. Microwave Symp. Dig.*, Long Beach, CA, pp. 525–528.
[31] D. Leistner, W. Schmid, and G. Eggers, "Application of coplanar waveguide microwave integrated circuits at C- and Ku-band frequencies," in *Proc. 20th European Microwave Conf.*, Sept. 1990, pp. 1021–1026.
[32] "CAD oriented numerical techniques for the analysis of microwave and MM-wave transmission-line discontinuities and junctions," in *Proc.* Int. Workshop of the German IEEE MTT/AP Chapter, Stuttgart, Sept. 13, 1991.
[33] R. F. Harrington, *Field Computation By Moment Methods*. New York: Macmillan, 1968.
[34] K. C. Gupta, R. Garg, and I. J. Bahl, *Microstrip Lines and Slotlines*. Dedham, MA: Artech House, 1979.
[35] N. Dib and P. Katehi, "Characterization of nonsymmetric coplanar waveguide discontinuities," in *1992 IEEE MTT-S Int. Microwave Symp. Dig.*, Albuquerque, NM, June 1–5.
[36] K. Koshiji, E. Shu, and S. Miki, "An analysis of coplanar waveguide with finite conductor thickness—Computation and measurement of characteristic impedance," *Electronics and Communications in Japan*, vol. 64-B, no. 8, pp. 69–78, 1981.
[37] W. P. Harokopus and P. B. Katehi, "Characterization of microstrip discontinuities on multilayer dielectric substrates including radiation losses," *IEEE Trans. Microwave Theory Tech.*, vol. 37, pp. 2058–2065, Dec. 1989.

Nihad Dib received the B.Sc. and M.Sc. degrees in electrical engineering from Kuwait University in 1985 and 1987, respectively.

He then worked as a Laboratory Engineer in the ECE Department at Kuwait University for two years. He has been with the Radiation Laboratory, University of Michigan, since Sept. 1988, where he obtained his Ph.D. degree in October 1992.

Mr. Dib was a recipient of a Pre-Doctoral Rackham Fellowship, University of Michigan, during the academic year 1991–1992. His research deals mainly with the construction of CAD programs for the analysis of Coplanar Waveguide structures and other printed lines.

George Ponchak received the B.E.E. degree from Cleveland, State University, Cleveland, OH, in 1983 and the M.S.E.E. from Case Western Reserve University, Cleveland, OH, in 1987.

He joined the NASA Lewis Research Center, Cleveland, in July 1983 as a member of the Space Communications Division. Since joining NASA he has been engaged in research in solid-state technology development, transmission lines, and monolithic microwave integrated circuits (MMIC's). He is currently pursuing his Ph.D. degree with the University of Michigan.

Linda P. B. Katehi (S'81-M'84-SM'84) received the B.S.E.E. degree from the National Technical University of Athens, Greece, in 1977 and the M.S.E.E. and Ph.D. degrees from the University of California, Los Angeles, in 1981 and 1984, respectively.

In Sept. 1984 she joined the faculty of the EECS Department of the University of Michigan, Ann Arbor. Since then, she has been involved in the modeling and computer-aided design of millimeter and near-millimeter wave monolithic circuits and antennas.

In 1984 Dr. Katehi received the W. P. King Award and in 1985 the S. A. Schelkunoff Award from the Antennas and Propagation Society. In 1987 she received an NSF Presidential Young Investigator Award and an URSI Young Scientist Fellowship. She is a member of Sigma Xi and URSI Commision D.

N94-20503

COPLANAR WAVEGUIDE RADIAL LINE STUB

R. N. Simons and S. R. Taub

Indexing terms: Waveguides, Resonators, Silicon

A coplanar waveguide radial line stub resonator is experimentally characterised with respect to stub radius, sectoral angle, substrate thickness and relative dielectric constant. A simple closed-form design equation, which predicts the resonance radius of the stub, is presented.

Introduction: Coplanar waveguide (CPW) technology is emerging as a viable alternative to stripline and microstrip line for monolithic microwave integrated circuits [1]. There are several applications in which a CPW radial line stub resonator is necessary; these include: bias line filters requiring a point of virtual RF ground, mixer and frequency multiplier circuits that require a reactance to terminate the diodes and the harmonics, respectively. In addition, a grounded CPW

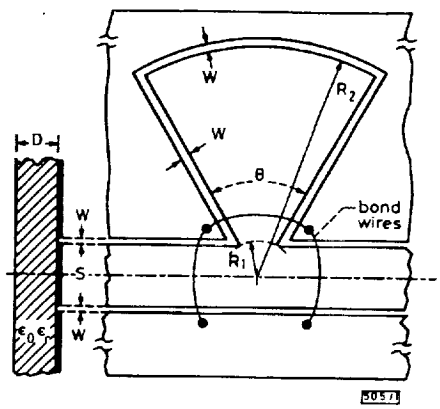

Fig. 1 *Schematic diagram of CPW radial line stub*

(GCPW) radial line stub resonator has application in oscillator circuits for active antennas [2]. In general, the advantages of a radial line stub over a straight 50Ω stub are the smaller resonance length, wider bandwidth and smaller discontinuity reactance at the junction with the main line [3].

This Letter presents, for the first time, CPW and GCPW radial line stub resonators, characterised by measuring the resonance frequency. The resonance frequency is measured for stubs with different radii, sectoral angles, substrate thicknesses and substrate relative dielectric constants. A closed-form design equation, which predicts the resonance radius of the stub, for a given set of parameters, is also presented.

Design and fabrication: Fig. 1 shows a schematic diagram of the CPW radial line stub resonator. The inner and outer radius of the stub are denoted as R_1 and R_2, respectively. The sectoral angle is denoted as θ. The CPW stubs are fabricated on Duroid (relative dielectric constants $\varepsilon_r = 6$ and 10·5) and on high resistivity silicon ($\varepsilon_r = 11{\cdot}7$, $\rho = 5000$–$10\,000\,\Omega$cm) substrates. The GCPW stubs are fabricated on Duroid with $\varepsilon_r = 2{\cdot}2$. Three bond wires near the plane of discontinuity ensure equal potential at all ground planes. The CPW centre strip conductor with width S and slot width W, are chosen to be compatible with the coaxial launchers of the Wiltron universal test fixture. Thus, the characteristic impedance Z_0 of the main line is 55Ω.

Experimental results and closed-form equation: The measured return loss and insertion loss of a CPW radial line stub are compared with those of a straight CPW stub in Fig. 2. In this experiment θ and R_2 for the radial stub are arbitrarily chosen as 60° and 5·08 mm, respectively. The length L of the straight stub is 7 mm. The measurements show that for identical ε_r and resonance frequency f_0, the radius R_2 is 37% smaller than the length L. Further, the radial line stub has a wider bandwidth. The bandwidth of the two structures as a function of the attenuation is compared in Table 1. The excess loss defined as $1 - |S_{11}|^2 - |S_{21}|^2$, and determined from the measured S parameters, is small. It is of the order of 0·09 and 0·05 for the radial line stub and straight stub, respectively.

A GCPW radial line stub with $\varepsilon_r = 2{\cdot}2$, $D = 0{\cdot}254$ mm and θ and R_2 the same as for the CPW radial line stub, has a much wider bandwidth. The characteristics for the GCPW radial line stub are also included in Table 1. The excess loss is of the order of 0·04.

Table 1 PERCENTAGE BANDWIDTH OF STRAIGHT AND RADIAL LINE STUB

	Stub configurations		
Attenuation	Straight	CPW radial	GCPW radial
dB	%	%	%
10	18·3	25·7	58·1
20	5·6	8·0	15·8
30	1·6	2·5	3·5

For a CPW radial line stub, the measured f_0 as a function of θ for a fixed R_2 is shown in Fig. 3. The f_0 decreases by 20% as θ increases from 30 to 90°. It is also worth noting that R_1 does not remain constant but increases with θ. The excess loss is small and decreases from 0·12 to 0·06 as θ increases from 30 to 90°.

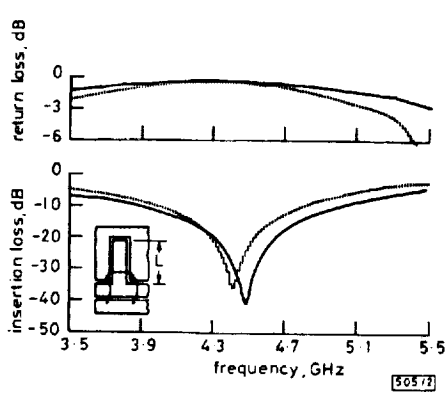

Fig. 2 *Measured return loss and insertion loss of CPW radial line stub and CPW straight stub*

$S = 0{\cdot}33$ mm, $W = 0{\cdot}234$ mm, $D = 0{\cdot}635$ mm, $\varepsilon_r = 10{\cdot}5$, $R_1 = 0{\cdot}191$ mm, $R_2 = 5{\cdot}08$ mm, $\theta = 60°$, $L = 7$ mm
——— radial line stub
····· straight stub

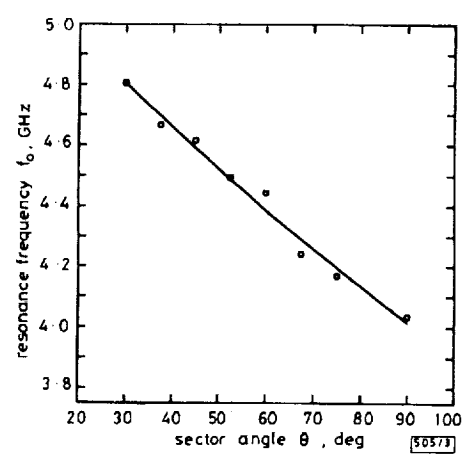

Fig. 3 *Measured resonance frequency of CPW radial line stub against sector angle*

$S = 0{\cdot}33$ mm, $W = 0{\cdot}234$ mm, $D = 0{\cdot}635$ mm, $\varepsilon_r = 10{\cdot}5$, $R_2 = 5{\cdot}08$ mm

© Reprinted, with permission, from IEE Electronics Letters, vol. 29, no. 4, 18th February 1993, pp. 412-413.

PRECEDING PAGE BLANK NOT FILMED

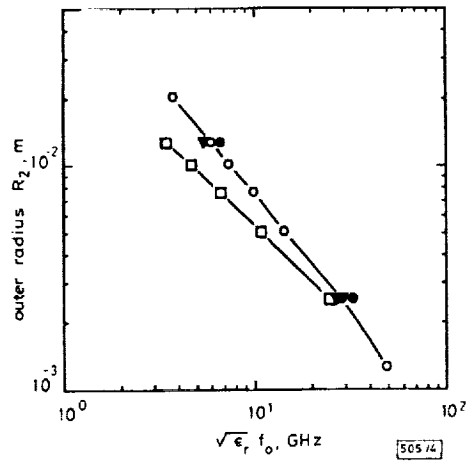

Fig. 4 *Measured resonance frequency against outer radius of radial stub for $\theta = 60°$*

(i) *GCPW:*
□ (*a*) $S = 0{\cdot}518$ mm, $W = 0{\cdot}127$ mm, $D = 0{\cdot}254$ mm, $\varepsilon_r = 2{\cdot}2$, $R_1 = 0{\cdot}3$ mm
(ii) *CPW:*
○ (*b*) $S = 0{\cdot}33$ mm, $W = 0{\cdot}234$ mm, $D = 0{\cdot}635$ mm, $\varepsilon_r = 10{\cdot}5$, $R_1 = 0{\cdot}191$ mm
● (*c*) $S = 0{\cdot}33$ mm, $W = 0{\cdot}185$ mm, $D = 0{\cdot}254$ mm, $\varepsilon_r = 10{\cdot}5$, $R_1 = 0{\cdot}191$ mm
▽ (*d*) $S = 0{\cdot}508$ mm, $W = 0{\cdot}155$ mm, $D = 0{\cdot}635$ mm, $\varepsilon_r = 6$, $R_1 = 0{\cdot}3$ mm
▼ (*e*) $S = 0{\cdot}152$ mm, $W = 0{\cdot}114$ mm, $D = 0{\cdot}381$ mm, $\varepsilon_r = 11{\cdot}7$, $R_1 = 0{\cdot}092$ mm

Fig. 4 shows the product of $\sqrt{(\varepsilon_r)}$ and measured f_0 as a function of R_2 for CPW and GCPW radial line stubs. By curve fitting the measured data, the coefficients of a simple closed-form equation to predict R_2 are determined using a sigma plot. The equations for CPW and GCPW are as follows:

$$\log(R_2) = C_1 \log[\sqrt{(\varepsilon_r)} f_0] + C_2 \log(D) + C_3 \log(R_1) + C_4$$

$$\log(R_2) = C_5 \log[\sqrt{(\varepsilon_r)} f_0] + C_6[\log(D) + \log(R_1)]$$

where f_0 is in gigahertz, R_1, R_2, and D are in metres. The coefficients were determined to be: $C_1 = -1{\cdot}0496$, $C_2 = 0{\cdot}098375$, $C_3 = -0{\cdot}1401$, $C_4 = -1{\cdot}297$, $C_5 = -0{\cdot}82462$ and $C_6 = 0{\cdot}21201$, respectively. These equations are valid for the geometry and the range of parameters given in Fig. 4. The range of parameters considered are those typically used in microwave circuit design. The standard error of the equation is at most 0·18 and 0·01% for the CPW and GCPW, respectively.

Conclusions: A CPW radial line stub resonator is experimentally characterised in terms of its radius, sectoral angle, substrate thickness and relative dielectric constant. A simple closed-form design equation which predicts the resonance radius of the stub for a given set of parameters is also presented. The radial line stub, when compared to a straight stub, has a wider bandwidth and shorter length.

Acknowledgment: The authors are thankful to P. G. Young for fabricating the circuits on silicon substrates.

4th January 1993

R. N. Simons and S. R. Taub (*Mail Stop 54-5, NASA Lewis Research Center, 21000 Brookpark Road, Cleveland, Ohio 44135, USA*)

References

1 KUMAR, M. (Ed.): IEEE 1991 Microwave and Millimeter-Wave Monolithic Circuits Symp. Dig. of Papers (91CH3016-3)
2 SIMONS, R. N., and LEE, R. Q.: 'Planar dielectric resonator stabilized HEMT oscillator integrated with CPW/aperture coupled patch antenna'. IEEE MTT-S Int. Microwave Symp. Dig., 1992, Vol. I, pp. 433–436
3 ATWATER, H. A.: 'The design of the radial line stub: A useful microstrip circuit element', *Microwave J.*, 1985, **28**, (11), pp. 149–156

N94-20504

ATTENUATION AND ε_{EFF} OF COPLANAR WAVEGUIDE TRANSMISSION LINES ON SILICON SUBSTRATES

Susan R. Taub and Paul G. Young
NASA-Lewis Research Center
Cleveland, OH

Abstract

Attenuation and ε_{eff} of Coplanar Waveguide (CPW) transmission lines have been measured on Silicon substrates with resistivities ranging from 400 to greater than 30,000 ohm-cm, that have a 1000 angstrom coating of SiO_2. Both attenuation and ε_{eff} are given over the frequency range 5 to 40 GHz for various strip and slot widths. These measured values are also compared to the theoretical values.

Introduction

Historically, Silicon has not been the material of choice for microwave applications because of its extremely high loss and its lack of high frequency active devices. Recently, however, high frequency Silicon devices have become available. In addition, Silicon Germanium (SiGe) shows great promise for high frequency Silicon based devices [1].

Theoretical work has been done in calculating the attenuation of microstrip lines on Silicon as a function of resistivity and frequency [2]. There has also been some work on Coplanar Waveguide (CPW) lines on Silicon on Insulator (SOI) [3] as a function of resistivity. This paper presents both measured and theoretical attenuation and ε_{eff} data of CPW lines on Silicon as a function of resistivity, strip and slot width and frequency.

Results

Groups of CPW lines were fabricated on five different Silicon wafers. The wafers were 8 mils thick and had resistivities of 400-720 ohm-cm, 2500-3300 ohm-cm, 5000 ohm-cm, 5000-10,000 ohm-cm, and greater than 30,000 ohm-cm. A 1000 angstrom layer of SiO_2 was deposited on the wafers, followed by a 2.5μm thick Au layer. The CPW lines were fabricated using etch back. Each group of CPW lines consisted of on open, thru, and four delay lines with a different strip width (s) and slot width (w) for each group. The s and w of each of the groups were: s=2 w=1, s=4 w=2, and s=6 w=3. The impedance of these lines was approximately 50 ohms. The CPW lines were on wafer probed using PicoProbes and an HP8510 Automatic Network Analyzer. The data from each group was analyzed using NIST's DEEMBED software to obtain values for the attenuation and ε_{eff}.

Figure 1 shows the measured attenuation of a CPW line with s=4 w=2 on Silicon substrates of varying resistivities. As the resistivity of the material increases, the attenuation decreases. This is attributed to the reduction of dielectric loss. Loss also increases with frequency, due to an increase in the effective length of the line. Note that for substrates of medium resistivity (400-720 ohm-cm), the loss is twice that of those with resistivities greater than 2,500 ohm-cm. However, the improvement in attenuation for substrates with resistivities greater than 2,500 ohm-cm is small.

Figure 2 shows the attenuation of CPW lines on a Silicon wafer with resistivity of 2,500-3,300 ohm-cm as a function of s and w. Measured and theoretical curves are shown.

© 1993 IEEE. Reprinted, with permission, from the Eleventh Annual Benjamin Franklin Symposium on Antenna and Microwave Technology in the 1990s, May 1993, pp. 8-11.

The theoretical curves were given by Gupta [4]. As was predicted by the theory, the loss of the CPW lines decrease with increasing s and w; however, the measured values of attenuation are slightly lower than the theory predicts.

ε_{eff} is not a function of resistivity but of s and w. Figure 3 shows theoretical and measured values for ε_{eff} of CPW lines with s=6 w=3. The theoretical values were again given by Gupta [4]. The value of ε_{eff} is virtually independent of resistivity and closely matches the theoretical value.

Conclusions

Both measured and theoretical values for attenuation and ε_{eff} for CPW lines on Silicon wafers were shown as a function of resistivity, strip and slot width and frequency. Losses for CPW lines on Silicon can be minimized if the resistivity of the wafer is kept above 2,500 ohm-cm. Thus making Silicon a viable microwave material.

Acknowledgment

The authors would like to thank Dr. Roger Marks of NIST for his help with the software and Dr. Rainee Simons for his support during this project.

References

[1] Patton, G., et al. "75 GHz f_t SiGe-Based Heterojunction Bipolar Transistor", IEEE Electron Device Lett., 1990, EDL-11, (4), pp. 171-173.

[2] Rosen, A., et al. "Silicon as a Millimeter-wave Monolithically Integrated Substrate-a New Look", RCA Rev., 1981, 42, pp. 633-660.

[3] Caviglia, A., et al. "Microwave Performance of SOI n-MOSFET's and Coplanar Waveguides", IEEE Electron Device Lett., 1991, EDL-12, (1), pp. 26- 27.

[4] Gupta, K.C., R. Garg, I.J. Bahl. Microstrip Lines and Slotlines. Artech House, Inc. 1979. pp. 285-287 and 275-276.

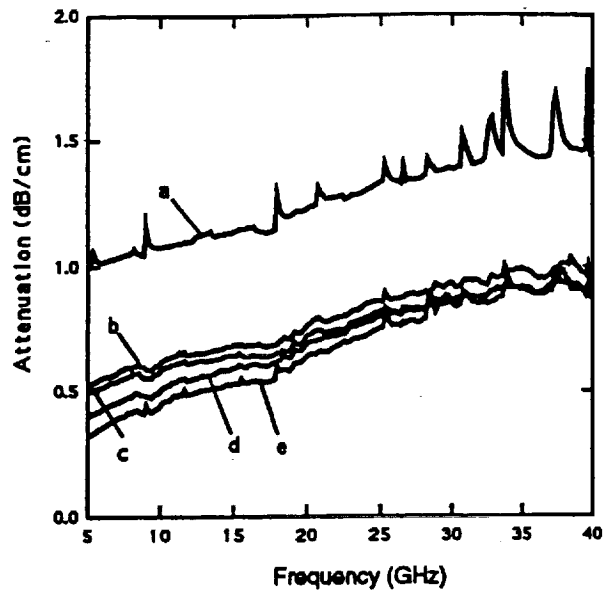

Figure 1: Measured attenuation of CPW lines on Silicon substrates with resistivities: a) 400-720 ohm-cm b) 2500-3300 ohm-cm c) 5000 ohm-cm d) >30,000 ohm-cm

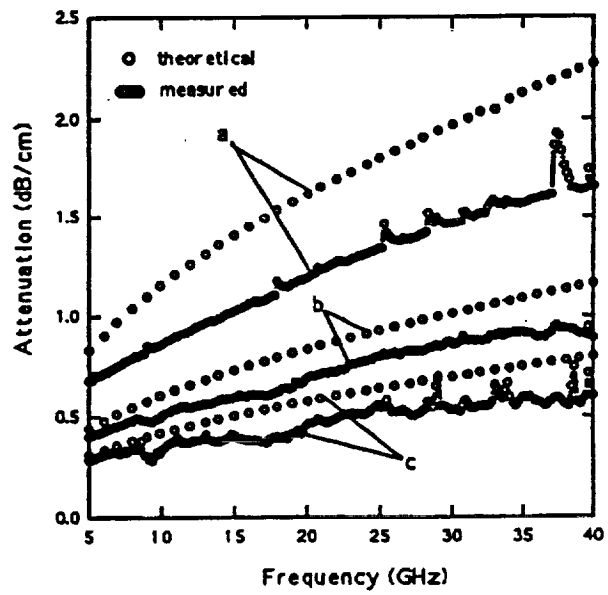

Figure 2: Measured and theoretical attenuation of CPW lines on a Silicon substrate, resistivity= 2500-3300 ohm-cm: a) s=2,w=1 b) s=4, w=2 c) s=6, w=3

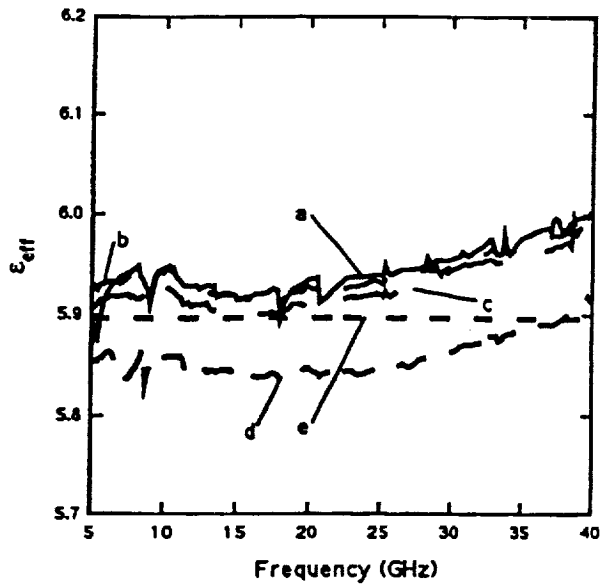

Figure 3: ε_{eff} of CPW lines on Silicon substrates, s=6 w=3, with resistivities: a) 400-720 ohm-cm b) 2500-3300 ohm-cm c) 5000 ohm-cm d) >30,000 ohm-cm e) theory

NOVEL COPLANAR WAVEGUIDE TO SLOTLINE TRANSITION ON HIGH RESISTIVITY SILICON

R. N. Simons, S. R. Taub and P. G. Young

Indexing terms: Coplanar waveguide, High resistivity silicon

Two novel coplanar waveguide (CPW) to slotline transitions have been fabricated and tested on high resistivity silicon. The first transition uses an air bridge to couple RF power from the CPW line to the slotline and has the entire circuit on the top side of the wafer. In the second transition, the grounded CPW (GCPW) line and the slotline are on opposite sides of the wafer and are coupled electromagnetically. The measured average insertion loss and return loss per transition are better than 1.5 and 10 dB, respectively, with a bandwidth greater than 30% at C-band frequencies.

Introduction: Recently, $Si_{1-x}Ge_x$-on-silicon devices have emerged as a viable alternative to GaAs- and InP-based heterostructure devices [1]. It appears that this material technology will be suitable for monolithic microwave integrated circuits (MMICs) for a number of reasons, some of which are the following: The technology is compatible with existing silicon technology which is extensively used for digital circuits and the low cost of silicon wafers. The active devices such as transistors and diodes are fabricated on the heterostructure while the interconnections would be laid out over the silicon substrate. By choosing a silicon substrate with sufficiently high resistivity it is possible to make the dielectric attenuation constant of the interconnecting microwave transmission lines approach those of GaAs [2]. For this to be possible, the transmission line interconnects must be characterised on silicon.

This Letter presents two new CPW to slotline transitions fabricated on high resistivity silicon substrates. A transition between a coplanar waveguide (CPW) and a slotline on a high resistivity silicon substrate has several applications. These include: facilitating fast and inexpensive testing of CPW and slotline MMICs using on-wafer RF probes, functioning as a balun in mixer circuits, and providing interconnection between CPW MMIC phase shifters or amplifiers and linearly tapered slot antennas in phased arrays. In the past, several investigators have worked on conventional CPW to slotline transitions on alumina and GaAs substrates [3, 4]. In these transitions the CPW line and the slotlines are orthogonal to each other.

Transition design and fabrication: The first transition presented in this Letter uses an air bridge to couple RF power from the CPW line to the slotline and has the entire circuit on the same side of the wafer. In the second transition, the grounded CPW (GCPW) line and the slotline are on opposite sides of the wafer and are coupled electromagnetically. In both cases

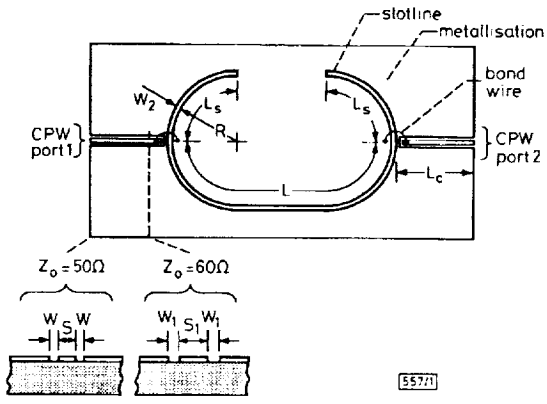

Fig. 1 *Schematic diagram of air-bridge coupled CPW to slotline transition*

$S = S_1 = 0{\cdot}1524$ mm, $W = 0{\cdot}0838$ mm, $W_1 = 0{\cdot}1524$ mm. $L = 19{\cdot}77$ mm, $L_s = 6{\cdot}83$ mm, $L_c = 5{\cdot}08$ mm, $R = 4{\cdot}35$ mm, and $W_2 = 0{\cdot}157$ mm

these circuits, the CPW line and the slotline are collinear. Both transitions are fabricated on a single 5000–10 000 Ω cm resistivity silicon wafer. The thickness D of the wafer is 0·381 mm with $\varepsilon_r = 11{\cdot}7$. The thickness T of the gold metallisation is about three times the skin depth at the centre frequency f_0 of 6 GHz.

(*a*) *Air-bridge coupled CPW to slotline transition:* An air-bridge coupled CPW to slotline transition is illustrated in Fig. 1. At the input port the characteristic impedance Z_0 is 50 Ω for compatibility with on-wafer RF testing. The line transforms to a 60 Ω line that terminates in an open circuit. The Z_0 of the slotline is 60 Ω. The circular bend at the feed end of the slotline provides a smooth transition. A 1 mil diameter bond wire between the open end of the CPW centre strip conductor and the opposite edge of the slotline functions as an air bridge and couples RF energy. The length L_s is $\sim\lambda_{g(slotline)}/4$ at f_0.

(*b*) *Electromagnetically coupled GCPW to slotline transition:* Fig. 2 shows a transition with electromagnetic coupling between a GCPW and a slotline which are on opposite sides of a wafer. At the input port Z_0 is 50 Ω, and in the centre region Z_0 is 60 Ω. This is realised by gradually flaring the GCPW slots. At the open end the top ground planes are terminated in two open circuited stubs of length L_g. Owing to the lack of CPW discontinuity models, these stubs are model-

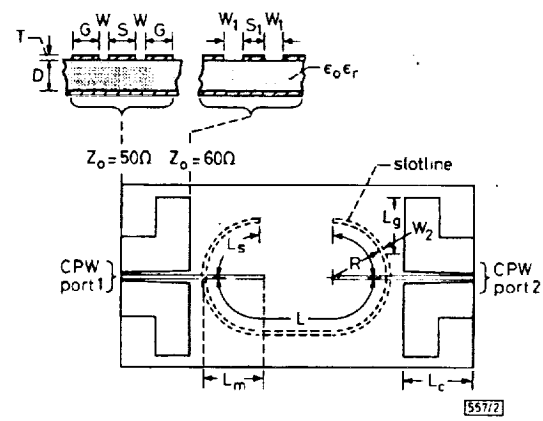

Fig. 2 *Schematic diagram of electromagnetically coupled CPW to slotline transition*

Top side circuit pattern:
$S = S_1 = 0{\cdot}1524$ mm, $W = 0{\cdot}1067$ mm, $W_1 = 0{\cdot}2515$ mm, $G = 2{\cdot}54$ mm, $L_m = 4{\cdot}6$ mm, $L_g = 3{\cdot}98$ mm, $L_c = 5{\cdot}08$ mm
Bottom side circuit pattern:
$L = 18{\cdot}7$ mm, $L_s = 6{\cdot}83$ mm, $R = 4{\cdot}35$ mm and $W_2 = 0{\cdot}157$ mm

led as microstrip lines of very low Z_0 ($\sim 10\,\Omega$) and length about $\lambda_{g(microstrip)}/4$. They provide a virtual short circuit between the top ground planes of the GCPW and the slotline. In addition, the GCPW has a finite ground plane of width G to suppress the parallel plate waveguide mode [5]. The Z_0 of the slotline is 60 Ω. Once again, owing to a lack of CPW discontinuity models, the centre strip conductor of the GCPW which extends beyond the terminated ground planes of the GCPW to form the transition is modelled as a microstrip line. The distances L_s and L_m are $\sim\lambda_{g(slotline)}/4$ and $\lambda_{g(microstrip)}/4$, respectively, at f_0.

Transition performance and discussions: During testing, the circuits were suspended 10 mm above the probe station stage. The insertion loss and return loss were measured using Cascade Microtech on-wafer probes. For two back-to-back air-bridge coupled CPW to slotline transitions, with a short length of slotline in between, the measured characteristics are shown in Fig. 3. The insertion loss and return loss per transition are ~1·5 dB, and better than 10 dB, respectively, over greater than 30% bandwidth centred at f_0. The above insertion loss includes the insertion loss of the two air bridges and the following which were not practical to calibrate out: the 19·8 mm length of slotline between the transitions, and two

© Reprinted, with permission, from IEE Electronics Letters, vol. 28, no. 24, 19th November 1992, pp. 2209-2210.

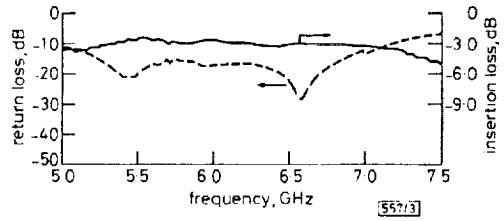

Fig. 3 *Measured insertion loss and return loss of air-bridge coupled CPW to slotline transition*

5·08 mm long CPW lines located at the input and output ports. Fig. 4 shows the measured insertion loss and return loss, respectively, for the electromagnetically coupled GCPW to slotline transitions with a short length of slotline in between. The insertion loss and return loss per transition are ~1·5 dB, and better than 10 dB, respectively, over greater than 40% bandwidth centred at 4·55 GHz. The above insertion loss includes the insertion loss of the two junctions and the following which were not practical to calibrate out: the

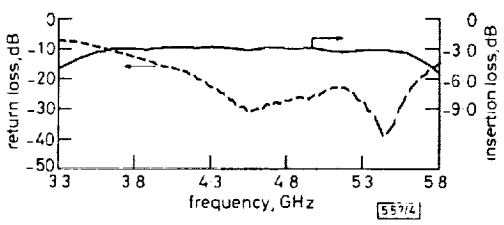

Fig. 4 *Measured insertion loss and return loss of electromagnetically coupled CPW to slotline transition*

18·7 mm length of slotline between the transitions, and two 5·08 mm long GCPW lines at the input and output ports. The return loss of this transition is observed to be better than the previous design because of better impedance match between the strip and the slot. However, the shift in the centre frequency from 6 to 4·55 GHz is caused by discontinuity effects which were not fully accounted for in the design.

Conclusions: Two novel CPW to slotline transitions on high resistivity silicon substrates have been experimentally demonstrated. The transitions are fabricated either on the same side or on opposite sides of a wafer and use an air bridge or electromagnetic coupling, respectively, to couple power. The measurements show that the transitions have good insertion loss, return loss and bandwidth characteristics.

2nd October 1992

R. N. Simons, S. R. Taub and P. G. Young (*Mail Stop 54-5 NASA Lewis Research Center, 21000 Brookpark Road, Cleveland, Ohio 44135, USA*)

References

1 PATTON, G., *et al.*: '75 GHz f_T SiGe-based heterojunction bipolar transistors', *IEEE Electron Devices Lett.*, 1990, **EDL-11**, (4), pp. 171–173

2 ROSEN, A., *et al.*: 'Silicon as a millimeter-wave monolithically integrated substrate—a new look', *RCA Rev.*, 1981, **42**, pp. 633–660

3 HOUDART, M., and AURY, C.: 'Various excitation of coplanar waveguide'. IEEE MTT-S Int. Microwave Symp. Dig., 1979, pp. 116–118

4 HIROTA, T., TARUSAWA, Y., and OGAWA, H.: 'Uniplanar MMIC hybrids—a proposed new MMIC structure', *IEEE Trans.*, 1987, **MTT-35**, (6), pp. 576–581

5 SIMONS, R. N., and LEE, R. Q.: 'Coplanar waveguide aperture coupled patch antenna with ground plane/substrate of finite extent', *Electron. Lett.*, 1992, **28**, (1), pp. 75–76

MICROWAVE CHARACTERIZATION OF SLOTLINE ON HIGH RESISTIVITY SILICON FOR ANTENNA FEED NETWORK

Rainee N. Simons, Susan R. Taub,
Richard Q. Lee, and Paul G. Young
National Aeronautics and Space Administration
Lewis Research Center
Cleveland, Ohio 44135

ABSTRACT

This paper presents, the effective dielectric constant (ε_{eff}) and attenuation constant (α) of a unshielded slotline on a high resistivity (5000 to 10,000 Ω-cm) silicon wafer. The ε_{eff} (DC to 40 GHz) and α (DC to 26.5 GHz) are determined from the measured resonant frequencies and the corresponding insertion loss of a slotline ring resonator. The measurements are carried out at room temperature and without the application of a DC bias. The attenuation for slotline on silicon are compared with microstrip line and coplanar waveguide on other semiconductor substrate materials. Finally, applications of the slotline to antenna feed network are addressed.

I. INTRODUCTION

There are several reasons why silicon is now a viable microwave material. One reason is that silicon MOSFET's with cutoff frequencies as high as 89 GHz have been reported (ref.1). Another, is that silicon MMIC amplifiers, mixers and IMPATT diodes are now commericially available (refs. 2 thru 4). The final reason is that transmission lines, such as, microstrip line (refs. 5 thru 9) and Coplanar Waveguide (CPW) (ref. 10) with low loss have been demonstrated on high resistivity silicon. Silicon has several advantages over GaAs and InP technologies, such as: better thermal conductivity, higher reliability, higher circuit complexity, availability of wafers of very large diameters, better mechanical properties, and lower cost (ref. 9). Furthermore, integration of MMIC's with digital control circuits and radiating elements on a single silicon wafer is possible. This can enhance the reliability, efficiency and lower the cost of phased array antenna systems. However, silicon substrates do have slightly higher dielectric loss than traditional microwave substrates. DC bias and high operating temperatures can increase this loss. Additional loss can be introduced, if during processing, the wafers are exposed to temperatures high enough to significantly lower their resistivity (ref. 9).

Conventional silicon wafers have low resistivity and consequently an unacceptably high value of dielectric attenuation. Therefore, microwave circuits for phased array antenna systems fabricated on these wafers have low efficiency. By choosing a silicon substrate with sufficiently high resistivity it is possible to make the dielectric attenuation of the interconnecting microwave transmission lines approach those of GaAs or InP (refs. 6 and 7).

In order to fabricate microwave circuits on silicon, the transmission lines on this material must be characterized. Recently, the attenuation of microstrip transmission lines on high resistivity, bare and passivated silicon as a function of frequency, temperature and DC bias have been measured (ref. 9). Also, attenuation and ε_{eff} of CPW lines as a function of resistivity, frequency and geometry on silicon substrates has been examined experimentally and theoretically (ref. 10). This paper presents the effective dielectric constant (ε_{eff}) and attenuation constant (α) of an unshielded slotline on a high resistivity (5000 to 10,000 Ω-cm) silicon wafer over the frequency ranges DC to 40 GHz and DC to 26.5 GHz respectively. The measurements are carried out at room temperature and without the application of a DC bias.

II. THEORY

An experimental slotline ring resonator is shown in figure 1. The advantage of a ring resonator over a series gap coupled linear resonator is that the ring resonator is free of end effects. The loaded Q-factor, Q_L, of the resonator is determined from the following equation relating the measured resonance frequency, f_0, and the frequency range, Δf, between the 3-dB points on either side of the resonance:

$$Q_L = f_0 \ / \ \Delta f. \tag{1}$$

The unloaded Q-factor, Q_u, of the resonator is determined from the following equation relating the measured peak insertion loss, L, at resonance and Q_L:

$$L \ (dB) \ = 20 \ Log \ \{1 - [Q_L/Q_u]\}. \tag{2}$$

The ε_{eff} is determined from the following equation:

$$\varepsilon_{eff} = (30 \ n/f_0 \ l)^2 \tag{3}$$

Where n is an integer and denotes the order of resonance. Therefore for n resonances of a particular resonator, n values of ε_{eff} can be obtained. l is the mean circumference of the ring in cm. f_0 is in GHz.

The phase velocity, v_{ph}, of the electromagnetic wave on the slotline is equal to

$$v_{ph} = 3x10^8 \ /\sqrt{\varepsilon_{eff}} \quad (mt/sec). \tag{4}$$

Finally, the attenuation constant α of the slotline is determined from the relation:

$$\alpha = \pi \ f_0 \ /Q_u \ v_{ph} \quad (Np/mt). \tag{5}$$

III. RESONATOR FABRICATION AND EXPERIMENTAL RESULTS

The slotline ring resonator is fabricated on a silicon wafer which is coated sequentially with 700 Å of silicon dioxide, 200 Å of chromium and 2.5 μm of gold. The thickness, T, of the gold metalization is greater than three times the skin depth at 8.5 GHz and above. The measured resistivity of the silicon dioxide layer is 10^{14} Ω-cm. The ε_{eff} and α are determined by substituting the measured resonant frequencies and the corresponding insertion loss in equations 1 thru 5. Figure 2 presents the ε_{eff} as a function of the frequency. In this figure the slot width W, wafer thickness D, and relative dielectric constant ε_r, are equal to 0.1 mm, 0.381 mm and 11.7, respectively. Also shown in Fig.2 is the computed ε_{eff} which is obtained as described in ref.11. The measured and computed ε_{eff} are in good agreement.

The intrinsic peak insertion loss L of the resonator is corrected for the insertion loss due to the microstrip feed lines and the coaxial connectors of the fixture. This is done by subtracting the feed and connector loss from the overall measured insertion loss. These excess losses are determined from a separate set of measurements using a thru line of length equal to the sum of the feed line lengths in the test fixture. Figure 3 presents the measured attenuation α as a function of the frequency. The W, D and ε_r of the slotline are the same as those in Fig. 2. The attenuation of slotline is compared in Table 1 with the measured results from the open literature for microstrip line and coplanar waveguide on various other semiconductor substrate materials. It is worth mentioning here that the attenuation values quoted in Table 1 depend on the substrate thickness, metalization thickness and also the strip conductor width and/or slot width which are not the same in all cases.

IV. CONCLUSIONS AND DISCUSSIONS

The ε_{eff} and α for a slotline on a high resistivity silicon substrate have been experimentally obtained. The attenuation constant for slotline has been compared with that of microstrip line and coplanar waveguide on other semiconductor substrate materials. The value of attenuation for slotline was found to be comparable to other transmission lines. This, however, can only be a rough comparison because attenuation depends upon the substrate thickness, metalization thickness and strip conductor width and/or slot width which are not the same in all the cases. However our experiments demonstrate the viability of high resistivity silicon for low loss antenna feed network. Application of this information to the feed network will be presented at the symposium.

REFERENCES

1. Yan, R.H., et al.: 89-GHz f_T Room-Temperature Silicon MOSFET's, IEEE Electron Device Letters, Vol. 13, No. 5, pp. 256-258, May 1992.

2. Hanes, M.H., et al.: MICROX™ -An All-Silicon Technology for Monolithic Microwave Integrated Circuits, IEEE Electron Device Letters, Vol. 14, No.5, pp. 219-221, May 1993.

3. Hewlett Packard Communications Components, GaAs and Silicon, Designers Catalogue, Section 8, 1993.

4. Hughes millimeter Wave Products Catalogue.

5. Hyltin, T.M.: Microstrip Transmission on Semiconductor Dielectrics, IEEE Trans. Microwave Theory Tech., Vol.MTT-13, No.6, pp.777-781, Nov. 1965.

6. Young, L. and H. Sobel (Editors), Advances in Microwaves, Vol.8, Academic Press, New York, New York, 1974, pp. 19-25.

7. Rosen, A., et al.: Silicon as a Millimeter-Wave Monolithically Integrated Substrate - A New Look, RCA Rev., Vol. 42, pp. 633-660, 1981.

8. Caviglia, A.L. et al.: Microwave Performance of SOI n-MOSFET's and Coplanar Waveguides, IEEE Electron Device Letters, Vol.12, No.1, pp.26-27, Jan. 1991.

9. Levesque, K., et al.: Microwave Characterization of High Resistivity Silicon, Microwave Hybrid Circuits Conf., Oct. 1992.

10. Taub, S.R. and P.G. Young: Attenuation and ε_{eff} of Coplanar Waveguide Transmission Lines on Silicon Substrates, Eleventh Annual Benjamin Franklin Symposium on Antenna and Microwave Technology in the 1990s Digest, pp.8-11, May 1993.

11. Simons, R,N.: Suspended Slot Line Using Double Layer Dielectric, IEEE Trans. Microwave Theory Tech., Vol. MTT-29, No. 10, pp.1102-1107, Oct.1981.

12. Higgins J.A.: Microwave GaAs FET Monolithic Circuits, 1979 IEEE Inter. Solid-State Circuits Conf. Digest of Tech. Papers, pp. 120-121.

13. Haydl, W.H. et al.: Millimeterwave Coplanar Transmission Lines on Gallium Arsenide, Indium Phosphide and Quartz with Finite Metalization Thickness, 1991 IEEE MTT-S Inter. Microwave Symp. Digest, pp. 691-694, 1991.

14. Haydl, W.H.,: Experimentally Observed Frequency Variation of the Attenuation of Millimeter-Wave Coplanar Transmission Lines with Thin Metalization, IEEE Microwave & Guided Wave Letters, Vol.2, No.8, pp.322-324, Aug. 1992.

TABLE 1
Comparision of Attenuation Constant of Microwave Transmission Lines on Semiconductor Substrates

TRANSMISSION LINE	SUBSTRATE MATERIAL	DIMENSIONS (Inch)	ATTENUATION @ 10 GHz (dB/cm)	REFERENCE
Microstrip (Z_0 = 50 Ω)	SI GaAs	D = 0.025 W = 0.025 T = 3 μm*	0.105	12
Coplanar Waveguide (CPW) (Z_0 ≈ 50 Ω)	SI GaAs	D = 0.025 S = 0.025 W = 0.0125 T = 3 μm*	0.16	12
Coplanar Waveguide (CPW)[1] (Z_0 ≈ 35 Ω)	SI InP	D = 0.5 mm S = 88 μm W = 16 μm T = 0.25 μm*	4.5	14
Coplanar Waveguide (CPW) (Z_0 = 50 Ω)	SI GaAs	D = 0.5 mm S = 75 μm W = 56 μm T = 3 μm*	0.45	13
Microstrip (Z_0 = 50 Ω)	High Res. silicon (1.5 k Ω-cm)	D = 0.01 W = 0.006$	0.5	5
Microstrip (Z_0 ≈ 50 Ω)	High Res. Silicon (8 k Ω-cm)	D = 0.021 W = 0.016 T ≈ 3 μm	0.16	9
Coplanar Waveguide (CPW)[2] (Z_0 ≈ 50 Ω)	High Res. Silicon (2.5 - 3.3 k Ω-cm)	D = 0.008 S = 0.004 W = 0.002 T = 2.5 μm*	0.62	10
Coplanar Waveguide (CPW)[2] (Z_0 ≈ 60 Ω)	High Res. Silicon (4 k Ω-cm)	D = 400 μm S = 30 μm W = 35 μm T = 1 μm$	3	8
Slotline[2] (Z_0 = 60 Ω)	High Res. Silicon (5 - 10 k Ω-cm)	D = 0.015 W = 0.004 T = 2.5 μm*	0.25	This work

D is substrate thickness and T is metalization thickness
Microstrip: W is strip width
Coplanar Waveguide: S is center strip width and W is slot width
[1]Metal thickness less than one skin depth
[2]A SiO_2 interfacial layer is present
*Gold conductors, $Aluminium conductors

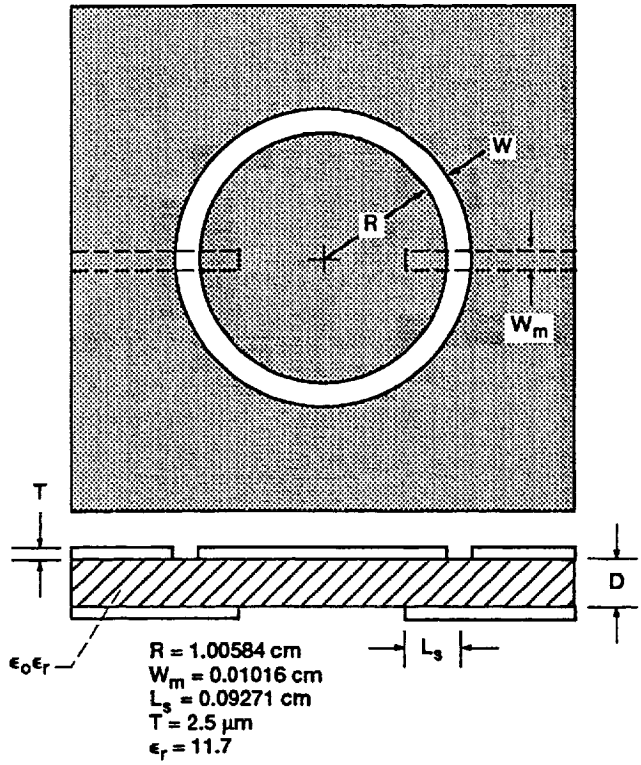

Figure 1.—Slotline ring resonator electromagnetically coupled to microstrip feed lines.

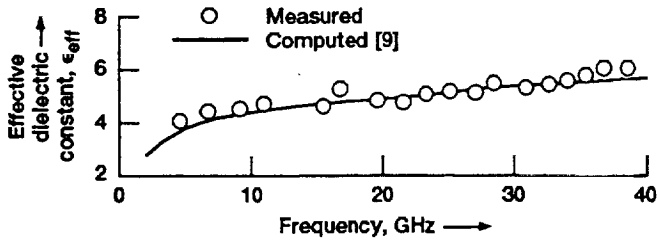

Figure 2.—Effective dielectric constant.

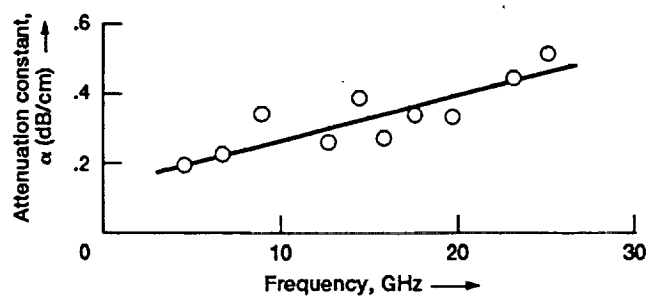

Figure 3.—Attenuation constant.

NEW COPLANAR WAVEGUIDE FEED NETWORK FOR 2 × 2 LINEARLY TAPERED SLOT ANTENNA SUBARRAY

Rainee N. Simons, Thomas D. Perl, and Richard Q. Lee
Mail Stop 54-5
NASA Lewis Research Center
21000 Brookpark Road
Cleveland, Ohio 44135

KEY TERMS

Coplanar waveguide, linearly tapered slot antenna, slot line, array antenna

ABSTRACT

A new technique for exciting 2 × 2 subarray of linearly tapered slot antennas (LTSAs) with coplanar waveguide (CPW) is presented. rf power is coupled to each element through a CPW-to-slotline transition by a coax-to-CPW in-phase four-way radial power divider. The transition and the power divider are coupled by a novel nonplanar CPW right-angle bend. Measured results at 18 GHz show excellent radiation patterns and return-loss characteristics. © 1992 John Wiley & Sons, Inc.

I. INTRODUCTION

Linear tapered slot antennas (LTSAs) are useful in applications which require high gain, narrow beamwidth and wide bandwidth [1]. The most common approach of exciting a single-element LTSA is with a microstrip/slotline transition. Recently, the use of coplanar waveguide feeding a single-element LTSA has been demonstrated [2]. For LTSA arrays, finline-to-waveguide [1] and slotline-to-microstrip [3] feed structures have been reported. The former feeding approach is bulky in size, while the latter could produce spurious radiation.

This article proposes a new technique for exciting a 2 × 2 LTSA subarray using a CPW-to-slotline transition in conjunction with a coax-to-CPW in-phase four-way radial power divider. The transition and the power divider are coupled by a novel nonplanar CPW right-angle bend. This compact feed design is easy to integrate, and using CPW as the transmission medium produces less spurious radiation.

II. CPW FEED NETWORK AND SUBARRAY DESIGN

Figure 1 illustrates the construction of the 2 × 2 LTSA subarray. The feed network for this subarray consists of a CPW-to-slotline transition and a coax-to-CPW in-phase four-way, radial power divider [4] on separate dielectric substrates coupled by a novel nonplanar CPW right-angle bend.

a. LTSA and CPW-to-Slotline Transition. The LTSA and the CPW feed are etched on opposite sides of the circuit board and electromagnetically coupled, as shown in Figure 1. The LTSA is formed by gradually flaring the width of the slotline by an angle 2α. In general, a symmetric beam is required to illuminate a reflector for maximum aperture efficiency, this is achieved by choosing 2α equal to 10.6 degrees [1]. Similarly, to optimize the radiation efficiency of the LTSA, H is chosen to be 0.75 λ_0, where λ_0 is the free-space wavelength at the center frequency f_0 of 18 GHz. The length L of the antenna as determined by α and H is 4.1 λ_0.

To couple power to the antenna, the center strip conductor of the CPW is extended to form a CPW-to-slotline transition with the LTSA. The distances from the short-circuit termination of the slotline and the open termination of the extended center strip conductor, to the CPW-to-slotline junction is approximately a quarter of a wavelength at f_0. To provide a smooth transition, the slotline at the feed end of the LTSA has a circular bend instead of a right-angle bend. The radius of curvature of the bend is approximately $\lambda_{g(slot)}/6$. The finite ground planes of the CPW lines are connected to the antenna ground plane via holes to ensure odd-mode excitation. Further, the CPW ground planes are tapered to provide good impedance match.

The coax-to-CPW in-phase four-way radial power divider circuit board is also shown in Figure 1. Design details for the radial power divider are given in [4].

b. Nonplanar CPW Right-Angle Bend. The nonplanar CPW right-angle bend is illustrated in Figure 2. In this bend, the center strip conductor of the CPW line is enlarged, forming a circular island that facilitates drilling a hole for a pin con-

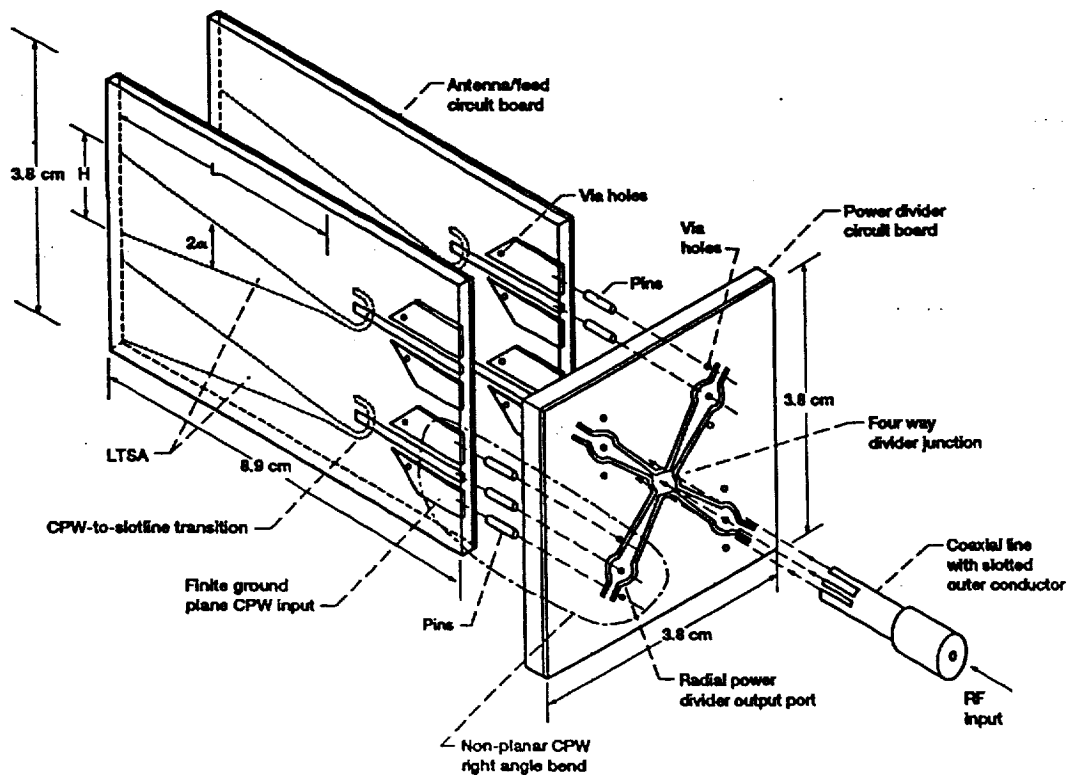

Figure 1 Schematic diagram illustrating the construction of 2 × 2 LTSA subarray

© Microwave and Optical Technology Letters/vol. 5, no. 9, 1992. Reprinted by permission of John Wiley & Sons, Inc.

PRECEDING PAGE BLANK NOT FILMED

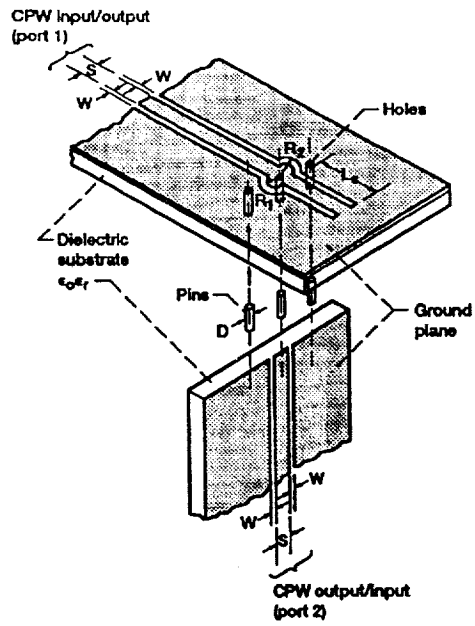

Figure 2 Schematic diagram illustrating nonplanar CPW right-angle bend

nection. Further, the CPW line beyond the island is terminated in a short-circuited stub for impedance matching. The radius of the island R_1, the surrounding slot region R_2, the diameter of the pin D, and the length of the CPW short-circuited stub L_s were experimentally optimized to obtain the best insertion loss and return loss characteristics. R_1, R_2, D, and L_s are approximately 0.043 λ_g, 0.063 λ_g, 0.024 cm, and 0.2 λ_g, respectively, where λ_g is the CPW guide wavelength at f_0. The power divider network as well as the subarray are fabricated on 0.0508-cm-thick RT/Duroid 5880 (ϵ_r = 2.2) circuit board.

III. CPW RIGHT ANGLE BEND AND SUBARRAY PERFORMANCE

The measured insertion loss (S_{21}) of the nonplanar CPW right-angle bend is shown in Figure 3. The measured insertion loss

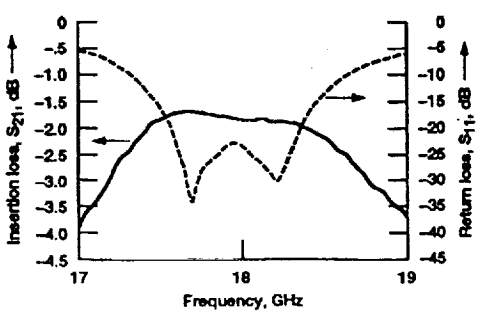

Figure 3 Measured insertion loss (S_{21}) and return loss (S_{11}) of the nonplanar CPW right-angle bend

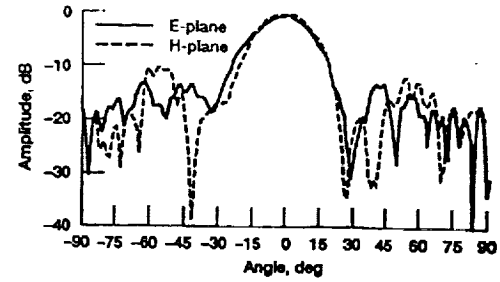

Figure 4 Measured radiation pattern of 2 × 2 LTSA subarray. (a) E plane, (b) H plane

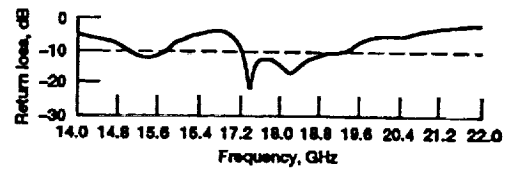

Figure 5 Measured return loss at coaxial input port of the 2 × 2 LTSA subarray

includes the losses occurring in the bend, the attenuation of 2.54-cm length of CPW line on either side of the bend, and that of the two coaxial connectors used at the measurement ports. Also superimposed on Figure 3 is the return loss (S_{11}), which is better than −10 dB and has a bandwidth of 1.45 GHz centered at f_0.

The measured E- and H-plane radiation patterns of the 2 × 2 LTSA subarray at f_0 are shown in Figure 4. The 3-dB beamwidth is approximately 23 degrees in the principal planes, and the measured cross-polarization is less than −16 dB. The measured gain of the single-element LTSA is approximately 11 dB, and hence the gain of the 2 × 2 LTSA subarray is estimated to be 17 dB. Last, as shown in Figure 5, the measured return loss at the coaxial input port of the subarray is better than −10 dB, and the 2:1 VSWR bandwidth is the same as the CPW right-angle bend.

IV. CONCLUSIONS AND DISCUSSIONS

A new feeding technique for a 2 × 2 LTSA subarray using a CPW-to-slotline transition and a coax-to-CPW in-phase four-way radial power divider have been demonstrated. The characteristics of a novel nonplanar CPW right-angle bend have also been presented. The subarray has excellent radiation patterns and symmetric beamwidth. Because of its compactness, this subarray module is suitable as a feed for a reflector antenna or as building blocks for large arrays.

REFERENCES

1. K. S. Yngvesson et al., "The Tapered Slot Antenna—A New Integrated Element for Millimeter-Wave Applications," *IEEE Trans. Microwave Theory Tech.*, Vol. MTT-37, No. 2, Feb. 1989, pp. 365–374.
2. A. Nesic, "Endfire Slot Line Antennas Excited by a Coplanar Waveguide," *IEEE AP-S Int. Symp. Digest*, 1991, pp. 700–702.
3. D. Rascoe et al., "K_a-Band MMIC Beam Steered Planar Array Feed," *1990 IEEE MTT-S Int. Microwave Symp. Digest*, pp. 809–812.
4. R. N. Simons and G. E. Ponchak, "Coax-to-Channelized Coplanar Waveguide In-Phase N-Way, Radial Power Divider," *Electron. Lett.*, Vol. 26, No. 11, May 1990, pp. 754–755.

Received 2-17-92

N94-20505

LINEARLY TAPERED SLOT ANTENNA WITH DIELECTRIC SUPERSTRATE

Rainee N. Simons* and Richard Q. Lee
NASA Lewis Research Center
MS 54-8
Cleveland, Ohio 44135

ABSTRACT

The effect of dielectric superstrate on a linearly tapered slot antenna (LTSA) was investigated experimentally. It was observed that the dielectric superstrate improves the directivity but generally at the expense of higher sidelobe level. The dielectric superstrate could be used to reduce the physical length and to improve the radiation characteristics of the LTSA.

INTRODUCTION

In recent years, research on linearly tapered slot antennas (LTSA) have been extensive [1],[2]. Most of these studies concerns with the performance characteristics and feeding techniques of the LTSA, and there is disproportionately little effort devoted to the study of superstrate effects on linearly tapered slot antennas. These effects are important in a stacked array antenna in which a dielectric spacer between two arrays inadvertently serves as a superstrate. The superstrate alters the guide wavelength of the LTSA and thus impacts the overall antenna design. In this paper, the effects of dielectric superstrate on the directivity and radiation patterns of a full length and reduced length LTAS will be presented and discussed.

ANTENNA CONFIGURATION

The LTSA used in the experiment is shown in Fig. 1. The LTSA having an aperture width L of 1.27 cms, a taper angle, 2α, of 11.2° and an aperture width H of 1.27 cms is etched on a 0.0508 cm RT/Duroid 5880 substrate (ϵ_r =2.2). The LTSA is electromagnetically coupled to a coplanar waveguide (CPW) with the center strip conductor of the CPW extented to form a CPW-to-slotline transition with the LTSA. The distances L_s from the short circuit termination of the slotline and L_w from the open termination of the extented center strip conductor to the CPW-to-slotline junction are about a quarter of a wavelength at 20 GHz. The ground

©1993 IEEE. Reprinted, with permission, from Proceedings of IEEE Antennas and Propagation Society International Symposium, Ann Arbor, Michigan, June 1993, pp. 1482-1485.

plane of the CPW is connected to the antenna ground plane through via holes to ensure good impedance match and odd mode operation.

RESULTS AND DISCUSSIONS

In our experiment, the effect of superstrate was examined for LTSA with various lengths. Fig. 2 shows the measured H- and E- patterns of the regular length (L = 6.6 cm) LTSA without superstrate at 11.67, 20.15 and 22.8 GHz. Results indicate that the patterns are generally symmetrical, and the directivity increases faster in the H-plane than in the E-plane with frequency. The measured gain of the LTSA is about 11 dB.

The superstrate increases the electrical length as well as the effective aperture of the antenna, and thus enhances the antenna directivity. The increase in directivity is evident from the measured antenna pattern which shows a narrower main lobe. Fig. 3(a)-(b) displays the measured H- and E-plane patterns with and without a superstrate. As indicated, the effect of the superstrate is more pronounced in the H-plane than in the E-plane. The beamwidths of the the LTSA with and without superstrate have been recorded for frequencies ranging from 10 to 20 GHz. The results are plotted in Fig. 4. With superstrate, the beamwidth is generally narrower; however, the sidelobe level is also higher.

By reducing the length ,L, of the LTSA, the radiation patterns become broader indicating a reduction in antenna gain. The superstrate increases the electrical length of the LTSA and enhances its directivity. The improvement in directivity results in narrower beamwidth for the LTSA with superstrate as indicated in Fig. 5. Fig. 6 shows the measured patterns of the reduced length LTSA with and without superstrate at 11 GHz. The patterns appear symmetrical with the superstrate.

CONCLUSION

The effect of superstrate on a LTSA has been studied. Results indicate that the superstrate improves the patterns and directivity of the antenna by increasing the electrical length and effective aperture of the antenna. A superstrate can also be used to reduce the physical length of the antenna without compromising the pattern quality.

REFERENCES

[1] K. S. Yngvesson, T. L.Korzeniowski, Y. S. Kim, E. L. Kollerg and J. F. Johansson, "The tapered

slot antenna-a new integrated element for millimeter-wave applications", IEEE Trans. Microwave Therory Tech., Vol. 37, No. 2, Feb. 1989, pp.365-374.

[2] R. N. Simons, R. Q. Lee and T.D. Perl, "New tech nique for exciting linearly tapered slot antennas with coplanar wave guide", Electronics Letters, Vol. 28, No. 7, March 1992, pp. 620-621.

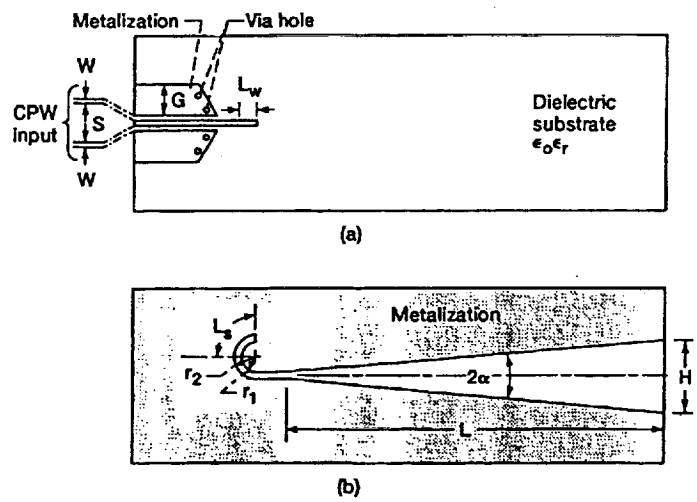

Fig. 1. Schematic for the LTSA and the CPW feed circuit S=0.762 mm, W=0.254 mm, G=5.08 mm, L_w=2.951 mm, r_1=2.171 mm, r_2=2.425 mm, L_s=3.43 mm.
(a) Top metalization is the feed structure.
(b) Bottom metallization is the antenna.

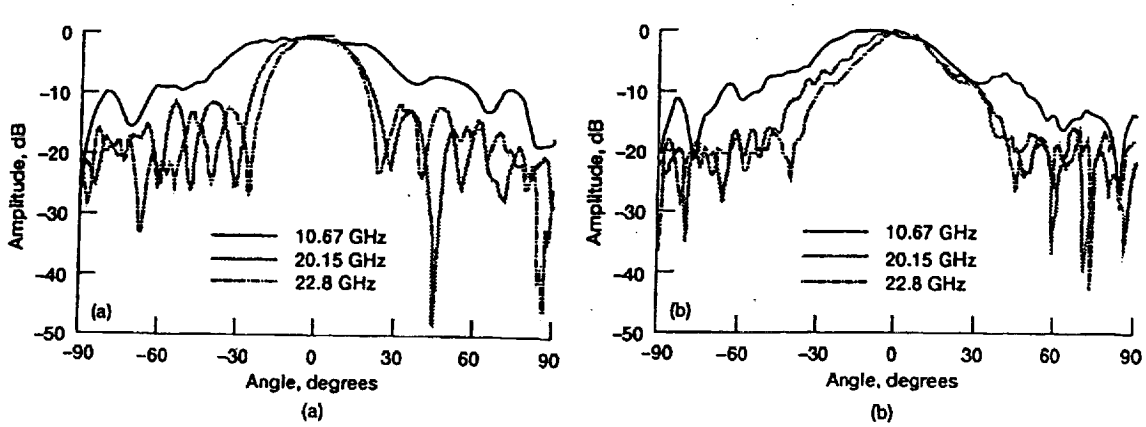

Fig. 2. Measured radiation patterns of the LTSA without a superstrate: (a) H-plane and (b) E-plane.

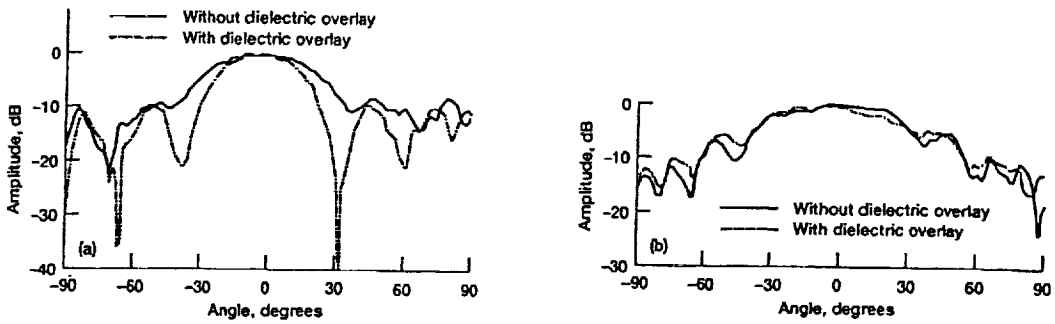

Fig. 3. Measured radiation patterns of the LTSA with and without a superstrate at 11 GHz: (a) H-plane and (b) E-plane.

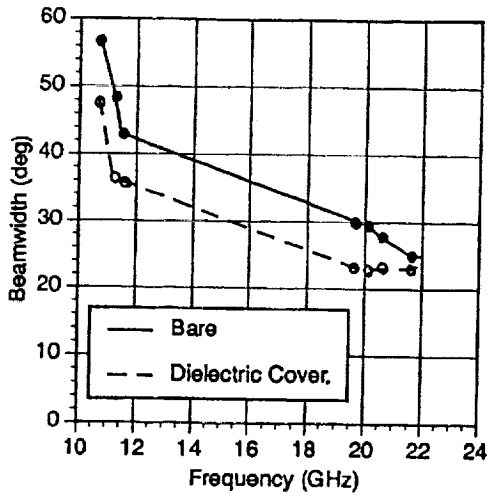

Fig. 4. Measured beamwidth vs. frequency for the LTSA with and without superstrate at 11 GHz.

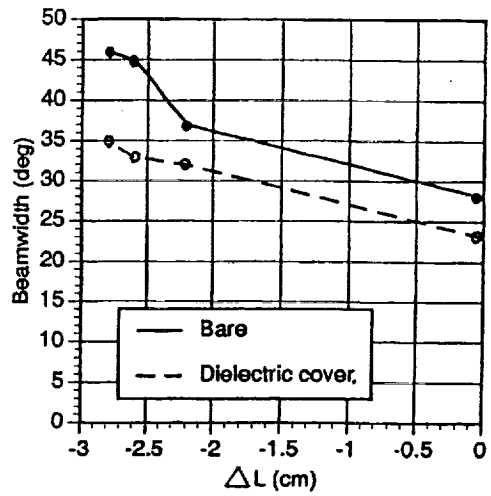

Fig. 5. Measured beamwidth vs. reduced lengths of the LTSA with and without superstrate at 11 GHz.

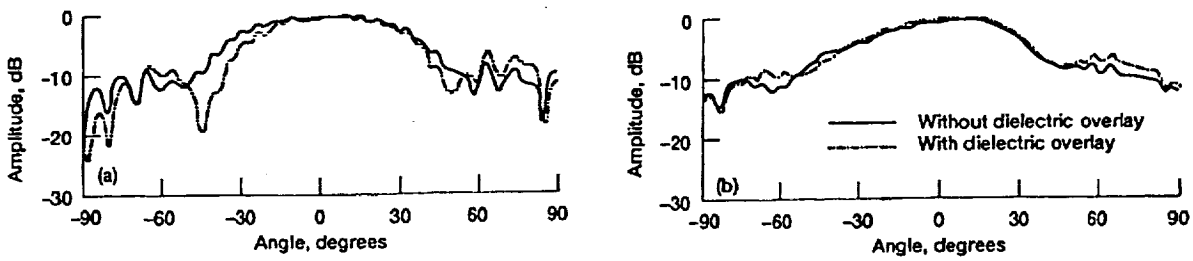

Fig. 6. Measured radiation patterns of the reduced length LTSA with and without superstrate at 11 GHz: (a) H-plane and (b) E-plane.

EFFECT OF A DIELECTRIC OVERLAY ON A LINEARLY TAPERED SLOT ANTENNA EXCITED BY A COPLANAR WAVEGUIDE

Rainee N. Simons, Richard Q. Lee, and Thomas D. Perl
NASA Lewis Research Center
Mail Stop 54-5
21000 Brookpark Road
Cleveland, Ohio 44135

John Silvestro
Electrical Engineering Department
Clemson University
Clemson, South Carolina

KEY TERMS

Slot antenna, coplanar waveguide, antenna feed

ABSTRACT

A linearly tapered slot antenna (LTSA) with a dielectric overlay was experimentally investigated. The presence of dielectric overlay alters the guide wavelength of the LTSA, and thus the radiation characteristics of the antenna. Results indicate that dielectric overlay could be used to reduce the physical length and to improve the radiation characteristics of the LTSA. © *1993 John Wiley & Sons, Inc.*

I. INTRODUCTION

The linearly tapered slot antenna (LTSA) has been developed for potential millimeter-wave applications, e.g., as a radiating element for reflector or lens antennas. Compared to other types of printed circuit antennas, these end-fire antennas have higher directivity, broader bandwidth, and less spatial constraint for solid-state device integration [1]. The LTSA has been studied extensively in the past decade. Most of these studies concern the performance characteristics and feeding techniques of the LTSA [2, 3]. Recently, a LTSA of nonplanar geometry fed with a balanced microstrip line has also been reported to have excellent radiation and bandwidth characteristics [4]. Despite all these efforts, little information is available on the effects of dielectric overlays on linearly tapered slot antennas. These effects are important in a stacked array antenna in which a dielectric spacer between two arrays inadvertently serves as an overlay. In addition, the dielectric overlay changes the guide wavelength of the LTSA and thus impacts the overall antenna design. In this article we report our experimental findings of the effects of dielectric overlay and also the effects of reduction in physical length of the LTSA on the radiation patterns.

II. DESIGN AND FABRICATION

Figure 1 shows the layout of the LTSA which has a physical length L of 6.6 cm, a taper angle, 2α, of 11.2 degrees, and an aperture width H of 1.27 cm. The LTSA is electromagnetically coupled to a coplanar waveguide (CPW) feed etched on the opposite side of a 0.0508-cm RT/Duroid 5880 substrate ($\epsilon_r = 2.2$). The finite ground plane of the CPW is connected to the antenna ground plane via holes to ensure good impedance match and odd-mode operation. For efficient power coupling, the center strip conductor of the CPW is extended to form a CPW-to-slot-line transition with the LTSA. The distance L_s from the short-circuit termination of the slot line, the L_w from open termination of the extended center strip conductor, to the CPW-to-slot-line junction are about a quarter of a wavelength at the center frequency of 20 GHz. To provide a smooth transition, the slot line at the feed end has a circular bend instead of a right-angle bend.

III. RESULTS AND DISCUSSIONS

In our experiments, the effect of dielectric overlay was examined for LTSA with regular and reduced lengths. These results were compared to those of identical LTSA without dielectric overlay. The experimental findings are summarized below.

A. Regular-Length LTSA Performance. The measured return loss is displayed in Figure 2, which shows a 2:1 VSWR bandwidth of 20 GHz over a frequency range of 10–30 GHz. These results indicate that the regular-length (L = 6.6 cm) LTSA without overlay has ultrawideband characteristics and good impedance match. Typical measured H- and E-plane radiation patterns are shown in Figures 3(a) and 3(b), respectively. The patterns are generally symmetrical over a wide range of frequencies. Results also indicate that the directivity increases faster in the H plane than in the E plane with increasing frequency. The measured gain of the LTSA is about 11 dB.

B. Overlay Effect. The effect of the overlay was found to have a significant effect on the regular-length LTSA at the lower end of the frequency band. At these frequencies, the

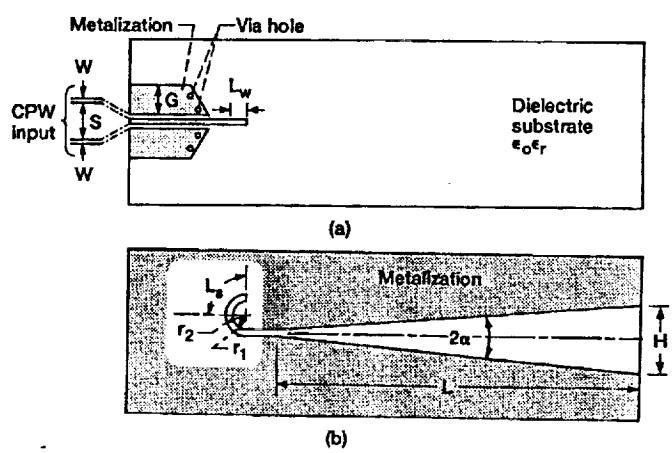

Figure 1 Schematic for the LTSA and the CPW feed circuit. (a) Top metallization is the feed structure. (b) Bottom metallization is the antenna. S = 0.762 mm, W = 0.254 mm, G = 5.08 mm, L_w = 2.951 mm, r_1 = 2.171 mm, r_2 = 2.425 mm, L_s = 3.43 mm

© Microwave and Optical Technology Letters/vol. 6, no. 4, 1993. Reprinted by permission of John Wiley & Sons, Inc.

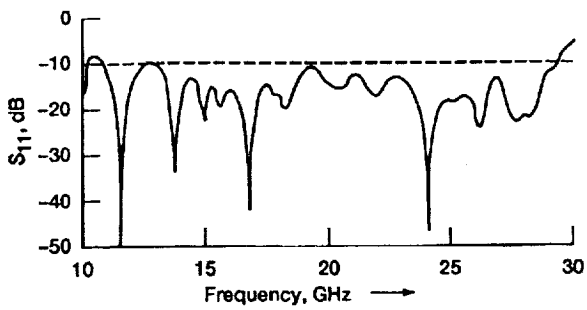

Figure 2 Measured return loss (S_{11}) as a function of frequency.

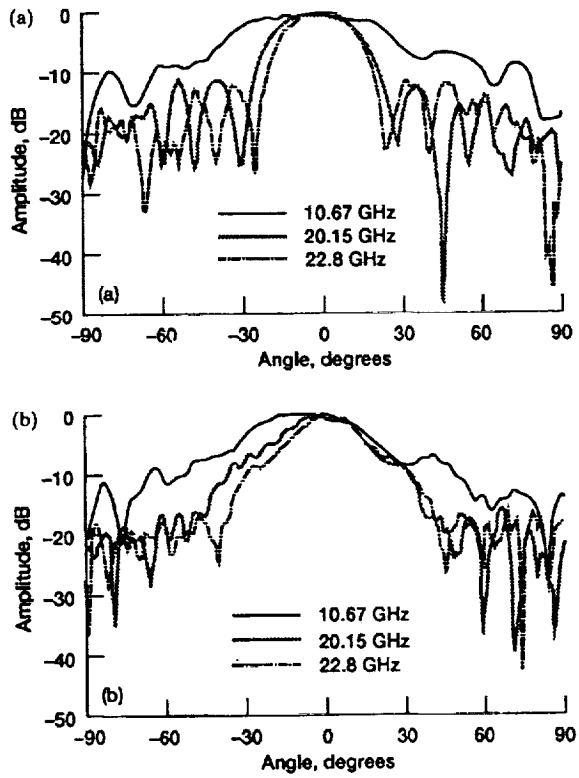

Figure 3 Measured radiation patterns of the regular-length LTSA without a dielectric overlay at 10.67, 20.15, and 22.8 GHz. (a) *H* plane, (b) *E* plane

electrical length and the effective aperture are small; hence the directivity is low and the beamwidth is broad. By introducing an overlay, the electrical length as well as the effective aperture are increased, thus enhancing the directivity. The increase in directivity is evident from the measured antenna pattern which now has a narrower main lobe. Figures 4(a) and 4(b) illustrate the measured *H*- and *E*-plane radiation patterns without and with an overlay. These patterns further indicate that the effect of overlay is more pronounced in the *H* plane than in the *E* plane. This is due to the fact that in the *E* plane, the incident wave is perpendicular to the plane of the substrate.

C. Reduced-Length LTSA Performance. By reducing the length *L* from 6.6 to 4.4 cm the radiation pattern broadens due to reduction in gain. By providing a dielectric overlay the

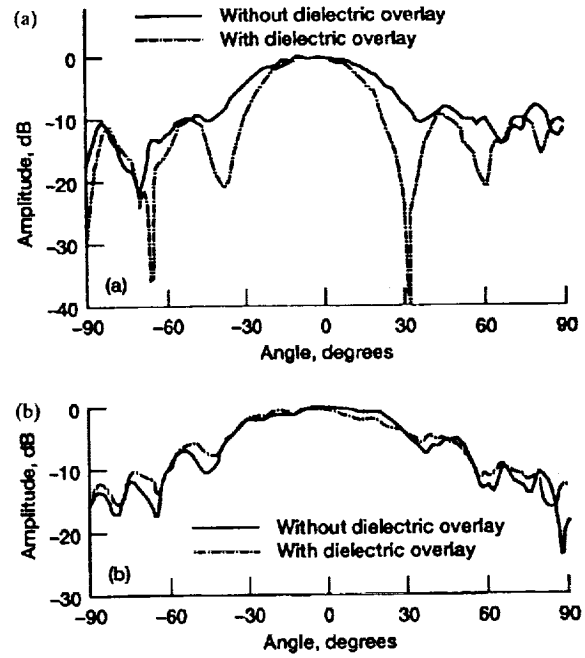

Figure 4 Measured radiation patterns of the regular-length LTSA without and with a dielectric overlay at 11 GHz. (a) *H* plane, (b) *E* plane

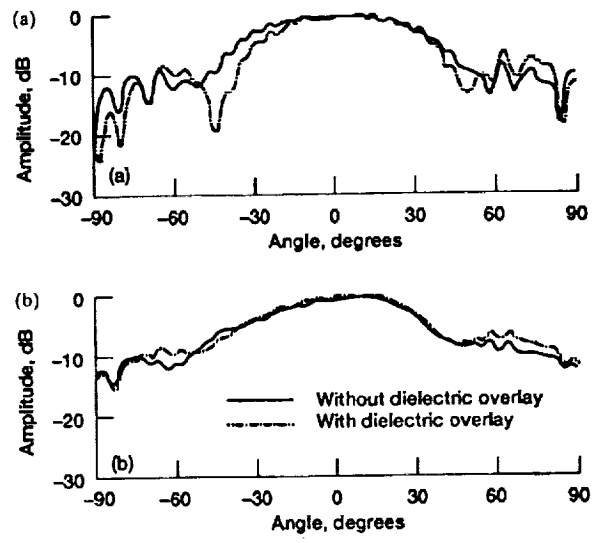

Figure 5 Measured radiation patterns of the *reduced*-length LTSA without and with a dielectric overlay at 11 GHz. (a) *H* plane, (b) *E* plane

electrical length of the LTSA increases and the directivity improves. The improvement in directivity is evident from the patterns shown in Figures 5(a) and 5(b).

IV. CONCLUSION

The effect of dielectric overlay on a LTSA has been studied. The LTSA under study exhibits very wide bandwidth and excellent radiation patterns. A dielectric overlay improved the patterns and directivity of the antenna by increasing the electrical length and effective aperture of the antenna. A

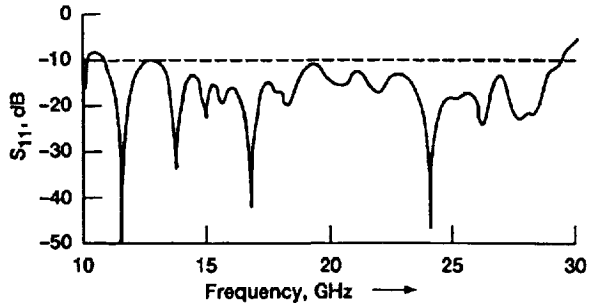

Figure 2 Measured return loss (S_{11}) as a function of frequency.

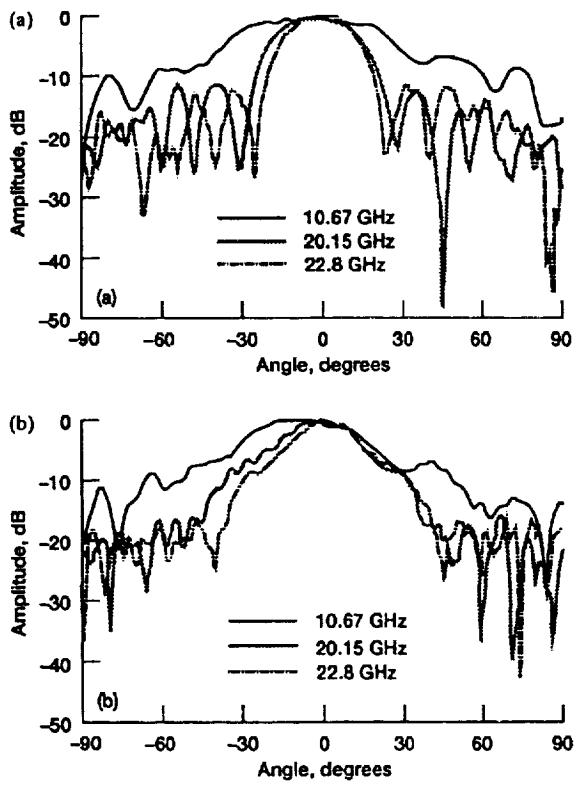

Figure 3 Measured radiation patterns of the regular-length LTSA without a dielectric overlay at 10.67, 20.15, and 22.8 GHz. (a) *H* plane, (b) *E* plane

electrical length and the effective aperture are small; hence the directivity is low and the beamwidth is broad. By introducing an overlay, the electrical length as well as the effective aperture are increased, thus enhancing the directivity. The increase in directivity is evident from the measured antenna pattern which now has a narrower main lobe. Figures 4(a) and 4(b) illustrate the measured *H*- and *E*-plane radiation patterns without and with an overlay. These patterns further indicate that the effect of overlay is more pronounced in the *H* plane than in the *E* plane. This is due to the fact that in the *E* plane, the incident wave is perpendicular to the plane of the substrate.

C. Reduced-Length LTSA Performance. By reducing the length *L* from 6.6 to 4.4 cm the radiation pattern broadens due to reduction in gain. By providing a dielectric overlay the

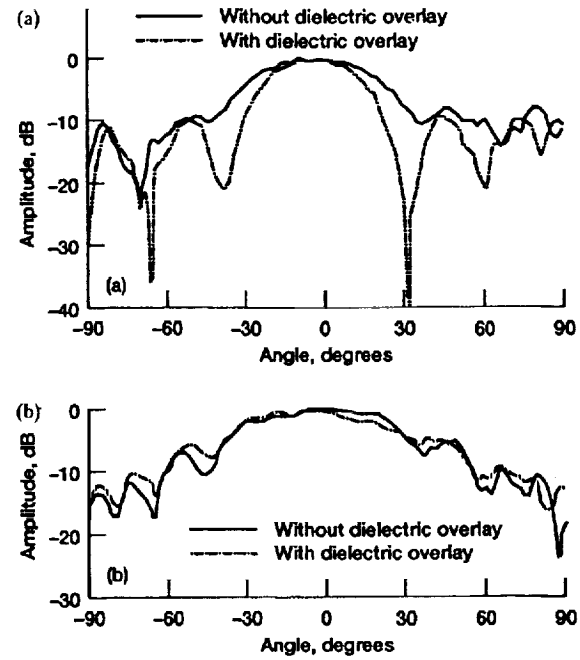

Figure 4 Measured radiation patterns of the regular-length LTSA without and with a dielectric overlay at 11 GHz. (a) *H* plane, (b) *E* plane

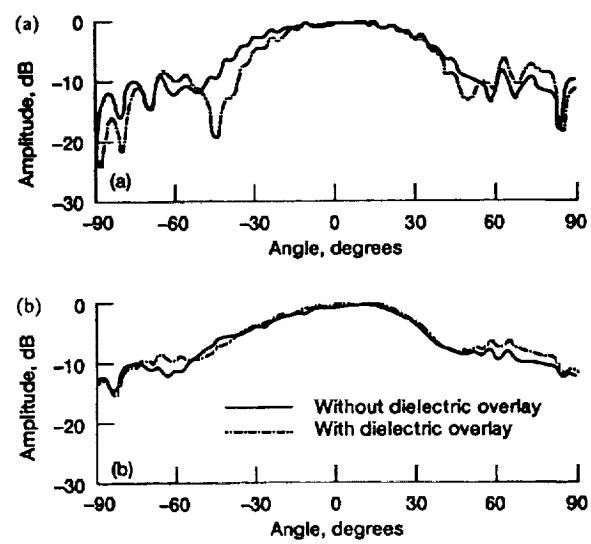

Figure 5 Measured radiation patterns of the *reduced*-length LTSA without and with a dielectric overlay at 11 GHz. (a) *H* plane, (b) *E* plane

electrical length of the LTSA increases and the directivity improves. The improvement in directivity is evident from the patterns shown in Figures 5(a) and 5(b).

IV. CONCLUSION

The effect of dielectric overlay on a LTSA has been studied. The LTSA under study exhibits very wide bandwidth and excellent radiation patterns. A dielectric overlay improved the patterns and directivity of the antenna by increasing the electrical length and effective aperture of the antenna. A

dielectric overlay can also be used to reduce the physical length of the antenna without compromising the pattern quality.

REFERENCES

1. K. S. Yngvesson, T. L. Korzeniowski, Y. S. Kim, E. L. Kollberg, and J. F. Johansson, "The Tapered Slot Antenna—A New Integrated Element for Millimeter-Wave Applications," *IEEE Trans. Microwave Theory Tech.*, Vol. MTT-37, No. 2, Feb. 1989, pp. 365–374.
2. A. Nesic, "Endfire Slotline Antennas Excited by a Coplanar Waveguide," *IEEE Antennas and Propagation Society International Symposium Digest*, 1991, pp. 700–702.
3. R. N. Simons, R. Q. Lee, and T. D. Perl, "New Technique for Exciting Linearly Tapered Slot Antennas with Coplanar Waveguide," *Electron. Lett.*, Vol. 28, No. 7, March 1992, pp. 620–621.
4. R. N. Simons, R. Q. Lee, and T. D. Perl, "Non-Planar Linearly Tapered Slot Antenna with Balanced Microstrip Feed," *1992 IEEE Antennas and Propagation International Symposium Digest*, Vol. 4, pp. 2109–2112.

Received 9-25-92

CHARACTERISTICS OF LINEARLY TAPERED SLOT ANTENNA WITH CPW FEED ON HIGH RESISTIVITY SILICON

Rainee N. Simons
Sverdrup Technology, Inc.
Lewis Research Center Group
Brook Park, Ohio 44142

and

Susan R. Taub and Richard Q. Lee
National Aeronautics and Space Administration
Lewis Research Center
Cleveland, Ohio 44135

SUMMARY

A linearly tapered slot antenna (LTSA) has been fabricated on a high resistivity silicon substrate and tested at C-Band frequencies. The LTSA is electromagnetically coupled to a coplanar waveguide (CPW) feed. In this paper, the measured radiation patterns, gain and return loss are presented and discussed.

INTRODUCTION

Linearly tapered slot antennas (LTSA's) have many exceptional features such as narrow beamwidth, high element gain, wide bandwidth and small transverse spacing between elements in an array. These features make them attractive in satellite communication antennas (ref. 1). Previously reported LTSA antennas are fabricated on low dielectric constant RT-5880 Duroid substrate (refs. 2 to 4). This paper describes the design and performance of a LTSA constructed on a high resistivity silicon substrate. By choosing a silicon substrate with sufficiently high resistivity it is possible to make the dielectric attenuation constant of the microwave transmission line for the feed network approach that of GaAs (ref. 5). Compared to designs presented earlier, the new design has smaller dimensions because of the higher dielectric constant of silicon. In addition, the use of silicon provides for the potential of integration with silicon MMIC's and digital control circuits. Lastly, when compared with GaAs, silicon wafers are available in much larger diameters and at lower cost thus facilitating integration of active devices, antenna and control circuits on a single wafer.

ANTENNA DESIGN AND FABRICATION

The antenna and the feed network are fabricated on a single 5000 to 10,000 Ω-cm silicon wafer. The thickness of the wafer is 0.381 mm with $\varepsilon_r = 11.7$. The thickness of the gold metalization is about 2.5 μm which is about three times the skin depth at the center frequency f_o of 6 GHz. This substrate has an effective thickness ratio (ref. 1) of 0.02 which is within the optimum range for high gain and low side lobes. Figure 1 shows a feed with electromagnetic coupling between a grounded CPW (GCPW) and slotline which are on opposite sides of a silicon wafer (ref. 6). At the GCPW input port, Z_o is 50 Ω while close to the transition to the slotline Z_o is 60 Ω. The Z_o of the slotline is 70 Ω. The distances L_s and L_m are $\sim\lambda_{g(slotline)}/4$ and $\lambda_{g(microstrip)}/4$, respectively at f_o. The LTSA is formed by gradually flaring the width of the slotline by an angle 2α. When 2α is close to 11 degrees a symmetric beam width is achieved for an antenna on Duroid (ref. 1). A symmetric beam results in high aperture efficiency if used for illuminating a reflector. The width H of the antenna is

arbitrarily chosen as 0.3 $\lambda_{g(slotline)}$. The length L of the antenna as determined by α and H which is 1.5 $\lambda_{g(slotline)}$. Figure 2 shows a picture of the fabricated antenna.

ANTENNA PERFORMANCE AND DISCUSSIONS

The measured return loss (S_{11}) at the coaxial input port of the feed network is shown in figure 3. The return loss is observed to be better than −10 dB (2:1 VSWR) over a frequency range extending from 6 to 8 GHz. Although, the antenna has been designed at 6 GHz, the best return loss occurs at about 7 GHz. This could be due to double side processing of the wafer which might have inadvertently offset the feed resulting in a shorter stub length. Typical measured E- and H-plane radiation patterns are shown in figure 4. The patterns are found to have good characteristics. The measured gain of the antenna is 5, 7, and 9 dB at 5, 7, and 9.4 GHz, respectively. Lastly, optimization of the LTSA on silicon has not been carried out and better performance might be expected with improvements.

CONCLUSIONS

The design and performance characteristics of a LTSA fabricated on high resistivity silicon wafer is presented. The LTSA exhibits good impedance match and radiation patterns.

ACKNOWLEDGMENT

The authors would like to thank Paul G. Young for the fabrication of the antenna.

REFERENCES

1. Yngvesson, K.S., et al.: The Tapered Slot Antenna - A New Integrated Element for Millimeter-Wave Applications. IEEE Trans. Microwave Theory Tech., vol. MTT-37, no. 2, Feb. 1989, pp. 365-374.

2. Yngvesson, K.S., et al.: Endfire Tapered Slot Antennas on Dielectric Substrates. IEEE Trans. Antennas Propagat., vol. AP-33, no. 12, Dec. 1985, pp. 1392-1399.

3. Nesic, A.: Endfire Slot Line Antennas Excited by a Coplanar Waveguide. IEEE Antennas and Propagation Society International Symposium Digest, vol. 2, IEEE, Piscataway, NJ, 1991, pp. 700-702.

4. Simons, R.N., et al.: New Techniques for Exciting Linearly Tapered Slot Antennas with Coplanar Waveguide. Electron. Lett., vol. 28, no. 7, Mar. 1992, pp. 620-621.

5. Rosen, A., et al.: Silicon as a Millimeter-Wave Monolithically Integrated Substrate – A New Look. RCA Rev., vol. 42, Dec. 1981, pp. 633-660.

6. Simons, R.N., et al.: Novel Coplanar Waveguide to Slotline Transition on High Resistivity Silicon. Electron. Lett., vol. 28, no. 24, Nov. 1992, pp. 2209-2210.

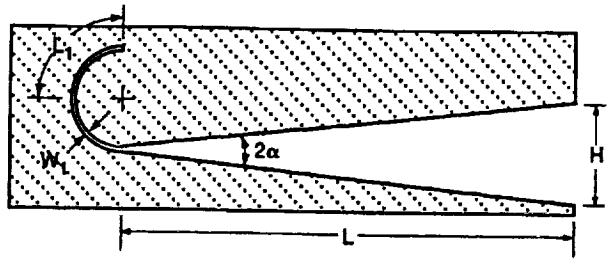

(a) Front side metalization.

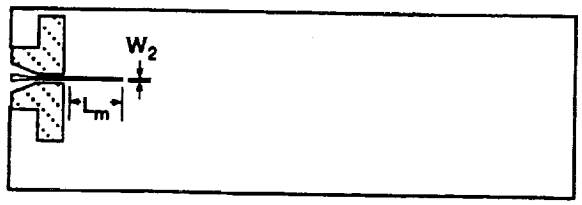

(b) Back side metalization.

Figure 1.—Schematic of the linearly tapered slot antenna. W_s = 0.16 mm, W_m = 0.15 mm.

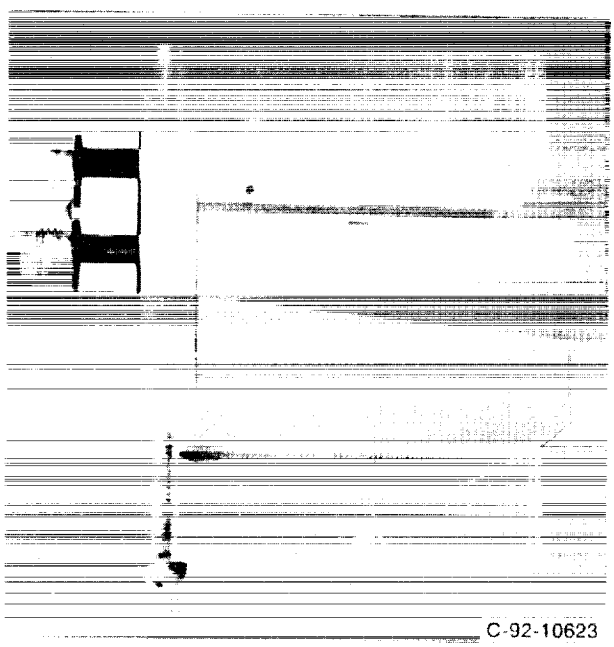

(a) Linearly Tapered Slot Antenna (LTSA) on silicon.

(b) Coplanar Waveguide Feed (CPW) for Linearly Tapered Slot Antenna on silicon.

Figure 2.—Photograph of the antenna.

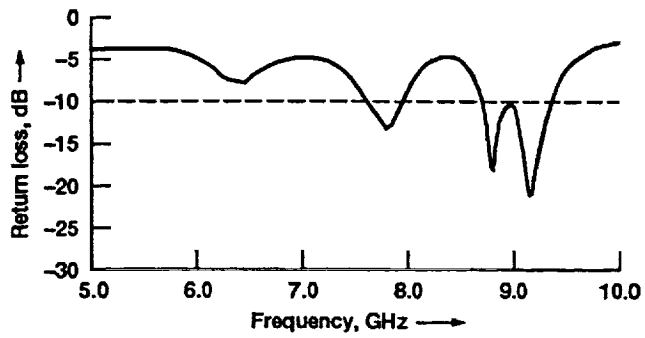

Figure 3.—Measured return loss (S_{11}) at the coaxial input port.

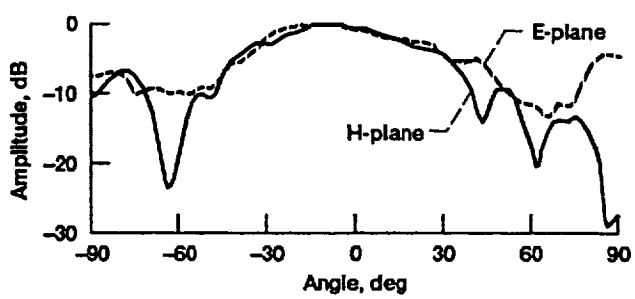

Figure 4.—Measured radiation pattern of the LTSA at 7 GHz.

NONPLANAR LINEARLY TAPERED SLOT ANTENNA WITH BALANCED MICROSTRIP FEED

Rainee N. Simons
Sverdrup Technology, Inc.
Lewis Research Center Group
Brook Park, Ohio 44142

Richard Q. Lee
National Aeronautics and Space Administration
Lewis Research Center
Cleveland, Ohio 44135

and

Thomas D. Perl
University of Akron
Akron, Ohio 44325

ABSTRACT

A nonplanar linearly tapered slot antenna (LTSA) has been fabricated and tested at frequencies from 8 to 32 GHz. The LTSA is excited by a broadband balanced microstrip transformer. The measured results include the input return loss as well as the radiation pattern of the antenna.

INTRODUCTION

Linearly tapered slot antennas (LTSAs) have many salient features such as narrow beam width, high element gain, wide bandwidth and small transverse spacing between elements in an array. These features make them attractive in satellite communication antennas involving beam shaping and switching (ref. 1). Previously reported LTSA antennas are excited either by a fin line (ref. 2), coplanar waveguide (CPW) (ref. 3), or by a microstrip to slot line transition (ref. 3). The latter makes use of quarter wavelength stubs for impedance matching and hence the 2:1 VSWR bandwidth of the circuit is very small (ref. 3).

This paper describes the design and performance of a LTSA excited by a balanced microstrip (fig. 1). Compared to the fin line feed, the new design is smaller, less complex, and is not limited to a waveguide band. In addition, when compared to CPW or microstrip/slot line feed, the new design eliminates the necessity of quarter wavelength stubs and hence has a much wider bandwidth.

BALANCED MICROSTRIP FEED DESIGN

The feed system, as shown in figure 1, consists of a conventional microstrip on a dielectric substrate of thickness D with the ground plane tapered to a width equal to the strip width W (0.071 cm) to form a balanced microstrip. The radius R_2 of the arc is arbitrarily chosen as half free space wavelength ($\lambda_0/2$) at the design frequency (f_0) of 18 GHz. The taper helps to match the characteristic impedance of the conventional microstrip (50 Ω) to the balanced microstrip. The characteristic impedance of the balanced microstrip is chosen as $\approx$160 Ω which is equal to the input impedance of the LTSA. This input impedance is twice the input impedance of a regular half LTSA above a ground plane ($\approx$80 Ω) (ref. 2). The electric field lines at various cross sections along the feed and the antenna are shown in figure 2. The electric field lines which are spread out in the conventional microstrip concentrate between the metal strips of the balanced microstrip and finally rotate while travelling along the axis of the antenna.

NONPLANAR LTSA DESIGN

The nonplanar LTSA is formed by gradually flaring the strip conductors of the balanced microstrip on opposite sides of the dielectric substrate by an angle α with respect to the antenna axis. A symmetric beam width is necessary while illuminating a reflector for maximum aperture efficiency; this is achieved is 2α is close to 11° (ref. 1). Hence α is chosen as 5.3° in our design. The radius R_1 of the arc is arbitrarily chosen as 0.9 λ_0. In order for the LTSA to operate as a travelling wave antenna, the width H must be greater than $\lambda_0/2$ (ref. 1); hence, H is chosen as 0.75 λ_0. The length L of the antenna as determined by α and H is 4.3 λ_0. The entire circuit is fabricated on 0.0508 cm thick RT/Duroid 5880 ($\varepsilon_r = 2.2$) substrate. This substrate has an effective thickness ratio of 0.03 which is within the optimum range for high gain and low side lobes (ref. 1).

ANTENNA PERFORMANCE AND DISCUSSIONS

The measured return loss (S_{11}) at the coaxial input port of the feed network is shown in figure 3. The return loss is observed to be better than -10 dB (2:1 VSWR) over a frequency range extending from 8 to 32 GHz. This is a significant improvement over the LTSA reported in the literature (ref. 3).

The measured E- and H-plane radiation patterns at three different frequencies are shown in figures 4(a) and (b) respectively. The measured patterns are found to be excellent.

The measured H-Plane cross-polarized radiation is -16 dB below the copolarized radiation at f_0. Further improvement could be achieved by varying the substrate thickness.

CONCLUSIONS

The design and performance characteristics of a LTSA with a balanced microstrip feed network has been presented. A LTSA fed with this feed network exhibits very broad bandwidth extending from X-band to Ka-band with good impedance match and excellent radiation patterns.

REFERENCES

1. Yngvesson, K.S., et al.: The Tapered Slot Antenna - A New Integrated Element for Millimeter-Wave Applications. IEEE Trans. Microwave Theory Tech., vol. MTT-37, no. 2, Feb. 1989, pp. 365-374.

2. Yngvesson, K.S., et al.: Endfire Tapered Slot Antennas on Dielectric Substrates. IEEE Trans. Antennas Propag., vol. AP-33, no. 12, Dec. 1985, pp. 1392-1399.

3. Nesic, A.: Endfire Slot Line Antennas Excited by a Coplanar Waveguide. IEEE AP-S International Symposium Digest, IEEE, New York, 1991, pp. 700-702.

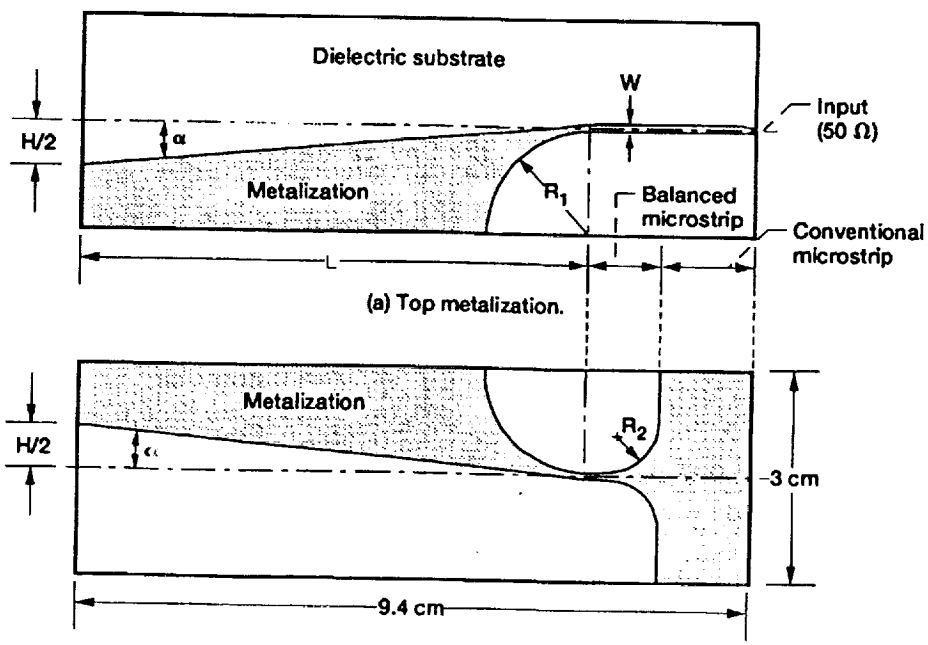

(b) Bottom metalization.

Figure 1.—Non-planar linearly tapered slot antenna and feed network.

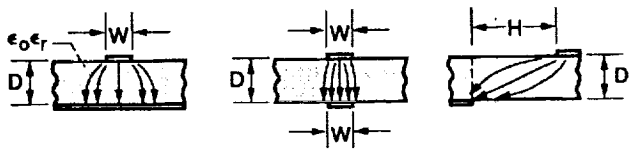

(a) Conventional microstrip. (b) Balanced microstrip. (c) Antenna radiating edge.

Figure 2.—The electric field distribution at various cross sections.

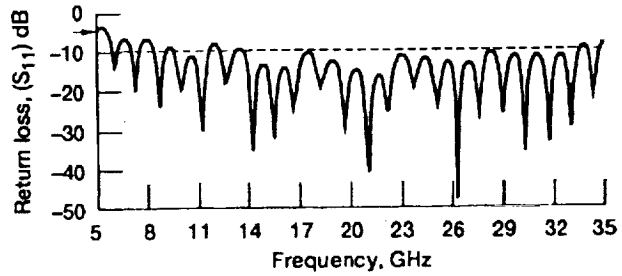

Figure 3.—Measured return loss (S_{11}) at the coaxial input port.

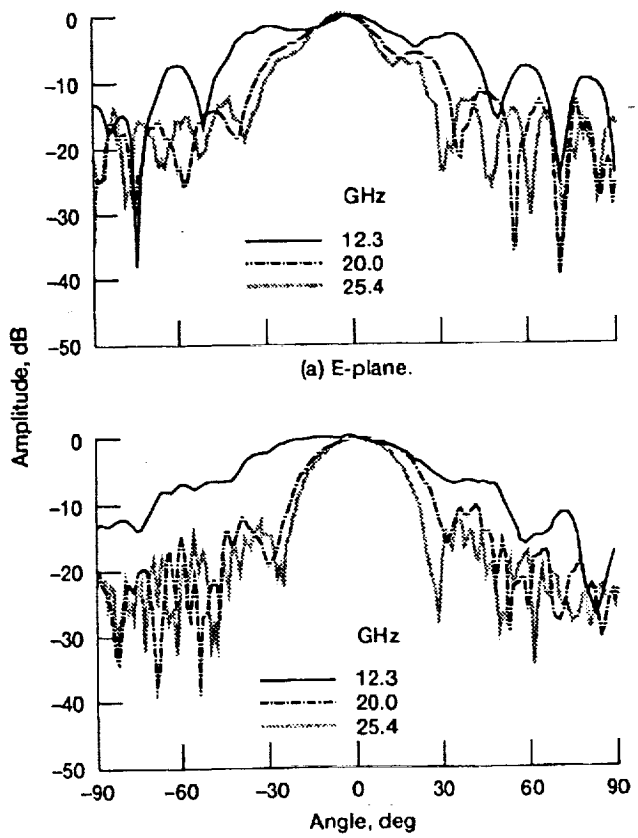

Figure 4.—Measured radiation pattern of the non-planar LTSA.

C-2

N94-20506

SLOT-COUPLED PATCH ANTENNA WITH COPLANAR WAVEGUIDE FEED

Richard Q. Lee* and Rainee N. Simons
NASA Lewis Research Center
MS 54-8
Cleveland, OH 44135

ABSTRACT

Two slot-coupled feeding techniques for exciting a patch antenna with a coplanar waveguide (CPW) were experimentally investigated. In the first technique, a CPW with two notches on both sides of the slot lines is used to couple power to the antenna through a narrow rectangular slot. In the second technique, a grounded CPW with a series gap in the center strip conductor is used to couple power to the antenna through a 'dumbbell' slot. Results indicated that both techniques are feasible and yield high coupling efficiency.

INTRODUCTION

Previous work on slot-coupled patch antennas concerns mainly with feed structure of microstrip type. Only recently, slot-coupled feeding technique with coplanar waveguide (CPW) feed has been demonstrated [1]. Compared to direct probe feeding approach, slot-coupled feeding requires no physical contact with the antenna, has wider bandwidth, and allows independent optimization of antennas and feed networks by using substrates of different thickness and permittivity. Further, the use of CPW as transmission media can reduce circuit radiation losses, and facilitates monolithic microwave integrated circuit (MMIC) device integration.
In this paper, we report two feeding techniques where the patch antenna is excited by coupling power electromagnetically through a slot from a CPW feed. The two techniques differ from each other in the CPW feed structure and slot designs. The first technique uses a grounded CPW with notches on both sides of the slot lines and a narrow rectangular slot, while the second technique uses a CPW with a series gap in the center strip conductor and a 'dumbbell' slot. The latter permits insertion of solid state devices in the series gap of the CPW and thus, is suitable for use in active antenna or quasi-optical combiner/mixer designs. To optimize the coupling efficiency, three different slot/gap designs have been tested.

DESIGN DESCRIPTION

Figure 1 (a) shows the slot-coupled patch antenna excited by a CPW with notches on both sides of the slot lines. The patch and the CPW feed structure are fabricated on separate substrates with the rectangular slot located in the common ground plane directly above the notches. The slot width and length are initially chosen to be 0.254 mm and $\lambda_{g(\text{slot line})}/2$ respectively, where λ_g is the wavelength of an uniform slot line [2]. The slot length is then

© 1992 IEEE. Reprinted, with permission, from Proceedings of IEEE Antennas and Propagation Society International Symposium, Chicago, Illinois, July 1992, pp. 1048-1051.

slightly reduced to account for the slot end effects. The notch has a width of 0.762 mm and an end-to-end distance approximately equal to the slot length. To ensure good coupling and odd mode operation, the CPW is terminated in a short circuit at a distance of approximately $\lambda_{g(cpw)}/2$ from the center of the notch, and a pair of bond wires is inserted on both sides of the notches.
Figure 1 (b) shows the slot-coupled patch antenna excited by a CPW with a series gap in the center strip conductor. The inset in Figure 3 shows the three different slot/gap designs tested. In the first design, the dimensions of the series gap and the rectangular slot are (L_1, S) and (L_2, W_2) respectively. In the second design, the width of the series gap is enlarged from S to S_1 by flaring the center strip conductor of the CPW near the gap location. In the third design, the rectangular slot is replaced by a 'dumbbell' slot of identical length and width. The design parameters are given in the figure caption.

RESULTS AND DISCUSSIONS

Measured input impedance on Smith chart for the patch antenna with CPW/notch feed structure is shown in Figure 2. At the best impedance match frequency of 14 GHz, the return loss is greater than 20 dB and the 2:1 VSWR bandwidth is 4.2 %. Figure 3 shows the measured return losses for the three different feed configurations. As indicated, the return losses are improved from -8.2 dB for (a) to -13.2 dB for (b) to -16.9 dB for (c). Results indicate that the coupling efficiency was improved by more than 3 dB each by using an enlarged series gap or a 'dumbbell' slot. However, the geometrical change in the series gap and slot of the feed structure produced a slight change in the resonance frequency. Measured H- and E-plane patterns for the patch antenna excited by a CPW through notch/slot and gap/slot coupling are displayed in Figure 4 (a) and (b) respectively. The patterns appear symmetrical. The measured front-to-back ratio is about 14 dB which is typical for slot-coupled antenna configurations.

CONCLUSION

Two slot-coupled techniques for exciting patch antennas with CPW feeds have been demonstrated. Techniques for improving coupling efficiency are also described and discussed. Measured results indicate excellent patterns and coupling efficiency.

REFERENCES:

[1] R. N. Simons, R. Q. Lee and G. R. Lindamood, "Electromagnetic coupling between coplanar waveguide and microstrip antennas," to be published in the Microwave and Opical Technology Letters, Vol. 5, February 1992.
[2] R. N. Simons, "Suspended slot line using double layer dielectric," IEEE Trans. Microwave Theory Tech., Vol. MTT-29, No. 10, Oct. 1981, pp. 1102-1107.

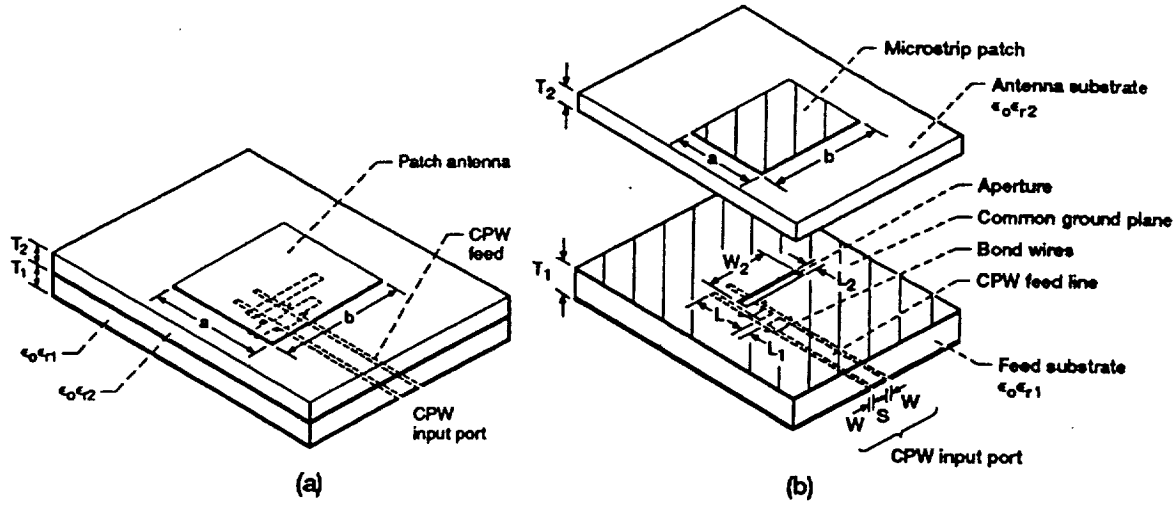

Fig. 1 Schematic of the CPW fed patch antenna with: (a) notch/slot coupling and (b) gap/slot coupling L_1=0.025 cm, L=0.711 cm, L_2=0.025 cm, W_2=0.69 cm, a=0.76 cm, b=1.14 cm, T_1=0.051 cm, T_2=0.025 cm, S=o.076 cm, W=0.025 cm, ϵ_{r1}=2.2, ϵ_{r2}=2.2

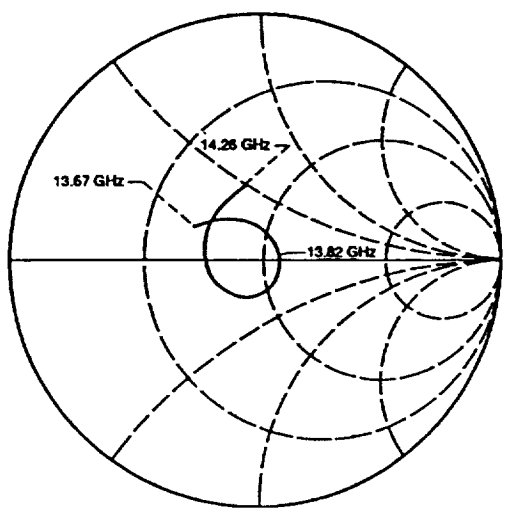

Fig. 2 Measured input impedance of the CPW fed patch antenna with notch/slot coupling.

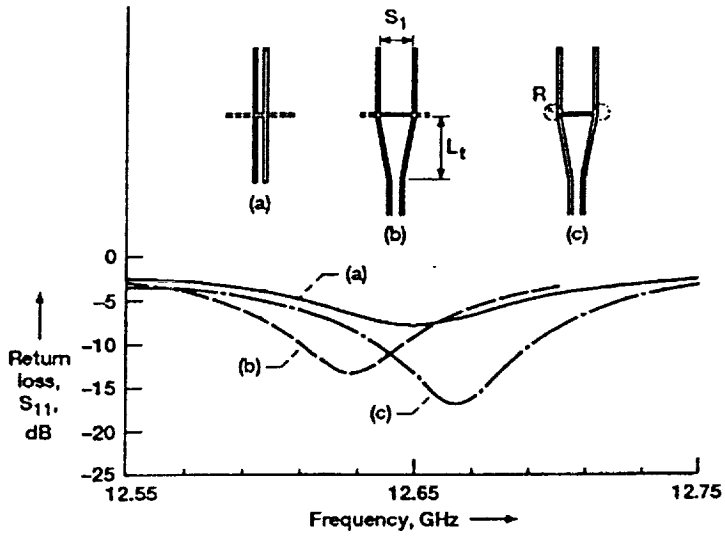

Fig. 3 Measured return losses vs. frequency for feed structures with: (a) a series gap and a rectangular slot, (b) an enlarged series gap and a rectangular slot, and (c) an enlarged series gap and a 'dumbbell' slot. (S_1=0.355 cm, L_t=0.711cm, and R=0.0843 cm)

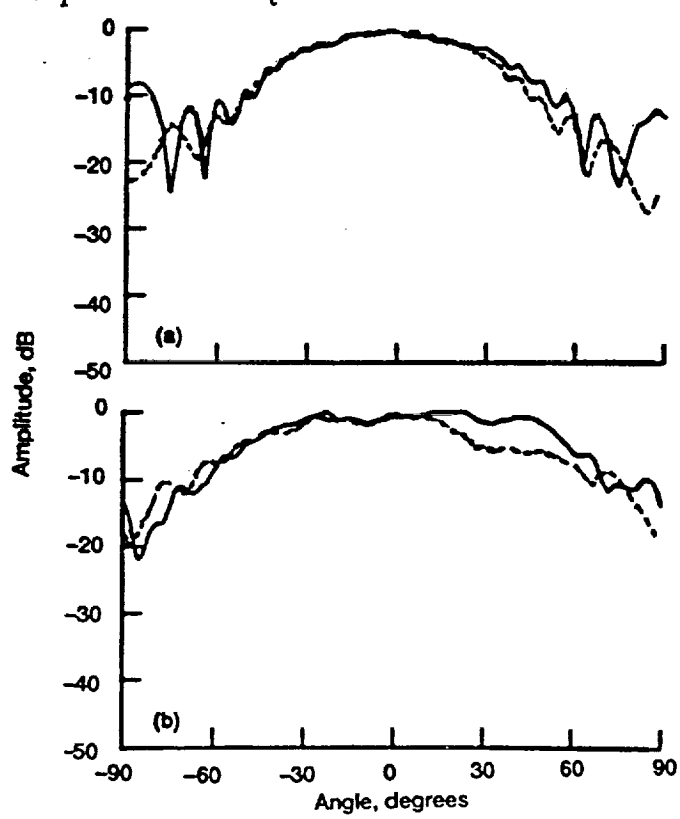

Fig. 4 Measured radiation patterns for the CPW fed patch antennas with (——) notch/slot and (---) gap/slot coupling: (a) H-plane and (b) E-plane.

N94-20507

BANDWIDTH ENHANCEMENT OF DIELECTRIC RESONATOR ANTENNAS

Richard Q. Lee* and Rainee N. Simons
NASA Lewis Research Center
MS 54-8
Cleveland, Ohio 44135

ABSTRACT

This paper reports an experimental investigation of bandwidth enhancement of dielectric resonator antennas (DRA) using parasitic elements. Substantial bandwidth enhancement for the $HE_{11\delta}$ mode of the stacked geometry and for the $HE_{13\delta}$ mode of the coplanar collinear geometry have been demonstrated. Excellent radiation patterns for the $HE_{11\delta}$ mode were also recorded.

INTRODUCTION

A dielectric resonator placed over a ground plane can serve as an effective radiator [1-2]. Compared to printed antennas, the DRA has lower ohmic losses and higher radiation efficiency particularly at high frequencies. However, because of high Q factor, the DRA has very narrow bandwidth which severely limits its usefulness as an antenna. It has been demonstrated that significant bandwidth enhancement can be achieved for microstrip antennas by placing closely spaced parasitic elements on both sides of or directly above a driven patch [3]. It appears that parasitic elements can also be used to enhance the bandwidth of a DRA. This paper is concerned with an experimental investigation of the effects of parasitic elements on dielectric resonator antennas.

THE EXPERIMENT

The single DRA as shown in Fig. 1(a) is placed on a ground plane and aperture coupled to a notched coplanar waveguide (CPW) through a slot. The slot is positioned along the y-axis (ϕ=90°) so the $HE_{11\delta}$ and the $HE_{13\delta}$ modes can be excited [4]. Bond wires are used to keep the CPW ground planes at equal potential and suppress the slotline even mode. The DRA of diameter D and height H of 6.223 mm and 2.489 mm respectively is constructed from $ZrSnTiO_4$ material of relative permittivity $\epsilon_{r2} \simeq$ 36.0, and the CPW feed is fabricated from 20 mil (0.508 mm) RT-5880 Duroid substrate of ϵ_{r1} = 2.2. In the experiment, identical dielectric resonators were placed directly above and on both sides of the driven DRA.

© 1993 IEEE. Reprinted, with permission, from Proceedings of IEEE Antennas and Propagation Society International Symposium, Ann Arbor, Michigan, June 1993, pp. 1500-1503.

RESULTS AND DISCUSSIONS

The measured return losses for the single DRA is shown in Fig. 2(a). Results indicate that with proper aperture lengths, either the $HE_{11\delta}$ or the $HE_{13\delta}$ mode can be strongly excited. The aperture length was found to have a strong impact on the bandwidth of the DRA. The $HE_{11\delta}$ mode excited with an aperture L_1 = 0.40 cm has a 2:1 VSWR bandwidth of 8.8 %, while the $HE_{13\delta}$ excited with an aperture L_1 = 0.68 cm has a bandwidth of only 2.5 %.The return losses are less than -10 dB for both modes indicating strong coupling. Figure 3(a) shows the measured patterns for the $HE_{11\delta}$ which has a broader main lobe in the ϕ=90° plane than in the ϕ=0° plane. The pattern is asymmetrical along the ϕ=0° plane due to interference from the test fixture.

Figure 1(b) shows the collinear geomtry where two identical dielectric resonators are proximity coupled to a driven DRA along the ϕ=0° plane with one on each side of the DRA. The separation between resonators is 1 mm. It was observed that placing the parasitic dielectric along the ϕ=0° plane produces strong coupling with the $HE_{13\delta}$ mode, while along the ϕ=90° plane produces strong coupling with the $HE_{11\delta}$ mode. The strong coupling is caused by high field concentrations of the $HE_{13\delta}$ and $HE_{11\delta}$ in the ϕ=0° and ϕ=90° plane respectively. Figure 2(b) shows the measured return losses which are less than -18 dB for the $HE_{13\delta}$ mode with ϕ=o° orientation and about -50 dB for the $HE_{11\delta}$ with ϕ=90° orientation. The parasitic elements has increased the 2:1 VSWR bandwidth of the $HE_{13\delta}$ from 2.5 % to 3.7 %. The measured patterns for the $HE_{11\delta}$ mode as shown in Fig. 3(b) exhibits excellent broadside characteristics.

Figure 1(c) shows the stacked geomtry. The overlaying parasitic resonator was found to couple strongly to the $HE_{11\delta}$ mode where the electric field is maximum near the top surface of the driven DRA [6]. As indicated in Fig. 2(c), the measured return loss is less than -20 dB for the $HE_{11\delta}$ mode with the higher order mode sup- pressed. The parasitic resonator increases the 2:1 VSWR bandwidth of the $HE_{11\delta}$ mode to over 5.3 %. As with the previous case, excellent radiation patterns have been obtained for the $HE_{11\delta}$ mode. These patterns are displayed in Fig. 3(c).

CONCLUSIONS

Substantial enhancement in bandwidth has been demonstrated for the HE_{11} and the HE_{13} modes with the parasitic resonators placed directly above and on both sides of the DRA respectively. Because of excellent

return loss and radiation characteristics, the DRA should be excited in HE_{11} mode when used as radiating elements in an array.

REFERENCES

[1] S.A. Long, M.W. Mcallister and L.C. Shen, "The resonant cylindrical dielectric cavity antenna," IEEE Trans. Ant. & Prog., Vol.AP-31, No.3, PP.406-412, May 1983.

[2] J.T.H. St.-Martin, Y.M.M. Antar, A.A. kishk, A. Ittipiboon, and M. Cuhaci, "Dielectric resonator antenna using aperture coupling," Electron. Lett. Vol.26, No.24, pp.2015-2016, Nov. 1990.

[3] R.Q. Lee, K.F. Lee anf J. Bobibchak, "Characteris tics of a two-layer electromagnetically coupled rectangular patch antenna," Electron. Lett., Vol.28, No.1, pp.75-76, Jan. 92.

[4] D. Kajfez, A.W. Glisson and J. James, "Computed model field distributions for isolated dielectric resonators," IEEE Trans. Microwave Theory tech., Vol.MTT-32, No.12, pp.1609-1616, Dec. 1984.

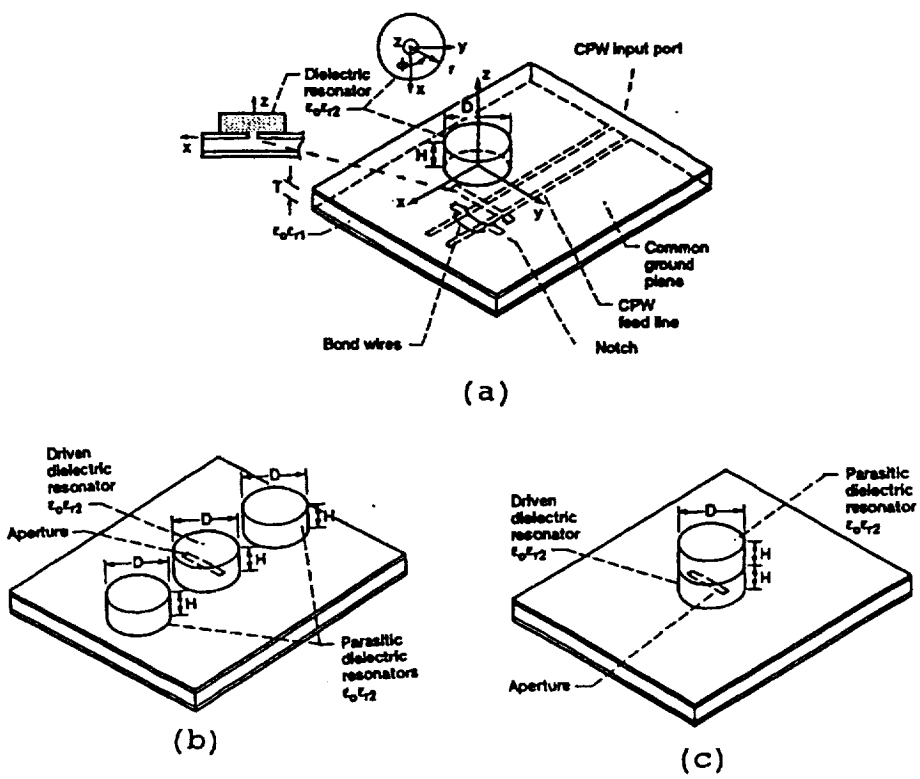

Fig. 1 Schematic Illustrating a Grounded Dielectric Resonator Aperture Coupled to a Notched CPW feed: (a) Single , (b) multiple and (c) Stacked Dielectric Resonator Antenna.

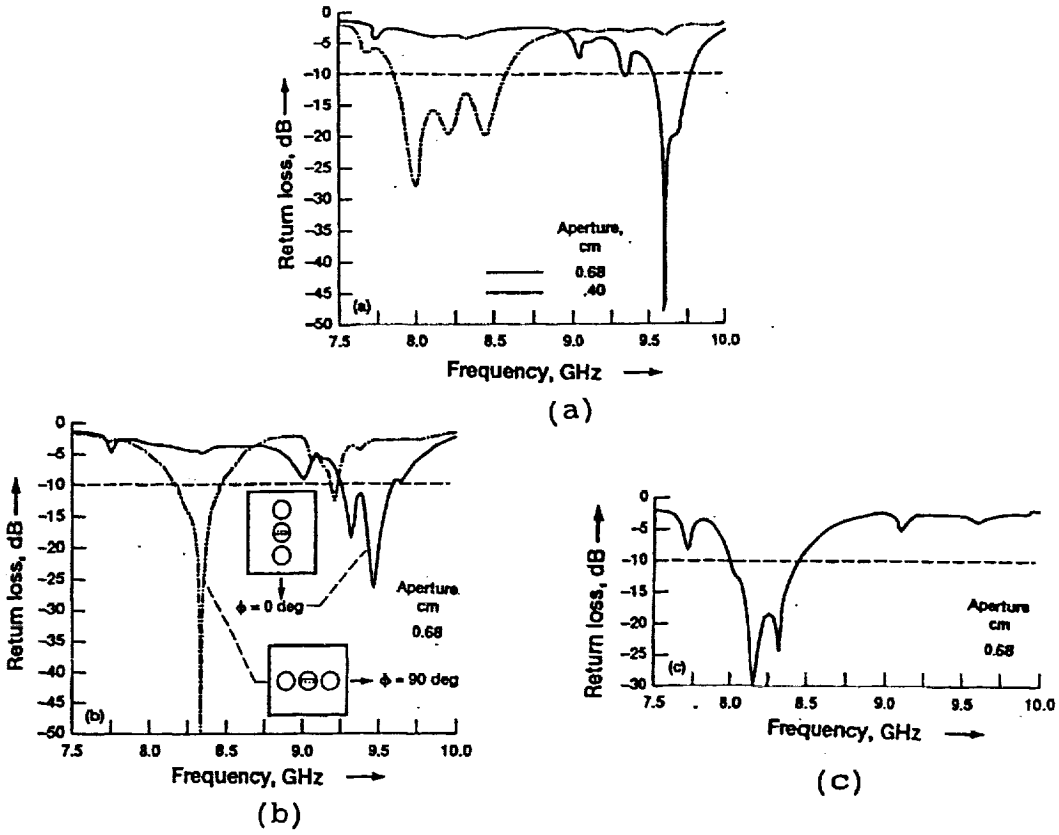

Fig. 2 Measured Return Losses for: (a) Single, (b) Multiple and (c) Stacked Dielectric Resonator Antenna.

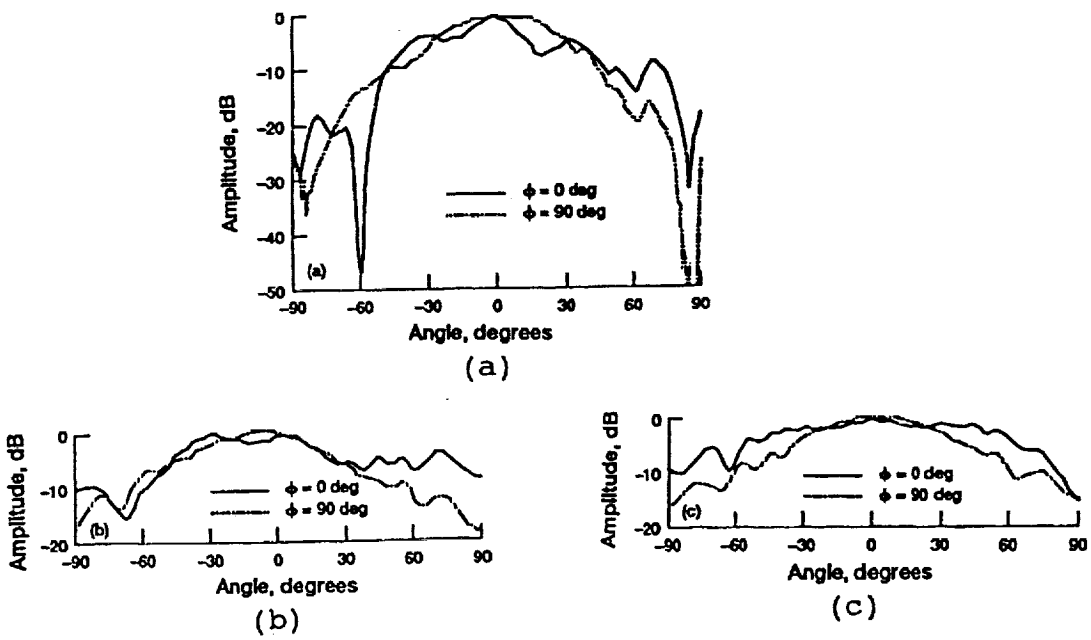

Fig. 3 Measured Radiation Patterns for the $HE_{11\delta}$ Mode for: (a) Single, (b) Multiple and (c) Stacked Dielectric resonator Antenna (f= 8.2 GHz).

SPACE POWER AMPLIFICATION WITH ACTIVE LINEARLY TAPERED SLOT ANTENNA ARRAY

Rainee N. Simons and Richard Q. Lee

National Aeronautics and Space Administration
Lewis Research Center
Cleveland, Ohio 44135

Abstract

A space power amplifier composed of active linearly tapered slot antennas (LTSAs) has been demonstrated and shown to have a gain of 30 dB at 20 GHz. In each of the antenna elements, a GaAs monolithic microwave integrated cir-cuit (MMIC) three-stage power amplifier is integrated with two LTSAs. The LTSA and the MMIC power amplifier have a gain of 11 dB and power added efficiency of 14 percent respectively. The design is suitable for constructing a large array using monolithic integration techniques.

Introduction

The power output as well as the dynamic range of microwave solid state devices decreases as the frequency of operation increases. Hence to obtain high power at fundamental frequencies of several tens of GHz, the output from all the devices have to be combined using either conventional power combiners or quasi-optical power combiners.[1] In the case of conventional power combiners, the combining is done with Wilkinson, radial line, and hybrid coupled networks. In the case of quasi-optical combiners, oscillators constructed with IMPATT diodes,[2] Gunn diodes,[3] MESFETs,[4] or HEMTs[5] are integrated with microstrip patch antennas or linearly tapered slot antennas (LTSAs)[6] to form an active antenna array which combines power radiatively in free space. The advantages of quasi-optical power combiners over conventional power combiners are higher combining efficiency because of lower conductor losses and larger dimensional tolerances with the absence of resonance modes. In addition both antennas and devices can be integrated on a single semiconductor wafer thus simplifying the array construction. The disadvantage of oscillator based quasi-optical combiners is that the individual oscillators have to be phase locked to a reference source or the active array has to be placed in a Fabry-Perot resonator to produce coherent radiation.

Another way to obtain high power is to construct a spatial amplifier. One such scheme is the grid amplifier.[7] Each unit cell of the grid amplifier consists of a pair of packaged GaAs MESFETs with the sources connected together to form a differential amplifier and with the gate and drain terminals extending radially to form a pair of orthogonal strip antennas. Radiation to and from a planar array of identical unit cells is quasi-optically coupled by a vertically or a horizontally polarized beam respectively.

This paper presents for the first time a spatial amplifier with GaAs monolithic microwave integrated circuit (MMIC) multi-stage power amplifiers. In this approach an array of active antenna modules constructed from nonplanar LTSAs[8] and GaAs MMIC amplifiers receives signals at lower power, and after amplification re-radiates signals into free space. The two advantages of the spatial amplifier over the spatial oscillator are that only a single stable lower power source is required (thus greatly simplifying the combiner construction) and that the amplifiers can be individually optimized. Figure 1 schematically illustrates a possible arrangement for space power amplification.

Active Antenna Module Characteristics

The experimental three-element array module is showns chematically in Figure 2. The array elements are constructed by integrating a GaAs MMIC multi-stage power amplifier between two nonplanar LTSAs.

Linearly Tapered Slot Antenna

The feed system of the nonplanar LTSA consists of a conventional microstrip with the ground plane tapered to form a balanced microstrip. The strip conductors of the balanced microstrip are gradually flared with respect to the antenna axis to form the nonplanar LTSA. The design of the non-planar LTSA and its characteristics are reported in Ref. 8. The antenna is fabricated on a 0.02 inch thick RT-5880 Duroid substrate. The measured gain of the LTSA is about 11 dB at the center frequency of 20 GHz. The LTSA has a return loss S_{11} of 10 dB (2:1 VSWR) over a bandwidth extending from 10 to 30 GHz.

GaAs MMIC Multi-Stage Power Amplifier

The GaAs MMIC three-stage power amplifier was designed and fabricated by Texas Instruments for NASA Lewis Research Center.[9] A photograph of the amplifier chip is shown in Figure 3. The amplifier is constructed on a GaAs substrate with an active layer doping level of 2.5×10^{17} cm^{-3}. The gate widths of the three stages are 1.2, 2.4, and 6.0 mm, respectively, and the gate length is 0.5 μm in all the stages. The chip size is about 4.0 by 3.0 by 0.1 mm. The bias network is incorporated on the chip. The drain voltage V_d and current I_d is 6.3 V and 1.9 A, respectively. The gate voltage

V_g is -0.6 V. The measured gain (S_{21}) on a HP 8510B ANA with a 40 dB coaxial attenuator on the drain side of a typical amplifier is shown in Figure 4. The gain is greater than 10 dB over the frequency range of 18 to 21 GHz. The saturated output power measured on a Pacific Instruments scalar network analyzer at 20 GHz is about 1.8 W with a gain of 10 dB and power added efficiency of 14 percent.[9]

Experimental Results and Discussions

A simple measurement procedure has been developed to estimate the gain of the space amplifier. This procedure involves the LTSAs at the input terminals are space fed from a single horn antenna while those at the output terminals radi-ate into free space. The free space radiation is picked up by a second horn antenna which is placed at a far field distance from the array. The ratio of the measured received power with and without bias to the MMIC amplifiers provides an estimate of the gain of the space amplifier. In the setup, the two horn antennas are orthogonally polarized but the LTSAs are oriented to have the same polarization as their respective horn antennas, thus good isolation between the transmitting and the receiving horn antennas is established. Also, for comparison purposes, a single LTSA was tested as a receive antenna. The H-plane pattern is shown in Figure 5 which exhibits a power gain of 6.7 dB with the MMIC amplifier turned ON.

Three-Element Array Module

In this experiment, the LTSAs at the amplifier input and output are oriented with the H and E vectors of the receiving horn, respectively as shown in Figure 6(a). This arrange-ment allows the horn to excite the three LTSAs with equal amplitude. The measured radiation pattern is shown in Figure 7(a) with the amplifiers turned ON and OFF, respectively. The gain increases by as much as 30 dB when the amplifiers are turned ON which is in good agreement withthe measured gain of the amplifiers.

A second experiment, as shown in Figure 6(b), is carried out with the LTSAs at the input and output oriented with the H and E vectors of the receiving horn, respectively. The measured radiation pattern is shown in Figure 7(b). In this arrangement the gain increases by 25 dB when the amplifiers are turned ON. The gain is lower in this case because the LTSAs on either side of the center element are excited with a lower amplitude due to the amplitude taper of the electric field distribution of the transmitting horn. The experimental three element LTSA MMIC array module is shown in Figure 8.

Conclusions

A space power amplifier composed of active LTSA antennas has been demonstrated and shown to have a gain of 30 dB at 20 GHz. In each of the antenna elements, a MMIC three-stage power amplifier is integrated with two LTSAs. The GaAs MMIC power amplifier and the LTSA have a power added efficiency of 14 percent and a gain of 11 dB, respectively. The design is suitable for constructing a large array using monolithic integration techniques.

References

1. K. Chang, and C. Sun, "Millimeter-wave power-combining techniques," IEEE Trans. Microwave Theory Tech., vol. MTT-31, no. 2, pp. 91-107, Feb. 1983.

2. N. Camilleri, and B. Bayraktaroglu, "Monolithic millimeter-wave IMPATT oscillator and active antenna," IEEE Trans. Microwave Theory Tech., vol. 36, no. 12, pp. 1670-1676, Dec. 1988.

3. K. Chang, K.A. Hummer, and J.L. Klein, "Experiments on injection locking of active antenna elements for active phased arrays and spatial power combiners," IEEE Trans. Microwave Theory Tech., vol. 37, no. 7, pp. 1078-1084, July 1989.

4. J. Birkeland, and T. Itoh, "FET-based planar circuits for quasi-optical sources and transceivers," IEEE Trans. Microwave Theory Tech., vol. 37, no. 9, pp. 1452-1459, Sept. 1989.

5. R.N. Simons, and R.Q. Lee, "Planar dielectric resonator stabilized HEMT oscillator integrated with CPW/aperture coupled patch antenna," IEEE MTT-S Int. Microwave Symp. Dig., vol. I, pp. 433-436, 1992. (Also, NASA TM-105752, pp. 21-23, 1992.)

6. J.A. Navarro, Y.H. Shu, and K. Chang, "Wideband integrated varactor-tunable active notch antennas and power combiners," IEEE MTT-S Int. Microwave Symp. Dig., vol. III, pp. 1257-1260, 1991.

7. M. Kim, J.J. Rosenberg, R.P. Smith, R.M. Weikle, J.B. Hacker, M.P. DeLisio, and D.B. Rutledge, "A grid amplifier," IEEE Microwave Guided Wave Lett., vol. 1, no. 11, pp. 322-324, Nov. 1991.

8. R.N. Simons, and R.Q. Lee, "Nonplanar linearly tapered slot antenna with balanced microstrip feed," IEEE Antennas Propag. Soc. Int. Symp. Dig., vol. IV, pp. 2109-2112, 1992.

9. "20 GHz Monolithic Power Amplifier Module Development," NAS 3-23781.

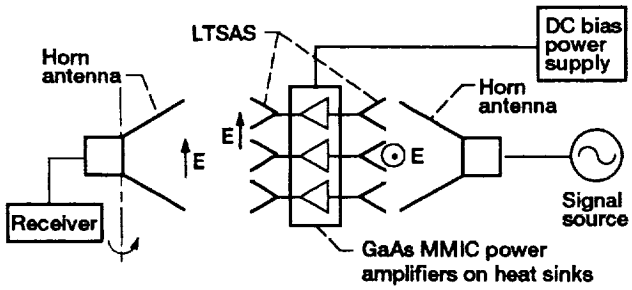

Figure 1.—Schematic illustrating a possible arrangement for space amplification.

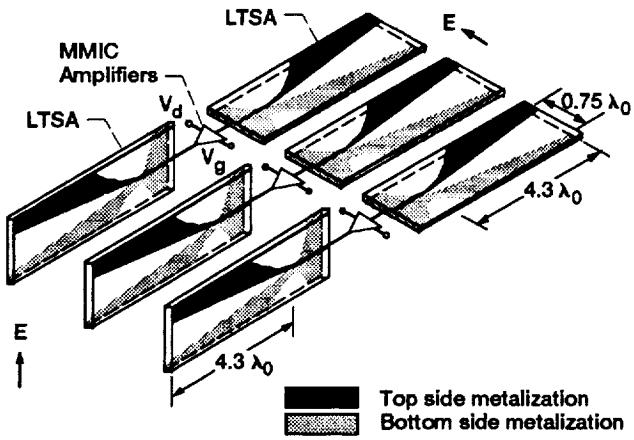

Figure 2.—Schematic illustrating the three-element array module. (λ_0: free space wavelength.)

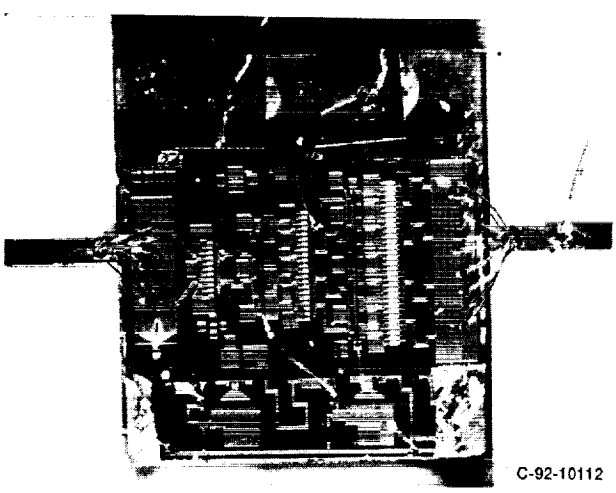

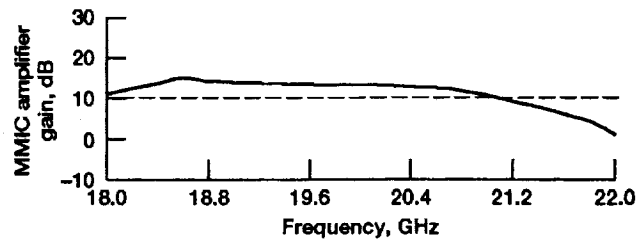

Figure 4.—Typical measured gain of MMIC amplifier.

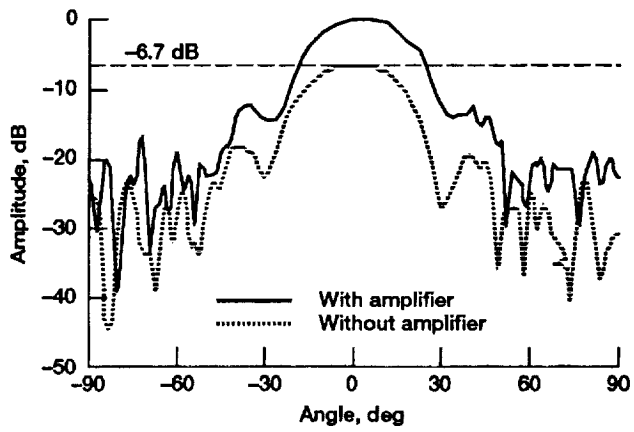

Figure 5.—The measured H-plane radiation pattern of a single LTSA with and without the amplifier.

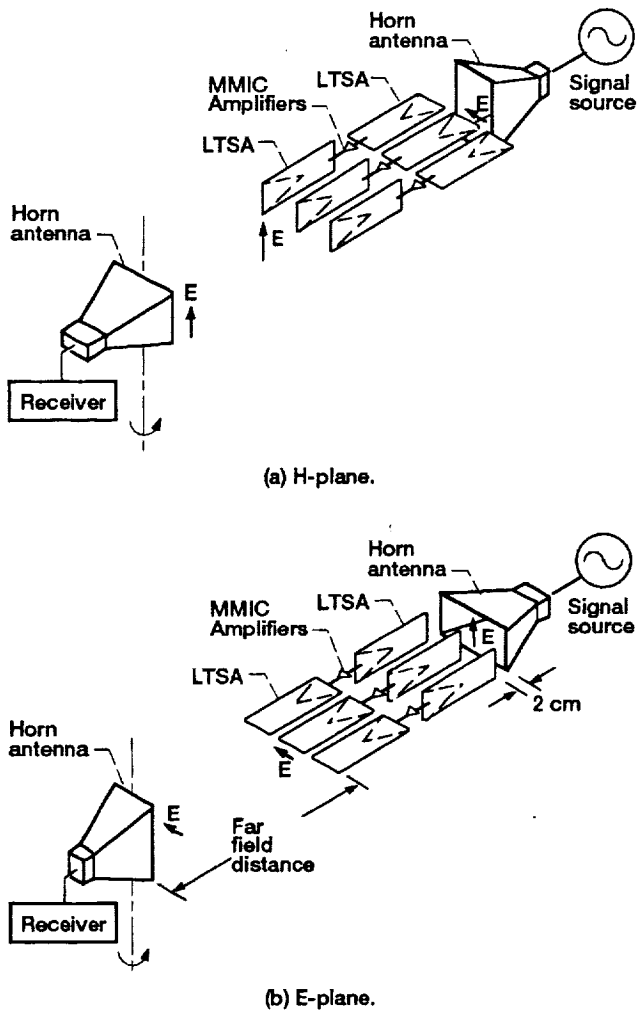

Figure 6.—LTSA orientation in the three-element array module for gain measurement.

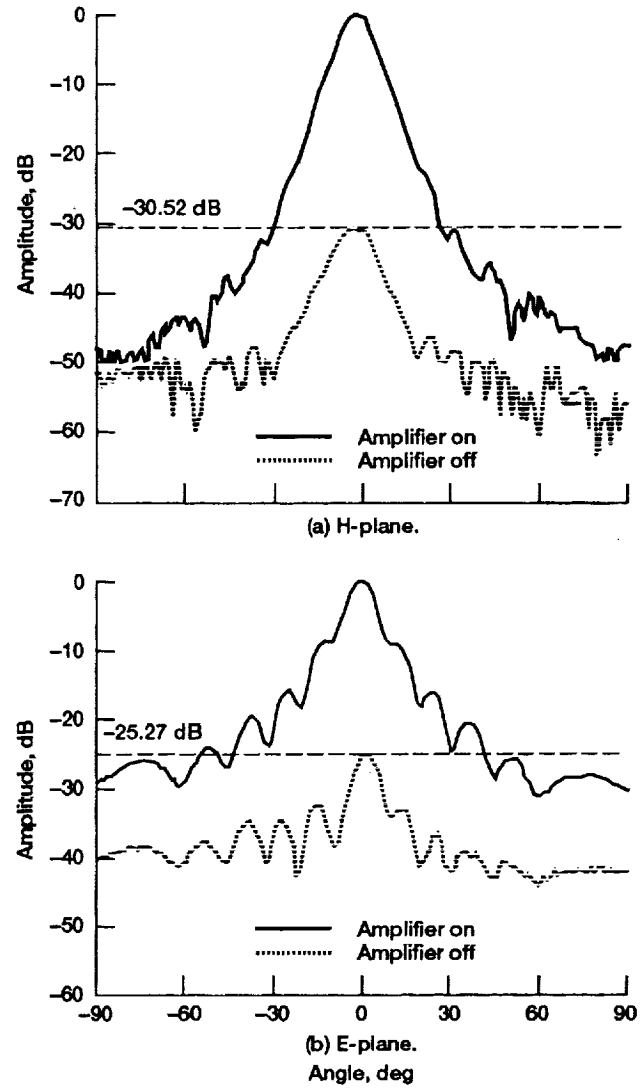

Figure 7.—The measured radiation pattern of the horn antenna showing space power amplification.

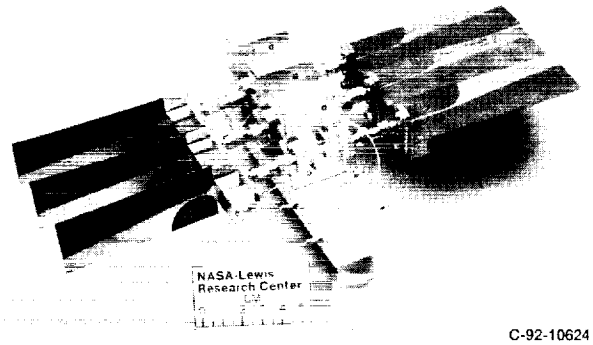

Figure 8.—The experimental three element LTSA MMIC array module.

AN ANALYSIS OF THE FREQUENCY LIMITATIONS OF AN $Al_xGa_{1-x}As/GaAs$ OPTICAL MODULATOR

M. Tabib-Azar and P. C. Claspy
Electrical Engineering and Applied Physics Department
Case Western Reserve University
Cleveland, Ohio

C. Chorey and K. B. Bhasin
National Aeronautics and Space Administration
Lewis Research Center
Cleveland, Ohio

KEY TERMS

Optical modulators, heterojunction devices, interferometers

ABSTRACT

Frequency response of an optical modulator, operating at $\lambda = 0.83$ μm and utilizing the linear electro-optic (Pockels) effect in a Mach-Zehnder configuration using an $Al_xGa_{1-x}As/Al_yGa_{1-y}As$ double heterostructure, is analyzed. We show that in semiconductor modulators, electroabsorption should be taken into account in optimizing the frequency response of the device. © *1993 John Wiley & Sons, Inc.*

I. INTRODUCTION

Light modulators, integrated with optoelectronics, have attracted intense research activities in recent years. Speed and inherent parallelism of all-optical signal processing usually justify overall larger size of the optical components, and much activity is devoted to establishing fabrication sequences that result in reliable integrated devices and waveguides [1, 2]. Electro-optic modulators based on the linear electro-optic effect are expected to have very fast response, limited only by the transit times and RCs (R is the resistance and C is the capacitance) of the geometry and, in the case of traveling-wave modulators, walk off between the light and the microwave. They are also relatively insensitive to the frequency of the light and their RCs and characteristic impedances do not change under illumination. On the other hand, the performance of electroabsorption modulators is very sensitive to the wavelength of the light and their time constants and characteristic impedances are affected by absorption. However, they can be made in much smaller sizes than the electro-optical modulators.

In most cases where one wishes to construct an electro-optic modulator from semiconductor materials, some electroabsorption cannot be avoided. This leads to slower response speeds, because the capacitance of the structure increases as electron-hole pairs (EHPs) are optically excited, as well as higher than expected attenuation. Particularly, the presence of impurity levels in the band gap can considerably contribute to the electroabsorption. In this article we analyze the performance of a $Al_xGa_{1-x}As/GaAs$ optical modulator based on the above considerations.

II. THEORETICAL CONSIDERATIONS

A typical semiconductor-based Mach-Zehnder electro-optic modulator is depicted in Figure 1(a) [2]. In this device, the integrated optical waveguide separates into two parallel branches which form the arms of the interferometer. Electrodes situated in a push-pull configuration produce the electric fields which rotate the polarization vector of the light and change its phase (the electro-optic effect) in the two arms. When the light that is traveling through these two arms is

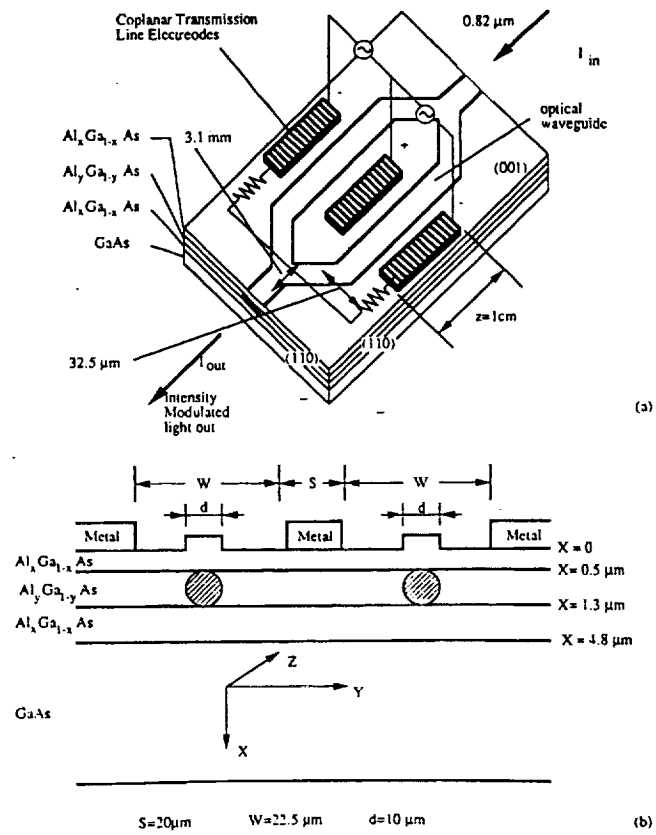

Figure 1 (a) Schematic diagram of a Mach-Zehnder modulator. (b) The cross section of the Mach-Zehnder modulator fabricated on AlGaAs/GaAs

recombined, due to mode conversion, its intensity is modulated.

A cross-sectional schematic through the parallel branches [Figure 1(b)] shows the epitaxial structure that constitutes the waveguide. It consists of three layers of $Al_xGa_{1-x}As$ grown on a semi-insulating GaAs substrate. The middle AlGaAs layer acts as the guiding channel for the light and the upper and lower layers of the AlGaAs act as cladding. The refractive indices of different AlGaAs layers are tailored by adjusting the molar ratio of the Al to Ga. The higher concentration of aluminum results in lower index of refraction. To minimize

© Microwave and Optical Technology Letters/vol. 6, no. 1, 1993. Reprinted by permission of John Wiley & Sons, Inc.

the free-carrier absorption, all these layers are undoped. In addition, the lower layer also isolates the optical field from the GaAs substrate which has a higher refractive index than the optical channel. Two-dimensional waveguides are formed by etching ridges in the upper cladding layer, which increases the effective index of refraction in the region beneath it. The epitaxial layer thickness and ridge dimensions, shown in Figure 1(b) were chosen to produce single mode guides [3]. Figure 2(a) schematically shows ideal electro-optic modulator.

The induced phase shift in the electro-optic effect is linearly proportional to the electric field (E) and the interaction length (Z) [5]: $\Theta \propto n_0^3 r_{41} EZ$ (where n_0 is the refractive index; r_{41}, the electro-optic coefficient, for GaAs is 1.1×10^{-12} m/V). Therefore, at photon energies near the band-gap energy of the waveguide, the electro-optic effects are quite small compared to the electroabsorption which manifests itself through the exponential dependence on the absorption coefficient α: $I(z) = I_0 e^{-\alpha z}$ [where $I(z)$ is the transmitted light power at position z; I_0 is the input power]. Depending on the photon energies, α depends on the band structure (band gap), and the applied electric field (this dependence has a form of $Ee^{(-c/E)}$ as discussed later). The electroabsorption, then, with the exponential dependence on the electric field, can overwhelm the electro-optic effect. When electroabsorption occurs, the absorbed light generates electron-hole pairs (EHP). Therefore, the capacitance and the resistance of the structure changes under illumination. The change is intensity and frequency dependent.

Figure 2(b) shows the band diagram of an n-type semiconductor used in metal-insulator-semiconductor electroabsorptive modulator and Figure 2(c) after the interface. The analysis directly applies to p-type semiconductors as well. The modulating electric field, when it is positive, results in accumulation at the surface, and when it is negative, it results in depletion at the surface. The band bending is exponential in accumulation and it has square-root dependence in depletion. This yields different probabilities of light absorption, through the Franz-Keldysh effect [4], under accumulating and depleting electric fields. Also, high carrier concentration reduces the refractive index, which results in a shift in the confinement of the light. The shift is away from the interface under accumulation and it is toward the interface under depletion.

When an insulator is not used between the semiconductor and the metal electrode, accumulating electric fields result in large current conduction and cannot be used. Thus, in Schottky diode structures only depleting electric fields are used. This is a serious drawback since a depleting dc bias voltage should be applied to prevent forward conduction by a microwave. Under reverse bias, dark current flows through the diode, and depending on the heterostructure quality and the magnitude of the reverse bias, the dark current changes as a function of time, deteriorating the modulator performance.

The second problem is generation of photocurrent, which increases the power consumption of the device. The photocurrent is generated due to EHP generation and clearly it is light-intensity and frequency dependent. Any impurity levels in the band gap will contribute to the current in two ways: (i) they increase the dark current, and (ii) they modify the carrier lifetime modifying the photocurrent. The most important factor determining the response time, however, is the capacitance associated with the depletion width in the waveguide and the series resistance. The capacitance is voltage, light-intensity, and frequency dependent. As light is absorbed, the width of the depletion region becomes smaller, increasing the capacitance.

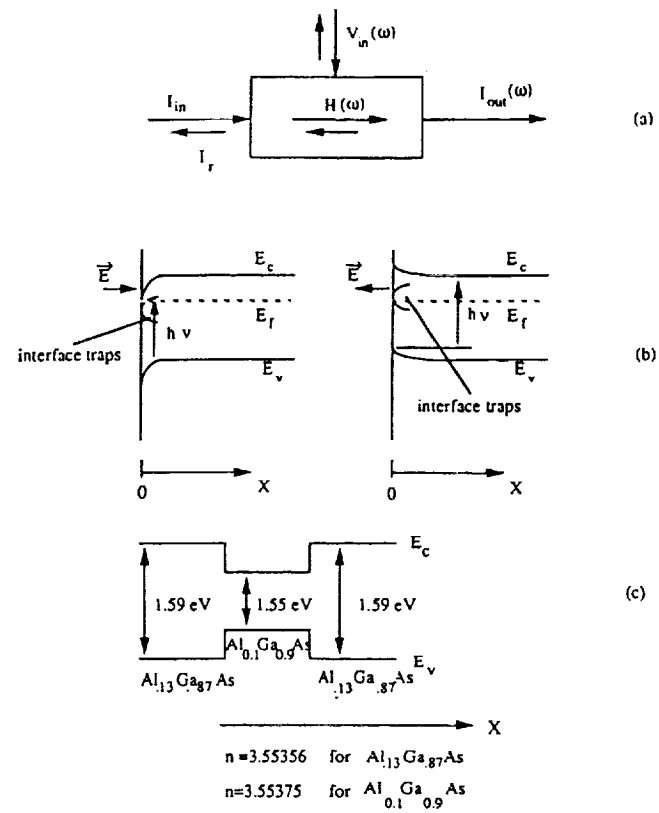

Figure 2 (a) A "black box" representation of a light modulator. (b) The band structure of a semiconductor under applied electric field. Both accumulating and depleting electric field polarities result in Franz-Keldysh effect in metal-insulator-semiconductor structures (c) The band-diagram of the modulator. The modulating electric field is applied through the high Al concentration layer at the surface

Using the above considerations, we proceed to determine the frequency characteristics of depletion capacitance of a Schottky diode when the optical generation rate and trap density are nonzero. The electric field dependence of g_{op} can be estimated as follows. First, it is easily shown that for unity quantum efficiency (i.e., one electron-hole pair per absorbed photon) the average number of EHPs generated per unit volume per second is given by $g_{op} = (1/Y)(1/Lh\nu) \int_0^L (I_0 - I)\, dx$ (where V is the volume, L is the interaction length, $h\nu$ is the photon energy, and I's are as defined before). Assuming a unit area and small α (for below band-gap illumination), it is easy to show that g_{op} is proportional to α ($g_{op} \approx \alpha \mathbf{n}/2$, $\mathbf{n}$ is the average number of electron-hole pairs generated per unit area per second). According to the Franz-Keldysh effect, the electric field dependence of the absorption coefficient is given by [5] $\alpha = (KE/\Delta E) \exp(-C(\Delta E)^{1.5}/E)$ (where K and C are

material constants and $\Delta E = E_g - h\nu$). Using the numerical values of the constants in GaAs, and for large fields ($E/4.74 \times 10^4 > 1$), we get $g_{op} \approx 1.24 \times 10^{-2} \mathbf{n} E$.

Next, using the semiconductor constitutive equations in one dimension (x) in n-type materials, and using the above g_{op}, we arrive at the following well-known linearized fourth-order partial differential equation for the potential V inside the semiconductor:

$$\partial^4 V/\partial x^4 - (1/\tau D + i\omega/D + q\mu N_D/\varepsilon_s D)\, \partial^2 V/\partial x^2 - q\mathbf{n}\alpha/2\varepsilon_s D\, \partial V/\partial x = 0, \quad (1)$$

where ρ is the charge density, ε_S is the dielectric constant of the semiconductor, n is the free carrier density, and δn is the excess carrier density. Moreover, τ is the carrier recombination lifetime, J_x is the current density, q is the elementary charge, μ is the carrier mobility, D is the diffusion constant, E_x is the electric field, and N_D is the doping concentration (all ionized: $N_D = N_{\bar{D}}$). The direction x is shown in Figure 1(b). In deriving the above equation, it is also assumed that the potential carrier density has a $e^{i\omega t}$ time dependence (ω is the radial frequency of the modulating microwave). Assuming that the position dependence of the potential is of the form $e^{\gamma x}$, γ's are given by the roots of the following algebraic equation:

$$\gamma^3 - (1/\tau D + i\omega/D + q\mu N_D/\varepsilon_s D)\gamma - q\mathbf{n}\alpha/2\varepsilon_s D = 0. \quad (2)$$

In general the potential V is given by

$$V(x) = \sum_{i=1}^{3} V_i e^{\gamma_i x} \quad (3)$$

where V_i's are determined from the boundary conditions.

The following values, which are typical in GaAs at room temperature [4], are used in solving for γ's: $\tau = 1 \times 10^{-9}$ sec, $D = 100$ cm^2/sec, $\varepsilon_s = 13 \times 8.854 \times 10^{-14}$ F/cm, $N_D = 10^{12}$ cm^{-3}, $\Delta E = 20$ meV, $q = 1.6e-.19$ coulomb, $k_B T/q = 0.0259$ eV (k_B is the Boltzmann constant, and T is temperature in degrees Kelvin), and $D/\mu = k_B T/q$. The values in AlGaAs, with low concentration of Al, are close to the above values, which are more exactly known in GaAs. For these values, one of the roots (γ_1) has a positive real part. Therefore, $V_1 = 0$ for V to stay bounded as x becomes large.

The ability of a modulator to properly modulate the light is closely related to the ability of an externally applied signal to modulate the potential $V(x)$ inside the semiconductor. In Figure 3, γ_2 and γ_3 as a function of frequency for different optical flux density ($\mathbf{n}$) are shown. These plots are equivalent to the plots of $\log(V_2(x))$ and $\log(V_3(x))$ as a function of $\log(f)$ curves at $x = 1$ μm. From Figure 3 it can be seen that the 3-dB point of the $\log(V_2)$ moves from 1 to 30 GHz as the $\mathbf{n}$ changes from 10^{21} photons/sec cm^2 to 10^{24} photons/sec cm^2. For values of $\mathbf{n}$ less than 10^{21} photons/sec cm^2 the change in the $\log(V_2)$ curve is negligible. Of course, this would not be the case for different values of τ and N_D.

Optical flux density of 10^{22} photons/sec cm^2 corresponds to a laser with 100-μW power operating at 1.5-eV photon energy emitting into an area of 10^6 (1000 × 1000) μm^2. With $\mathbf{n} = 10^{22}$ photons/sec cm^2, and the rest of the parameters as given above, γ versus $\log(f)$ plots are generated with τ as a variable as shown in Figure 4. It is interesting to note that

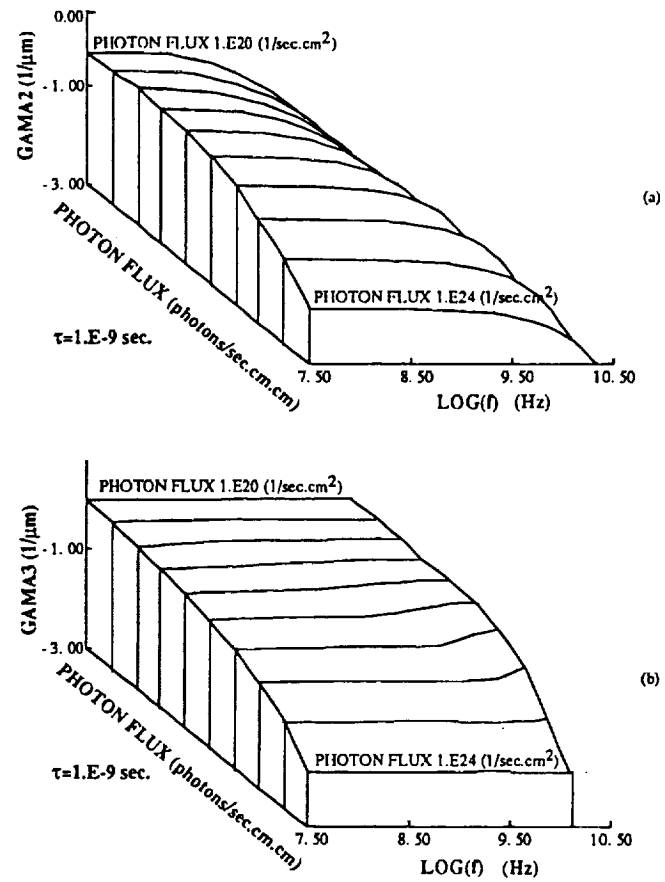

Figure 3 (a) γ_2 and γ_3 as a function of frequency and $\mathbf{n}$ (photons/sec cm^2). (b) γ_2 and γ_3 as a function of frequency and carrier lifetime τ (sec) in GaAs

shorter τ results in wider bandwidths but smaller γ_2 with γ_3 being nearly zero. Smaller γ_2 results in a potential that decays much faster inside the semiconductor. This in turn results in narrower space charge region where the gradient of the potential is not negligible.

The capacitance of the structure is approximately proportional to the inverse of the space charge width. As τ decreases or as $\mathbf{n}$ increases, the capacitance increases. If the response of the modulator is limited by the RC of the structure, larger capacitance results in larger RCs and, hence, smaller bandwidths.

III. EXPERIMENTAL RESULTS

The design and fabrication of traveling-wave Mach-Zehnder configuration electro-optic modulator, shown in Figure 1(a), has been reported elsewhere [1, 2]. Fiber optics were used to couple light in and out of the modulator. Optical coupling was accomplished by butt coupling from a single mode fiber pigtailed to a laser diode (Ortel LD-620s, peak wavelength

of 826.6 mm ~ 1.5 eV). The end facets of the modulator were prepared by cleaving; no antireflection coatings were applied. The output was monitored by an IR-sensitive camera and/or an optical power meter during alignment.

Measurements with zero applied voltage showed that the insertion loss was approximately 24 dB: this includes losses from: (1) Fresnel reflection, (2) mode mismatching between the fiber and the waveguide, and (3) absorption and scattering within the waveguide which includes losses at bends and the Y branch. The modulator 3-dB bandwidth was experimentally

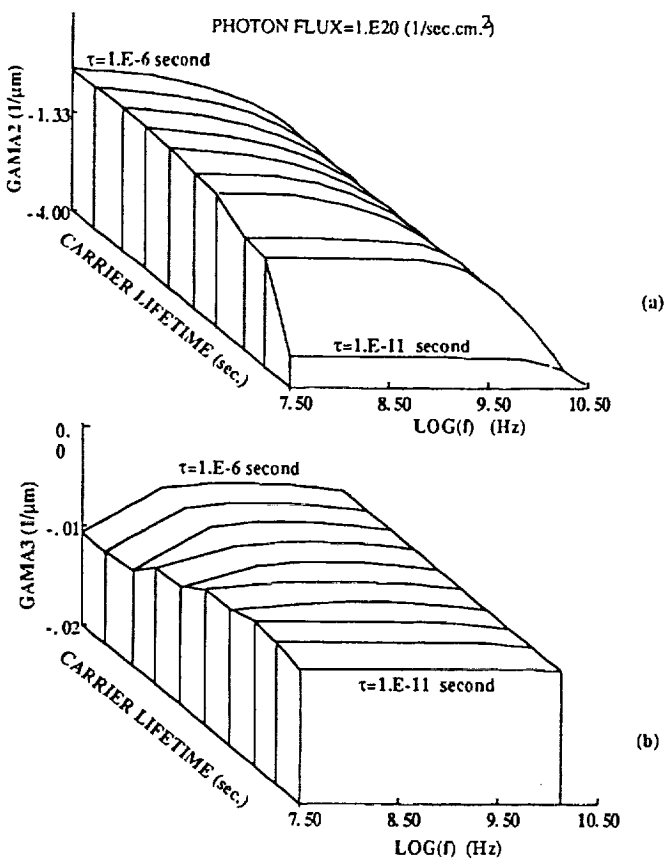

Figure 4 (a) γ_2 and γ_3 as a function of the optical flux density **n** (photons/sec cm^2). (b) γ_2 and γ_3 as a function of the carrier lifetime τ (sec) at f = 1 GHz in GaAs

measured to be 0.5 GHz [2]. The modulator was designed to have an 11-GHz bandwidth.

The observed transmitted optical intensity and the calculated $\cos^2 \phi$ intensity, expected for electro-optic modulation, as a function of applied voltage is shown in Figure 5. The observed intensity versus voltage behavior does not match the $\cos^2 \phi$ behavior, but more closely resembles a continuous exponential decrease. Observations on straight sections of waveguide (i.e., without an interferometer configuration) showed a similar decrease in intensity with applied voltage.

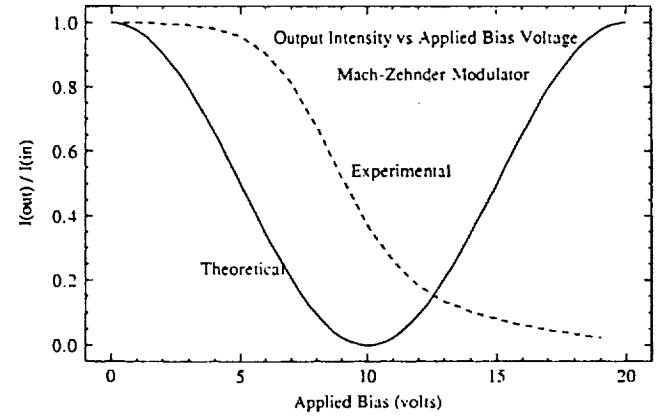

Figure 5 Theoretical output intensity versus voltage of a Mach-Zehnder modulator and the experimentally measured output intensity versus voltage

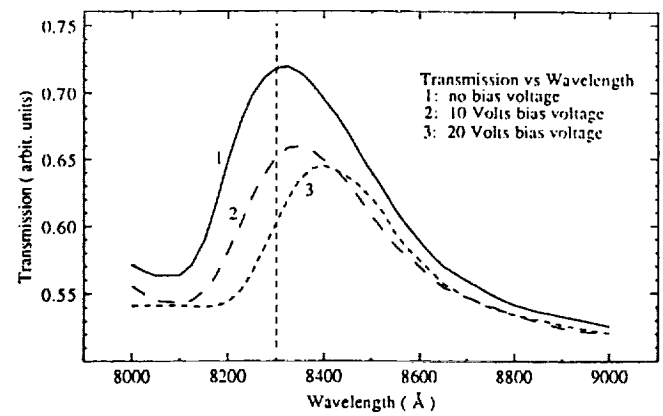

Figure 6 Experimental output intensity versus photon wavelength under different applied bias voltages

Spectroscopy was performed on the waveguides, and Figure 6 shows the observed transmission through the waveguide as a function of wavelength for applied voltages of 0, 10, and 20 V. The application of a voltage shifts the absorption edge from 814 nm (1.523 eV) at 0 V to 821 nm (1.510 eV) at 20 V, a shift of 0.013 eV. The transmission drops off at higher wavelengths partly due to waveguide cutoff and partly due to somewhat lower output of the monochromator and lower detection efficiency of the detector at larger wavelengths.

IV. DISCUSSION

According to Figure 6, the absorption edge at $V = 0$ is around 814 nm (1.52 eV). The relationship between the E_g and the composition index y when $0 < y < 0.35$ is [4] $E_g = 1.424 + 1.247y$ (eV). The 1.52-eV absorption edge means that the effective y is around 0.08 (8% Al) instead of the expected value of 0.1 (10% Al). This discrepancy can also be caused by a nonzero internal electric field when $V = 0$. From the position of the laser diode at 826 nm (1.501 eV) it is obvious that the applied voltage significantly increases the absorption. From Figures 5 and 6 it is clear that the observed intensity modulation with applied voltage is due to electroabsorption.

Any change related to the electro-optic effect is rendered unobservable by the much larger absorption effect.

To determine the bandwidth of the modulator, we note that as the light is absorbed in the $Al_yGa_{1-y}As$ layer, EHPs are generated. In the presence of an electric field, EHPs are spatially separated. Since this layer has lower Al concentration than the adjacent layers, its band gap is lower. Thus, it can contain the EHPs forming a two-dimensional low-resistivity layer. This sheet of charge provides a relatively good conducting layer. Therefore, the effective distance between the metallic electrodes is shortened and the capacitance between them is increased. Assuming that the top $Al_xGa_{1-x}As$ layer is semi-insulating, the characteristic impedance of the electrodes and the modified structure is calculated, using standard microwave programs to be 2.31 Ω. With such a large mismatch between the line impedance (50 Ω) and the modulator. With such a large mismatch between the line impedance (50 Ω) and the modulator impedance, most of the microwave power is reflected. Only at relatively low frequencies is the transmitted microwave able to modulate the potential inside the waveguide to any appreciable width. This is discussed in the previous section.

In terms of lumped parameters, the capacitance per unit area is 1.15 nf/cm^2 ($= \varepsilon_s/2d$, $d = 0.5$ μm, and $\varepsilon_s = 13 \times 8.854 \times 10^{-14}$), which results in an RC of 1.15×10^{-9} sec ($f \approx 0.87$ GHz). This is in good agreement with the experimentally observed bandwidth of our modulator.

V. CONCLUSION

In semiconductors the Franz-Keldysh effect, which results in an increase in optical generation rate, can increase the capacitance of the structure, lowering the bandwidth of the modulator. The effects that are discussed here can also be incorporated to increase the figure of merit, for example, by including the effect of optical generation rate, and hence the excess carrier generation on the refractive index change. This also suggests the possibility of using a second light beam to modulate light with an applied electric field as an adjustable variable that determines the coupling between the two light beams through the band bending. It can also be concluded that by incorporating an insulator (a semiconductor with a large band gap) between the metallic electrode and the channel [5, 6], the capacitance of the electroabsorptive modulator can be kept low at a reasonable value under the worst conditions.

REFERENCES

1. R. G. Walker, *J. Lightwave Technol.*, Vol. LT-5, No. 10, 1987, pp. 1444–1453.
2. C. M. Chorey, A. Ferendeci, and K. B. Bhasin, 1988 IEEE MTT-S International Microwave Symposium, New York, NY.
3. S. Y. Wang and S. H. Lin, *J. Lightwave Technol.*, Vol. 6, No. 6, 1988, p. 758.
4. S. Wang, *Fundamentals of Semiconductor Theory and Device Physics*, Prentice-Hall, Englewood Cliffs, NJ, 1989, pp. 618–620.
5. M. Tabib-Azar et al., *Proceedings of 163rd Electroch. Society Meeting*, 1983, pp. 186–190.
6. W. T. Tsang, *Appl. Phys. Lett.*, Vol. 33, 1978, p. 426.

Received 3-13-92; revised 9-28-92

SECTION TWO

SEMICONDUCTOR MATERIAL CHARACTERIZATION

PRECEDING PAGE BLANK NOT FILMED

Ellipsometric characterization of $In_{0.52}Al_{0.48}As$ and of modulation doped field effect transistor structures on InP substrates

S. A. Alterovitz
NASA Lewis Research Center, Cleveland, Ohio 44135

R. M. Sieg
EE Department, Cleveland State University, Cleveland, Ohio 44115

J. Pamulapati and P. K. Bhattacharya
EECS, University of Michigan, Ann Arbor, Michigan 48109

(Received 27 August 1992; accepted for publication 24 December 1992)

The dielectric function of a thick layer of $In_{0.52}Al_{0.48}As$ lattice matched to InP was measured by variable angle spectroscopic ellipsometry in the range 1.9–4.1 eV. The $In_{0.52}Al_{0.48}As$ was protected from oxidation using a thin $In_{0.53}Ga_{0.47}As$ cap that was mathematically removed for the dielectric function estimate. The $In_{0.52}Al_{0.48}As$ dielectric function was then verified by ellipsometric measurements of other $In_{0.53}Ga_{0.47}As/In_{0.52}Al_{0.48}As$ structures, including modulation doped field effect transistors (MODFET), and is shown to provide accurate structure layer thicknesses.

In this letter, we present a measurement of the dielectric function of $In_{0.52}Al_{0.48}As$ and apply it to the ellipsometric characterization of $In_{0.53}Ga_{0.47}As/In_{0.52}Al_{0.48}As$ heterostructures. The main application of $In_{0.52}Al_{0.48}As$ is as a high band gap semiconductor in $In_{0.53}Ga_{0.47}As/In_{0.52}Al_{0.48}As$ heterostructures lattice matched to InP, which are used in a variety of microwave and optical applications.[1] An important property of $In_{0.52}Al_{0.48}As$ is the fact that, unlike InP, it can be grown in thin film form by solid molecular beam epitaxy (MBE), as opposed to phosphorus containing III-V semiconductors which require gas sources. Important parameters for any applications that can be measured by ellipsometry are the thicknesses of the layers, interface quality, and surface contaminations, roughness and oxidation. In addition, the dielectric function of $In_{0.52}Al_{0.48}As$ in the visible may be useful in applications involving waveguides in this spectral range.

Ellipsometry, particularly variable-angle spectroscopic ellipsometry (VASE) in the visible and near UV, has been used to characterize, nondestructively, a variety of modulation doped field effect transistors (MODFETs)[2,3] and optoelectronic structures[4] grown on GaAs substrates. Dielectric functions of the constituents necessary for the ellipsometric analysis were taken from the literature. However, at this time no reliable experimental dielectric function of $In_{0.52}Al_{0.48}As$ has been published. Ellipsometry has been used twice in the past[5,6] to obtain the dielectric function of $In_{0.52}Al_{0.48}As$ in the visible. In Ref. 5, only results for the refractive index were published, while in Ref. 6, the dielectric function of $In_{0.52}Al_{0.48}As$ was estimated by scaling the InP values and using an effective medium model with a 3% negative voids fraction. Clearly, a direct experimental dielectric function for $In_{0.52}Al_{0.48}As$ is preferable.

In most aluminum containing III-V semiconductor ternaries, the top layer of the material will oxidize in air[7] in a time scale of hours. As ellipsometry is very sensitive to the surface conditions, we protected the top layer with $In_{0.53}Ga_{0.47}As$. We kept the thickness of this cap layer to a minimum in order to get reliable results for the $In_{0.52}Al_{0.48}As$ dielectric function in the near UV, where the light penetration depth is very small. As a check of the accuracy of our result, we used our experimental $In_{0.52}Al_{0.48}As$ dielectric function to fit two other $In_{0.53}Ga_{0.47}As/In_{0.52}Al_{0.48}As$ structures using two parameter fits only. Finally, we used our result to analyze five MBE grown $In_{0.53}Ga_{0.47}As/In_{0.52}Al_{0.48}As$ complete MODFET structures. The MODFETs were grown at two laboratories to make sure that no systematic error in the analysis was carried over from a systematic error in the growth parameters of one group.

All samples, except three MODFETs, were grown at the University of Michigan. The $In_{0.52}Al_{0.48}As$ growth temperature used was the optimum value of 520 °C that was found to result in smooth films with the least amount of clustering.[8] Some of the MODFET structures were grown at 500 °C. The growth rate was in the range 0.6–1.2 μm per hour. The ellipsometric measurements[9] were taken at 3–7 angles of incidence in the range 300–750 nm (i.e., spectral range with reasonable experimental reflectivity) with 10 nm increments. The calibration sample was measured in 5 nm increments for better resolution. Marquardt least square fits were used to estimate the desired parameters.

The calibration sample was a 1-μm-thick $In_{0.52}Al_{0.48}As$ on top of a 30 period 3 nm/3 nm $In_{0.53}Ga_{0.47}As/In_{0.52}Al_{0.48}As$ buffer. For ellipsometry purposes, the $In_{0.52}Al_{0.48}As$ was treated as the substrate, assuming it to be optically thick. The free parameters of the model were the oxide and cap layer thicknesses and the values of the $In_{0.52}Al_{0.48}As$ dielectric function at all experimental wavelengths. The calibration functions for the oxide[10] and $In_{0.53}Ga_{0.47}As$[11] were taken from the literature. The resulting $In_{0.52}Al_{0.48}As$ dielectric function ϵ is shown in Fig. 1. The values of the dielectric function for energies below 1.9 eV ($\lambda > 650$ nm) are not as accurate as those above that energy due to the light penetrating into the superlattice region. Conventionally, a layer is considered optically thick if its thickness is greater than 2δ, where δ is the light

© Appl. Phys. Lett. 62 (12), 22 March 1993. Reprinted, with permission, from American Institute of Physics.

PRECEDING PAGE BLANK NOT FILMED

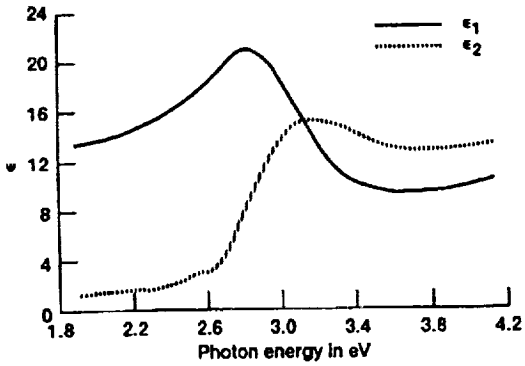

FIG. 1. Dielectric function ϵ of $In_{0.52}Al_{0.48}As$ in the range 1.9–4.1 eV. ϵ_1 and ϵ_2 are the real and imaginary parts of the dielectric function, respectively.

penetration depth.[12] We choose to be more conservative and use a 3δ cutoff criterion. The ellipsometric result also provided best fit values of 2.2 nm of oxide and 1.3 nm of $In_{0.53}Ga_{0.47}As$, which are reasonable values for a native oxide thickness and a nominal 2 nm $In_{0.53}Ga_{0.47}As$ cap. We obtained a mean square error (MSE) for the tan Ψ and cos Δ fit[3] of 1.0×10^{-5}, where Ψ and Δ are the ellipsometric experimental results. This exceedingly low value of MSE is due to the large number of parameters.

Next, two samples of thick $In_{0.52}Al_{0.48}As$ layers were measured, both grown on InP without a superlattice buffer. Sample A had a nominal 2-μm-thick $In_{0.52}Al_{0.48}As$ while sample B had a little over a 1-μm-thick layer. Both had a thicker $In_{0.53}Ga_{0.47}As$ cap layer than the calibration sample. The ellipsometric model used for these samples included two parameters only, the thicknesses of the oxide and the $In_{0.53}Ga_{0.47}As$ cap layer. The $In_{0.52}Al_{0.48}As$ dielectric function used was the result obtained here in the first stage of the work. The results for samples A and B are summarized in Table I. The values of the MSE for these two parameter fits, especially for sample A, are extremely good. In both cases, the $In_{0.53}Ga_{0.47}As$ layer thickness estimated by ellipsometry is smaller than the nominal value. We believe some of the material was oxidized and some error may be due to the growth calibration. However, we did not encounter this discrepancy in MODFET samples made at another laboratory, as will be shown below.

The MODFET structures shown in Table II were made at both the University of Michigan (sample Nos. 1 and 2) and by a commercial vendor[13] (sample Nos. 3, 4, and 5). All structures had complex buffer layers. For example, the University of Michigan samples had the following layers: starting from the semi-insulating InP substrate, a 30 period 3 nm/3 nm $In_{0.53}Ga_{0.47}As/In_{0.52}Al_{0.48}As$ buffer layer and a 400 nm undoped $In_{0.52}Al_{0.48}As$ as the lower part of the conduction channel quantum well. The other samples (Nos. 3, 4, and 5) had additional layers below the 30 period lattice, but they had the same buffer structure just below the conduction channel. As the ellipsometric analysis was limited to the device active layers, the 400 nm $In_{0.52}Al_{0.48}As$ layer was regarded as substrate. Thus, we limited our analyses to wavelengths below 540 nm. The layer thicknesses, as estimated by RHEED, are given in Table II. In all samples, the active layers included an undoped $In_{0.53}Ga_{0.47}As$ channel, an $In_{0.52}Al_{0.48}As$ donor layer, and an $In_{0.53}Ga_{0.47}As$ cap layer. The $In_{0.52}Al_{0.48}As$ donor layer had a doped (5×10^{18} cm^{-3}, Si) 15 nm layer on top of a 5 nm undoped spacer. The cap layer was also *n* doped, at 3×10^{18} cm^{-3}, Si. In the ellipsometric model, doping effects on the dielectric function were neglected.[2,3] The nominal ellipsometric models, including all layer thicknesses for the five samples, are given in Table II under the heading "Nominal." A summary of the ellipsometric results is given in Table II under the heading "VASE." The errors shown are the 90% confidence limits obtained from the least squares fitting.[14] Representative tan Ψ and cos Δ model fits for sample number 5 are given in Figs. 2(a) and 2(b). In general, the quality of the fits, as given by the MSE, is very good, except for sample No. 3. The results for the samples made by the commercial vendor are very illuminating. Sample Nos. 3 and 4 were grown in 1991 and were nominally equivalent, except for the cap layer thickness. The VASE results show that in both samples the $In_{0.52}Al_{0.48}As$ donor layers and the $In_{0.53}Ga_{0.47}As$ channels are much thicker than the nominal values. However, the MSE is much larger for sample No. 3, denoting a poorer

TABLE I. Best fits for layer thicknesses in nm for samples made of a thick $In_{0.52}Al_{0.48}As$ layer, considered as substrate. Analysis range 300–620 nm.

	Oxide		$In_{0.53}Ga_{0.47}As$		MSE
Sample	Nominal	VASE	Nominal	VASE	$\times10^{-4}$
A	···	2.20±0.02	20	13.3±0.1	2.7
B	···	1.3±0.1	40	32.3±0.4	5.1

TABLE II. Best fits for $In_{0.53}Ga_{0.47}As/In_{0.52}Al_{0.48}As$ MODFET layer thicknesses (in nm). Analysis wavelength range 300–405 nm. 400 nm $In_{0.52}Al_{0.48}As$ layer used as substrate.

Sample	Oxide		$In_{0.53}Ga_{0.47}As$ Cap layer		$In_{0.52}Al_{0.48}As$ Donor layer		$In_{0.53}Ga_{0.47}As$ Channel layer		
number	Nominal	VASE	Nominal	VASE	Nominal	VASE	Nominal	VASE	MSE$\times10^{-4}$
1	···	4.6±0.1	10	4.8±0.1	40	42.2±0.3	55	53.9±0.7	1.6
2	···	2.4±0.1	15	8.8±0.2	45	47.9±0.4	55	56.1±1.0	2.4
3	···	2.6±0.1	5	2.3±0.3	40	46.4±0.3	40	51.2±0.6	4.9
4	···	1.0±0.04	35	40.6±0.4	40	48.4±0.5	40	54.1±1.4	0.7
5	···	1.4±0.1	35	32.9±0.5	40	43.4±1.1	40	41.5±2.1	2.4

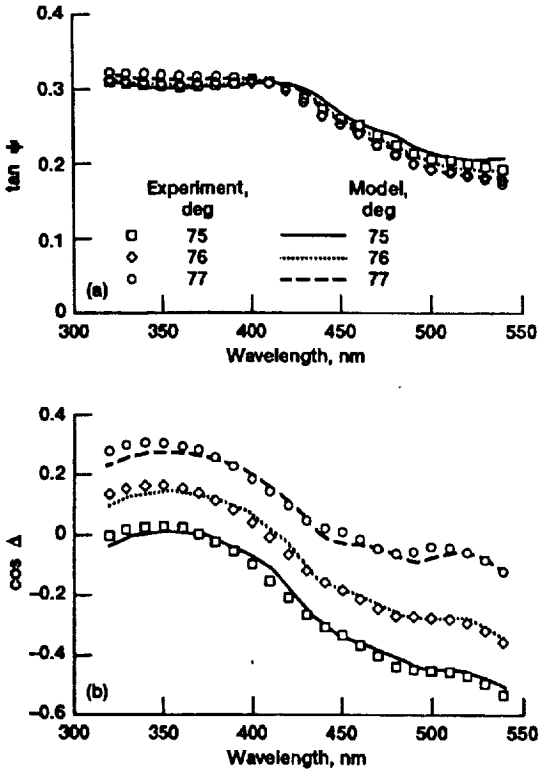

FIG. 2. Experimental and model simulation for (a) tan Ψ (b) cos Δ vs wavelength for sample number 5, Table II, for the following three angles of incidence: □ 75°, ◇ 76°, ○ 77°.

model. We speculate that the problem in this sample originates from the very thin thickness of the cap layer. The $In_{0.53}Ga_{0.47}As$ top layer may be too thin for protecting the $In_{0.52}Al_{0.48}As$ from oxidation, and the sample model shown here did not take this into account. Oxidation problems are encountered in all thin capped MODFET structures (samples No. 1, 2, and 3), where the VASE determined $In_{0.53}Ga_{0.47}As$ layer thickness is very small (see Table II). The large discrepancy between the nominal and the VASE thicknesses of the donor and channel layers in samples 3 and 4 as compared with that of sample 5 can be explained as follows. Sample No. 5 was grown 10 months after the other two samples. In the meantime, several improvements in the nominal thickness calibrations were implemented,[15] including repositioning of the RHEED gun, adjusting the shutters to reduce transients, and a better correlation between RHEED results and ternary alloy thicknesses. Indeed, for sample No. 5, the nominal and VASE thicknesses are the same to within 8% for all layers.

We also analyzed all MODFET samples using the suggested $In_{0.53}Al_{0.47}As$ dielectric function from Ref. 6. The results looked unreliable: the MSE were a factor of 5 to 18 higher for the thin $In_{0.53}Ga_{0.47}As$ capped samples; there was no consistency between sample Nos. 3 and 4; and most thicknesses were far away from the nominal values.

In summary, we have experimentally determined the dielectric function of $In_{0.52}Al_{0.48}As$ in the range 300–650 nm and have successfully applied it in the determination of the active layers' thicknesses of MODFET devices lattice matched to InP grown by MBE. This ellipsometric nondestructive characterization of high performance MODFET's that include $In_{0.52}Al_{0.48}As$ layers not only provided a confirmation of the nominal layer thickness values, but also identified problems in thickness calibrations during growth, as well as cap layer oxidation problems.

We would like to thank W. Weisbecker and L. W. Kapitan from Quantum Epitaxial Design, Inc., for making three samples and for sending private communication on their system improvements, and to D. E. Aspnes for supplying us with his $In_{0.53}Ga_{0.47}As$ results in a digital form.

[1] See, for example, *Proceedings of the Third International Conference on InP and Related Materials* (IEEE, New York, 1991).
[2] P. G. Snyder, M. C. Rost, G. H. Bu-Abbud, J. A. Woollam, and S. A. Alterovitz, J. Appl. Phys. **60**, 3293 (1986).
[3] S. A. Alterovitz, P. A. Sekula-Moise, R. M. Sieg, M. N. Drotos, and N. A. Bogner, Thin Solid Films **220**, 241 (1992).
[4] S. A. Alterovitz, J. A. Woollam, and P. G. Snyder, Solid State Technol. **31**, 99 (1988).
[5] J. Krauser, C. Borholdt, H. Kunzel, H. W. Dinges, M. Druminski, R. Gessner, and K. H. Zschauer, *Proceedings of the 4th European Conference on Integrated Optics* (SETG, Glasgow, 1987), p. 75.
[6] C. Pickering, N. S. Garawal, D. Lancefield, J. P. Piel, and R. Blunt, Appl. Surf. Sci. **50**, 346 (1990).
[7] D. E. Aspnes, S. M. Kelso, R. A. Logan, and R. Bhat, J. Appl. Phys. **60**, 754 (1986).
[8] J. E. Oh, P. K. Bhattacharya, and Y. C. Chen, J. Electron. Mater. **19**, 435 (1990).
[9] S. A. Alterovitz, R. M. Sieg, N. S. Shoemaker, and J. J. Pouch, Mater. Res. Soc. Symp. Proc. **152**, 21 (1989).
[10] D. E. Aspnes, G. P. Schwartz, G. J. Gualtieri, A. A. Studna, and B. Schwartz, J. Electrochem. Soc. **128**, 590 (1981).
[11] D. E. Aspnes and H. J. Stocker, J. Vac. Sci. Technol. **21**, 413 (1982).
[12] J. Humlicek, M. Garriga, M. I. Alonso, and M. Cardona, J. Appl. Phys. **65**, 2827 (1989).
[13] Quantum Epitaxial Design, Bethlehem, PA. 18015.
[14] D. E. Aspnes, SPIE **276**, 188 (1981).
[15] L. W. Kapitan (private communication).

Ellipsometric study of metal–organic chemically vapor deposited III–V semiconductor structures

Samuel A. Alterovitz
NASA Lewis Research Center, Cleveland, OH 44135 (USA)

Patricia A. Sekula-Moise
Spire Corporation, Bedford, MA 01730 (USA)

Robert M. Sieg*, Mark N. Drotos* and Nancy A. Bogner*
Cleveland State University, Cleveland, OH 44115 (USA)

Abstract

Metal–organic chemical vapor deposition was used to grow epitaxial layers of AlGaAs, GaAs and InGaAs on semi-insulating GaAs substrates. The ternary composition of the thick layers was determined by double-crystal X-ray diffraction (DCXRD). Variable angle spectroscopic ellipsometry was used to characterize several types of structures including relaxed single-component thick films and strained lattice multilayer structures. The thick film characterization included ternary alloy composition as determined by a numerical algorithm and interface quality. The results for the alloy composition were equal to the DCXRD results, to within the experimental errors except for the top layer of a thick AlGaAs film. The strained layer multistructures were analyzed for all layer thicknesses and alloy compositions. For most layers, the thickness was equal to the nominal values, to within the experimental errors. However, in all three $In_{0.3}Ga_{0.7}As$ samples, the indium concentration estimated from the relaxed layer's InGaAs algorithm was around 21%, *i.e.* much lower than the nominal value. This result indicates a shift in the critical points of the dielectric function, owing to strain effects.

1. Introduction

The most common technique of growing epitaxial III–V semiconductors films on III–V substrates is by molecular beam epitaxy (MBE). However, the technique of metal organic chemical vapor deposition (MOCVD) is more versatile than MBE, as it can be used to grow a larger selection of group V materials, *e.g.* phosphorus. In addition, MOCVD can produce film growth on several wafers concurrently compared with a single wafer in MBE. The materials of interest in this study are AlGaAs, InGaAs and GaAs, as they are needed to grow the multistructure needed to produce modulation-doped field effect transistors (MODFETs). This MODFET device was developed by MBE in the mid-1980s [1]. MOCVD is being used to grow strained layer InGaAs on GaAs [2, 3] but MOCVD growth of the combination of a AlGaAs layer adjacent to strained InGaAs is not common. The commercial applications of this MODFET are widespread [4], especially for materials grown on GaAs substrates. The conduction channel, made of InGaAs, is under strain. However, if the thickness of the channel is below a critical thickness h_c [5], the strained layer grows pseudomorphically on GaAs. These strain effects have essentially no effect on the electrical properties of the MODFET, but they can be important for optoelectric applications [6].

The most common technique to calibrate a MOCVD reactor for growth rate and alloy composition is to measure mechanically or by microscopy the layer thickness and to use double-crystal X-ray diffraction (DCXRD) for composition. However, DCXRD needs a relatively thick layer of material to give a reliable value of alloy concentration. A much larger thickness is needed to assume a strain-free layer and to avoid corrections to the X-ray results, as a result of strain.

In this paper we will show several ways that ellipsometry can be used to help in calibrating the MOCVD growth parameters. We will also show instances in which ellipsometry was able to pinpoint problems in the layer composition or interfaces. In addition, a quantitative measure of the strain effect on the dielectric function of $In_{0.3}Ga_{0.7}As$ will be estimated.

*Undergraduate student intern at NASA Lewis Research Center, Cleveland, OH 44135, USA.

© Reprinted with the kind permission of Elsevier Sequoia, Lausanne, Switzerland, publishers of the journal Thin Solid Films, no. 220, pp. 241-246.

PRECEDING PAGE BLANK NOT FILMED

2. Experimental details

All samples were grown by MOCVD at Spire Corporation, on semi-insulating GaAs(001) substrates, using low pressure MOCVD in an SPI-MO CVD™450 reactor. The growth temperature and pressure used for all samples were 650 °C and 53 Torr respectively. Source regeants used for these layers include trimethylgallium, trimethylindium, trimethylaluminum, and 100% arsine (AsH_3) with a palladium-diffused hydrogen carrier gas. Two sets of samples were selected for ellipsometry work: (a)thick films; (b) MODFET structures. In set a, two aluminum gallium arsenide ($Al_xGa_{1-x}As$) films were supplied from the same run (M4-2128) with an aluminum molar fraction of 18% (averaged over both samples) as measured by DCXRD. The $Al_xGa_{1-x}As$ film thickness was 8500 Å; the growth rate for this layer was 2.6 Å s^{-1}. The $Al_xGa_{1-x}As$ was protected by a thin (50 Å) GaAs cap. Two indium gallium arsenide ($In_YGa_{1-Y}As$) compositions were calibrated for Y by DCXRD. The first, M4-2093-2 has an indium concentration of 25.6% and was grown at a rate of 3.5 Å s^{-1} for a total thickness of 1.75 μm. M4-2116-2 is a 1.8 μm film of InGaAs with 30% In concentration; the growth rate for this composition was slightly higher at 4.4 Å s^{-1}. Set b contains three samples. All have the nominal structure given in Fig. 1, but with slight differences. Two of the samples have a 100 Å InGaAs channel, while one has a 50 Å channel. Also, one sample had originally a 300 Å GaAs cap layer. Some variations in the buffer among the samples were also present, but their thickness was always 1 μm with at least 9000 Å of GaAs. As elliposmetry cannot distinguish easily between doped and undoped material, we show in Fig. 1 also the initial model for ellipsometric purposes.

MODFET STRUCTURE

Nominal Structure		Nominal Structure for Ellipsometry		
		t_1	GaAs Oxide	20 Å
n GaAs	100 Å 300 Å	t_2	GaAs	100 Å 300 Å
n $Al_{0.2}Ga_{0.8}As$	400 Å			
i $Al_{0.2}Ga_{0.8}As$	50 Å	t_3	$Al_XGa_{1-X}As$	450 Å
i $In_{0.3}Ga_{0.7}As$	50 Å 100 Å	t_4	$In_YGa_{1-Y}As$	50 Å 100 Å
Buffer	10,000 Å		GaAs Substrate	
SI GaAs Substrate				

Fig. 1. Nominal structure used for ellipsometry compared with the actual nominal structure. The ternary concentrations X and Y are variables in the ellipsometric analysis.

The ellipsometric technique was described previously [7] and will only briefly be described here. In order to increase accuracy, many measurements were made using two-zone averaging [8] and/or estimating the angle of incidence by using a known sample (GaAs wafer in this case) and obtaining the correct angle by least-squares analysis. We found these corrections to be very small. A model calculation of the ellipsometric parameters tan Ψ_c, cos Δ_c was least-squares fitted to the experimental tan Ψ_e, cos Δ_e, using the Marquardt algorithm to minimize the mean square error σ;

$$\sigma \equiv (N-P)^{-1} \sum_i [(\tan \Psi_{e,i} - \tan \Psi_{c,i})^2 + (\cos \Delta_{e,i} - \cos \Delta_{c,i})^2]$$

Here N is the number of experimental points and P is the number of free parameters in the model. Data at all relevant experimental angles of incidence and wavelengths are included. The dielectric functions of $Al_xGa_{1-x}As$ for any value of the aluminum concentration X were calculated using the numerical algorithm and the critical points given in ref. 10. The functions needed for $In_YGa_{1-Y}As$ for all Y values were calculated using a numerical algorithm similar to that of ref. 10, but using the following critical points (in electron-volts): from ref. 11: $E_0(Y) = 1.424 - 1.53Y + 0.45Y^2$; $E_1(Y)$ was taken as a linear approximation between GaAs and the experimental results [12] at $Y = 0.3$, $E_2(Y) = 4.8$. In this numerical calculation we found that very little difference was introduced in the dielectric functions if the E_1 critical point was exchanged with almost equal energy value of the peak in ε_1, which is much easier to deduce from the experimental result in ref. 12.

3. Results and discussion

All four thick samples were measured as received, in the wavelength range 3200–7500 Å at five angles of incidence each (around 75°). Results for the two InGaAs samples are given in Table 1. As these films were over 1.75 μm thick, we could not penetrate the thickness of the film. Thus we had only two parameters, the top oxide film thickness and the indium molar concentration Y. In Table 1 we show two results for sample M4-2093-2. In the second measurement the value of σ has improved by a factor to 2.5 because of a better angle of incidence definition obtained from measurement of a GaAs wafer.

The results for Y are basically equal to the experimental DCXRD data, to within both techniques' experimental error, indicating the reproducibility of our results compared with the sample in ref. 12 and the validity of the algorithm. The excellent values for σ

TABLE 1. Best fits for $In_yGa_{1-y}As$ thick layers, wavelength range 3200–7500 Å

	M4-2093-2		M4-2093-2		M4-2116-2	
	Nominal	Best fit	Nominal	Best fit	Nominal	Best fit
Oxide thickness	—	30.3 ± 0.6	—	27.9 ± 0.3	—	25.8 ± 0.4
In concentration (%)	25.6	24.1 ± 1.0	25.6	24.0 ± 0.5	30.0	29.9 ± 0.5
σ	—	6.4×10^{-4}	—	2.5×10^{-4}	—	7.8×10^{-4}

denote a smooth film and reliable parameter values. The results for the two AlGaAs films are given in Table 2. Here t_1(Å), t_2(Å) and t_3(Å) are the oxide, GaAs and AlGaAs thicknesses respectively and X(%) is the aluminum molar concentration. Comparison of experimental and calculated tan Ψ and cos Δ for sample M4-2128-3 before etching are shown in Fig. 2. An H_3PO_4:H_2O_2:H_2O (3:1:75) etch was performed on each sample independently. This etch can remove both GaAs and AlGaAs material. After the etch, the samples were measured in a dry nitrogen environment at an angle of incidence of 75°, with two-zone averaging. Two measurements were made on each sample, one immediately following the etch, the other 3 h later. Absolutely no change was observed as a function of the measurement delay time. Table 2 shows that, with the etch, the top oxide layer thickness increased and the AlGaAs thickness decreased as expected. We see two problems with the results in Table 2: the large values of σ compared with Table 1 and the extremely small values of GaAs thicknesses t_2 before etch. In addition, the fits given in Fig. 2 reveal very systematic discrepancies between the calculated and the experimental tan Ψ and cos Δ values in the wavelength range below 5000 Å, *i.e.* near the surface.

In order to clarify this last problem, we made fits of the data in the range 3200–5500 Å. The results are shown in Table 3. Here t_4 is the thickness of an interface layer of $Al_{0.2}Ga_{0.8}As$ with f_1(%) being the volume fraction of Al_2O_3. The very small amount of Al_2O_3 could have been formed either by the aluminum gettering action during deposition or by post-deposition oxidation from the air, through the very thin GaAs cap layer. The penetration depth of light in $Al_{0.2}Ga_{0.8}As$ in this range is always below 2000 Å. Thus, it turns out that the parameter t_3 of Table 2 cannot be estimated accurately from results in this restricted wavelength range, and therefore the $Al_xGa_{1-x}As$ was treated as a substrate. The most important result from Table 3 is that, before the etch, the top layer of the 8500 Å thick AlGaAs film does not behave like $Al_{0.2}Ga_{0.8}As$, irrespective of the interface model or the quality of fit. It seems that a long MOCVD growth of AlGaAs followed by GaAs gives a poor quality interface layer, showing up in ellipsometry by a larger aluminum concentration in the top layer than in the bulk of the film and a small amount of Al_2O_3. The etch depth of sample M4-2128-1 was about 125 Å (from Table 2), while that of sample M4-2128-3 was about 225 Å. From Table 3 we see that the X value is reduced with etching, with higher reduction for deeper etch. An approximately 225 Å etch was required to obtain the same quality AlGaAs at the top and bottom interfaces. Then, the ellipsometrically determined values of X for all wavelength range analyses are in excellent agreement with the DCXRD value. This result shows that, except for the top approximately 200 Å layer, the AlGaAs film is of good quality, with the aluminum concentration constant over all the film thickness. We have also performed best fits for the wavelength range 5600–7500 Å. In these cases we always obtained results for X and σ similar to those in Table 2. The large value of σ is probably due to inhomogeneities in the very thick AlGaAs film. This can be seen from the resonances above 6000 Å in Fig. 2, where the experimental and the calculated functions

TABLE 2. Best fits for $Al_xGa_{1-x}As$ thick films, wavelength range 3200–7500 Å

Sample	Etch	σ	t_1 (Å)	t_2 (Å)	t_3 (Å)	X (%)
M4-2128-1	Before	2.32×10^{-3}	13.8 ± 0.7	0.8 ± 2.8	8515 ± 9	20.0 ± 0.1
M4-2128-1	After	3.23×10^{-3}	32.6 ± 1.6	—	8392 ± 13	20.7 ± 0.1
M4-2128-3	Before	1.87×10^{-3}	12.2 ± 0.8	2.5 ± 2.5	8745 ± 9	19.7 ± 0.1
M4-2128-3	After	1.52×10^{-3}	23.9 ± 0.7	—	8521 ± 10	18.1 ± 0.2
Nominal values				50	8500	18

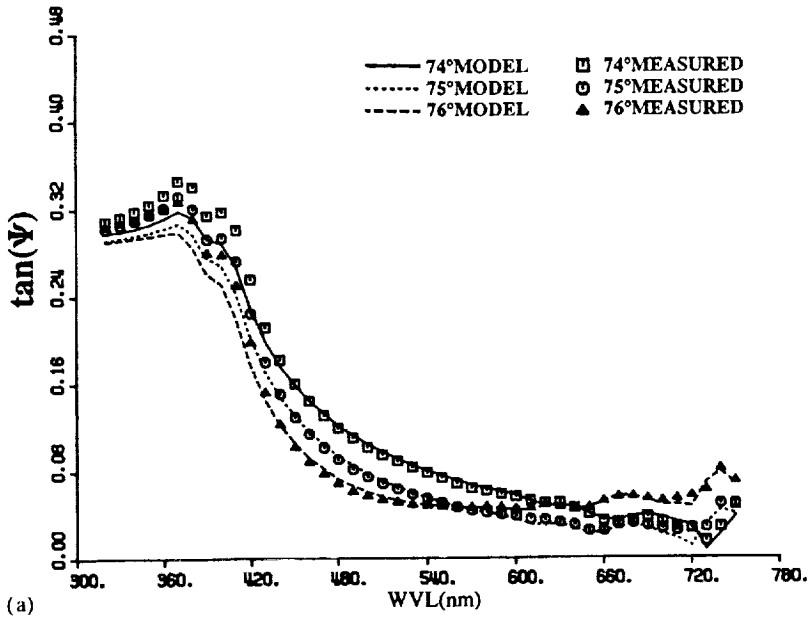

(a)

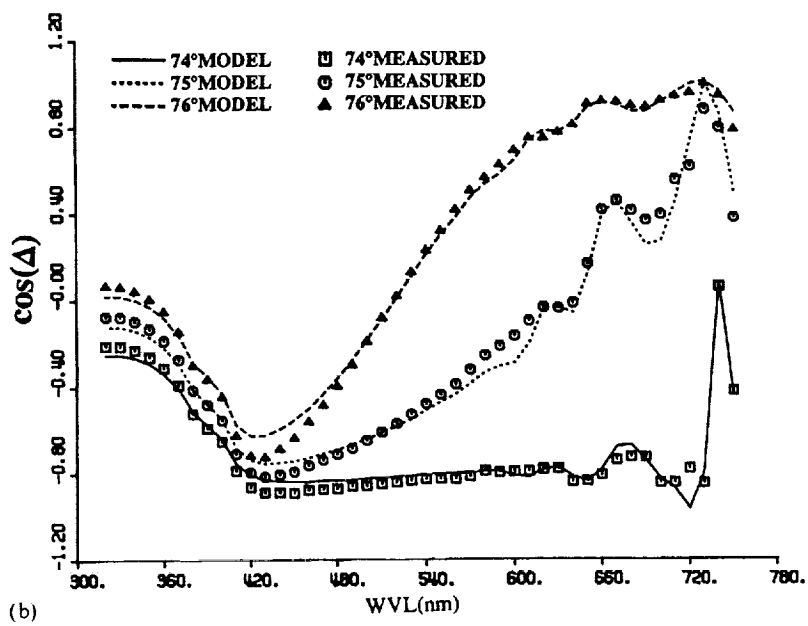

(b)

Fig. 2. Experimental and model calculated values for (a) tan Ψ and (b) cos Δ *vs.* wavelength at three angles of incidence for sample M4-2128-3 before etching.

TABLE 3. Best fits for $Al_xGa_{1-x}As$ thick films, wavelength range 3200–5500 Å

Sample	Etch	σ	t_1 (Å)	t_2 (Å)	t_4 (Å)	f_1 (%)	X (%)
M4-2128-1	Before	1.8×10^{-4}	15.8 ± 0.3	26.0 ± 1.0	—	—	28.8 ± 0.4
M4-2128-1	Before	7.3×10^{-5}	18.3 ± 0.6	13.1 ± 1.4	78 ± 7	0.8 ± 0.3	30.2 ± 0.5
M4-2128-1	After	6.6×10^{-5}	31.2 ± 0.3	—	—	—	26.2 ± 0.4
M4-2128-3	Before	2.0×10^{-4}	13.9 ± 0.3	26.3 ± 1.1	—	—	28.1 ± 0.5
M4-2128-3	Before	9.3×10^{-5}	13.6 ± 0.6	14.6 ± 1.6	75 ± 8	0.7 ± 0.4	29.5 ± 0.6
M4-2128-3	After	8.5×10^{-5}	22.1 ± 0.2	—	—	—	20.5 ± 0.3
Nominal values				50			18

have the same shape, but the magnitudes are a little different.

Results for the three MODFET structures are summarized in Table 4. Preliminary results were given in ref. 9, where no InGaAs algorithm was used. The nominal values were obtained from the prior calibration of deposition rates. The low aluminum concentrations in two of the samples are believed to be related to a possible problem in these particular runs. For all three samples, we found a correlation parameter a'_{ij} of 0.91–0.95 between the GaAs and the AlGaAs thicknesses. For the samples with the lower a'_{ij}, *i.e.* MO6-332-1 and MO6-334-1, thicknesses of all layers including both InGaAs and AlGaAs are in excellent agreement with the nominal values. For sample MO6-316-1, with $a'_{ij} = 0.95$, the value of the sum of the GaAs and AlGaAs thicknesses is within 7% of the nominal value. However, in all cases the value of Y, the indium concentration in the strained layer, is much smaller than the nominal value. For the 100 Å strained layer samples, we obtain an apparent concentration $Y = 23\%$ while for the 50 Å layer we obtain $Y = 18\%$. This result is quantitative, compared with the qualitative results obtained in ref. 9 for MBE-grown samples around $Y = 53\%$. It must be mentioned that the experimental critical thickness h_c for $In_{0.3}Ga_{0.7}As$ is around 90 Å. Thus the 100 Å InGaAs layer may be more relaxed than the thinner film, and therefore the strain effect is more pronounced for the thinner film. However, as seen from Table 4, the errors in Y make the results of all three samples overlap, around $Y = 21\%$.

In order to increase our sensitivity and to decrease the 90% confidence limits on the value of Y, we etched the thick GaAs layer of sample MO6-316-1 and remeasured it at five angles of incidence. An excellent result, with $\sigma = 8 \times 10^{-5}$, was obtained using a composite top layer, with an oxide layer thickness of 34.7 ± 3.5 Å and a 72 ± 11 Å thick layer composed of a mixture of $Al_{0.2}Ga_{0.8}As$ and $(11 \pm 4.5)\%$ of Al_2O_3. The remaining structure included the AlGaAs layer with $t_3 = 295 \pm 5.6$ Å and $X = 19.8 \pm 0.4$, and the InGaAs with $t_4 = 94.3 \pm 5.6$ Å and $Y = 21.6 \pm 0.9$. This result for Y has the lowest confidence limit. We checked the correlation of Y with the other parameters, as shown in Table 5 for sample MO6-316-1. No correlation was found, except with the InGaAs layer thickness. In all samples including the etched sample, the InGaAs thicknesses are very near to the nominal values, therefore increasing our confidence in the values of Y. Thus we believe that the value of $Y = 21\%$ for a coherently strained $In_{0.3}Ga_{0.7}As$ is reliable.

This result can be explained by changes in the critical points $E_i(Y)$, $i = 0, 1, 2$, with strain ε. Recalling the way the InGaAs algorithm was structured, we expect $E_i(\varepsilon)$ to change in an opposite way to $E_i(Y)$, *i.e.* both $E_0(\varepsilon)$ and $E_1(\varepsilon)$ to increase with ε, while E_2 will remain constant. The biaxial strain dependence of critical points in III–V semiconductors is treated theoretically

TABLE 4. Best fits for three modulation-doped field effect transistor structure samples, wavelength range 3500–6800 Å

Sample	σ	t_1 (Å)	t_2 (Å)	t_3 (Å)	X (%)	t_4 (Å)	Y (%)
MO6-316	2.4×10^{-4}	20.5 ± 0.5	337 ± 4	367 ± 6	19.7 ± 0.5	91 ± 13	24.1 ± 2.7
MO6-316	Nominal	—	300	450	20	100	30
MO6-332	5.2×10^{-4}	16.3 ± 0.5	93 ± 3	437 ± 4	14.3 ± 0.4	94 ± 6	23.5 ± 2.1
MO6-332	Nominal	—	100	450	20	100	30
MO6-334	4.7×10^{-4}	16.9 ± 0.5	99 ± 3	488 ± 5	13.7 ± 0.4	65 ± 14	18.3 ± 3.5
MO6-334	Nominal	—	100	450	20	50	30

TABLE 5. Best fits for modulation-doped field effect transistor structure sample MO6-334 using constant indium concentration values

Y (%)	σ	t_1 (Å)	t_2 (Å)	t_3 (Å)	X (%)	t_4 (Å)
10	5.19×10^{-4}	16.5 ± 0.5	99 ± 3	482 ± 5	13.3 ± 0.5	109 ± 13
15	4.74×10^{-4}	16.6 ± 0.5	99 ± 3	487 ± 5	13.4 ± 0.4	78 ± 8
17	4.68×10^{-4}	16.8 ± 0.5	99 ± 3	488 ± 5	13.6 ± 0.4	69 ± 7
18	4.66×10^{-4}	16.9 ± 0.5	99 ± 3	488 ± 5	13.6 ± 0.4	66 ± 6
19	4.66×10^{-4}	16.9 ± 0.5	99 ± 3	488 ± 5	13.7 ± 0.4	63 ± 6
20	4.67×10^{-4}	16.9 ± 0.5	99 ± 3	488 ± 5	13.7 ± 0.4	60 ± 6
22	4.70×10^{-4}	17.0 ± 0.5	99 ± 3	487 ± 5	13.7 ± 0.4	55 ± 5
25	4.74×10^{-4}	17.1 ± 0.5	100 ± 3	485 ± 5	13.8 ± 0.4	49 ± 5
30	4.88×10^{-4}	17.3 ± 0.5	100 ± 3	483 ± 5	13.9 ± 0.4	43 ± 4

in ref. 13. $E_0(\varepsilon)$ is split and both $E_0(\varepsilon)$ and $E_1(\varepsilon)$ go up with the strain. We found out, by using several values for E_0 in our algorithm, that the calculated value of the InGaAs dielectric function in our experimental range is only slightly dependent on the value of E_0 (E_0 is below 1.14 eV, for $Y > 20$). Thus, the changes in E_0 with strain can be neglected as a first approximation for small values of ε. E_1 is linear [13] for small ε, and so is the E_1 dependence on the indium concentration Y for coherently strained layers. Thus the strain dependence can be exchanged for composition dependence in our algorithm approximation. Therefore the measured 30% reduction in the value of Y with strain, together with the assumptions of linearity, gives us a simple way to measure the correct Y_c value from the measured ellipsometric result Y_e, using $Y_c = 0.7 Y_c$.

4. Conclusions

A two-prong ellipsometric study of MOCVD-grown layers of AlGaAs and InGaAs was performed, including thick films and strained layer complex structures. The study shows that the ternary composition of thick non-strained layers can be accurately determined to within experimental errors using numerical algorithms. In the case of complex structures, thicknesses of all layers and the alloy composition of non-strained layers can be determined simultaneously, provided that the correlations between parameters is no higher than 0.9. The composition of strained InGaAs can be estimated from the experimental result using a correction factor based on a linear approximation of the dependence of the critical point E_1 on composition and strain.

References

1 W. T. Masselink, A. Ketterson, J. Klem, W. Kopp and H. Morkoc, *Electron. Lett.*, *21* (1985) 937.
2 G.-W. Wang, R. Kaliski and J. B. Kuang, *IEEE Electron Device Lett.*, *11* (1990) 394.
3 W. C. Hsu, C. M. Chen and R. T. Hsu, *Appl. Phys. Lett.*, *59* (1991) 1075.
4 R. Ramanchandran and G. Metze, *Microwave J.*, *34* (1991) 113.
5 T. G. Anderson, Z. G. Chen, V. D. Kulakovskii, A. Uddin and J. T. Vallin, *Appl. Phys. Lett.*, *51* (1987) 752.
6 H. K. Choi and C. A. Wang, *Appl. Phys. Lett.*, *57* (1990) 321.
7 S. A. Alterovitz, R. M. Sieg, N. S. Shoemaker and J. J. Pouch, *Mater. Res. Soc. Symp. Proc.*, *152* (1989) 21.
8 J. M. M. de Nijs and A. van-Silfhout, *J. Opt. Soc. Am. A*, *5* (1988) 535.
9 S. A. Alterovitz, R. M. Sieg, H. D. Yao, P. G. Snyder, J. A. Woollam, J. Pamulapati, P. K. Bhattacharya and P. A. Sekula-Moise, *Thin Solid Films*, *206* (1991) 288.
10 P. G. Snyder, J. A. Woollam, S. A. Alterovitz and B. Johs, *J. Appl. Phys.*, *68* (1990) 5925.
11 Z. Hang, D. Yan, F. H. Pollack, G. D. Pettit and J. M. Woodall, *Phys. Rev. B*, *44* (1991) 10546.
12 S. A. Alterovitz, R. M. Sieg, H. D. Yao, P. G. Snyder, J. A. Woollam, J. Pamulapati, P. K. Bahattacharya and P. A. Sekula-Moise, *Proc. ICEM-90*, MRS Int. Proc., Pittsburgh, PA, 1990, p. 187.
13 F. H. Pollak, in T. P. Pearsall (ed.), *Semiconductors and Semimetals*, Vol. 32, Academic Press, Boston, MA, 1990, p. 17.

Enhancement of Shubnikov–de Haas oscillations by carrier modulation

S. E. Schacham,[a] E. J. Haugland, and S. A. Alterovitz
NASA Lewis Research Center, M/S 54-5, Cleveland, Ohio 44135

(Received 16 January 1992; accepted for publication 19 May 1992)

A drastic enhancement of the Shubnikov–de Haas (SdH) pattern is obtained by recording the *changes* in the quantum oscillations of magnetoresistance due to modulation of the carrier concentration. The technique enables measurement of the SdH waveform at relatively high temperatures and in samples with moderate mobilities. The modulated waveform shows selective enhancement of the low-frequency SdH oscillations associated with the upper subband. Thus, we were able to record very clear oscillations generated by a carrier concentration well below 5×10^{10} cm^{-2}. The theory for this selective enhancement is provided.

Several fundamental aspects concerning transport properties of carriers in a two-dimensional electron gas (2DEG) are still unresolved. As the second subband starts to be populated, does the electron concentration in the ground subband (n_1) continue to increase?[1,2] Is the mobility of electrons in the second subband larger than that at the ground level?[1–3] Does the carrier mobility drop as soon as the upper subband starts filling up[3] or even before?[4]

The primary techniques for determining most transport parameters are the Shubnikov–de Haas (SdH) oscillatory magnetoresistance, the Hall effect, and conductivity measurements. While the total carrier concentration n_T is obtained from the Hall voltage, the frequency (in $1/B$, where B is the magnetic field) of the SdH oscillation renders the electron concentration in the subbands of the 2DEG. The presence of carriers in the second subband is manifested by a superposition of the two frequencies corresponding to the concentration of electrons in the ground subband n_1 and in the upper one n_2. Most frequently $n_2 < n_1$ and the determination of n_2 is extremely difficult, in particular for lower concentrations ($n_2 < 5\times10^{10}$ cm^{-2}).[3,5]

In this letter, we present a novel technique by which we are able to drastically enhance the SdH pattern. The technique is based on measuring the change in the magnetoresistance due to a carrier generated by a modulated light source. In addition to the overall enhancement of the SdH waveform, the technique has an important property of selectively increasing the amplitude of the slower oscillations due to carriers in the second subband much more than oscillations generated by the ground subband electrons.

The experimental setup used to generate the modulated oscillatory magnetoresistance waveform is a conventional SdH setup with an additional lock-in amplifier and a chopped laser. The sample is cooled down in an open-flow He cryostat with an optical axis to enable excitation of the carriers. The magnetic field is swept up to 1.4 T. The change in the longitudinal voltage drop is measured by a lock-in amplifier with reference frequency provided by the chopper.

Figure 1 shows the raw data obtained using the modulated SdH technique (a), followed by a regular SdH measurement (b). Both measurements were taken at 4.2 K on an InGaAs/AlGaAs high electron mobility transistor (HEMT) structure with a 200 Å $In_{0.1}Ga_{0.9}As$ well, a 100-Å-wide $Al_{0.15}Ga_{0.85}As$ spacer, and a 2×10^{18} cm^{-3} Si-doped barrier of the same composition. The identical frequency of oscillation of 12.4 T seen in Figs. 1(a) and 1(b) indicates a carrier concentration of 6.01×10^{11} cm^{-2} in the 2DEG. The *raw* modulated waveform is as good as the best computed SdH pattern derived after background subtraction and normalization. The experimentally modulated results are superior to those obtained by taking the numerical

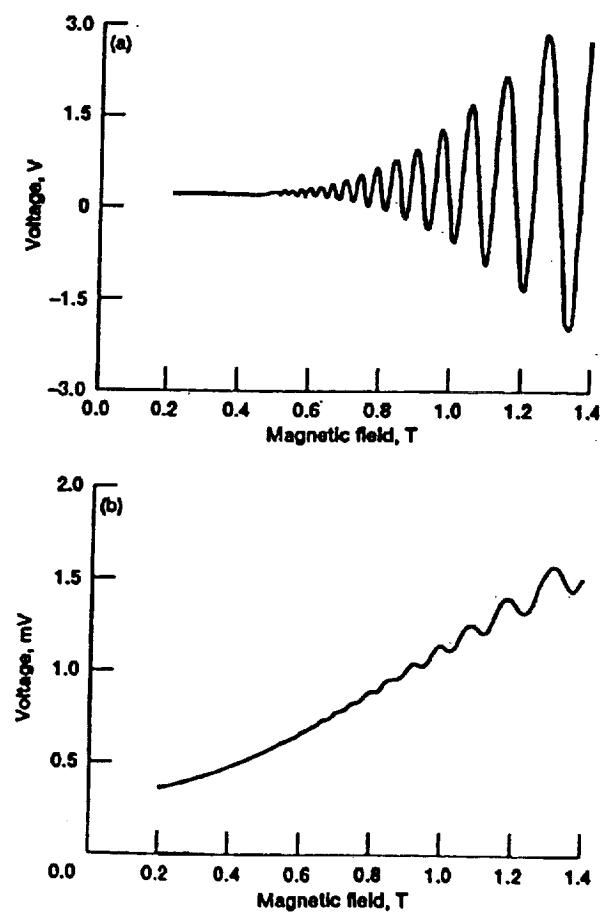

FIG. 1. SdH oscillations at 4.2 K on an $In_{0.1}Ga_{0.9}As/Al_{0.15}Ga_{0.85}As$ HEMT structure with $n = 6.01\times10^{11}$ cm^{-2} and $\mu_e = 97\,000$ cm^2/V s. (a) Raw modulated data. (b) Regular SdH.

[a]National Research Council–NASA Senior Research Associate, on leave from the Dept. of Electrical Engineering and Solid State Institute, Technion–Israel Institute of Technology, Haifa 32000, Israel.

© Appl. Phys. Lett. 61 (5), 3 August 1992. Reprinted, with permission, from American Institute of Physics.

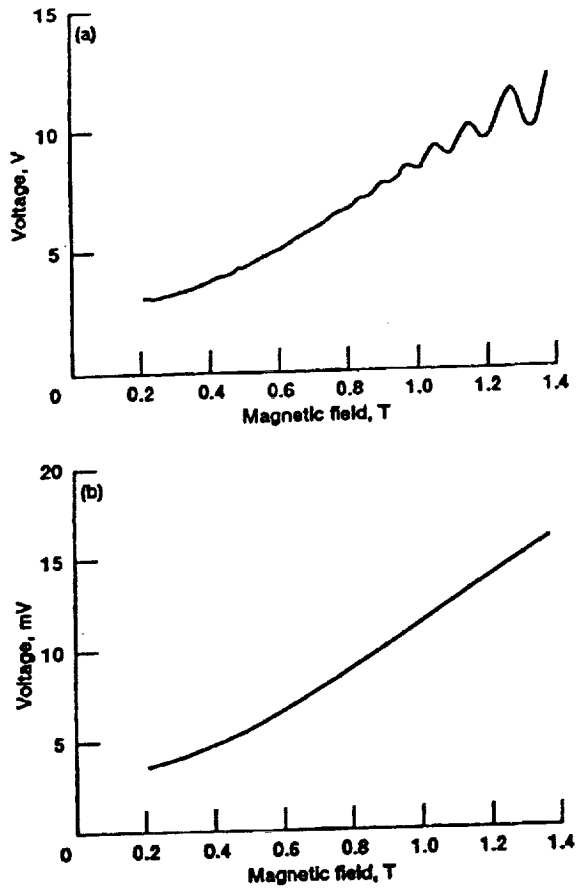

FIG. 2. Same as Fig. 1, taken at 9.1 K.

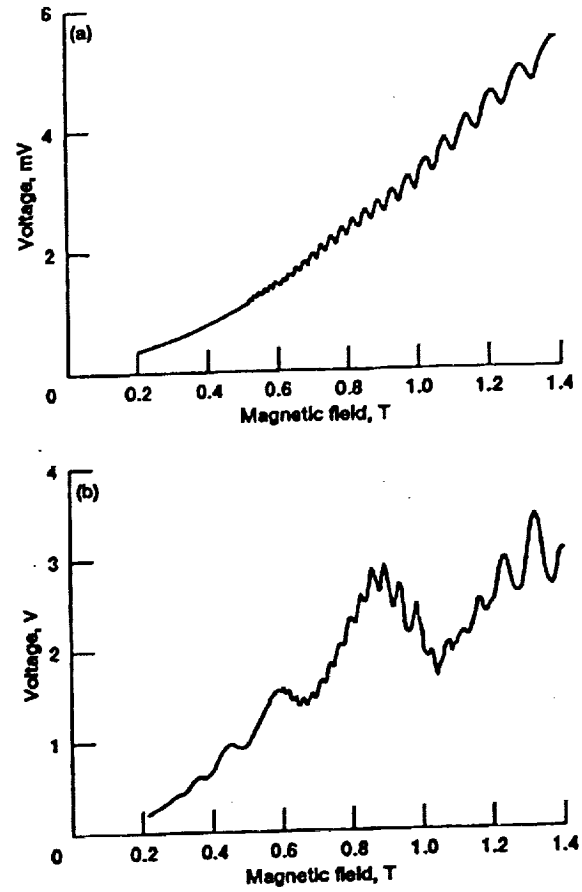

FIG. 3. SdH oscillations at 1.95 K on an $Al_{0.3}Ga_{0.7}As/GaAs$ HEMT structure. (a) Regular SdH. (b) Raw modulated data. Note the clear low-frequency oscillations.

derivative with respect to the magnetic field,[6] as will be discussed below. Figure 2 shows SdH waveforms for the same sample measured at 9.1 K. The enhancement of the waveform by the carrier modulation technique is obvious. The oscillations obtained with this carrier modulation method are very clear at this relatively high temperature, even though the electron mobility is not too large ($\mu_e = 97\,000$ cm^2/V s at 4.2 K).

The technique has an important property of selectively increasing the amplitude of the slower oscillations due to carriers in the upper subband much more than oscillations generated by the ground subband electrons. This selective enhancement is demonstrated in Fig. 3 on an $Al_{0.3}Ga_{0.7}As/GaAs$ HEMT structure grown on semi-insulating GaAs. The undoped AlGaAs spacer is 60 Å and the dopant concentration is 3×10^{18} cm^{-3}. The measurements are taken at 1.95 K. Figure 3(a) shows the raw data for a regular SdH measurement, from which the modulation at the lower frequency can be extracted only after background subtraction. The raw data for modulated SdH is shown in Fig. 3(b). The amplitude of oscillation at the lower frequency is significantly larger than that generated by the ground subband. The Fourier transform of the modulated SdH shows a very clear peak at a frequency corresponding to a second subband concentration of 8.4×10^{10} cm^{-2} as compared to 9.7×10^{11} cm^{-2} for the ground one. The Hall concentration n_T is 1.06×10^{12} cm^{-2} and the Hall mobility is $\mu_e = 410\,000$ cm^2/V s.

The selective enhancement can be caused either by an uneven distribution of the carriers between the two subbands, or by the different effect of the excess carriers on the amplitudes of oscillation. The ratio between the oscillatory resistance ΔR_{xx} and its zero-field value R_0 for a two subband system is given by[1]

$$\frac{\Delta R_{xx}}{R_0} = A_1\frac{\Delta g_1}{g_0} + A_2\frac{\Delta g_2}{g_0} + B_{12}\frac{\Delta g_1 \Delta g_2}{g_0^2}, \qquad (1)$$

where A_1 and A_2 are the amplitudes of oscillations at either frequency while B_{12} represents the intermodulation term. The zero-field density of states is g_0, while is oscillatory parts are given by

$$\Delta g_i = 2g_0 \sum_s D_T(sX)\exp\left(\frac{-s\pi}{\omega_c\tau_{q_i}}\right)\cos\left(\frac{h\pi n_i}{qB} + s\pi\right), \qquad (2)$$

where $D_T(Y) = Y/\sinh(Y)$, $X = 2\pi^2 kT/\hbar\omega_c$, T is the temperature, ω_c the cyclotron frequency, τ_{q_i} the quantum re-

laxation time, and $i=1,2$ denotes the subband. Practically the first Fourier component $s=1$ suffices to describe most oscillations.[7]

The modulation of the carrier concentration results in a change in the oscillatory resistance $\delta(\Delta R_{xx})$ given by

$$\delta\left(\frac{\Delta R_{xx}}{R_0}\right)=\left[\left(\frac{\partial A_1}{\partial n_1}+\frac{\partial B_{12}}{\partial n_1}\frac{\Delta g_2}{g_0}\right)\frac{\Delta g_1}{g_0}+\left(\frac{A_1}{g_0}+B_{12}\frac{\Delta g_2}{g_0^2}\right)\frac{\partial \Delta g_1}{\partial n_1}\right]\delta n_1+\left[\left(\frac{\partial A_2}{\partial n_2}+\frac{\partial B_{12}}{\partial n_2}\frac{\Delta g_1}{g_0}\right)\frac{\Delta g_2}{g_0}+\left(\frac{A_2}{g_0}+B_{12}\frac{\Delta g_1}{g_0^2}\right)\frac{\partial \Delta g_2}{\partial n_2}\right]\delta n_2, \quad (3)$$

where the excess concentration δn_T is divided between the two subbands as δn_1 and δn_2. A straightforward interpretation for the enhancement of oscillations due to the upper subband would be that the electron concentration at the ground subband remains almost unchanged once the second subband starts getting populated,[2] and therefore, $\delta n_2 \gg \delta n_1$. However, most reported data indicate that the electron concentration in the ground subband continues to increase, as were our measurements on the samples described above. Moreover, it is reported that δn_1 is larger than δn_2.[8] Therefore, this cannot be the cause of the selective enhancement.

Next, the derivative terms in Eq. (3) are investigated. The derivative of the density of state is given by

$$\frac{\partial \Delta g_i}{\partial n_i}=2g_0 D_T(X)\exp\left(-\frac{\pi}{\omega_c \tau_{q_i}}\right)\times\left[\frac{\pi}{\omega_c \tau_{q_i}^2}\frac{\partial \tau_{q_i}}{\partial n_i}\cos\left(\frac{h\pi n_i}{qB}+\pi\right)+\frac{h\pi}{qB}\sin\left(\frac{h\pi n_i}{qB}\right)\right]. \quad (4)$$

This result obtained for carrier modulation should be compared with the technique of differentiating with respect to the magnetic field.[6] Taking the derivative with respect to B results in a multiplication by n_i, and since $n_1 \gg n_2$, that technique greatly enhances the signal due to the *ground* subband. It should be emphasized that the carrier modulation technique provides experimentally a derivative with respect to n. Since $\omega_c = qB/m^*$, both terms in the square brackets in Eq. (4) are multiplied $1/B$. Thus, there is a relative increase in the amplitudes at low fields. The first term depends on the change in quantum relaxation time with subband population. Little data is available on this dependence. A theoretical analysis is provided by Isihara and Smrcka,[9] from which one can derive that

$$\tau_q \propto \left[\frac{\epsilon_F}{\epsilon_F^2+[\epsilon_\sigma-3(\epsilon_\tau^2/\epsilon_\sigma)]\epsilon_F+\epsilon_\tau^2}\right]^2, \quad (5)$$

where ϵ_F is the Fermi energy and ϵ_τ and ϵ_σ are the energies at which the relaxation time and the conductivity reach their maximum. Since the electron concentration depends linearly on the Fermi level, Eq. (5) can be transformed to a dependence on n. Thus, τ_q increases steeply with increasing population at low values of n since at low energies the states become localized and resonant scattering dominates. It reaches a maximum at a concentration corresponding to ϵ_τ, and dropping from there on as the electrons can get closer to the scattering impurities.[10] Therefore, the contribution of this derivative term is much larger for the upper subband, with its low concentration. The quantum lifetime of electrons in the ground subband may have reached its peak, i.e., the derivative is close to zero. Thus, the contribution of this term to the oscillations waveform is much larger for the second subband.

The last part to be analyzed is the derivatives of the amplitudes of oscillations and the intermodulation. Expressions for the amplitudes were derived by Coleridge[1] based on the effect of various scattering mechanisms on the relaxation time. It can be shown for the case of $n_1 \gg n_2$ that

$$A_1 \simeq 2-\frac{P_{12}}{P_{11}+P_{12}}; \quad A_2 \simeq B_{12} \simeq \frac{P_{12}}{P_{11}+P_{12}}, \quad (6)$$

where P_{11} is the intraground subband scattering probability and P_{12} is the intersubband scattering probability. It is clear from the equation that if A_2 increases, A_1 decreases and vice versa. Following the drop of mobility at the onset of population of the second subband, the mobility increases with increasing carrier population. Since the dominant scattering mechanism is due to the ionized impurities, this scattering is reduced by additional carriers screening this potential. Thus, it can be deduced that the intrasubband scattering decreases with increased carrier concentration. Reviewing Eqs. (3) and (6), one can expect a positive contribution to the modulated signal generated by carriers in the upper subband due to the positive derivative of A_2, but a negative contribution to the modulated amplitude by excess carriers in the ground subband since the derivative of A_1 is negative. The derivatives of the intermodulation are both positive, but as long as the oscillations are not very large (as is usually the case when the modulated SdH technique is used), this term, proportional to the square of the oscillations, is negligible.

[1] P. T. Coleridge, Semicond. Sci. Technol. 5, 961 (1990).
[2] H. L. Stormer, A. C. Gossard, and W. Wiegmann, Solid State Commun. 41, 707 (1982).
[3] J. J. Harris, D. E. Lacklison, C. T. Foxon, F. M. Stelten, A. M. Suckling, R. J. Nicholas, and K. W. J. Barnham, Semicond. Sci. Technol. 2, 783 (1987).
[4] R. Fletcher, E. Zaremba, M. d'Iorio, C. T. Foxon, and J. J. Harris, Phys. Rev. B 41, 10 649 (1990).
[5] R. J. Nicholas, M. A. Brummel, and J. C. Portal, J. Cryst. Growth 68, 356 (1984).
[6] D. R. Leadley, R. J. Nicholas, J. J. Harris, and C. T. Foxon, Semicond. Sci. Technol. 4, 885 (1989).
[7] P. T. Coleridge, R. Stoner, and R. Fletcher, Phys. Rev. B 39, 1120 (1989).
[8] D. Delagebeaudeuf and N. T. Linh, IEEE Trans. Electron Devices ED-29, 955 (1982).
[9] A. Isihara and L. Smrcka, J. Phys. C 19, 6777 (1986).
[10] See Fig. 3 of Ref. 14.

TEMPERATURE INDEPENDENT QUANTUM WELL FET WITH DELTA CHANNEL DOPING

P. G. Young, R. A. Mena, S. A. Alterovitz, S. E. Schacham, and E. J. Haugland

Indexing terms: Field-effect transistors, Transistors, Semiconductor devices and materials

A temperature independent device is presented which uses a quantum well structure and delta doping within the channel. The device requires a high delta doping concentration within the channel to achieve a constant Hall mobility and carrier concentration across the temperature range 300–1·4 K. Transistors were RF tested using on-wafer probing and a constant G_{max} and F_{max} were measured over the temperature range 300–70 K.

Introduction: In most semiconductor devices, the gain changes as a function of temperature. For a high electron mobility transistor (HEMT), as the temperature is lowered, the gain is enhanced due to lower electron scattering while maintaining an acceptable carrier concentration. When designing circuits and devices for applications requiring operation over a large temperature range, this enhancement of the carrier mobility has to be taken into account. Previous studies on delta doped channel structures [1–4] have shown that the delta doping creates band bending within the channel allowing for the quantisation of the carrier states within the doped region.

We propose a temperature independent FET with a heavily delta doped GaAs quantum well channel using molecular beam epitaxy (MBE). In the channel doped structure, temperature independence is achieved via proper ion sheet densities within the channel region that degrades the peak mobility of the carrier but creates a constant mobility and carrier concentration from 300 to 1·4 K. This doping technique is contrary to typical HEMT devices where the doping occurs outside the channel in order to reduce ion scattering at low temperatures.

Device structures and characterisation: The nominal structures grown by MBE for this work are shown in Fig. 1. The conduction channel is a GaAs layer of 150 Å confined between two $Al_{0.3}Ga_{0.7}As$ layers to form a quantum well. The channel layer is delta doped in the centre with silicon to nominal concentrations of $1{\cdot}8 \times 10^{12}/cm^2$ or $6 \times 10^{12}/cm^2$. The different dopant concentrations were used to determine the effect of the dopant concentration level on the parametric temperature dependance. The quantum well structure is used to reduce parallel conduction and improve the output conductance of the resulting device.

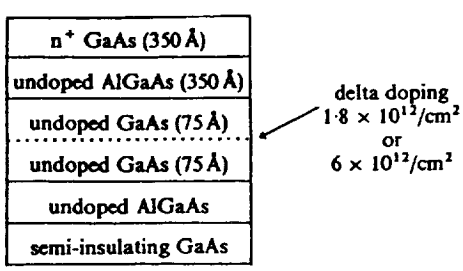

Fig. 1 *Device structure cross-section*

Fabrication of transistors and Hall bar structures was carried out using wet mesa isolation techniques. The transistors are a dual, Ti/Au gate design with gate lengths and width of 0·8–1·2 μm and 200 μm, respectively. Ohmic contacts consist of sequentially evaporated Au/Ge/Au/Ni/Au metal.

Testing of the devices was carried out to determine material transport parameters and transistor performance. The transport properties of the structures were measured by Hall and Shubnikov-de Haas (SdH) techniques over a temperature range 300–1·4 K with a maximum magnetic field of 1·4 T and carrier light modulation capability. Transistors were RF tested using an HP8510 ANA and an in-house fabricated cryostat mounted with Design Techniques probes capable of on-wafer probing of the device *S* parameters down to 65 K.

Results and discussion: Fig. 2*a* and *b* show the measured Hall mobility and carrier concentrations for the two devices as a

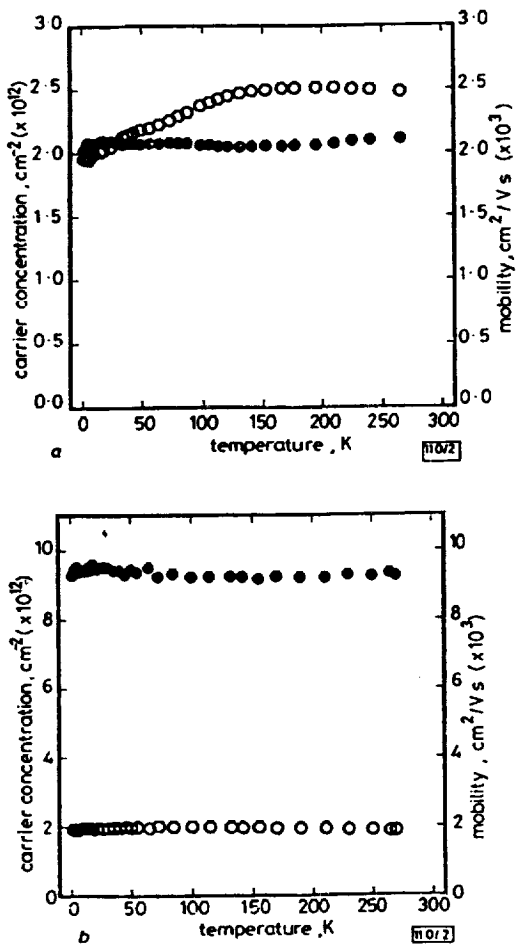

Fig. 2 *Hall mobility and carrier concentration against temperature*

O mobility
● carrier concentration
a Nominal silicon doping $2 \times 10^{12}/cm^2$
b Nominal silicon doping $6 \times 10^{12}/cm^2$

© Reprinted, with permission, from Electronics Letters, vol. 28, no. 14, 2nd July 1992, pp. 1352-1354.

PRECEDING PAGE BLANK NOT FILMED

function of temperature. As can be seen, the Hall mobility for the lower doped structure varied by 27% over the temperature range with maximum a Hall mobility of 2500 cm^2/Vs. The temperature dependence below 125 K is consistent with scattering from ionised impurities. The carrier concentration variation of only 5% is considered to be temperature independent and indicates there is no carrier freeze out.

When the delta doping concentration is increased by a factor 3·3 to a nominal level of $6 \times 10^{12}/cm^2$, the structure experiences a fluctuation of the electron mobility of only 7% over the same temperature range but at the expense of the magnitude of Hall mobility. The Hall mobility was measured to be $\sim 2000\,cm^2/Vs$ which is a 20% decrease over that of the lower doped sample at room temperature. The carrier concentration also showed a small 5% variation over the temperature range. Thus a stable carrier concentration is obtained over the temperature range for both dopant levels but only the higher doped sample experiences constant Hall mobility.

Finally, very high 2-D carrier concentrations were observed in these structures. For the lower doped sample, a dark Hall electron concentration of $2{\cdot}1 \times 10^{12}/cm^2$ was measured as compared to a value of $2{\cdot}7 \times 10^{12}/cm^2$ under illumination. The large photoconductivity (PC) effect leads to an enhanced signal of the SdH oscillation enabling quantitative measurements and positively confirm the 2-D character of the carriers. Quantitatively, we found carrier concentrations under illumination for the ground and first excited sub-bands of $2{\cdot}1 \times 10^{12}/cm^2$ and $5{\cdot}3 \times 10^{11}/cm^2$, respectively. This shows that for the low doped sample, only two sub-bands are populated. We could not resolve all the sub-bands by SdH for the higher doped sample, but we expect more sub-bands to be populated. This larger number of populated sub-bands is the main reason for temperature independent mobility, as the electrons in the higher sub-bands are spatially less affected by the ionised impurity scattering [5].

To demonstrate the temperature independence of the structure, FETs made from the highly doped structures were tested from 70 to 300 K. The S parameters were measured on-wafer to determine F_{max} and G_{max} at 5 GHz as a function of temperature. G_{max} and F_{max} are shown in Fig. 3. An average G_{max} of 7·3 dB was measured over the whole temperature range at 5 GHz with a variation of only $\pm 0{\cdot}35$ dB. The devices were

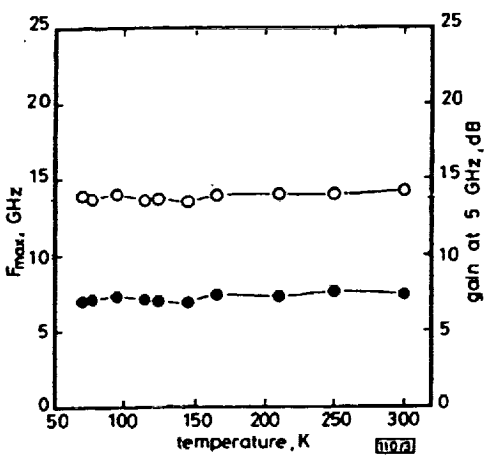

Fig. 3 G_{max} and F_{max} against temperature for 1 μm device
○ F_{max}
● G_{max}

stable across the frequency range and this constant stability appears to be characteristic of the structures with channel delta doping. Results for F_{max} show a similar effect with F_{max} being only affected by system noise and not dependent on temperature.

Conclusion: A device quantum well structure with channel doping has been demonstrated with temperature independent parameters. Electron Hall mobility and carrier concentration were almost constant against temperature independence of the RF performance for the transistors. With G_{max} and F_{max} remaining unchanged over the whole temperature range, the need for temperature compensation is eliminated and cryogenic design of circuits using the room temperature S-parameters is viable.

26th May 1992

P. G. Young*, R. A. Mena, S. A. Alterovitz, S. E. Schacham† and E. J. Haugland (*NASA Lewis Research Center Cleveland, Ohio 44135, USA*)

* Permanent address: Department of Electrical Engineering, University of Toledo, Toledo, Ohio 43606, USA
† Permanent address: Department of Electrical Engineering, Technion-Israel Institute of Technology, Haifa 32000, Israel

References

1 HONG, W., HARRISON, J., FLOREZ, L., and ABELES, J.: 'DC and AC characteristics of Delta-Doped GaAs FET', *IEEE Electron Device Lett.*, 1989, **19**, pp. 310–311
2 SHUBERT, E., CUNNINGHAM, J., and TSANG, W.: 'Self-aligned enhancement-mode and depletion mode GaAs field-effect transistors employing the delta doping technique', *Appl. Phys. Lett.*, 1986, **49**, pp. 1729–1731
3 MAKIMOTO, T., KOBAYASHI, N., and HORIKOSHI, Y.: 'Electron conduction in GaAs atomic layer doped with Si', *J. Appl. Phys.*, 1988, **63**, pp. 5023–5026
4 ZRENNER, A., REISINGER, N., and KOCH, F.: 'Electron subband structure of a δ(z)-doped layer in n-GaAs'. 17th Int. Conf. on Phys. of Semiconductors, 1984, San Francisco, CA, August, pp. 325–328
5 SHUBERT, E., CUNNINGHAM, J., and TSANG, W.: 'Electron-mobility enhancement and electron-concentration enhancement in delta-doped n-GaAs at T = 300 K', *Solid State Commun.*, 1987, **63**, pp. 591–594

Room-temperature determination of two-dimensional electron gas concentration and mobility in heterostructures

S. E. Schacham,[a] R. A. Mena, E. J. Haugland, and S. A. Alterovitz
National Aeronautics and Space Administration, Lewis Research Center, Cleveland, Ohio 44135

(Received 30 September 1992; accepted for publication 11 January 1993)

A technique for determination of room-temperature two-dimensional electron gas (2DEG) concentration and mobility in heterostructures is presented. Using simultaneous fits of the longitudinal and transverse voltages as a function of applied magnetic field, we were able to separate the parameters associated with the 2DEG from those of the parallel layer. Comparison with the Shubnikov–de Haas data derived from measurements at liquid helium temperatures proves that the analysis of the room-temperature data provides an excellent estimate of the 2DEG concentration. In addition we were able to obtain for the first time the room-temperature mobility of the 2DEG, an important parameter to device application. Both results are significantly different from those derived from conventional Hall analysis.

Two of the most important physical parameters governing the performance of devices based on two-dimensional electron gas (2DEG) are the concentration of carriers forming the 2DEG and their mobility. In the past, the main effort was placed on increasing the carrier mobility by separating the doped layer from the conduction channel. This was realized using either homogeneous or planar doping in the barrier while the conduction took place in the channel, i.e., a modulation doped (MOD) structure. Lately the trend is to obtain as high a 2DEG concentration as possible. Dopants are introduced into the channel,[1,2] drastically reducing the carrier mobility, defeating the concept of a MOD structure. There is a tradeoff between increased doping level and mobility of the carriers in the channel. In all cases, the determination of the 2DEG concentration and mobility is an essential part of the characterization of high speed devices.

Unfortunately the determination of the concentration and mobility of carriers is frequently complicated by the presence of a parallel conducting path, in most cases in the barrier layer, since it is usually heavily doped. Typical room-temperature concentrations in the parallel conduction path, AlGaAs for GaAs based devices, and InAlAs for InP based devices, are of the order of 10^{18} cm^{-3}. Even though the mobility of these carriers is substantially smaller than that of carriers in the 2DEG, in particular in MOD structures, their presence may significantly modify the Hall coefficient R_H and conductivity data.[3] Thus, it becomes essential to resort to measurements performed at cryogenic temperatures, in order to determine the 2DEG concentration, assuming it remains constant as a function of temperature.

In this letter we propose a technique that enables the determination of the 2DEG concentration using only room-temperature measurements. At the same time the room-temperature 2DEG mobility is derived, which is a parameter of utmost importance in development of high speed devices. The technique is based on recording of both the longitudinal and transverse (Hall) voltages across the sample versus magnetic field, determining the physical magnetoresistance and the change in the Hall voltage as a function of field.

The general expressions for the longitudinal and transverse resistivities as a function of magnetic field B (in the z direction) in the presence of two carriers are given by:[3]

$$\rho_{xx}=E_x/J_x=D_{12}/(D_{12}^2+A_{12}^2), \tag{1}$$

$$\rho_{yx}=E_y/J_x=R_H B=-A_{12}/(D_{12}^2+A_{12}^2), \tag{2}$$

with

$$D_i=n_i e^2\tau_i/m_i(1+\omega_{ci}^2\tau_i^2)$$

$$A_i=\omega_{ci}\tau_i D_i$$

$$D_{12}=D_1+D_2$$

$$A_{12}=A_1+A_2.$$

In this letter we assume that the carriers in the conduction channel of the heterostructure form a 2DEG and we will denote these carriers with index 1 and those in the parallel path with index 2. The concentrations of the two carriers are n_i, their effective masses are m_i and the scattering times are τ_i, with $i=1,2$ for the two carriers. E is the electric field while the longitudinal current density is denoted by J_x (see insert in Fig. 1). The Hall concentration and mobility will be denoted by n_H and μ_H and the Hall scattering factor is assumed to be equal to 1. The magnetic field dependence is introduced through the cyclotron frequency, $\omega_{ci}=eB/m_i$, where e is the electron charge. At zero magnetic field the longitudinal resistivity is equal to the parallel combination of the resistivities of the two carriers, while at very large fields ($\omega_{ci}\tau_i \gg 1$) the Hall concentration is equal to the sum of the two concentrations. If, for example, the two concentrations are of comparable magnitude, but the mobility of the first is much larger than that of the second one, $\mu_1 \gg \mu_2$, the low field Hall concentration equals n_1. At high fields, under the same conditions, the longitudinal resistivity is given by:

$$\rho_{xx}\approx n_2/e\mu_1(n_1+n_2)^2.$$

[a]National Research Council-NASA Senior Research Associate, on leave from the Dept. of Electrical Engineering and Solid State Institute, Technion-Israel Institute of Technology, Haifa 32000 Israel.

© Appl. Phys. Lett. 62 (11), 15 March 1993. Reprinted, with permission, from American Institute of Physics.

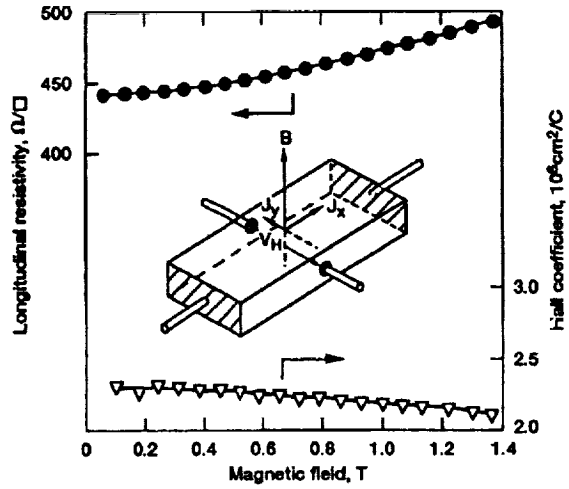

FIG. 1. Theoretical fit to experimental data of longitudinal resistivity ρ_{xx} (circles) and Hall coefficient R_H (triangles) as a function of magnetic field for sample Q12I. Insert shows test configuration.

In our experimental setup we recorded the longitudinal voltage and the Hall voltage continuously versus the magnetic field up to the highest field accessible, 1.4 T. Then, using a nonlinear least-squares method we fitted both sets of experimental data simultaneously to Eqs. (1) and (2). Thus we obtained an estimate of the four variables: n_1, n_2, μ_1, and μ_2. Two problems are faced during this process. First the Hall voltage increases almost linearly with the magnetic field which would result in an improper balance of the computation by underweighting the low field and by overweighting the high field Hall data. To overcome this issue we fitted the Hall coefficient which varies much less with magnetic field. A second problem is present in a simultaneous fitting process when one set of numbers is significantly larger than the other. In this case the latter set would have a marginal effect on the derived parameters. Therefore we introduced a normalization factor. A point in mid-field range was chosen for which the resistivity and Hall coefficient were calculated. The ratio between these figures forms a normalization factor by which the Hall data were multiplied, making these data comparable in magnitude to the resistivity data. Upon completion of the computation the data were renormalized.

Several aspects regarding the accuracy of the procedure were examined. The standard deviation of the parameters derived from the fitting process was found to be better than 0.5%. Second, the procedure was applied to different ranges of magnetic fields to determine the consistency of the results. While the scatter between derived parameters obtained for different ranges was less than 2% at intermediate temperatures (typically between 50 and 200 K), this scatter at higher temperatures may be over 10% in concentration and 5% in mobility. Caution must be taken when choosing the range of fit of the Hall data. Since we fit the Hall coefficient, which is derived from the measured transverse voltage by division with the magnetic field, small errors in the low field data may result in a substantial

TABLE I. Carrier concentrations and mobilities for three samples. Concentrations are in 10^{12} cm^{-2} and mobilities in cm^2/V s.

	300 K						4.2 K	
Sample	n_1	n_2	μ_1	μ_2	n_H	μ_H	n_H	n_{SdH}
Q12H	1.09	3.22	7570	1850	2.80	5080	1.11	0.96
Q12I	1.05	3.17	7710	1920	2.78	5150	1.16	1.01
Q11A	0.557	4.13	8080	1810	2.92	4060	0.624	0.48

deviation of the entire fit. Another source of inaccuracy may be due to the presence of a large transverse voltage at zero field. If the parallel concentration becomes much lower than the 2DEG concentration, the accuracy of the values derived for n_2 and μ_2 may be worse than 10%. This is frequently the case with better samples at the lowest temperatures (and not exposed to light). Under these conditions, $\mu_1 n_1 \gg \mu_2 n_2$, so that the conduction data are dom-

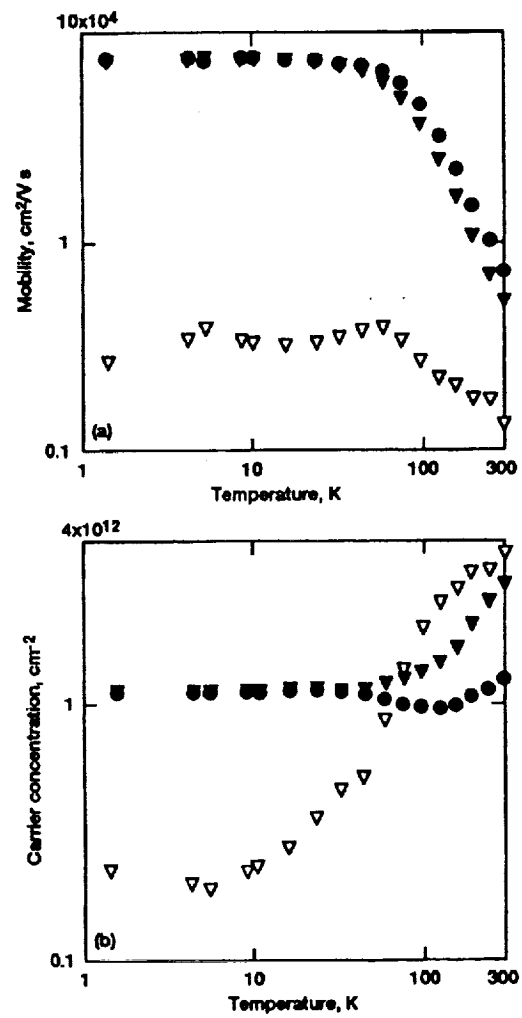

FIG. 2. Hall data and parameters derived from fitting procedure as function of temperature for sample Q12H: (a) carrier concentrations: n_1 (circles), n_2 (empty triangles), and n_H (full triangles); (b) mobilities: μ_1 (circles), μ_2 (empty triangles), and μ_H (full triangles).

inated entirely by the 2DEG carriers. The actual accuracy of the derived 2DEG concentration was evaluated by comparing it to the results obtained from the SdH and Hall experiments performed at liquid helium temperatures.

Table I summarizes the results of the analysis performed on three samples. The samples were MBE grown MOD structures consistent of AlGaAs barrier with 30% Al and a GaAs well. In samples Q12H and Q12I the barrier was delta-doped with Si at a concentration of 3.5×10^{12} cm^{-2}, while in sample Q11A the barrier was homogeneously doped at a concentration of 10^{18} cm^{-3}. Sample Q12I is identical to sample Q12H except that it was removed from the GaAs substrate by an epitaxial liftoff process.[4] The 2DEG concentrations are compared with the concentrations derived from the Shubnikov–de Haas (n_{SdH}) oscillations and the Hall data (n_H) taken at liquid helium temperatures. No second subband population was evident from the SdH data on either sample.

For all the samples examined at room temperature, the derived 2DEG concentration n_1 falls between the measured low-temperature SdH and Hall concentration. The difference between these and the room-temperature Hall concentration is very significant. Altogether the high-temperature Hall data are much closer to that of the parasitic parallel layer. It should be pointed out that this large parallel concentration n_2 is typical for these types of structures. The concentration n_2 drops drastically with temperature and reaches 2×10^{11} cm^{-2} below 50 K. The relatively larger error in room temperature n_1 for sample Q12H is due to a large zero field transverse voltage (0.1 mV with a current of 2 μA). At the lowest field this voltage is more than half of the recorded signal.

Figure 1 shows the experimental points and the results of the fitting process to the data measured at room temperature on sample Q12I. The fit of ρ_{xx} is excellent, while that of R_H exhibits some fluctuations at the lowermost magnetic fields, due to the division by B, as explained before. Even for these points, the error is below 2%.

As an extension of the method we used it to estimate the four parameters n_1, n_2, μ_1, and μ_2 as a function of temperature. Figure 2(a) shows the carrier concentrations and Fig. 2(b) the mobilities as function of temperature for sample Q12H. The low-temperature 2DEG parameters almost coincide with the Hall data because of the low parallel concentration in this temperature range. It is interesting to note that the mobility of the parallel layer μ_2 increases as n_2 decreases with descending temperatures. However, μ_2 remains fairly constant at lower temperatures as might be expected in degenerate semiconductors.

In conclusion we have shown that the simultaneous fit of the magnetic field dependent longitudinal and transverse resistivities can serve as a useful tool in characterization of quantum well structures both enabling room-temperature determination of 2DEG concentration and mobility as well as exploration of the effect of parallel conductance. This may be particularly helpful in better understanding of persistent photoconductivity in these structures.[5]

[1] P. P. Ruden, M. Shur, A. I. Akinwande, J. C. Nohava, D. E. Grider, and J. Baek, IEEE Trans. Electron. Devices ED-37, 2171 (1990).
[2] K. Ploog, M. Hauser, and A. Fischer, Appl. Phys. A 45, 233 (1988).
[3] M. J. Kane, N. Apsley, D. A. Anderson, L. L. Taylor, and T. Kerr, J. Phys. C 18, 5629 (1985).
[4] P. G. Young, R. A. Mena, S. A. Alterovitz, and E. D. Smith, IEEE Trans. Electron. Devices (in press).
[5] S. E. Schacham, R. A. Mena, E. J. Haugland, and S. A. Alterovitz, Mater. Res. Soc. Symp. Proc. 240, 517 (1992).

N94-20508

Spectroscopic ellipsometry studies of HF treated Si (100) surfaces

Huade Yao and John A. Woollam
University of Nebraska, Center for Microelectronic and Optical Materials Research, and Department of Electrical Engineering, Lincoln, Nebraska 68588-0511

Samuel A. Alterovitz
NASA Lewis Research Center, Cleveland, Ohio 44135

(Received 26 October 1992; accepted for publication 3 April 1993)

Both *ex situ* and *in situ* spectroscopic ellipsometry (SE) measurements have been employed to investigate the effects of HF cleaning on Si surfaces. The hydrogen-terminated (H-terminated) Si surface was modeled as an equivalent dielectric layer, and monitored in real time by SE measurements. The SE analyses indicate that after a 20-s 9:1 HF dip without rinse, the Si (100) surface was passivated by the hydrogen termination and remained chemically stable. Roughness of the HF-etched bare Si (100) surface was observed, in an ultrahigh vacuum (UHV) chamber, and analyzed by the *in situ* SE. Evidence for desorption of the H-terminated Si surface-layer, after being heated to ~550 °C in the UHV chamber, is presented and discussed. This is the first use of an *ex situ* and *in situ* real-time, nondestructive technique capable of showing state of passivation, the rate of reoxidation, and the surface roughness of the H-terminated Si surfaces.

In the fabrication of ultralarge-scale integrated circuits, preparation of native oxide free Si surfaces, the monitor and control of Si surface passivation and reoxidation are extremely important issues. Aqueous HF etching of Si surfaces removes the surface oxide and terminates the Si surface with atomic hydrogen.[1,2] The hydrogen termination retards the Si surface oxidation, and protects the surface from chemical attack.[3,4] Therefore, the HF cleaning of Si surfaces has received increasing attention. However, the properties of hydrogen-terminated (H-terminated) Si surfaces under various conditions, and the degree of surface passivation and reoxidation are still under investigation.[4–7] In this letter, we report results of *ex situ* and *in situ* spectroscopic ellipsometry (SE) studies of HF cleaned Si (100) surfaces.

SE is a surface-sensitive, nondestructive optical technique used to characterize surface overlayer thicknesses, multilayer structures, optical constants of bulk materials, and surface changes.[8,9] Ellipsometry determines the complex ratio of reflectance R_p to R_s, defined as

$$\rho = R_p/R_s = \tan(\psi)e^{i\Delta}, \tag{1}$$

where R_p and R_s are the reflection coefficient of light polarized parallel to (p) or perpendicular to (s) the plane of incidence, and the values of $\tan(\psi)$ and Δ are the amplitude and phase of the complex ratio.

The pseudodielectric function $\langle\epsilon\rangle$ can be obtained from the ellipsometrically measured values of ρ, assuming a two-phase model (ambient/substrate)[8] regardless of the possible presence of surface overlayers. For samples with surface overlayers or multilayer structures, SE data must be numerically fitted according to an assumed model (e.g., a three-phase model: ambient/surface overlayer/substrate). Assuming such a model, values of $\psi^c(h\nu_i,\Phi_j)$ and $\Delta^c(h\nu_i,\Phi_j)$, defined as in Eq. (1), are calculated. Here $h\nu$ is the photon energy and Φ is the external angle of incidence. A regression analysis is established to vary the model parameters (e.g., layers thicknesses) until the calculated and experimental values match as closely as possible. This process is done by minimizing the mean square error (MSE) function as described in Refs. 10 and 11. In our study, *ex situ* and *in situ* SE measurements were made using a Woollam Co. Variable Angle Spectroscopic Ellipsometer (VASE™), which was equipped with a beam-chopped, rotating analyzer to increase the stray light rejection and signal to noise ratio.

Si (100) surfaces covered with native oxide from a virgin p-type wafer of 14–22 Ω cm resistivity were employed to study the effects of HF treatments on Si. A piece from the wafer was dipped in 9:1 (volume ratio of deionized water to 49% HF) HF solution for approximately 20 s with no rinse. SE measurements were made in air, at a 75° angle of incidence, before and after the HF dip. During the measurement, the automated polarizer azimuth angle P was set to vary with changes of the measured $\psi(h\nu_i,\Phi_j)$ to minimize experimental errors in the ellip-

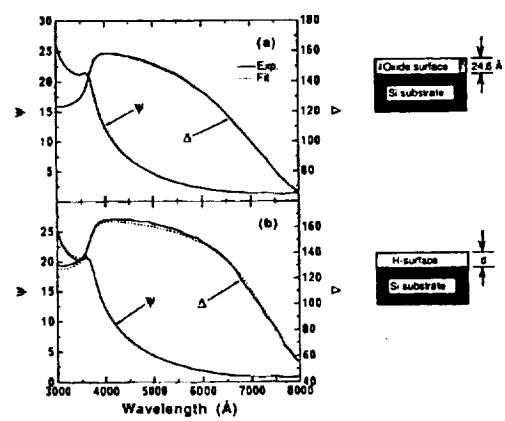

FIG. 1. Ψ and Δ values of *ex situ* SE measurements on a Si (100) surface: (a) before and (b) after the HF treatment. The solid line represents the experimental data, and the dashed line is the best fit of the SE analysis. Assumed models for the SE analysis, in each case, are sketched with the plots.

© Appl. Phys. Lett. 62 (25), 21 June 1993. Reprinted, with permission, from American Institute of Physics.

PRECEDING PAGE BLANK NOT FILMED

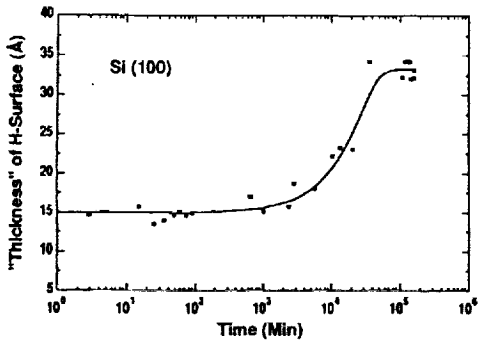

FIG. 2. Changes in effective thickness of the H-terminated Si surface (H surface) as a function of time, after the 20-s 9:1 HF dip, monitored by the *ex situ* SE measurements.

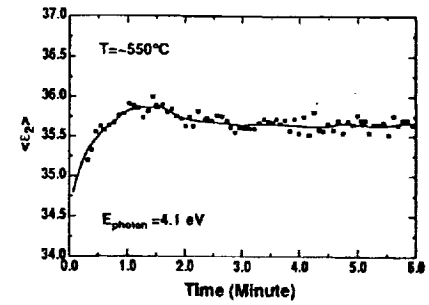

FIG. 3. Real time $\langle\epsilon_2\rangle$ data from the HF-treated Si (100) surface, inside the UHV chamber, at ~550 °C, near the E_2 critical-point energy.

someter system.[12] It was set such that $P=\psi$ with $P_{min}=10°$. The spectral scan, ranging from 3000 to 8000 Å, with an increment of 100 Å, was completed within 2–3 min. The SE analysis indicated that an approximately 25 Å thick native oxide covered the virgin Si surface as shown in Fig. 1(a). After the HF cleaning, the Si native oxides were removed and the Si surface was terminated with H-silicon bonds.[1,2] This H-terminated Si surface was modeled as an equivalent dielectric layer described by the optical constants of SiO_2[13] [for the SE analysis shown in Fig. 1(b)]. The optical constants of Si used for the calculations in the SE regression analysis are from Ref. 14. A typical "thickness" of the H-terminated Si surface (H surface) immediately after the HF cleaning, as indicated by the SE regression analysis, was in the range 14–17 Å. Notice that the thickness referred to here as an H surface was not the actual thickness of the H-surface layer, but the effective thickness of the modeled equivalent dielectric layer of SiO_2, which includes possible Si surface microroughness after HF etching (as discussed below). The value of this thickness as measured by SE was used to monitor the changes in the H surface.

SE measurements were made on this H surface in air at room temperature (RT) over a period of several months after the HF cleaning. Changes in thickness of the H surface were monitored as a function of time as shown in Fig. 2. The figure shows that the H-terminated Si surface remained unchanged for over 2 h, and very little reoxidation took place within 3–4 days. After two months the reoxidized Si surface layer saturates at a thickness of ~33 Å, which is thicker than the native oxide before the HF etching. The SE study indicates that remarkable surface passivation has been achieved by the hydrogen termination of Si surface dangling bonds, which contributes to the retardation of the Si surface oxidation during air exposure. The apparent larger thickness of the reoxidized layer provides a clue to the Si surface roughness after the HF etching.

In situ SE was employed to study changes of the H-terminated Si surface at elevated temperatures and the bare Si surface conditions after HF etching. During the *in situ* measurements, the ellipsometer was attached to an UHV chamber, fitted with a pair of low-strain fused-quartz windows.[11,15] A Si (100) sample was introduced into the UHV chamber, immediately after a 20-s 9:1 HF dip, and clamped on a resistor-heater plate that could be rotated and tilted by a rotary drive, inside the chamber. Temperatures were measured and controlled by two *K*-type thermocouples, which were calibrated by an infrared (IR) optical pyrometer. The typical base pressure of the UHV was $\sim 1\times 10^{-9}$ Torr.

The HF-cleaned Si (100) surface was heated to ~550 °C inside the UHV chamber, and real time ellipsometric measurements of one set of Ψ and Δ data were made periodically in time (about once every 5 s) at a photon energy of ~4.1 eV, corresponding to the critical point energy E_2 (i.e., ~4.1 eV for Si at ~550 °C),[16] while maintaining the sample at ~550 °C. These data were converted simultaneously to a pseudodielectric function $\langle\epsilon\rangle=\langle\epsilon_1\rangle+i\langle\epsilon_2\rangle$. In general, it has been established[9,11,15] that the peak value of the imaginary part $\langle\epsilon_2\rangle$ in semiconductors is very sensitive to the presence of surface overlayers (e.g., H surface) and any possible surface defects such as surface microscopic roughness. A reduction of the thickness of surface overlayer or surface roughness leads to increasing values of $\langle\epsilon_2\rangle$. The highest value $\langle\epsilon_2\rangle$ corresponds to the cleanest and smoothest bulk surface condition. Therefore, changes in the H surface induced at elevated temperatures can be monitored in real time by measuring the changes of $\langle\epsilon_2\rangle$.

Figure 3 shows changes in $\langle\epsilon_2\rangle$ in real time at

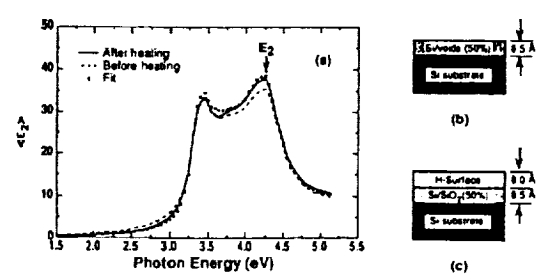

FIG. 4. (a) $\langle\epsilon_2\rangle$ spectrum of HF-treated Si at RT, measured by *in situ* SE, before (dashed line) and after (solid line) being heated to ~550 °C in the UHV chamber. The dotted line is the fit for the rough Si surface model, sketched in (b). (c) A sketch of the H-surface structure, containing the surface roughness formed by HF etching.

~550 °C. An obvious increase of $\langle\epsilon_2\rangle$ within the first minute at ~550 °C indicates the desorption of H-terminated Si surface at ~550 °C. A flat plateau followed the desorption of the H surface indicates a stabilized Si surface. The plateau remained unchanged during further extended heating. This also suggests that there is no evidence of the surface quality deterioration (e.g., increasing surface roughness induced by heating) at this elevated temperature.[15]

SE data for the H-terminated Si surfaces were taken at RT before and after the heating, as shown in Fig. 4(a). A comparison of the two $\langle\epsilon_2\rangle$ spectra at RT, shows a ~7% higher $\langle\epsilon_2\rangle$ peak value at the E_2 critical point energy (~4.3 eV at RT) after the heating. This further confirms the desorption of the H surface after heating to ~550 °C. The evidence for desorption observed in this experiment is consistent with results obtained by thermally stimulated desorption measurements as described in Ref. 5.

The RT $\langle\epsilon_2\rangle$ peak value at the E_2 energy after the desorption of the H surface, as shown in Fig. 4(a) (solid line), is considerably lower than the known value (~46) of Si from literature.[14] This indicates a roughened Si surface induced by the HF etching. The surface roughness was modeled as a top Si layer containing 50% voids, as shown in Fig. 4(b). The thickness of this rough Si layer was calculated by the regression analysis, under the assumption of the Bruggeman effective-medium approximation (EMA).[17] Good fit was obtained with a thickness of 8.5 Å, as shown in Fig. 4(a) (dotted line). It indicates an approximate 1–2 monolayer surface microroughness formed from the HF etching.

This model of rough Si surface was applied to characterize the H surface measured at RT in vacuum, before the heating, as shown in Fig. 4(c). In this case, the voids were replaced by SiO_2 to model the H termination of the rough Si layer, while the thickness of this rough layer was kept the same as in Fig. 4(b). On top of the rough Si surface, a pure H-surface layer was modeled and described by the optical constants of SiO_2, as we have discussed previously. The thickness of ~8 Å of this pure H-surface layer was calculated through the regression analysis. Notice that by modeling a rough interface between the top H surface and Si substrate, the top pure H surface has an effective thickness of ~8 Å, which is consistent with an expected monolayer H termination of Si surface.

Same surface-roughness model [as in Fig. 4(c)] was used to reanalyze the *ex situ* RT SE measurements shown in Fig. 1. The results show a reduced effective thickness of the initial top H surface, after the HF dip, of ~5.4 Å, and a saturated reoxide layer is ~21.7 Å. This value is quite consistent with the thickness of a fresh native oxide surface layer. The small difference between the two initial thicknesses of H surface (i.e., 8.0 and 5.4 Å) are likely due to different degrees of surface roughness of the two individual HF treated Si samples.

In summary, HF treated Si (100) surfaces were investigated by *ex situ* and *in situ* SE measurements. The SE analysis indicated that the Si (100) surface was well passivated via a ~20-s 9:1 HF dip with no rinse. Real-time SE data showed evidence for desorption of the H-terminated Si surfaces at ~550 °C in the UHV chamber. Si (100) surface roughness induced by HF etching was observed in a UHV chamber, and analyzed by the *in situ* SE. It was shown that a ~1–2 monolayer surface roughness was formed after our HF etching. This unique surface characterization, by *in situ* SE, provides a useful means of studying and monitoring various Si surface conditions after HF cleaning.

The authors wish to thank Dr. Y. J. Chabal and AT&T Bell Laboratories for his helpful discussions. This work was partially supported by NASA-Lewis Grant NAG3-154.

[1] E. Yablanovitch, D. L. Allara, C. C. Chang, T. Gmitter, and T. B. Bright, Phys. Rev. Lett. 57, 249 (1986).
[2] M. Grundner and H. Jacob, Appl. Phys. A 39, 73 (1986).
[3] G. S. Higashi, Y. J. Chabal, G. W. Trucks, and K. Raghavachari, Appl. Phys. Lett. 56, 656 (1990).
[4] P. Jakob, P. Dumas, and Y. J. Chabal, Appl. Phys. Lett. 59, 2968 (1991).
[5] N. Hirashita, M. Kinoshita, I. Aikawa, and T. Ajioka, Appl. Phys. Lett. 56, 451 (1990).
[6] M. Morita, T. Ohmi, E. Hasegawa, M. Kawakami, and M. Ohwada, J. Appl. Phys. 68, 1272 (1990).
[7] P. Jakob and Y. J. Chabal, J. Chem. Phys. 95, 2897 (1991).
[8] R. M. A. Azzam and N. M. Bashara, *Ellipsometry and Polarized Light* (North-Holland, Amsterdam, 1977).
[9] D. E. Aspnes, in *Handbook of Optical Constants of Solids*, edited by E. D. Palik (Academic, New York, 1985), p. 89.
[10] G. H. Bu-Abbud, N. M. Bashara, and J. A. Woollam, Thin Solid Films 138, 27 (1986).
[11] H. Yao, P. G. Snyder, and J. A. Woollam, J. Appl. Phys. 70, 3261 (1991).
[12] D. E. Aspnes, J. Opt. Soc. Am. 64, 639 (1974).
[13] H. R. Philipp, Ref. 9, p. 759.
[14] G. E. Jellison, Jr., Opt. Mater. 1, 41 (1992).
[15] H. Yao and P. G. Snyder, Thin Solid Films 206, 283 (1991).
[16] H. Yao (unpublished data).
[17] D. E. Aspnes and J. B. Theeten, Phys. Rev. B 20, 3292 (1979).

HIGH FREQUENCY PERFORMANCE OF $Si_{1-x}Ge_x/Si_{1-y}Ge_y/Si_{1-x}Ge_x$ HBTs

D. Rosenfeld and S. A. Alterovitz

Indexing terms: Bipolar devices, Transistors, Semiconductor devices and materials

The results of a theoretical study of the performance of high speed SiGe HBTs is presented. The study includes a group of SiGe HBTs in which the Ge concentration in the base is 20% higher than that in the emitter and collector (i.e. $y = x + 0{\cdot}2$). It is shown that the composition dependences of f_T and the f_{max} are non-monotonic. As the Ge composition in the emitter and collector layers is increased, f_T and f_{max} first decrease, then remain constant and finally increase to attain their highest values.

Introduction: The main interest in SiGe alloys stems from their potential use in high speed heterostructure transistors for microwave and digital switching applications. In the last two decades a large number of HBTs based on III-V materials have been fabricated and characterised. However, it is only during the last few years that material growth and processing techniques compatible with silicon technology have been developed. The new SiGe growth technologies, as well as the recently published promising results of $Si/Si_{1-x}Ge_x/Si$ HBTs, have generated considerable need among material growers and device engineers for theoretical estimation of the potential performance of these SiGe devices. The composition dependence of the SiGe HBT figures of merit, such as the current gain, the cutoff frequency (f_T) and the maximum frequency of oscillation (f_{max}), has not been experimentally or theoretically estimated.

In this Letter, the results of a theoretical study of the composition dependence of f_T and f_{max} are presented. In the study, the high frequency characteristics of a series of *npn* SiGe HBTs with different emitter and collector compositions were calculated. To maintain the advantages of an HBT, the Ge concentration of the base in each of the HBTs was set to be 20% higher than that of the collector and emitter composition (i.e. $y = x + 0{\cdot}2$). The composition dependences of the emitter-to-collector transit time (τ_{ec}) and the base-resistance collector-capacitance product ($R_b C_c$) were computed and consequently, the dependences of f_T and f_{max} on the emitter and base compositions were derived.

Geometry and structure: We followed the design rules presented in Reference 1, and obtained device dimensions and dopant concentrations similar to those obtained in Reference 2. The chosen parameters were not meant to project the ultimate performance potential of SiGe HBTs and, therefore, the high frequency figures of merit are somewhat inferior to those recently published [3]. Because the study was comparative in nature all devices examined had the same areas (emitter and base $2 \times 8\,\mu m^2$, collector $10 \times 8\,\mu m^2$), same layer thicknesses (300, 500, 5000, 5000 Å in the emitter, base, collector and subcollector, respectively), same dopant profiles (10^{19}, 5×10^{18}, 10^{17} and $10^{20}\,cm^{-3}$) and same operating conditions (1 V base–collector bias). The HBTs differ in the emitter and collector Ge concentrations and in the base concentration, which was always set to be 20% higher than the former.

Device model and material properties: f_T and f_{max} were analysed using widely used formulas:

$$f_T = (2\pi \cdot \tau_{ec})^{-1} \quad (1)$$

$$f_{max} = (4\pi)^{-1} \cdot (\tau_{ec} \cdot R_b C_c)^{-1/2} \quad (2)$$

where τ_{ec} is given by

$$\tau_{ec} = \tau_e + \tau_b + \tau_{cib} + \tau_{sl} + \tau_c \quad (3)$$

In eqn. 3 τ_e and τ_c are the emitter and collector charging times, τ_b is the base transit time, τ_{cib} is the transit time associated with the current induced base at high current levels and τ_{sl} is the transit time through the base–collector depletion region (or collector–subcollector depletion region at high currents).

The above transit times depend strongly on the basic properties of the materials such as dielectric constants, mobilities, saturation velocities, bandgaps and dopant concentrations. The material properties, in turn, depend on the Ge concentration and hence it is expected that f_T and f_{max} will show a dependence on composition.

The SiGe material properties and their composition dependences were adopted from the literature. The resistances, the junction capacitances, and the built-in voltages were calculated using the expressions given in Reference 4. For the composition dependence of the bandgaps, the intrinsic carrier concentrations and the dielectric functions, we use the formulas published in References 5–7, respectively. The bandgap discontinuities and their composition dependences were taken from Reference 8. The expressions for the carrier mobilities in SiGe are based on the theoretical calculation presented in Reference 9. For the saturation velocity of electrons in SiGe alloys we employed a linear fit between the saturation velocities of electrons in Si and Ge. The influence of the high current on the width and location of the base–collector depletion region was calculated according to Reference 10.

Results and discussion: The calculated f_T and f_{max}, plotted against the collector current density J_c for several SiGe HBTs, are shown in Figs. 1 and 2. All transistors were identical in

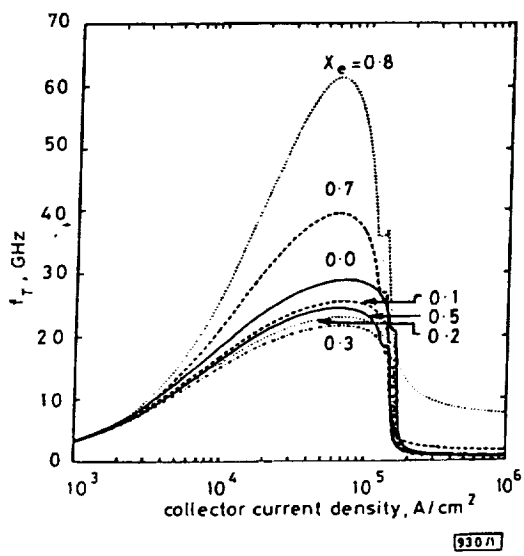

Fig. 1 *Cutoff frequency f_T of $Si_{1-x}Ge_x/Si_{1-y}Ge_y/Si_{1-x}Ge_x$ HBTs against collector current density, plotted for several values of emitter composition*

$X_c = X_e$ and $X_b = X_e + 0{\cdot}2$

© Reprinted, with permission, from Electronics Letters, vol. 29, no. 3, 4th February 1993, pp. 260-261.

PRECEDING PAGE BLANK NOT FILMED

geometry and dopant profile. However, they differed in the compositions of the layers. The emitter and collector compositions were varied from $X_e = X_c = 0$ to $X_e = X_c = 0{\cdot}8$ and the base composition varied from 0·2 to 1.

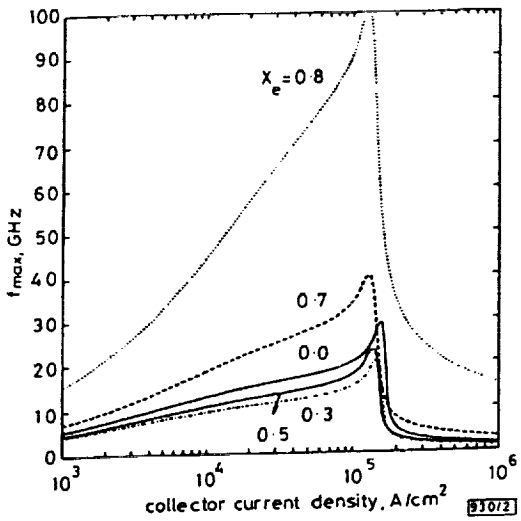

Fig. 2 *Maximum oscillation frequency f_{max} of $Si_{1-x}Ge_x/Si_{1-y}Ge_y/Si_{1-x}Ge_x$ HBTs against collector current density, plotted for values of emitter composition*

$X_c = X_e$ and $X_b = X_e + 0{\cdot}2$

Figs. 1 and 2 demonstrate the non-monotonic behaviour of both f_T and f_{max}. For $X_e = 0$ (pure silicon in the emitter and collector), the highest f_T and f_{max} (29 GHz) are obtained at collector currents of 72 kA cm^{-2} and 162 kA cm^{-2}, respectively. Increasing the emitter and collector compositions to 0·4 (and the base composition to 0·6), the highest f_T and f_{max} *decrease* to 23 GHz, and are obtained for collector currents of 68 kA cm^{-2} and 150 kA cm^{-2}. Further increasing the emitter composition to 0·8 (and pure Ge in the base), the peak values

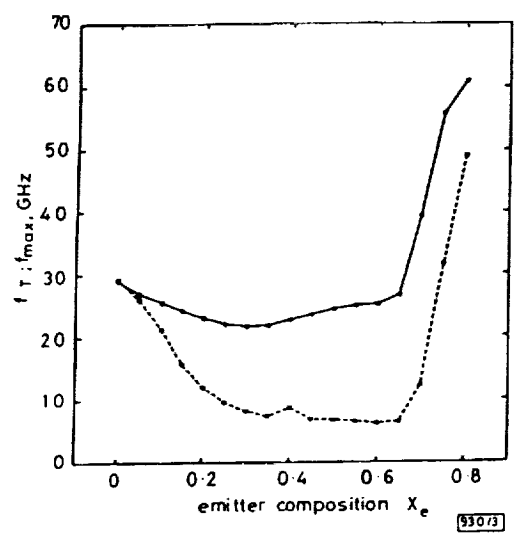

Fig. 3 *f_T at $J_c = 72$ A cm^{-2} and f_{max} at $J_c = 162$ A cm^{-2} against emitter composition*

At these current densities f_T and f_{max} attain their highest values for $X_e = 0{\cdot}2$

——— f_T at 72 kA/cm^2

- - - - f_{max} at 162 kA/cm^2

of f_T and f_{max} *increase* to 62 and 100 GHz, obtained for $J_c = 72$ kA cm^{-2} and 162 kA cm^{-2}. Fig. 3 emphasises the non-monotonic behaviour of f_T and f_{max}, by showing the f_T and f_{max} values (calculated for $J_c = 72$ kA cm^{-2} and $J_c = 172$ kA cm^{-2}, respectively), plotted against the emitter composition.

Conclusion: We have demonstrated the non-monotonic behaviour of f_T and f_{max}. As the Ge composition in the emitter and collector layers (as well as the base) is increased, f_T and f_{max} first decrease, then remain almost constant and finally increase to attain their highest values.

6th November 1992

D. Rosenfeld* and S. A. Alterovitz (*NASA—Lewis Research Center, Mail Stop 54-5, 21000 Brookpark Rd., Cleveland, OH 44135, USA*)

* National Research Council Resident at NASA—Lewis Research Center, USA. Permanent address: Faculty of EE, Technion IIT, Haifa 32000, Israel

References

1 PATTON, G. L., COMFORT, J. H., STORK, B. S., MEYERSON, B. S., CRABBE, E. F., SCILLA, G. J., DEFRESART, E., STORK, J. M. C., SUN, J. Y. C., HARMAN, D. L., and BURGHARTZ, J. N.: '75 GHz f_t SiGe-base heterojunction bipolar transistors', *IEEE Electron Device Lett.*, 1990, **EDL-11**, pp. 171–173

2 CHEN, J., GAO, G. B., and MORKOC, H.: 'Comparative analysis of the high frequency performance of $Si/Si_{1-x}Ge_x$ heterojunction and Si bipolar transistors', *Solid-State Electron.*, 1992, **35**, pp. 1037–1044

3 CRABBE, E. F., COMFORT, J. H., LEE, W., CRESSLER, D., MEYERSON, B. S., MEGDANIS, A. C., SUN, J. Y. C., and STORK, M. C.: '73 GHz self aligned SiGe base bipolar transistors with phosphorus doped polysilicon emitters', *IEEE Electron Device Lett.*, 1992, **13**, pp. 259–261

4 MILNES, A. G., and FEUCHT, D. L.: 'Heterojunctions and metal–semiconductors junctions' (Academic Press, New York, 1972), pp. 34–94

5 KARLSTEEN, M., and WILLANDER, M.: 'Optimized frequency charcterisetics of Si/SiGe heterojunction and conventional bipolar transistors', *Solid-State Electron.*, 1990, **33**, pp. 199–204

6 KLAUSMEIER-BROWN, M. E., LUNDSTROM, M. N., and MELLOCH, M. R.: 'The effects of heavy impurity doping on AlGaAs/GaAs bipolar transistors', *IEEE Trans.*, 1989, **ED-36**, pp. 2146–2155

7 SUTHERLAND, J. E., and HAUSER, J. R.: 'A computer analysis of heterojunction and graded composition solar cells', *IEEE Trans.*, 1977, **ED-24**, pp. 363–372

8 PEOPLE, R., and BEAN, J. C.: 'Band alignment of coherently strained Ge_xSi_{1-x}/Si heterostructures on ⟨001⟩ Ge_ySi_{1-y}', *Appl. Phys. Lett.*, 1986, **48**, pp. 538–540

9 KRISHMANURTHY, S., CHER, A., and CHEN, A.: 'Generalized Brooks' formula and the electron mobility in Ge_xSi_{1-x} alloys', *Appl. Phys. Lett.*, 1985, **47**, pp. 160–162

10 ROULSTON, D. J.: 'Bipolar semiconductor devices' (McGraw-Hill Publishing Company, NY, NY, 1990), pp. 254–258

N94-20509

Ellipsometric study of $Si_{0.5}Ge_{0.5}$/Si strained-layer superlattices

R. M. Sieg[a)]
Cleveland State University, Cleveland, Ohio 44115

S. A. Alterovitz
NASA Lewis Research Center, Cleveland, Ohio 44135

E. T. Croke and M. J. Harrell
Hughes Research Laboratories, Malibu, California 90265

(Received 2 September 1992; accepted for publication 7 January 1993)

We present an ellipsometric study of two $Si_{0.5}Ge_{0.5}$/Si strained-layer superlattices grown by MBE at low temperature (500 °C), and compare our results with x-ray diffraction (XRD) estimates. Excellent agreement is obtained between target values, XRD, and ellipsometry when one of two available Si_xGe_{1-x} databases is used. We show that ellipsometry can be used to nondestructively determine the number of superlattice periods, layer thicknesses, Si_xGe_{1-x} composition, and oxide thickness without resorting to additional sources of information. We also note that we do not observe any strain effect on the E_1 critical point.

Semiconductor superlattices (SL) and strained-layer superlattices (SLS) are most commonly characterized by x-ray diffraction (XRD) and transmission electron microscopy (TEM). Neither of these methods are ideal. The first technique is very accurate, but only directly gives the SL period and an average value of composition,[1,2] while the second technique requires very tedious sample preparation and is destructive. In this letter, we will show that variable angle-of-incidence spectroscopic ellipsometry (VASE) as applied to $Si_{0.5}Ge_{0.5}$/Si SLS yields simultaneously the SL period, the layer thicknesses, the Si_xGe_{1-x} layer composition, the number of periods, and the overlayer oxide thickness. In addition, strain effects on the dielectric function of the Si_xGe_{1-x} layer will be estimated by VASE. The effect of strain on the dielectric function of Si_xGe_{1-x} grown on silicon is presently an area of active research. Both single wavelength[3,4] and spectroscopic[5–7] ellipsometry, as well as photoreflectance[8] have been used on high Si concentration ($x>0.75$) Si_xGe_{1-x} thin films, showing conflicting results. Most spectroscopic measurements,[6–8] which give an overall picture of the strain on the dielectric function, have estimated the effect of strain on the critical points, particularly E_1 and E_0'. The E_1 critical point is a crucial parameter in the energy shift algorithm[9] and a change in its position will be reflected in a change of the estimated value of x.[10] Published results claim either no change in E_1,[6,8] decrease in E_1 with increasing strain,[7] or an effective increase.[5] In this work, the low Si content ($x\approx0.5$) and small Si_xGe_{1-x} layer thickness (~5 nm) of our SLS should make any lattice mismatch effect on E_1 readily detectable.

Two nominally identical 15 period $Si_{0.5}Ge_{0.5}$/Si SLS samples, identified here as samples A and B, were grown by molecular beam epitaxy[2] (MBE) using a Perkin–Elmer (model 430S) Si MBE system. The growth temperature was 500 °C. The upper layer of each SLS was silicon. Target parameter values are given in Table I. Both samples were measured by XRD which, together with the knowledge of the shutter opening times, gives the SLS period, the average Si concentration throughout the SLS, and the Si_xGe_{1-x} layer thickness. The XRD pattern for sample B was of excellent quality, while that of sample A was somewhat degraded. However, an accurate estimate of the SLS period and average Si concentration in the SLS was obtained for both samples. All results are included in Table I. The average Si concentration is given as x(avg); values determined using shutter timing information are labelled with asterisks. The XRD results show excellent agreement with the target values for both samples.

The VASE measurements were taken with a rotating analyzer ellipsometer described elsewhere.[11] This instrument measures the complex reflection ratio $\rho=\tan(\Psi)e^{j\Delta}$ where Ψ and Δ are the conventional ellipsometric parameters used to represent the amplitude and phase of ρ. Measurements of the SLS samples were taken over the spectral range 300–760 nm for sample A and 300–780 nm for sample B, both in 5 nm increments. Each sample was measured at three angles-of-incidence: 75°, 76°, and 77°. These incident angles were selected to be near to the principal angle for most of the spectral range, providing maximum sensitivity.[12] Experimental results of $\tan(\Psi)$ and $\cos(\Delta)$ for sample A are shown in Fig. 1; the results for sample B are very similar.

Analysis of VASE data involves a least squares fit of the data to an appropriate model, with the quality of the fit defined by a mean-square-error σ.[10] A four parameter model was used to fit the SLS samples. The parameters were: Si and Si_xGe_{1-x} layer thicknesses, silicon concentration x in the Si_xGe_{1-x} layer, and the native oxide thickness. All periods of the superlattice were assumed to be exactly identical in terms of thicknesses and optical properties. The optical constants of silicon were taken from Ref. 13. There are currently two available databases for Si_xGe_{1-x} in the literature.[14,15] J. Humliček *et al.*[14] have published the results of measurements of bulk Si_xGe_{1-x} grown by the Czochralski method and also of thick films grown by liquid-phase epitaxy. These measurements cover the entire compositional range. Optical measurements were taken[14]

[a)]Undergraduate student intern at NASA Lewis Research Center, Cleveland, OH 44135.

© Appl. Phys. Lett. 62 (14), 5 April 1993. Reprinted, with permission, from American Institute of Physics.

TABLE I. VASE and XRD analyses of the SLS samples. The ellipsometric fitted parameters are the oxide, Si and SiGe layer thicknesses (d), and the silicon concentration x of the SiGe layer. The period is the sum of the Si and the SiGe layer thicknesses. x(avg) is the average silicon concentration in one period.

Sample	Source	$d(SiO_2)$ (nm)	Period (nm)	d(Si) (nm)	d(SiGe) (nm)	x(avg)	x	σ
···	target	···	35.0	30.0	5.0	0.929	0.5	···
A	XRD	···	35.3	30.0[a]	5.3[a]	0.922	0.47[a]	···
A	VASE	1.89	34.8	30.11	4.67	0.942	0.5690	0.0021
	Ref. 14[b]	±0.08		±0.08	±0.05		±0.0035	
A	VASE	1.83	34.8	29.88	4.96	0.926	0.4709	0.0013
	Ref. 15[c]	±0.04		±0.06	±0.04		±0.0037	
B	XRD	···	38.3	32.8[a]	5.5[a]	0.931	0.50[a]	···
B	VASE	3.08	37.6	32.42	5.19	0.945	0.6031	0.0025
	Ref. 14[b]	±0.08		±1.00	±0.06		±0.0022	
B	VASE	2.96	37.7	32.36	5.33	0.931	0.5145	0.0016
	Ref. 15[c]	±0.06		±0.07	±0.05		±0.0031	

[a]Estimated from growth times.
[b]Fitted $\lambda < 650$ nm.
[c]All data fitted.

using a rotating analyzer ellipsometer (RAE). There are several difficulties with this database: first, because RAE does not measure low absorption substrates accurately, data at high wavelengths are unreliable.[14,15] Probably for this reason, data are available in the infrared only down to 1.7 eV (729 nm). This is a problem for our analyses, as the silicon layer of the first period is only penetrated for $\lambda > 370$ nm, so that the information on the superlattice is contained mostly in the high wavelength measurements. Second, the compositions were determined only by ellipsometry,[14] using the measurement at the He-Ne line (632.8 nm), where the RAE is inaccurate. Recently, Jellison, Haynes, and Burke[15] have published an independent database using the results of measurements of thick (7–8 μm on Si) relaxed Si_xGe_{1-x} films grown by conventional high-temperature chemical vapor deposition. Optical measurements were taken using a two-channel spectroscopic polarization modulation ellipsometer (2-C SPME) which measures low absorption substrates accurately;[15] data are available to 840 nm. Compositions were determined by electron microprobe and Rutherford backscattering measurements. This database also covers the entire compositional range. However, there is a variation between a sample grown on a silicon substrate and another sample of similar composition grown on a germanium substrate. Therefore, in our analyses, only Ref. 15 spectra taken from samples grown on silicon will be used. Because the databases of Refs. 14 and 15 show significant differences, each SLS was analyzed using each database and the results will be compared. In order to use the databases, an algorithm for interpolating between the compositions is needed. The energy shift algorithm[9] which has been applied previously to Si_xGe_{1-x} using the Ref. 14 database[5,6] was used. This algorithm requires the location of the main critical points to be expressed as a function of alloy composition. Because of the significant differences between the databases of Refs. 14 and 15, different critical point functions must be used. For both databases, the indirect band gap function $E_0(x) = 0.68 + 0.44x$ was used.[16] This function, which is a simple linear interpolation between the fundamental indirect band gaps of silicon and germanium, was found to give identical results in our analyses, as compared with more complex $E_0(x)$ functions, because the range of measurement is far away from $E_0(x)$. $E_1(x)$ for the database of Ref. 14 was

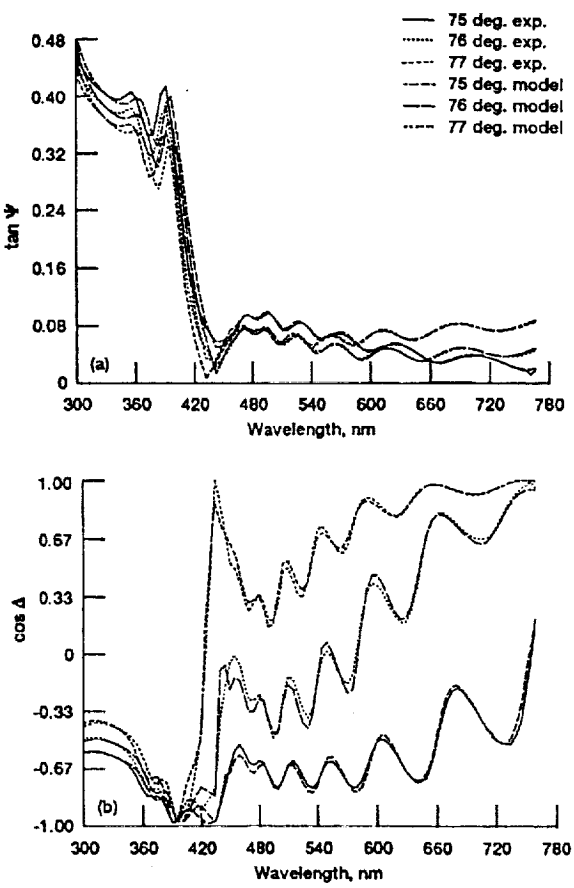

FIG. 1. Sample A experimental data vs model for the four parameter fit (using Ref. 15 database). Graphs show (a) tan(Ψ) and (b) cos(Δ).

given in that reference, while $E_2(x)=4.39+0.03x$ was taken from Ref. 6. For the database of Ref. 15, critical points $E_1(x)$ and $E_2(x)$ were obtained by fitting the spectra to critical point line shapes.[17] $E_2(x)$ was found to be approximately constant at 4.30 eV, while the linear fit $E_1(x)=2.357+0.9393x$ was found to describe $E_1(x)$ well, especially in the range $0.47<x<0.85$.

Comparison of experimental VASE and best fit model results using the Ref. 15 database for sample A are shown in Fig. 1. Full numerical VASE results for both samples are given in Table I along with the associated 90% confidence limits. Note that analyses using Ref. 14 are limited to $\lambda<650$ nm, due to the range of reference data and the nature of the energy shift algorithm. Analyses using Ref. 15 include all measured data. In all cases, the values determined by XRD were used as initial conditions. Statistical analyses of the fits indicated no significant parameter correlations. The results using both Si_xGe_{1-x} databases are very similar, except for the x value of the Si_xGe_{1-x} layers. The composition obtained using Ref. 15 data agrees very well with the XRD results, while the x value obtained using Ref. 14 is about 0.1 higher for both superlattices. This, along with the higher σ values obtained using the Ref. 14 database, supports our belief in the greater accuracy of the Ref. 15 database. The XRD data and the VASE results all show a 0.03 difference in the x values between the two samples, strongly indicating this difference is real. This indicates that the precision of both the XRD and VASE techniques for determining the value of Si_xGe_{1-x} composition x is better than 0.03.

XRD can verify the number of periods provided the sample is of extremely good quality. To examine the ability of VASE to verify this parameter, we refitted sample B using the Ref. 15 database assuming 14, 16, and 17 periods. For the 14 period model, σ is a factor of 3 higher than the 15 period model and x increases to 0.607. For 16 periods and 17 periods, the x value decreased below 0.47 (the lowest available reference spectrum) and had to be held constant there: the resultant σ were 1.2 and 4.2 times higher, respectively. Adding or subtracting a period clearly degrades the fit, either by increasing σ or by unreasonably decreasing the composition; we thus conclude VASE can be used to verify the number of periods.

To examine potential parameter correlations, the measurement of sample B was refitted using an initial Si_xGe_{1-x} layer thickness of 6.6 nm and concentration $x=0.60$, maintaining the XRD value $x(\text{avg})=0.93$. The fit converged to the same values as given in Table I to four significant digits. This means VASE can separate the Si_xGe_{1-x} layer composition and thickness, i.e., they are not significantly correlated. VASE thus provides an independent verification of shutter opening times, which are used in the XRD analysis.

The strain effect, if any, on the dielectric function will be observed as a shift in the x value. As seen from Table I, using the Ref. 15 database which is deemed more reliable in our wavelength range, we do not observe any strain effect. The good agreement between XRD and the fit using Ref. 15 indicates that the E_1 critical point is not strongly affected by the strain, since the energy shift algorithm used was based upon this critical point.[9] The $E_1+\Delta_1$ and E_0' critical points are not checked with this method, as they are weaker and influence the spectrum only above the E_1 energy region, where the top period silicon layer largely shields the superlattice.

In conclusion, we have obtained excellent agreement between XRD and VASE results for two $Si_{0.50}Ge_{0.50}$/Si SLS samples using Ref. 15 data for unstrained Si_xGe_{1-x}. We have shown that VASE can be used to determine the number of periods, layer thicknesses, Si_xGe_{1-x} layer composition, and native oxide.

The authors would like to thank G. E. Jellison for providing a diskette of his Si_xGe_{1-x} database and L. D. Warren for assisting with the XRD measurements.

[1] V. S. Speriosu and T. Vreeland, Jr., J. Appl. Phys. 56, 1591 (1984).
[2] R. J. Hauenstein, B. M. Clemens, R. H. Miles, O. J. Marsh, E. T. Croke, and T. C. McGill, J. Vac. Sci. Technbl. B 7, 767 (1989).
[3] G. M. W. Kroesen, G. S. Oehrlein, E. de Frésart, and G. J. Scilla, Appl. Phys. Lett. 60, 1351 (1992).
[4] M. Racanelli, C. I. Drowley, N. D. Theodore, R. B. Gregory, H. G. Tompkins, and D. J. Meyer, Appl. Phys. Lett. 60, 2225 (1992).
[5] H. D. Yao, J. A. Woollam, P. J. Wang, M. J. Tejwani, and S. A. Alterovitz, Appl. Surf. Sci. 63, 52 (1993).
[6] C. Pickering, R. T. Carline, D. J. Robbins, W. Y. Leong, S. J. Barnett, A. D. Pitt, and A. G. Cullis, J. Appl. Phys. 73, 239 (1993).
[7] F. Ferrieu, F. Beck, and D. Dutartre, Solid State Commun. 82, 427 (1992).
[8] Y. Yin, F. H. Pollak, P. Auvray, D. Dutartre, R. Pantel, and J. A. Chroboczek, Thin Solid Films 222, 85 (1992).
[9] P. G. Snyder, J. A. Woollam, S. A. Alterovitz, and B. Johs, J. Appl. Phys. 68, 5925 (1990).
[10] S. A. Alterovitz, P. A. Sekula-Moise, R. M. Sieg, M. N. Drotos, and N. A. Bogner, Thin Solid Films 220, 241 (1992).
[11] S. A. Alterovitz, R. M. Sieg, N. S. Shoemaker, and J. J. Pouch, Mater. Res. Soc. Symp. Proc. 152, 21 (1989).
[12] P. G. Snyder, M. C. Rost, G. H. Bu-Abbud, J. A. Woollam, and S. A. Alterovitz, J. Appl. Phys. 60, 2393 (1986).
[13] G. E. Jellison, Jr., Opt. Mater. 1, 41 (1992).
[14] J. Humliček, M. Garriga, M. I. Alonso, and M. Cardona, J. Appl. Phys. 65, 2827 (1989).
[15] G. E. Jellison, T. E. Haynes, and H. H. Burke, Opt. Mater. (to be published).
[16] E. S. Yang, *Microelectronic Devices* (McGraw-Hill, New York, 1988).
[17] P. Lautenschlager, M. Garriga, L. Viña, and M. Cardona, Phys. Rev. B 36, 4821 (1987).

N94-20510

Spectroscopic ellipsometric characterization of $Si/Si_{1-x}Ge_x$ strained-layer supperlattices

H. Yao *, J.A. Woollam

Center for Microelectronic and Optical Materials Research, and Department of Electrical Engineering, University of Nebraska, Lincoln, NE 68588-0511, USA

P.J. Wang, M.J. Tejwani

IBM Semiconductor R&D Center, Hopewell Junction, NY 12533, USA

and

S.A. Alterovitz

Lewis Research Center, National Aeronautics and Space Administration, Cleveland, OH 44135, USA

Received 2 June 1992; accepted for publication 31 July 1992

Spectroscopic ellipsometry (SE) was employed to characterize $Si/Si_{1-x}Ge_x$ strained-layer superlattices. An algorithm was developed, using the available optical constants measured at a number of fixed x values of Ge composition, to compute the dielectric function spectrum of $Si_{1-x}Ge_x$ at an arbitrary x value in the spectral range 1.7 to 5.6 eV. The ellipsometrically determined superlattice thicknesses and alloy compositional fractions were in excellent agreement with results from high-resolution X-ray diffraction studies. The silicon surfaces of the superlattices were subjected to a 9:1 HF cleaning prior to the SE measurements. The HF solution removed silicon oxides on the semiconductor surface, and terminated the Si surface with hydrogen–silicon bonds, which were monitored over a period of several weeks, after the HF cleaning, by SE measurements. An equivalent dielectric layer model was established to describe the hydrogen-terminated Si surface layer. The passivated Si surface remained unchanged for > 2 h, and very little surface oxidation took place even over 3 to 4 days.

1. Introduction

The $Si/Si_{1-x}Ge_x$ strained-layer superlattice (SLS) plays an important role in band-gap engineering and Si-based fast electronic device applications [1,2]. This structure can be grown by low-temperature growth processes, such as molecular beam epitaxy (MBE) or ultrahigh vacuum/chemical vapor deposition (UHV/CVD) [3,4]. In both processes, it is critically important to have tight control on the structural growth parameters such as layer thicknesses, alloy compositions and interfacial roughness. In this paper, we report results of spectroscopic ellipsometry (SE) characterization of layer thicknesses, pseudo-alloy-compositions and surface conditions of $Si/Si_{1-x}Ge_x$ SLSs grown by the UHV/CVD technique.

2. Spectroscopic ellipsometry

SE is a non-destructive optical technique. It is extremely sensitive to thickness, alloy composition, and surface and interfacial conditions of the sample structure [5,6]. SE is designed to accu-

* To whom correspondence should be addressed.

© 1993 Elsevier Science Publishers B.V. Reprinted, with permission, from Applied Surface Science, vol. 63, 1993, pp. 52-56.

PRECEDING PAGE BLANK NOT FILMED

rately determine the values of $\tan(\psi)$ and $\cos(\Delta)$, which are the amplitude and projected phase of the complex ratio

$$\rho = R_p/R_s = \tan(\psi)\, e^{i\Delta}, \quad (1)$$

where R_p and R_s are the complex reflection coefficients of light, measured from the sample, polarized parallel to (p) or perpendicular to (s) the plane of incidence. The results of the SE experimental measurements can be expressed as $\psi(h\nu_i, \Phi_j)$ and $\Delta(h\nu_i, \Phi_j)$ where $h\nu$ is the photon energy and Φ is the external angle of incidence.

In the simplest case, i.e., the sample can be ideally described as a two-phase model (ambient/substrate), R_p and R_s are the Fresnel reflection coefficients. In the case of multilayer-structured samples, a model has to be assumed, and the SE data must be numerically fitted. The values of $\psi^c(h\nu_i, \Phi_j)$ and $\Delta^c(h\nu_i, \Phi_j)$ are calculated as in eq. (1), by an assumed model, for comparison with experimentally measured values. A regression analysis is used to vary the model parameters (e.g., layer thickness or alloy composition) until the calculated and measured values match as closely as possible. This process is done by minimizing the mean square error (MSE) function, defined as:

$$\text{MSE} = \frac{1}{N}\sum_{i,j}\left\{\left[\tan\psi(h\nu_i, \Phi_j) - \tan\Psi^c(h\nu_i, \Phi_j)\right]^2 + \left[\cos\Delta(h\nu_i, \Phi_j) - \cos\Delta^c(h\nu_i, \Phi_j)\right]^2\right\}. \quad (2)$$

The pseudodielectric function of the sample $\langle\epsilon\rangle$ is obtained from the ellipsometrically measured values of ρ, in a two-phase model (ambient/substrate) [5]:

$$\langle\epsilon\rangle = \langle\epsilon_1\rangle + i\langle\epsilon_2\rangle = \epsilon_a\left[\left(\frac{1-\rho}{1+\rho}\right)^2 \sin^2\Phi\,\tan^2\Phi + \sin^2\Phi\right], \quad (3)$$

regardless of the possible existence of surface overlayers or multilayer structures. The ϵ_a in eq. (3) represents the ambient dielectric function (e.g., $\epsilon_a = 1$ in vacuum). To compute the dielectric functions of $Si_{1-x}Ge_x$ at an arbitrary x value, we used a group of dielectric functions of bulk $Si_{1-x}Ge_x$ measured at fixed x values [7–9], shown in fig. 1, as the basis of our calculation. From fig. 1, it is noticeable that as the x value increases, each critical point of the energy band, such as E_2 or E_1, shifts by different amounts. Considering the nature of the non-rigid shifts of the $\langle\epsilon\rangle$ spectrum as the x value changes, an energy-shift model [10] is employed to calculate the $\langle\epsilon\rangle$ spectrum for any x values of Ge. This model has been described in detail in ref. [10]. In this procedure the $\langle\epsilon\rangle$ spectrum is computed for an arbitrary x value of Ge by interpolating between the two known adjacent spectra which are above and below the x value, with weighted averages of the two shifted spectra [10]. For $Si_{1-x}Ge_x$, three critical-point transitions are considered: E_2 (~ 4.37 eV); E_1 (2.1–3.4 eV); $E_{g,ind}$ (0.76–1.1 eV). The $E_{g,ind}$ is outside the measuring energy range, but it is needed to interpolate the $\langle\epsilon\rangle$ spectrum at photon energies between $E_{g,ind}$ and E_1 [10]. Contributions of $E_1 + \Delta_1$ and E_0' to the $\langle\epsilon\rangle$ spectrum are not considered separately here since the positions of these two critical points are very close to that of E_1. The energy positions of the critical-point transitions E_2, E_1, and $E_{g,ind}$ are given in refs. [11], [7] and [12], respectively:

$$E_2 = 4.372 - 0.069(1-x)\ \text{eV}, \quad (4)$$

$$E_1 = 2.108 + 1.134(1-x) + 0.153(1-x)^2\ \text{eV}, \quad (5)$$

$$E_{g,ind} = 0.8941 + 0.0421(1-x) + 0.1691(1-x)^2\ \text{eV} \quad (0 \leqslant x \leqslant 0.85), \quad (6)$$

$$E_{g,ind} = 0.7596 + 1.0860(1-x) + 0.3306(1-x)^2\ \text{eV} \quad (0.85 < x \leqslant 1), \quad (7)$$

where $E_{g,ind}$ refers to the indirect energy gap of $Si_{1-x}Ge_x$ with the X and L minima crossing near $x = 0.85$ [12].

Based on this algorithm, the x value was treated as a parameter in fitting the SE data for the $Si_{1-x}Ge_x$ SLSs to find the best-fit pseudo-alloy-composition values x, regardless of the possible influence of strain.

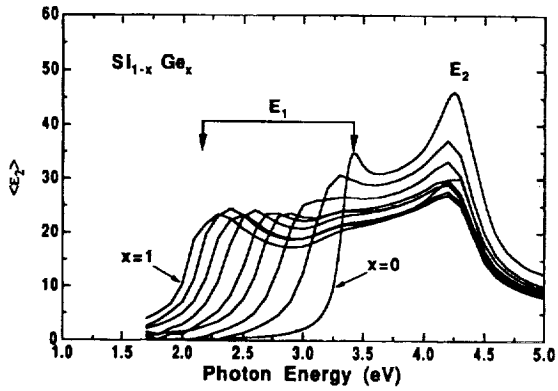

Fig. 1. Imaginary part of the pseudodielectric function $\langle\epsilon_1\rangle + i\langle\epsilon_2\rangle$ measured for bulk $Si_{1-x}Ge_x$, with x decreasing from left to right. The data with $x = 1$ are from ref. [8], those with $x = 0$ are from ref. [9], while the data with other x values: 0.218, 0.389, 0.513, 0.635, 0.75, 0.831 and 0.914 are from ref. [7]. The energy intervals between data points are 0.1 eV for all x, except that for $x = 1$, which is much smaller [8].

3. Experimental results and discussions

3.1. Sample surface cleaning and passivation

The $Si/Si_{1-x}Ge_x$ SLSs are generally covered with oxides. This oxide surface overlayer has to be modeled for the SE characterization. Si oxide surface is usually modeled as a SiO_2 layer for the SE analysis. However, since the oxide overlayer generally consists of roughness, as well as mixtures of constituents it is necessary to remove the surface oxide and clean the Si surface to obtain the better SE characterization results for $Si/Si_{1-x}Ge_x$ SLSs. Therefore, SE studies of Si surface HF cleaning were carried out prior to the characterization of $Si/Si_{1-x}Ge_x$ SLSs.

p-Type Si wafers (100) of 14–22 $\Omega \cdot$cm resistivity were used to study the effects of HF treatments on Si surfaces covered with native oxide. A piece from the wafer was dipped in 9:1 HF for ~20 s with no rinse. SE measurements were made before and after the HF dip, at a 75° angle

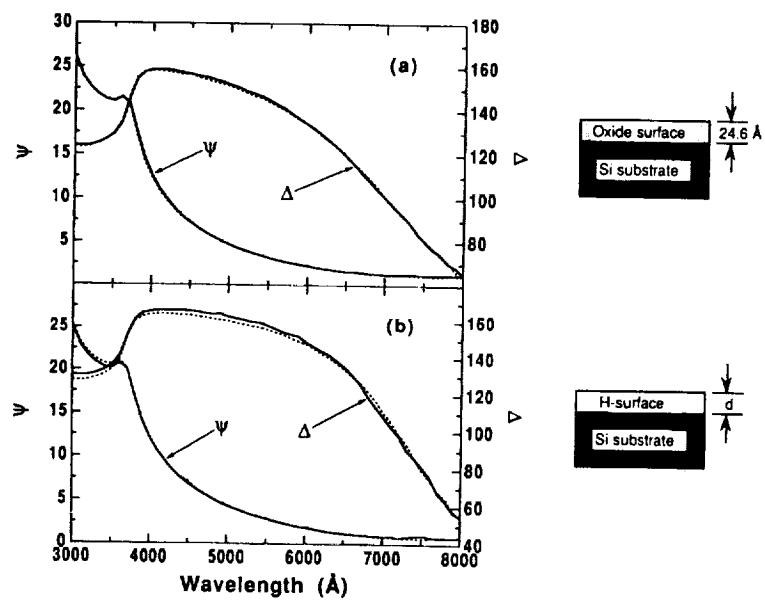

Fig. 2. ψ and Δ values of SE measurements on a Si(100) surface: (a) before and (b) after the HF cleaning. The solid line represents the experimental data, and the dashed line is the best fit of the SE analysis. Assumed models for the SE analysis, in each case, are sketched with the plots.

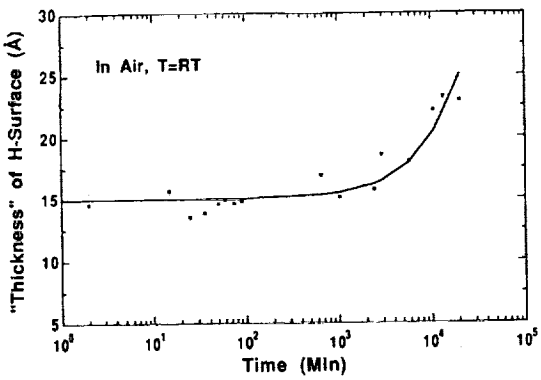

Fig. 3. Changes in effective "thickness" of the hydrogen-terminated Si surface (H-surface) as a function of time, monitored by the SE measurements after the 9:1 HF dip.

of incidence, as shown in figs. 2a and 2b, respectively. As indicated by the SE analysis, this Si sample was initially covered by a native oxide layer with a thickness of 24.6 Å (fig. 2a). After the 9:1 HF dip, the Si oxides were removed and the Si surface was terminated with hydrogen–silicon bonds. This hydrogen-terminated Si surface was modeled as an equivalent dielectric layer described by the optical constants of SiO_2, for the SE analysis shown in fig. 2b. The "thickness' of the hydrogen-terminated Si surface (H-surface), indicated by the SE study, was ~ 14.6 Å right after the HF cleaning. Notice that the "thickness" referred to here as an "H-surface" was not the actual thickness of the H-surface layer, but the thickness of the modeled equivalent dielectric layer of SiO_2. The value of this "thickness" as measured by SE was used to monitor the changes in the H-surface of Si.

SE measurements were made on this H-surface in air at room temperature (RT) over a period of several weeks, after the HF cleaning. Changes in "thickness" of the H-surface were monitored as a function of time as shown in fig. 3. The figure shows that the hydrogen-terminated Si surface remained unchanged for > 2 h, and very little surface reoxidation took place within 3 to 4 days. Full reoxidation occurred after two weeks. The SE study indicates that the hydrogen termination of the Si surface dangling bonds effectively retards the Si surface oxidation during air exposure.

3.2. SE characterization of the $Si/Si_{1-x}Ge_x$ SLSs

$Si/Si_{1-x}Ge_x$ SLSs with a Ge atomic molar fraction of 8% were grown on Si(100) substrates, at 520°C, by the UH[illegible]D technique [13]. These $Si/Si_{1-x}Ge_x$ superlattices consist of 20 alternating layers, with a nominal thickness of 200 Å for each layer.

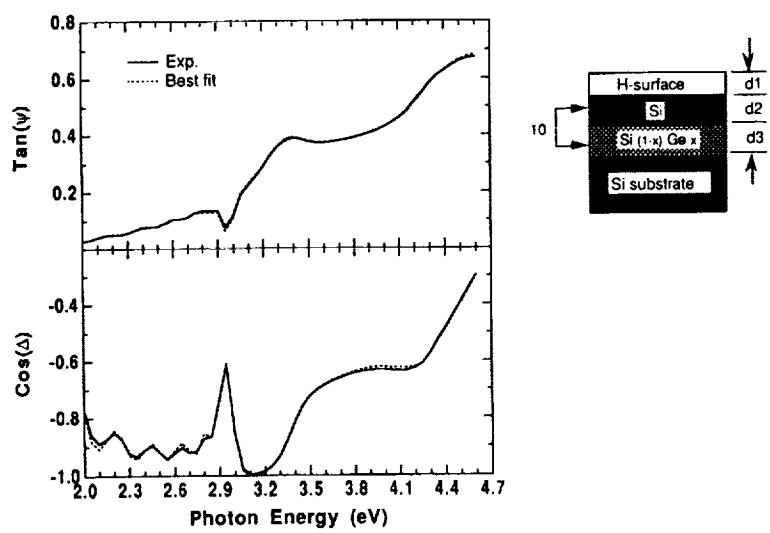

Fig. 4. Results of the SE characterization of the $Si/Si_{1-x}Ge_x$ SLSs. The best fit of the SE analysis is based on the model sk[illegible]hed in this figure, with $d1 = 12.5 \pm 0.2$ Å, $d2 = 216.6 \pm 2.3$ Å, $d3 = 183.9 \pm 2.6$ Å and $x = 0.0610 \pm 0.0008$.

The $Si/Si_{1-x}Ge_x$ SLSs were subjected to a 9:1 HF dip for ~20 s prior to SE characterization. SE measurements were made in air, with an angle of incidence of 75°, in the spectral range 2.0 to 4.6 eV, with an energy interval of 0.05 eV between data points. A sketch of the assumed model for these superlattices, for SE analysis, is shown in fig. 4. In this model, 10 periods of $Si/Si_{1-x}Ge_x$ layers, with thicknesses of $d2/d3$, were established on a Si substrate. The top hydrogen-terminated surface layer of "thickness" $d1$ was modeled as an equivalent dielectric layer of SiO_2, as described in the previous section of this paper. All thicknesses parameters: $d1$, $d2$, $d3$, and the values of pseudo-alloy-composition x were allowed to vary. No interfacial roughness was modeled at this time. Fig. 4 shows the experimental SE data and the best fit from the SE analysis. The best-fit results are: Si 216.6 ± 2.3 Å, $Si_{1-x}Ge_x$ 183.9 ± 2.6 Å and $x = 0.0610 \pm 0.0008$. These results are in excellent agreement with the values of Si 206 ± 5 Å, $Si_{1-x}Ge_x$ 185 ± 5 Å and $x = 0.0825$, from studies of high-resolution double-crystal X-ray diffraction (HRXRD) and cross-sectional transmission electron microscopy (XTEM) by Wang et al. [13]. A MSE value of 3.73×10^{-5} indicates a good fit, and it also reflects high quality of this $Si/Si_{1-x}Ge_x$ SLS with excellent thickness and composition uniformity, grown by the UHV/CVD technique.

Notice that the x value obtained from SE characterization is smaller than that from HRXRD. This is evidence of the strain effects on the $Si_{1-x}Ge_x$ layer. As indicated in ref. [14] and ref. [15], the refractive index of strained $Si_{1-x}Ge_x$ tends to shift towards smaller value, which corresponds to unstrained bulk $Si_{1-x}Ge_x$ with smaller alloy composition value x. It needs to be pointed out that the x value obtained from the HRXRD study considered the strain effects by employing Poisson ratios [13]. The SE measurements seem to magnify the same strain effects on a larger scale. The real reason is not clear.

4. Conclusions

Non-destructive optical SE measurements have been used to characterize the $Si/Si_{1-x}Ge_x$ SLSs grown by the UHV/CVD technique. Good fits were obtained by SE analysis, with model parameter values consistent with results from HRXRD and XTEM studies. A smaller pseudo-alloy-composition x value is indicative of the strain in the $Si_{1-x}Ge_x$ layer. Ex-situ SE studies of HF cleaning show that the hydrogen termination of the Si surface dangling bonds effectively retards surface reoxidation.

Acknowledgement

This work was partially supported by NASA-Lewis Grant NAG-3-154.

References

[1] T.P. Pearsall, Thin Solid Films 184 (1990) 451.
[2] S.S. Iyer, G.L. Patton, J.M.C. Stork, B.S. Meyerson and D.L. Harane, IEEE Trans. Electron Devices 36 (1989) 2043.
[3] J.C. Bean, L.C. Feldman, A.T. Fiory, S. Nakahara and J.K. Robinson, J. Vac. Sci. Technol. A 2 (1984) 436.
[4] G.L. Parron, J.H. Comfort, B.S. Meyerson, E.F. Crabbé, G.L. Scilla, E. de Frésart, J.M.C. Stork, J.Y.-C. Sun, D.L. Harame and J.N. Burghartz, IEEE Electron Device Lett. 11 (1990) 171.
[5] R.M.A. Azzam and N.M. Bashara, Ellipsometry and Polarized Light (North-Holland, Amsterdam, 1977).
[6] D.E. Aspnes, in: Handbook of Optical Constants of Solids, Ed. E.D. Palik (Academic Press, New York, 1985) p. 89.
[7] J. Humliček, M. Garriga, M.I. Alonso and M. Cardona, J. Appl. Phys. 65 (1989) 2827.
[8] D.E. Aspnes and A.A. Studna, Phys. Rev. B 27 (1983) 985.
[9] G.E. Jellison, Jr., Opt. Mater. 1 (1992) 41.
[10] P.G. Snyder, J.A. Woollam, S.A. Alterovitz and B. Johs, J. Appl. Phys. 68 (1990) 5925.
[11] J. Humliček, F. Lukeš and E. Schmidt, Solid State Commun. 42 (1983) 387.
[12] S. Krishnamurthy, A. Sher and A. Chen, Appl. Phys. Lett. 47 (1985) 160.
[13] P.J. Wang, M.S. Goorsky, B.S. Meyerson, F.K. LeGoues and M.J. Tejwani, Appl. Phys. Lett. 59 (1991) 814.
[14] G.M.W. Kroesen, G.S. Oehrlein, E. de Frésart and G.J. Scilla, Appl. Phys. Lett. 60 (1992) 1351.
[15] M. Racanelli, C.I. Drowley, N.D. Theodore, R.B. Gregory, H.G. Tompkins and D.J. Meyer, Appl. Phys. Lett. 60 (1992) 2225.

DEVELOPMENT OF $Si_{1-x}Ge_x$ TECHNOLOGY FOR MICROWAVE SENSING APPLICATIONS

Rafael A. Mena, Susan R. Taub, and Samuel A. Alterovitz
National Aeronautics and Space Administration
Lewis Research Center
Cleveland, Ohio 44135

Paul E. Young
University of Toledo
Toledo, Ohio 43606

Rainee N. Simons
Sverdrup Technology, Inc.
Lewis Research Center Group
Brook Park, Ohio 44142

and

David Rosenfeld*
National Aeronautics and Space Administration
Lewis Research Center
Cleveland, Ohio 44135

Abstract

This report discusses the progress for the first year of the work done under the Director's Discretionary Fund (DDF) research project entitled, "Development of $Si_{1-x}Ge_x$ Technology for Microwave Sensing Applications". This project includes basic material characterization studies of silicon-germanium (SiGe), device processing on both silicon (Si) and SiGe substrates, and microwave characterization of transmission lines on silicon substrates. The material characterization studies consisted of ellipsometric and magneto-transport measurements and theoretical calculations of the SiGe band-structure. The device fabrication efforts consisted of establishing SiGe device processing capabilities in the Lewis cleanroom. The characterization of microwave transmission lines included studying the losses of various Coplanar transmission lines and the development of novel transitions on silicon. This report discusses, individually, each part of the project and presents the findings for each. Future directions are also discussed.

Introduction

Silicon technology has never been considered viable for microwave applications because of its lack of high frequency active devices and the extremely high dielectric loss associated with silicon substrates. But silicon technology provides many benefits for microwave applications. Among them are: integration with digital circuitry, mature, well-defined processing procedures and low cost. Recently, a new material, SiGe (silicon-germanium), has emerged that can produce high frequency active devices in a silicon based technology. Using SiGe it is possible to fabricate devices with a two-dimensional electron gas (2DEG). This type of structure has advantages in terms of frequency of operation, noise

*National Research Council—NASA Research Associate at Lewis Research Center.

PRECEDING PAGE BLANK NOT FILMED

performance and performance improvements at low temperatures. To reduce the dielectric losses associated with silicon substrates, it has been theorized that silicon of sufficiently high resistivity must be used [1].

The purpose of this research project is the development and characterization of microwave devices, both passive and active, using newly-developed SiGe technology at frequencies required for microwave sensing applications. This effort has included basic material studies of SiGe, the development of high electron mobility transistor (HEMT) devices and characterization of microwave transmission lines on high resistivity silicon.

In order to carry out the goals of the program, a working group was established consisting of several members of the Solid State Technology Branch. In this manner, people representing different areas of expertise were brought together. Material, device and circuit experts were all present from the onset of the program. This allowed all areas to be taken into account during planning. Since Lewis does not have the facilities necessary to grow SiGe material, industry and universities were relied upon for the preparation of the SiGe samples. Collaboration was established with UCLA, University of Michigan, Cornell University, Hughes and Spire Corporation. These universities and companies have provided HEMT structures, both n-type and p-type, as well as single strained layers for material characterization studies and device fabrication. It was important to find several sources for material preparation because SiGe technology is in its infancy and there are many uncertainties involved in its growth.

The program consisted of three different areas of research while maintaining a common objective among the members of the working group. The research areas consisted of: basic material studies, device processing and, microwave characterization studies. In a relatively short period of time, many of the goals of this three year program have been accomplished. This report describes the progress for the first year and discuss future directions.

Basic Material Characterization Studies

Theoretical Study

The objective of the theoretical study was to gain a better understanding of the relationships between the physical parameters of the layers in a SiGe structure (composition, grading, doping, and mobility), and the device performance parameters (unity current gain frequency and maximum oscillation frequency). The knowledge of these relationships is required in order to design an optimum structure for high-speed, low-temperature applications.

The procedure used to analyze these relationships was to calculate the band structure of the layers and then calculate the performance which results from that band structure. Because of the complexity of the mathematical problem associated with these calculations, as well as some other non-trivial aspects, a collaboration with the Computational Material Lab at NASA Lewis was established. This lab specializes in complicated matter-related numerical calculations. With the help of the Computational Material Lab, the creation of a sophisticated computer code that solves the Poisson equations and calculates the band structure and the currents of SiGe was recently completed. The I-V characteristics of some simple SiGe structures have been calculated and plotted.

Ellipsometry Work

SiGe material samples were obtained from Spire, UCLA, University of Michigan and Hughes. They included: single SiGe strained layers on silicon, Supperlattice SiGe-silicon, and n- and p-type HEMT structures. Only the results obtained for the n-type MODFET

structures provided by UCLA and Spire will be discussed here. These samples consisted of a strained silicon layer for improved carrier confinement and are labeled as follows: 1) Spire D-5983, 2) UCLA MT-115. The results of Ellipsometric characterization of these samples is shown in Table 1.

Ellipsometric characterization of the samples included three steps: measurement, modeling and linear regression analysis. In the first step, the change in the state of polarization of a monochromatic light, that is reflected from the sample, is measured. This change in polarization is represented quantitatively using the ellipsometric parameters φ and Δ. The measurement was repeated for approximately 50 wavelengths and several angles of incidence. Thus, a large number of experimental φ and Δ are estimated. The sample is modeled using the estimated composition and thickness of all the layers in the sample. In the present case, the model consisted of the nominal compositions and thicknesses of all layers as supplied by the sample grower. They are denoted "nominal" in Table 1. The last step included a linear regression least square fit of all the experimental φ and Δ to the theoretically evaluated φ and Δ associated with the model. The minimization parameters were the composition of the SiGe layer and all layer thicknesses. The theoretical φ and Δ associated with the model were calculated using standard Fresnel reflection equations, and published dielectric functions of all material constituents.

The calculation was done using unpublished calibration functions supplied by J. Jellison from Oak Ridge National Laboratories. The dielectric functions supplied by Jellison were interpolated using a numerical algorithm. These functions were measured on relaxed layers of SiGe on silicon. Measurements were done at 3-5 angles of incidence in the range 3000-7500A using 100A steps. The wavelength (λ) range was limited so that the light did not penetrate the SiGe buffer layer into the silicon substrates. The concentration 'x' in the SiGe top layer and the "substrate" was assumed to be the same and no roughness was assumed. Graphs of the experimental DELTA (Δ) and PSI (φ) verses model calculations are shown in Fig. 1a,1b,1c,1d.

The reason the strained silicon layers have a lower thickness than the nominal value is probably due to the fact that the unstrained calibration function was used. This was done, because, as of now, no strained silicon calibration function exists. The results for D-5983 indicate that it was a poor quality sample, because the thickness and composition were very different from the nominal values. In comparison, sample UCLA MT-115 appeared much better.

Magneto-Transport Measurements

The most important characteristic of a HEMT structure is the two dimensional nature of its transport properties. This characteristic enables very high speed, low noise performance in active semiconductor devices. SiGe n-type structures have been shown to have very high mobilities, as high as 10^5 $cm^2/V \cdot s$ at low temperatures, which indicate that this is an excellent structure for microwave applications. It is very difficult however, to obtain two dimensionality in this structure since the conduction band discontinuity between silicon and SiGe is very small. This makes it difficult to achieve quantization of the carriers at the interface of the two layers. Two dimensional transport has only been obtained in the n-type structures by growing a strained silicon layer on top of a fully relaxed SiGe layer. The strain pushes down on the conduction band of the higher bandgap silicon layer, relative to the SiGe conduction band and thus makes possible the quantization. High quality strained layers are very difficult to grow as a result of misfit dislocations that arise from the lattice mismatch growth of the epitaxial layers. Because of this, the transport characteristics of the received samples had to be characterized.

N-type SiGe structures have been received from Spire, UCLA, University of Michigan and AT&T. Hall and Shubnikov-de Haas measurements were carried out using a 1.4 Tesla magnet at temperatures from room temperature down to 1.4K. Two dimensional transport was not detected in any of the structures. Therefore, transport must have occurred in either the bulk of the silicon or SiGe layers; as evident by the large carrier freeze-out at lower temperatures and the large magneto-resistance observed in the samples. Carrier freeze-out in a two dimensional electron gas (2DEG) leads to only a small decrease in the carrier concentration. In the structures examined here, the carrier concentration decreased by orders of magnitude as the temperature decreased. For example, the Spire sample went from a concentration of $7.22 \cdot 10^{12}/cm^2$ at 300K to a concentration of $1.5 \cdot 10^{7}/cm^2$ at 22K. This type of behavior was typical of all the samples. The freeze-out temperature of the samples varied between 20K and 50K.

Two dimensional transport was detected in the p-type structure provided by Hughes. As compared with the n-type structures, two dimensional transport in p-type structures is easier to achieve. This is due to the larger band discontinuity in the valance band of the silicon and SiGe layers. Doping the layers is also more simple for p-type structures and thus more accurately controlled. The mobility increased with decreasing temperature due to a reduction in phonon scattering effects. The drop in concentration is consistent with carrier freeze-out in the quantized states.

These results have been provided to the material suppliers and has led to modifications in their growth process. UCLA is attempting to lower the concentration of the capping layer (used for contact purposes), in order to reduce the band bending that occurs at such high concentrations. At Lewis, there is an attempt being made to etch away some of the doped layers, with the intent of reducing the band bending and increasing the energy discontinuity.

Device Processing

Much like the GaAs based high electron mobility transistor (HEMT) technology, SiGe HEMT technology offers the ability to fabricate active devices with low noise and high speed performance. SiGe HEMT technology has the added advantage of silicon's native oxide for metal-oxide-semiconductor (MOS) devices. The advantages of the MOS structure is the decrease in gate leakage and the improvement in device stability as compared to Schottky barrier structures.

To achieve device fabrication capability at Lewis, initial design and fabrication development projects were conducted. The intention of these projects was to develop processing techniques necessary for the fabrication of devices. Etching of SiGe materials was the first processing step required to achieve device patterning and was also needed to expose material layers for further device fabrication. Experiments were conducted to characterize etch rates for SiGe materials.

To achieve optimum device operation, low resistance contacts are critical. Therefore, development of a contact structure has been investigated. The focus of this research has been on antimony based contacts and ion implantation of the contact regions. Antimony based contacts studies were conducted using metal type, metal thickness, alloy temperature and alloy time as variables to determine optimum contact resistance. Figure 2 illustrates some of the results used to determine the proper contact procedure for SiGe devices. The figure shows the effect of various alloying temperatures on the series resistance on contacts of various composition. Studies were also conducted by ion implanting phosphorus ions into the material to create contact regions suitable for aluminum based contacts. Because a heterostructure is being used, contact to the 2DEG is required to provide ohmic contact to the

carriers. Ion implantation is used because it creates a conduction path from the upper contact region to the channel.

In order to fabricate MOS type devices, an oxide is necessary. Oxide characteristics were investigated by examining C-V and I-V measurements. To insure that no interdiffusion of the germanium or donor impurity into the silicon channel layer occurred, a low temperature plasma enhanced chemical vapor deposition (PECVD) technique was used. A characteristic C-V curve is shown in Figure 3. It illustrates the ability to invert the channel region under the oxide and good saturation in the accumulation region. Analysis of the interface state density shows a minimum of $3 \cdot 10^{10}$ states/cm^2 using the Terman method. The capacitor turn on voltage can be adjusted via processing techniques to plus or minus 5 volts to compensate for charge screening at the inversion layer of the oxide, thus achieving an effective modulation of the 2D carriers.

This work was then used to fabricate a preliminary transistor design. Ion implantation was used in fabricating the contacts. A cross section of the device structure and a finished device are shown in Figures 4 and 5, respectively. Initial evaluation of the device indicated a suppressed transconductance. This was most likely caused by poor material. Contact and oxide resistivities were acceptable but the modulated carrier concentration was extremely low. This resulted in poor device performance. Future device fabrication will be conducted on improved materials. At that time, rf performance as a function of temperature will be measured.

Microwave Transmission Line Studies

To make microwave applications on silicon possible, silicon with sufficiently high resistivity must be used to minimize the dielectric loss. The aim of this segment of the DDF is to investigate the effective dielectric constant (ε_{eff}) and attenuation of various transmission lines on silicon as a function of resistivity. We investigated Coplanar Waveguide (CPW), Coplanar slotline and Coplanar stripline structures.

The CPW structures were evaluated theoretically and experimentally. The theoretical analysis was based on the expressions in [2] for ε_{eff} and attenuation. The data for attenuation is shown in Figure 6. These calculations are for 2μm gold lines on 203μm thick silicon wafers. In this figure, dielectric loss is shown as a function of silicon resistivity for CPW lines of various geometries. Conductor loss is not shown because it is independent of the substrate. It can be seen that the loss is independent of CPW geometry. Losses for wafers of low resistivities are extremely high, but they decreases quickly with increasing resistivity. At a resistivity of 3000 ohm-cm, the dielectric loss is approximately 0.1 dB/cm, which is acceptable. The effective dielectric constant, ε_{eff} was calculated to be 6.06 for a CPW line, S=100μm, W=50μm. Experimentally, the ε_{eff} and attenuation were obtained by deembeding these parameters from measurements of several CPW lines on silicon using software from NIST. The theoretical results showed that if silicon with resistivity of 3000 ohm-cm was used, the losses would be comparable with those of the same CPW lines on GaAs (Gallium Arsenide). CPW lines of varying geometries were fabricated on silicon with resistivity of 3000-4000 ohm·cm. The values obtained for ε_{eff} and attenuation are shown in Figures 7 and 8 respectively. For the data shown, S=50μm, W=25μm, wafer thickness = 300μm and the gold thickness is approximately 1.7μm. Although no exact theoretical calculations have been done for these particular lines, the measured values are in the expected range. The noise in both curves around 34 GHz was found to be due to cable resonances.

The Coplanar Stripline and slotline structures were evaluated experimentally using resonator methods (since the NIST deembeding software only works for CPW structures).

These methods were first validated on a much cheaper and easier to handle microwave material - RT Duriod 5810.5. This material has a dielectric constant (ε_r) of 10.5 (silicon has one of 11.7) and a loss tangent of 0.0028. The slotline structure was evaluated using a ring resonator that produces multiple resonances allowing many frequencies to be evaluated. The Coplanar stripline was evaluated using a series gap coupled straight resonator. The results, experimental and theoretical are summarized in Table 2.

In order to test the slotline, a transition from a CPW to the slotline was developed, since CPW lines can be wafer-probed and slotlines cannot. Two different transitions were developed. The first makes use of a finite ground plane coplanar waveguide (FCPW) which is electromagnetically coupled to a slotline. The second makes use of a conventional CPW which is coupled to the slotline with an airbridge. The average measured performance of both transitions (measured using two back-to-back transitions with about 0.8" of slotline in between) on Duroid substrate gave a maximum insertion loss of -1.5 dB and return loss of better than -10 dB over the frequency range of 3 to 8 GHz.

Second Year Objectives

The efforts of the second year will focus on continuing the collaboration that has been established with the various universities and corporations. The team at Lewis will work more closely with these organizations in the growth and preparation of the SiGe material structures. Results obtained from ellipsometric and magneto-transport measurements carried out at Lewis, will be used to calibrate the growth process and to further understand the material characteristics of various SiGe structures.

The device processing efforts established during this first year will also be continued. The focus will be on improving the performance of the MOS transistor fabricated here at Lewis. Higher quality material, as well as a more complete understanding of processing procedures, will help make this possible. Once suitable material has been obtained and a device fabricated, the rf performance as a function of temperature, will be characterized using an custom variable temperature cryostat. Dramatic improvement in the rf performance is expected at the lower temperatures because of the increase in the mobility of the majority carriers.

Microwave studies will continue and expand to include the development of passive microwave applications on silicon. This will include determining loss as a function of resistivity for CPW lines and the continuing development of slotline and CPW striplines on silicon. Applications such as: phase shifters and antennas will be developed. This is in preparation for the third year effort which will involve combining the microwave passive with the active devices to form truly integrated SiGe circuits.

Conclusion

We have been successful in establishing collaboration with universities and industry for the growth of the SiGe structures. Results obtained from ellipsometric and magneto-transport measurements, carried out at Lewis, were used in the calibration of the growth process as well as to further understand the material characteristics of SiGe. Also, theoretical calculations of the band structure and I-V characteristics of some simple structures, were carried out using a code that was developed at Lewis. We have also been successful in establishing a SiGe device processing capability in the Lewis cleanroom. Preliminary results have been obtained for a MOS transistor device. Finally, we have favorably ascertained the feasibility of silicon as a substrate for microwave applications. Theoretical calculations have shown that transmission line losses are similar to those of GaAs if the substrate resistivity is

kept above a certain value. We have also evaluated experimentally Coplanar Stripline and slotline structures using resonator methods.

References

[1] Rosen, A., et al. "Silicon as a Millimeter-wave Monolithically Integrated Substrate-a New Look", RCA Rev., 1981, 42, pp. 633-660.

[2] Gupta, K.C., R. Garg, I.J. Bahl. Microstrip Lines and Slotlines. Artech House, Inc. 1979. pp. 285-287 and 275-276.

a) Layer	Nominal	Ellipsometry
SiO_2	---------	6±1
Silicon	200 angstroms	113±3
$Si_{1-x}Ge_x$	500 angstroms	498±6, x=0.233±0.011
Silicon	500 angstroms, x=0.30	114±11
$Si_{1-x}Ge_x$	x=0.30	x=0.233±0.011
	Substrate	

b) Layer	Nominal	Ellipsometry
SiO_2	----------	26±1
Silicon	400 angstroms, x=0.35	428±3
$Si_{1-x}Ge_x$	150 angstroms	0.338±0.004
Silicon	x=0.35	135±4
$Si_{1-x}Ge_x$	Substrate	0.338±0.004

Table 1: Results of ellipsometric study of SiGe structures. a) D-5983,mean square error= 7×10^{-4} b) UCLA MT-115, $\lambda \leq$ 6400 angstroms mean square error= 2×10^{-3}

a) Slotline

Frequency (GHz)	Measured ε_{eff}	Computed ε_{eff}	Measured Attenuation
25.4	4.1918	4.2093	0.4374
18.8	4.0415	3.9413	0.3471
12.1	3.7996	3.5932	0.2189

b) Coplanar Stripline

Frequency (GHz)	Measured ε_{eff}	Computed ε_{eff}	Measured Attenuation	Computed Attenuation
6.2	•	3.9872	0.139	0.111
11.0	•	4.7451	0.158	0.150

Table 2: Characteristics of ring resonators on high resistivity silicon a) Slotline b) Coplanar Stripline

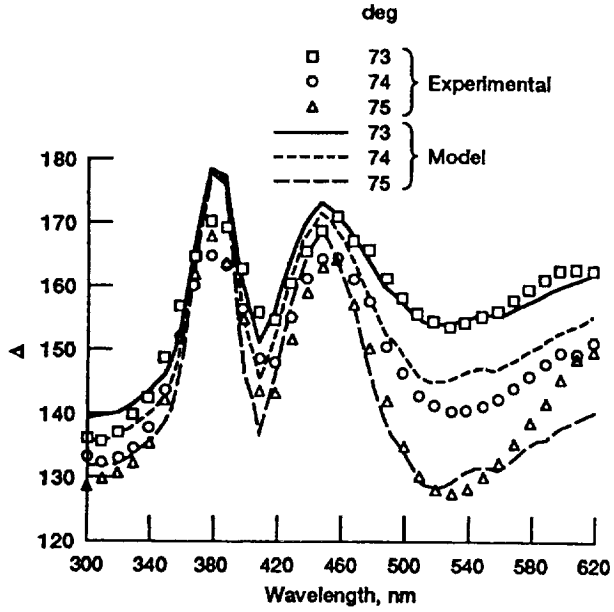

(a) Spire Corporation D-5983; measurement versus model.

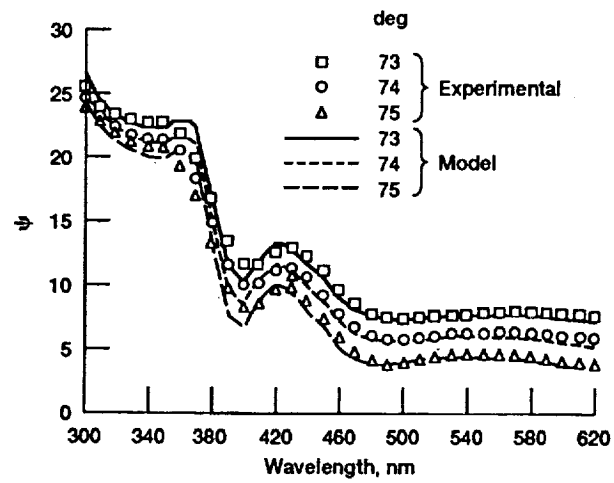

(b) Spire Corporation D-5983; measurement versus model.

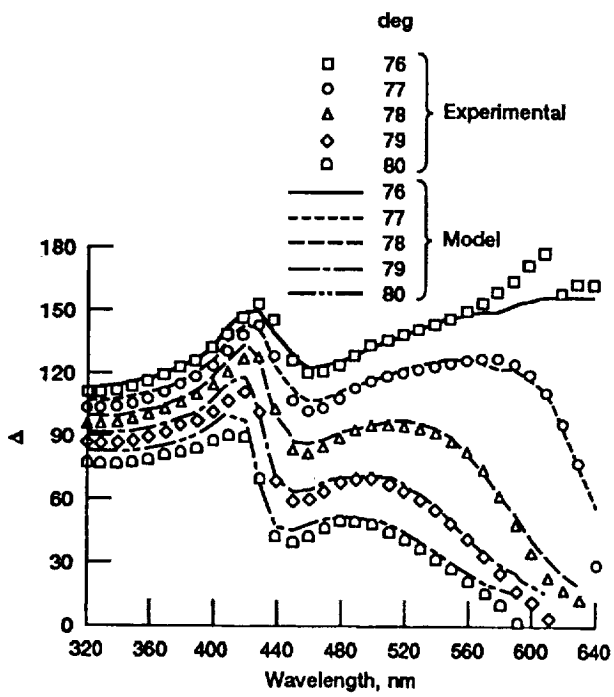

(c) UCLA MT-115; measurement versus model.

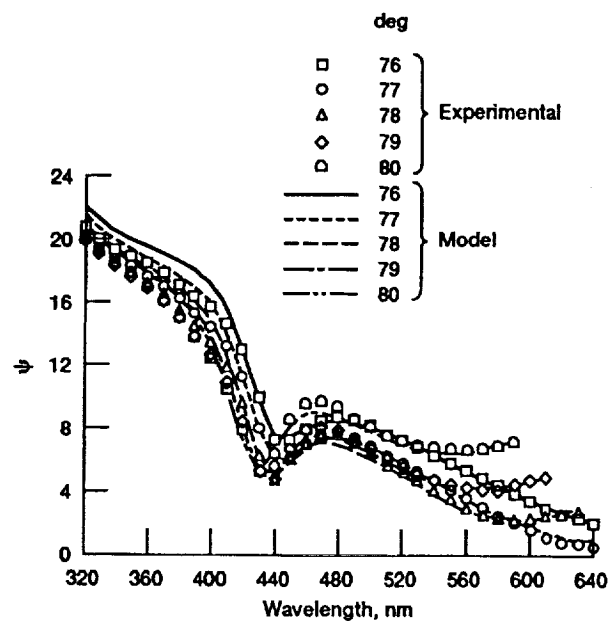

(d) UCLA MT-115; measurement versus model.

Figure 1.—Ellipsometry data.

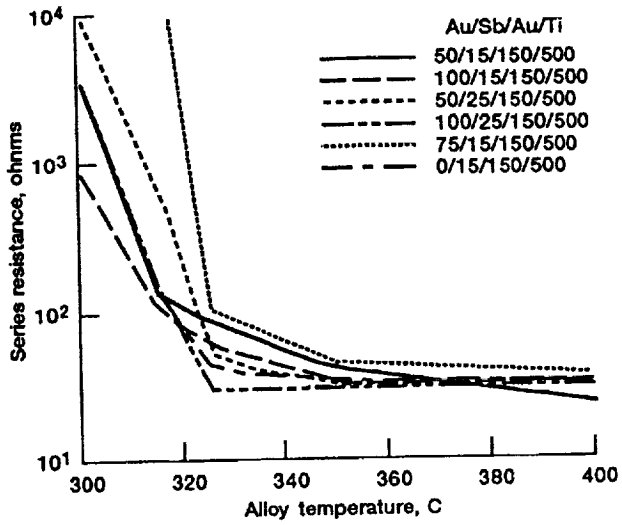

Figure 2.—Series resistance as a function of temperature for various Au/Sb/Au/Ti contacts on silicon.

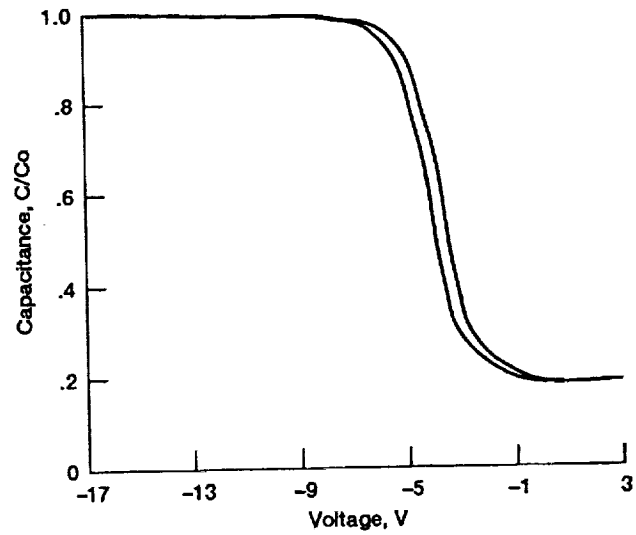

Figure 3.—C-V curve of oxide on SiGe.

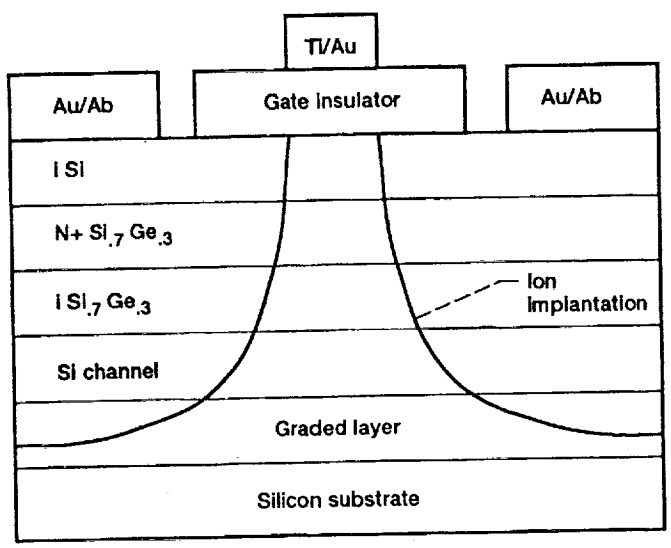

Figure 4.—Self gate aligned SiGe MOS-MODFET-device structure.

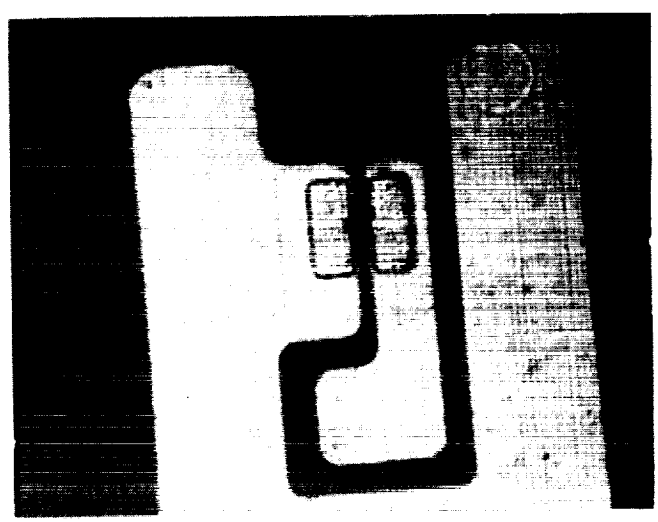

Figure 5.—Self gate aligned SiGe MOS-MODFET finished device.

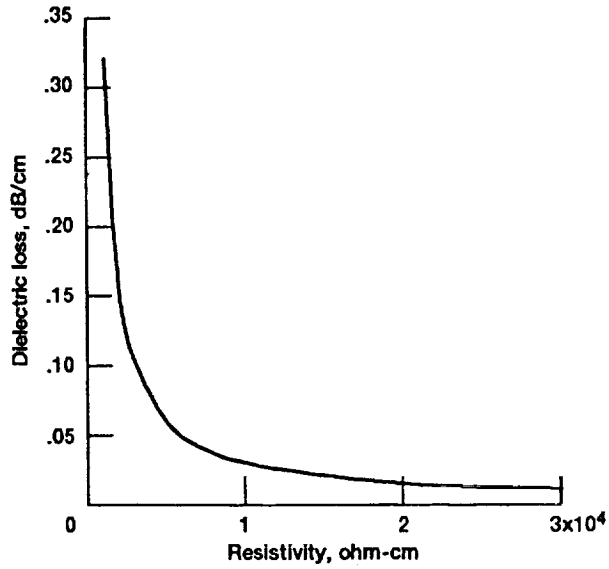

Figure 6.—Theoretical dielectric losses of CPW lines on silicon as a function of resistivity.

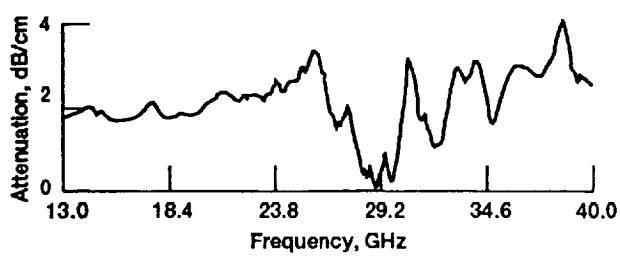

Figure 7.—Measured attenuation.

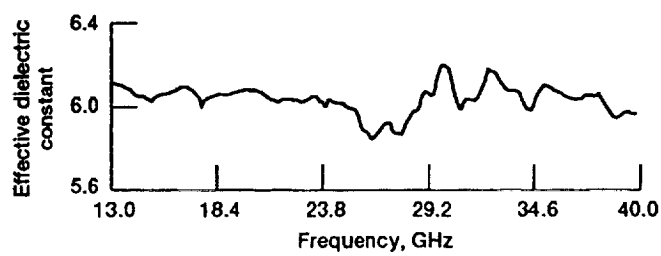

Figure 8.—Measured effective dielectric constant.

N94-20511

New technique for oil backstreaming contamination measurements

S. A. Alterovitz and H. J. Speier
NASA Lewis Research Center, Cleveland, Ohio 44135

R. M. Sieg[a] and M. N. Drotos[a]
Cleveland State University, Cleveland, Ohio 44115

J. E. Dunning[a]
Michigan State University, East Lansing, Michigan 48824

(Received 4 October 1991; accepted 6 January 1992)

Due to the large size and the number of diffusion pumps, space simulation chambers cannot be easily calibrated by the usual test dome method for measuring backstreaming from oil diffusion pumps. In addition, location dependent contamination may be an important parameter of the test. We have measured the backstreaming contamination in the Space Power Facility (SPF) near Sandusky, Ohio, the largest space simulation vacuum test chamber in the U.S.A. We used small size clean silicon wafers as contamination sensors placed at all desired measurement sites. The facility used diffusion pumps with DC 705 oil. The thickness of the contamination oil film was measured using ellipsometry. Since the oil did not wet uniformly the silicon substrate, two analysis models were developed to measure the oil film: (1) continuous, homogeneous film and (2) islands of oil with the islands varying in coverage fraction and height. In both cases, the contamination film refractive index was assumed to be that of DC 705. The second model improved the ellipsometric analysis quality parameter by up to two orders of magnitude, especially for the low coverage cases. Comparison of the two models for our case shows that the continuous film model overestimates the oil volume by $<50\%$. Absolute numbers for backstreaming are in good agreement with published results for diffusion pumps. Good agreement was also found between the ellipsometric results and measurements done by x-ray photoelectron spectroscopy (XPS) and by scanning electron microscopy (SEM) on samples exposed to the same vacuum runs.

I. INTRODUCTION

The Space Power Facility (SPF) near Sandusky, Ohio is the largest vacuum space simulation test chamber in the U.S.A. The SPF was designed to simulate space environment over a wide range of thermal and vacuum conditions for testing advanced propulsion and space power systems. SPF's unique size and high vacuum pumping capacity have facilitated testing of complete spacecrafts, two-stage medium weight rockets, and upper atmosphere phenomena with minimal wall effects. The facility is operated by NASA Lewis Research Center. Starting in 1994, the Space Station Freedom (SSF) program will require testing of the SSF electrical power system hardware in a simulated space environment. The SPF was chosen for the tests. One of the concerns of testing the SSF electrical power system hardware is the possibility of contaminating the test article, with a possible subsequent reduction in performance. One of the very important possible contamination sources is oil backstreaming, especially of diffusion pump oil. However, other contamination sources, both organic (e.g., from lubricants and paints) and inorganic (e.g., dust particles) can also contribute. Due to the large size of the SPF vacuum chamber and possible temperature gradients, the contamination is expected to be location dependent.

This work was initiated to obtain a reliable quantitative estimate of the contamination in the SPF in a space simulation test. The usual method of measuring oil backstreaming, i.e., the test dome method, could not be used due to the chamber size. Several techniques[1] have been tried, namely ellipsometry, x-ray photoelectron spectroscopy (XPS), residual gas analysis (RGA), nonvolatile residue (NVR) wipe samples, and scanning electron microscopy (SEM). This paper will report in detail the results obtained by ellipsometry. This technique gave location dependent quantitative results which were in qualitative agreement with the XPS and SEM data. To date, the other two methods (RGA and NVR) were not pursued beyond the initial tests and were not used in the final contamination estimate.

The paper is divided into three parts: experimental, results, and discussion. A short description of the SPF and the ellipsometric technique will be given in the experimental part. The second part describes the results obtained using two ellipsometric models, namely the island and the continuous film models, as function of position. The last part includes a discussion of the two models for analyzing the ellipsometric data, and an evaluation of ellipsometry versus the other techniques used in the SPF contamination experiments.

II. EXPERIMENTAL

The Space Power Facility (SPF) vacuum chamber has a 100-ft (30.5-m) diameter and a 121-ft (36.9-m) height. It offers the user 800 000 cubic feet (22 653.477 m^3) of usable unobstructed volume. The vacuum system consists of 32 48-in.-diam liquid nitrogen (LN) baffled diffusion pumps mounted in the chamber floor. The diffusion pumps

© Appl. Phys. Lett. 73 (4), 1 Jul/Aug 1992. Reprinted, with permission, from American Institute of Physics.

PRECEDING PAGE BLANK NOT FILMED

are backed by a five-stage roughing train consisting of four stages of roots blowers in series and a single stage of three rotary-piston-type mechanical vacuum pumps in parallel. Under dry, clean, empty conditions, the chamber will achieve a pressure of 10^{-7} Torr. The pumpdowns conducted during this test program yielded a chamber pressure of 5×10^{-6} Torr without complete LN flow to the baffles. The samples for ellipsometry consisted of small clean silicon wafers that were positioned at a variety of locations inside the vacuum chamber. Commercial silicon wafers were cut into roughly 1×1-cm pieces and were thoroughly cleaned for possible organic and inorganic contamination using the following procedure: boiling tri-chloroethylene, boiling acetone, boiling methanol, 30-s dip in 1:10 HF: H_2O, and rinse with deionized water. These silicon pieces will be named slides in this paper. For each vacuum pumpdown, slides were located within 2 ft of each diffusion pump and at eight other locations throughout the chamber, at different orientations and distances from the diffusion pumps.

The ellipsometer used in this work is a variable angle spectroscopic unit that was described previously and will not be repeated here.[2] For a detailed description of ellipsometry, see Ref. 3. The instrument measures changes in the polarization of monochromatic light upon reflection from the sample in terms of the ellipsometric parameters ψ_e and Δ_e (or $\tan \psi_e$ and $\cos \Delta_e$). Here ψ_e and Δ_e are defined by

$$\tan \psi_e e^{i\Delta_e} = R_p / R_s, \tag{1}$$

where R_p and R_s are the complex effective reflection coefficients for light polarized parallel and perpendicular to the plane of incidence, respectively. The measurement of ψ_e, Δ_e is repeated at a variety of wavelengths (in the range of 3200–7500 Å) and angles of incidence (mostly 75°). The usual method of estimating the thicknesses d_j of one or more overlayers on a substrate when the complex refractive index of all the films and the substrate are known consist of two steps. First, R_p and R_s are calculated[3] assuming continuous, homogeneous films with interfaces parallel to each other and to the substrate. Using Eq. (1), the calculated values ψ_c and Δ_c are estimated. In the second step, a least square minimization procedure is used to find the values of d_j that minimize the function

$$\sigma = (N - P)^{-1} \sum_i [(\tan \psi_{e,i} - \tan \psi_{c,i})^2 + (\cos \Delta_{e,i} - \cos \Delta_{c,i})^2]. \tag{2}$$

The summation is over all N experimental points, i.e., all wavelengths and angles of incidence. P is the number of free parameters, d_j in this case. In the oil contamination work, several slides, unexposed to the vacuum, were used as reference. They were analyzed in terms of crystalline Si (c-Si) with a SiO_2 overlayer, using published results for the complex refractive index versus wavelength.[4,5] We obtained SiO_2 thicknesses in the range of 22–34 Å, but the values of σ were higher than expected for a perfect SiO_2 film. However, we used this structure as the composite substrate in all our analyses, as it was not the accuracy limiting factor in this study. The oil contaminated samples were analyzed in two ways. First, we assumed a continuous oil film and used the procedure outlined above to find the thickness of this layer on top of the composite substrate. The oil used in the diffusion pumps was Dow Corning 705 (DC 705), which according to the published data[6] has a refractive index of 1.579. This oil has very small absorption in the wavelength range of 3200–7500 Å used here,[7] and thus the constant 1.579 value was used. Some of the results showed very poor fits to this simple model with rather large σ values. In parallel, a scanning electron microscope (SEM) was used to observe the morphology of the contaminated samples. The SEM pictures show a discontinuous coverage of the slides. Thus, a second ellipsometric model was used, namely the islands' model.[8,9] In the islands' model, the characteristic dimensions, i.e., the islands sizes and the interisland distances, are assumed to be much larger than the light wavelength. Thus, one of the main assumptions of the most common model for the optical behavior of a mixture, namely the effective medium approximation[10] (EMA) is violated, and thus EMA and the islands' model do not overlap. In the islands' model, we also assume that the characteristic dimensions are smaller than the coherence length of the incident light.[9] Thus, the reflectivity of the islands and the bare substrate will be independent, but will have to be added up due to the large light coherence length. Both these assumptions are well obeyed in the oil contamination samples for light in the visible and a spectral width of 20 Å. A detailed discussion of the conditions required for the application of the islands' model to the oil contamination problem as compared to the EMA will be given elsewhere.[11] We found that the EMA model is not applicable in this particular case. In the islands' model, the reflected light from the overlayer covered composite substrate and the bare surface are superimposed in a coherent way, i.e.,

$$R_\nu = f R_{\nu,c} + (1 - f) R_{\nu,b}, \tag{3}$$

Here $\nu = p$ or s polarizations, $R_{\nu,c}$ and $R_{\nu,b}$ are the reflection coefficients for the covered and bare surface, respectively, and f is the fraction of the surface covered by the overlayer.

III. RESULTS

Four pumpdowns were performed, with the following durations in hours: 28, 74, 100, and 72. Silicon slides were located at 39 points in the SPF vacuum chamber for each one of the 28-, 74-, and 72-h runs, and at 12 points for the 100-h run. The 32 diffusion pumps were divided into two groups: 16 in the north group and 16 in the south group. Besides the 32 slides located by the diffusion pumps, 7 others were located at important points in the chamber, e.g., east and west doors, top center, crane, RGA location, and others. An example of the way results were summarized is given in Table I. The example shows the ellipsometric analysis results for the 32 slides located by the 32 diffusion pumps: slides 1–16 are in the south side group and slides 17–32 are in the north side group. Besides the

TABLE I. Ellipsometrically determined oil contamination of all diffusion pumps in the SPF, using two analysis methods.

Pump number	Continuous film		Islands' model			
	σ (10^{-2})	d (Å)	σ (10^{-2})	t (Å)	f	$t \cdot f$ (Å)
1	0.626	220	0.316	268	0.7070	189.3
2	3.18	55.5	0.023	562	0.0743	41.73
3	0.167	301	0.083	322	0.8948	287.8
4	0.439	338	0.427	347	0.9552	331.4
5	0.178	240	0.112	259	0.8759	226.7
6	3.64	72.4	0.029	524	0.1002	52.46
7	0.133	366	0.088	383	0.9349	357.6
8	1.56	256	1.41	286	0.8061	230.8
9	1.38	88.9	0.039	312	0.2066	64.48
10	1.10	113	0.025	276	0.3043	83.93
11	4.19	137	0.132	453	0.2049	92.86
12	2.24	193	1.19	335	0.3959	132.7
13	1.23	282	0.937	322	0.7761	249.9
14	1.14	284	1.14	289	0.9681	279.3
15	0.746	282	0.550	314	0.8206	257.9
16	5.66	90.2	0.094	586	0.1106	64.77
17	1.70	34.6	0.029	597	0.0448	26.75
18	5.03	101	0.503	542	0.1284	69.59
19	2.60	287	1.06	401	0.5119	205.3
20	3.97	279	1.12	465	0.3795	176.5
21	5.61	199	0.643	511	0.2469	126.2
22	0.467	366	0.175	411	0.8406	345.5
23	6.53	207	1.10	538	0.2343	126.0
24	7.24	152	0.805	576	0.1690	97.34
25	1.52	95.8	0.162	323	0.2115	68.31
26	0.444	310	0.283	339	0.8589	291.2
27	6.76	141	0.767	563	0.1628	91.66
28	2.00	39.2	0.042	602	0.0498	29.98
29	2.73	55.9	0.052	545	0.0762	41.53
30	3.47	84.8	0.400	491	0.1201	58.97
31	4.51	116	0.677	494	0.1570	77.56
32	3.08	78.4	0.358	484	0.1139	55.13

pump number, Table I has the following columns: the continuous film trigonometric mean square errors (trig MSE) σ, and thicknesses d; and the islands' model results, namely the trig MSE σ, the average island height t, the island coverage fraction f, and the parameter $t \cdot f$. The $t \cdot f$ parameter, measured in Å, is the equivalent oil thickness obtained in the islands' model, and should be compared with the continuous film thickness d. We will use the $t \cdot f$ parameter as an effective oil thickness throughout this paper. Table I clearly shows that the values of σ for the continuous film model are higher by up to two orders of magnitude as compared to those obtained using the islands' model. However, above $f = 0.70$, the islands' model converges into the continuous film model, giving almost the same σ values. A graph of the σ (trig MSE) values versus the islands fraction for the samples in Table I is given in Fig. 1. It shows that the islands' model gives good fits to the experimental data at all coverage fractions f, but the quality of the fits is really excellent for f values at or below approximately 0.10, with σ at or below 10^{-3}. These excellent fits were also obtained for the 28-h run where all 39 samples had $f < 0.10$. In this short run, the islands' model σ values were in the range $4 \times 10^{-5} < \sigma < 2.5 \times 10^{-4}$. For comparison, the continuous film model for the 28-h run gave the range $3 \times 10^{-4} < \sigma < 1.7 \times 10^{-2}$. A more detailed quantitative comparison of the two models used here will be given elsewhere.[10]

A SEM picture of one of the slides (No. 32 in Table I) is given in Fig. 2. Several important results were obtained from the SEM picture: (1) Oil contamination gives a dis-

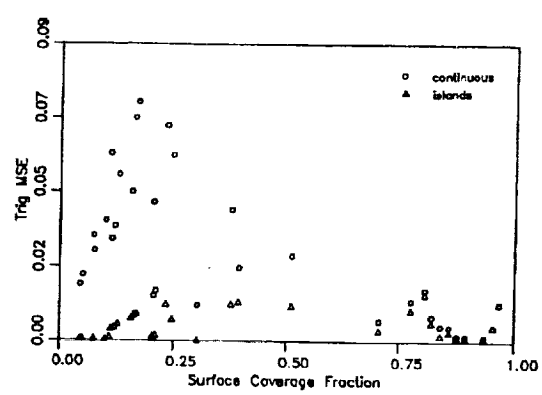

FIG. 1. Trigonometric mean square error (trig MSE) σ vs the islands coverage fraction f obtained using the continuous film and the islands' models, for the slides given in Table I.

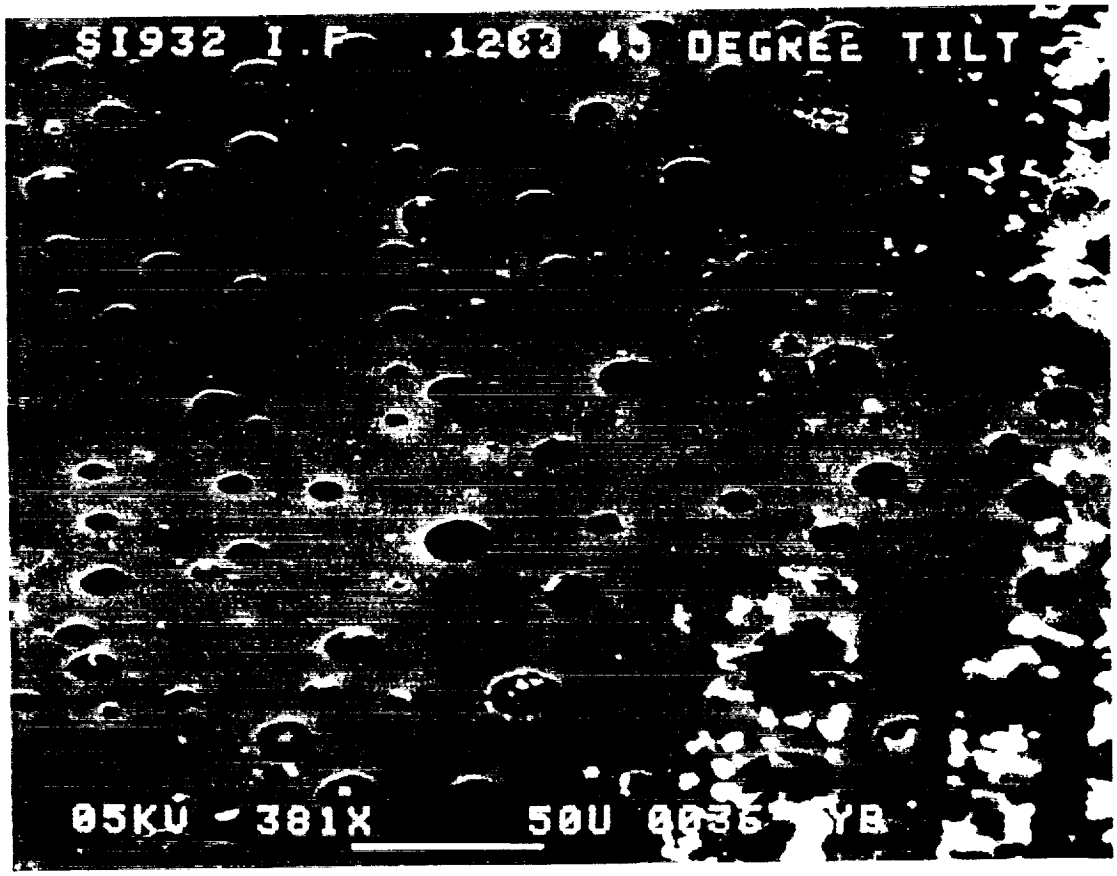

FIG. 2. Scanning electrón microscope (SEM) picture of an oil contaminated slide showing the islands' structure.

continuous film that covers the substrate in the form of disconnected islands. (2) The coverage value obtained by ellipsometry (0.114) is in good agreement with a visual estimate of 0.1. (3) The ideal islands' model is not completely applicable, as a small part of the islands start to wet the substrate and/or do not maintain their original shape. We repeated the SEM work on some of the slides several months later, and the number of broken up islands grew considerably. In addition, most of the higher coverage samples have a larger percentage of nonideal islands morphology. This fact explains the higher values of σ obtained for these samples, as shown in Fig. 1.

Practical application of this method for discontinuous film effective thickness measurement will be enhanced if a simpler model is used. Many ellipsometers can measure the thickness of one continuous film. In Fig. 3 we compare the results of the effective thickness $t \cdot f$ measured in the 72-h "proof of performance" run versus the results for the thickness d obtained from the continuous film analysis on the same slides. We can clearly see two regimes: large and small thicknesses, and a crossover. As expected, at very high coverage fractions, i.e., near the continuous film regime with $f > 0.70$, corresponding to films with thicknesses d over 220 Å, the slope of the curve approaches 1. This result is reinforced by another measurement. In addition to the work on the SPF, we tested other vacuum chambers. In one of these tests, highly contaminated samples show continuous film coverage. For example, one sample had the

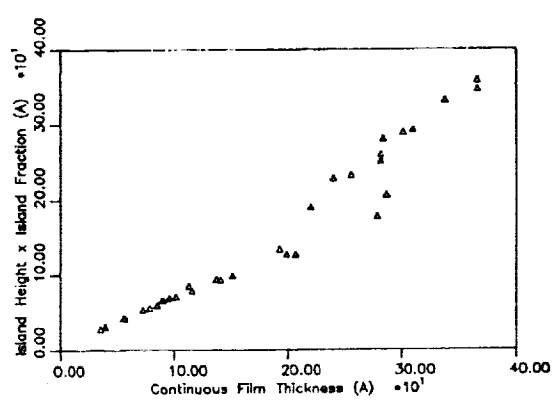

FIG. 3. The effective thickness $f \cdot t$ as determined from the islands' model vs the continuous film model thickness d for the 72-h run.

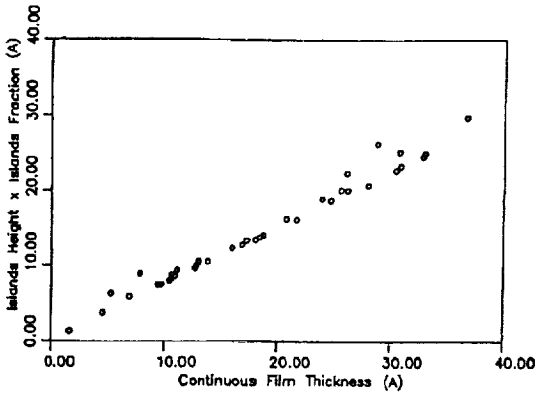

FIG. 4. The effective thickness $f \cdot t$ as determined from the islands' model vs the continuous film model thickness d for the 28-h run.

following results: continuous film model $d = 229.1$ Å and $\sigma = 2.5 \times 10^{-5}$, islands' model $t = 228.2$ Å, $f = 1.008$, and $\sigma = 2.4 \times 10^{-5}$. In this case, the islands' model is clearly not needed, although it converges to the correct answer, and it corresponds to a slope of 1 in Fig. 3. The small thicknesses regime in Fig. 3 corresponds to small coverage fractions and to a more ideal islands structure. Figure 3 clearly shows a linear dependence of $t \cdot f$ on d, for $d < 100$ Å. We also examined the $t \cdot f$ versus d relationship for the 28-h run and the result is shown in Fig. 4. A completely linear dependence was obtained, with a slope of 0.77 and a correlation coefficient of 0.990 showing excellent linearity. As will be shown in the discussion part, this result is only applicable for oil contamination work using our experimental 3200–7500-Å wavelength range.

Other observations obtained from analyzing the ellipsometric results were:

(1) The slides from the 28-h run had the thinnest films of all four pumpdowns. This run gave an average $t \cdot f$ value of 15.7 Å versus thicknesses of over 150 Å for other runs. In addition, this run has also the lowest deposition rate.

(2) The south side diffusion pump slides show more contamination than the north side group. For example, in the 72-h run, the south side pumps have an average $t \cdot f$ value of 184 Å versus only 118 Å for the north side group.

(3) The oil films thicknesses decrease as the distance from the diffusion pump increases. For example, in the 72-h run, the slides by the diffusion pumps have a 151-Å average thickness versus only 34.2 Å for the other seven slides.

(4) Backstreaming rate was calculated directly from the thickness of the oil films on the slides by the diffusion pumps, the length of the run and the oil density.[6] For the three long runs an average backstreaming value of 0.37 $\times 10^{-6}$ mg/cm^2/min was obtained. In contrast, the short 28-h run gave only 0.1 $\times 10^{-6}$ mg/cm^2/min backstreaming rate.

IV. DISCUSSION

This part is divided in two main sections: (1) Comparison of ellipsometry to other oil contamination characterization methods used in the SPF calibration work,[1] and its applicability for backstreaming estimates. (2) Discussion on the applicability of the continuous film results to quantitative oil contamination analysis.

Comparison of the ellipsometry work with SEM results was already discussed. Comparison with XPS is rather complex, as XPS is an excellent technique for characterizing the type of contaminant, but not as good in estimating the depth of the film. Ellipsometry and XPS are complementary techniques. In the SPF work, the conclusions from the XPS analysis[12] compared to ellipsometry were the following:

(1) The oil contamination is probably DC 705, as Si peaks were observed. In the ellipsometry work we used this result, i.e., it was an assumption.

(2) For all samples, both the substrate and the silicon oil contamination were observed simultaneously, by XPS, denoting incomplete coverage. In ellipsometry, the islands' model gave much better fits than the continuous film model, pointing to the same result.

(3) The short 28-h run gave almost undetectable silicon oil by XPS. Ellipsometry gave an average thickness (i.e., $t \cdot f$ value) of 15.7 Å for the slides near the diffusion pumps, and 7.4 Å for other locations, accompanied by a very small ($f < 0.10$) coverage.

(4) The presence of silicon oil contamination by XPS decreased as distance from the diffusion pumps increased. This result was also found by ellipsometry, as given in the "results" part.

(5) XPS shows that the south diffusion pump group had more silicon oil than the north group. This result was also found by ellipsometry, and it was consistent, i.e., it was measured for all four pumpdowns. Even in the case of the 28-h run, the south group had an average thickness (i.e., $t \cdot f$ value) of 19.7 Å and the north group only 11.7 Å. Thus, an excellent agreement was found between XPS, SEM, and ellipsometry: XPS gave more information on the type of contamination, SEM showed the islands-type morphology, and ellipsometry gave the effective thickness and, thus, the backstreaming rate.

The backstreaming calculated from the ellipsometrically determined film thicknesses $t \cdot f$ will now be compared with published data obtained for oil diffusion pumps using DC 705 and baffles. The present average result of 0.4 $\times 10^{-6}$ mg/cm^2/min is lower than the value 5.3 $\times 10^{-6}$ mg/cm^2/min reported by Hablanian[13] on a 6-in. diffusion pump, but is in excellent agreement with the results obtained by Langdon and Fochtman.[14] In Ref. 14, a chevron-baffled diffusion pump gave backstreaming values in the range 0.1–1.0 $\times^{-6}$ mg/cm^2/min, with most of the pumpdowns giving values around 0.5 $\times 10^{-6}$/cm^2/min. The SPF also uses chevron-baffled diffusion pumps. However, an additional parameter should be considered in the backstreaming comparison and it is the oil molecules' sticking coefficient. The average backstreaming rate of 0.4 $\times 10^{-6}$ mg/cm^2/min is based on a sticking coefficient

near unity for the oil molecules that strike the silicon slide. As the sticking coefficient deviates from unity, the measured backstreaming rate would deviate from the actual rate. Additional work is required to quantify the sticking coefficient. A sticking coefficient would be required for both the oil molecules on silicon slides and oil molecules on oil.

We will now discuss the general applicability of the results shown in Figs. 3 and 4 for the continuous film to quantitative oil contamination analysis. We checked the universality of the experimental slope (0.77) found in Fig. 4 using a simulation. Assuming an ideal oil islands' model, we calculated ψ_c and Δ_c in the wavelength range 3200–7500 Å for films with different values of t (300 Å$\leqslant t \leqslant$500 Å) and f ($0.02 \leqslant f \leqslant 0.15$), on top of a 22-Å SiO_2 on c-Si substrate. From these ψ_c, Δ_c values we calculated, using a least square fit, the thickness d of a continuous oil film and the accompanying σ. We obtained a completely linear $t \cdot f$ dependence on d, with a slope of 0.74 and a correlation coefficient of 0.9999 for the linear fit. The values of the calculated σ changed in a similar way to the experimental ones, i.e., increasing very fast with increasing coverage fraction f. This comparison with theory again shows that our oil contamination samples with low values of f, are closely described by the ideal islands' model. However, the calculated value of 0.74 for the slope is not universal. We recalculated the same $t \cdot f$ versus d dependence by simulation, using two wavelength ranges: 3200–5300 and 5301–7500 Å. We found only approximate linear dependencies, with slopes of roughly 1.1 and 0.5 for the two wavelength ranges, respectively, and for $f \leqslant 0.1$. In conclusion, the continuous film model generally gives only a rough approximation for the value of the effective oil thickness, and probably an error by a factor of 2 is possible for low coverage fractions. However, for our experimental range, the continuous film approximation is much better, and errors are smaller than 50%.

We will now comment on the anomalous low $t \cdot f$ values for two points in Fig. 3. These points have continuous film thicknesses d near 300 Å. These two points correspond to coverage fractions of 0.51 and 0.38, whereas all other points with $d > 240$ Å have $f \geqslant 0.78$. This result shows that in the f range around 0.5, the $t \cdot f$ versus d graph also depends on f. It turns out that the north and south diffusion pump groups gave slightly different types of islands, with the north group average island height of 429 Å (standard deviation 86 Å), while the south group had an average $t = 365$ Å (standard deviation 107 Å). Thus, the two groups do not have the same morphology versus thickness, and the crossover between the islands' model and the continuous film occurs at different values of the continuous film thicknesses.

V. CONCLUSIONS

A new technique for measuring oil backstreaming and other contamination in large vacuum chambers was demonstrated, namely ellipsometry. This technique can measure thicknesses of both continuous films of contaminants as well as discontinuous, island type of deposits. This last type was found in the DC 705 oil backstreaming experiment in the SPF. In either case, an *a priori* knowledge of the (complex) refractive index of the contaminants is required. This method is quantitative and it shows excellent agreement with results obtained by XPS and SEM. For an accurate determination of the contamination, the islands' model is required. However, relatively good estimates of backstreaming can be obtained by the simplest ellipsometric model of a single continuous contamination film.

ACKNOWLEDGMENT

The authors would like to thank N. Bogner for part of the data analysis and for typing the manuscript.

[a]Student interns at NASA Lewis Research Center, Cleveland, OH 44135.

[1] H. J. Speier, Preliminary Information Report PIR No. 250, Space Station Freedom Directorate, Lewis Research Center.
[2]S. A. Alterovitz, R. M. Sieg, N. S. Shoemaker, and J. J. Pouch, Mater. Res. Soc. Symp. Proc. **152**, 21 (1989).
[3]R. M. A. Azzam and N. M. Bashara, *Ellipsometry and Polarized Light* (North-Holland, Amsterdam, 1977).
[4]D. E. Aspnes and A. A. Studna, Phys. Rev. B **27**, 985 (1983).
[5]I. H. Malitson, J. Opt. Soc. Am. **55**, 1205 (1965).
[6]D. J. Crawley, E. D. Tolmie, and A. R. Huntress, *Transactions of the Ninth National Vacuum Symposium* (McMillan, New York, 1962), p. 399.
[7]R. L. Kroes, Appl. Opt. **12**, 2075 (1973).
[8]R. H. Muller and J. C. Farmer, Surf. Sci. **135**, 521 (1983).
[9]M. J. Armstrong and R. H. Muller, J. Appl. Phys. **65**, 3056 (1989).
[10]D. E. Aspnes, J. B. Theeten, and F. Hottier, Phys. Rev. B **20**, 3292 (1979).
[11]S. A. Alterovitz, H. J. Speier, R. M. Sieg, and M. N. Drotos (to be published).
[12]D. Jayne, as reported in Ref. 1.
[13]M. H. Hablanian, J. Vac. Sci. Technol. **6**, 265 (1969).
[14]W. M. Langdon and E. G. Fochtman, *Transactions of the 10th National Vacuum Symposium* (McMillan, New York, 1963), p. 128.

N94-20512

The quantum efficiency of HgCdTe photodiodes in relation to the direction of illumination and to their geometry

D. Rosenfeld[a] and G. Bahir
Kidron Microelectronics Research Center, Department of Electrical Engineering, Technion—I.I.T., Haifa, Israel 32000

(Received 6 January 1992; accepted for publication 22 June 1992)

In this paper a theoretical study of the effect of the direction of the incident light on the quantum efficiency of homogeneous HgCdTe photodiodes suitable for sensing infrared radiation in the 8–12 μm atmospheric window is presented. The probability of an excess minority carrier to reach the junction is derived as a function of its distance from the edge of the depletion region. Accordingly, the quantum efficiency of photodiodes is presented for two geometries. In the first, the light is introduced directly to the area in which it is absorbed (opaque region), while in the second, the light passes through a transparent region before it reaches the opaque region. Finally, the performance of the two types of diodes is analyzed with the objective of finding the optimal width of the absorption area. The quantum efficiency depends strongly on the way in which the light is introduced. The structure in which the radiation is absorbed following its crossing the transparent region is associated with both higher quantum efficiency and homogeneity. In addition, for absorption region widths higher than a certain minimum the quantum efficiency in this case is insensitive to the width of the absorption region.

I. INTRODUCTION

The present technology of choice for present and future infrared imaging systems is photovoltaic linear arrays and two-dimensional matrices, which can be coupled with a Si signal processor in the focal plane. The extensive interest in thin films of HgCdTe (either grown on a semi-insulating transparent substrate or thinned from bulk material) is associated with the possibility of illuminating the diodes from one side, and connecting the signal processor on the other side.

For the sake of simplicity we shall consider here only diodes in which the photocurrent is dominated by the contribution of photons absorbed only in one side of the diode. This is frequently the case that occurs when the diffusion length in one side of the junction is very short, or when one of the sides is either based on a wide-band-gap material or is too thin to absorb a significant number of photons. Hence, the photodiodes considered here are based on two different quasineutral regions—a transparent region and an opaque region in which the light is absorbed.

Theoretical and technological considerations usually dictate whether to realize frontside-illuminated diodes with a backside signal processor, or backside-illuminated diodes with a frontside signal processor. However, the analysis shows that the crucial parameter determining the quantum efficiency is the distance of the absorption site from the edge of the depletion region, rather than the side of illumination.

Our investigation will focus on two structures shown in Fig. 1. In the first one, presented in Fig. 1(a), the light reaches the transparent side first (TSF), passes through it and through the depletion region and then is absorbed in the opaque side. In the second structure [Fig. 1(b)], the light reaches the opaque side first (OSF), is partly absorbed there, and only then passes through the depletion region and reaches the transparent side.

Most of the present HgCdTe photodiodes fabricated for the purpose of thermal imaging are included within the above two categories as, for example, the following.

Ion-implanted n^+p photodiodes fabricated on a thin HgCdTe film: due to the small thickness of the implanted n^+ region and to the low-minority-carrier lifetime there, the contribution of the n^+ side to the photocurrent is negligible. As demonstrated by Fig. 1, backside illumination is associated with the OSF configuration, while the frontside illumination is associated with the TSF configuration.

Pn or *Np* diodes realized on heterostructures: usually a structure of a thin narrow-band-gap material layer between a thin wide-band-gap material layer and a semi-insulating transparent substrate. In the case of a one-dimensional array the light can be introduced from either sides of the diodes, while in the case of two-dimensional arrays the light is usually introduced through the semi-insulating substrate (OSF configuration). Regardless of the direction of the illumination, photons with longer wavelengths are absorbed in the narrow-band-gap material only.

Hg-diffused diodes: realized by diffusing Hg into a heavily doped p-type material, forming a thin n-type area. Due to the short minority-carrier lifetime in the p side, the photocurrent is dominated by the contribution of the light absorbed in the n side. The Hg-diffused diodes are usually illuminated through the n side (therefore, OSF). In the case of a thin epitaxially grown p layer the diodes can be illuminated from the opposite side as well (TSF).

In this paper we present a theoretical study of the quantum efficiency of photodiodes fabricated on homogeneous thin films, to determine which of the two geometries renders higher quantum efficiency. Other figures of merit,

[a]Current address: NASA Lewis Research Center, 21000 Brookpark Rd., M/S 54-5, Cleveland, OH 44135.

© J. Appl. Phys. 72 (7), 1 October 1992. Reprinted, with permission, from American Institute of Physics.

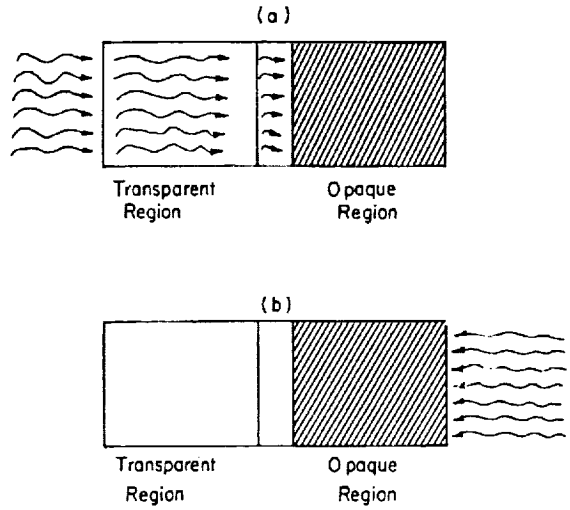

FIG. 1. The two geometrical instances of illumination: (a) the transparent side first (TSF) case, and (b) the opaque side first (OSF) case.

such as noise equivalent temperature difference (NETD) and D_λ^* are proportional to the quantum efficiency. For instance, in the case of background limited-in-performance (BLIP) operation, D_λ^* is given by

$$D_\lambda^* = \frac{R(\lambda)}{[2q(I_d+I_\lambda)]^{1/2}} \cong \frac{\eta(\lambda)\lambda}{hC(2A_d N_0 \eta_{av})^{1/2}}, \qquad (1)$$

where R is the responsivity of the photodiode, I_d and I_λ present the dark current and photocurrent, A_d is the detector's optical area, and N_0 is the photon flux. q, h, and c are constant with their regular meaning. $\eta(\lambda)$ and η_{av} represent the quantum efficiency at wavelength λ and the average quantum efficiency in the relevant spectral region.

The effect of the structure of the device on the quantum efficiency, and the correlation between the quantum efficiency and other figures of merit of the photodiodes, have led to the publication of many works in the literature. van der Wiele[1] solved the one-dimensional diffusion equation in silicon, and presented the quantum efficiency associated with both frontside and backside illuminations. More recently, Rogalsky and Rutkowsky[2] used the above-mentioned equations, and analyzed the quantum efficiency of a PbSnTe one-dimensional diode. Other interesting works are those by Shappir and Kolodny,[3] Levy, Schacham, and Kidron,[4,5] and Briggs[6] who, based on numerical and analytical approaches, presented computer solutions for the two-dimensional and three-dimensional cases.

Most of the published works do not deal with HgCdTe in particular, and therefore rightly ignore the asymmetrical structure which characterize the HgCdTe diodes. Their published analytical equations, for both frontside or backside cases, are rather complicated and therefore the geometrical dependence is concealed. In addition, the wavelength dependence of the absorption coefficient is usually ignored. Levy and co-workers[4,5] did not ignore both the wavelength dependence of the absorption coefficient and the geometrical effects; however, their approach, based on two-dimensional Fourier series, totally concealed the geometrical dependence of the quantum efficiency.

One of the objectives of the theoretical study presented here is to emphasize the geometrical dependence of the quantum efficiency in homogeneous photodiodes and to determine whether the OSF or TSF illumination is preferable. We therefore present in Sec. II a one-dimensional analytical equation which describes the probability of the minority carriers generated at a known distance from the edge of the depletion region, to reach the junction and to participate in the photocurrent. We show that this probability depends strongly on the distance of the absorption site from the edge of the depletion region, and emphasize the importance of absorption close to the junction. In Sec. III we use the above-calculated probability, and Plank's radiation law, and compute the quantum efficiency of OSF and TSF HgCdTe photodiodes in the 8–12 μm region. In Sec. IV we demonstrate the superiority of the TSF geometry by presenting an example based on two HgCdTe photodiodes.

Our study does not take into account effects caused by variation in composition or doping which sometimes occur close to the junction. Thin layers grown by liquid-phase epitaxy and more recently by molecular-beam epitaxy (MBE) or metalorganic chemical-vapor deposition (MOCVD) have composition variation throughout the layer. The resulting electric field accelerates minority carriers toward the junction, regardless of the direction of the illumination, and therefore yields higher quantum efficiencies in both OSF and TSF photodiodes. The gradient in composition results in variations of the absorption coefficient, band gap, intrinsic concentration, and other material parameters, and therefore the complex diffusion equations that yield the quantum efficiency can only be solved using numerical methods. Hence, the study of the quantum efficiency in nonhomogeneous photodiodes is performed separately and will be published elsewhere.

Even though it is shown that the TSF configuration is preferable for photodiodes fabricated on homogeneous material, frequently technological considerations rather than fundamental physical principles dictate the use of the OSF configuration. One of the important technological limitations is that caused by the metal layer which can shield a significant fraction of the incoming light. This limitation, which is usually associated with frontside illumination, can place another limit on the quantum efficiency of both OSF and TSF photodiodes. Consequently, both the TSF and OSF structures are fully analyzed in this paper. The maximal quantum efficiencies as well as the optimal thickness of the absorption volumes, in terms of diffusion lengths, surface recombination velocities, and absorption coefficients, are presented.

II. QUANTUM EFFICIENCY AS A FUNCTION OF ABSORPTION DEPTH

In this section the probability of a minority carrier generated at a distance X_0 from the junction to reach the

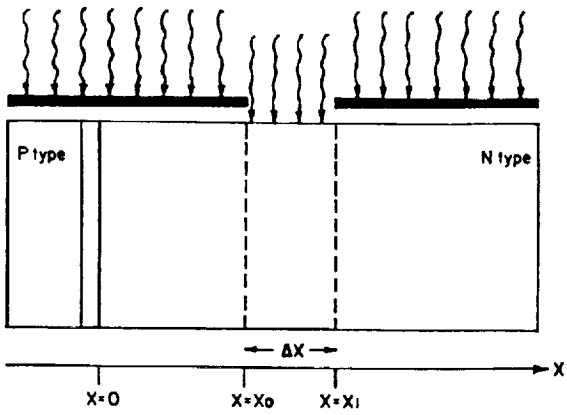

FIG. 2. A photodiode in which the light is uniformly absorbed at a distance of $X_0 < X < X_1$ from the edge of the depletion region.

junction is calculated. This probability is equal to the quantum efficiency associated with photons absorbed at the same distance.

Our assumptions are that both the length and the width of the diode are larger than the diffusion length and therefore the one-dimensional treatment is valid.[5] We also assume low injection conditions, an abrupt junction, a very thin depletion layer, a constant minority-carrier lifetime and a constant dopant concentration along the quasineutral regions.

Let us consider the diode of Fig. 2. Assume that somehow the light is uniformly absorbed only in a narrow n-type volume $A_j\,(X_1-X_0)$ at a distance $X_0<X<X_1$ from the edge of the depletion region. In order to calculate the resulting photocurrent, the steady state of the minority-carrier distribution close to the junction must be found, and therefore the continuity equations for the three regions must be solved,

$$D_p\frac{d^2\hat{p}_1}{dx^2}-\frac{\hat{p}_1}{\tau_p}=0, \qquad 0<x<x_0, \tag{2a}$$

$$D_p\frac{d^2\hat{p}_2}{dx^2}-\frac{\hat{p}_2}{\tau_p}+G_L=0, \qquad x_0<x<x_1, \tag{2b}$$

$$D_p\frac{d^2\hat{p}_3}{dx^2}-\frac{\hat{p}_3}{\tau_p}=0, \qquad x_1<x<d_n, \tag{2c}$$

where p_1, p_2, and p_3 are the minority-carrier concentrations. d_n, D_p, and τ_p represent the width of the neutral region and the minority-carrier diffusion coefficient and lifetime, respectively. The uniform optical generation rate is given by $G_L=N_0/(X_1-X_0)$, where N_0 is the induced photon flux.

The boundary conditions for the problem are

$$\hat{p}_1(0)=\frac{n_i^2}{N_D}\,(e^{qV/kT}-1), \quad \left.\frac{d\hat{p}_3}{dx}\right|_{x=d_n}=\frac{-S_n}{D_p}\,\hat{p}_3(d_n), \tag{3a}$$

$$\hat{p}_1(x_0)=\hat{p}_2(x_0), \quad \hat{p}_2(x_1)=\hat{p}_3(x_1), \tag{3b}$$

$$\left.\frac{d\hat{p}_1}{dx}\right|_{x=x_0}=\left.\frac{d\hat{p}_2}{dx}\right|_{x=x_0}, \quad \left.\frac{d\hat{p}_2}{dx}\right|_{x=x_1}=\left.\frac{d\hat{p}_3}{dx}\right|_{x=x_1}, \tag{3c}$$

where S_n is the surface recombination velocity. Solving the problem for the short-circuit condition, one obtains for the first zone

$$\hat{p}_1(x)=2A\cosh(x/L_p), \tag{4}$$

$$A=-\frac{N_0L_p^2}{D_p(1+K)}\left(\frac{e^{X_0/L_p}-Ke^{-X_0/L_p}-e^{X_1/L_p}+Ke^{-X_1/L_p}}{(X_1-X_0)}\right),$$

$$K=e^{2(d_n/L_p)}\left(\frac{1+\beta}{1-\beta}\right), \quad \beta=S_nL_p/D_p,$$

where L_p is the diffusion length of the minority carriers, given by $L_p=(D_p\tau_p)^{1/2}$. Knowing $p_1(x)$ the diffusion photocurrent can be obtained by

$$I_\lambda=-qA_jD_p\left.\frac{d\hat{p}_1}{dx}\right|_{x=0}$$
$$=qA_jN_0\left(\frac{e^{X_0/L_p}-Ke^{-X_0/L_p}-e^{X_1/L_p}+Ke^{-X_1/L_p}}{(1+k)(X_1-X_0)/L_p}\right). \tag{5}$$

The term in the large parentheses represents the fraction of holes that is collected by the junction, and forms the photocurrent. This fraction can be treated as the quantum efficiency of the diode, while illuminated in the way shown in Fig. 2. Rewriting the quantum efficiency as

$$\left(\frac{e^{X_0/L_p}-Ke^{-X_0/L_p}-e^{X_1/L_p}+Ke^{-X_1/L_p}}{(1+k)(X_1-X_0)/L_p}\right)$$
$$=\frac{1}{(1+K)}\left(\frac{e^{X_0/L_p}(1-e^{\Delta X/L_p})}{\Delta X/L_p}+K\frac{e^{-X_0/L_p}(1-e^{-\Delta X/L_p})}{-\Delta X/L_p}\right), \tag{6}$$

where $\Delta x=X_1-X_0$, and using

$$\lim_{y\to 0}[(1-e^y)/y]=1, \tag{7}$$

we finally obtain

$$\eta'(X_0)=\frac{1}{(1+K)}\,(e^{X_0/L_p}+Ke^{-X_0/L_p}), \tag{8}$$

where η' represents the density of the quantum efficiency of holes generated at a distance X_0 from the edge of the depletion region. It should be emphasized that this quantum efficiency depends on three parameters only: the carrier's initial distance from the depletion region X_0, the parameter β, and the width of the neutral region d_n. It does not depend on the way in which the light is introduced, or on optical parameters such as the absorption coefficient and the photon's energy.

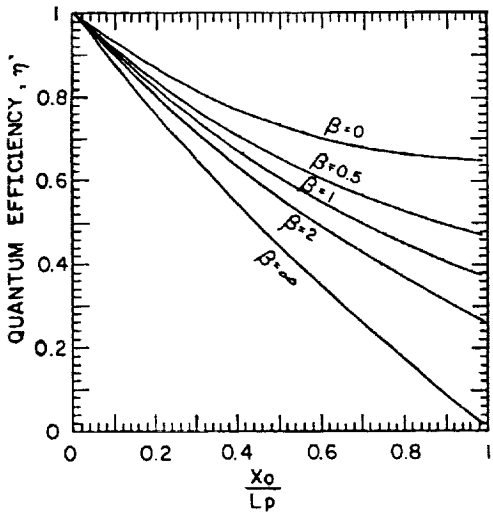

FIG. 3. The quantum efficiency η' given by Eq. (8) as a function of the carrier's initial distance from the junction, with the surface quality as a parameter.

Figure 3 presents the quantum efficiency η' given by Eq. (8) as a function of the distance from the depletion region, with the surface quality as a parameter. It is clearly seen that for all surface conditions, the quantum efficiency dramatically decreases as X_0 increases. Since the distribution of the absorbed photons (and therefore the generated carriers) strongly depends on the way in which the light is introduced, we expect the overall quantum efficiency to be completely different in each configuration. Hence, the preferred side for illumination is the side which is associated with a higher number of photons absorbed close to the junction.

III. THE OVERALL QUANTUM EFFICIENCIES FOR TSF AND OSF CONFIGURATIONS

Let us assume that the photodiodes of Fig. 1 are illuminated with monochromatic photon flux either from their transparent side (a) or from their opaque side (b). Let us further assume that the reflected photon flux in both geometries is negligible. The generation function due to monochromatic photon flux N_0, with wavelength λ, is given in the TSF case by

$$G_L(X,\lambda)=\alpha(\lambda)N_0\,e^{-\alpha(\lambda)X}, \tag{9}$$

where $\alpha(\lambda)$ is the absorption coefficient. Similarly, in the OSF configuration the generation function G_L is given by

$$G_L(X,\lambda)=\alpha(\lambda)N_0\,e^{\alpha(\lambda)(X-d_n)}, \tag{10}$$

where d_n is the width of the quasineutral region.

Since the continuity equation is a linear one, Eqs. (9) and (10) can be used to calculate the quantum efficiencies associated with monochromatic photon flux. For the TSF photodiode the quantum efficiency η_{TSF} is given by

$$\eta_{\mathrm{TSF}}(\lambda)=\int_0^{d_n}\alpha(\lambda)e^{-\alpha(\lambda)X}\frac{1}{(1+K)}\left(e^{X/L_p}+Ke^{-X/L_p}\right)dx$$
$$=\frac{\alpha L_p}{1-\alpha^2L_p^2}\left(\frac{-(\beta-\alpha L_p)e^{-\alpha d_n}+\beta\cosh(d_n/L_p)+\sinh(d_n/L_p)}{\cosh(d_n/L_p)+\beta\sinh(d_n/L_p)}-\alpha L_p\right) \tag{11}$$

while for the OSF photodiode the quantum efficiency η_{OSF} is given by

$$\eta_{\mathrm{OSF}}(\lambda)=\int_0^{d_n}\alpha(\lambda)e^{\alpha(\lambda)(X-d_n)}\frac{1}{(1+K)}\left(e^{X/L_p}+Ke^{-X/L_p}\right)dx$$
$$=\frac{\alpha L_p}{1-\alpha^2L_p^2}\left(\frac{-(\beta+\alpha L_p)+[\beta\cosh(d_n/L_p)+\sinh(d_n/L_p)]e^{-\alpha d_n}}{\cosh(d_n/L_p)+\beta\sinh(d_n/L_p)}-\alpha L_p\,e^{-\alpha d_n}\right). \tag{12}$$

Equations (11) and (12), which present the quantum efficiency in terms of surface conditions, dimensions, and absorption coefficients, are widely known and used in the literature;[1,7,8] however, they give the quantum efficiency associated with the uncommon case of monochromatic photon flux. HgCdTe photodiodes packaged in infrared imaging systems are usually exposed to radiation emitted from bodies with temperatures of about 300 K. Hence, the flux is usually composed of photons of different wavelengths as described by Plank's radiation law. Therefore, the relevant quantum efficiency for both the OSF and the TSF cases should be obtained by integrating the relative contributions of all photons. While doing so, the dependence of the absorption coefficient on the photons' wavelength should be taken into account (see the Appendix). Hence,

$$\eta_{\mathrm{T}}=\frac{\int_{\lambda_{\mathrm{on}}}^{\lambda_{\mathrm{off}}}\eta_{\mathrm{TSF}}(\alpha,\lambda)n(\lambda,T)d\lambda}{\int_{\lambda_{\mathrm{on}}}^{\lambda_{\mathrm{off}}}n(\lambda,T)d\lambda}, \tag{13}$$

$$\eta_{\mathrm{O}}=\frac{\int_{\lambda_{\mathrm{on}}}^{\lambda_{\mathrm{off}}}\eta_{\mathrm{OSF}}(\alpha,\lambda)n(\lambda,T)d\lambda}{\int_{\lambda_{\mathrm{on}}}^{\lambda_{\mathrm{off}}}n(\lambda,T)d\lambda}, \tag{14}$$

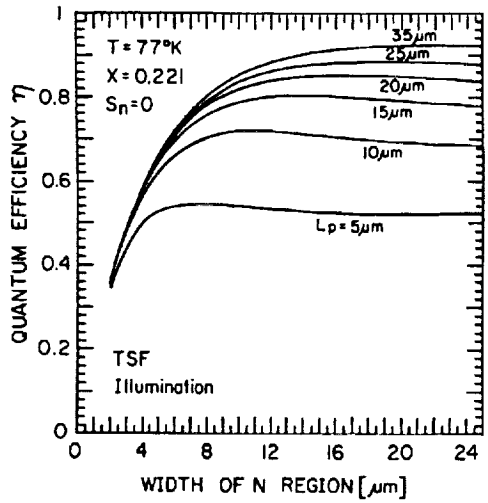

FIG. 4. The quantum efficiency of TSF illuminated $Hg_{1-x}Cd_xTe$ photodiode vs the thickness of the n-type layer with the diffusion length of the holes as a parameter. The bulk composition is $x=0.221$, the hole mobility coefficient is $\mu_p=1000$ cm^2/V S (Ref. 16) and the surface recombination velocity is $S_n=0$.

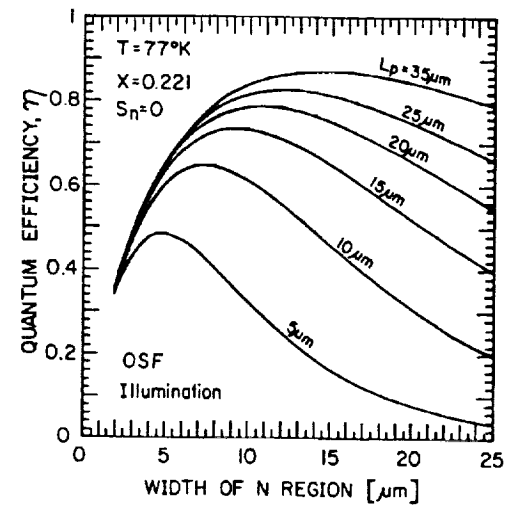

FIG. 5. The same as Fig. 4 for the OSF configuration.

where η_{TSF} and η_{OSF} are given by Eqs. (11) and (12), λ_{on} and λ_{off} are the system's cut-on and cut-off wavelengths, $n(\lambda,T)$ (photons/cm^2 s μm) is the spectral radiant photon emittance of the target as given by Planck's radiation law,[9] and T is the temperature of the target.

IV. RESULTS

Technological considerations rather than fundamental physical principles usually dictate the fabrication of photodiodes based on p-type material, although the longer lifetime of the minority carriers in the n-type material makes it preferable for infrared sensing. However, since our objective is to emphasize the physical and geometrical principles, here we disregard the technological obstacles by assuming that the substrate is a high-quality n-type material. This high-quality material is characterized by high values of both mobility and lifetime of the minority carriers. In addition, we assume in our two example photodiodes excellent surface recombination velocities in both diodes, which yield electrical reflecting conditions for the holes. Hence, the two above-mentioned photodiodes differ only in the direction of illumination.

Figures 4 and 5 show the quantum efficiencies obtained in the two configurations as calculated from Eqs. (13) and (14). Both figures show the quantum efficiency versus the width of the absorption volume with the diffusion length of the minority carriers as a parameter. The hole mobility coefficient was assumed to be $\mu_p=1000$ cm^2/V S (Ref. 10) and the surface recombination velocity was assumed to be very low ($S_n=0$). The hole lifetime varies from 38 nS up to 2 μS which yields minority diffusion lengths from 5 up to 35 μm. We chose $Hg_{1-x}Cd_xTe$ with $x=0.221$ which yields a reasonable value for the cut-off wavelength (11 μm) for a hole lifetime of 100 nS, at 77 K.[11] Consequently, λ_{on} and λ_{off} were taken to be 8 and 11 μm, respectively.

The superiority of the TSF photodiode in the case of reflecting surface conditions is clearly seen. To begin with, the quantum efficiency obtained for the TSF photodiode is always larger than that obtained for the OSF photodiode. In the case of the material with a minority-carrier diffusion length of 35 μm, the maximal quantum efficiencies obtained are 92% and 87%, for the TSF and OSF configuration, respectively. For materials with shorter diffusion lengths the relative difference between the two configurations is even more significant. For example, in the case where $L_p=5$ μm, the maximal values of the quantum efficiencies were 54% and 48%, for the TSF and OSF configurations, respectively.

In addition to the differences in the values of the quantum efficiency, the difference in the sensitivity of the two photodiodes to the width of the n-type layer is obviously noticed. It is clearly seen that in the case of the OSF configuration there is an "optimal" thickness of the n-type layer for each value of the diffusion length. It is also clearly seen that the quantum efficiency is rapidly degrading as the n-type layer thickness deviates from its optimal value; however, in the case of the TSF configuration the quantum efficiency reaches a saturation value which is very close to the maximal value. Therefore, the term "optimal thickness" of the n-type layer, used in the OSF illuminated diode, is not valid, and the term "minimal thickness" should be applied.

The strong dependence of the quantum efficiency on the width of the absorption region, as it exists in OSF illuminated photodiodes, is a serious limitation, since the width of the n-type region can vary along an array of photodiodes. This results in a severe nonhomogeneity in the quantum efficiencies and in the performance of the photodiodes. This yields a significant degradation in the system's figures of merit, such as NET.[12,13]

Excellent surface conditions in HgCdTe are not easily

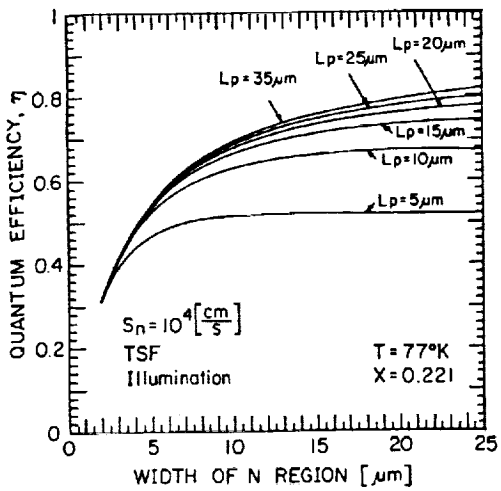

FIG. 6. The same as Fig. 4 but $S_n = 10^4$ cm/s.

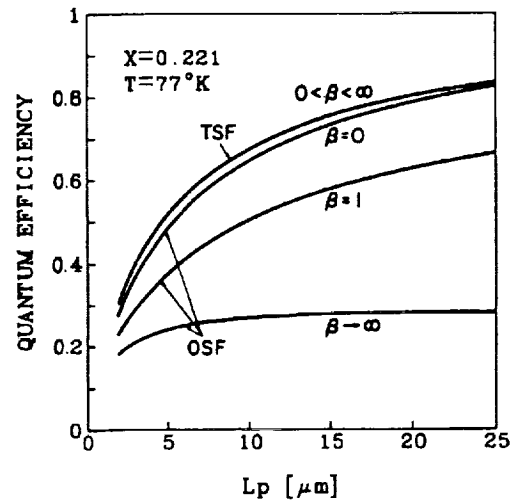

FIG. 8. The maximal quantum efficiency obtained for the OSF case with β as a parameter, and the saturation value of the quantum efficiency obtained for the TSF case.

achieved.[14] Most of the published data concerning the surface recombination velocity in n-type material is related to photoconductors. Since the photoconductors require accumulation conditions, the reported data is of no value to $Hg_{1-x}Cd_xTe$ photodiodes with $x \cong 0.2$, which require a weak depletion condition.[15] Hence, we chose the surface recombination velocity in our example diodes to be 10^4 cm/S, which is a practical value for p-type material.[16]

Figures 6 and 7 show the quantum efficiencies obtained for $S_n = 10^4$ cm/s in the two configurations. Once again, the superiority of the TSF configuration (in terms of high quantum efficiency and homogeneity) is seen very clearly. In addition to the two above-mentioned advantages of the TSF configuration, Figs. 4–7 demonstrate a third one: The TSF illuminated diodes reach a saturation value, and therefore are less sensitive to the surface recombination velocity in the edge of the n-type layer.

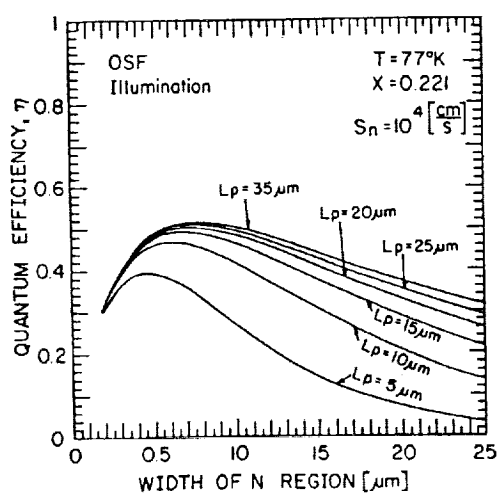

FIG. 7. The same as Fig. 6 for the OSF configuration.

Figure 8 shows the maximal quantum efficiency obtained for the OSF configuration with β as a parameter, as well as the saturation value of the quantum efficiency obtained for the TSF case (which is close to the maximal value). It should be noted, however, that the surface recombination velocity S_n is not constant along the horizontal axis since the diffusion length is changing, and $S_n = (\beta D_p/L_p)$, as indicated by Eq. (4). Figure 8 demonstrates clearly the two advantages of the TSF illumination case: For the same quality of the material (i.e., the same diffusion length) the quantum efficiency associated with the TSF case is always higher than that associated with the OSF case, and does not depend upon the surface condition.

Figure 9 shows the optimal thickness of the n-type layer versus the hole diffusion length with $\beta = 0$, for both TSF and OSF cases. It should be mentioned that in the OSF case, the width drawn in Fig. 9 is the optimal width, and the quantum efficiency rapidly degrades when a different width is applied. In the TSF case, however, the plotted width is the minimal width, and the associated quantum efficiency remains constant for values higher than the minimum.

Figure 9 indicates an additional advantage of the TSF case. For the same diffusion length the thickness of the optimal absorption region associated with the TSF configuration is smaller than that associated with the OSF configuration; hence, there is less diffusion leakage current in the TSF diode.

V. SUMMARY

We have presented a theoretical study of the quantum efficiency of HgCdTe photodiodes fabricated on thin films, with the objective to emphasize the geometrical depen-

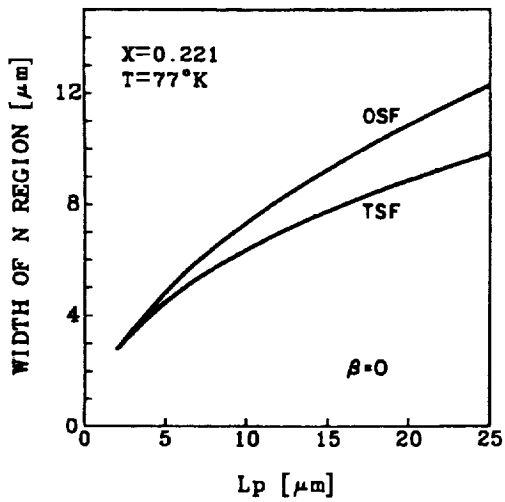

FIG. 9. The thickness of the n-type layer (for which the maximal quantum efficiencies are obtained), vs the diffusion lengths of the holes. This thickness is the minimal thickness in the TSF case, and the optimal thickness in the OSF case.

dence of the quantum efficiency and to determine whether the OSF or TSF configuration is preferable. In particular, we calculated the probability of a carrier to be collected at the junction as a function of its initial distance from the edge of the depletion region. Using the above probability function, we pointed out the importance of inducing absorption close to the junction and suggested that the light should be absorbed after it passes through the transparent region (TSF). Following that, we have calculated the quantum efficiencies for both TSF and OSF illuminated diodes, and showed that the quantum efficiencies associated with the TSF configuration are always higher than those associated with the OSF configuration. In addition, we pointed out the difference in the sensitivity to the thickness of the absorption region. Our calculations show that the quantum efficiency in the OSF instance is dramatically degraded when the absorption thickness differs from the optimal one. We have also shown that, in the TSF case, the quantum efficiency reaches a saturation value, and therefore does not depend on the thickness of the absorption region. Our final conclusion is that the TSF illuminated diodes are much superior sensors for IR thermal imaging.

ACKNOWLEDGMENTS

The authors wish to thank Y. Betser for his help with the numerical calculations, S. Schacham for his helpful remarks, and P. Eliyau for her technical assistance. The editorial assistance of I. Rosenfeld is also acknowledged with thanks.

APPENDIX

The absorption coefficient in semiconductor materials such as HgCdTe is given for energies higher than the band gap by

$$\alpha(x,T,E)=\gamma(E-E_g)^{1/2}, \tag{A1}$$

where E is the energy of the photon, E_g is the band gap, and γ is a coefficient that depends on the material and temperature only. Radiation is absorbed also at energies lower than the band gap, a process known as the Urbach tail.[17] The absorption coefficient associated with the Urbach tail in HgCdTe is given by[18]

$$\alpha(x,T,E)=\alpha_0 e^{[\sigma(E-E_0)/W]}, \tag{A2}$$

where x is the composition, T is the temperature, E is the energy of the photon, and α_0, σ, W, and E_0 are fitting parameters. Finkman and Schacham[19] measured the absorption coefficient over the temperature range 80 K $< T <$ 300 K and obtained

$$E=hc/\lambda \ \text{(eV)},$$

$$\alpha_0=\exp(53.61x-18.88) \ (\text{cm}^{-1}),$$

$$\sigma=3.267\times10^4(1+x) \ \text{(K/eV)},$$

$$W=81.9+T \ \text{(K)},$$

$$E_0=1.838x-0.3424+0.148x^4 \ \text{(eV)}.$$

In a previous work[20] an expression for γ was derived, based on the assumption that the absorption coefficient and its derivative are continuous. Hence,

$$\gamma=(2\sigma e/W)^{1/2}\alpha_0 e^{[\sigma(E_g-E_0)/W]}, \tag{A3}$$

where e is the base of the natural logarithm.

[1] F. van der Wiele, in *Solid State Imaging*, edited by P. G. Jespers, F. van der Wiele, and M. H. White (Leydon, Noordhoff, 1976), p. 47.
[2] A. Rogalsky and J. Rutkowski, Infrared Phys. 22, 199 (1982).
[3] J. Shappir and A. Kolodny, IEEE Trans. Electron Devices ED-24, 1093 (1977).
[4] D. Levy, S. E. Schacham, and I. Kidron, IEDM Tech. Dig. 18, 373 (1986).
[5] D. Levy, S. E. Schacham, and I. Kidron, IEEE Trans. Electron Devices ED-34, 2059 (1987).
[6] R. J. Briggs, IEDM Tech. Dig., p. 165 (1981).
[7] M. B. Reine, A. K. Sood, and T. J. Tredwell, in *Semiconductors and Semimetals*, edited by R. K. Willarson and A. C. Beer (Academic, New York, 1981), Vol. 18, Chap. 6.
[8] E. Zand and Y. Nemirovsky, Infrared Phys. 25, 591 (1985).
[9] J. M. Lloyd, *Thermal Imaging Systems* (Plenum, New York, 1975).
[10] Y. Shacham-Diamond and I Kidron, J. Appl. Phys. 56, 1104 (1984).
[11] Y. Nemirovsky and D. Rosenfeld, J. Appl. Phys. 63, 2435 (1988).
[12] F. D. Shepherd, Proc. SPIE 930, 2 (1988).
[13] N. Bluzer, Proc. SPIE 930, 64 (1988).
[14] Y. Nemirovsky and G. Bahir, J. Vac. Sci. Technol. A 7, 450 (1989).
[15] G. Bahir and D. Rosenfeld (unpublished).
[16] E. Finkman and S. E. Schacham, J. Vac. Sci. Technol. A 7, 464 (1989).
[17] F. Urbach, Phys. Rev. 92, 1324 (1953).
[18] E. Finkman and Y. Nemirovsky, J. Appl. Phys. 50, 4356 (1979).
[19] E. Finkman and S. E. Schacham, J. Appl. Phys. 56, 2896 (1984).
[20] D. Rosenfeld, D.Sc. thesis, Technion—I.I.T, Haifa, Israel, 1989.

SECTION THREE

HIGH TEMPERATURE SUPERCONDUCTIVITY

PRECEDING PAGE BLANK NOT FILMED

N94-20513

Space Applications of Superconducting Microwave Electronics at NASA Lewis Research Center

R. F. Leonard, K. B. Bhasin, R. R. Romanofsky, and C. D. Cubbage
NASA Lewis Research Center
Cleveland, Ohio

C. Z. Chorey
Sverdrup Corp.
Cleveland, Ohio

ABSTRACT

Since the discovery of high temperature superconductivity in 1987, NASA Lewis Research Center has been involved in efforts to demonstrate its advantages for applications involving microwave electronics in space, especially space communications. The program has included thin film fabrication by means of laser ablation. Specific circuitry which has been investigated includes microstrip ring resonators at 32 GHz, phase shifters which utilize a superconducting, optically activated switch, an 8x8 32 GHz superconducting microstrip antenna array, and an HTS-ring-resonator stabilized oscillator at 8 GHz. The latter two components are candidates for use in space experiments which will be described in other papers. Experimental data on most of the circuits will be presented as well as, in some cases, a comparison of their performance with an identical circuit utilizing gold or copper metallization.

THIN FILM FABRICATION

High quality thin films of YBCO have been deposited by means of ablation of stoichiometrically correct targets by a pulsed excimer laser [1,2]. The facility is shown schematically in Figure 1

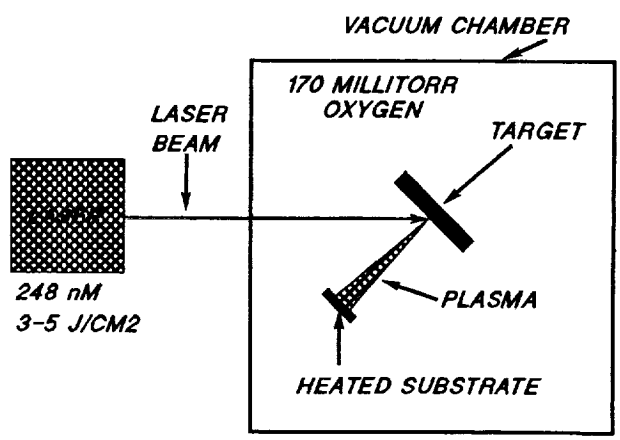

Figure 1. Laser Ablation Facility

A typical deposition is carried out by evacuating the sample chamber to $3x10^{-7}$ torr or less, warming the substrate to near 500C, introducing a continuous flow of oxygen (120 sccm) into the chamber, and heating the sample to 775°C. During deposition, chamber pressure is approximately 170 mtorr. The laser wavelength is 248 nm; the energy density is typically 1.5 J/cm^2/pulse, with a pulse repetition rate of 4 pps. Following deposition, the oxygen pressure is raised to 1

© Reprinted from Applied Superconductivity, vol. 1, nos. 7-9, pp. 1341-1347, 1993, with kind permission from Pergamon Press Ltd., Headington Hill Hall, Oxford 0X3 0BW, UK.

PRECEDING PAGE BLANK NOT FILMED

atmosphere and the sample allowed to cool prior to removal from the chamber.

Using this technique, strongly c-axis oriented YBCO films have been deposited on strontium titanate, lanthanum aluminate, and MgO. The most useful of these, in terms of the film characteristics and the microwave properties of the substrate, are those on lanthanum aluminate, where a Tc of 90.6K was achieved, with a critical current density of $2x10^6$ amps/cm^2 at 77K. A typical measurement of DC resistance vs. temperature is shown in Figure 2.

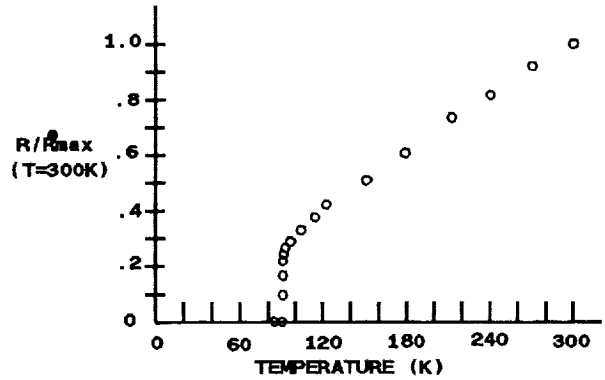

Figure 2. Measured DC Resistance of YBCO Film

MICROWAVE CIRCUITS

Microstrip Ring Resonators

Among the first microwave circuits to be fabricated and tested was the microstrip ring resonator at 35 GHz [3,4]. A schematic diagram of this device is shown in Figure 3.

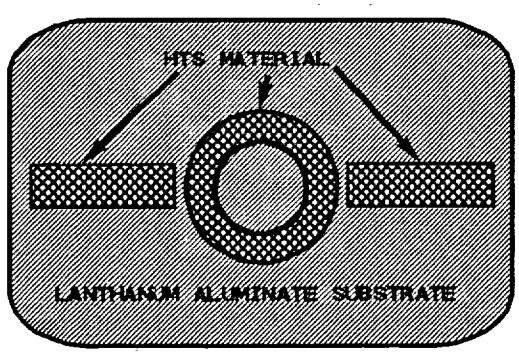

Figure 3. Microstrip Ring Resonator

Q-values of such devices yield realistic estimates of the microwave performance of superconducting circuits since they reflect both conductor and dielectric losses, as would a functional application. Results for two such resonators, one fabricated from YBCO and the other from $Tl_2Ca_2Ba_2Cu_3O_x$ (TCBCO), deposited at the University of Cincinnati, are shown in Figure 4.

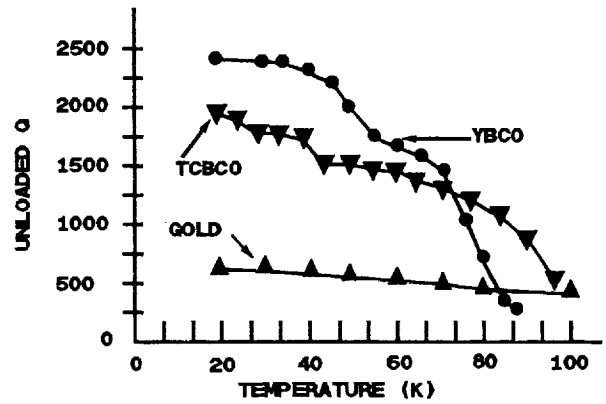

Figure 4. Unloaded Q Values for Ring Resonators at 35 GHz

Both circuits use a normal metal ground plane. It is clear that at 35 GHz, neither superconducting resonator is much superior to an identical gold circuit. At lower temperatures, however, the Q of the YBCO resonator is four to five times that of gold, while the TCBCO one is approximately three times that of gold.

Superconducting Phase Shifters

One device which, in principle, could benefit greatly from the use of superconductivity is the true-time-delay phase shifter. Such a circuit, which is required for electronically steered phased array antennas, switches an RF signal between two alternate paths, one of which is physically longer than the other so as to provide a true time delay phase shift. Such devices, using a field effect transistor as the active switching element, will typically exhibit insertion losses of one or two dB, so that a five bit phase shifter, as would be required in order to obtain phase resolution of 11.5 degrees would suffer a loss of 5 to 10 dB. The use of a superconducting patch as the switching element should provide considerable improvement. The layout for such a phase shifter is shown in Figure 5.

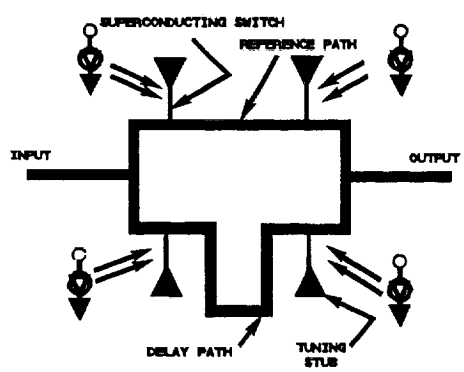

Figure 5. Optically Activated HTS Phase Shifter

Such a device, utilizing bolometric switching from normal to superconducting state, with the heat being delivered optically via optical fiber, has been fabricated at NASA Lewis. Preliminary results indicate that switching times on the order of 100 milliseconds are achievable in this manner. Unfortunately, this is only marginal for most antenna beam steering applications. Thermal analysis indicates that

faster switching times are unlikely unless a low thermal conductivity substrate with acceptable microwave properties can be identified. A possible candidate for such a material is yttrium-stabilized zirconia (YSZ), which has been used in the fabrication of another device. Data for this circuit are not yet available.

Microstrip Array Antennas

Dinger [5] has shown that the gain of a multielement microstrip array at millimeter wave frequencies is limited by the ohmic losses in the power divider network, which becomes increasingly complex as the number of radiating elements increases. Work at NASA Lewis, carried out in collaboration with Ball Aerospace, has produced a 64 element (8x8) array antenna operating at 35 GHz. The superconducting film is TCBCO, which is deposited on a two-inch diameter lanthanum aluminate substrate. The TCBCO film was fabricated by Superconductor Technologies Inc., while the array was designed and fabricated by Ball and tested at NASA Lewis. A photograph of the array in its test fixture is shown in Figure 6.

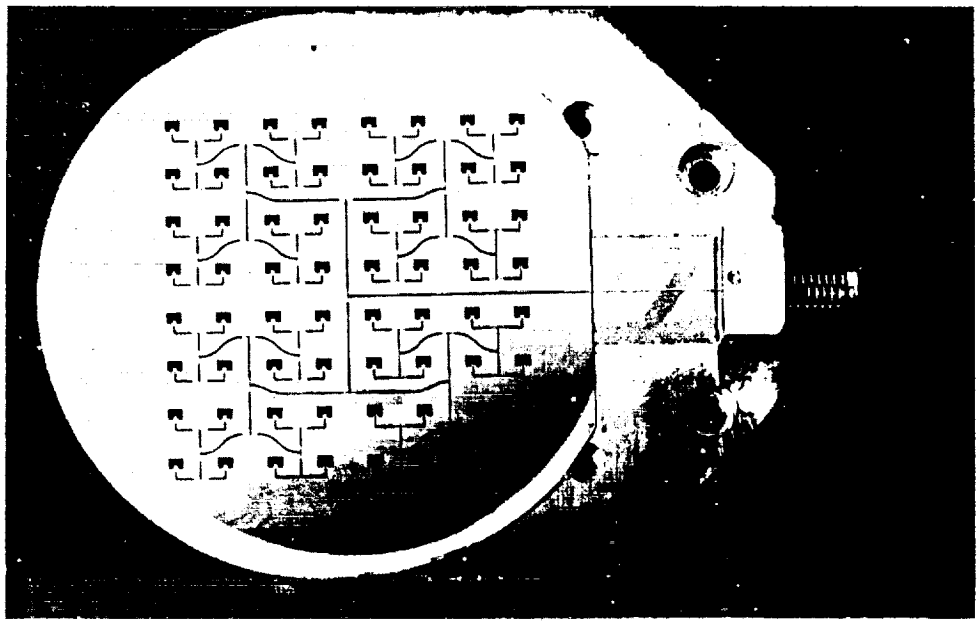

Figure 6. 64-Element Microstrip Antenna Array

Results of gain tests, using the antenna as a receiver are shown in Figure 7.

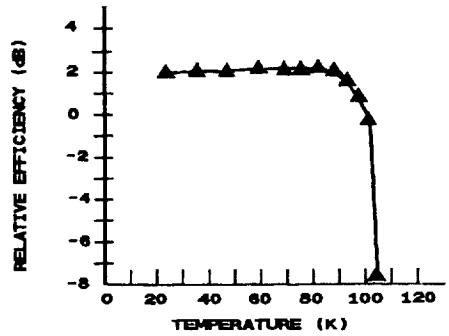

Figure 7. Efficiency of 8x8 Superconducting Array Relative to an Identical Gold Array at the Same Temperature.

As is clearly demonstrated, at 35 GHz, the superconducting 8x8 array and power divider network have approximately 2 dB higher gain than an equivalent cooled gold antenna. Relative to a gold array at room temperature, the HTS antenna exhibited an improvement of approximately 5 dB at temperatures below 90K.

HTS-Resonator-Stabilized Oscillator

By using planar resonators fabricated from superconducting films, it should be possible to implement stable microwave oscillators, such as are now designed using crystal oscillators or dielectric-resonator-stabilized oscillators (DRO). Such a structure would be highly amenable to integration with semiconductor components and would have the advantages of reduced circuit complexity and increased reliability, with only a small sacrifice in performance. Typically, one would anticipate unloaded Q's near 10,000 (at 8 GHz) from a planar superconducting resonator, as compared with the 10,000 to 20,000 possible from a DRO, and the 1000 possible for a planar structure using normal metals. Such a Q should make possible a superconductor-stabilized oscillator with a phase noise better than -100dBc/Hz. Although data is not yet available, the design for such a resonator is complete, and is shown in Figure 8.

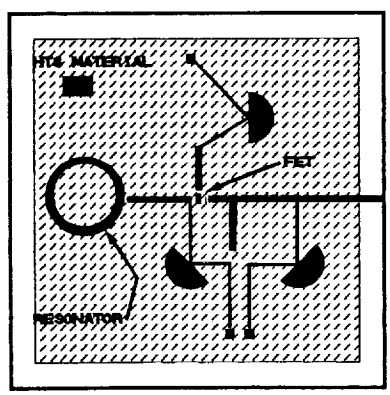

Figure 8. Layout of an HTS-Resonator-Stabilized Oscillator

CANDIDATE FLIGHT EXPERIMENTS

Shuttle/ACTS Communications Experiment

The antenna described above, combined with an appropriate phase shifter is intended to be the forerunner of a steerable array which can

be installed on the space shuttle to form the receive terminal of an earth-to-geo-leo 30/20 GHz communications link. A schematic representation of the experiment is shown in Figure 9.

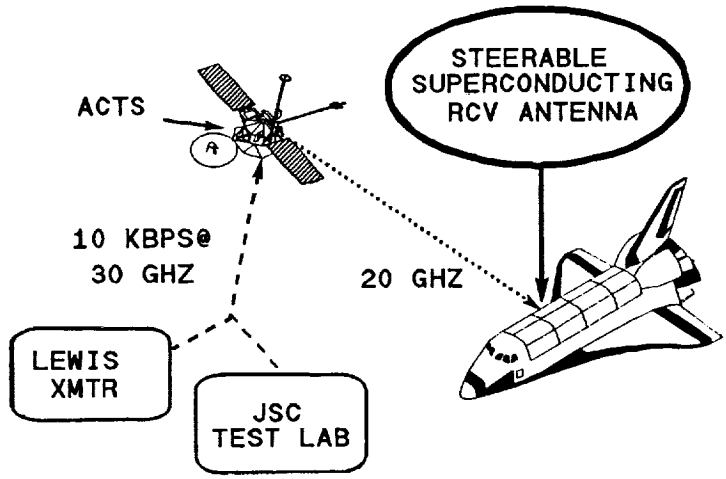

Figure 9. Schematic Representation of ACTS/Shuttle Communications Experiment Using an HTS Antenna

Details of the experiment are described in another paper [6] at this conference.

HTSSE-II

Together with JPL, NASA Lewis is developing a low noise receiver as a candidate to be flown on NRL's HTSSE-II flight experiment [7]. An overall block diagram of the receiver is shown in Figure 10.

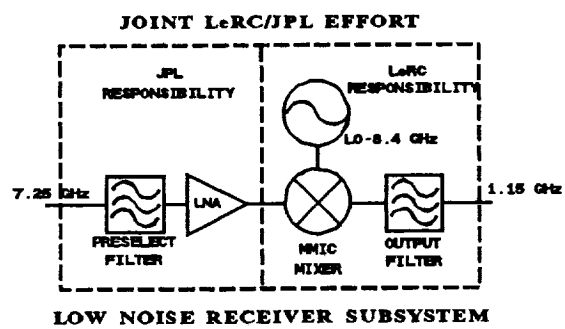

Figure 10. Block Diagram of Lewis/JPL HTSSE-II Receiver

The receiver will employ the superconducting oscillator described earlier in this paper, a superconducting input filter, together with cryogenically-cooled, normal metal low noise amplifier and mixer, both of which will utilize conventional semiconductor components. More details of the experiment are given in another paper at this meeting [8].

REFERENCES

1. Warner, J.D., Bhasin, K.B., Varaljay, N.C., Bohman, D.Y., and Chorey, C.M., "Growth and Patterning of Laser Ablated Superconducting $YBa_2Cu_3O_7$ Films on $LaAlO_3$ Substrates, NASA Technical Memorandum 102346. Prepared for the 36th National Symposium and Topical Conference sponsored by the American Vacuum Society, Boston MA, October 23-27, 1989.

2. Warner, J.D., Meola, J.E., and Jenkins, K.A., "Study of Deposition of $YBa_2Cu_3O_{7-x}$ on Cubic Zirconia. NASA Technical Memorandum 102350, 1989.

3. Chorey, C.M., Kong. K., Bhasin, K.B., Warner, J.D., and Itoh, T., "YBCO Superconducting Ring Resonators at Millimeter Wave Frequencies", IEEE Transactions on Microwave Theory and Techniques, 39, pp. 1480-1486 (1991).

4. Bhasin, K.B., Warner, J.D., Romanofsky, R.R. Heinen, W.O., and Chorey, C.M., IEEE MTT-S International Microwave Symposium Digest, 1, pp.269-272, (1990).

5. Dinger, R.J., "Some Potential Antenna Applications of High Temperature Superconductors", Journal of Superconductivity, 3, pp. 287-296, (1990).

6. Ngo,P., Krishen,K., Arndt,D., Raffoul,G., Karasak,G., Bhasin,K., and Leonard,R., "A High Temperature Superconductivity Communications Flight Experiment", Proceedings of 3rd International World Congress on Superconductivity, September, 1992.

7. Lichtenberg,C.L., Kawecki,T.G., Johnson,M.S., and Niesenoff,M., "The High Temperature Superconductivity Space Experiment", Proceedings of 3rd International World Congress on Superconductivity, September, 1992.

8. Chew,W., Barner,J.B., Bautista,J.J., Bhasin,K.B., Chorey,C.M., Foote,M.C., Fujiwara,B.H., Hunt,B.D., Leonard,R.F., Ortiz,G.G., Rascoe,D.L., Romanofsky,R.R., and Vasquez,R.P., "Low Noise Receiver Downconverter Using High Critical Temperature Superconductor Films", Proceedings of 3rd International World Congress on Superconductivity, September, 1992.

N94-20514

Y-Ba-Cu-O SUPERCONDUCTING/GaAs SEMICONDUCTING HYBRID CIRCUITS FOR MICROWAVE APPLICATIONS

K. B. Bhasin*, S. S. Toncich*, C M. Chorey**, N. J. Rohrer*** and G.J. Valco***
* National Aeronautics and Space Administration
Lewis Research Center, Cleveland, Ohio 44135
** Sverdrup Technology, Brook Park, Ohio 44142
*** Department of Electrical Engineering
Ohio State University, Columbus, Ohio 43210

ABSTRACT

We have combined a two pole superconducting bandpass filter with a packaged GaAs low noise amplifier, and have designed, fabricated, and tested a superconducting X-band oscillator. Both circuits have been compared to normal metal circuits at 77K. This paper presents the results of these experiments, technical issues, and potential applications.

INTRODUCTION

Before the discovery of high temperature superconducting (HTS) materials, the integration of low-Tc superconductors with semiconducting devices was not feasible since many semiconducting devices experience carrier freeze-out below 10K. Demonstrations of HTS passive microwave components operating at liquid nitrogen (77K) temperatures [1,2] has enhanced the feasibility of integrating HTS passive components with semiconductors to achieve high performance microwave systems [3]. GaAs and heterostructure microwave semiconducting devices make strong candidates for integration since they have much lower noise figures at 77K [4,5] than at 300K, while the operating temperature of 77K also avoids the problem of carrier freeze-out. To achieve the maximum benefit of HTS materials the level of integration between passive and active elements must be increased to the point where entire systems can operate reliably at liquid nitrogen temperatures for extended periods of time.

Integration of passive HTS devices with semiconductor devices can be achieved from the discrete component level up to the system level. Such a progression is shown in Figure 1. Levels 1 and 2 are now feasable due to the demonstration of high Tc superconducting microwave devices. Level 3 work is in the early stages at the present time. To determine the performance advantages at the subsystem level, we have combined a two pole superconducting bandpass filter with a packaged GaAs low noise amplifier (LNA), and compared its performance with a gold filter/LNA hybrid circuit down to 35K. At the circuit level, we have designed, fabricated, and tested an X-band hybrid superconducting/GaAs oscillator on a single lanthanum aluminate substrate, where a high Q superconducting resonator is used for stabilization of the oscillator. High quality Y-Ba-Cu-O (YBCO) superconducting films were used in both experiments.

BPF/LNA HYBRID CIRCUIT

Several two-pole bandpass filter were designed with a 2.5 percent bandwidth, 0.5 dB passband ripple, and 7.5 GHz center frequency. The filters were fabricated using laser ablated YBCO superconducting films (approx. 5000A) on a 0.01 inch lanthanum aluminate substrate. Gold film deposited by E-beam evaporation on the opposite side of the substrates formed ground planes for the circuits. An identical filter using gold film for the microstrip was also fabricated.

The LNA selected was an Avantek PGM 11421 with a specified bandwidth of 4 to 11 GHz, a gain of 8.0 dB, and a noise figure of 2.5 dB. A diagram of the hybrid is shown in Figure 2. The devices were connected by 0.010 inch gold bond wires to a 50 ohm microstrip line that was fabricated on a 0.01 inch thick Duroid (ϵ_r=2.3) substrate. The hybrid was mounted on a brass test fixture using a conductive epoxy. SMA female flange connectors were used for the microstrip to coax transition.

All cryogenic measurements were made inside a closed cycle cryostat which has semi-rigid coaxial cables providing a connection between the

PRECEDING PAGE BLANK NOT FILMED

two temperature environments. An HP 8510B automatic network analyzer (ANA) was used to measure insertion gain or loss. A full two port calibration was performed inside the cryostat so as to move the reference planes of the ANA to the ends of these cables. Since this experiment is concerned only with relative changes in system performance, a two port cal was chosen over a TRL or LRL, that would have moved the reference planes of the ANA onto the test fixture. Noise figure measurements were made on a HP8970A noise figure meter, with loss compensation used to account for the test fixture's contribution to the system noise figure.

The LNA and filters were tested individually to determine their gain or loss and noise figures at T=300K and 77K. The HTS filter showed a significantly smaller insertion loss than the gold filter at 77K, due to the near elimination of conductor loss in the YBCO film compared to the gold conductor. Most of the HTS filter loss is due to the gold ground plane; if it were replaced with HTS material the insertion loss would be nearly eliminated. At 77K the gold hybrid shows a noise figure improvement of 3.5 dB compared to 300K, while the HTS hybrid shows a 5.5 dB improvement compared to gold at 300K. These results are shown in Figure 3. The gain of the HTS hybrid is greater than the gold hybrid due to lower insertion loss in the HTS filter [6].

SUPERCONDUCTING OSCILLATOR

The high "Q" observed in superconducting resonator circuits [7] can be exploited in low phase noise hybrid oscillator design. These oscillators have the potential to replace dielectric resonator stabilized oscillators in cryogenic applications.

Several hybrid GaAS/superconducting microwave oscillators were fabricated on $1cm^2$ lanthanum aluminate substrates and tested. The design used a ring resonator in the reflection mode. A ring with a resonant frequency of 10 GHz was placed a quarter wavelength from the drain of the FET, parallel coupled to the output transmission line with a coupling gap 40 microns long. The oscillator output was taken at the drain. The best circuit had an output power of 6.4 dBm at 77K, which corresponds to an efficiency of 10.4%. The layout of the oscillator circuit is shown in Figure 4. For the HTS circuits, the transmission lines, rf chokes (radial stubs), and bias lines were fabricated using YBCO films, only the ground planes were fabricated in gold.

Toshiba low noise GaAs FETs (JS8830-s) were used in the design. Their S-parameters were measured from 4 to 26.5 GHz, over temperatures from 300K to 40K under a bias of I_{ds}=10ma and V_{ds}=3V. V_{gs} was adjusted from -1.04V at 300K to -1.19V at 40K to maintain the desired bias condition. Of all the S-parameters measured, the magnitude of S_{21} showed the most variation over temperature, due to the increased electron mobility as the temperature was decreased. The S-parameter measurements from 15 to 26.5 GHz were unreliable due to a loss of calibration at those frequencies at the lower temperatures. This was most noticable in the values for S_{22}. This problem has been reported before [8]. The oscillator circuit design based on the measured S-parameters at 77K, was performed, and then optimized using Touchstone [9].

Both copper and HTS circuits were fabricated and tested for comparison purposes. They were mounted on a brass test fixture inside a closed cycle cryostat. The circuits oscillated at 10 and 20 GHz, the 20 GHz signal was 20 dB below the fundamental. The copper circuit showed little frequency sensitivity to temperature, varying about -70 kHz/K from 25K to 100K. The best HTS circuit showed a sensitivity of -10 MHz/K in the vicinity of 77K. This oscillator worked up to 87K. Figure 5 plots output power vs. temperature for several circuits and Figure 6 shows output frequency vs. temperature.

The frequency of the copper circuit changed very little. The power decreased from 4.8 dBm at 25K to 2.8 dBm at 100K. The efficiency of the circuit at these bias conditions at 77K was 4.1%.

TECHNICAL ISSUES

It should be noted that temperature cycling of devices or systems is probably the most stressful thermal condition that can be placed on them. On the other hand, operation at stable cryogenic temperatures for extended periods of time should enhance the performance of semiconducting devices. Besides lower noise figures, cryogenic operation will in general lead to lower power consumption, longer device life due to the ease with which device power

may be dissipated, and more uniform device characteristics.

Our closed cycle cryocooler relies on a pump to achieve the desired temperature. The pump introduces a vibration into the cold finger on which the device under test (DUT) is mounted. We have found that this vibration can lead to broken external bond wires if insufficient attention is paid to layout and assembly of the DUT. Internal bonds in the packaged device appear to be unaffected. The vibration also caused instability in the HTS oscillator circuit.

CONCLUSIONS

A two-pole HTS BPF/LNA hybrid has been fully characterized at 77K and its performance compared to that of a normal metal hybrid. The hybrid showed a 2.1 dB noise figure improvement and a 0.5 dB gain improvement at 77K as compared to the gold filter/ LNA hybrid. Repeated cycling over temperature showed no adverse effects on the hybrid or in the performance of the commercial LNA. There was no loss in the hermeticity of the package. Several other LNAs were also tested and similar results obtained.

The power supply to the LNA's was turned on during the entire time the hybrid was being cooled. The resulting power dissipation inside the package undoubtedly raised the temperature inside the package above 77K and prevented the nitrogen gas backfill from condensing. This was seem as a benefit since condensation of the backfill in the package could have caused short circuits. Also, the primary goal of the experiment was to integrate the HTS BPF with a commercial LNA at 77K, any further system level performance improvement due to cooling the LNA is an added benefit.

The results of superconducting oscillators were presented and their performance compared to that of similar circuits fabricated from copper. The oscillator designs were optimized for operation at 77K, rather than designed for room temperature operation and then cooled.

In deep space communications, radio astronomy and radiometer applications, low noise/low loss requirements are usually met by cooling microwave components. Long term system reliability is also critical, since there is usually no option to service the equipment once it is launched. The ability to integrate larger systems in a cryogenic environment is contingent on reliable unattended performance. Our results on the BPF/LNA hybrid and the superconducting oscillator would indicate that reliable operation is possible without radical departures from present design techniques used for space systems.

REFERENCES

1. IEEE Trans. Microwave Theory and Tech. Special Issue on Microwave Applications of Superconductivity, vol.39, September 1991.

2. D.C. Webb and M. Nisenoff,"The High Temperature Superconductivity Space Experiment," Microwave Journal, September 1991, pp 85-91.

3. T. Van Duzer, "Superconductor-semiconductor hybrid devices, circuits and systems", Cryogenics, Vol. 28, pp.527-531, 1988

4. M.W. Pospieszalski, S. Weinreb, R.D. Norrod, and R. Harris, "FET's and HEMT's at cryogenic temperatures-their properties and use in low-noise amplifiers,"IEEE Trans. Microwave Theory and Tech., Vol.36, pp.552-560, 1988.

5. S.S. Toncich, K.B. Bhasin, T.K Chen, and P.C. Claspy,"Performance of a wideband GaAs low noise amplifier at cryogenic temperatures" to be published in the July 1992 issue of Microwave and Optical Tech. Lett.

6. K.B. Bhasin, S.S. Toncich, C.M. Chorey, R.R. Bonetti, and A.E. Williams, "Preformance of a Y-Ba-Cu-O superconducting filter/GaAs low noise amplifier hybrid circuit," 1992 MTT-S International Microwave Symposium, Albuquerque, NM, June 2-4, 1992.

7. C.M. Chorey, K. Kong, K.B. Bhasin, J.D. Warner, and T. Itoh," YBCO Superconducting ring resonator at millimeter wave frequencies", IEEE Trans. on Microwave Theory and Tech., Vol. 39, No. 9, p. 1480, Sept. 1991.

8. J.W. Smuk, M.G. Stubbs, and J.S. Wight,"Vector measurement of microwave device at cryogenic temperatures", IEEE Trans. Microwave Theory and Tech., Vol. MTT-S, p. 1195, 1989.

9. EEsof, Westlake Village, CA

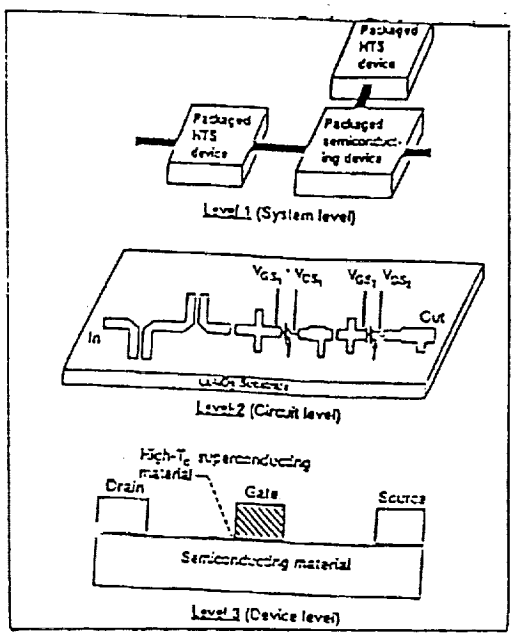

Figure 1
Possible levels of integration

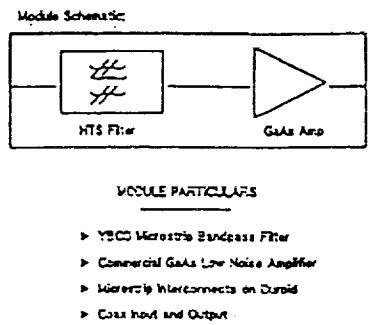

Figure 2
BPF/LNA combination

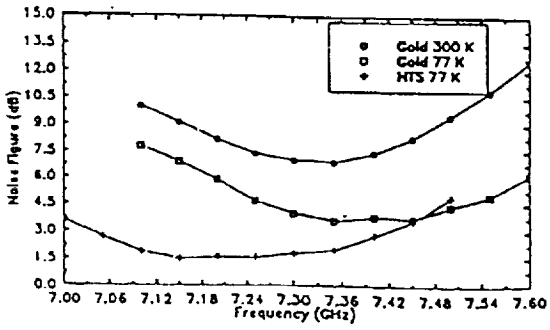

Figure 3
Noise figure for BPF/LNA combination

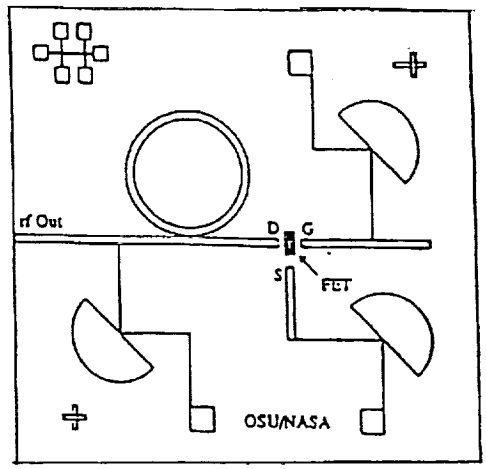

Figure 4
Oscillator layout

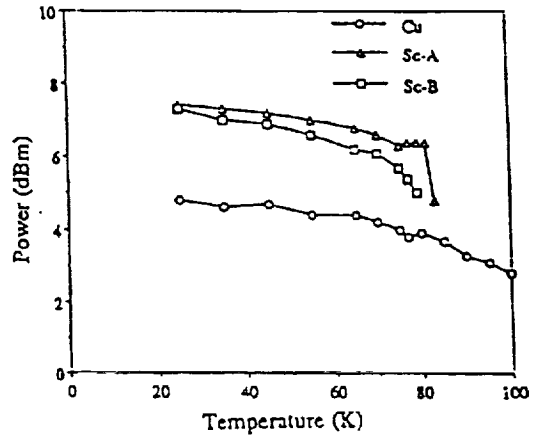

Figure 5
Output power vs. temperature

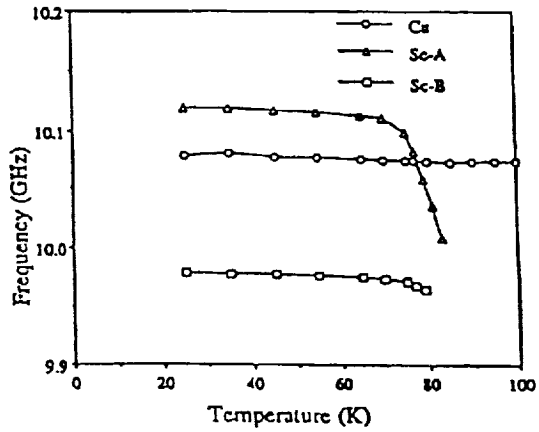

Figure 6
Output frequency temperature

A HIGH TEMPERATURE SUPERCONDUCTIVITY COMMUNICATIONS FLIGHT EXPERIMENT

P. Ngo, K. Krishen, and D. Arndt
NASA Johnson Space Center
Houston, Texas

G. Raffoul and V. Karasak
Lockheed
Houston, Texas

K. Bhasin and R. Leonard
NASA Lewis Research Center
Cleveland, Ohio

ABSTRACT

A high-temperature superconductivity (HTSC) flight experiment from the payload bay of the Space Shuttle Orbiter to the Advanced Communications Technology Satellite (ACTS) is being breadboarded. This proposed experiment, a joint project between the Johnson Space Center and the Lewis Research Center, would use a Ka-band (20 GHz) HTSC phased array antenna and front-end electronics (low-noise amplifier) to receive a downlink communications signal from the ACTS. A conventional receiver demodulates the encoded telemetry signal which is then turned around and transmitted back to ACTS and the ground.

The HTSC phased array has nine 4 x 4 microstrip patch antenna subarrays which when properly phased, provide approximately 24 dB of boresight gain. A 2 x 2 HTSC microstrip patch has been built and tested. A Ka-band receiver, transmitter, modem, encoder, decoder, etc., are now being built and tested. Link analyses and interface problems with the Orbiter are addressed in the paper in addition to the design, fabrication, and testing of various subsystems used in the communication link.

1.0 INTRODUCTION

The recent discovery of high temperature superconductors (HTSC) has focused attention towards the search for applications that will enhance the performance of communications systems. With the natural cooling abilities of space under certain conditions, potential space applications are attractive. One application is the use of HTSC materials in microwave and millimeter-wave feed networks for large antenna arrays. This application could enhance the communications system performance primarily by reducing front-end losses, but also allowing the replacement of bulky waveguide feed structures with smaller, high performance planar structures.

© Reprinted from Applied Superconductivity, vol. 1, nos. 7-9, pp. 1349-1361, 1993, with kind permission from Pergamon Press Ltd., Headington Hill Hall, Oxford 0X3 0BW, UK.

This paper describes a proposed HTSC millimeter-wave communications flight experiment between a Shuttle Orbiter in low-earth-orbit and the Advanced Communications Technology Satellite (ACTS) in geosynchronous orbit. The experiment involves a Ka-band, superconducting phased array antenna with the front-end electronics developed by the Lewis Research Center (LeRC) and the receiver, with appropriate interfaces in an Orbiter's payload bay developed by Johnson Space Center personnel. Breadboard hardware for the various experiment is 1996. The advantages of such an experiment include: (1) the first use of a complete HTSC communications system operating in a manned spacecraft environment, (2) an evaluation of the thermal interfaces, cooling rates, and interfaces required for an HTSC system to work in an operational space environment, (3) provide direct distribution of data from the ground to a spacecraft without the additional hops involved in the present communication links through the Whites Sands facility, and (4) the first utilization of the 19.7 GHz forward link from the ACTS to an orbiting spacecraft.

2.0 SYSTEM CONFIGURATION

The ACTS is an experimental, geosynchronous satellite scheduled to be launched in July 1993 with a 4-year expected operational lifetime. This satellite which has been designed and developed by the LeRC, provides spot beams to fixed ground locations within the United States. It also has a 1.1 meter, computer steerable antenna which can communicate with low-earth orbiting (LEO) spacecraft. The system configuration, as shown in Figure 1, has an uplink subsystems are being built and tested. The expected time-frame for the

signal at 29.5 GHz which is transmitted from the Electronic Systems Test Laboratory at JSC or from the LeRC to the ACTS. The signal is received by the 2.2m antenna on the ACTS, routed via a matrix switch to the 1.1m antenna which transmits the signal at 19.7 GHz to the Orbiter. This is a bent-pipe mode within the ACTS with a 900 MHz IF bandwidth. The maximum Doppler shift during the experiment is approximately 500 MHz which exceeds the capability of the ACTS baseband processing mode (demodulation/modulation).

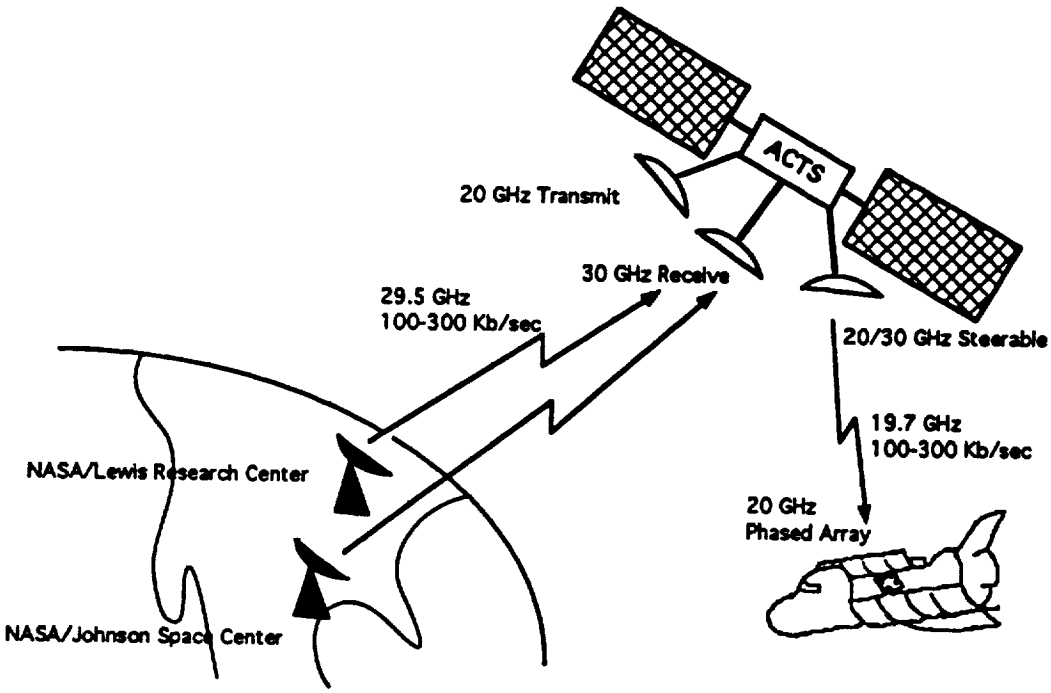

Figure 1 - ACTS 20/30 GHz Flight Experiment

The experiment program includes development of the space hardware for the Orbiter as well as ground transmitting equipment needed in the ESTL. In addition, the program includes certification testing and documentation required for flight on the Orbiter, integration into the payload bay, and the interfaces with the other Orbiter equipment. Certification testing includes four areas: thermal vacuum, vibration, structural loads, and electromagnetic interference (EMI). The experiment is categorized as a Class C payload (economically reflyable or repeatable) with no Orbiter impacts in the event of an experiment failure.

A detailed block diagram of the spacecraft equipment is given in Figure 2. The HTSC antenna could be a circular polarized phased array with nine subarrays; each subarray has 4 x 4 microstrip patch antennas. This antenna will be discussed in detail later in the paper. The antenna has approximately 25 dB of gain with a 10° half-power beamwidth. Each of the nine subarray feeds a low-noise amplifier (LNA), followed by a monolithic microwave integrated circuit (MMIC) phase shifter. The phase shifters are controlled by a dedicated antenna controller which takes the Orbiter's state vector available from the payload interface panel and calculates the required phase shifter settings to electronically point the beam. Mechanical pointing requirements, as determined by the 3 dB beamwidth of a subarray, is approximately +/- 15° for boresight alignment.

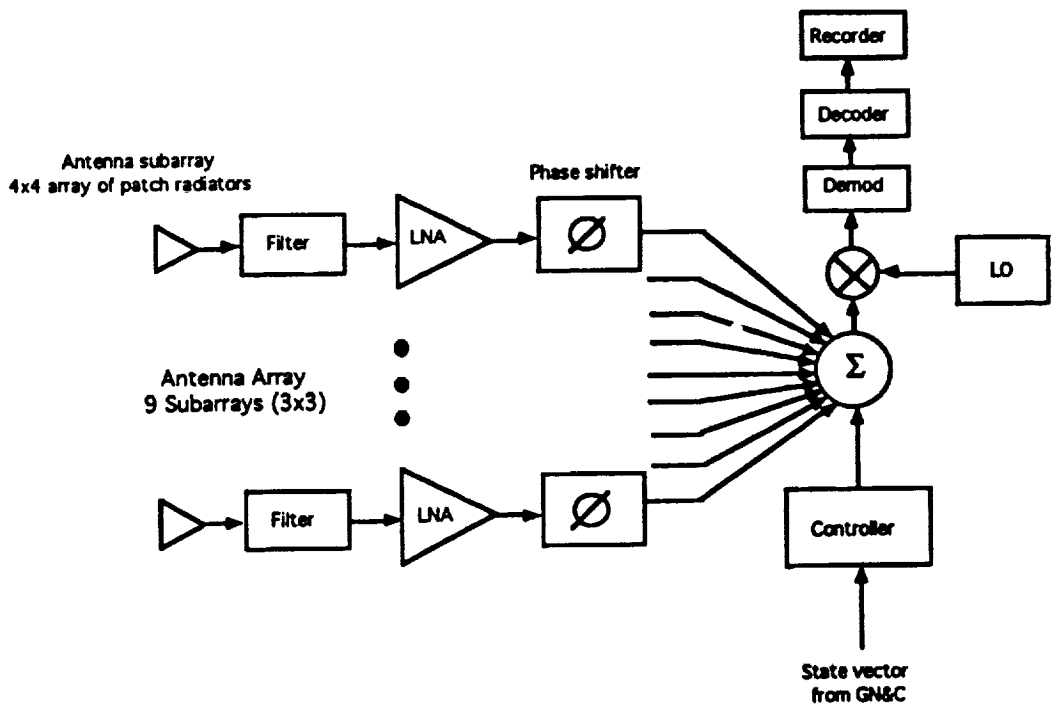

Figure 2 - Electronic Equipment Onboard the Orbiter

2.1 Ground Equipment

The ground terminal at JSC has a 1.2m parabolic antenna which is manually pointed to the ACTS. A baseband signal, 100 Kbps to 300 Kbps with convolutional encoding, is biphase modulated onto uplink carrier. The type of modulation data has not been determined.

2.2 Spacecraft Receiver

The spacecraft receiver requires either a large sweep bandwidth in order to acquire the doppler shifted signal of +/- 500 MHz with a maximum rate of change of .6 KHz/sec., or the ground transmitter must have a preprogrammed emphemeris to compensate for the doppler shift. It will probably be easier and less costly to doppler compensate on the ground. It has also not been decided whether to record the uplink data for post mission evaluation or to turn around the the data and transmit back to the ground via the normal Ku-band Tracking Data Relay Satellite System (TDRSS) link or to use the Ka-band return link of the ACTS.

3.0 LINK PERFORMANCE

The circuit margin calculations for the forward link are shown in Table 1. There is a 3 dB polarization loss in the ACTS/Orbiter link due to the linear polarized ACTS antenna and the circular polarized Orbiter antenna. The ACTS is operating in a bent-pipe configuration with a 900 MHz bandwidth; there could be signal suppression in the satellite's limiter and a power sharing loss in the output power amplifier. However, recent test data taken on a prototype ACTS system indicated little or no power sharing losses or signal suppression (private communications). Accordingly, these losses are zero in the calculations. A coding gain of 5 dB for the data is used to provide 2.9 dB of link margin for 300 Kbps of data.

4.0 THERMAL LOADING

Several thermal loading configurations were calculated for payloads located in the Orbiter's payload bay. The general equation for thermal balance is:

$$Q_{in} = Q_{out} \tag{1}$$

Solar + Earth + System Heating = Radiation to Space + Radiation to Payload Bayliner + Conduction to Orbiter Structure

$$\alpha_s A_n Q_{solar} + \varepsilon_{ir} A_n Q_{earth} + Q_{system} = \sigma \Im A_n (T^4_{system} - T^4_{space}) + \sigma \Im A_n (T^4_{system} - T^4_{liner}) + (kA_{cond}/l)(T_{system} - T_{beam}) \tag{2}$$

where

α_s = Solar absorptivity

A_n = area of node n

Q_{solar} = 429 BTU/ft^2/hour
ε_{ir} = emissitivity of infrared (dependent upon surface coating)
Q_{earth} = 70 BTU/ft^2/hour
Q_{system} = heat dissipation in receiver(assumed 0 watts)
σ = Stefan Boltzmann's Constant
$\Im$ = view factor(percent of viewing surface area)
T_{system} = temperature environment of HTSC component
T_{liner} = temperature of payload bay liner
T_{space} = temperature of outer space (0° Kelvin)
l = length between two nodes for conduction
T_{beam} = temperature of payload bay beam that the payload is attached to (+50° to 90°F for sun viewing, +15°F for earth viewing, and -50°F for cold space viewing)
A_{cond} = effective cross-sectional area of conducting beam (perpendicular to payload structure
k = thermal conductivity of attachment beam

The analyses were performed using the Thermal Radiation Analyzer System (TRASYS) model to produce radiation conductors and heating rates for various orbit attitudes; the TRASYS output is used as an input for Systems Improved Numerical Differencing Analyzer (SINDA) model to calculate temperatures for 136 nodes (points) within the Orbiter's payload bay. Three orbital attitudes are shown in Figure 3: (1) bay to space (cold); Beta = 90° (polar orbit), (2) bay to sun (hot); Beta = 90° (polar orbit), and (3) bay to earth (warm); Beta = 0° (equatorial orbit).

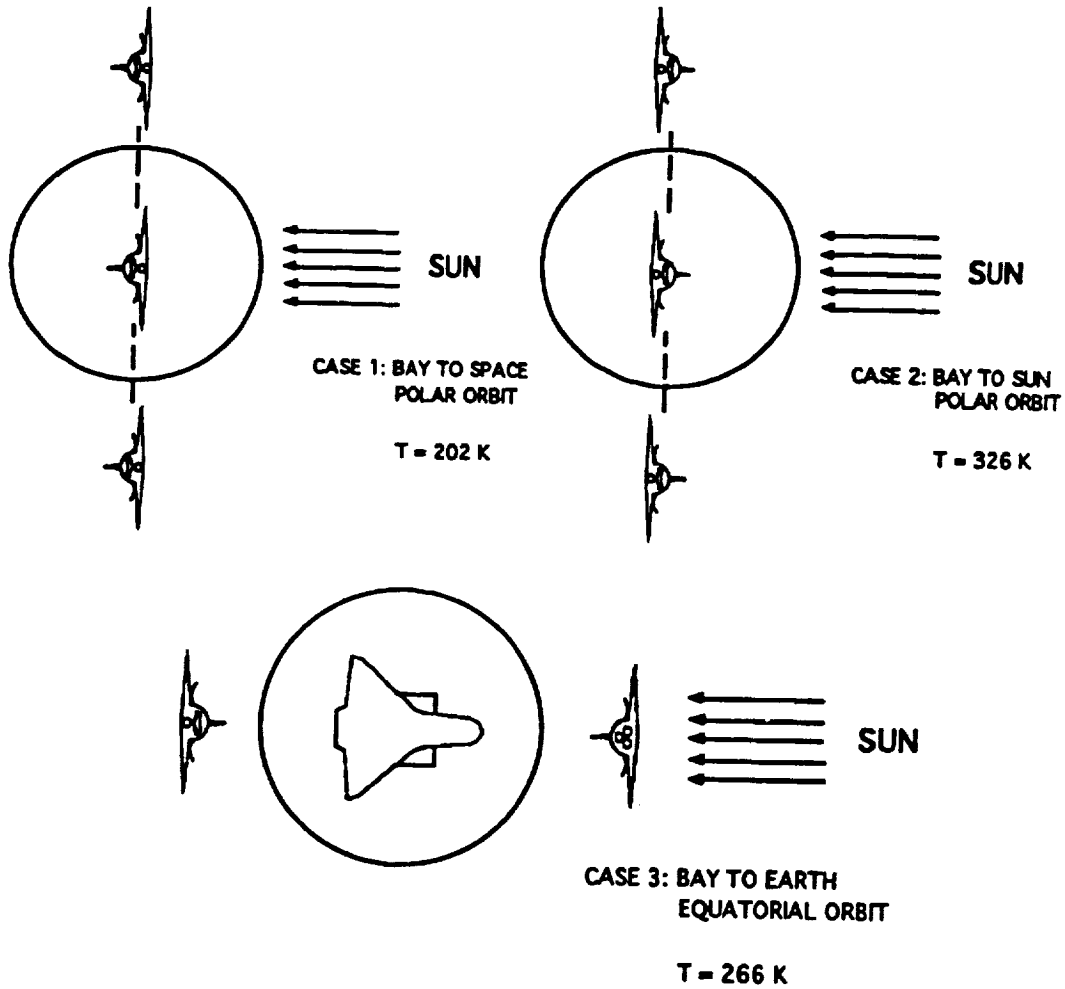

Figure 3 - Orbital Configurations for Thermal Analyses

For the earth-facing orbit, the temperature of the earth is 0°F with a heating rate of 70 BTU/ft^2/hour; for the sun-facing orbit, the heating rate is 429 BTU/ft^2/hour; for the cold (space-facing) orbit, the heating rate is 0 BTU/ft^2/hour. With an assumed initial temperature of 70° F, the steady-state results as shown in Figure 4 are:

Case 1	Payload bay to cold space	T = - 95° F (203°K)
Case 2	Payload bay to sun	T = + 128° F
Case 3	Payload bay facing earth	T = + 20°F

The reason for the relatively high temperature (- 95°F) in the payload bay facing cold space is due to the conduction from warmer parts of the Orbiter to the payload bay. The bottom of the Orbiter is still heated by the sun and there is a finite thermal mass within the Orbiter's structure. It is possible to achieve colder payload bay temperatures by flying in polar orbit with the bottom of the Orbiter facing the earth and the nose towards the sun.

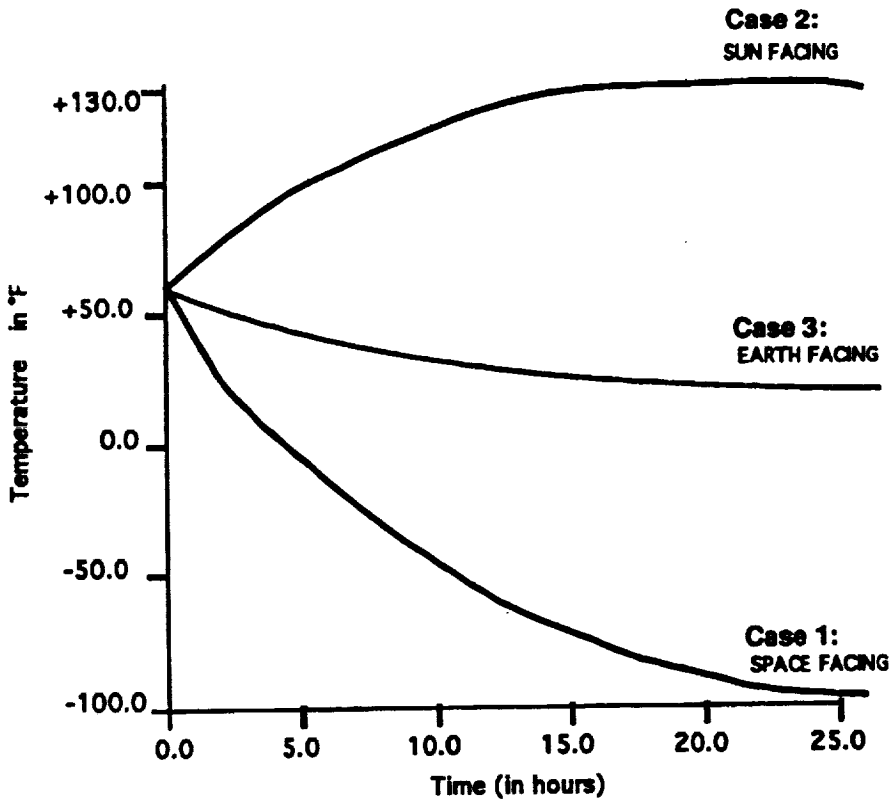

Figure 4 - Thermal Conditions in The Orbiter's Payload Bay

A payload bay temperature of - 250° F (113° K) could be achieved with even colder temperatures by using thermal isolator between the equipment and the payload bay structure. Regardless, a small cooling refrigerator will probably be necessary for the HTSC equipment.

5.0 SUPERCONDUCTING ANTENNA ARRAY

The use of HTSC materials in antenna designs will increase any antenna's radiation efficiency by reducing the ohmic losses in the structure. This appears as an increase in the gain of the antenna since gain and radiation efficiency are in direct proportion. The use of HTSC materials will have a negligible effect on the shape of the antenna's radiation pattern.

Although the gain of all normal-metal antennas can be increased to some extent via the use of superconductors, millimeter-wave arrays appear to have the greatest potential for practical improvement. For a corporate-fed array with a uniform excitation across its aperture, the gain of the array is

$$G(dB) = 10 \log(4\pi A/\lambda^2) - \alpha L \qquad (3)$$

where A is the aperture area, λ is the wavelength of operation, α is the attenuation (dB/unit length), and L is the length of the transmission line from the array feed point to any radiating element. Figures 5 and 6 show how the length of the feed lines increase with increasing array size and how the feed network losses affect the gain of the array, respectively. As can be seen, if losses can be neglected (α=0), an arbitrarily large gain can be obtained if the physical size of the array is not limited by other constraints. However, as the length of the array side increases linearly, the length of the path from the array feed point to any element increases exponentially. Eventually, any losses in the feed network become large enough to limit the maximum available gain of the structure. These calculations were done at a frequency of 20 GHz, with lossless radiating elements separated by 1/2 λ. The loss value of 0.25 dB/in is typical for room-temperature CU/PTFE microstrip or stripline transmission lines at this frequency. Often, waveguide feed networks are used to reduce loss at the expense of physical size.

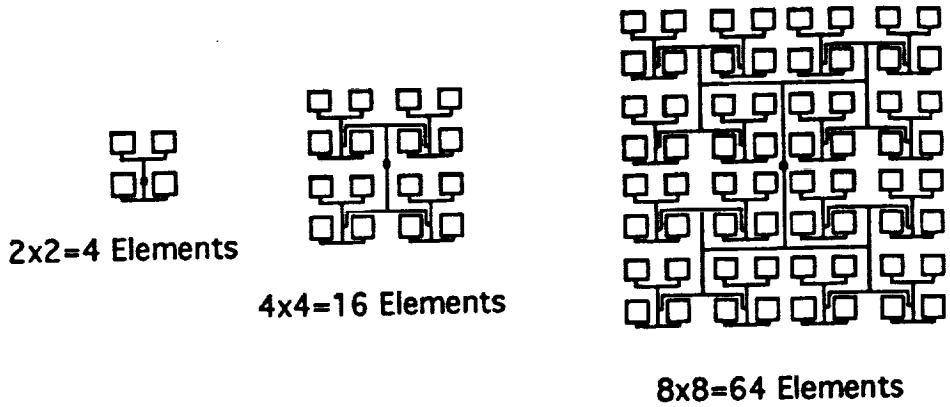

Figure 5 - Feed Network Complexity Increases Exponentially as Corporate-Fed Array Side Lenght Increases Linearly

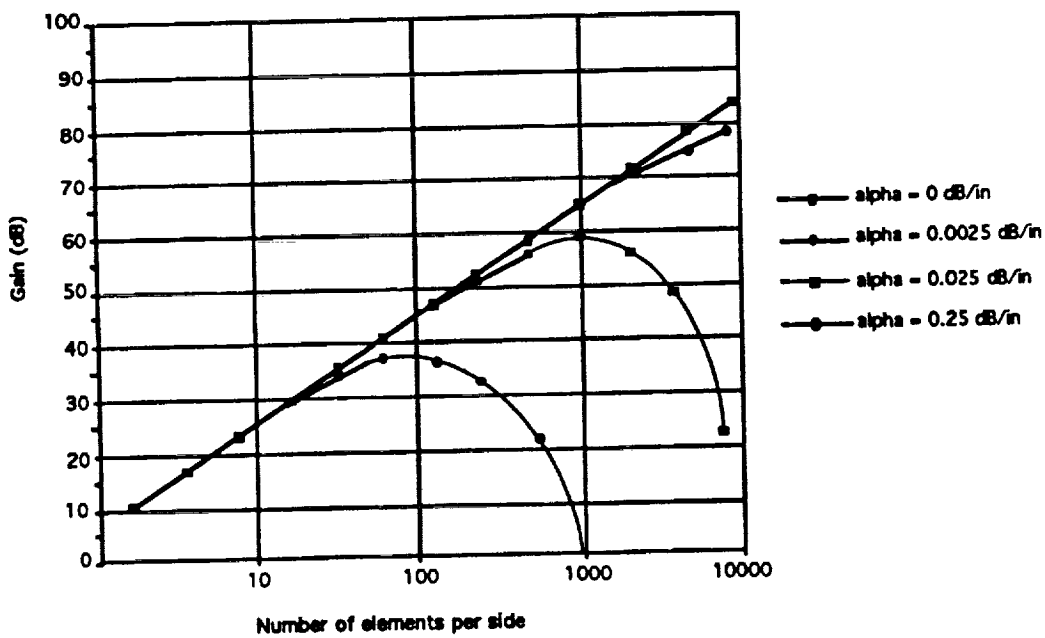

Figure 6 - Array Gain Versus Size as a Function of Feed Line Losses

Researchers at NASA/LeRC have fabricated and tested a 64-element thallium-film superconducting microstrip array operating at 30 GHz [1]. The array is fabricated on a 10 milli-inch lanthanum aluminate substrate and both the radiating elements and the microstrip corporate feed network share the same side of the substrate. At 77 K, the device has shown a 2 dB higher gain than an identical antenna pattern with gold metallization at the same temperature, and 4 dB higher gain than the room temperature gold antenna.

In the antenna described above, both the feed network and the radiating elements were fabricated from HTSC material. It is known that superconducting patch radiators show only a modest increase in efficiency over that of normal-metal designs unless the patches are fabricated on relatively thin or high-dielectric substrates [2]. In fact, microstrip patch antennas are usually fabricated on thick (~ $\lambda_0/20$), low dielectric constant ($\varepsilon_r < 10$), low-loss ($\tan\delta < 0.001$) substrates. The substrates that are presently compatible with HTSC films do not meet all these criteria. A design, presently underway at NASA/JSC, that combines a HTSC stripline feed network and normal-metal patch radiators fabricated on a relatively thick, low dielectric constant substrate is shown in Figure 7.

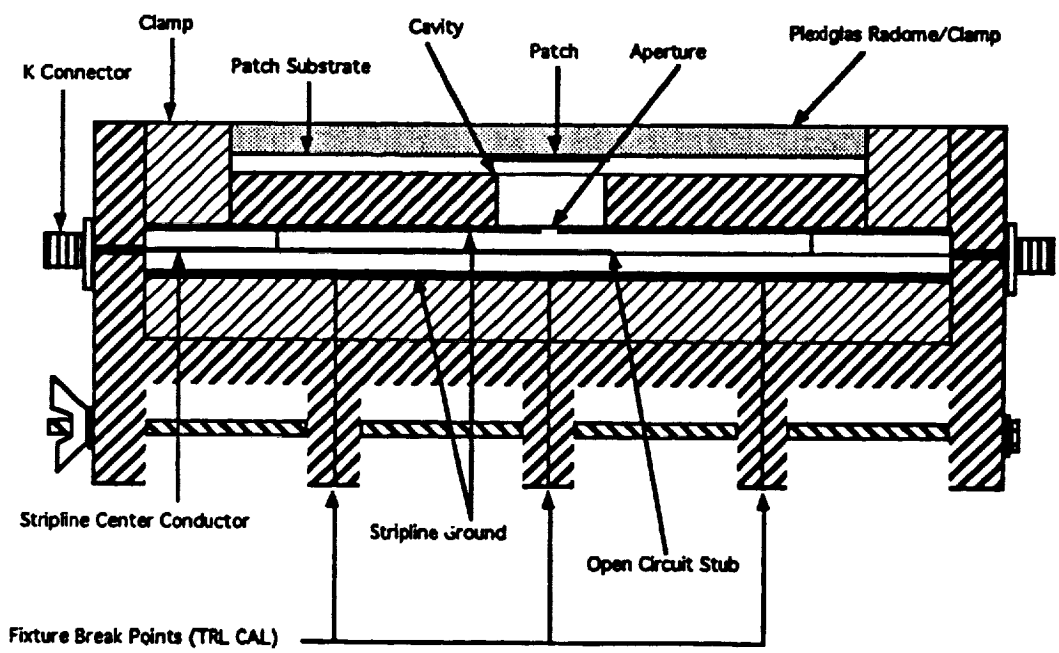

Figure 7 - Single Aperture-Coupled Patch Antenna and Test Fixture - Cross Section

Table I

ACTS-to-Orbiter Link Calculations (300 Kbps)

Parameters	Values	Remarks
1. ACTS transmit power, dBw	16.3	43 watts
2. ACTS transmit circuit loss, dB	-3.0	
3. ACTS transmit antenna gain, dB	42.0	1.1m antenna
4. ACTS transmit EIRP, dBw	55.3	Sum 1 thru 3
5. ACTS power sharing loss due, dB to 900 MHz bandwidth	0.0	
6. Spaceloss, dB	-210.5	40744Km, 19.7 GHz
7. Polarization loss, dB	-3.0	Linear to Circular
8. Pointing loss, dB	-.5	Estimate
9. Orbiter antenna receive, gain, dB	25.0	9 subarrays; 16 microstrip patches/sub-array
10. Orbiter receive circuit loss, dB	-0.5	HTSC lines to input LNA
11. Orbiter total receive power, dBw	-134.2	Sum 4 thru 10
12. System noise temperature, dBk	29.6	NF = 5 dB, Ta = 290°K
13. Noise spectral density (No) dB/KHz	-228.6	Boltzmann's Constant
14. Received C/No, dBHz	64.8	Lines 11 - (12 + 13)
15. Bit rate bandwidth, dBHz	54.8	300 Kbps
16. Received S/N, dB	10.0	Lines 14-15
17. Theoretical required S/N, dB	9.6	1.E-5 BER
18. Coding gain	5.0	(R = 1/2, K = 7)
19. Implementation loss, dB	-1.5	Estimate
20. Demodulation loss, dB	-1.0	Estimate
21. Required S/N, dB	7.1	Lines 17 - (18+19+20)
22. Link circuit margin, dB	2.9	Lines 16-21

6.0 REFERENCES

[1] Lewis, L.L., Koepf, G., Bhasin, K.B., and Richard, M. A. "Performance of TlCaBaCuO 30 GHz 64 Element Antenna Array," To be presented at 1992 Applied Superconductivity Conference, Chicago.

[2] Karasack, V.G. "High-Temperature Superconductor Antenna Investigations," *Superconductivity Applications for Infrared and Microwave Devices*, Kul B. Bhasin, Vernon O. Heinen, Editors, Proc. SPIE 1292, 93-106 (1990).

C-BAND SUPERCONDUCTOR/SEMICONDUCTOR HYBRID FIELD-EFFECT TRANSISTOR AMPLIFIER ON A $LaAlO_3$ SUBSTRATE

J.J. Nahra
University of Cincinnati
Cincinnati, Ohio

K.B. Bhasin and S.S. Toncich*
Lewis Research Center
Cleveland, Ohio

G. Subramanyam and V.J. Kapoor
University of Cincinnati
Cincinnati, Ohio

Abstract—A single-stage C-band superconductor/semiconductor hybrid field-effect transistor (FET) amplifier was designed, fabricated, and tested at 77K. The large-area (1 inch x 0.5 inch) high temperature superconducting (HTS) Tl-Ba-Ca-Cu-O (TBCCO) thin film was rf magnetron sputtered onto a Lanthanum Aluminate ($LaAlO_3$) substrate. The amplifier showed a gain of 5.75 dB and a 3dB bandwidth of 150 MHz centered at 7.915 GHz at 77K. An identical gold amplifier was also tested at 77K for purposes of comparison, it had a gain of 5.46 dB centered at 7.635 GHz with a 3dB bandwidth of 100 MHz.

I. INTRODUCTION

Since the discovery of high temperature superconductors (HTS) in the Thallium-Barium-Calcium-Copper-Oxide (-TBCCO) and Yttrium-Barium-Calcium-Copper-Oxide (YBCO) systems [1,2], the idea of using superconductors in combination with semiconductor devices in hybrid microwave integrated circuits became feasible at liquid nitrogen temperatures [3]. Semiconductor devices such as Metal Semiconductor Field-Effect Transistors (MESFET's) and High Electron Mobility Transistors (HEMT's) have been shown to have improved device characteristics at cryogenic temperatures [4]. With the development of High T_c superconducting thin films, and Gallium Arsenide (GaAs) monolithic microwave integrated circuits high performance superconductor/semiconductor hybrid integrated circuits can now be realized. The use of superconductors and semiconductors together in microwave circuits has been demonstrated recently [5]. By combining superconducting material with semiconductor devices in microwave circuits, improved performance can be achieved in terms of decreased conductor losses, reduced noise figure (NF), and increased gain [6]. Also, by operating the amplifier at cryogenic temperatures, natural increase in gain due to increased conductivity in the transistor at low temperatures can be exploited.

*National Research Council-NASA Research Associate.

The objective of this work is to determine the advantage of using High T_c superconducting thin films in the input and output impedance matching networks of a GaAs FET microstrip amplifier. In deep space communications and radio astronomy where ultra low-noise amplifiers (LNA's) are very important because very weak signals need to be detected, the use of superconducting matching networks could provide for lower insertion loss, resulting in improved performance. The amplifier design, fabrication, and results are presented in the following sections.

II. AMPLIFIER DESIGN AND FABRICATION

A single-stage microstrip amplifier was designed for a gain of 6 dB at a center frequency of 8 GHz and a 3dB bandwidth of 500 MHz. The amplifier circuit was designed using TOUCHSTONE [7] on a Sun Workstation. For the purpose of obtaining an optimized cryogenic design the Scattering Parameters (S-Parameters) of a Toshiba GaAs transistor were measured at 77K. The S-Parameters are shown in Figure 1.

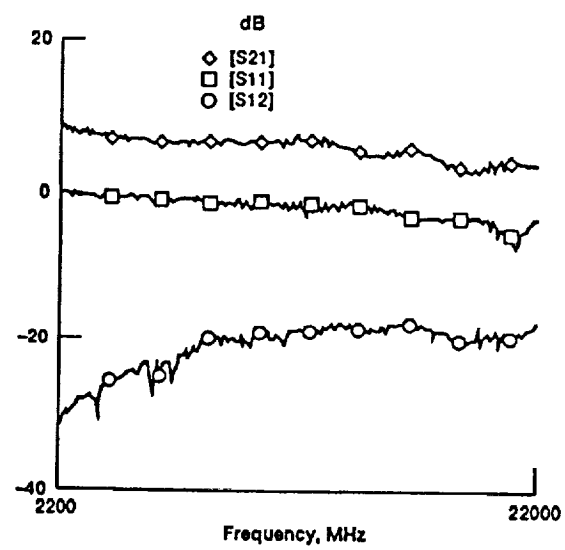

Fig. 1 S-Parameters of Toshiba GaAs FET at T= 77K

PRECEDING PAGE BLANK NOT FILMED

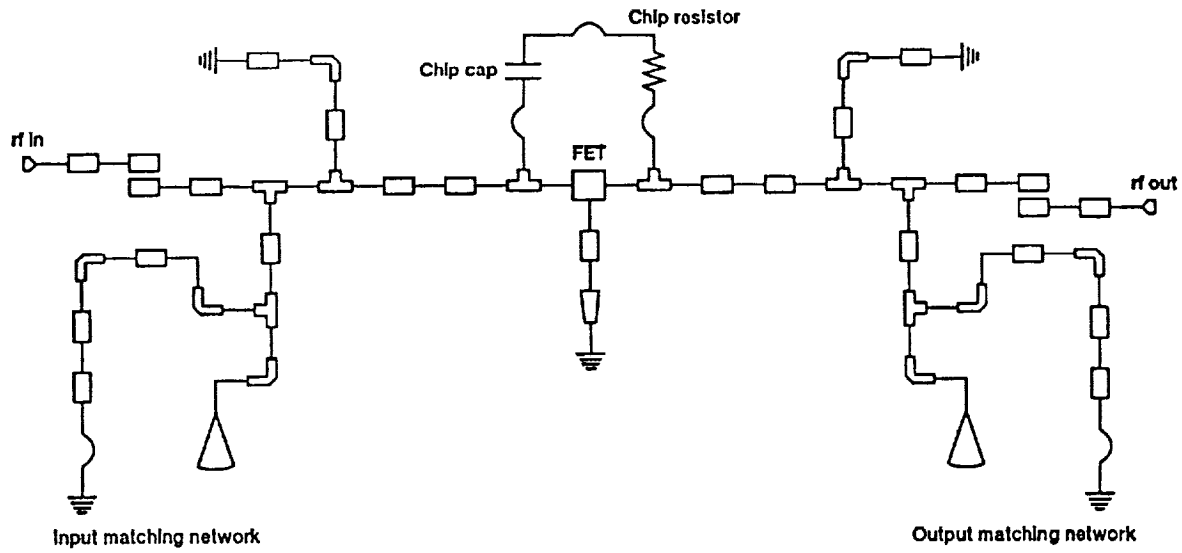

Fig. 2 Schematic of Amplifier Generated in TOUCHSTONE

The measured S-Parameter data was used to design the input and output single-stub impedance matching networks. A schematic of the design is shown in Figure 2. Input and output 50Ω feed lines are followed by coupled lines which function as dc blocks. Impedance matching was done using transmission lines of different length and width, and open-circuited shunt stubs to avoid the problem of fabricating high quality wide band short circuits. The grounding of the source terminal of the transistor was performed by using a low impedance transmission line terminated in a low impedance tapered line. The end of the tapered line came to the edge of the substrate and silver paint was applied to this edge in order to provide an rf ground path to the test fixture.

The amplifier matching and dc bias networks were fabricated by rf magnetron sputtering a TBCCO film from a single composite powder target of $Tl_2Ba_2Ca_2Cu_3O_x$ to a thickness of 3750Å onto a 20 mil thick $LaAlO_3$ substrate [8]. Gold contact areas for wire bonding purposes were formed through a lift-off process and 2.5μm of silver was thermally evaporated on the opposite side of the substrate which acted as the ground plane. A Toshiba GaAs FET was mounted on the substrate using silver-filled conductive epoxy and cured at 150°C for 1 hour. A feedback network consisting of a chip resistor and chip capacitor was added to the amplifier design in order to ensure stability because the amplifier had a tendency to oscillate. The FET, chip capacitor, and chip resistor were connected to the appropriate microstrip lines with 0.7 mil diameter gold bond wires. The amplifier was mounted in a brass test fixture inside a cryogenic chamber on a cold-head platform. Inside the chamber semi-rigid coaxial lines connected the input and output ports of the amplifier to the outside of the cryogenic chamber. Input and output 3.5mm SMA female connectors provided a coax to microstrip feed line transition. Silver paint was used to ensure electrical contact between the launcher pin and the microstrip line. A photograph of the amplifier in its test fixture is shown in Figure 3. An identical amplifier using gold film for the microstrip lines and ground plane was also fabricated for use as a comparison to the hybrid amplifier.

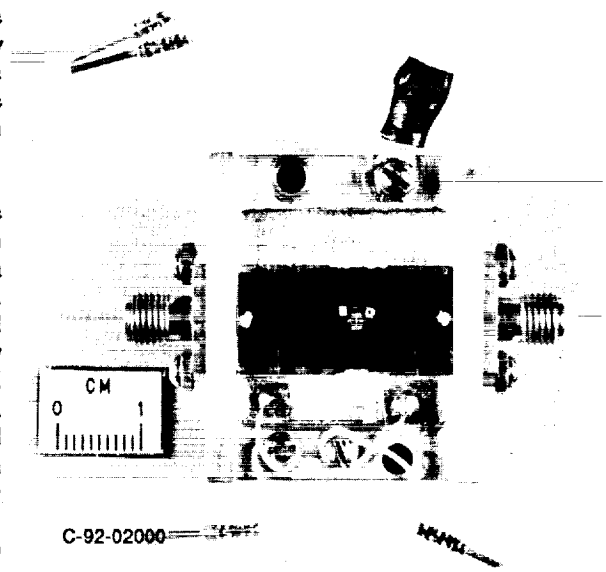

Fig. 3 Photograph of Hybrid Amplifier in Test Fixture

III. MEASUREMENTS AND RESULTS

An HP8510B Vector Network Analyzer and a model 22C Cryodyne closed-cycle refrigeration system made by CTI-

Cryogenics were used to measure the S-Parameters of the amplifiers at 77K. The amplifier was mounted in the cryogenic chamber and the semi-rigid coaxial lines were connected to the input and output ports respectively. The chamber was evacuated to 50 milli torr and the transistor dc bias was applied. The corresponding S-Parameters were measure and recorded. The forward gain of the hybrid and gold amplifiers are shown in Figures 4 and 5 respectively.

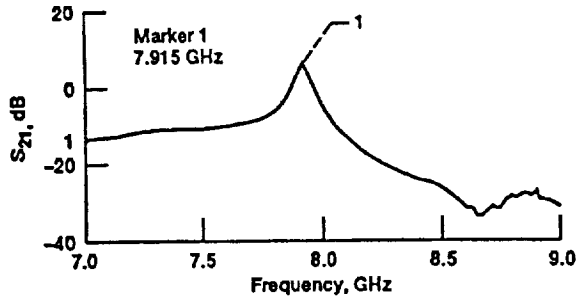

Fig. 4 Measured Gain of Hybrid Amplifier at T= 77K

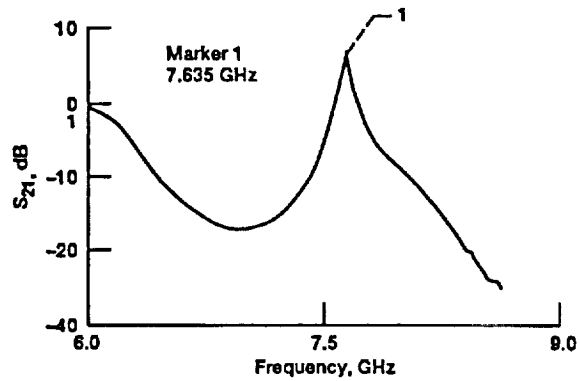

Fig. 5 Measured Gain of Gold Amplifier at T= 77K

The primary advantage of using TBCCO matching networks instead of gold is that the conductor losses are decreased and the NF can also be reduced. Since the superconducting material reacts differently than gold in terms of impedance one must design the matching networks taking into account in the simulation the properties of the superconducting material (i.e. surface resistance, thickness, and film uniformity) as compared to the properties of the gold film.

A comparison of the results obtained for the hybrid amplifier and the gold amplifier are shown in Table 1. Even though the results of the two circuits are not exactly comparable because of the differences in the impedance of the two materials it can be seen from Table 1 that the hybrid amplifier results were closer to the original design goals. This is because the properties of the superconducting material, such as thickness and resistivity, were taken into account in the design.

IV. CONCLUSIONS

A single-stage TBCCO/GaAs FET amplifier was fabricated and its S-Parameters were measured at 77K. An identical gold film amplifier was also fabricated and characterized at 77K. The hybrid amplifier showed a gain of 5.75 dB at a center frequency of 7.915 GHz while the gold amplifier showed a gain of 5.46 dB at a center frequency of 7.635 GHz. The hybrid amplifier was 1.0 inches long and 0.5 inches wide.

ACKNOWLEDGMENTS

This work was performed under a grant from NASA Lewis Research Center, grant number NCC3-33.

REFERENCES

[1] M.K. Wu, J.R. Ashburn, and C.J. Torng, "Superconductivity at 93K in a New Mixed-Phase Y-Ba-Cu-O Compound System at Ambient Pressure", Physical Review Letters, vol. 58, No.9, pp. 908-910, March 2,1987.

[2] Z.Z. Sheng and A.M. Herman, "bulk Superconductivity at 120K in the Tl-Ca/Ba-Cu-O System", Nature, vol. 332, pp. 138-139, March 10, 1988.

[3] T. Van Duzer, "Superconductor - Semiconductor Hybrid Devices, Circuits and Systems", Cryogenics, vol. 28, pp. 527-531, August 1988.

[4] M.W. Pospieszalski, S. Weinreb, R.D. Norrod, and R. Harris, "FET's and HEMT's at Cryogenic Temperatures - Their Properties and Use in Low-Noise Amplifiers", IEEE Transactions on Microwave Theory and Techniques, vol. 36, No. 3, pp. 552-560, March 1988.

Table 1. Comparisons of Results of Hybrid and Gold Amplifiers at 77K

Amplifier Type	Gain (dB)	Center Frequency (GHz)	3dB Bandwidth (MHz)
Hybrid, T=77K	5.75	7.915	150
Gold, T=77K	5.46	7.635	100

[5] K.B. Bhasin, S.S. Toncich, C.M. Chorey, R.R. Bonetti, A.E. Williams, "Performance of a Y-Ba-Cu-O Superconducting Filter/GaAs Low Noise Amplifier Hybrid Circuit", IEEE Microwave Theory and Techniques International Microwave Symposium Digest, vol. 1, pp. 481-483, 1992.

[6] T. Van Duzer, "Superconductor Electronics", Cryogenics, vol. 30, pp. 980-995, December 1990.

[7] EESOF, Inc., Westlake Village, CA, 1992.

[8] G. Subramanyam, F. Radpour, V.K. Kapoor, " Fabrication of Tl-Ca-Ba-Cu-O Superconducting Thin Films on $LaAlO_3$ Substrates", Applied Physics Letters, vol. 56, pp. 1799-1801, 30 April 1990.

N94-20515

10 GHz $YBa_2Cu_3O_{7-\delta}$ superconducting ring resonators on $NdGaO_3$ substrates

H Y To†, G J Valco† and K B Bhasin‡

† Department of Electrical Engineering, Ohio State University, Columbus, Ohio 43210, USA
‡ National Aeronautics and Space Administration, Lewis Research Center, Cleveland, Ohio 44135, USA

Abstract. $YBa_2Cu_3O_{7-\delta}$ thin films were formed on $NdGaO_3$ substrates by laser ablation. Critical temperatures greater than 89 K and critical current densities exceeding 2×10^6 A cm^{-2} at 77 K were obtained. The microwave performance of films patterned into microstrip ring resonators with gold ground planes was measured. An unloaded quality factor six times larger than a that of a gold resonator of identical geometry was achieved. The unloaded quality factor decreased below 70 K for both the superconducting and gold resonators due to increasing dielectric losses in the substrate. The temperature dependence of the loss tangent of $NdGaO_3$ was extracted from the measurements.

1. Introduction

A major area of interest for application of high-temperature superconductors is microwave electronics. The characterization of these materials at microwave frequencies is important for understanding their potential for practical use. Strontium titanate ($SrTiO_3$), a cubic pervoskite, has been used as a substrate for the formation of a thin film of high-temperature superconductor [1] and films on $SrTiO_3$ have among the best DC properties. However, its large dielectric constant and loss tangent make it unsuitable for microwave applications.

Lanthanum aluminate ($LaAlO_3$), which has a similar structure to $SrTiO_3$, has been widely used as the substrate for microwave applications of thin film $YBa_2Cu_3O_{7-\delta}$ (YBCO). This substrate has a lattice mismatch with YBCO of less than one per cent. $LaAlO_3$ has a loss tangent of less than 10^{-4} at 10 GHz [2] and a dielectric constant of 24.5 [3] below the critical temperature (T_c) of YBCO. However, $LaAlO_3$ has a second-order phase transition around 500°C [4]. This causes the substrate to have a high density of twinning and may have a detrimental effect on the microwave performance of the YBCO films.

A search for crystals with similar lattice dimensions reveals that neodymium gallate ($NdGaO_3$) is a promising substrate [4, 5]. $NdGaO_3$ is a perovskite which has about 0.8% lattice mismatch with the YBCO superconductor. Furthermore, the dielectric constant of $NdGaO_3$ is comparable to that of $LaAlO_3$, and this crystal is twin free [6, 7]. The crystal has a second-order phase transition at 950°C which is higher than the typical processing temperature of *in situ* annealed high-temperature superconductors.

Recently, there have been reports on the growth of epitaxial YBCO films on $NdGaO_3$ [8, 9, 10]. The microwave properties of YBCO superconducting films deposited on $NdGaO_3$ have been measured by other researchers [11]. However, to our knowledge, no measurements on resonators fabricated using the YBCO film on $NdGaO_3$ have been reported at frequencies higher than 5 GHz or as a function of temperature.

In this report, YBCO superconducting thin films were deposited on (001) $NdGaO_3$ and patterned into ring resonators. The advantage of a ring resonator over a linear resonator is that the ring resonator does not have radiation losses from an open end. The reflection coefficients of the resonator were measured as a function of temperature. The unloaded quality factors at 10 GHz were calculated and the effective surface resistance was extracted from the loaded Q-factors. Further, the loss tangent of $NdGaO_3$ was determined as a function of temperature.

2. Sample preparation

A two-inch (5.1 cm) diameter, 20 mils (0.51 mm) thick, (001) $NdGaO_3$ substrate, polished on both sides, was cut into typical sizes of 1 cm x 1 cm and 0.8 cm by 0.4 cm for microwave and DC transport characterization, respectively. YBCO thin films were deposited on to the substrates by laser ablation. Prior to deposition of the films, the substrates were cleaned in acetone and methanol with ultrasonic agitation for 5 minutes each. They were then rinsed in deionized water (DI) for 5 minutes followed by 1 minute in DI:HCl (10:1). Lastly, the substrates were rinsed in DI water for 5 minutes and blown dry with filtered nitrogen.

© 1992 IOP Publishing Ltd. Reprinted, with permission, from Supercond. Sci. Technol., vol. 5, 1992, pp. 421-426.

Ablation was performed with a KrF excimer laser. The 248 nm illumination was focused to a typical spot size of 7 mm x 3 mm on a one inch diameter, 95% dense YBCO target. The energy density at the target was 0.8 J cm^{-2}. The laser beam was incident at 45°. The target was rotated at 7 rpm and the laser spot was scanned from the centre to the edge of the target with a period of 65 s. The substrate was mounted with silver paste on a three inch diameter heater located 6 cm away from the target. Depositions were performed with a laser pulse rate of two per second. After the sample was loaded, the vacuum chamber was evacuated to 5×10^{-7} Torr while the substrate was heated to the deposition temperature, which was controlled through a thermocouple embedded in the heater. Oxygen was introduced to the chamber to a pressure of 170 mTorr during deposition. The duration of the depositions was typically one hour. After the deposition, the temperature of the heater was ramped down to 450° C at a rate of 2° C min^{-1} while the oxygen pressure was increased to 1 atm. The substrates were held at this temperature for 2 hours and then ramped down at a rate of 2° C min^{-1}.

Following the deposition of the films, their resistance was measured as a function of temperature. This measurement was done in a closed cycle cryostat using a four-probe method. One micron diameter gold wires were ultrasonically bonded directly to the surface of the superconductor for these measurements. A constant current of 0.1 mA was passed through the two outer leads while the voltage across the inner two leads was measured.

For measurement of the critical current density (J_c), the films were patterned into a 10 μm and 5 μm wide, 2.77 mm long meander test structure. Positive photolithography was used to form the structure on the superconductor films using Shipley 1400-31 positive photoresist. The YBCO films were etched in DI:H_3PO_4 (100:1).

Lift-off photolithography was employed to form metal contacts on the superconductor. Patterns were formed with Shipley AZ1400-37 photoresist. A 15 minute soak in chlorobenzene prior to development was used to form a reentrant photoresist profile for the lift-off. After deposition of 0.7 μm of silver and 0.3 μm of gold, a 15 minute soak in N-methyl-2-pyrrolidone was used to swell the photoresist. The lift-off of the excess metal was completed by soaking the samples in warm acetone for 10 minutes. 1 μm diameter gold wire was bonded to the metal contacts for electrical connections. The resistance versus temperature of the patterned test structure was measured using 1 μA of current. Below the critical temperature (T_c), the critical current was measured by increasing the amount of the current to the sample until the measured voltage exceeded the 1 μV cm^{-1} criteria.

YBCO films on 1 cm x 1 cm substrates were patterned into ring resonators by standard photolithographic steps as described above. The geometry of the resonator is shown in figure 1. The dimensions were: width of the microstrip (w) = 99 μm, gap size

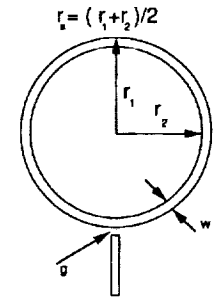

Figure 1. Layout of the microstrip ring resonator.

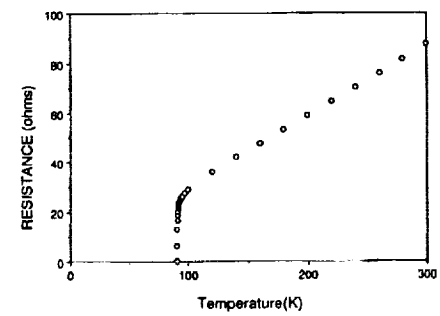

Figure 2. Resistance as a function of temperature of sample F.

(g) = 27 μm, substrate thickness (h) = 508 μm, and average radius = 2.45 mm. It had a characteristic impedance of 50 Ω and a fundamental resonant frequency of 5 GHz. Microwave measurements were performed at the first harmonic. The ground plane consisted of a 2.5 μm thick layer of gold on the back of the substrate. A resonator was also fabricated using 2.8 μm thick gold transmission lines for comparison.

3. Results

YBCO films were deposited on to seven $NdGaO_3$ substrates at five different substrate temperatures. X-ray diffraction spectroscopy showed the films to be epitaxial with the c axis perpendicular to the surface of the substrate. Table 1 lists the deposition temperatures, film thicknesses, critical temperatures before and after patterning, and critical current densities at 77 K. Samples A to E were patterned for critical current density measurements. The critical current densities of samples F and G were not measured since they were patterned into ring resonators. Figure 2 shows the resistance as a function of temperature for sample F after patterning. The critical temperature of this film was 89.7 K and the transition width was 1 K.

From table 1 it can be seen that the critical temperature after patterning is usually slightly higher than that before patterning. This is probably a result of non-uniformity in the film and the location of the measurement. Prior to patterning, the measurements were

Table 1. Deposition temperature and DC properties of YBCO films.

Sample	T_d (°C)	T_c (K) before	T_c (K) after	t (μm)	$J_c \times 10^{-6}$ (A cm^{-2})
A	715	87.1	88.3	0.37	1.50
B	735	87.9	88.5	0.26	0.22
C	745	88.0	89.1	0.35	2.25
D	755	87.4	86.6	0.38	0.45
E	785	—	87.5	0.24	0.44
F	785	88.6	89.7	0.30	resonator
G	785	87.8	87.3	0.38	resonator

performed by wire bonding directly to the films with the contacts located near the edge of the sample to prevent mechanical damage in the centre. The patterned test structures, on the other hand, were located near the centre of the samples suggesting that the quality of the films was higher near the centres than at the edges. Sample D was unintentionally over etched. Its critical temperature showed a decrease after patterning.

If the samples are ranked according to critical temperature after patterning it can be seen that, with the exception of sample B, higher critical current densities correspond to higher critical temperatures. Sample B, which had a relatively high critical temperature, also had the lowest critical current density. Inspection of this sample with an optical microscope revealed a large particle in the 10 μm wide YBCO line used for the critical current density measurement. This probably accounts for the anomalously low J_c.

The scattering parameters of the ring resonators fabricated on samples F and G were measured as a function of temperature. The magnitude of S_{11} is plotted as a function of frequency for sample G at 79 K in figure 3, showing the resonance at 10.14 GHz. The unloaded quality factor of the resonance was determined from the S_{11} data using the 3 dB frequencies, resonant frequency, reflection coefficients on and off resonance and phase information to account for the coupling coefficient and coupling losses. The details of the technique are describe elsewhere [12–14]. The unloaded quality factors (Q_0) were determined as a function of temperature for samples F and G at 10 GHz. At 77 K they had unloaded quality factors of 326 and 876 respectively. Note that although sample F had a higher critical temperature, sample G had better microwave performance. This is probably a result of surface morphology. A rough film will exhibit more loss than a smooth film with otherwise identical properties [15]. The surface of sample F had cloudy spots, which we have correlated with roughness by optical and scanning electron microscopy on other samples.

The unloaded quality factors of samples F and G are plotted as a function of temperature in figure 4. As expected, Q_0 increases rapidly as the temperature is decreased below T_c. However, as the temperature is further decreased Q_0 reaches a maximum and then decreases. This is particularly apparent in sample G, which had the higher Q_0. This phenomenon was observed when the measurement was performed with either increasing or decreasing temperatures. The measurements were repeatable. This is quite different from the expected behaviour, such as observed for YBCO resonators on $LaAlO_3$ substrates, for which Q_0 tends to levels off but not decrease at low temperatures. This suggests that the losses in the $NdGaO_3$ substrate increase as the temperature is decreased.

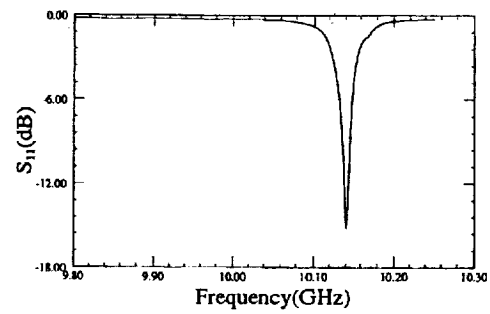

Figure 3. Magnitude of S_{11} as a function of frequency for the ring resonator patterned from film G measured at 79 K.

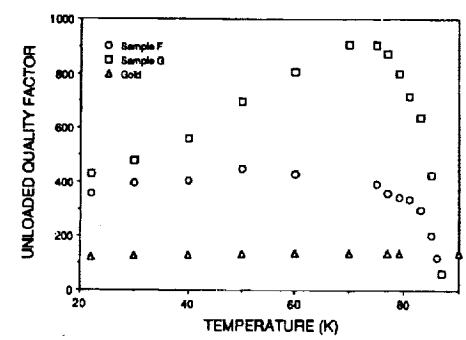

Figure 4. Unloaded quality factors at 10 GHz of samples F (circles) and G (squares) and the gold resonator (triangles) from 20 K to room temperature.

To verify that the decrease in the quality factor is due to the substrate and not due to the properties of YBCO on $NdGaO_3$, the reflection coefficient for a gold resonator on $NdGaO_3$ was also measured from 20 K to room temperature. The results of this measurement are shown in figure 5. The decrease in Q_0 at low temperatures was observed here as well. To facilitate comparison with the superconducting resonators, the data for the gold resonator below 90 K are also plotted in figure 4.

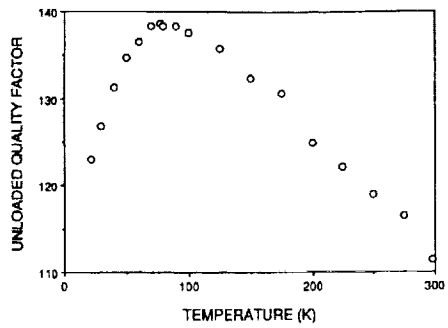

Figure 5. Unloaded quality factor at 10 GHz of the gold resonator from 20 K to room temperature.

4. Discussion

To determine the surface resistance of the YBCO films, the losses in the substrate and to radiation must be accounted for. The loss by radiation is assumed to be negligible due to shielding of the circuit. The losses in the dielectric are clearly not negligible, however, especially at low temperature. We have attempted to extract the losses in the dielectric from the measurements on the gold resonator by three techniques. The first two were not successful. For the first technique we calculated the expected conductor quality factor from measured DC values of the resistivity of thin films of gold. For the second technique we used conductor quality factors obtained by scaling values measured at 35 GHz, reported in reference [14], to 10 GHz. The loss tangent of the dielectric was then calculated from the unloaded quality factor of the gold resonator using

$$\tan\delta = \frac{1}{Q_d} = \frac{1}{Q_{oAu}} - \frac{1}{Q_{cAu}} \qquad (1)$$

where $\tan\delta$ is the loss tangent, Q_d is the dielectric quality factor and Q_0 and Q_c are the unloaded quality factor and conductor quality factor respectively. The loss tangent is actually proportional to $1/Q_d$ but the constant of proportionality is very near unity in this case and is assumed to be unity hereafter. Both of these techniques produced values of $\tan\delta$ that implied greater loss in the dielectric than the total measured loss for samples F and G, that is $Q_d < Q_0$, which is inconsistant. This is most probably due to the difficulty in scaling the surface resistance of gold for the frequency changes since the effects of non-idealities such as surface roughness were neglected.

The data shown in figure 4 suggest that near T_c the losses are dominated by those in the superconductor while at low temperatures the losses in the substrate dominate. We can take advantage of this to help separate the two components of the loss. Young *et al* have reported $\tan\delta = 3 \times 10^{-4}$ for $NdGaO_3$ at 77 K [11] and 5 GHz. We have used this value as a starting point in an iterative technique for extracting the temperature dependence of the loss tangent from the unloaded quality factors of sample G and the gold resonator. The technique basically consists of the following steps.

(i) Extrapolate the conductor loss at low temperature from its value at 77 K.

(ii) Estimate the dielectric loss below 70 K, where it is dominant, from the unloaded quality factor and the extrapolated conductor loss.

(iii) Use a curve fit to extrapolate the dielectric loss above 77 K to T_c.

(iv) Use the extrapolated dielectric loss to recalculate the conductor loss between 77 K and T_c and use a curve fit to refine the estimate of the conductor loss from 0 K to T_c.

(v) Use the refined estimate of conductor loss to redetermine the dielectric loss from 0 K to T_c.

(vi) Compare the resulting dielectric loss tangent at 77 K to the reported value of 3×10^{-4}, adjust the initial estimate of conductor loss at 77 K, and repeat the process.

The extrapolation of conductor loss is based on the two-fluid model for losses in superconductors while the extrapolation of dielectric loss is based on a fit to an exponential. A detailed description of the procedure follows. The values reported in the description are for the final iteration of the process.

Using a starting estimate of 4.4×10^{-4} for the loss tangent (3×10^{-4} for the first iteration), the conductor quality factor for sample G at 77 K is found to be 1425 through equation (1). The quality factor of the superconducting resonator varies little for temperatures sufficiently below T_c. (77 K is not quite far enough below T_c. This accounts for the difference between the starting estimate of 4.4×10^{-4} for the final iteration and the value of 3×10^{-4} with results at the end of the iteration.) Assuming Q_{cG}, the conductor quality factor of sample G, has a value equal to that at 77 K for all lower temperatures allows determination of a first estimate of the loss tangent of the substrate. It is shown on a semi-logarithmic plot in figure 6. The loss tangent was found to fit quite well

$$\tan\delta = Ke^{-\gamma T} \qquad (2)$$

over this temperature range. T is the absolute temperature and K and γ are fitting parameters. The results of the fit were used to extrapolate the loss tangent above 77 K to T_c. The conductor quality factor is changing rapidly above 77 K, where the subtractive approach of equation (1) assuming Q_c constant would be invalid.

The loss tangents calculated from this fit were then used in equation (1) to extract an estimate of Q_{cAu} the conductor quality factor of the gold resonator, as a function of temperature. An estimate of the surface resistance of the gold films, R_{sAu}, was calculated from Q_{cAu} through equation (3) [16, 17].

$$R_{sAu} = \frac{4\pi Z_0}{B(2C+D)}\frac{\pi}{\lambda}\left(\frac{1}{Q_{cAu}}\right) \qquad (3)$$

$$B = 1 - \left(\frac{w'}{4h}\right)^2 \qquad (4)$$

$$C = \left(1 - \frac{t}{\pi w'}\right)\Big/ h \qquad (5)$$

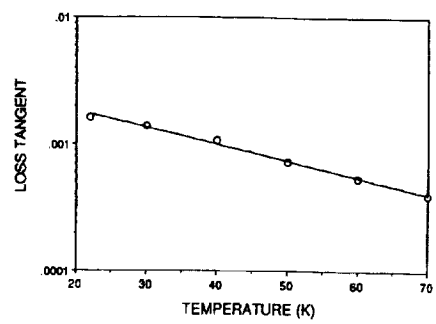

Figure 6. First estimate of the loss tangent of $NdGaO_3$ from 20 K to 70 K obtained by assuming the conductor quality factor of sample G is constant below 77 K. The circles are the data and the full line is the exponential fit.

$$D = 2\left(\pi + \ln\left(\frac{2h}{t}\right)\right) \Big/ \pi w' \tag{6}$$

$$w' = w + \frac{t}{\pi}\left(\ln\left(\frac{2h}{t}\right) + 1\right). \tag{7}$$

Z_0 is the characteristic impedence of the microstrip, λ is the guided wavelength and t is the thickness of the gold film.

Using equation (1) with the gold resonator and sample G we can write

$$\frac{1}{Q_{cG}} = \frac{1}{Q_{cAu}} - \left(\frac{1}{Q_{oAu}} - \frac{1}{Q_{oG}}\right) \tag{8}$$

Also, for a superconducting microstrip with a gold ground plane we have

$$\frac{1}{Q_{cG}} = \frac{\lambda}{\pi}\alpha_{cG} = \frac{\lambda}{\pi}\frac{B'\left((C'+D')\,R_{sG} + C'R_{sAu}\right)}{4\pi Z_0} \tag{9}$$

where α_{cG} is the conductor loss in sample G, R_{sG} is the effective surface resistance of the superconductor in sample G and B', C' and D' are determined from equations (4) to (7) using the thickness of the superconductor in sample G. Combining equations (3), (8) and (9) yields

$$R_{sG} = \left(\frac{B\,(2C+D) - B'C'}{B'\,(C'+D')}\right) R_{sAu} - \frac{4\pi Z_0}{B'\,(C'+D')}\frac{\pi}{\lambda}\left(\frac{1}{Q_{oAu}} - \frac{1}{Q_{oG}}\right) \tag{10}$$

which was used to estimate the effective surface resistance of the superconductor in sample G. The surface resistance calculated here is an effective value since corrections for the actual current distribution in the superconductor are not made [18].

A fit to the effective surface resistance thus determined was performed using the following equation

$$R_{sG} = R_0 + A\,(T/T_c)^4 \Big/ \left(1 - (T/T_c)^4\right)^{3/2} = R_0 + Af(\tau). \tag{11}$$

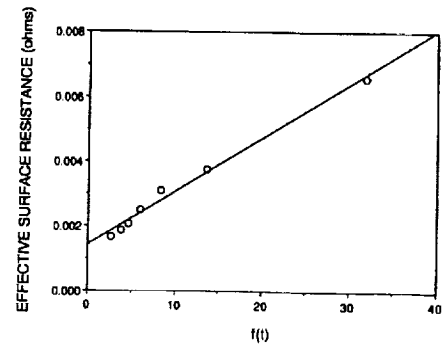

Figure 7. Effective surface resistance of sample G between 70 and 85 K calculated using the exponential from the curve fit of figure 6 to account for dielectric losses. The circles show the data and the line is the fit to the data using the two fluid model. See equation (11) for the definition of $f(\tau)$.

The first term, R_0, is a residual surface resistance, the second term is the surface resistance from the two fluid model [19] and $\tau = T/T_c$. The fitting parameters were R_0 and A. The effective surface resistances determined from equation (10) are shown in figure 7. The line shows the result of the fit. The data points shown correspond to temperatures from 70 to 85 K, the region in which the effective surface resistance is rapidly changing and the losses are dominated by the superconductor. The effective surface resistances at lower temperatures were not included to minimize the influence of errors in the estimation of the dielectric losses. The dielectric losses are large at low temperatures, and errors there could dominate the results of the fit. While equation (11) oversimplifies the temperature dependence of the surface resistance near T_c, where the pentration depth and the film thickness are comparable, it does allow an improvement in the extraction of $\tan\delta$ at low temperatures. The results of this fit are used to include the temperature dependence of Q_{cG} below 77 K, which was previously assumed constant.

Equation (10) was used to recalculate the surface resistance of gold using R_{sG} calculated from the fit and the measured values for Q_{oAu} and Q_{oG}. New values for the conductor quality factor for the gold resonator were then calculated using equation (3). Finally equation (1) was used to determine the loss tangent as a function of temperature. The value at 77 K was compared with 3×10^{-4} and, if needed, an adjustment to the original estimate of the conductor quality factor of sample G at 77 K was made and another iteration was performed. Figure 8 shows the loss tangent of $NdGaO_3$ as a function of temperature after the final iteration. The loss tangent is seen to increase by more than a factor of five from 77 K to 22 K.

The effective surface resistance of sample F was calculated using equation (10). The effective surface resistances for both superconducting resonators and the surface resistance of the gold resonator are plotted as a function of temperature in figure 9.

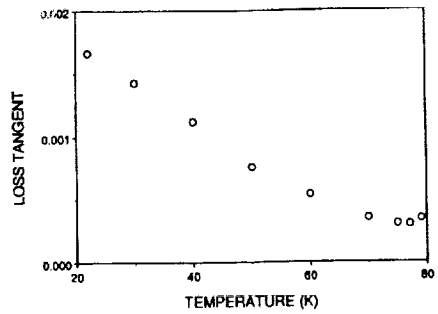

Figure 8. Loss tangent of $NdGaO_3$ from 20 K to 80 K extracted from the 10 GHz measurements on superconducting resonator G and the gold resonator.

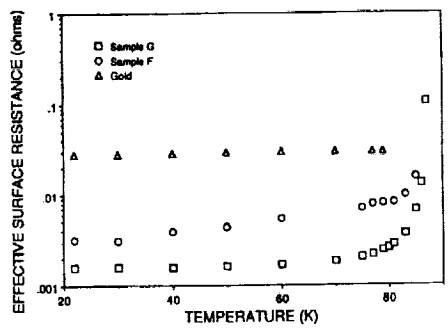

Figure 9. Effective surface resistance at 10 GHz as a function of temperature for superconducting resonators F (circles) and G (squares) and the gold resonator (triangles).

5. Conclusions

$YBa_2Cu_3O_{7-\delta}$ thin films were formed on $NdGaO_3$ substrates by laser ablation. The best films had critical temperatures greater than 89 K and critical current densities exceeding 2×10^6 A cm^{-2} at 77 K. Two films were patterned into microstrip ring resonators with gold ground planes. The better of the two resonators had an unloaded quality factor of 876 at 77 K, which was six times larger than that of a gold resonator of identical geometry. The unloaded quality factor increased to 910 at 70 K but then decreased as the temperature was further lowered. Qualitatively similar temperature dependence was observed for the gold resonator indicating that the losses at low temperature were being dominated by dielectric losses in the substrate.

The temperature dependence of the loss tangent was extracted from the measured quality factors of the gold and superconducting resonators for temperatures from 22 K to 80 K. The method employed to extract the temperature dependence of the loss tangent uses a previously reported value of 3×10^{-4} at 77 K [11]. The loss tangent was found to increase from 3×10^{-4} at 77 K to 1.7×10^{-3} at 22 K. These loss tangents are large compared to those for $LaAlO_3$, particularly at low temperatures, and $LaAlO_3$ is a better substrate than $NdGaO_3$ for microwave applications of high-temperature superconductors.

Acknowledgments

The authors are grateful to Mr Norman Rohrer for his assistance with the microwave measurements. This research was supported by the National Aeronautics and Space Administration under Award No. NCC-3-197.

References

[1] Laibowitz R B, Koch R H, Chaudhari P and Gambino R J 1987 *Phys. Rev.* B **35** 8822
[2] Simon R W, Platt C E, Lee A E, Lee G S, Daly K P, Wire M S, Laine J A and Urbanik M 1988 *Appl. Phys. Lett.* **53** 2677
[3] Samara G A, 1990 *J. Appl. Phys.* **68** 4214
[4] O'Bryan H M, Gallagher P K, Berkstresser G W and Brandle C D 1990 *J. Mater. Res.* **5** 183
[5] *Synoptics, Synthetic Crystal and Optical Products Data sheet*
[6] Giess E A *et al* 1990 *IBM J. Res. Develop.* **34** 916
[7] Sasaura M, Miyazawa S and Mukaida M 1990 *J. Appl. Phys.* **68** 3643
[8] Phillips J M, Siegal M S, Perry C L and Marshall J H 1991 *IEEE Trans. Magn.* **27** 1006
[9] Koren G, Gupta A, Giess E A, Segmiller A and Laibowitz R B 1989 *Appl. Phys. Lett.* **54** 1054
[10] Mukaida M, Miyazawa S, Sasaura M and Kuroka K 1990 *Japan. J. Appl. Phys.* **29** L936
[11] Young K H, Negrete G V, Sun J Z and James T W 1991 *Japan. J. Appl. Phys.* **30** L1355
[12] Romanofsky R R 1989 *NASA Technical Paper* TM-2899
[13] Rohrer N J, To H Y, Valco G J, Bhasin K B, Chorey C M and Warner J D 1990 *Science and Technology of Thin Film Superconductors 2* (New York: Plenum) p 615
[14] Chorey C M, Kong K S, Bhasin K B, Warner J D and Itoh T 1991 *IEEE Trans. Microwave Theory Tech.* **MTT-39** 1480
[15] Valco G J, Blemker A R and Bhasin K B 1992 *Microwave and Optical Technology Letters*
[16] Takamoto J, Oshita F and Fetterman H 1989 *IEEE Trans. Microwave Theory Tech.* **MTT-37** 1650
[17] Pucel R A, Masse D J and Hartwig C P 1968 *IEEE Trans Microwave Theory Tech.* **MTT-16** 342
[18] Sheen D M, Ali S M, Oates D E, Withers R S and Kong J A 1991 *IEEE Trans. Appl. Supercond.* **ASC-1** 108
[19] Van Duzer T and Turner C W 1981 *Principles of Superconductive Devices and Circuits* (New York: Elsevier) p 131

N94-20516

.CaBaCuO HIGH Tc SUPERCONDUCTING MICROSTRIP RING RESONATORS DESIGNED FOR 12 GHZ

G.Subramanyam and V.J.Kapoor
Microwave Electronics Laboratory
Department of Electrical and Computer Engineering
University of Cincinnati, Cincinnati, OH-45221-0030

C.M.Chorey
Sverdrup Technology Inc., (NASA Lewis Group)

K.B.Bhasin
NASA Lewis Research Center, Cleveland, OH-43435

ABSTRACT

Microwave properties of sputtered Tl-Ca-Ba-Cu-O thin films were investigated by designing, fabricating and testing microstrip ring resonators. Ring resonators designed for 12 GHz fundamental resonance frequency, were fabricated and tested. From the unloaded Q values for the resonators, the surface resistance was calculated by separating the conductor losses from the total losses. The penetration depth was obtained from the temperature dependence of resonance frequency, assuming that the shift in resonance frequency is mainly due to the temperature dependence of penetration depth. The effective surface resistance at 12 GHz and 77 K was determined to be between 1.5 and 2.75 mΩ, almost an order lower than Cu at the same temperature and frequency. The effective penetration depth at 0 °K is approximately 7000 Å.

1. INTRODUCTION

Among the high Tc materials, thallium based superconductors are very attractive for elecronic applications, as they have shown the highest Tc[1], high Jc[2-3], and the lowest values for microwave surface resistance(Rs)[3-4]. The foremost applications of high Tc thin films is

© Reprinted from Applied Superconductivity, vol. 1, nos. 10-12, pp. 1605-1614, 1993, with kind permission from Pergamon Press Ltd., Headington Hill Hall, Oxford 0X3 0BW, UK.

expected to be in the area of 'passive microwave devices' such as resonators, filters and delay lines. High Tc superconductors have a greater impact on passive microwave devices because of their lower surface resistance in thin films of high Tc superconductors, compared to Cu and Au, corresponding to higher Q and improved performance in passive microwave devices. The second advantage is the frequency independent penetration depth as compared to frequency dependent skin depth in normal conductors. This means, dispersion introduced in superconducting components will be negligible upto frequencies as high as 1 THz. Compact delay lines[5], filters[6], and resonators are possible, with lower losses.

This paper addresses the design, fabrication and characterization of $Tl_2Ca_1Ba_2Cu_2O_x$ (2122) thin film based microstrip ring resonators.

2. EXPERIMENTAL

A microstrip ring structure resonates if its electrical length is an integral multiple of the guide wavelength. A simple ring resonator device was designed which consisted of a ring structure separated from the feed line by a small coupling gap. The size of the coupling gap determines the coupling between the feed line and the ring resonator. A ring resonator designed for 10 mil thick $LaAlO_3$ substrates ($\epsilon_r = 24.5$), for a fundamental resonance at 12 GHz is shown in figure 1.

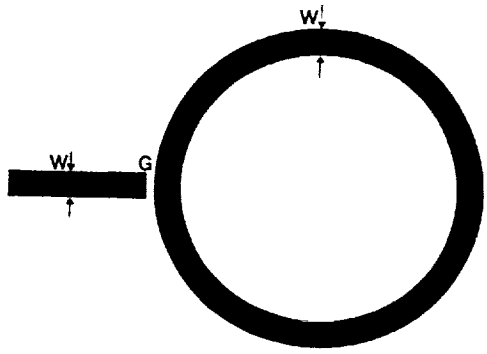

Fig.1 The ring resonator device designed for 12 GHz resonance

In the figure, the linewidth of the ring and the microstrip feed line is W = 5.6 mils, the coupling gap G = 1.75 mils, and the mean radius of the ring $R = (R_1 + R_2)/2$ = 77 mils. The characteristics impedance of the microstrip is 41 Ohms at 12 GHz. The design of the ring resonator has been described by Chorey et al[7].

TlCaBaCuO ring resonators were fabricated by patterning 0.3 μm thin films using AZ 1421 positive photoresist photolithography and wet chemical etching techniques. The fabrication and patterning of TlCaBaCuO thin films is described in detail elsewhere[8]. The ring resonators were annealed using our standard annealing procedures[8-9]. The samples were divided into two groups: one set of samples with 1 μm gold film on the bottom side of the $LaAlO_3$ substrate for the ground plane formation and the second set with 0.3 μm TlCaBaCuO superconducting thin film ground plane. The ground plane side superconductor was deposited and post-processed using our routine post-deposition methods, after the microstrip ring resonator was fabricated on the top side.

A ring resonator was mounted in a gold plated Copper test fixture of 1" wide, 2" long and 1" thickness. The test fixture was placed on the cold head of the helium gas closed cycle cryogenic system. Connections to the HP 8720 network analyzer were made using a 0.141" semi-rigid co-axial cable of 50 ohms characteristic impedance. Before measurements were performed on ring resonators, standard one port calibration was performed at room temperature.

The resonator quality factor(Q) was obtained from the swept frequency reflection measurements[7,10]. The unloaded Q is obtained by separating the external losses in the feed line and due to coupling. The loaded Q and the unloaded Q are related through the reflection coefficients at resonance and far from the resonance[10]. The determination of whether the resonator was overcoupled or undercoupled was made from the Smith chart and also the phase response of the resonator. Typically, the ring resonators were overcoupled. Measurements for the superconducting

resonator were performed at the fundamental resonance frequency of 12 GHz, and an input power level of -30 dBm.

3. RESULTS

Unloaded Q versus temperature characteristics for an all-superconducting ring resonator is shown in figure 2. The curve A is the data for the high Tc thin film ring resonator with a superconducting ground plane. For comparison, data for the gold resonator is also shown in curve B.

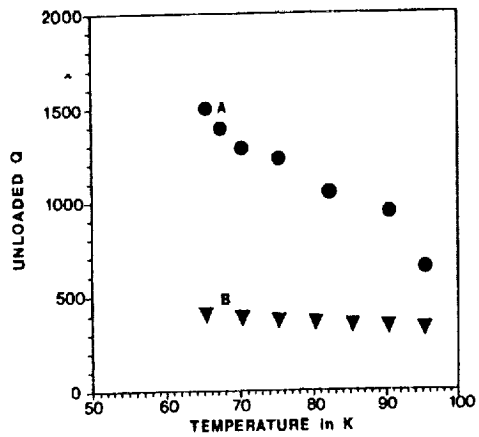

Fig.2. The unloaded Q vs Temperature for an all-superconducting resonator

The unloaded Q of the ring resonator with superconducting ground plane is approximately four times higher than the gold resonator at 65 °K. In addition, the unloaded Q of the superconducting ring resonator shows an increasing trend in Q with decreasing temperature, whereas the superconducting ring resonators with gold ground plane show a saturation of Q at low temperatures due to the dominance of ground plane conductor losses.

The effective surface resistance (R_s) of the superconducting thin films, were obtained from ring resonator quality factor (Q) measurements. By separating the conductor and dielectric losses, the Rs was calculated using the standard microstrip loss equations described by Pucel et al[11]. The Rs at 12 GHz, and 77 °K was determined to be typically between 1.5 and 2.75 mΩ, almost an order lower than Rs of Cu at the same temperature and

frequency. The swept frequency reflection measurements performed at several temperatures, is also used in determining the penetration depth of the TlCaBaCuO superconducting thin films. The resonance frequency was measured at each temperature for ring resonators. A typical measured resonance frequency shift with respect to temperature for a superconducting ring resonator with approximately 1 μm thick gold ground plane is shown in figure 3.

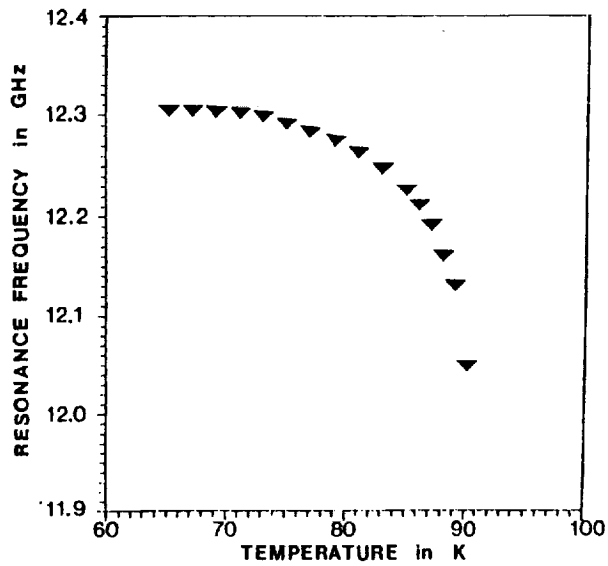

Fig.3. Resonant frequency vs Temperature characteristics for a resonator

The shift in resonance frequency with temperature is mainly due to the temperature dependence of the penetration depth of the superconductor. Thus, the resonance frequency shift is an indirect method of determining the penetration depth. From the figure, the change in resonance frequency below 70 °K is almost negligible. The detailed analysis of this figure to determine the penetration depth of the superconducting thin films, is given in the next section.

4. ANALYSIS AND DISCUSSIONS

The phase velocity of a superconducting microstrip transmission line with a superconducting ground plane is given by[12],

$$v_{ph} = c/\sqrt{\epsilon_{eff}} * \{1 + 2 * \lambda/h * \coth(t/\lambda)\}^{-0.5} \qquad \text{--->(1)}$$

where c is the velocity of light, ϵ_{eff} is the effective dielectric constant, h is

the substrate thickness, t is the thickness of the microstrip, λ the penetration depth of the superconducting microstrip. The penetration depth is temperature dependent based on the Gorter-Casimir relationship[13] ie.,

$$\lambda(T) = \lambda(0)*[1-(T/Tc)^4]^{-0.5} \quad \text{---> (2)}$$

for temperature T less than Tc. $\lambda(0)$ is the penetration depth at T=0 °K. The resonance frequency of the ring resonator is given by the equation

$$f = n*v_{ph}/(2*L) \quad \text{---> (3)}$$

where f is in GHz, L is the mean circumference of the ring in mm, and n is the integer order of resonance. From the temperature dependence of resonance frequency measurements and the above equations, the best value of $\lambda(0)$ was determined to be 6890 Å. The typical value ranges between 7000 Å and 8000 Å. Since the thin films are only 0.3-0.4 μm thick, the penetration depth depends upon the properties of the superconductor through the entire film.

A theoretical model based on the Phenomenological loss Equivalence Method (PEM) approximation[14-15] was employed to determine the theoretical variation of conductor losses with temperature for the cases of superconducting microstrip/gold ground plane, and superconducting microstrip/superconducting ground plane. Both these cases were compared to the attenuation constant of a gold microstrip on $LaAlO_3$ substrate.

The attenuation constant for a superconducting microstrip is calculated from the formula[15],

$$\alpha = (T/Tc)^4/[1-(T/Tc)^4]^{3/2} * G_1/4 * \sigma_n/Z * w^2 * \mu^2 * \lambda(0)^3 * \coth(X) + X \operatorname{cosec}^2(X) \ \text{Np/m} \quad \text{---> (4)}$$

where $X = A * G_1/\lambda(0) * [1-(T/Tc)^4]^{1/2}$.

G_1 is the geometric factor given by the equation

$$G_1 = 1/(\pi h)*[1-(W_e/(4h))^2]*[1/2+h/W_e+h/(\pi W_e)*\ln(2h/t) \quad \text{---> (5)}$$

W_e is the effective width of the microstrip, and A is the area of cross-section of the microstrip, T is the measurement temperature below Tc, and $\lambda(0)$ the penetration depth at 0 °K of the superconductor.

The parameters assumed for the calculations are the relative dielectric

constant (ϵ_r) of $LaAlO_3$ to be 24.5[7], the loss tangent (tan δ) of $LaAlO_3$ to be $8.3*10^{-5}$ below 100 °K[7], the substrate thickness (h) of 10 mil, the width of the microstrip (W) of 142 μm, corresponding to a characteristic impedance of 41 ohms at 12 GHz, the thickness of the superconducting microstrip(t) to be 0.3 μm, the ground plane thickness of 1 μm for gold ground plane and 0.3 μm for superconducting ground plane, the zero resistance Tc of the TlCaBaCuO thin films was to be 100 °K, and the normal conductivity at Tc (σ_n) of $1.5*10^6$ S/m.

The ground plane conductor losses can be calculated by the same method, using the geometric factor G_2 instead of G_1 in the equation 4.

$$G_2 = 1/(2\pi h) * [1-(W_e/4h)^2] \quad \text{---> (6)}$$

Figure 4 shows temperature variation of the attenuation due to conductor losses for a gold microstrip (curve A), a superconducting microstrip with a gold ground plane (curve B), and a superconducting microstrip with a superconducting ground plane (curve C) as determined using equations 4-6.

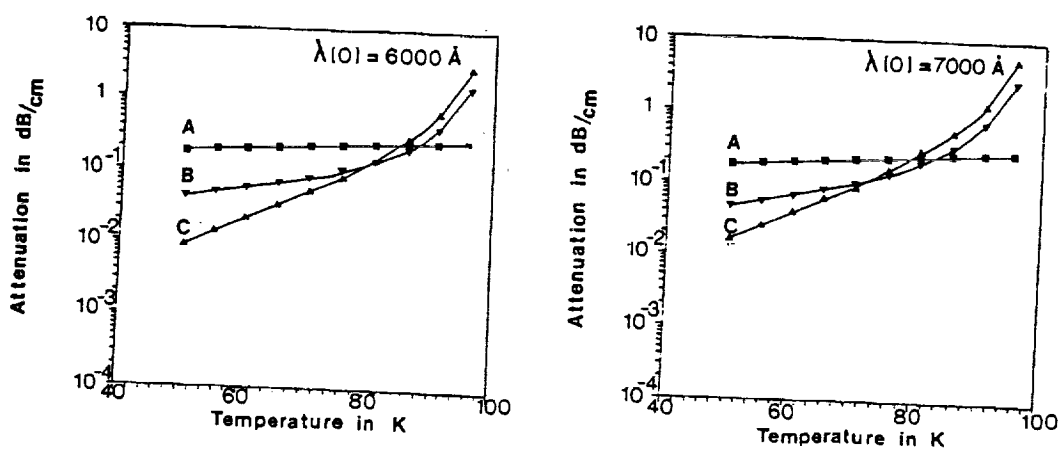

Fig.4. Theoretical attenuation loss vs temperature characteristics for superconducting microstrip with gold ground plane (B), and superconducting ground plane (C), compared to a gold microstrip (A).

The diagram in the left is for $\lambda(0)$ of 6000 Å, and the one in the right is for $\lambda(0)$ of 7000 Å. The figures show lower attenuation for the microstrip with superconducting ground plane (curve C) compared to the one with gold ground-plane (curve B), below 77 °K.

The surface resistance of the superconducting thin film can be obtained from the attenuation equation

$$R_s = 2 Z_0 \alpha / G_1 \qquad \text{---> (7)}$$

where Z_0 is the characteristic impedance of the microstrip.

The microwave properties of TlCaBaCuO thin films obtained from the ring resonator measurements were used in designing a reflection type hybrid phase shifter circuit based TlCaBaCuO thin film components and GaAs MESFETs. The design of the superconducting microstrips included the effects due to complete field penetration in the films. The phase bits were designed for 90 and 180 degrees phase shift, operating at 4 GHz center frequency, 25% bandwidth and phase error less than 5 degrees. Each phase bit consists of a 3 dB Lange coupler, impedance transforming networks and GaAs MESFET switches. A 180 degrees phase bit circuit was fabricated and tested using gold microstrip. The circuit showed a phase shift of 180.06 degrees at 3.9277 GHz. The insertion loss of the circuit was as low as -2.12 dB in the off state of the switching devices, and -2.523 dB in the on state. The input and output reflection losses were above 10 dB. The results of the superconductor/semiconductor hybrid phase shifters will be published elsewhere[16].

5. SUMMARY

The microwave properties of TlCaBaCuO thin films were investigated by designing, fabricating and characterizing a microstrip ring resonator. The resonator was designed for a fundamental resonance frequency of 12 GHz, and for fabrication on 10 mil thick $LaAlO_3$ substrates. Ring resonators with gold ground plane of 1 μm thickness and TlCaBaCuO superconducting

ground plane of 0.3 μm thickness were fabricated and characterized at cryogenic temperatures. The unloaded Q for the superconducting resonators were above 1500 at 65 °K, compared to 370 for a gold resonator. The surface resistance of the TlCaBaCuO thin films obtained by separating conductor losses from the Q measurements is typically between 1.5 and 2.75 m-Ohms at 12 GHz and 77 °K, almost an order lower than Cu and Au at the same temperature and frequency. The penetration depth at 0 °K, was calculated from the resonance frequency shift with temperature measurements. The typical values for the penetration depth at 0 °K is approximately between 7000 and 8000 Å.

The conductor losses in the superconducting microstrips with superconducting ground plane were compared to the ones with gold ground plane using a theoretical model called the Phenomenological loss Equivalence Method (PEM). This model predicted lower conductor losses for the microstrip with superconducting ground plane, below 77 °K.

ACKNOWLEDGEMENTS

This research was supported by NASA Lewis Research Center. The authors acknowledge the support and encouragement of Dr.Regis Leonard of NASA Lewis Research Center.

REFERENCES

1. Parkin, S.S.P., Lee, V.Y., Engler, E.M., Nazzal, A.I., Huang, T.C., Gorman, G., Savoy, R., and Beyers, R., Phys.Rev.Lett., 60, 2539 (1988).
2. Ginley, D.S., Kwak, J.F., Venturini, E.L., Morosin, B., and Baughman, R.J., Physica C, 160, 42 (1989).
3. Lauder, A., Wilker, C., Kountz, D.J., Holstein, W.L., and Face, D.W., "High performance superconducting thin films on large area substrates", presented at the IEEE Applied Superconductivity Conference, August 24-28, 1992, Chicago, IL.

4. Application Notes from "Superconductor Technologies", Santa Barbara, CA, July 1992.

5. Bourne L.C, Hammond R.B, Robinson McD., Eddy M.M, Olson W.L, and James T.W, Appl.Phys.Lett. 56, 2333 (1990).

6. Hammond, R.B., Negrete, G.V., Schmidt, M.S., Moskowitz, M.J., Eddy, M.M., Strother, D.D., and Skoglund, D.L., IEEE MTT symposium, June 1990.

7. Chorey, C.M., Kong, K.S., Bhasin, K.B., Warner, J.D., and Itoh, T., IEEE Trans. Microwave Theory Tech. 39, 1480 (1991).

8. Subramanyam, G., Radpour, F., Kapoor, V.J., and Lemon, G.H., J.Appl.Phys. 68, 1157 (1990).

9. Subramanyam, G., Kapoor, V.J., Chorey, C.M., and Bhasin, K.B., to be published in J. Appl.Phys., 15 September 1992.

10. Aitken, J., Proc.of Inst.Elec.Eng. 123, 855 (1976).

11. Pucel, R.A., Masse, D.J., and Hartwig, C.P., IEEE Trans. Microwave Theory Tech., 16, 342 (1968). Also "Correction to losses in microstrip", IEEE Microwave Theory Tech., 16, 1064 (1968).

12. Kautz, R.L., J.Appl.Phys. vol.49, 308 (1978).

13. Van Duzer, T., and Turner, C.W., 'Principles of Superconductive devices and circuits', chapter 3, pp 92-138. Elsevier North Holland Inc., New York, 1981.

14. Lee, H.-Y, and Itoh, T., IEEE Trans. Microwave Theory Tech., 37, 1904 (1989).

15. Baiocchi, O.R., Kong, K.-S., Ling, H., and Itoh, T., IEEE Microwave and Guided Wave Lett. 1, 2 (1991).

16. Subramanyam, G., Kapoor, V.J., and Bhasin, K.B., manuscript under preparation.

Conductor-Backed Coplanar Waveguide Resonators of $YBa_2Cu_3O_{7-\delta}$ on $LaAlO_3$

Félix A. Miranda, *Member, IEEE*, Kul B. Bhasin, *Senior Member, IEEE*, Keon-Shik Kong, *Member, IEEE*, Tatsuo Itoh, *Fellow, IEEE*, and Mark A. Stan

***Abstract*— Conductor-backed coplanar waveguide (CBCPW) resonators operating at 10.8 GHz have been fabricated from laser ablated and off-axis magnetron sputtered $YBa_2Cu_3O_{7-\delta}$ (YBCO) high-temperature superconducting (HTS) thin films on $LaAlO_3$. These resonators were tested in the temperature range from 14 to 92 K. The unloaded quality factor (Q_0) at 77 K of the HTS CBCPW resonators was 3 to 4 times that of a similar gold (Au) resonator. To our knowledge, these results represent the first reported measurements of HTS-based CBCPW resonators.**

I. Introduction

THE coplanar waveguide (CPW) structure is advantageous for HTS-based microwave IC fabrication mainly because of its geometrical attribute of having the signal ground planes on the same surface as the signal transmission line [1]–[3]. To improve thermal contact between the substrate of the CPW and the cooling fixture, a layer of a good conducting material can be deposited onto the reverse side of the substrate. This conducting layer also acts as an additional ground plane for the structure. When such a ground plane is added, the resulting structure is known as a conductor-backed coplanar waveguide (CBCPW). To date, coplanar superconducting circuit tests have been reported for structures without a back-ground plane, and only at 77 K and 4.2 K [1]–[4]. This letter represents the first report of measurements on several $YBa_2Cu_3O_{7-\delta}$ (YBCO) HTS-based CBCPW resonators from 14 K to 92 K and at 10.8 GHz. The performance of these resonators, as compared with that of an Au-based counterpart is presented.

II. Experimental

The CBCPW resonators analyzed in this study were patterned on laser ablated and off-axis magnetron sputtered $YBa_2Cu_3O_{7-\delta}$ (YBCO) thin films on 1.0 × 1.0 × 0.05 cm (100) $LaAlO_3$ substrates. A schematic of the CBCPW resonator is shown in Fig. 1. This pattern was transferred to the HTS films using standard photolithography techniques and a subsequent "back-etching" process using a 1% phosphoric acid (H_3PO_4) solution. Afterwards, the ground plane on the opposite side of the substrate was formed by evaporation of a Au layer ~2.5 μm thick on top of a Chromium layer (~150 Å) previously evaporated on the $LaAlO_3$ to improve Au adhesion. For comparison purposes, a similar resonator was made with its CPW part consisting of an evaporated Au layer ~1.2 μm thick. The length (L2) and width (S) of the center conductor were 7.020 mm and 0.200 mm, respectively. The gaps on each side (W) and at the bottom (G2) of the resonator were 0.530 mm, and G3 was 0.630 mm. The coupling between the external coaxial lines and the resonator was achieved through an SMA launcher. The center pin of the connector was placed in direct contact with the feed line that tapered from 0.559 mm to the width of the center conductor over a length L1 of 1.000 mm. Coupling to the resonator was achieved across a gap (G1) 0.050 mm wide. To improve the contact between the launcher and the feed line, silver (Ag) contacts (~2500 Å thick) were evaporated onto the end of the feed line and the coplanar ground planes. The transition temperature ($T_c(R=0)$) of the resonators after being patterned was measured using standard four-point probe techniques. The measured T_c values were 91.1 K, 89.9 K, and 84 K, for samples 1 (laser ablated), 2 (magnetron sputtered), and 3 (laser ablated), respectively. Each resonator was mounted on a brass test fixture which was bolted to the cold finger of a close-cycle-helium-gas refrigerator and enclosed inside a vacuum can. The reflection coefficient of the circuit was measured using an HP-8510C network analyzer, and was used to determine the unloaded quality factor (Q_0) of the resonator according to the procedure described in [5]. The network analyzer was calibrated with short, open, and load standards before the beginning of each measurement cycle.

III. Results

The results of the measurements on the CBCPW resonators are summarized in Table I. Films thickness and T_c values were measured after patterning. The Q_0's versus temperature for the resonators tested in this study are shown in Fig. 2. The results show that sample 2 has the highest Q_0 values for the temperature range in common for all the resonators. Its Q_0 at 77 K and 10.8 GHz was 470, which is approximately four times better than that of the Au resonator at the same temperature and frequency. However, this value is approximately 0.4 of the best reported value for laser ablated YBCO-based CPW structures at 8.8 GHz and 77 K [6]. This reduction may be due to the effect of adding a back conductor.

Manuscript received March 6, 1992. Editorial decision made by S. Maas.

F. A. Miranda and K. B. Bhasin are with the National Aeronautics and Space Administration, Lewis Research Center, Cleveland, OH 44135.

K.-S. Kong is with the Electrical and Computer Engineering Department, University of Texas at Austin, Austin, TX 78712.

T. Itoh is with the Department of Electrical Engineering, University of California at Los Angeles, 66–147A Engineering IV, 405 Hilgard Avenue, Los Angeles, CA 90024–1594.

M. A. Stan is with the Department of Physics, Kent State University, Kent, OH 44242.

IEEE Log NUmber 9201477.

1992 IEEE. Reprinted, with permission, from IEEE Microwave and Guided Wave Letters, vol. 2, no. 7, July 1992, pp. 287-288.

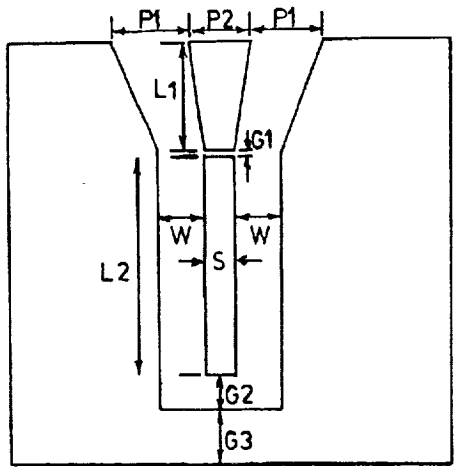

Fig. 1. Top view of the conductor-backed coplanar waveguide (CBCPW) resonator (9.230 × 9.230 mm). P1 = 0.533 mm, P2 = 0.559 mm, L1 = 1.000 mm, L2 = 7.020 mm, W = 0.530 mm, S = 0.200 mm, G1 = 0.050 mm, G2 = 0.530 mm, and G3 = 0.630 mm. The relative dielectric constant (ϵ_r) of the substrate is 22.

TABLE I
FILM PROPERTIES OF CONDUCTOR-BACKED COPLANAR WAVEGUIDE RRESONATORS

Sample	Deposition Temp. (°C)	Film Thickness (nm)	T_c(K)[a]	Q_0(77 K)[b]	f_0(GHz; @ 77 K)[c]
Au		1200		110	10.803
1	715	350	91.1	412	10.805
2		350	89.9	470	10.755
3	715	310	84.0	159	10.662

[a] dc transition temperature.
[b] Unloaded quality factor.
[c] Resonance frequency.

For microwave applications an HTS-based resonator should be characterized by a high T_c (~90 K), a rapid increase in Q_0 as the sample is cooled below T_c, and a fast stabilization of the Q_0 with respect to temperature at temperatures not far below T_c. Of the three resonators under study, samples 1 and 2 seem to satisfy these demands. However, although resonances for samples 1 and 2 were observed around the same temperature (~91 K), the increase in Q_0 with decreasing temperature for sample 1 is not as sharp as that for sample 2. The behavior of sample 1 as compare with sample 2 could be associated with a higher degree of homogeneity for the sputtered film than that attained for the laser ablated one for which the more gradual change of the Q_0 with temperature may be a consequence of a distribution of T_c's from grain to grain and other film inhomogeneities. However, the closeness of the Q_0 values for these samples indicates that films suitable for microwave applications can be obtained by off-axis magnetron sputtering as well as laser ablation.

IV. CONCLUSION

Conductor-backed coplanar waveguide (CBCPW) resonators

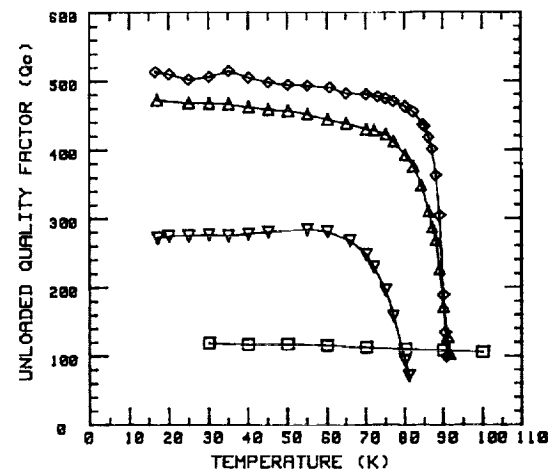

Fig. 2 Unloaded quality factor (Q_0) versus temperature for a Au (□), and YBCO CBCPW resonators on $LaAlO_3$; sample 1 (△; laser ablated), sample 2 (◇; off-axis magnetron sputtered), sample 3 (▽; laser ablated).

have been patterned on laser ablated and off-axis magnetron sputtered YBCO HTS thin films on $LaAlO_3$. These resonators were tested in the temperature range from 14 to 92 K and an unloaded quality factor Q_0 as high as 470 was obtained at 10.8 GHz and 77 K. This value is four times higher than that of a similar all Au resonator at the same frequency and temperature. We found that similar Q_0 values were obtained for CBCPW resonators fabricated on both off-axis magnetron sputtered and laser ablated YBCO thin films of comparable T_c's.

ACKNOWLEDGMENT

The authors wish to thank Mr. J. Olsavsky, Mr. C. Hulbert, and Mr. N. Varaljay for technical assistance. The authors also acknowledge Mr. C. M. Chorey for helpful discussions and suggestions, and for critical reading of the manuscript.

REFERENCES

[1] A. A. Valenzuela, and P. Russer, "High-Q coplanar transmission line resonator of $YBa_2Cu_3O_{7-x}$ on MgO," *Appl. Phys. Lett.*, vol. 55, pp. 1029–1031, 1989.
[2] A. A. Valenzuela, B. Daalmans, and B. Roas, "High-Q coplanar transmission line resonator of $YBa_2Cu_3O_{7-x}$ on $LaAlO_3$," *Electron. Lett.*, vol. 25, pp. 1435–1436, 1989.
[3] M. R. Namordi, A. Mogro Campero, L. G. Turner, and D. W. Hogue, "Comparison of high-temperature-superconductor and metal-based resonators," *IEEE Trans. Microwave Theory Tech.*, vol. 39, pp. 1468–1474, Sept. 1991.
[4] R. Klieber, R. Ramisch, A. A. Valenzuela, R. Weigel, and P. Russer, "A coplanar transmission line high-T_c superconductive oscillator at 6.5 GHz on a single substrate," *IEEE Microwave Guided Wave Lett.*, vol. 2, pp. 22–24, Jan. 1992.
[5] C. M. Chorey, K. S. Kong, K. B. Bhasin, J. D. Warner, and T. Itoh, "YBCO superconducting ring resonators at millimeter-wave frequencies," *IEEE Trans. Microwave Theory Tech.*, vol. 39, pp. 1480–1487, Sept. 1991.
[6] G. J. Valco, A. R. Blemker, and K. B. Bhasin, "Laser ablated $YBa_2Cu_3O_{7-\delta}$ high-temperature superconductor coplanar waveguide resonator," *Microwave Opt. Technol. Lett.*, vol. 5, pp. 234–236, 1992.

CONDUCTOR-BACKED COPLANAR WAVEGUIDE RESONATORS OF Y-Ba-Cu-O AND Tl-Ba-Ca-Cu-O ON $LaAlO_3$

F.A. Miranda and K.B. Bhasin
National Aeronautics and Space Administration
Lewis Research Center
Cleveland, Ohio 44135

M.A. Stan
Kent State University
Department of Physics
Kent, Ohio 44242

K.S. Kong
TRW
Redondo Beach, California 90278

T. Itoh
University of California at Los Angeles
Department of Electrical Engineering
Los Angeles, California 90024

Abstract--Conductor-backed coplanar waveguide (CBCPW) resonators operating at 10.8 GHz have been fabricated from Tl-Ba-Ca-Cu-O (TBCCO) and Y-Ba-Cu-O (YBCO) thin films on $LaAlO_3$. The resonators consist of a coplanar waveguide (CPW) patterned on the superconducting film side of the $LaAlO_3$ substrate with a gold ground plane coated on the opposite side. These resonators were tested in the temperature range from 14 to 106 K. At 77 K, the best of our TBCCO and YBCO resonators have an unloaded quality factor (Q_u) 7 and 4 times, respectively, larger than that of a similar all-gold resonator. In this study, the Q_u's of the TBCCO resonators were larger than those of their YBCO counterparts throughout the aforementioned temperature range.

I. INTRODUCTION

Since their discovery in 1986, high transition temperature superconducting (HTS) compounds have been employed in the development of passive microwave transmission structures such as resonators, filters, and delay lines [1-3]. Ease of fabrication and performance reliability are two requirements that these HTS compounds should meet in order to be used in microwave circuits. Because of its geometrical attribute of having the ground planes on the same surface as the signal transmission line, coplanar waveguide (CPW) structures are advantageous for HTS-based microwave integrated circuits. When a good conducting layer is deposited on the opposite side of the CPW supporting substrate the structure is known as a conductor-backed coplanar waveguide (CBCPW).

Recently, reports on YBCO-based CPW and CBCPW resonators have been published [4-7]. Until now, a comparative study to determine which type of HTS compound is more appropriate for the optimization of these structures for microwave applications has not been done. In this paper we present our results on the performance of CBCPW resonators fabricated from TBCCO and YBCO thin films on $LaAlO_3$.

II. EXPERIMENTAL

Figure 1 shows a schematic representation of the CBCPW resonators analyzed in this study. The TBCCO resonators were custom made by Superconductor Technologies Inc. from laser ablated films (~800 nm thick) deposited onto 1.0x1.0x0.05 cm (100) $LaAlO_3$ substrates. The YBCO resonators were patterned by us on laser ablated (NASA-Lewis) and magnetron sputtered (Conductus Inc.) thin films (~350 nm) on $LaAlO_3$ substrates of the aforementioned dimensions and crystallographic orientation. The pattern shown in Fig. 1 was transferred to the HTS films using standard photolithography techniques followed by a "back-etching" process using a 1% phosphoric acid (H_3PO_4) solution. The ground plane on the opposite side of the substrate was formed by successive evaporations of a 150 Å thick chromium layer and a ~2.5 μm thick gold layer. A similar all-gold CBCPW resonator, with its CPW layer ~ 1.2 μm thick, was also fabricated for comparison purposes. The testing of the resonators was done by mounting them on a brass test fixture bolted to the cold finger of a closed-cycle-helium-gas refrigerator and enclosed inside a vacuum can with feedthroughs to allow coupling between the resonator and a coaxial waveguide. The coupling between the coaxial line and the resonators was achieved through an SMA launcher. The center pin of the connector was placed in direct contact with the feed line that tapered from 0.559 mm to the width of the center conductor over a length (L1) of 1.000 mm. Coupling to the resonator was achieved across a gap (G1) 0.050 mm wide. The reflection coefficient of the resonators was measured using an HP-8510C network analyzer, and was used

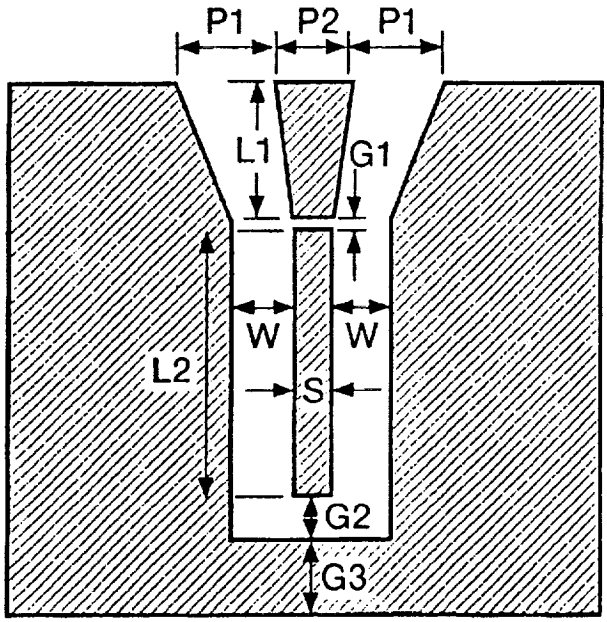

Fig. 1 Top view of the conductor-backed coplanar waveguide resonator (9.230x9.230 mm). P1=0.533 mm, P2=0.559 mm, L1=1.000 mm, L2=7.020 mm. W=0.530 mm, S=0.200 mm, G1=0.050 mm, G2=0.530 mm, and G3=0.630 mm. The relative dielectric constant (ε_r) of the substrate is 22. The crosshatched sections represent the HTS material.

to determine the unloaded quality factor (Q_u) of the resonator according to the procedure described in [8]. Before the beginning of each measurement cycle the network analyzer was calibrated with short, open, and load standards.

In order to improve the contact between the launcher and the feed line, silver contacts (~250-300 nm thick) were evaporated onto the end of the feed line and the coplanar ground planes. Immediately after the evaporation the resonators were annealed in flowing oxygen (~1 SLM). The YBCO resonators were annealed at 450°C for 1 hr, and cooled afterwards at a rate of 2°C/min to room temperature. The TBCCO resonators were annealed at 450°C for 10 min, followed by a rapid cooling on a fire brick. The contact resistivity was measured by a three-point probe method, and was found to be ~2.7×10^{-6}, 9.0×10^{-8}, and 4.5×10^{-9} $\Omega\,cm^2$ for the laser ablated YBCO, the magnetron sputtered YBCO, and the TBCCO films, respectively. The transition temperature ($T_c(R=0)$) of the resonators was measured before and after silver contacts deposition and annealing using a standard four-point probe technique.

III. RESULTS

Table 1 shows a summary of the results of the characterization of the CBCPW resonators. The T_c values and film thicknesses correspond to measurements performed after patterning and annealing of the films. The Q_o's versus temperature of the resonators analyzed in this work are shown in Fig.2.

Table 1. Properties of Conductor-Backed Coplanar Waveguide Resonators at 77 K.

Sample	Film Thickness (nm)	T_c(K)[a]	Q_o[b]	R_s(mΩ)[c]	f_o(GHz)[d]
Au	1200		110	24.0	10.803
1 (YBCO)	310	84.0	159	16.6	10.662
2 (YBCO)	350	91.1	412	6.4	10.805
3 (YBCO)	350	89.9	470	5.6	10.755
4 (TBCCO)	800	103.5	471	5.6	10.742
5 (TBCCO)	800	103.0	577	4.6	10.750
6 (TBCCO)	800	104.2	823	3.2	10.680

[a] dc transition temperature after patterning and annealing.
[b] Unloaded quality factor.
[c] Effective surface resistance.
[d] Resonance frequency.

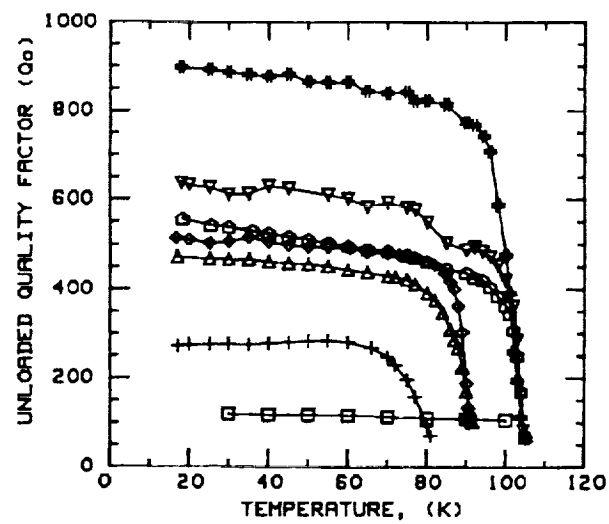

Fig. 2 Unloaded quality factor (Q_u) versus temperature for CBCPW resonators on $LaAlO_3$. Sample 1 (LA YBCO, +), sample 2 (LA YBCO, △), sample 3 (MS YBCO, ◇), sample 4 (LA TBCCO, ⌂), sample 5 (LA TBCCO, ▽), and sample 6 (LA TBCCO, ⋔). A Au resonator (□) is also shown for comparison.

These data were found to be independent of applied power within the range of -5.0 to -26.0 dBm. The lowest Q_u observed in this study for any of the HTS resonator corresponded to a laser ablated (LA) YBCO film (sample 1, Tab. 1). This film exhibited a T_c=84 K after annealing, and although Scanning Electron Microscopy (SEM) micrographs showed a smooth surface, some porosity was noticeable on one of the coplanar ground planes which gave it a hazy appearance. A very smooth surface was also observed for YBCO sample 2, also laser ablated, but not for YBCO sample 3 (magnetron sputtered, MS) which exhibits outgrowths on its surface ranging in size from 1-3 μm. Note that in spite of their different surface morphologies, the Q_u's of these

two resonators were comparable which shows that surface roughness does not necessarily equate to a poorer microwave performance, at least for YBCO thin films deposited by the two techniques considered here. This is consistent with microwave results obtained by power transmission measurements in the same type of YBCO thin films [9]. The highest Q_o's amongst the YBCO resonators were exhibited by sample 3. Its Q_o at 77 K was 470 which is ~ 4.3 times better than that of the gold resonator at the same frequency and temperature. This value is lower than reported Q_o's for YBCO-based CPW resonator at the same temperature and at frequencies close to 10 GHz [6]. The lower Q_o may be due to the effect of adding a back conductor to the CPW structure. However, direct comparison between different resonant structures should be done cautiously due to the differences in their geometrical configuration. X-ray diffraction (XRD) analysis showed that the YBCO films considered here have a crystallographic orientation where the c-axis is predominantly oriented perpendicular to the substrate plane. No evidence of change in the XRD patterns was observed for these films after the annealing process.

The TBCCO resonators shown in Table 1. are representative of two different deposition batches, with samples 4 and 5 originating from the same batch and sample 6 from a separate batch. From Fig. 2 it can be seen that the Q_o's for the TBCCO resonators were larger than those obtained for their YBCO counterparts. For the best TBCCO resonator (sample 6, Fig. 2) a Q_o of 823 was obtained at 77 K. This value is ~ 7.4 times that of the gold resonator and is ~1.75 times larger than the Q_o of our best YBCO resonator. It was observed that after the annealing the Q_o's of the resonators increased (almost by a factor of 2 for sample 6) with respect to those obtained before the annealing. The enhanced Q_o's can be correlated with an increase in oxygen content in the films as reflected by the rise in T_c with respect to that measured before the annealing process. For the YBCO films this increase was ~1.0-1.3 K while for the TBCCO films it was ~ 2.0-3.0 K. Observe that for the YBCO resonators (especially for the two laser ablated ones) the discrepancies in Q_o's are well correlated with their T_c values. However, for the TBCCO resonators, although the difference between their T_c values after the annealing was less than 1.3 K, and the temperature at which a measurable resonance was first observed was almost the same (~105 K), still there was a large discrepancy between their respective Q_o's. This difference can be associated with the morphology of the films. The XRD patterns contain only the (00ℓ) reflections for both the 2212 and the 2223 phases. Based upon the relative peak intensities it appears that the films are similar in composition and composed primarily of the 2212 phase. However, SEM analysis revealed that samples 4 and 5 are characterized by a "terrace-like" surface morphology which is absent in sample 6. As such, we believe that the effective thickness of sample 4 and 5 is less than that of sample 6 and thus is responsible for their lower Q_o's.

The effective surface resistance (R_s) for the YBCO and TBCCO HTS films was determined from the unloaded quality factor [10]. The surface resistance of the all-gold resonator was determined from measurements of the dc resistivity (ρ) and using the expression $R_{s,Au}=(\mu_o\omega\rho/2)^{1/2}$, where μ_o is the permeability of free space and $\omega=2\pi f$, where f is the frequency. Values of R_s at 77 K for the HTS-based and all-Au based CBCPW resonators are shown in Tab. 1. Note that the lowest R_s for YBCO is ~0.25 of that for Au, and compares well with those reported by others [6,10] if we assume that the R_s of the superconductor is proportional to the square of the frequency. For TBCCO, our lowest R_s is ~0.13 of that for Au. However, the R_s values obtained in this study for our best TBCCO resonator is ~6 times larger than the value obtained by others from ring resonators fabricated on films from the same source as ours (R_s~6 mΩ at 35 GHz and 77 K; R_s~0.5 mΩ at 10 GHz and 77 K, assuming a $R_s \alpha f^2$) [1]. This may be explained in terms of the current distribution in the conductors of the resonator. In the CPW section of the CBCPW resonator the currents are concentrated near the edges of both the center conductor and the ground planes. Therefore this structure is more sensitive to defects at the edges of the conductors that may arise during the patterning process, resulting in an increase in R_s [11].

IV. CONCLUSIONS

Conductor-backed coplanar waveguide resonators have been patterned on YBCO and TBCCO HTS thin films on $LaAlO_3$. These resonators were tested in the temperature range from 14 to 106 K. Unloaded quality factors Q_o as high as 823 and 470 were obtained at 77 K and 10.8 GHz for TBCCO and YBCO resonators, respectively. The highest Q_o's at 77 K for the TBCCO and YBCO resonators were nearly a factor of 7 and 4, respectively, better than that of an all-gold resonator of the same geometry at the same temperature and frequency. In this study, the Q_o's of the TBCCO resonators were larger than those of their YBCO counterparts throughout the aforementioned temperature range. Our results support the observation that a high T_c does not always correlate with a good microwave performance. In addition, they suggest that the TBCCO films may be the material of choice for cryogenic microwave applications given the fact that there is still room for improvement of aspects such as the porosity of the films. However, more work is necessary to correlate Q_o with porosity for films having similar T_c's.

ACKNOWLEDGEMENT

The authors wish to thank Mr. G. Subramanyam, of the University of Cincinnati, for silver contact deposition onto the TBCCO resonators. The authors also acknowledge Mr. J. Olsavsky and Mr. J. Meola for technical assistance. Our thanks to Mr. R. Garlick and Ms. R. Cipcic for XRD measurements.

Helpful discussions with Mr. C. M. Chorey and Dr. V. O. Heinen are gratefully acknowledged.

REFERENCES

[1] M. S. Schmidt, R. J. Forse, R. B. Hammond, M. M. Eddy, and W. L. Olson, "Measured Performance at 77 K of Superconducting Microstrip Resonators and Filters," *IEEE Trans. Microwave Theory Tech.*, Vol. 39, pp. 1475-1479, Sept. 1991.

[2] S. H. Talisa, M. A. Janocko, C. Moskowitz, J. Talvacchio, J. F. Billing, R. Brown, D. C. Buck, C. K. Jones, B. R. McAvoy, G. R. Wagner, and D. H. Watt, "Low-and High-Temperature Superconducting Microwave Filters," *IEEE Trans. Microwave Theory Tech.*, Vol. 39, pp. 1448-1454, Sept. 1991.

[3] W. G. Lyons, R. S. Withers, J. M. Hamm, A. C. Anderson, P. M. Mankiewich, M. L. O'Malley, and R. E. Howard, " High-T_c Superconductive Delay Line Structures and Signal Conditioning Networks," *IEEE Trans. Magn.*, Vol. 27, pp. 2932-2935, March 1991.

[4] A. A. Valenzuela and P. Russer, "High-Q Coplanar Transmission Line Resonator of $YBa_2Cu_3O_{7-x}$ on MgO," *Appl. Phys. Lett.*, Vol. 55, pp. 1029-1031, Sept. 1989.

[5] R. Klieber, R. Ramisch, A. A. Valenzuela, R. Weigel, and P. Russer, "A Coplanar Transmission Line High-T_c Superconductive Oscillator at 6.5 GHz on a Single Substrate," *IEEE Microwave Guided Wave Lett.*, Vol. 2, pp. 22-24, Jan. 1992.

[6] G. J. Valco, A. R. Blemker, and K. B. Bhasin, "Laser Ablated $YBa_2Cu_3O_{7-\delta}$ High-Temperature Superconductor Coplanar Waveguide Resonator," *Microwave Opt. Technol. Lett.*, Vol. 5, pp. 234-236, May 1992.

[7] F. A. Miranda, K. B. Bhasin, K. S. Kong, T. Itoh, and M. S. Stan, "Conductor-Backed Coplanar Waveguide Resonators of $YBa_2Cu_3O_{7-\delta}$ on $LaAlO_3$," *IEEE Microwave Guided Wave Lett.*, Vol. 2, pp. 287-288, July 1992.

[8] C. M. Chorey, K. S. Kong, K. B. Bhasin, J. D. Warner, and T. Itoh, "YBCO Superconducting Ring Resonators at Millimeter-Wave Frequencies," *IEEE Trans. Microwave Theory Tech.*, Vol. 39, pp. 1480-1487, Sept. 1991.

[9] F. A. Miranda, W. L. Gordon, K. B. Bhasin, V. O. Heinen, and J. D. Warner, "Microwave Properties of $YBa_2Cu_3O_{7-\delta}$ High-Transition-Temperature Superconducting Thin Films Measured by the Power Transmission Method," *J. Appl. Phys.*, Vol. 70, pp. 5450-5462, Nov. 1991.

[10] M. R. Namordi, A. Mogro Campero, L. G. Turner, and D. W. Hogue, "Comparison of High-Temperature-Superconductor and Metal Based Resonators," *IEEE Trans. Microwave Theory Tech.*, Vol. 39, pp. 1468-1474, sept. 1991.

[11] K. S. Kong, K. B. Bhasin, and T. Itoh, "Design Aspects and Comparison Between High T_c Superconducting Coplanar Waveguide and Microstrip Line," *SPIE Proc.* 1477,city, s[illegible] month 1991, pp. 57-65.

N94-20517

A 10 GHz Y-Ba-Cu-O/GaAs Hybrid Oscillator Proximity Coupled to a Circular Microstrip Patch Antenna

Norman J. Rohrer, M. A. Richard, *Student Member, IEEE,* George J. Valco, *Member, IEEE,* and Kul B. Bhasin, *Senior Member, IEEE*

***Abstract*—A 10 GHz hybrid Y-Ba-Cu-O / GaAs microwave oscillator proximity coupled to a circular microstrip antenna has been designed, fabricated and characterized. The oscillator was a reflection mode type using a GaAs MESFET as the active element. The feedline, transmission lines, rf chokes, and bias lines were all fabricated from $YBa_2Cu_3O_{7-x}$ superconducting thin films on a 1 cm × 1 cm lanthanum aluminate substrate. The output feedline of the oscillator was wire bonded to a superconducting feedline on a second 1 cm × 1 cm lanthanum aluminate substrate, which was in turn proximity coupled to a circular microstrip patch antenna. Antenna patterns from this active patch antenna and the performance of the oscillator measured at 77 K are reported. The oscillator had a maximum output power of 11.5 dBm at 77 K, which corresponded to an efficiency of 10%. In addition, the efficiency of the microstrip patch antenna together with its high temperature superconducting feedline was measured from 85 K to 30 K and was found to be 71% at 77 K, increasing to a maximum of 87.4% at 30 K.**

I. Introduction

The application of high temperature superconducting (HTS) thin films to microwave circuits is advantageous since the films have a lower surface resistance than gold or copper at microwave frequencies. Passive circuits such as ring resonators [1], [2], filters [3], transmission lines [4], and antennas [5] fabricated from HTS films have shown substantial improvements in performance over identical circuits fabricated with normal metals. Several authors have suggested that HTS technology may be very beneficial in phase-array antenna systems [6], [7]. To date, a limited amount of work in the area of passive microstrip antennas has been reported [5]. However, for HTS to be useful in phased array antennas, active circuits such as oscillators, phase shifters and power amplifiers, will need to be integrated with radiating elements so that beam control and/or scanning may be realized. Because of the limited amount of available space in high frequency arrays, some authors have suggested the use of an active patch antenna as the radiating element. By using active patch antennas, the problem of rf distribution to each radiating element is minimized and space is made available for phase shifters and power amplifiers.

In this paper, we report a first demonstration of a HTS/GaAs hybrid active patch antenna consisting of a hybrid oscillator on one substrate, and a feedline proximity coupled to a circular microstrip patch antenna on a second substrate. The patch antenna was printed on alumina ($\epsilon_r = 9.9$) to reduce the effective permittivity seen by the radiator. The performance of this active antenna was measured at 77 K.

II. Design

Since our objective was to implement the entire oscillator on a single substrate to be cooled to 77 K, the S-parameters of the transistors were first obtained by measurements at cryogenic temperatures for use in the design of the oscillator. The active device used in the oscillator was a low noise MESFET with a gate length of 0.25 μm (Toshiba GaAs MESFET, part no. JS8830-AS). The S-parameters of the FET for the frequency range of 2 GHz to 26 GHz were measured over a range from room temperature (300 K) to 40 K. The magnitude and angle of the S-parameters at 10 GHz as a function of temperature are shown in Fig. 1. The S-parameters as a function of frequency at 300 and 77 K will be presented elsewhere [8]. Of the S-parameters, the largest change in magnitude as a function of temperature occurred for the S_{21} values. This was due to an increase in the electron's mobility at the reduced temperatures. The variation in phase of S_{11} and S_{22} was the only other major change. The percent change of the magnitude and phase of the S-parameters at the design frequency of 10 GHz due to the change in the temperature from 300 K to 77 K is listed in Table I.

The oscillator was designed using simulations performed with a commercially available software package (Touchstone) under the assumption that the drain current would be held at $I_d = 10$ mA, and that the temperature would be held at 77 K. The design used a parallel coupled ring resonator in the matching network off the drain for the frequency stabilization. Using the small signal S-parameters that were measured at 77 K, the input reflection coefficient at the drain was made very large by

Manuscript received August 17, 1992; November 23, 1992. This work was supported by the National Aeronautics and Space Administration under award no. NCC-3-197. M. A. Richard was supported through the Ohio Aerospace Institute Doctoral Fellowship.

N. J. Rohrer and G. J. Valco are with the Department of Electrical Engineering, The Ohio State University, Columbus, OH 43210.

M. A. Richard is with the Department of Electrical Engineering, Case Western Reserve University, Cleveland, OH 44106.

K. B. Bhasin is with the National Aeronautics and Space Administration, Lewis Research Center, Cleveland, OH 44135.

IEEE Log Number 9206629.

© 1993 IEEE. Reprinted, with permission, from IEEE Transactions on Applied Superconductivity, vol. 3, no. 1, Mar. 1993, pp. 23-27.

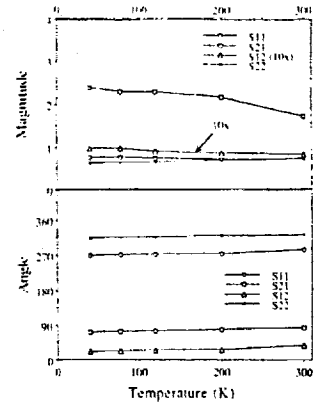

Fig. 1. Magnitude and angle of the S-parameters of the GaAsFET at 10 GHz as a function of temperature. The magnitude of S_{12} has been magnified by a factor of 10 for clarity.

TABLE I
PERCENT CHANGE OF THE S-PARAMETERS FROM 300 K TO 77 K AT 10 GHz

S_{11}		S_{21}		S_{12}		S_{22}	
Magnitude	Phase	Magnitude	Phase	Magnitude	Phase	Magnitude	Phase
3.4%	16.2%	25.6%	8.4%	4.8%	6.2%	26.7%	27.1%

varying the length of the transmission lines on the source and the gate. The selected lengths of the transmission lines from the source and gate were 1.57 mm and 2.79 mm, respectively. Both were open circuited lines. The ring resonator, with a fundamental resonant frequency of 10 GHz, which was used to select the frequency of operation was place $\lambda_g/4$ from the drain of the transistor, parallel coupled to the output transmission line using a 40-μm wide coupling gap. The matching network, including the ring resonator, was designed such that the magnitude of the real part of the impedance of the matching network was less than the magnitude of the real part of the impedance looking into the drain of the FET. The magnitude of the imaginary part of the impedance was equal to zero at the resonant frequency. With this criterion met, the 10-GHz oscillation will start upon proper biasing of the FET. The output of the oscillator was taken off the drain. The physical layout of this reflection mode oscillator is shown in Fig. 2.

The antenna used for this investigation was a circular microstrip patch which was proximity coupled to a microstrip feedline. The feedline for the antenna was patterned on a second substrate for two reasons: this method allowed for the testing of both the oscillator and the antenna separately to determine their performance, and secondly, a HTS thin film with an area large enough to pattern the entire circuit was available.

The resonant frequency of the circular antenna patch was found from the formula [9]:

$$f = \frac{1.841c}{2\pi a_e \sqrt{\epsilon_{eq}}} \tag{1}$$

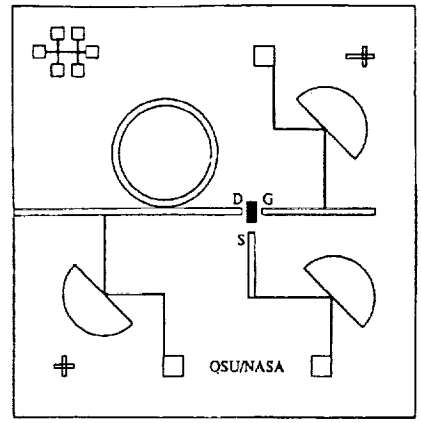

Fig. 2. Physical layout of the hybrid 10 GHz superconductor/GaAs oscillator designed using the reflection method.

where a_e is the effective radius of the patch

$$a_e = a\left[1 + \frac{2d}{\pi a \epsilon_{eq}}\left(\ln\frac{a}{2d} + (1.41\epsilon_{eq} + 1.77) + \frac{d}{a}(0.268\epsilon_{eq} + 1.65)\right)\right]^{1/2} \tag{2}$$

Here, d is sum of the thickness of the two substrates between the patch and the ground plane and a is the physical radius of the patch. Because the patch was printed on an alumina ($\epsilon_1 = 9.9$) substrate with a thickness of 254 μm while the feedline and ground plane were on lanthanum aluminate ($\epsilon_2 = 23$) with a thickness of 508 μm, the value for the net ϵ_{eq} of this dual layer substrate to use in (1) and (2) was found using a static capacitor model

$$\epsilon_{eq} = \frac{3\epsilon_1\epsilon_2}{2\epsilon_1 + \epsilon_2} \tag{3}$$

to be 16.0, resulting in the diameter of the patch equaling 4.02 mm. Measurements showed that a slightly larger diameter of 4.71 mm resulted in a resonance closer to the desired frequency of 10 GHz. The resonant frequency of the patch was tuned to match the output frequency of the oscillator by adjusting the position of the patch over the feedline.

III. EXPERIMENTAL DETAILS

An HTS film was patterned into the oscillator using standard positive photolithographic techniques and etched with an aqueous solution of deionized water : H_3PO_4 :: 100 : 1. This film was a commercially purchased film deposited using an off-axis sputtering technique and had a critical temperature of 88.6 K after patterning. Contacts to the superconductor for the rf output and wire bonding pads were made of silver with a gold overlayer patterned by lift-off photolithography. Wire bonding pads were located at the bias pads as well as at the ends of the transmission lines near the FET. The GaAs FET was epoxied onto the substrate and wire bonds were made to

the transmission lines with 0.7 mil gold wire by thermosonic bonding. A copper ground plane with a thickness of 2.4 μm was deposited on the backside of the substrate.

A second HTS thin film was used for the antenna feedline. A $YBa_2Cu_3O_{7-x}$ thin film was deposited by pulsed laser deposition onto this substrate [10]. The film had a critical temperature of 86 K. This film was patterned in the same way as the oscillator into a 50 ohm transmission line that was 160 μm wide and 5 mm in length. A silver/gold contact was deposited at the end of the feedline for ribbon bonding, and a 2-μm copper ground plane was evaporated on the backside of the substrate. An alumina substrate with the patterned antenna patch was placed on top of the feedline and held in place with small amounts of fingernail polish at the edges.

The performance of the oscillator was measured on a spectrum analyzer at 77 K by mounting the circuit in a sealed brass test fixture and submerging the fixture in liquid nitrogen. Details of the procedures used for measurement will be presented elsewhere [8]. The antenna with its HTS feedline was measured by placing the circuit on a copper test fixture and mounting the fixture on the second stage of a closed cycle gas refrigerator. A high density polyethylene radome served as a vacuum chamber. Details of the experimental apparatus and procedures have been presented elsewhere [5].

The efficiency of the antenna together with its HTS feedline was measured using the Wheeler Cap method [11]. To do this, the input impedance of the antenna at resonance was measured with and without a radiation shield from 30 K up to 85 K. The efficiency (η) was then calculated as:

$$\eta = 1 - \frac{R_w}{R_{wo}} \tag{4}$$

where R_w and R_{wo} are the input resistances with and without the radiation shield, respectively. For this work, an aluminum cap with an inner dimension of 12-mm wide × 12-mm deep by 6.8 mm high was used as the radiation shield. Electrical contact to the test fixture was ensured with silver paint.

The oscillator and antenna circuits were then mounted with silver paint onto a brass test fixture. The rf connection between the two substrates was made by ribbon bonding to the contacts on the feedline of antenna and the output of the oscillator (Fig. 3). The test fixture was then mounted in the closed-cycle gas refrigerator and covered with the high density polyethylene radome. An X-band horn attached to a pivoting arm served as the receive antenna to measure the radiation pattern of the active patch antenna in the far field as a function of angle.

IV. Results and Discussion

The output power and frequency of operation of the hybrid oscillator were measured to verify its performance before bonding the oscillator to the antenna circuit. The maximum power attainable from the oscillator at 77 K

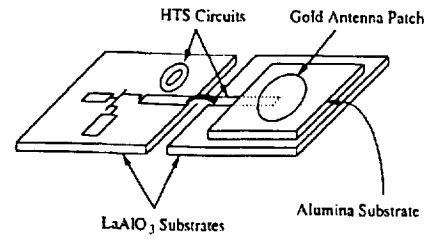

Fig. 3. Physical layout of the active antenna. The gold patch was on an alumina substrate place over a superconducting feedline on a $LaAlO_3$ substrate. The oscillator and patch antenna were ribbon bonded together.

was 11.5 dBm at a bias of V_{ds} = 4.0 V and V_{gs} = 0.0 V. The sensitivity of the frequency to temperature was −10 MHz/K at 77 K. Detailed results of the measurements performed on this oscillator as a function of temperature and bias will be presented elsewhere [8]. For the active antenna measurements at 77 K, the FET was biased at V_{ds} = 0.5 V and V_{gs} = −0.5 V which gave a current of I_d = 12 mA. For this bias condition, the frequency of the signal was 10.082 GHz with an output power of −2.0 dBm. The efficiency of the oscillator was 10.5%. The power of the second harmonic at 20.16 GHz was 35 dB less than the fundamental signal at 77 K.

The efficiency of the antenna was measured before bonding the antenna to the oscillator circuit. The efficiency as a function of temperature is shown in Fig. 4. As expected, the efficiency rises dramatically as the HTS film becomes superconducting and then increases slowly as the temperature decreases, due to the increase in the conductivity of the HTS feedline. This trend was in agreement with the measured performance of HTS ring resonators. The efficiency reaches a maximum of 87.4% at 30 K.

The measured antenna patterns with the superconducting oscillator driving the antenna are shown in Fig. 5, along with the patterns predicted for the co-polarization by the cavity model [12]. The H-plane shows good agreement with the model, while the E-plane deviates substantially due to surface waves and the feedline, neither of which are accounted for in the model used. This is in agreement with results published by Schaubert *et al.* [13] which demonstrated that antennas on high permittivity substrates are characterized by perturbations in the E-plane pattern. The 12 dB dip in the E-plane and the cross polarization patterns at an angle of 15 degrees was almost certainly due to radiation interference from the resonator and microstrip lines on the oscillator.

V. Conclusion

The performance of a 10 GHz active antenna employing a Y-Ba-Cu-O superconducting feedline and resonator stabilized oscillator has been demonstrated for the first time. The patch antenna and the hybrid oscillator were fabricated on separate $LaAlO_3$ substrates. The measurements on the antenna showed that it was 71% efficient at 77 K and 87.4% efficient at 30 K. The oscillator had a maximum power of 11.5 dBm and was 10.5% efficient at

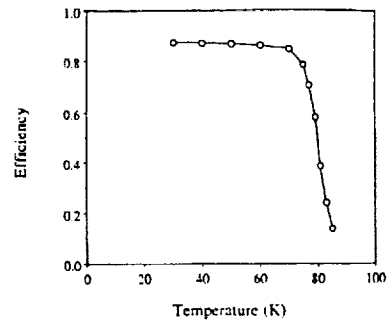

Fig. 4. Efficiency of the patch antenna as a function of temperature measured from 30 K to 85 K. The efficiency at 77 K was 71%.

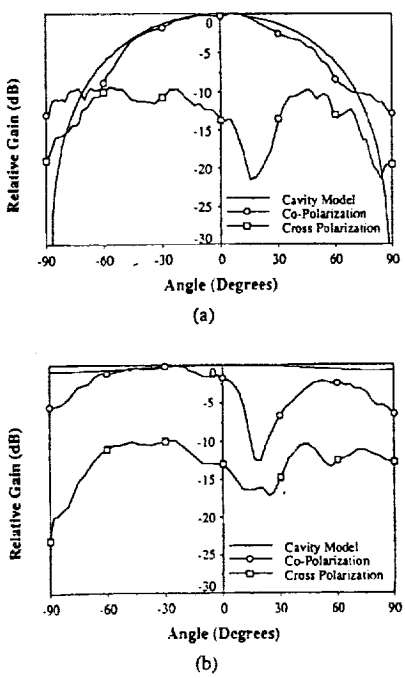

Fig. 5. Radiation patterns for the patch antenna at 77 K. a) H-plane radiation patterns comparing the cavity model (solid line) with the co-polarization data (open circles) and also displaying the cross polarization data (open squares). b) E-plane radiation patterns comparing the cavity model with the co-polarizaton data and also displaying the cross polarizaton data.

77 K. The sensitivity of the frequency as a function of temperature was -10 MHz/K. The radiation patterns for the oscillator were measured as a function of the angle and compared to a cavity model for a driving power from the oscillator of -2.0 dBm. The H-plane showed good agreement with the model, while interference due to the oscillator was present in each trace except the co-polarization of H-plane.

ACKNOWLEDGMENTS

The authors would like to thank Chris Chorey for his assistance in the testing of the transistor at cryogenic temperatures.

REFERENCES

[1] C. M. Chorey, K. Kong, K. B. Bhasin, J. D. Warner, and T. Itoh, "YBCO Superconducting ring resonator at millimeter-wave frequencies," *IEEE Trans. Microwave Theory Tech.*, vol. 39, no. 9, pp. 1480–1487, Sept. 1991.

[2] J. H. Takemoto, F. K. Oshita, H. R. Fetterman, P. Korbin, and E. Sovoro, "Microstrip ring resonator technique for measuring microwave attenuation in high-T_c superconducting thin films," *IEEE Trans. Microwave Theory Tech.*, vol. 37, pp. 1650–1652, 1989.

[3] W. G. Lyons, R. R. Bonetti, A. E. Williams, P. M. Mankiewich, M. L. O'Malley, J. M. Hamm, A. C. Anderson, R. S. Withers, A. Meulenberg, and R. E. Howard, "High-T_c superconductive microwave filters," *IEEE Trans. Magn.*, vol. 27, no. 2, pp. 2537–2539, Mar. 1991.

[4] E. B. Ekholm and S. W. McKnight, "Attenuation and dispersion for high-T_c superconducting microstrip lines," *IEEE Trans. Microwave Theory Tech.*, vol. 38, no. 4, pp. 387–395, Apr. 1990.

[5] M. A. Richard, K. B. Bhasin, C. Gilbert, S. Metzler, G. Keopf, and P. C. Claspy, "Performance of a four-element Ka-band high-temperature superconducting microstrip antenna," *IEEE Microwave Guided Wave Lett.*, vol. 2, no. 4, pp. 143–145, Apr. 1992.

[6] R. J. Dinger, "Some potential antenna applications of high temperature superconductors," *J. Superconduct.*, vol. 3, no. 3, pp. 287–196, 1990.

[7] R. C. Hansen, "Superconducting antennas," *IEEE Trans. Aerospace Electronic Syst.*, vol. 26, no. 2, pp. 345–354, Mar. 1990.

[8] N. J. Rohrer, G. J. Valco, and K. B. Bhasin, "Hybrid high temperature superconductor/GaAs 10 GHz microwave oscillator: Temperature and bias effects," *IEEE Trans. Microwave Theory Tech.*, (Accepted for publication).

[9] W. C. Chew and J. A. Kong, "Effects of fringing fields on the capacitance of circular microstrip disks," *IEEE Trans. Microwave Theory Tech.*, vol. 28, no. 2, pp. 98–104, Feb. 1990.

[10] J. D. Warner, K. B. Bhasin, N. J. Varljay, D. Y. Bowman, and C. M. Chorey, "Growth and patterning of laser ablated superconducting YBCO films on LaAlO3 substrates," NASA Report No. TM-102336.

[11] H. A. Wheeler, "The radiansphere around a small antenna," *Proc. IRE*, vol. 47, pp. 1325–1331, Aug. 1959.

[12] I. J. Bhal and P. Bhartia, *Microstrip Antennas*, Massachusetts: Artech House, 1980.

[13] D. H. Schaubert and K. S. Yngvesson, "Experimental study of a microstrip array on high permittivity substrate," *IEEE Trans. Antennas Propag.*, vol. 34, no. 1, pp. 92–97, Jan. 1986.

Norman J. Rohrer received the B.S. degree in physics and mathematics from Manchester College, North Manchester, Indiana in 1987, and the M.S. and Ph.D. degrees in electrical engineering from the Ohio State University, Columbus, Ohio, in 1990 and 1992, respectively.

As a graduate student, he was recipient of a NASA Graduate Student Research Fellowship under which he was able to complete his dissertation research on superconducting microwave oscillators. Since August of 1992, he has been employed by IBM, Burlington, Vermont, in the Technology Products Division.

M. A. Richard (S'92) received the B.A. in physics from Bluffton College in 1988 and the M.S. and Ph.D. degrees in electrical engineering from Case Western Reserve University in 1990 and January, 1993, respectively.

He was a recipient of an Ohio Aerospace Institute/NASA Space Grant Doctoral Fellowship. Dr. Richard has co-authored 15 technical papers, one of which won first place at the IEEE Antennas and Propagation Society's 1992 Student Paper Contest. He is currently a Research

Associate at Case Western Reserve University where he is continuing his investigation of superconducting antennas.

George J. Valco (M'86) received the B.S. and M.S. degrees in electrical engineering from Case Western Reserve University in 1979 and 1981, respectively. He received the Ph.D. in electrical engineering from the University of Cincinnati in 1986.

In 1986 he joined the faculty of the Ohio State University where he is currently an assistant professor of electrical engineering. His current research interests are electronic applications of high temperature superconductors, electronic properties of diamond films, photovoltaics, and compound semiconductor devices and technology.

Kul B. Bhasin (S'74–M'83–SM'89) received the M.S. and Ph.D. degrees from Purdue University and the University of Missouri-Rolla, respectively.

Since 1983 he has been a senior research scientist in the Solid State Technology Branch of the Space Electronics Division of the NASA Lewis Research Center in Cleveland, Ohio. Prior to joining NASA he was with Gould, Inc. from 1977 to 1983 as senior scientist and manager of technology. He is currently engaged in development of GaAs microwave devices and circuits, microwave photonics and superconducting electronics for space applications. He has authored many publications and co-edited the book, *Microwave Integrated Circuits*. He is the recipient of the IR-100 Award, the NASA Group Achievement Awards, the Gould Scientific Achievement Award and is on the editorial board of Microwave and Optical Technology Letters. He is a member of APS, Sigma Xi, and a member of the Fellow International Society for Optical Engineers.

PERFORMANCE OF TlCaBaCuO 30 GHZ 64 ELEMENT ANTENNA ARRAY

L. L. Lewis and G. Koepf
Ball Communications Systems Division,
Broomfield, CO 80038-1235
K. B. Bhasin
NASA Lewis Research Center,
Cleveland, OH 44135
M. A. Richard
Case Western Reserve University,
Cleveland, OH 44106

***Abstract*–A 64 element, 30 GHz, microstrip antenna array with corporate feed network was designed and built on a .254 mm (10 mil) thick lanthanum aluminate substrate. One antenna pattern was fabricated from gold film, and a second pattern used TlCaBaCuO high temperature superconductor. Both antennas used gold ground planes deposited on the reverse side of the substrate. Gain and radiation patterns were measured for both antennas at room temperature and at cryogenic temperatures. Observations agree well with simple models for loss and microwave beam width, with a gain on boresight of 20.3 dB and beam width of 15 degrees for the superconducting antenna.**

I. INTRODUCTION

When microstrip antenna design [1] is extended to microwave frequencies above 30 GHz, certain difficulties become apparent. Losses due to surface waves [2] and radiation [3] become more significant than at lower frequencies. Both of these losses may be reduced by decreasing the thickness of the substrate, drawing the ground plane closer to the microstrip traces. However, the trace widths must also be reduced in order to maintain a given transmission line impedance. The narrower lines have high resistive losses when conventional metals are used to form the traces. For copper traces on a .152 mm (6 mil) thick sapphire substrate, for example, a 30 GHz phased array with 40 dB directivity will have more than 25 dB of loss [4]. In order to reduce these resistive losses, high temperature superconducting (HTS) materials may be used to form the feed networks for high gain phased array antennas [5]. When a high quality HTS film on .254 mm (10 mil) lanthanum aluminate (LAO) is used instead of copper for a 30 GHz antenna of 40 dB directivity, the loss is only 3 dB [4]. This paper describes the design, construction, and performance of the first 30 GHz, 64 element phased array antenna that uses an HTS feed network. The successful implementation of HTS circuits with this relatively low gain antenna supports the position that high gain millimeter wave antennas would benefit from use of the new superconductors.

Manuscript received August 24, 1992. Research supported in part by NASA Headquarters, Satellite Communications Applications Research (SCAR) Program.

II. ANTENNA DESIGN

A. General Design

For ease in fabrication, and in order to compare HTS performance with copper performance, we selected an array design with 64 rectangular patches arranged in an 8 x 8 square pattern (Fig. 1). Element spacing was 4500 μm, which is slightly less than one-half of the free space wavelength. This reduced spacing allowed us to place the entire array on a 50.8 mm (2 inch) diameter wafer of LAO, without appreciably changing the radiation pattern of the antenna. Wafer thickness was chosen to be .254 mm (10 mils), with a gold ground plane on the reverse side. The corporate feed network uses 50 ohm lines, which are split to the patch elements by means of six levels of quarter wave microstrip transformers. The relative dielectric constant of LAO is approximately 24 [6], which results in a microstrip line width of 92 μm for this geometry.

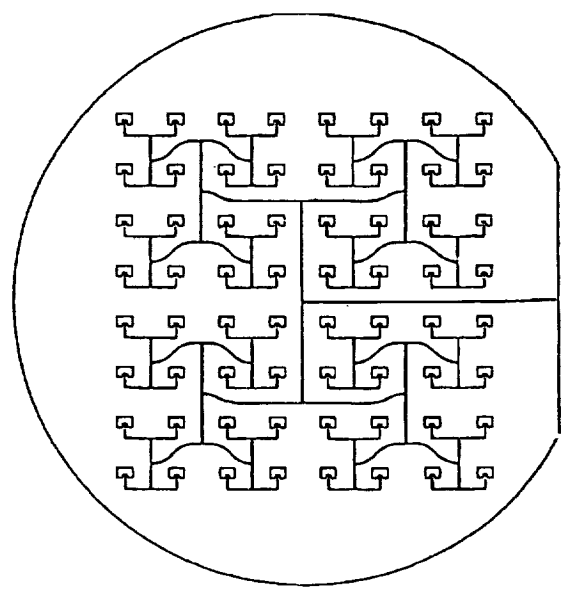

Fig. 1 Layout of patch elements and feed network for the 30 GHz phased array antenna. Wafer diameter is 50.8 mm (2 inches).

© 1993 IEEE. Reprinted, with permission, from IEEE Transactions on Applied Superconductivity, vol. 3, no. 1, Mar. 1993, pp. 2844-2847.

PRECEDING PAGE BLANK NOT FILMED

B. Antenna Patch Elements

Because of the uncertainty in material properties and the application of microwave design rules for substrates with such high dielectric constant, we designed, fabricated, and tested single patches at 15 GHz first, in order to determine the validity of our models for devices on LAO at MMW frequencies. We then extended the design to 30 GHz patches, which were then used in arrays. The patches are rectangular, with width W and length L (Fig. 2). A microstrip line feeds directly to a notched input of depth d. The calculation of the patch resonance frequency is not difficult, but an accurate calculation of patch impedance is nontrivial. We use a Mixed Potential Integral Equation (MPIE) approach [7]. This is one of several 'full wave' models, which should give good values for patch impedance, surface wave components, and radiation patterns. The patch impedance is needed in order to couple the microwave power efficiently into the patch. The antenna efficiency is determined in part by the resistive losses of the patch, and also by the energy lost to surface waves.

The edge impedance of a rectangular patch on LAO is very high, requiring the use of the notch, which allows coupling near the center of the patch, where the impedance goes to zero. We select a point where the impedance is 100 ohms, and use a quarter wave transformer to match the 50 ohm input line to this point. Typical values are W=3000 μm, L=2000 μm, and d=782 μm for a resonance frequency of 14.84 GHz, and theoretical input impedance of 78 ohms. The measured impedance in this case was 72 ohms. For the 64 element array, we used patches with W=1350 μm, L=900 μm, and d=337 μm. These elements have a predicted resonance frequency of 31.25 GHz, and input impedance of 100 ohms.

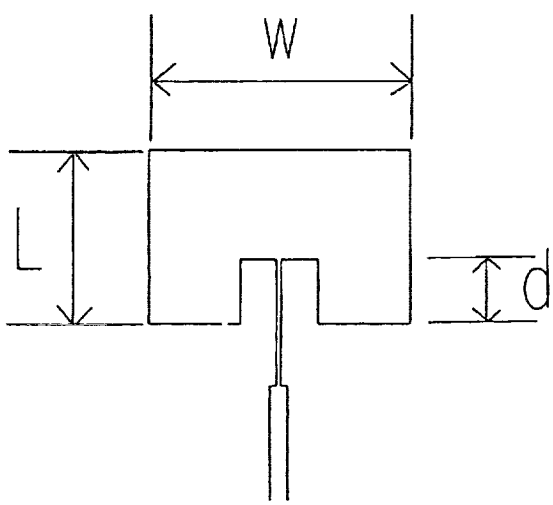

Fig. 2 Antenna patch element, showing quarter wave input transformer.

C. Surface Waves

The high dielectric constant of LAO means that even a .254 mm (10 mil) substrate is electrically thick. While the cutoff frequency for propagation of the TE_0 surface wave mode is about 60 GHz, the TM_0 mode is supported at all frequencies. This can be a source of energy loss. We have calculated the radiation efficiency of a single patch, using an electric surface current model [8] to estimate the surface wave losses. At 15 GHz, the single patch efficiency is about 84 percent. At 30 GHz, the efficiency drops to about 60 percent.

In theory, the efficiency of an array can be improved considerably over this value by carefully placing the radiating elements at the correct distance apart, so that the surface wave components destructively interfere. The spacing can also be chosen so that the spatial part of the radiation constructively interferes. Both are possible at the same time because the wavelength of the surface waves is nearly one fifth of the free space wavelength. In practice, however, the presence of the feed network makes it difficult to predict the exact propagation constants in the structure, so that surface waves can be suppressed.

III. FABRICATION

The preliminary single patches at 15 GHz and 30 GHz were fabricated at Ball using 4 μm thick gold on .254 mm (10 mil) thick LAO, with a titanium adhesion layer. Both plate up and etch down processes were used. Gold ground planes were deposited on the reverse side of the LAO. The diced patches were soldered with indium to gold plated metal carriers made of Alloy 48, which matches the coefficient of thermal expansion of the LAO. The carriers were then mounted in a test fixture, using gold ribbon bonds to microstrip launchers, which in turn were bonded to 'V-type' microwave connectors.

The 64 element array was patterned by Superconductor Technologies, Inc. on a 50.8 mm (2 inch) diameter, .254 mm (10 mil) thick LAO. One array was formed with 3 μm thick gold film, using a titanium-tungsten adhesion layer, and a second array was formed with $Tl_2CaBa_2Cu_2O_8$ high temperature superconductor. Both arrays used a gold ground plane deposited on the reverse side of the LAO. The 50 ohm microstrip feed line, as shown in Fig. 1, passes to the edge of the wafer, where a gold ribbon bond is made to a microstrip launcher. In the case of the HTS array, a gold contact strip is deposited over the superconductor near the end of the wafer, for bonding purposes. As with the single patches, the wafer is soldered to a gold plated fixture using an indium alloy. On both the gold and the HTS arrays, line widths were held to a tolerance of about 3 μm. Substrate thickness variations were less than .025 mm (1 mil).

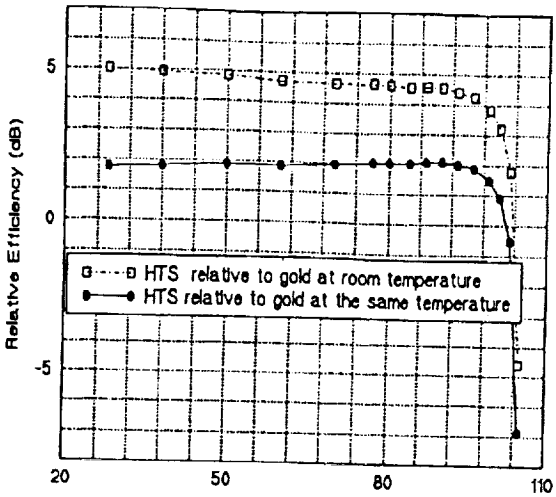

Fig. 3 Efficiency of HTS antenna relative to gold antenna.

IV. PERFORMANCE

The resonance frequency of both the gold and the HTS arrays was measured at Ball, at both room temperature and liquid nitrogen temperatures. The gold array was resonant at 30.7 GHz (room temperature) and 31.1 GHz (77 K). The HTS array was resonant at 30.55 GHz (77 K). A calibrated gain measurement of the gold array was made at Ball, at room temperature. The measured gain, on resonance and on boresight was 15.6 dBil (H-plane). The 3 dB beam width was 13 degrees. The relative gain of the gold and HTS antennas at cryogenic temperatures was then measured at NASA Lewis Research Center. We express the normalized gain, G, of an antenna in terms of the usual S-parameters:

$$G = \frac{|S_{21}|^2}{1-|S_{11}|^2} \quad (1)$$

Then the efficiency of the HTS antenna relative to the gold antenna is just

$$\varepsilon_{HTS-Au} = G_{HTS}/G_{Au} \quad (2)$$

Fig. 3 gives the efficiency of the HTS antenna relative to the gold antenna at 300 K and also relative to the gold antenna at the same temperature as the HTS antenna. At 77 K, the HTS antenna is 4.7 dB higher gain than the gold antenna at room temperature. We therefore conclude, using the calibrated gain measurements of the gold antenna, that the gain of the HTS antenna at 77 K is 20.3 dBi. This is to be compared with the maximum possible gain (no losses) of 22.2 dBi. The inferred loss of 1.9 dB can easily be attributed to losses in the microwave connectors, gold ground plane, and surface waves. Indeed, the predicted maximum loss due to surface waves alone is 2.2 dB. Using a simple model of resistive losses in the feed network, we expect the gold antenna losses at 300 K to be 3.8 dB, and 2.2 dB at 77 K. Similarly, we expect the HTS losses to be .4 dB at 77 K. The measured gains are in reasonable agreement with these estimates.

Fig. 4 and Fig. 5 give the E-plane and H-plane radiation pattern measurements for the HTS antenna at 77 K. These two measurements are in excellent agreement with the predicted patterns, showing the first side lobes at -13 dBc, with good symmetry. The slight skewing of the central lobe may be attributed to asymmetry in the measurement fixture.

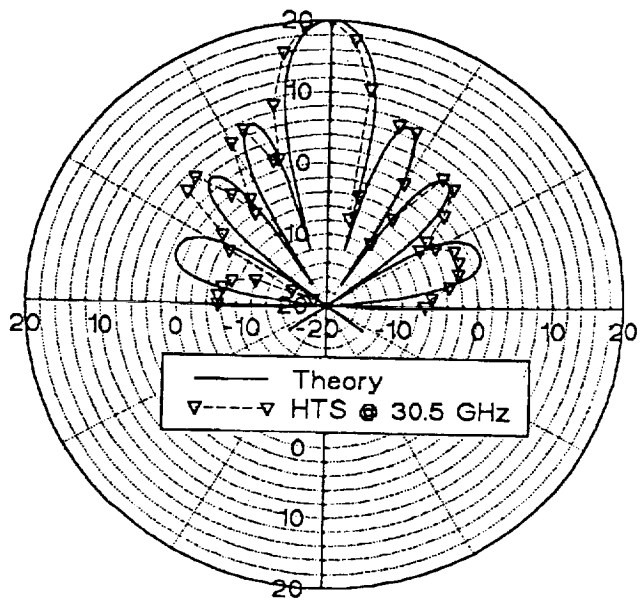

Fig. 4 E-plane radiation pattern, normalized to 20 dB.

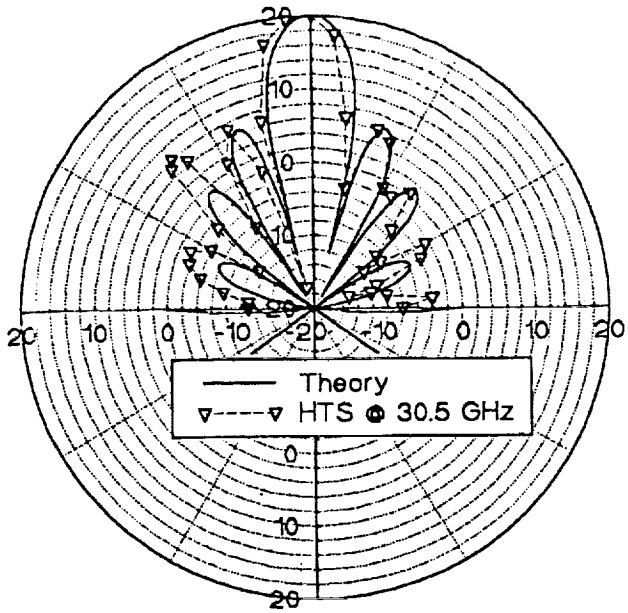

Fig. 5 H-plane radiation pattern, normalized to 20 dB.

V. SUMMARY

The measured performance of a 30 GHz, 64 element phased array antenna with a superconducting feed network agrees well with theory. The antenna loss is only 1.9 dB, and the radiation patterns behave as predicted. These results support the contention that significant gain improvements are possible in a high gain millimeter wave antenna that uses an HTS feed network.

REFERENCES

[1] P. Bhartia, K. V. S. Rao, and R. S. Tomar, *Millimeter-Wave Microstrip and Printed Circuit Antennas*, Boston: Artech House, 1991, 322 pp.

[2] Pisti B. Katehi and Nicolaos G. Alexopoulos, "On the Effect of Substrate Thickness and Permittivity on Printed Circuit Dipole Properties," IEEE Trans. on Antennas and Propagation, Vol. **AP-31**, No. 1, pp. 34-39, January, 1983.

[3] L. Lewin, "Radiation from Discontinuities in Strip-line," IEEE Monograph No. 358E, February 1960.

[4] Fred Schmidt, "Superconducting Antennas Applications and Architecture Study," Final Report, NASA contract No. NASW-4514, August, 1991, pp. 49-53.

[5] M. A. Richard, K. B. Bhasin, C. Gilbert, S. Metzler, and P. C. Claspy, "Measurement techniques for cryogenic Ka-Band microstrip antennas," Antenna Measurement Tech. Association Proc., pp. 1.13-1.17, 1991.

[6] Tsuneo Konaka, Makoto Sato, Hidefumi Asano, and Shugo Kubo, "Relative Permittivity and Dielectric Loss Tangent of Substrate Materials for High-T_c Superconducting Film," Journal of Superconductivity, Vol. 4, No. 4, pp. 283-288, 1991.

[7] J. R. Mosig, "Arbitrarily Shaped Microstrip Structures and their Analysis with a Mixed Potential Integral Equation," IEEE Trans. Microwave Theory and Techniques, Vol. 36, No. 2, pp. 314-323, February 1988.

[8] P. Perlmutter, S. Shtrikman, and D. Treves, "Electric Surface Current Model for the Analysis of Microstrip Antennas with Application to Rectangular Elements," IEEE Transactions on Antennas and Propagation, Vol. **AP-33**, No. 3, pp. 301-311, March 1985.

N94-20518

Microwave properties and characterization of co-evaporated BSCCO thin films

F A Miranda†, C M Chorey‡, M A Stan§, C E Nordgren‖, R Y Kwor¶ and T S Kalkur¶

† National Aeronautics and Space Administration, Lewis Research Center, Cleveland, OH 44135

‡ Sverdrup Technology, Inc. Lewis Research Center Group, Brook Park, OH 44142

§ Department of Physics, Kent State University, Kent, OH 44242

‖ Department of Physics, Case Western Reserve University, Cleveland, OH 44106

¶ Department of Electrical and Computer Engineering, University of Colorado at Colorado Springs, Colorado Springs, CO 80933, USA

Received 25 February 1992, in final form 21 April 1992

Abstract. An extensive characterization of Bi–Sr–Ca–Cu–O (BSCCO) thin films deposited by co-evaporation on $LaAlO_3$ and $SrTiO_3$ substrates has been performed. The films had a $T_c(R = 0)$ of ~78 K, and were predominantly *c*-axis oriented, with critical current densities (J_c) at 4.5 K of 1.6×10^6 and 1.1×10^6 A cm^{-2}, for the samples on $SrTiO_3$ and $LaAlO_3$ respectively. The microwave properties of the films were examined by three techniques. The complex conductivity ($\sigma^* = \sigma_1 - j\sigma_2$) and the magnetic penetration depth (λ) were measured by power transmission at 30.6 GHz; the surface resistance (R_s) was measured using a cavity resonator at 58.9 GHz, and the transmission line losses were determined by measuring the quality factor (Q) of a linear microstrip resonator at 10.4 and 20.2 GHz. The complex conductivity for the film on $LaAlO_3$ was determined to be $(2.0 - j10) \times 10^5$ S m^{-1} at 77 K. It was observed that in the superconducting state σ_1 deviates from both the Bardeen–Cooper–Schrieffer (BCS) theory and the two-fluid model. Values of λ were found to be ~2.0 and 1.1 μm at 77 K and 20 K respectively, and were obtained for the film on $LaAlO_3$. The value of λ at 20 K was approximately three times larger than that of BSCCO single crystals. R_s values of 865 and 1391 mΩ were obtained for the films on $SrTiO_3$ and $LaAlO_3$, respectively, at 77 K and 58.9 GHz. Unloaded Q factors at 20 K of ~1100 and 800 at 10.4 and 20.2 GHz respectively, were measured for the BSCCO resonator. Unloaded Q values of 290 and 405 at 20 K were obtained at 10.4 GHz and 20.2 GHz respectively, for an all gold (Au) resonator.

1. Introduction

High transition temperature superconductors (HTS) have potential for microwave applications due to their low loss and dispersion as compared with typically used conductors such as copper (Cu) and gold (Au). Therefore, it is not surprising that to date a large number of measurements at microwave frequencies on HTS properties such as surface resistance (R_s), complex conductivity ($\sigma^* = \sigma_1 - j\sigma_2$), and magnetic penetration depth (λ), have been reported. Most of the work so far has been performed on the $YBa_2Cu_3O_{7-\delta}$ (YBCO) compound [1–7], mainly because of its single phase and simplicity of fabrication. However, studies of the Bi–Sr–Ca–Cu–O (BSCCO) compound have been performed by several research groups since this material offers the advantage of being relatively insensitive to exposure to atmosphere and handling, and because of its great stability with respect to thermal cycling [8]. In spite of the number of studies on BSCCO thin films, data on R_s and σ^* at microwave frequencies are still scarce [9, 10].

In this paper we report on the structural, DC and microwave properties of two BSCCO thin films deposited by co-evaporation on $LaAlO_3$ and $SrTiO_3$ substrates. The films were characterized by scanning electron microscopy (SEM), x-ray diffraction (XRD) analysis, by DC transition temperature (T_c) and critical current density (J_c) measurements. The microwave properties of the films were determined from R_s measurements using resonant cavity techniques, and power transmission measurements. The R_s of the film on $LaAlO_3$ was also measured using a linear resonator

© 1992 U.S. Government. Reprinted, with permission, from the U.S. Government.

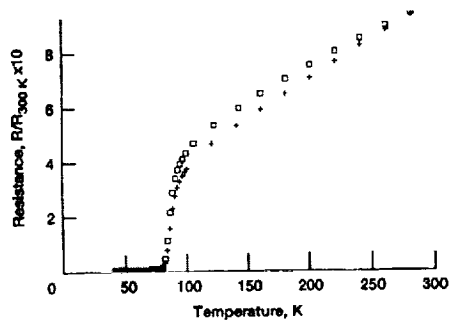

Figure 1. Normalized resistance against temperature for BSCCO thin films (3000 Å) on $SrTiO_3$ (+ : $T_c(R = 0) = 78.2$ K) and $LaAlO_3$ (□: $T_c(R = 0) = 78$ K) substrates.

method, since knowledge of the microwave signal propagation along transmission lines is of interest for practical microwave applications.

2. Structure and DC properties

Our measurements were made on BSCCO superconducting films approximately 3000 Å thick deposited by co-evaporation on to (100) $LaAlO_3$ and (100) $SrTiO_3$ substrates 0.010 in thick. The details of the BSCCO film preparation can be found elsewhere [11]. The $T_c(R = 0)$ of the films was determined using standard four-point-probe measurement techniques. T_c values of 78.2 and 78.0 K were measured for the films on $SrTiO_3$ and $LaAlO_3$ respectively (figure 1). Both films have a transition width (ΔT) of ~ 10 K, which is consistent with previously reported resistivity data for BSCCO thin films [12]. The zero temperature intercept (R_o) is lower for the film on $SrTiO_3$, and suggests a higher degree of c-axis texturing, where the c axis is perpendicular to the substrate plane.

Figure 2 shows SEM micrographs of the films under study. The observed surface roughness is typical of films grown by high temperature *ex-situ* anneal. However, surface roughness alone has not been shown to be detrimental to microwave properties of HTS thin films [7, 13]. Note that the background structure shows the plate-like structure typical of the BSCCO system. The typical grain size for these films was between 2 and 10 μm. XRD analysis of these films showed that they were predominantly oriented with the c axis perpendicular to the film plane, although unknown peaks were observed in both samples, as shown in figure 3. The c-axis lattice parameter agrees within 1 per cent of that corresponding to single crystals [14].

Magnetization hysteresis measurements were performed using a Quantum Design Magnetic Property Measurement System (MPMS). For these measurements, rectangular samples were cut from the films on $SrTiO_3$ and $LaAlO_3$, and the samples were oriented with the a–b plane normal to the magnetic field (H). Figure 4 shows magnetization hysteresis loops for both films.

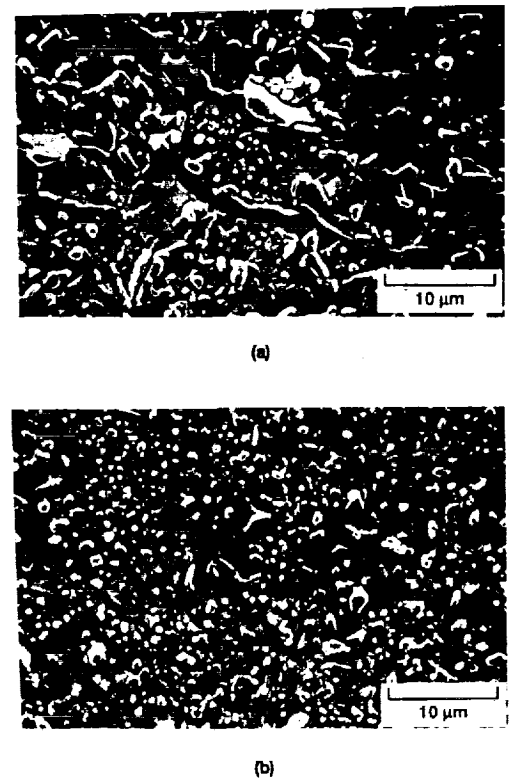

Figure 2. Scanning electron micrographs of the surface of co-evaporated (3000 Å) BSCCO thin films on (*a*) $SrTiO_3$, and (*b*) $LaAlO_3$.

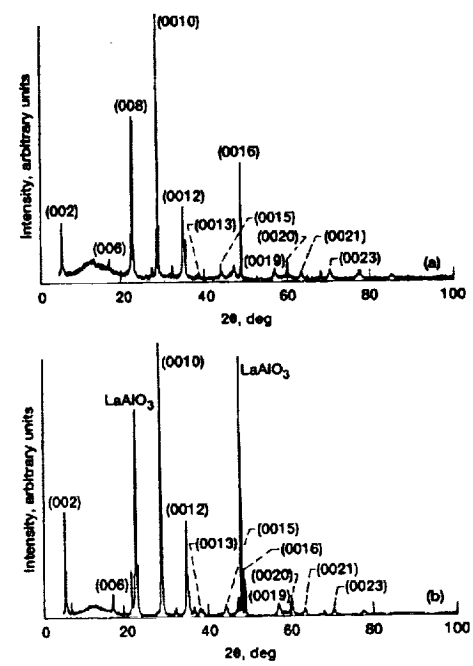

Figure 3. X-ray diffraction pattern of 3000 Å BSCCO HTS thin films on (*a*) $SrTiO_3$, and (*b*) $LaAlO_3$ substrates. The films are predominantly the $Bi_2Sr_2Ca_1Cu_2O_x$ (2212) phase with the c axis perpendicular to the substrate.

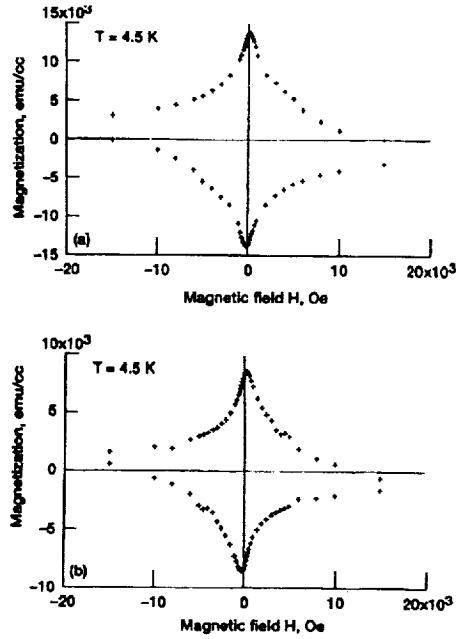

Figure 4. Magnetization hysteresis loops for BSCCO thin films (3000 Å) on (*a*) $SrTiO_3$, and (*b*) $LaAlO_3$; H parallel to the c axis.

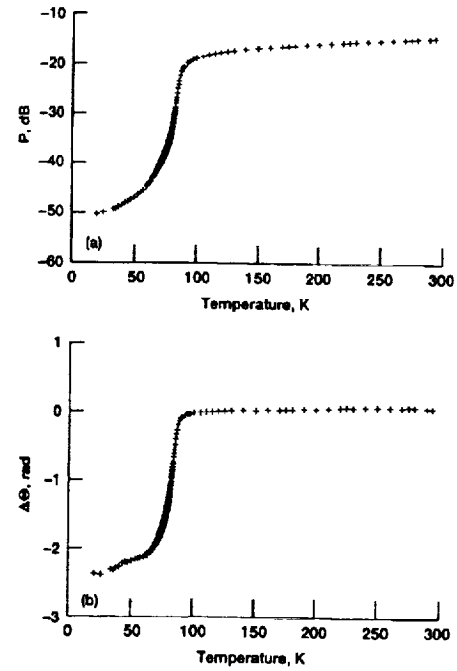

Figure 5. Magnitude, P, (*a*) and relative phase, $\Delta\theta = \theta_{300\,K} - \theta(T)$ (*b*) of the fractional transmitted power for a co-evaporated BSCCO thin film (3000 Å) on $LaAlO_3$ at 30.6 GHz.

Using Bean's model [15], and assuming a circular current path, we obtained J_c values at 4.5 K of 1.6×10^6 and 1.1×10^6 A cm^{-2} for the films on $SrTiO_3$ and $LaAlO_3$ respectively. J_c values for both films are listed in table 1 as a function of temperature. Note that for all temperatures the J_c obtained for the film on $SrTiO_3$ is larger than that for the film on $LaAlO_3$, which may be a result of better epitaxy on the $SrTiO_3$ substrate. In addition, the J_c values for both films at 40 K agree well with the $J_c \sim 1.5 \times 10^5$ A cm^{-2} reported at 40 K for laser-ablated BSCCO thin films ($\sim$3000 Å) on MgO [12].

3. Characterization of BSCCO films at microwave frequencies

3.1. Power transmission measurements

Power transmission measurements were performed on the samples at frequencies from 26.5 to 40.0 GHz (Ka-band), and at temperatures from 300 to 20 K. The details of the experimental configuration and measurement procedures have been previously reported [7]. The main components of the experimental apparatus are an HP-8510B network analyser and a closed-cycle helium gas refrigerator, both controlled by an HP 900-216 computer. The network analyser is coupled to the refrigerator by Ka-band rectangular waveguides. The measurement technique compares the transmitted signal with the incident microwave signal to determine the power transmission coefficient. All the measurements were made under vacuum ($<10^{-3}$ Torr) in a vacuum can with input/output ports for the waveguides designed for the refrigerator. Inside the vacuum can the sample was oriented perpendicular to the microwave source by clamping it between two waveguide flanges thermally connected to the cold head of the refrigerator through a gold-plated copper plate. The film side of the sample was directed towards the incident microwave signal. The system was calibrated before the beginning of each measurement cycle to account for the impedance and spurious reflections of the waveguide network. Background attenuation and phase corrections were made by subtracting the transmitted power as a function of temperature in the absence of the sample from the data obtained with the sample in place.

Figure 5 shows a plot of the magnitude (P) and relative phase ($\Delta\theta$, where $\Delta\theta = \theta_{RT} - \theta(T)$, with θ_{RT} the phase value at room temperature) at 30.6 GHz of the fractional transmitted power for the film on the $LaAlO_3$

Table 1. Magnetic J_c for BSCCO thin films on $SrTiO_3$ and $LaAlO_3$ substrates.

Temperature (K)	J_c (A cm^{-2})	
	$SrTiO_3$	$LaAlO_3$
4.5	1.6×10^6	1.1×10^6
20.0	1.0×10^6	6.7×10^5
40.0	2.7×10^5	1.0×10^5

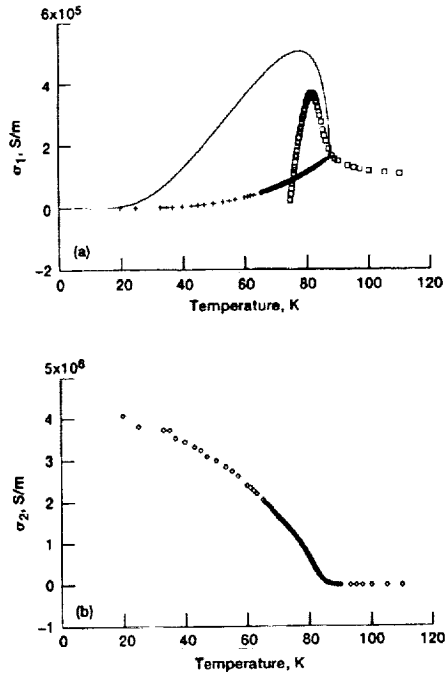

Figure 6. Real (*a*) and imaginary (*b*) parts of the complex conductivity against temperature at 30.6 GHz for a co-evaporated BSCCO thin film (3000 Å) on $LaAlO_3$. In (*a*) □ represents the experimental data, + represents σ_1 obtained using the two-fluid model approximation, and the solid line represents a fit using the BCS temperature dependence for σ_1.

substrate as a function of temperature. Since in this type of measurement the signal also interacts with the substrate, similar types of measurement were not performed with the film on $SrTiO_3$ because of the extreme temperature sensitivity of its dielectric constant and loss tangent [16, 17]. $LaAlO_3$ has more stable properties and has proved to be a suitable substrate for microwave applications [18, 19]. Observe that in the normal state P decreases monotonically with temperature while $\Delta\theta$ remains almost constant. However, at the beginning of the normal-superconducting phase transition ($\sim$88 K) both P and $\Delta\theta$ decrease very quickly, levelling off at low temperatures. This behaviour is consistent with previous reports for BSCCO and YBCO thin films [7, 20, 21].

The complex conductivity can be expressed in terms of the power transmission data according to the following relations [7],

$$R = \frac{\{(2n/P^{1/2})[n\cos(k_0 nt)\sin(k_0 t+\theta) - \sin(k_0 nt)\cos(k_0 t+\theta)] - n(n^2-1)\sin(k_0 nt)\cos(k_0 nt)\}}{k_0 d[n^2\cos^2(k_0 nt) + \sin^2(k_0 nt)]} \quad (1)$$

and

$$I = \frac{\{(2n/P^{1/2})[n\cos(k_0 nt)\cos(k_0 t+\theta) + \sin(k_0 nt)\sin(k_0 t+\theta)] - 2n^2\cos^2(k_0 nt) - (n^2+1)\sin^2(k_0 nt)\}}{k_0 d[n^2\cos^2(k_0 nt) + \sin^2(k_0 nt)]} \quad (2)$$

where R and I are the real and imaginary parts of the HTS thin film dispersion coefficient and are related to σ^* by $R = 1 + 4\pi\sigma_2/\omega\varepsilon$, and $I = 4\pi\sigma_1/\omega\varepsilon$, where $\omega/2\pi = f$ is the frequency of the wave and ε is the relative dielectric constant of the HTS material. P and θ were measured, and from these quantities σ^* was calculated.

Figure 6 shows plots of σ_1 and σ_2 against temperature for the BSCCO film on $LaAlO_3$. Observe that in the normal state σ_1 shows metallic behaviour, while σ_2 is close to zero as expected for a good conductor. When the superconducting transition begins (we refer to this temperature as T_c^{mw}, which in this case is $\sim$88 K), both conductivities increase rapidly. As the temperature decreases, σ_1 increases to a maximum and then decreases quickly to the extent that we were unable to determine its value for temperatures below $\sim$74 K, while σ_2 increased monotonically. This behaviour is consistent with that reported for YBCO and other BSCCO thin films [7, 20, 21]. The complex conductivity was determined to be $(2.0 - j10) \times 10^5$ S m^{-1} at 77 K. These values are approximately one order of magnitude larger than those obtained previously for BSCCO thin films on $LaAlO_3$ at the same temperature and frequency [10]. The same temperature behaviour for σ^* was observed for measurements at other frequencies within the Ka-band. From figure 6(*a*) it can be seen that the behaviour of σ_1 in the superconducting state does not follow that expected from the two-fluid model approximation [22] where,

$$\sigma_1(T) = \sigma_c(T/T_c)^4 \quad (3)$$

and σ_c is the conductivity at T_c. The measured data also deviated from σ_1 calculated using the BCS-based Mattis–Bardeen equations [23]

$$\sigma_1 = \sigma_c[2\Delta(k_B T)^{-1}]\exp[-\Delta/k_B T]\ln(\Delta/\hbar\omega) \quad \hbar\omega \ll 2\Delta \quad (4)$$

where k_B is Boltzmann's constant, $\omega = 2\pi f$ is the angular frequency, and Δ is the energy gap.

The values of σ_2 can be used to determine λ by using the expression $\lambda = (1/\mu\omega\sigma_2)^{1/2}$, valid for homogeneous superconductors. λ values of $\sim$1.97 and 1.09 μm at 77 and 20 K respectively, were obtained for the film on $LaAlO_3$. The value of λ at low temperature is less than that obtained in ion-beam-deposited BSCCO thin films on MgO ($\lambda \sim 1.3$ μm) [20], and compare well with those obtained using microstrip transmission lines fabricated with the same type of co-evaporated BSCCO films used in this study ($\lambda(0) \sim 1.11$ μm, where $\lambda(0)$ is the magnetic penetration depth at

$T = 0$) [24]. However, the values of λ are still large when compared with those reported for BSCCO single-crystals ($\lambda(0) \sim 0.3\ \mu m$) [25–27].

3.2. Surface resistance measurements

Cavity method The R_s of the films was measured by monitoring the change in the quality factor (Q) of a cylindrical, TE_{011} mode copper cavity, resonant at 58.9 GHz, with one of its end walls replaced with the BSCCO thin film. Using an HP-8510B network analyser and Ginzton's impedance method the loaded Q (Q_L) of the cavity was determined by measuring the reflection coefficient. Knowing Q_L, the unloaded quality factor (Q_0) of the cavity was obtained and the R_s of the BSCCO films were computed by the method in [28]. As shown in Figure 7, the R_s of the BSCCO films decreased monotonically with temperature for $T/T_c > 0.75$, levelling off at lower temperatures. Note that, except for very low temperatures, the R_s for the film on $SrTiO_3$ is less than that of its counterpart on $LaAlO_3$. Values of R_s of 865 and 376 mΩ for the film on $SrTiO_3$, and of 1391 and 370 mΩ for the film on $LaAlO_3$ were obtained at 77 and 20 K respectively. The R_s values at low temperatures are almost one-fifth of those measured at lower frequencies on BSCCO films on MgO using microstrip and cavity resonator techniques (~25 mΩ at 7 GHz and 25 K; $R_s \sim 1770$ mΩ at 58.9 GHz assuming $R_s \propto f^2$ dependence) [29]. They are also almost an order of magnitude less than those recently obtained by others from ring microstrip resonators fabricated on e-beam deposited BSCCO films on MgO (~34 mΩ at 4.2 K, 6 GHz, and 12 dB m incident RF power; 3276 mΩ at 4.2 K, 58.9 GHz, using $R_s \propto f^2$) [30]. Since the R_s of the film is larger than that of Cu for all temperatures (for very pure Cu and at 77 K, $R_s \sim 21.6$ mΩ at 58.9 GHz; the measured R_s value for a Cu sample at 77 K using the cavity was ~45.4 mΩ) the flat part of the curve may be associated with residual losses in the film and not with limitations in the sensitivity of the cavity, in contrast to measurements of good quality YBCO thin films on $LaAlO_3$ [7].

Linear resonator method Microstrip transmission line resonators were fabricated and tested to examine the losses of the BSCCO films in a structure that can be used in potential HTS passive microwave circuits such as filters, resonators or delay lines. The microstrip structure is shown in figure 8 and consisted of the BSCCO superconducting strip separated from a gold ground plane by the 0.010 in $LaAlO_3$ substrate (figure 8(*a*)). The strip width (W) was 300 μm with a length (L) of 7 mm (figure 8(*b*)). This resulted in a 30 Ω line impedance with the fundamental ($L = \lambda/2$) resonant frequency at 10.4 GHz and a second harmonic ($L = \lambda$) at 20.2 GHz. The resonant strip was capacitively coupled to a 30 Ω feed line by a 75 μm wide gap (G). Transition from the coaxial test cables to the microstrip feed line was accomplished by a coaxial 'spark-plug' launcher.

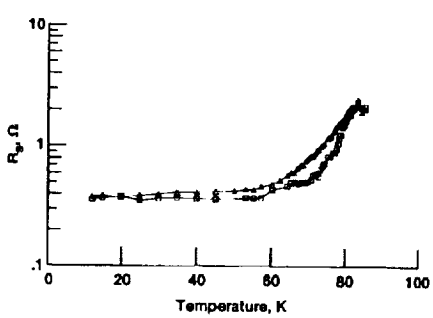

Figure 7. Surface resistance, R_s, at 58.9 GHz against temperature for co-evaporated BSCCO thin films (3000 Å) on $SrTiO_3$ (□) and $LaAlO_3$ (△).

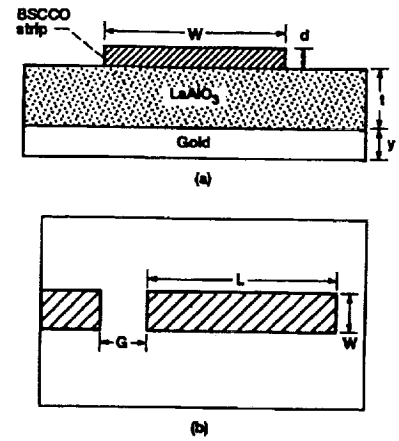

Figure 8. Cross section (*a*), and top view (*b*) of a BSCCO microstrip transmission line resonator. For this resonator $W = 300\ \mu m$, $L = 7$ mm, $G = 75\ \mu m$, $d = 3000$ Å, $t = 0.010$ in, and $y = 1.5\ \mu m$. The calculated line impedance was 30 Ω.

The circuit was tested using an HP 8510B network analyser and a closed-cycle refrigerator for cooling. The test cable was calibrated up to the spark-plug launcher using coaxial open, short, and load standards. The calibration was performed at room temperature but was used at low temperatures as well since only minor shifts in the calibration with decreasing temperature were observed. The reflection coefficient (S_{11}) was measured at temperatures from ~20 K upwards, giving the loaded Q of the circuit. Using the impedance method [31, 32] the unloaded Q was extracted from the reflection data.

Figure 9 shows a plot of the unloaded Q values against temperature for the superconducting and an identical gold (Au) resonator at 10.4 and 20.2 GHz. The Q values of the Au resonator are relatively flat over this temperature range with the Q values at 20.2 GHz larger than those at 10.2 GHz, as expected for a conductor loss-limited transmission line resonator where $Q \propto f^{1/2}$, and f is the frequency. A measurable response for the HTS resonators began just below the $T_c(R = 0)$ value measured for the films. As seen in figure 9, the Q values increased with decreasing temperature and exceeded the Q values of the Au resonator around 60 to 65 K. However, the BSCCO unloaded Q values above ~60 K

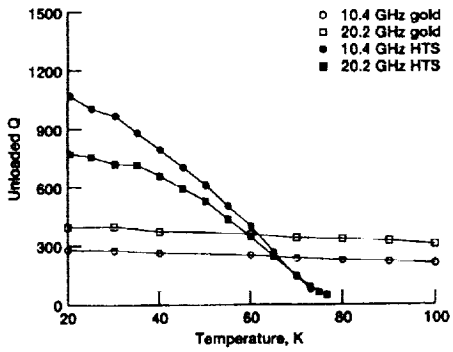

Figure 9. Linear resonator unloaded Q values for BSCCO HTS and gold strips.

are less than those for the Au resonator because the thinner BSCCO film (0.3 μm for BSCCO; 1.5 μm for Au) leads to overall higher conductor loss and lower Q. The Q values of the superconducting resonator kept increasing down to the lowest temperatures measured, reaching values of approximately four times that of the Au circuit Q at 10.4 GHz and 20 K, and approximately twice that of the Au circuit Q at 20.2 GHz and 20 K. It should be noted that for the superconducting resonator the 10.4 GHz resonance has a higher Q than the 20.2 GHz resonance, contrary to the observations for the Au resonator. This is due to the $R_s \propto f^2$ dependence for the superconducting film which leads to $Q \propto 1/f$ for a conductor loss-limited transmission line resonator.

The unloaded Q values of the resonator may be used to estimate the R_s of the BSCCO thin film [32]. The R_s values obtained at 10.4 and 20.2 GHz, and the R_s values corresponding to Au are plotted in figure 10. R_s values at 73 K of 13 and 22 mΩ were obtained for the BSCCO at 10.4 and 20.2 GHz respectively. At 20 K, R_s was $\sim$0.75 and 2.9 mΩ at 10.4 and 20.2 GHz respectively. These R_s values are less than those for the Au film at the same frequencies and temperatures, and are approximately eight times smaller than earlier values ($\sim$25 mΩ at 25 K) reported at 7 GHz [29]. Also plotted in figure 10 are the values of R_s for the BSCCO thin film at 20.2 GHz obtained assuming a $R_s \propto f^2$ dependence, where f is the frequency, and using the experimental values measured at 10.4 GHz. Note that although there is a noticeable discrepancy between the measured and calculated R_s values at 20.2 GHz at T near T_c, the agreement between the two sets of values improves at temperatures far below T_c.

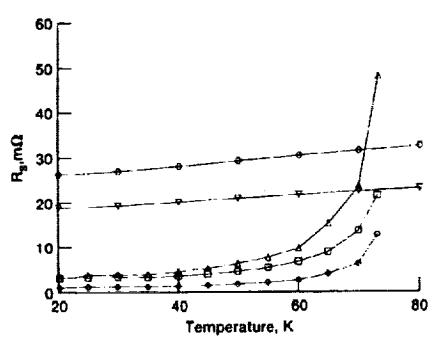

Figure 10. Surface resistance, R_s, for BSCCO HTS strip at 10.4 GHz (◇) and 20.2 GHz (□). The R_s of a gold strip at 10.4 (▽) and 20.2 (○) GHz are shown for comparison purposes. Also shown is the R_s for the BSCCO HTS strip at 20.2 GHz calculated from the measured R_s at 10.4 GHz assuming an $R_s \propto f^2$ dependence (△).

4. Discussion

We have characterized co-evaporated BSCCO thin films on $SrTiO_3$ and $LaAlO_3$ substrates. We have compared the films in terms of their T_c and J_c values, surface morphology and XRD patterns. It was observed that, although both films have similar DC T_c, the film on the $SrTiO_3$ substrate has a larger J_c from 4.2 to 40 K, a smoother surface morphology, and lower R_s than its counterpart on $LaAlO_3$. From the power transmission measurements we have shown that the conductivity in the superconducting state does not follow either the BCS or two-fluid model temperature dependence. However, the observed increase in σ_1 for $T < T_c$ is consistent with the observation of Ho *et al* [20] (for ion-beam-deposited BSCCO thin films on MgO at 60 GHz) who suggested that this trend below T_c is either an intrinsic temperature dependence of the homogeneous superconductor or the manifestation of the response of a composite consisting of superconducting regions growing in a normal conducting matrix. In the case of our films, although σ_1 increases very quickly upon cooling the sample below $\sim$88 K, we also observed that, contrary to the observations by Ho *et al* [20], it reaches a maximum at T not far below T_c^{mw} and then falls very quickly. This behaviour may be due to the better quality of the co-evaporated films under study as compared with those analysed by Ho *et al* [20], which have $T_c \sim 68$ K and $J_c \sim 5 \times 10^4$ A cm^{-2} at 10 K. Thus it may be reasonable to assume that as the quality of the material improves, i.e., as the normal conductor fraction in the material decreases, the behaviour below T_c could actually approach that expected from the two-fluid model. A more rigorous analysis should be performed along this line in the future.

From the R_s values obtained using the resonant cavity technique, one can see that the values at 77 K for the films on $SrTiO_3$ and $LaAlO_3$ are approximately 12 and 20 times, respectively, larger than those of pure Cu and Au at room temperature, and about 8 and 13 times, respectively, that of a Au-plated Cu sample. However, the R_s measured at 10.4 GHz using the linear resonator patterned on the film on $LaAlO_3$ ($\sim$13 mΩ) is similar to that of pure Cu and pure Au at the same frequency and temperature ($R_{s,Cu} \sim 10$ mΩ, $R_{s,Au} \sim 14.3$ mΩ), and lower than that of its Au counterpart ($\sim$23 mΩ). We

found that when the $R_s \propto f^2$ dependence was used to determine the R_s of the BSCCO film at 20.2 GHz using the resonator technique, the agreement between the calculated and measured values at this frequency improved for temperatures far from T_c. However, when the same approach was used to determine the R_s at 58.9 GHz ($R_s \sim 13$ mΩ at 10.4 GHz, and ~417 mΩ at 58.9 GHz) the resulting value was approximately one-third of that obtained by the cavity technique at temperatures near 77 K, the discrepancy becoming worse for lower temperatures. This deviation is not unexpected since we are dealing with an heterogeneous system in which the different components (superconducting, normal and possibly insulating) do not necessarily respond to frequency changes in the same way and therefore may alter the frequency dependence of the microwave losses that one expects for a homogeneous superconductor. In addition it will be interesting to see how the different measurement techniques contribute to the deviation especially when it has been suggested by others that calibration differences in different techniques to measure R_s can contribute to the lack of correlation between R_s values in HTS thin films [33].

We have also obtained λ for the BSCCO films under discussion. Low temperature values for $\lambda \sim 1.0$ μm were obtained. Although these values compare favourably with those obtained by others in BSCCO films, they are still approximately three times the values reported by others for BSCCO single crystals. This may be due to the inhomogeneity of the films under study as shown by the unknown peaks observed in the XRD pattern (figure 3). It has been shown by others that non-superconducting inclusions and weak link effects result in an increase of λ [34]. The fact that the low temperature λ is large compared with the values typically obtained at low temperatures for YBCO thin films (~0.14–0.3 μm) [5–7] may impose limitations in the use of this type of BSCCO thin film for microwave applications. In normal conductors, in order to have low conductor losses, the conductor thickness must be at least three times larger than the normal skin depth (δ). If, as in the YBCO films, the superconducting properties of the BSCCO films deteriorate as the film thickness goes beyond 0.5 μm, then it is clear that improvements in the BSCCO film growth are still necessary. Therefore careful study of the various microwave transmission lines, in terms of the contribution to total losses (i.e., conductor, substrate and radiation losses [35]) must be performed to determine, in view of the limitations described above, for which of these structures the BSCCO HTS film would be more suitable.

Nevertheless, since the values of T_c and J_c compared well with those of other BSCCO thin films deposited by other techniques, we believe that the microwave data presented here are representative of state-of-the-art BSCCO films. In view of this we can see that this type of film offers some possibilities for microwave applications at low frequencies (i.e., $\leqslant 20$ GHz), but potential applications at frequencies around 60 GHz and above will require further improvements in the material.

5. Conclusions

We have characterized co-evaporated BSCCO thin films on $SrTiO_3$ and $LaAlO_3$. The J_c values measured for these films are better than or equal to those reported by others for state-of-the-art BSCCO films deposited by other techniques. From the microwave power transmission measurements we were able to determine σ^*; it was found that the temperature dependence of σ^* for $T < T_c$ deviates from both the BCS theory and the two-fluid model. The low temperature values of λ agreed with those reported by others for BSCCO films, but were approximately three times larger than those of BSCCO single crystals. R_s values for the BSCCO thin films were measured at 10.4, 20.2, and 58.9 GHz. From the R_s data it is evident that the low-T_c phase BSCCO thin films could offer possibilities for microwave applications at low frequencies ($\leqslant 20$ GHz), but applications at frequencies around 60 GHz and above will require further improvements in the material. To our knowledge this is the first time a microwave characterization in terms of the transport parameters most relevant for transmission line applications has been performed on the same BSCCO film and in the frequency range from 10 to 60 GHz.

Acknowledgments

The authors would like to thank Ms Ruth Cipcic and Mr Ralph Garlick for the x-ray-diffraction measurements. The assistance of D Bohmann in obtaining the SEM micrographs of the films and measuring their thickness is deeply appreciated. We thank Ms C Cubbage for her assistance in measurements of the gold linear resonator. Finally we thank Dr V O Heinen for helpful discussions and suggestions.

This paper is declared a work of the US Government and is not subject to copyright protection in the United States of America.

References

[1] Klein N, Muller G, Piel H, Roas B, Schultz L, Klein U and Peiniger M 1989 *Appl. Phys. Lett.* **54** 757

[2] Drabeck L, Gruner G, Chang J J, Inam A, Wu X D, Nazar L, Venkatesan T and Scalapino D J 1989 *Phys. Rev. B* **40** 7350

[3] Harshman D R, Schneemeyer L F, Waszczak J V, Aeppli G, Cava R J, Batlogg B, Rupp L W, Ansaldo E J and Williams D L 1989 *Phys. Rev.* B **39** 851

[4] Qui X G, Cui C G, Zhang Y Z, Li S L, Zhao Y Y, Xu P and Li L 1990 *J. Appl. Phys.* **68** 884

[5] Anlage S M, Langley B W, Deutscher G, Halbritter J and Beasley M R 1991 *J. Phys. Rev.* B **44** 9764

[6] Kobrin P H, Ho W, Hall W F, Hood P J, Gergis I S and Harker A B 1990 *Phys. Rev.* B **42** 6259

[7] Miranda F A, Gordon W L, Bhasin K B, Heinen V O and Warner J D 1991 *J. Appl. Phys.* **70** 5450

[8] Maeda H, Tanaka Y, Fukutomi M and Asano T 1988 *Japan. J. Appl. Phys.* **27** L209
[9] Talvacchio J, Wagner G R and Talisa S H 1991 *Microwave J.* **34** 105
[10] Miranda F A, Bhasin K B, Heinen V O, Kwor R and Kalkur T S 1990 *Physica* C **168** 91
[11] Kalkur T S, Kwor R Y, Jernigan S and Smith R 1989 *Science and Technology of Thin Film Superconductors* ed R D McConnell and S A Wolf (New York: Plenum) p 487
[12] Narumi E, Lee J, Li C, Hosokawa S, Patel S and Shaw D T 1991 *Appl. Phys. Lett.* **59** 3180
[13] Xi X X *et al* 1991 *IEEE Trans. Magn.* **MAG-27** 982
[14] Yeh J J and Hong M 1989 *Appl. Phys. Lett.* **54** 769
[15] Bean C P 1962 *Phys. Rev. Lett.* **8** 250
[16] Gorshunov B P, Kozlov G V, Krasnosvobodtsev S I, Pechen E V, Prokhorov A M, Prokhorov A S, Syrotynsky O I and Volkov A A 1988 *Physica* C **153–154** 667
[17] Weaver H E 1959 *J. Phys. Chem. Solids* **11** 274
[18] Miranda F A, Gordon W L, Bhasin K B, Ebihara B T, Heinen V O and Chorey C M 1990 *Microwave Opt. Tech. Lett.* **3** 11
[19] Simon R W, Platt C E, Lee A E, Lee G S, Daly K P, Wire M S, Luine J A and Urbanik M 1988 *Appl. Phys. Lett.* **53** 2677
[20] Ho W, Hood P J, Hall W F, Kobrin P, Harker A B and DeWames R E 1988 *Phys. Rev.* B **38** 7029
[21] Kobrin P H, Ho W, Hall W F, Hood P J, Gergis I S and Harker A B 1990 *Phys. Rev.* B **42** 6259
[22] Hinken J H 1989 *Superconductor Electronics: Fundamentals and Microwave Applications* (Berlin: Springer)
[23] Tinkham M 1980 *Introduction to Superconductivity* (New York: McGraw-Hill)
[24] Byrne D P, Kwor R Y and Kalkur T S 1991 *J. Appl. Phys.* **69** 6693
[25] Mitra S, Cho J H, Lee W C, Johnston D C and Kogan V G 1989 *Phys. Rev.* B **40** 2674
[26] Gygax S, Xing W, Rajora O and Curzon A 1989 *Physica* C **162–164** 1551
[27] Ansaldo E J, Batlogg B, Cava R J, Harshman D R, Rupp L W, Riseman T M and Williams D 1989 *Physica* C **162–164** 259
[28] Miranda F A, Gordon W L, Bhasin K B and Warner J D 1990 *Appl. Phys. Lett.* **57** 1058
[29] Lichtenberg C L, Wosik J, Davis M and Wolfe J C 1989 *NASA TM-102159*
[30] Andreone A, Attanasio C, Dichiara A, Maritato L, Nigro A, Peluso G and Vaglio R 1991 *Physica* C **180** 272
[31] Ginzton E L 1957 *Microwave Measurements* (New York: McGraw-Hill)
[32] Chorey C M, Kong K S, Bhasin K B, Warner J D and Itoh T 1991 *IEEE Trans. Microwave Theory Tech.* **39** 1480
[33] Talvacchio J and Wagner G R 1990 *SPIE Proc.* **1292** 2
[34] Hylton T L, Kapitulnik A, Beasly M R, Carini J P, Drabeck L and Gruner G 1988 *Appl. Phys. Lett.* **53** 1343
[35] Kong K S, Bhasin K B and Itoh T 1991 *SPIE Proc.* **1477** 57

PROCESSING, ELECTRICAL AND MICROWAVE PROPERTIES OF SPUTTERED Tl-Ca-Ba-Cu-O SUPERCONDUCTING THIN FILMS

G. Subramanyam and V. J. Kapoor
Department of Electrical & Computer Engineering
University of Cincinnati
Cincinnati, OH 45221-0030

C. M. Chorey
Sverdrup Technology Inc. (NASA Lewis Group)
Cleveland, OH 44135

K. B. Bhasin
NASA Lewis Research Center
Cleveland, OH 44135

Abstract--A reproducible fabrication process has been established for TlCaBaCuO thin films on $LaAlO_3$ substrates by rf magnetron sputtering and post-deposition processing methods. Electrical transport properties of the thin films were measured on patterned four-probe test devices. Microwave properties of the films were obtained from unloaded Q measurements of all-superconducting ring resonators. This paper describes the processing, electrical and microwave properties of $Tl_2Ca_1Ba_2Cu_2O_x$ (2122) phase thin films.

I.INTRODUCTION

The high temperature superconducting thin films show great promise for electronic applications at 77 °K. Since the discovery of high T_c materials, there has been a substantial progress in the applications such as SQUIDs, passive microwave devices, IR detectors and interconnections in microelectronics. Among the high T_c materials, the TlCaBaCuO compound has proven to possess the highest T_c of 125 °K[1], and hence offers a wide margin of temperature range for applications at 77 °K. Thin films of TlCaBaCuO compound have shown T_c as high as 120 °K, and critical current density (J_c) greater than 10^6 A/cm^2 at 77 K[2]. Also, TlCaBaCuO thin films, primarily of 2122 phase have shown surface resistance (R_s) about 80 times lower than Cu at 10 GHz and 77 °K[3]. This research work primarily addresses a reproducible processing method for TlCaBaCuO thin films of 2122 phase, electrical transport measurements and also microwave ring resonator measurements.

This research was supported by NASA Lewis Research Center.
Manuscript received August 24, 1992.

II.PROCESSING OF TlCaBaCuO THIN FILMS

The TlCaBaCuO thin films were sputter deposited on (100) $LaAlO_3$ substrates from a single composite powder target in a CVC model 601 rf magnetron sputtering system. The target was a Tl enriched $Tl_2Ca_2Ba_2Cu_3O_x$ (2223) powder target, with 20% excess Tl_2O_3 to compensate for the loss of Tl during post-processing steps and to maintain sufficient composition for several deposition runs. The sputter depositions were performed at an rf power density of 0.7 W/cm^2, and the chamber pressure at 5 mTorr, in a pure argon atmosphere. The thin films were deposited at a deposition rate of approximately 30 Å/min. The sputter deposited thin films of 0.3-0.5 μm thickness were post-processed in two steps: first, sintering in air at 850 °C for 12-15 minutes in an optimum Tl_2O partial pressure, and the second, annealing in oxygen flow at 750 °C. These steps were performed in a box furnace with samples placed in an enclosed platinum crucible. The Tl_2O partial pressure was provided by placing 2223 pellets inside the crucible. Both the steps were performed with the same number of pellets placed inside the crucible. The Tl_2O partial pressure provided during the sintering process establishes the phase in the thin films. The details of the post-processing steps have been reported earlier[4-5].

To provide the optimum Tl_2O partial pressure during the post-processing steps, a simple technique was used to monitor the reduction in Tl content in the as-deposited thin films, after each sputtering run. Percentage reduction in Tl content from run to run was obtained by Auger Electron Spectroscopy(AES) surface analysis on the as-deposited samples. This percentage reduction in Tl gives an approximate estimate of additional Tl_2O partial pressure needed for the post-deposition processes. The estimated additional Tl_2O partial pressure was provided

© 1993 IEEE. Reprinted, with permission, from IEEE Transactions on Applied Superconductivity, vol. 3, no. 1, Mar. 1993, pp. 1749-1752.

by adding additional 2223 pellets in the crucible. This technique has yielded reproducible high T_c and high J_c thin films. The annealed thin films were essentially smooth in morphology. The superconducting thin films were characterized by X-ray diffraction(XRD) analysis to determine the phase purity. XRD spectra obtained on a TlCaBaCuO thin film is shown in figure 1. The characteristic peaks of 2122 and 2223 phases were present. The 2122 phase with c-axis oriented growth was the dominant phase in the thin films, as determined from the XRD data.

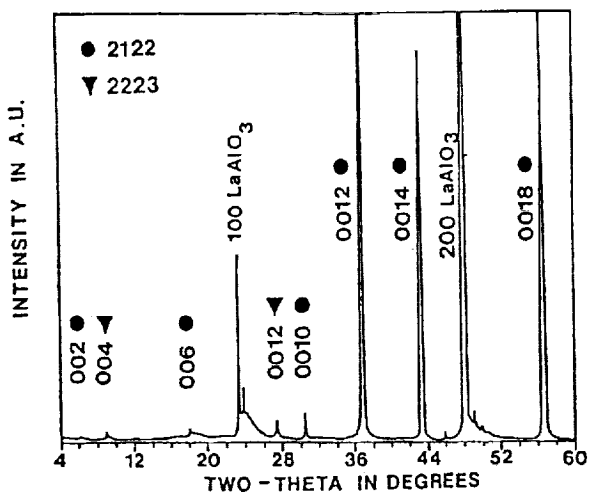

Fig.1 XRD spectra obtained on an annealed TlCaBaCuO thin film showing c-axis oriented 2122 and 2223 peaks.

III.ELECTRICAL TRANSPORT PROPERTIES

Electrical transport measurements were performed on patterned four-probe test devices 10, 25 and 50 μm wide, and 1 mm long. The test devices were patterned on as-deposited TlCaBaCuO thin films using standard positive photoresist photo-lithography, and wet chemical etching in a weak phosphoric acid. Positive photoresist AZ 1421 was used for the photo-lithography. The etching solution was a 1:100 phosphoric acid:DI H_2O heated to about 75 °C. The etch rate was approximately 30 Å/min. The patterned samples were post-processed using our standard procedures described above.

For reliable electrical measurements, a process for making low resistance gold contacts on TlCaBaCuO thin films was established. First, metal bonding pads were formed by thermally evaporating 6000 Å thick gold film on the superconducting pads of the four-probe device. The samples were annealed at 600 °C for 15 minutes in an oxygen flow of 1 liter/min, followed by a slow furnace cooling for 30 minutes after the furnace was switched off. Gold wires were bonded to the pads using an ultrasonic wedge bonder. Typically, the four-probe test devices showed zero resistance T_c between 97 and 100 °K. The measurements were performed at a constant applied current of 10 μA. The contact resistance obtained from the I-V measurements of the four-probe devices is typically a few mΩ at temperatures below Tc. The specific contact resistivity was approximately 3.65×10^{-5} Ω-cm^2 at 90 °K, and below 10^{-8} Ωcm^2 at 77 °K.

The zero-field transport current density (J_c) measurements were performed using dc and pulsed current techniques, using a 1 μV/mm electric field criterion. Figure 2 shows the J_c vs temperature measurements obtained on two four probe test devices. Zero-field J_c greater than 10^5 A/cm^2 at 77 °K was obtained in the four-probe devices tested.

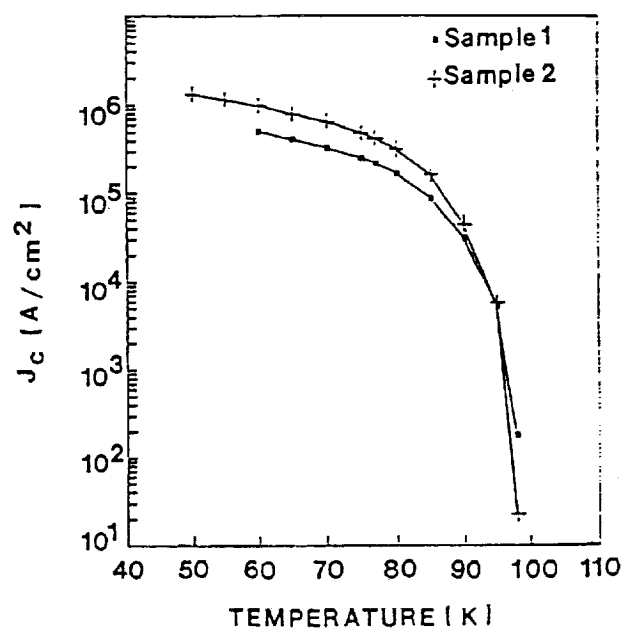

Fig.2 Zero-field J_c vs Temperature for two different TlCaBaCuO thin films measured using 1 μV/mm criterion.

III.MICROWAVE PROPERTIES

The microwave properties of the TlCaBaCuO thin films were obtained indirectly by measuring the unloaded Q of all-superconducting ring resonators. A ring resonator was designed for a fundamental resonance at 12 GHz. The device consisted of a ring structure separated from the feed line by a small coupling gap. The figure 3 shows a ring resonator designed for fundamental resonance at 12 GHz, for 10 mil

thick $LaAlO_3$ substrates(ϵ_r=24.5). In the figure, the linewidth of the ring and the microstrip feed line is W=5.6 mils, the coupling gap G=1.75 mils, and the mean radius of the ring R=77 mils.

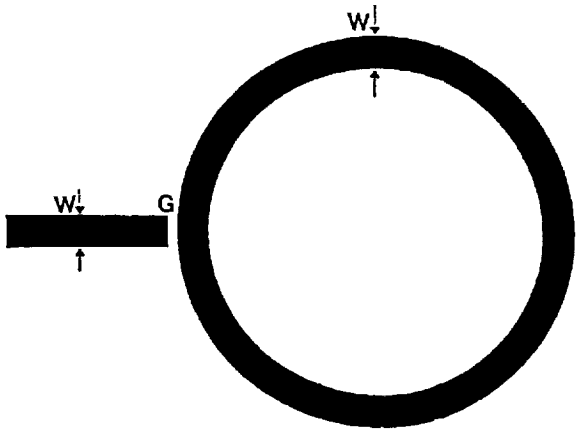

Fig.3 Microstrip ring resonator designed for 12 GHz

The TlCaBaCuO ring resonators were fabricated by patterning 0.3 μm thin films using AZ 1421 photolithography, and wet chemical etching techniques described before. After processing the top conductor side, the ground plane TlCaBaCuO thin film was deposited to a thickness of 0.3 μm, and post-processed using the same steps described in section II. The unloaded Q of the resonators were obtained by swept frequency reflection measurements[6] using a HP8720B network analyser. The unloaded Q versus temperature characteristics for an all-superconducting TlCaBaCuO ring resonator is shown in curve A of figure 4. For comparison, data for a gold resonator with gold ground plane is shown in curve B.

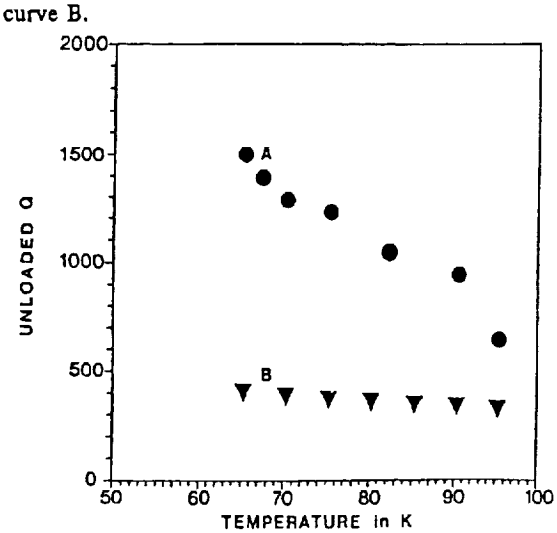

Fig.4 The unloaded Q vs temperature characteristics of an all-superconducting TlCaBaCuO ring resonator

The unloaded Q of the superconducting ring resonator is approximately four times higher than the gold resonator at 65 °K. The ring resonators offer an indirect method for measuring the surface resistance (R_s) of superconducting thin films. By separating the conductor and dielectric losses, the R_s of the TlCaBaCuO thin films were calculated using the standard microstrip loss equations described by Pucel et al[7]. The effective R_s at 12 GHz and 77 °K was determined to be typically between 1.5 and 2.75 mΩ, almost an order of magnitude lower than the R_s of Cu at the same frequency and temperature. The lowest surface resistance reported in $Tl_2Ca_1Ba_2Cu_2O_x$ thin films to date is 0.130 mΩ at 77 K and 10 GHz[3].

The swept frequency reflection measurements performed at several temperatures, were also used in determining the effective penetration depth in the TlCaBaCuO thin films. The shift in resonance frequency with temperature is mainly due to the temperature dependence of the penetration depth in the superconducting thin film. The phase velocity of a superconducting microstrip line with a superconducting ground plane is given by[8],

$$v_{ph} = c/\sqrt{\epsilon_{eff}}\{1+2(\lambda/h)\coth(t/\lambda)\}^{-0.5} \quad \text{--(1)}$$

where c is the velocity of light, ϵ_{eff} is the effective dielectric constant, h is the substrate thickness, t is the thickness of the microstrip, λ the penetration depth of the superconducting microstrip. The penetration depth is temperature dependent based on the Gorter-Casimir relationship, ie.,

$$\lambda(T) = \lambda(0)[1-(T/Tc)^4]^{-0.5} \quad \text{--(2)}$$

for temperature T less than Tc. $\lambda(0)$ is the penetration depth at T=0 °K. The resonance frequency of the ring resonator is given by the equation

$$f = nv_{ph}/(2L) \quad \text{--(3)}$$

where f is in GHz, L is the mean circumference of the ring in mm, and n is the integer order of resonance. From the above equations, the lowest value of the effective $\lambda(0)$ was determined to be 6890 Å. The typical value ranges between 7000 Å and 8000 Å. Since the thin films were only 0.3-0.4 μm thick, the penetration depth depends upon the properties of the superconductor through the entire film. This may be a reason for the higher penetration depth. The typical values of penetration depth reported in literature is between 4000 and 8000 Å in Tl 2122 phase thin films[9-10]. The higher value of penetration depth is also an indication of the film quality. Improvements in film quality should yield lower effective

penetration depth and lower R_s values.

IV.SUMMARY

A reproducible fabrication process has been established for TlCaBaCuO thin films of 2122 phase on $LaAlO_3$ substrates. Zero resistance T_c as high as 100 °K, and the zero-field J_c as high as $5x10^5$ A/cm^2 were obtained in four-probe test devices. The surface resistance of the TlCaBaCuO thin films obtained by separating the conductor losses from Q measurements in ring resonators is typically between 1.5 and 2.75 mΩ at 12 GHz and 77 °K. The effective penetration depth at 0 °K, calculated from the resonance frequency shift with temperature measurements was typically between 7000 and 8000 Å.

REFERENCES

[1] S. S. P. Parkin, V. Y. Lee, E. M. Engler, A. I. Nazzal, T. C. Huang, G. Gorman, R. Savoy and R. Beyers,"Bulk superconductivity at 125 °K in $Tl_2Ca_2Ba_2Cu_3O_x$", Phys. Rev. Lett., vol.60, pp 2539-42, 1988.

[2] W. Y. Lee, S. M. Garrison, M. Kawasaki, E. L. Venturini, B. T. Ahn, R. Boyers, J. Salem, R. Savoy, and J. Vasquez, "Low temperature formation of epitaxial $Tl_2Ca_2Ba_2Cu_3O_{10}$ thin films in reduced O_2 pressure", Appl. Phys. Lett., vol.60, pp 772-774, 1992.

[3] W. L. Holstein, L. A. Parisi, C. Wilker, and R. B. Flippen, "$Tl_2Ba_2Ca_1Cu_2O_8$ films with very low microwave surface resistance up to 95 K", Appl. Phys. Lett., vol.60, pp 2014-2016, 1992.

[4] D. S. Ginley, J. F. Kwak, E. L. Venturini, B. Morosin, and R. J. Baughman, "Morphology control and high critical currents in superconducting thin films in the TlCaBaCuO system", Physica C, vol.160, pp 42-48, 1989.

[5] G. Subramanyam, F. Radpour, V. J. Kapoor, and G. H. Lemon, "Fabrication and chemical composition of rf magnetron sputtered TlCaBaCuO high Tc thin films", J. Appl. Phys. vol.68, pp 1157-63, 1990.

[6] J. Aitken, "Swept frequency microwave Q factor measurements", Proc. of Inst. Elec. Eng. vol.123, pp 855-862, 1976.

[7] R. A. Pucel, D. J. Masse, and C. P. Hartwig, "Losses in microstrip", IEEE Trans. Microwave Theory Tech., vol.16, pp 342-350, 1968. Also "Correction to losses in microstrip", IEEE Microwave Theory Tech., vol.16, pp 1064, 1968.

[8] R. L. Kautz, "Picosecond pulses on superconducting strips", J. Appl. Phys. vol.49, pp 308-314, 1978.

[9] V. M. Hietala, J. S. Martens, D. S. Ginley, T. E. Zipperian, C. P. Tigges, M. S. Housel, and T. A. Plut, "Evaluation of superconducting Tl-Ca-Ba-Cu-O thin film surface resistance using a microstrip ring resonator", IEEE Microwave and Guided Wave Lett., vol.1, pp 84-86, 1991.

[10] Private Communications with Dr. Felix A. Miranda of NASA Lewis Research Center.

Electrical-transport properties and microwave device performance of sputtered TlCaBaCuO superconducting thin films

G. Subramanyam and V. J. Kapoor
Microwave Electronics Laboratory, Department of Electrical and Computer Engineering, University of Cincinnati, Cincinnati, Ohio 45221-0030

C. M. Chorey
Sverdrup Technology Inc., NASA Lewis Group, Cleveland, Ohio 44135

K. B. Bhasin
NASA Lewis Research Center, Cleveland, Ohio 44135

(Received 21 February 1991; accepted for publication 1 June 1992)

Tl-Ca-Ba-Cu-O high-temperature superconducting thin films were deposited on lanthanum aluminate substrates, by rf magnetron sputtering and postannealing methods. A reproducible fabrication process with low-resistance metal contacts has been established for high-T_c and high-J_c TlCaBaCuO thin films after patterning using standard microelectronic photolithography and wet chemical etching techniques. Low-resistance gold contacts on TlCaBaCuO thin films were obtained by annealing in an oxygen flow of 1 l/min followed by a slow furnace cooling. Specific contact resistivity was approximately 10^{-10} $\Omega\,cm^2$ below 77 K. High transition temperatures as high as 100 K, and current density at zero magnetic field greater than 10^5 A/cm^2 are routinely obtained in 0.3–0.5 μm TlCaBaCuO thin films. The morphology studies of the films using scanning electron microscopy show the correlation between J_c and the microstructure of the films. Films with featureless morphology have larger zero-field transport currents. The microwave properties of TlCaBaCuO thin films were investigated by designing, fabricating, and characterizing microstrip ring resonators with a fundamental resonance frequency of 12 GHz on 10-mil-thick lanthanum aluminate ($LaAlO_3$) substrates. Ring resonators with a superconducting ground plane of 0.3 μm thickness and a gold ground plane of 1 μm thickness were fabricated and characterized in the temperature range of 60–95 K. Typical unloaded quality factors Q for the ring resonators at 12 GHz were above 1500 at 65 K, compared to an unloaded Q of 370 for a gold ring resonator. A surface resistance as low as 1.5 mΩ at 12 GHz and 77 K was obtained in 0.3 μm TlCaBaCuO thin films using the ring resonator Q measurements. Typical values of penetration depth at 0 K in the TlCaBaCuO thin films were determined to be between 7000 and 8000 Å using the temperature variation of resonance frequency measurements.

I. INTRODUCTION

Since the discovery of a copper-oxide high transition temperature (T_c) superconductor by Bednorz and Muller in January 1986,[1] there has been substantial progress in superconducting electronics. Several new compounds such as YBaCuO,[2] BiSrCaCuO,[3] and TlCaBaCuO (Ref. 4) have been found to be superconducting above 90 K, thus making it feasible for electronic applications at liquid-nitrogen temperature (77 K). Currently, worldwide research is underway for developing high-T_c superconducting electronics. Already rapid progress has been made for applications of high-T_c materials in areas such as superconducting quantum interference devices (SQUIDs), passive microwave devices, IR detectors, and interconnections in microelectronics.[5-8]

Among the high-T_c materials, the TlCaBaCuO compound has proven to possess the highest T_c,[9] which means a wide margin of operational range is available for electronic applications at 77 K. The TlCaBaCuO thin films are very attractive for electronic applications, as they have shown high T_c and high critical current density J_c.[10,11] Fabrication of TlCaBaCuO thin films on lanthanum aluminate ($LaAlO_3$) substrates has been reported by the authors.[12-14] $LaAlO_3$ substrates have a good a-axis lattice match with TlCaBaCuO thin films to permit highly c-axis-oriented growth of TlCaBaCuO superconducting thin films. The dielectric constant of $LaAlO_3$ is 24.5 (Ref. 15) and the loss tangent is approximately 8.3×10^{-5} at 77 K.[15] The growth of TlCaBaCuO thin films on $LaAlO_3$ substrates offers promising applications in the area of microwave electronics. The only disadvantage of TlCaBaCuO compound is the toxicity of thallium (Tl) which needs very careful processing and handling procedures. For microelectronic and microwave applications of TlCaBaCuO thin films, it is very important to establish a reproducible fabrication process for superior electrical and microwave properties.

The foremost applications of high-T_c thin films is expected to be in the area of "passive microwave devices" such as resonators and filters. High-T_c superconducting thin films have lower surface resistance R_s compared to Cu and Au, corresponding to higher Q and improved performance in passive microwave devices. TlCaBaCuO thin-film-based passive microwave devices have shown superior

© J. Appl. Phys. 72 (6), 15 September 1992. Reprinted, with permission, from American Institute of Physics.

performances. Chang *et al.*[5] have reported a surface resistance at least an order smaller than Cu at 77 K and 9.5 GHz. Bourne *et al.*[6] reported a 1 ns microstrip delay line using thin films of TlCaBaCuO, again a factor of 10 improvement in loss was observed at 3.29 GHz and 77 K. Hammond *et al.*[7] reported a TlCaBaCuO microstrip resonator and its power handling performance at 77 K. At effective power levels in the resonator up to 100 W, the Q was still three times higher than a silver resonator at 2.6, 5.2, and 7.3 GHz. Linear resonators with loaded Q as high as 15 000 at 5 GHz have been demonstrated.[8]

This paper describes the processing and electrical transport measurements for achieving reproducible high-T_c, high current density J_c, low microwave surface resistance R_s TlCaBaCuO thin films on $LaAlO_3$ substrates, for microelectronic applications. A method for fabricating low-resistance contacts on TlCaBaCuO thin films for reliable electrical transport measurements is also addressed. The microwave properties of TlCaBaCuO thin films were investigated by designing, fabricating, and characterizing microstrip ring resonators for 12 GHz fundamental resonance frequency. This paper describes the results of these investigations.

II. EXPERIMENTAL

TlCaBaCuO thin films were sputter deposited from a single composite powder target in a CVC model 601 rf sputtering system operating at 13.56 MHz. The system was operated in the rf magnetron mode to improve the sputtering yields at low working pressures. The depositions were performed in a "sputter up" configuration on substrates placed face down. The $Tl_2Ca_2Ba_2Cu_3O_x$ powder target was prepared by the solid-state reaction of stoichiometric amounts of high-purity BaO, CaO, CuO, and Tl_2O_3 (in the ratio 2:2:2:3) powders. The target was enriched with 20% excess Tl_2O_3 to compensate for the loss of Tl during the postprocessing of the thin films, and to maintain sufficient composition for several deposition runs. The powder target was spread over an 8-in.-diam copper plate which was part of the cathode assembly, and pressed to obtain a uniform surface. The (100) $LaAlO_3$ substrates were degreased in acetone, methanol, rinsed in de-ionized (DI) water, and blown dry using nitrogen before loading into the vacuum chamber. Depositions were performed at a rf power density of 0.7 W/cm^2, and a chamber pressure at 5 mTorr, in a pure argon atmosphere. The thin films were deposited to a thickness of about 3000–5000 Å, at a deposition rate of approximately 30 Å/min, as determined by Dektak profilometer thickness measurements. The detailed fabrication process has been described earlier by the authors.[12]

The sputter-deposited thin films of 0.3–0.5 μm thickness were postprocessed in two steps: first, sintering in air at 850 °C (to create the Tl_2O liquid phase), in an excess Tl partial pressure; and second, annealing in flowing oxygen at about 750 °C in an excess Tl partial pressure. These processes were performed in a small box furnace with the samples placed in an enclosed platinum crucible in the free-surface configuration described by Ginley *et al.*[11]

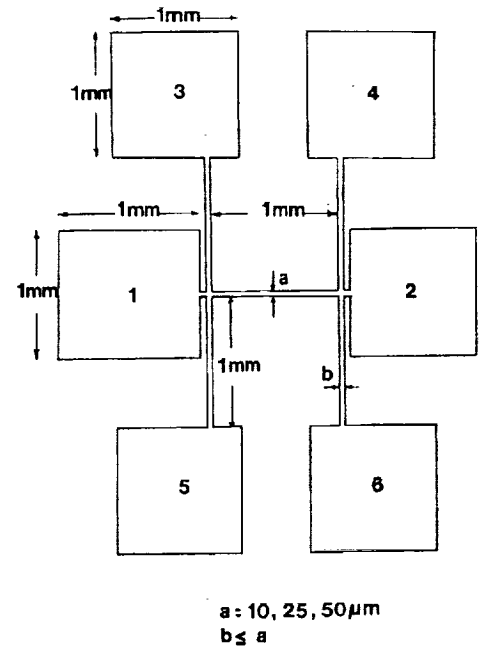

FIG. 1. The geometry of four-probe test devices with linewidths of 10, 25, and 50 μm for electrical-transport measurements. The voltage sense lines are 1 mm apart.

The thin films were placed on a $Tl_2Ca_2Ba_2Cu_3O_x$ pellet, with the film side facing the free surface in an enclosed platinum crucible. A second pellet was placed on a platinum wire mesh, approximately half an inch above the thin-film surface. The pellets provided the excess Tl partial pressure inside the crucible, mainly to minimize the loss of Tl from the thin films. The details of the post-processing heat treatments has been reported earlier.[11,12] For reproducible processing of TlCaBaCuO thin films, it was necessary to provide the optimum Tl partial pressure during postdeposition processes. A simple technique was used to monitor the reduction in Tl content in the as-deposited thin films, after each sputtering run. The percentage reduction in Tl content from run to run was obtained through Auger electron spectroscopy (AES) surface analysis on the as-deposited samples. The percentage reduction in Tl content compared to a standard reference 2223 pellet gives an approximate estimate of additional Tl partial pressure needed during the postdeposition processes. The estimated additional Tl partial pressure was provided for the postdeposition processes by adding additional 2223 pellets in the crucible. This technique has yielded reproducible high-T_c and high-J_c films.[14]

For the electrical-transport measurements, four-probe test devices were designed with linewidths of 10, 25, and 50 μm. The geometry of the test devices is shown in Fig. 1. The voltage sense lines were 1 mm apart, and the width of the sense lines was less than the linewidths in order to approximate a point contact as closely as possible. The test devices were patterned on as-deposited TlCaBaCuO thin films using standard photolithography and wet chemical

etching techniques. Positive photoresist AZ 1421 was used for the lithography. The as-deposited TlCaBaCuO thin films on $LaAlO_3$ substrates were prebaked at 180 °C for 20 min before the photoresist was spun. The photoresist AZ 1421 was spun on to a thickness of about 1 μm. The samples were soft baked at 90 °C for 20 min, followed by exposure to UV light in a mask aligner. The photoresist was developed in a 1:5 developer:DI H_2O solution for 45 sec. The samples were postbaked at 85 °C for 15 min to complete the photolithography process. A 1:90 phosphoric acid:DI H_2O solution was used for chemically etching the films. The solution was kept at a constant temperature of 75 °C. The etch rate was approximately 40 Å/min. After the etching process was completed, the photoresist was removed by immersing the samples in acetone for 25 s, followed by a 30 s rinse in DI H_2O. The patterned samples were postprocessed using our standard methods described above.

For electrical measurements on the test devices, metal bonding pads were formed by thermally evaporating 6000-Å-thick gold film on the superconducting pads, through a shadow mask. In order to obtain low-resistance contacts, the samples were annealed in an oxygen flow of 1 l/min, for about 15 min at 600 °C, followed by slow furnace cooling for 30 min after the furnace was switched off. The samples were removed when the furnace temperature was approximately 300 °C. Gold wires of 1 mil diameter were bonded to the gold pads using a Kulicke and Soffa Model 4123 ultrasonic wedge bonder. The bonding process did not require sample heating. For redundancy, multiple bonds were attached on the contact pads.

The zero-resistance T_c of the test devices was determined by measuring the resistivity versus temperature characteristics. The critical transport J_c was measured using dc and pulsed-current techniques, using a 1 μV/mm electric-field criterion. A Keithley model 181 nanovoltmeter and a Keithley model 224 current source were used for the dc transport measurements. The specimen temperature was controlled using a Lakeshore model 805 temperature controller, connected to a closed-cycle helium gas refrigeration system. The error in temperature measurement was less than 0.25 K. Thermal equilibrium was established before measurements at each temperature below T_c. The dc current method was not used above a current density of 10^4 A/cm^2, since sample heating at higher currents could cause the films to crack before measurements could be completed.

The pulsed current measurements were performed using two EG&G PARC 5210 lock-in amplifiers, a HP 214B pulse generator, and an adjustable current source capable of supplying 1 A. The pulse generator supplies a 10 V, 1 KHz pulse train with a 10% duty cycle. The pulsed current is applied to the test device, and the corresponding voltage pulse is measured across the sample using the lock-in amplifiers. The amplitude of the current pulse at which the voltage across the sample exceeds 1 μV yields the critical current at a particular temperature. The pulsed current measurements were compared to the dc values at as many temperatures as possible to insure the accuracy and compatibility of the two methods. The morphology of the finished TlCaBaCuO devices was examined in an ISI SX-30 scanning electron microscope (SEM). The morphology was evaluated in order to study the correlation between J_c and the microstructure of the films.

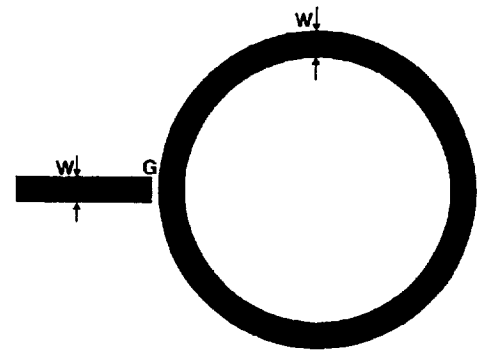

FIG. 2. Microstrip ring resonator designed for the fundamental resonance at 12 GHz. The coupling gap G and width W were chosen at 1.75 and 5.6 mils, respectively.

A microstrip resonator is a useful device for measurement of dispersion, phase velocity, and effective dielectric constants of dielectric substrates. Ring resonators are being widely used for realizing filters, and stabilization of oscillators. A microstrip ring structure resonates if its electrical length is an integral multiple of the guide wavelength. A simple ring resonator device was designed that consisted of a ring structure separated from the feed line by a small coupling gap. The size of the coupling gap determines the coupling between the feed line and the ring resonator. Loose coupling is desired to minimize excessive loading effects.[15] A ring resonator designed for 10-mil-thick $LaAlO_3$ substrates ($\epsilon r = 24.5$), for a fundamental resonance at 12 GHz is shown in Fig. 2. In the figure, the linewidth of the ring and the microstrip feed line is $W = 5.6$ mils, the coupling gap $G = 1.75$ mils, and the mean radius of the ring $R = (R1 + R2)/2 = 77$ mils. The characteristics impedance of the microstrip is 41 Ω at 12 GHz. The details of the design of the ring resonator have been described by Chorey *et al.*[15]

TlCaBaCuO ring resonators were fabricated by patterning 0.3 μm thin films using AZ 1421 positive photoresist photolithography and wet chemical etching techniques similar to the process used for fabricating the four-probe test devices described above. The ring resonators were annealed using the same annealing procedure described above. The samples were divided into two groups: one set of samples with 1 μm gold film on the bottom side of the $LaAlO_3$ substrate for the ground plane formation and a second set with a 0.3 μm TlCaBaCuO superconducting thin-film ground plane. The ground plane side superconductor was deposited and postprocessed using our routine postdeposition methods described above, after the microstrip ring resonator was fabricated on the top side.

A ring resonator was mounted in a gold-plated copper test fixture of 1 in. wide, 2 in. long, and 1 in. thick. The test

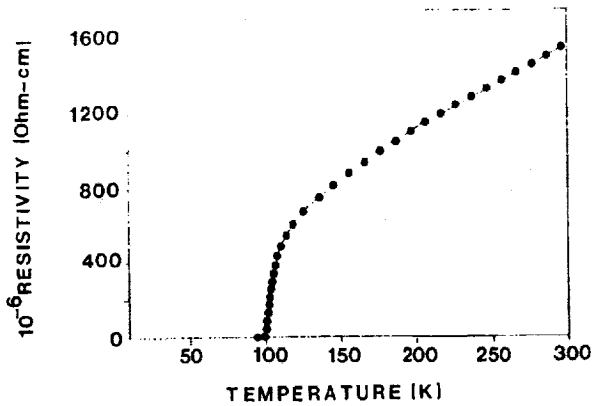

FIG. 3. The resistivity vs temperature characteristics of a patterned TlCaBaCuO thin-film test device, after lithography, chemical etching, and annealing, showing the onset of T_c at 106 K and zero resistivity at 98.5 K.

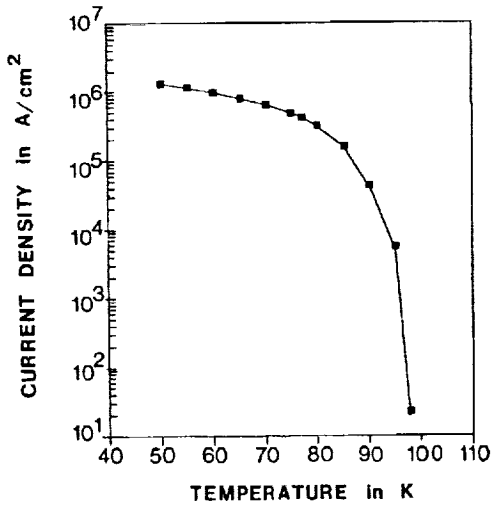

FIG. 4. Typical zero-field current density J_c vs temperature characteristics of a TlCaBaCuO four-probe test device obtained using the 1 μV/mm electric-field criterion.

fixture was placed on the cold head of the helium gas closed-cycle cryogenic system.[12] Electrical connection to the feed line was obtained by mechanical contact of a launcher at the input side of the test fixture. Connections to the HP 8720 network analyzer were made using a 0.141 in. semirigid coaxial cable of 50 Ω characteristic impedance. Before measurements were performed on ring resonators, standard one-port calibration was performed at room temperature. The calibration was performed using an open, a short, and a broadband load to effectively remove the test system imperfections introduced by the interconnecting cables, adapters, etc. The calibration was also valid at lower temperatures.

III. RESULTS

The resistivity versus temperature characteristics of a 50-μm-wide four-probe test device is shown in Fig. 3. The measurements were taken at a constant applied current of 10 μA. The onset of superconductivity occurred at 106 K, and the device showed zero resistance at 98.5 K. The room-temperature resistivity was 1.5×10^{-3} Ω cm. Zero resistance T_c between 97 and 100 K is routinely obtained. The T_c is low because of the $Tl_2Ca_1Ba_2Cu_2O_x$ (2122) phase, which is the dominant phase in these films. The thin films were also characterized by x-ray-diffraction analysis (XRD), and the results showed the characteristic peaks of 2122 and 2223 phases. The 2122 phase with c-axis-oriented growth was the dominant phase in the TlCaBaCuO thin films, as determined from the XRD data. The details of the XRD analysis are reported by the authors elsewhere.[13]

The contact resistance obtained from four-probe resistance measurements is typically a few mΩ, at temperatures below the T_c. The specific contact resistivity calculated from the four-probe resistance measurements range from 3.65×10^{-5} Ω cm^2 at 90 K, to 10^{-10} Ω cm^2 below 77 K. These results were reproducible from sample to sample and are comparable with the results for Au contacts on YBaCuO high-temperature superconducting thin films.

Figure 4 shows the typical zero-field current density J_c versus temperature measurements obtained on the four-probe test devices. Current densities at zero magnetic field as high as 5×10^5 A/cm^2 at 77 K an approximately 1×10^6 A/cm^2 at 60 K were obtained. The resistivity of the sample calculated from the I-V measurements is approximately 2.38×10^{-11} Ω cm at 77 K, much lower than any normal conductors at this temperature. The surface morphology of one of the test devices is shown in Fig. 5. The surface was essentially featureless and very smooth, typical of high-quality films. The current density of such films exceeded 10^5 A/cm^2 at 77 K. Films with numerous intergrain boundaries showed lower current densities below 10^4 A/cm^2 at 77 K.

The resonator quality factor Q, the ratio of the energy stored in the resonator to the energy dissipated in the resonator, was obtained from swept frequency reflection mea-

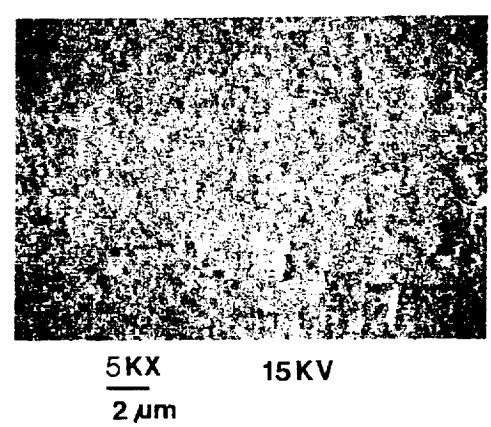

FIG. 5. Scanning electron micrograph of a TlCaBaCuO thin-film surface showing a smooth featureless morphology. The marker is 2 μm long.

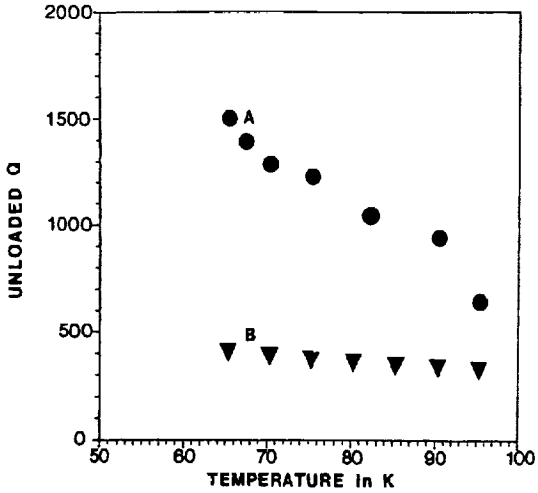

FIG. 6. The unloaded Q vs temperature characteristics of a TlCaBaCuO microstrip ring resonator. Curve A is for a superconducting ring resonator with a 0.3 μm TlCaBaCuO ground plane, and curve B is for a gold ring resonator.

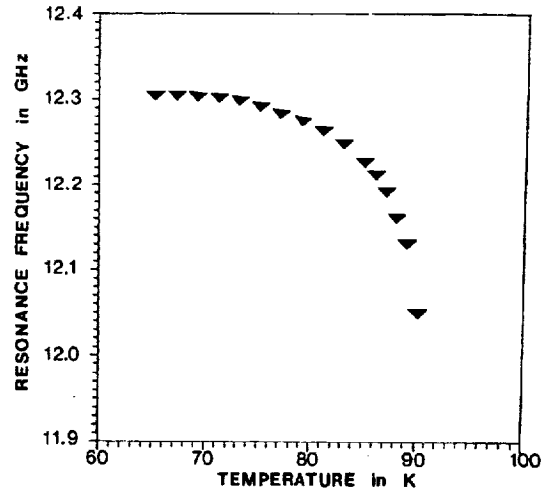

FIG. 7. The resonance frequency shift vs temperature characteristics of a TlCaBaCuO ring resonator.

surements.[15,16] The Q value is a figure of merit for a resonator, and is inversely proportional to the total losses in the circuit. The measured Q (called the loaded Q) is a measure of the circuit losses including the coupling loss and the loss through the feed line. The actual Q of the ring resonator (called the unloaded Q) is a measure of the losses only in the resonator. The unloaded Q is obtained by separating the external losses in the feed line and due to coupling. The loaded Q and the unloaded Q are related through the reflection coefficients at and far from resonance.[16] The derivation for the relationship between the loaded Q and the unloaded Q is described by Aitken.[16] A computer program was written to compute the unloaded Q values from the measured loaded Q and the magnitude of reflection coefficients at and far from resonance. The determination of whether the resonator was overcoupled or undercoupled was made from the Smith chart and also the phase response of the resonator. Typically, the ring resonators were overcoupled. Measurements for the superconducting resonator were performed at the fundamental resonance frequency of 12 GHz and an input power level of -30 dBm.

Unloaded Q versus temperature characteristics for two ring resonators is shown in Fig. 6. Curve A is the data for the high-T_c thin-film ring resonator with a superconducting ground plane. For comparison, data for the gold resonator with a gold ground plane is shown by curve B. The unloaded Q of the ring resonator with superconducting ground plane is approximately four times higher than the gold resonator at 65 K. In addition, the unloaded Q of the superconducting ring resonator shows an increasing trend in Q with decreasing temperature, whereas the superconducting ring resonators with gold ground plane show a saturation of Q at low temperatures due to the dominance of ground plane conductor losses.

The superconducting ring resonators offer an indirect method for measuring the surface resistance R_s of the superconducting thin films. This microwave surface resistance is the fundamental quantity responsible for the conductor losses at high frequencies. The R_s of sputtered thin films were obtained from ring resonator quality factor Q measurements. By separating the conductor and dielectric losses, the surface resistance of the TlCaBaCuO thin films was calculated using the standard microstrip loss equations described by Pucel, Masse, and Hartwig.[17] The R_s at 12 GHz and 77 K was determined to be typically between 1.5 and 2.75 mΩ, almost an order of magnitude lower than R_s of Cu at the same temperature and frequency.

The swept frequency reflection measurements performed at several temperatures are also used in determining the penetration depth of the TlCaBaCuO superconducting thin films. The resonance frequency is the frequency at which the magnitude of the reflection coefficient is at the minimum. The resonance frequency was measured at each temperature for ring resonators. A typical measured resonance frequency shift with respect to temperature for a superconducting ring resonator with an approximately 1-μm-thick gold ground plane is shown in Fig. 7. The shift in resonance frequency with temperature is mainly due to the temperature dependence of the penetration depth of the superconductor. Thus, the resonance frequency shift is an indirect method of determining the penetration depth. From the figure, the change in resonance frequency below 70 K is almost negligible. The superconducting resonators with a 0.3-μm-thick superconducting ground plane showed a slightly higher dependence of resonance frequency with temperature due to the temperature dependence of penetration depths of the top and the ground plane superconductors. A detailed analysis of this figure to determine the penetration depth of the superconducting thin films is given in the following section.

IV. ANALYSIS AND DISCUSSIONS

The data from the zero-field current density J_c measurements shown in Fig. 4 were analyzed to investigate the

dependence of J_c with the temperature ratio T/T_c. The slope of the $\log J_c$ vs $\log(1-T/T_c)$ characteristics is an indication of the type of the superconductor. The slope of the line obtained from our measurements was approximately 1.5 for temperatures between 50 and 80 K. The $(1-T/T_c)^{3/2}$ dependence of J_c is consistent with earlier reports in high-T_c thin films.[18] This indicates that the thin films may contain grain boundaries that are either insulating or behave like a normal metal, or the thin films may be polycrystalline in nature. The presence of grain boundaries and weak flux pinning in TlCaBaCuO thin films may be the main reasons for the lower J_c in TlCaBaCuO thin films compared to epitaxial *in situ* grown YBaCuO thin films. However, among the polycrystalline high-T_c thin films, TlCaBaCuO thin films have shown superior electrical properties and hence are very attractive for electronic applications.

The penetration depth of TlCaBaCuO thin films can be determined from the resonance frequency versus temperature measurements, by comparing the experimental data shown in Fig. 7 with theoretical calculations. The resonance frequency shift in the ring resonators is assumed to be due to the change in penetration depth with temperature. Neglecting the effects due to the substrate contraction at lower temperatures, the penetration depth was extracted from the resonance frequency shift as discussed below.

The phase velocity of a superconducting microstrip transmission line with a superconducting ground plane is given by[19]

$$v_{ph}=c/\sqrt{\epsilon_{eff}}[1+2\lambda/h\coth(t/\lambda)]^{-0.5}, \quad (1)$$

where c is the velocity of light, ϵ_{eff} is the effective dielectric constant, h is the substrate thickness, t is the thickness of the microstrip, and λ is the penetration depth of the superconducting microstrip. The penetration depth is temperature dependent based on the Gorter–Casimir relationship,[20] i.e.,

$$\lambda(T)=\lambda(0)[1-(T/T_c)^4]^{-0.5}, \quad (2)$$

for temperature T less than T_c. $\lambda(0)$ is the penetration depth at $t=0$ K. The resonance frequency of the ring resonator is given by the equation

$$f=nv_{ph}/(2L), \quad (3)$$

where f is in GHz, L is the mean circumference of the ring in mm, and n is the integer order of resonance. From the temperature dependence of resonance frequency measurements and the above equations, the best value of $\lambda(0)$ was determined to be 6890 Å. The typical value ranges between 7000 and 8000 Å. This is an approximate estimate for the penetration depth along the c axis in the TlCaBaCuO thin films. Since the thin films are only 0.3–0.4 μm thick, the penetration depth depends upon the properties of the superconductor through the entire film. This may be a reason for the high penetration depth. Also, the patterned thin films have rough edges, and hence the penetration depth obtained using the above technique is an averaged value over the whole film area.

The surface resistance of the TlCaBaCuO superconducting thin films determined from the ring resonator Q measurements was compared with the theoretical surface resistance versus temperature characteristics for a given penetration depth. A theoretical model based on the phenomenological loss equivalence method (PEM) approximation[21,22] was employed to determine the theoretical variation of conductor losses and the surface resistance with temperature for the cases of superconducting microstrip/gold ground plane, and superconducting microstrip/superconducting ground plane. Both these cases were compared to the attenuation constant of a gold microstrip on $LaAlO_3$ substrate.

The attenuation constant for a superconducting microstrip is calculated from the formula[22]

$$\alpha=(T/T_c)^4/[1-(T/T_c)^4]^{3/2}(G_1/4)(\sigma_n/Z) \times w^2\mu^2[\lambda(0)^3]\coth(X)+X\,\mathrm{cosec}^2(X)(Np/m), \quad (4)$$

where

$$X=A[G_1/\lambda(0)][1-(T/T_c)^4]^{1/2}.$$

G_1 is the geometric factor given by the equation

$$G_1=1/(\pi h)\{1-[W_e/(4h)]^2\}[1/2+h/W_e +h/(\pi W_e)\ln(2h/t)], \quad (5)$$

where W_e is the effective width of the microstrip, A is the area of cross section of the microstrip, T is the measurement temperature below T_c, and $\lambda(0)$ the penetration depth at 0 K of the superconductor.

The parameters assumed for the calculations are the relative dielectric constant ϵ_r of $LaAlO_3$ of 24.5, the loss tangent ($\tan\delta$) of $LaAlO_3$ of 8.3×10^{-5} below 100 K, the substrate thickness h of 10 mil, the width of the microstrip W of 142 μm, corresponding to a characteristic impedance of 41 Ω at 12 GHz, the thickness of the superconducting microstrip t of 0.3 μm, the ground plane thickness of 1 μm for a gold ground plane and 0.3 μm for a superconducting ground plane, the zero resistance T_c of the TlCaBaCuO thin films of 100 K, and the normal conductivity at T_c (σ_n) of 1.5×10^6 S/m.

The ground plane conductor losses can be calculated by the same method, using the geometric factor G_2 instead of G_1 in Eq. (4),

$$G_2=1/(2\pi h)[1-(W_e/4h)^2]. \quad (6)$$

Figure 8 shows temperature variation of the attenuation due to conductor losses for a gold microstrip (curve A), a superconducting microstrip with a gold ground plane (curve B), and a superconducting microstrip with a superconducting ground plane (curve C) as determined using Eqs. (4)–(6). The upper diagram is for $\lambda(0)$ of 6000 Å, and the lower diagram is for $\lambda(0)$ of 7000 Å. Figure 8 shows the lower attenuation for the microstrip with superconducting ground plane (curve C) compared to the one with gold ground plane (curve B) below 77 K.

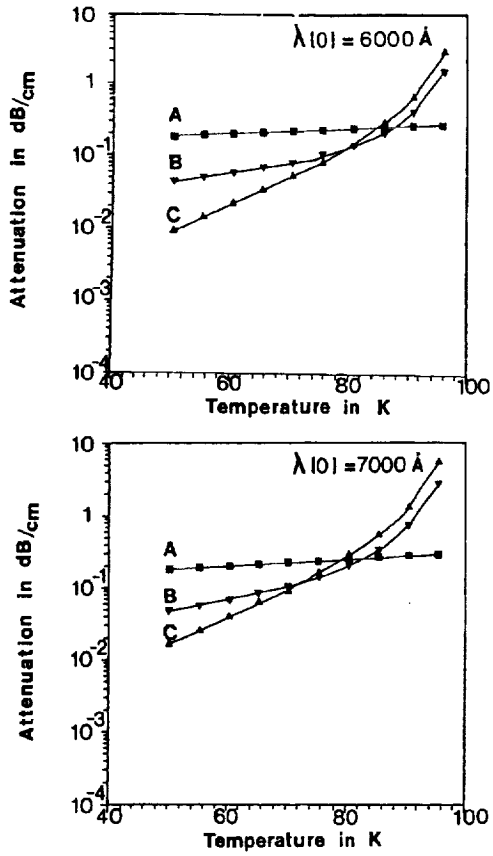

FIG. 8. Theoretical temperature variation of attenuation due to conductor losses for a gold microstrip (1-μm-thick gold for both sides: curve A), a superconducting microstrip (0.3 μm) with a gold ground plane (1 μm) in curve B, and a superconducting microstrip (0.3 μm) with a superconducting ground plane (0.3 μm) in curve C. The penetration depth at 0 K was assumed to be 6000 Å for the upper diagram and 7000 Å for the lower diagram.

The surface resistance of the superconducting thin film is obtained from the equation

$$R_s = 2Z_0\alpha/G_1, \tag{7}$$

where Z_0 is the characteristic impedance of the microstrip. The theoretical temperature variation of surface resistance of the superconducting microstrip with a superconducting ground plane determined using Eq. (7) is shown in Fig. 9, for $\lambda(0)$ of 6000 Å (curve C) and 7000 Å (curve B). For comparison, the surface resistance of a 1-μm-thick gold microstrip (curve A) on a $LaAlO_3$ substrate is plotted for the same microstrip geometry. The R_s calculated from the measured Q values of an all-superconducting ring resonator on a $LaAlO_3$ substrate (curve D) is also plotted in Fig. 9. The R_s obtained from the ring resonator Q measurements (curve D) deviates from the theoretical temperature dependence as seen in the figure. Since the TlCaBaCuO thin films do react with the $LaAlO_3$ substrate, it is possible that the region of interaction contributes to additional losses.

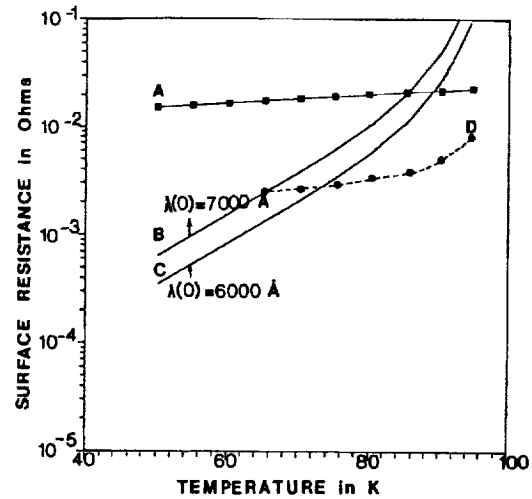

FIG. 9. Theoretical temperature variation of surface resistance for the all-superconducting ring resonator, for penetration depths at 0 K of 6000 (curve C) and 7000 Å (curve B). The surface resistance calculated from the measured Q values of the resonator is also shown in curve D. For comparison, the surface resistance of a gold microstrip is plotted in curve A.

V. SUMMARY

TlCaBaCuO superconducting thin films were fabricated on $LaAlO_3$ substrates by rf magnetron sputter deposition in a pure argon plasma and by using postannealing techniques. A reproducible fabrication process has been established for TlCaBaCuO thin films on $LaAlO_3$ substrates for high-T_c and high-J_c characteristics. The TlCaBaCuO thin films were patterned into four-probe test devices using standard microelectronic lithography and wet etching techniques. Low-resistance gold contacts on TlCaBaCuO thin films were obtained by annealing at 600 °C in an oxygen flow of 1 l/min followed by a slow furnace cooling for about 30 min. The critical current density measurements were performed using dc and pulsed current techniques under the electric-field criterion of 1 μV/mm. The zero-resistance T_c between 97 and 100 K are routinely obtained in patterned TlCaBaCuO thin films. Zero-field current density J_c as high as 5×10^5 A/cm^2 were obtained in four-probe test devices. The specific contact resistivity measured when the sample is superconducting ranges from 3.65×10^{-5} Ω cm^2 at 90 K, to 10^{-10} Ω cm^2 below 77 K.

The microwave properties of TlCaBaCuO thin films were investigated by designing, fabricating, and characterizing a microstrip ring resonator. The resonator was designed for a fundamental resonance frequency of 12 GHz, and for fabrication on 10-mil-thick $LaAlO_3$ substrates. Ring resonators with a gold ground plane of 1 μm thickness and a TlCaBaCuO superconducting ground plane of 0.3 μm thickness were fabricated and characterized at cryogenic temperatures. The unloaded Q for the superconducting resonators were above 1500 at 65 K, compared to 370 for a gold resonator. The surface resistance of the TlCaBaCuO thin films obtained by separating conductor losses from the Q measurements is typically between 1.5

and 2.75 m-Ω at 12 GHz and 77 K, almost an order lower than Cu and Au at the same temperature and frequency. The penetration depth at 0 K was calculated from the resonance frequency shift with temperature measurements. The typical values for the penetration depth at 0 K are approximately between 7000 and 8000 Å.

The conductor losses in the superconducting microstrips with superconducting ground plane were compared to the ones with gold ground plane using a theoretical model called the phenomenological loss equivalence method (PEM). This model predicted lower conductor losses for the microstrip with a superconducting ground plane, below 77 K. A theoretical temperature variation of the surface resistance R_s for different penetration depths was obtained for the all-superconducting microstrip (with superconducting ground plane). The R_s obtained from the Q measurements in the ring resonators deviates from the theoretical temperature dependence. This is possibly because of additional losses introduced in the devices due to interaction between the TlCaBaCuO thin films and the $LaAlO_3$ substrates. Nevertheless, the polycrystalline TlCaBaCuO thin films have almost an order-of-magnitude lower surface resistance compared to gold at 80 K. The design of the ring resonator was not optimized for the highest Q, but the results of our investigations show that TlCaBaCuO ring resonator devices fabricated with a superconducting ground plane do show higher Q compared to a gold resonator below 90 K, proving their usefulness for all-superconducting microwave circuit applications.

ACKNOWLEDGMENTS

The authors thank Dr. Regis Leonard for his continued support and encouragement. The authors thank Dr. Sam Alterovitz, Dr. Mark Stan, and Dr. John Pouch for useful discussions, and also thank Professor Punit Boolchand for his useful suggestions and discussions. This research was supported by NASA Lewis Research Center.

[1] J. G. Bednorz and K. A. Muller, Z. Phys. B **64**, 189 (1986).
[2] M. K. Wu, J. R. Ashburn, C. J. Torng, P. H. Hor, R. L. Meng, L. Gao, Z. J. Huang, Y. Q. Wang, and C. W. Chu, Phys. Rev. Lett. **58**, 908 (1987).
[3] H. Maeda, Y. Tanaka, M. Fukitomi, and T. Asano, Jpn. J. Appl. Phys. **27**, L209 (1988).
[4] Z. Z. Sheng and A. M. Hermann, Nature **332**, 138 (1988).
[5] L. D. Chang, M. J. Moskowitz, R. B. Hammond, M. M. Eddy, W. L. Olson, D. D. Casavant, E. J. Smith, M. Robinson, L. Drabeck and G. Gruner, Appl. Phys. Lett. **55**, 1357 (1989).
[6] L. C. Bourne, R. B. Hammond, McD. Robinson, M. M. Eddy, W. L. Olson, and T. W. James, Appl. Phys. Lett. **56**, 2333 (1990).
[7] R. B. Hammond, G. V. Negrete, M. S. Schmidt, M. J. Moskowitz, M. M. Eddy, D. D. Strother, and D. L. Skoglund, in Proceedings of the IEEE MTT Symposium, June 1990.
[8] C. Wilker, Z. Y. Shen, P. Pang, D. W. Face, W. L. Holstein, A. L. Mathews, and D. B. Laubacher, IEEE Microwave Theory Tech. **MTT-39**, 1462 (1991).
[9] S. S. P. Parkin, V. Y. Lee, E. M. Engler, A. I. Nazzal, T. C. Huang, G. Gorman, R. Savoy, and R. Beyers, Phys. Rev. Lett. **60**, 2539 (1988).
[10] W. Y. Lee, V. Y. Lee, J. Salem, T. C. Huang, R. Savoy, D. C. Bullock, and S. S. P. Parkin, Appl. Phys. Lett. **53**, 329 (1988).
[11] D. S. Ginley, J. F. Kwak, E. L. Venturini, B. Morosin, and R. J. Baughman, Physica C **160**, 42 (1989).
[12] G. Subramanyam, F. Radpour, V. J. Kapoor, and G. H. Lemon, J. Appl. Phys. **68**, 1157 (1990).
[13] G. Subramanyam, F. Radpour, and V. J. Kapoor, Appl. Phys. Lett. **56**, 799 (1990).
[14] G. Subramanyam, V. J. Kapoor, and G. H. Lemon, Bull. Am. Phys. Soc. **36**, 519 (1991).
[15] C. M. Chorey, K. S. Kong, K. B. Bhasin, J. D. Warner, and T. Itoh, IEEE Trans. Microwave Theory Tech. **39**, 1480 (1991).
[16] J. Aitken, Proc. Inst. Electr. Eng. **123**, 855 (1976).
[17] R. A. Pucel, D. J. Masse, and C. P. Hartwig, IEEE Trans. Microwave Theory Tech. **MTT-16**, 342 (1968); **16**, 1064 (1968).
[18] J. F. Kwak, D. S. Ginley, E. L. Venturini, B. Morosin, R. J. Baughman, J. C. Barbour, and M. O. Eatough, in *Studies of High Temperature Superconductors*, edited by A. Narlikar (Nova Science, New York, 1991), Vol. 7, pp. 45–73.
[19] R. L. Kautz, J. Appl. Phys. **49**, 308 (1978).
[20] T. Van Duzer and C. W. Turner, *Principles of Superconductive Devices and Circuits* (Elsevier/North-Holland, New York, 1981), Chap. 3, pp. 92–138.
[21] H. -Y. Lee and T. Itoh, IEEE Trans. Microwave Theory Tech. **MTT-37**, 1904 (1989).
[22] O. R. Baiocchi, K. -S. Kong, H. Ling, and T. Itoh, IEEE Microwave Guided Wave Lett. **MGWL-1**, 2 (1991).

N94-20519

The effect of fluctuations on the electrical transport behaviour in $YBa_2Cu_3O_{7-x}$

Satish Vitta†, S A Alterovitz and M A Stan‡
Lewis Research Center, NASA, Cleveland, OH 44135, USA

Received 15 April 1992, in final form 10 June 1992

Abstract. The excess conductivity behaviour of highly oriented $YBa_2Cu_3O_{7-x}$ thin films prepared by both coevaporation and laser ablation has been studied in detail in the reduced-temperature range $9 \times 10^{-4} < t < 1$. The excess conductivity in all the films studied was found to diverge sharply near T_c, in agreement with the conventional mean-field thoery. However, the detailed temperature dependence could not be fitted to either the power-law or the logarithmic functional forms as predicted by the theory. The excess conductivity of all the films was found to be exponentially dependent on the temperature over nearly three decades for $9 \times 10^{-4} < t < 10^{-1}$, in contradiction to the mean-field theory.

1. Introduction

The rounding of the superconducting phase transition has been conventionally attributed to fluctuations in the magnitude and lifetime of the order parameter. By considering fluctuations of magnitude less than the order parameter in the Ginzburg–Landau (GL) theory, a critical temperature region was predicted in which the GL theory will not be valid. For temperatures greater than the critical limit the excess contribution $\Delta\sigma$ to electrical conductivity is estimated using the mean-field value of the order parameter in the time-dependent GL (TDGL) theory. The excess conductivity $\Delta\sigma$ is defined as $\sigma_{exp} - \sigma_{calc}$ where σ_{exp} is the experimentally observed electrical conductivity and σ_{calc} the conductivity due to normal-electron scattering alone in the absence of superconducting fluctuations. It is found to follow a power-law-type temperature dependence given by

$$\Delta\sigma(T) \propto (t)^{-\eta} \tag{1}$$

where t is the logarithm of the reduced temperature given by $\ln(T/T_c^{mf}) \simeq [(T - T_c^{mf})/T_c^{mf}]$ for $t < 1$ (T_c^{mf} is the mean-field transition temperature) and η a constant which depends on the dimensionality of conduction [1]. For three-dimensional (3D) conduction it is $\frac{1}{2}$ and for two-dimensional (2D) conduction it is 1. Hence the temperature dependence of $\Delta\sigma$ has been extensively studied in order to determine η and, thus, the dimensionality of order parameter fluctuations, the nature

† Present address: Department of Metallurgy, Indian Institute of Technology, Bombay 400 076, India.
‡ Present address: Department of Physics, Kent State University, Kent, OH 44242, USA.

© 1992 IOP Publishing Ltd. Reprinted, with permission, from J. Phys.: Condens. Matter, vol. 4, 1992, pp. 7891-7898.

of contributions to excess conductivity and also to estimate the coherence length. In the case of $YBa_2Cu_3O_7$, equation (1) has been extensively used to determine the dimensionality of $\Delta\sigma$ in the range $10^{-3} < t < 1$ and it has been reported to be 3D, 2D and quasi-2D crossing over to a 3D behaviour close to T_c [2]. Recently, however, it was found that $\Delta\sigma$ does not exhibit the classical power-law dependence on t in the mean-field regime but instead has a logarithmic dependence [3]. The deviation from normal behaviour of the specific heat of an untwinned single crystal was also found to exhibit a logarithmic temperature dependence in the range $10^{-4} < t < 10^{-1}$ by Regan *et al* [4]. The contribution of fluctuations to diamagnetic susceptibility in bulk pellets on the other hand was found to obey the predictions of conventional GL theory [5]. Howson *et al* [6] have studied the variation in thermoelectric power up to T_c in single crystals and found that it exhibits an anomalous peak near T_c because of the presence of 3D divergent fluctuations. This large body of experimental results clearly indicates that the phenomenon of fluctuations and the length of the critical region in the oxide superconductors is still not completely understood.

In the present work we report the systematic study of $\Delta\sigma$ in highly oriented $YBa_2Cu_3O_{7-x}$ thin films prepared by two different techniques: coevaporation and laser ablation. The study of fluctuation effects requires the background or normal-state contribution to the overall conductivity to be accurately determined. Hence the normal-state behaviour was analysed in terms of both the linear metallic conduction phenomenon and the more recent resonating-valence-bond (RVB) model [7]. It was found that the film with the lowest room-temperature resistivity follows metallic conduction behaviour while the other films follow the RVB model. The temperature variation in $\Delta\sigma$ for all the films was found to deviate completely from that predicted by the conventional GL-based models.

2. Experimental methods

The thin films of $YBa_2Cu_3O_{7-x}$ were deposited onto $SrTiO_3$ (100) substrates by two methods: coevaporation and laser ablation. In the coevaporation, Y and Cu were electron beam evaporated while BaF_2 was resistively evaporated onto a cold substrate in an oxygen ambient. The thickness of the as-deposited film is 0.5 μm. The films were later annealed at 850 °C in wet flowing oxygen to form the superconducting phase. In the case of laser ablation the film (0.3 μm thick) was deposited onto a heated substrate in an oxygen atmosphere from a sintered $YBa_2C_3O_7$ target. Structural characterization of the films was done by scanning electron microscopy and large-angle x-ray diffraction. The DC transport behaviour as a function of T was studied by the standard four-probe method. Thin Au wires attached to the film surface by In solder were used as leads for electrical characterization. These provided very-low-resistance ohmic contacts to the film surface. In the transition region, data points were taken at 0.2 K intervals to facilitate accurate analysis. The normal-state conductivity σ_{calc} for $T < 110$ K was determined by extrapolation of the regression-fitted data in the range 110 K $< T <$ 180 K.

3. Results

The microstructure of the two coevaporated films (C1 and C2) were completely different although they were deposited and annealed under apparently identical conditions.

Film C1 has long cylindrical grains of about 0.25 μm diameter. The grains are highly oriented with their a–b plane along the film plane. Film C2, however, has a basket-weave-type grain morphology with an aspect ratio of about 16 in the film plane. The x-ray diffraction spectrum shows that the film has both c-axis- and a–b-axis-aligned grains along the film normal. The a–b-axis-aligned grains, however, were restricted to the top surface of the film [8]. The laser-ablated film (L) also shows a highly oriented cylindrical grain morphology similar to that of film C1. The film has a mirror-like smooth surface morphology, indicating that the surface roughness is much less than those of the coevaporated films.

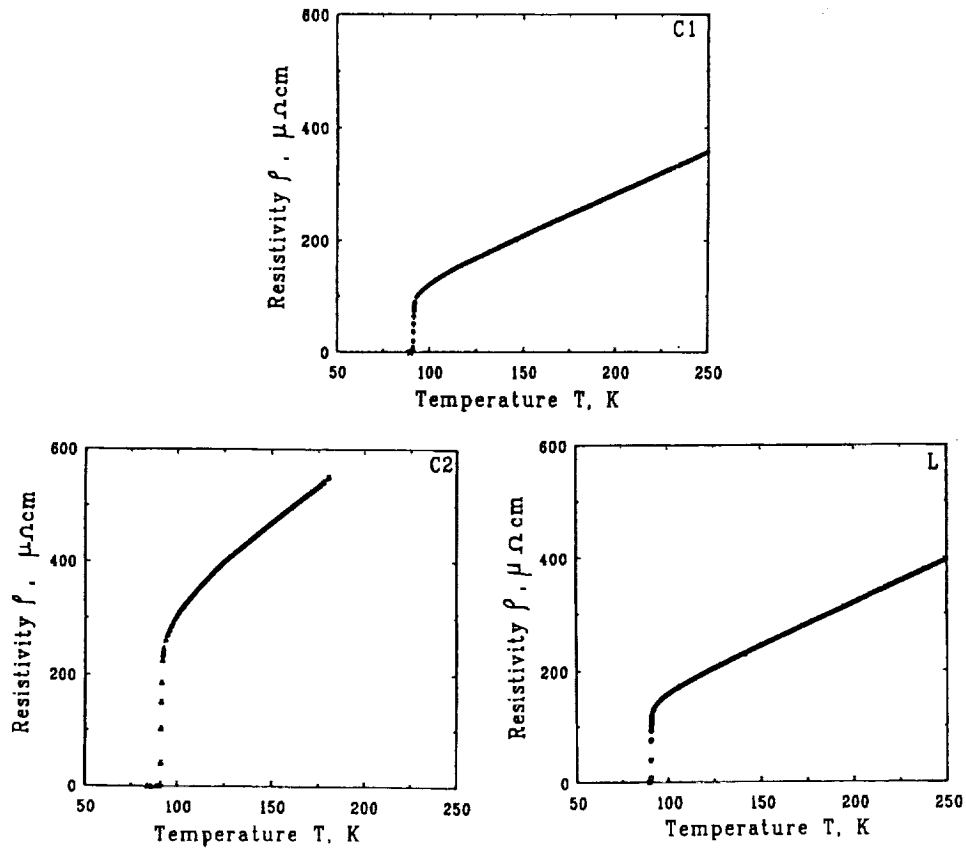

Figure 1. The variation in the resistivities ρ of the three films with temperature T.

The variation in the resistivities ρ with temperature of the three films C1, C2 and L shows a sharp transition into the superconducting state (figure 1). The transition width, defined as the width at half-maximum of the temperature-derivative curve, is about 0.4 K for all the films. The parameters that are important in any systematic study of $\Delta\sigma$ are

(i) determination of the mean-field transition temperature T_c^{mf} and

(ii) determination of the background or normal-state transport contribution to the overall conductivity.

It has been shown that the inflection temperature in the ρ–T curve can be

approximated as the mean-field transition temperature [9, 10]. This criterion was used in the determination of T_c^{mf} for the films and is given in table 1.

Table 1. The zero-resistance temperature $T_c(0)$, mean-field transition temperature T_c^{mf} and the transition width $\Delta T_c(0)$ to zero-resistance state of the three films.

Sample	$T_c(0)$ (K)	T_c^{mf} (K)	$\Delta T_c(0)$ (K)
C1	91.1	91.5	0.4
C2	90.5	91.4	0.5
L	90.2	90.5	0.3

4. Discussion

The low-temperature superconductors are of strong-coupling BCS type and their normal-state behaviour can be estimated using a linear temperature dependence for ρ based on the conventional electron scattering mechanisms. However, the scattering mechanisms in the normal state of the oxide superconductors are not clearly known. Both the Fermi-liquid-based models which predict a linear temperature dependence and the non-Fermi-liquid-based models are currently used to fit the normal-state transport behaviour [11]. According to the non-Fermi-liquid-based RVB model, the charge carriers are assumed to be confined to the Cu–O a–b planes of the crystal, thus leading to metallic conduction behaviour along the planes and phonon-activated hopping conduction in between the planes. The overall resistivity $\rho(T)$ in such an hypothesis is given by an expression of the form

$$\rho(T) = aT^{-1} + bT \tag{2}$$

where a and b are temperature-independent constants. In the present analysis, the ρ–T data of all the films were fitted to both the linear temperature dependence of the type $\rho(T) = \rho(0) + bT$ and the RVB dependence, equation (2), using the least-squares regression-fitting routine in the range 110 K $< T <$ 180 K. It was found that the best fit to film C1 was the linear relation while that for films C2 and L was the RVB-type relation. However, only the linear coefficient b of the two films C2 and L is in reasonable agreement with that predicted by the RVB model. The values of a in equation (2), 442.1 and 925.8 $\mu\Omega$ cm K, are orders of magnitude lower than the predicted values. The linear temperature coefficients b for the three films are 0.186 $\mu\Omega$ cm K^{-1}, 0.294 $\mu\Omega$ cm K^{-1} and 1.584 $\mu\Omega$ cm K^{-1}, respectively. These values are well within the average values observed for single crystals [2, 3] and indicate the phase purity of the films. Using the simple Drude relation for metallic conduction given by $\rho(T) = (3\pi\hbar/2)/e^2k_F^2l$ where l is the quasi-particle mean free path, e the electron charge, $\hbar$ the Planck constant and $k_F \simeq 4.46 \times 10^7$ cm^{-1} [12] the Fermi wavevector, the 'metallic parameter' k_Fl can be estimated for the three films. These were found to be 17, 7 and 14 for films C1, C2 and L, respectively, at 120 K, indicating that all the three films are very much on the metallic side of the Ioffe–Regel limit. This clearly shows that the microscopic conduction mechanism in these materials above T_c is not completely understood, although a mathematical fit

to the RVB model can be obtained. Recently, on the basis of mid-infrared phonon spectroscopy [13] and transport [14] studies on polycrystalline pellets it has been reported that the contribution from fluctuations persists up to temperatures as high as $2T_c$. This corresponds to the 'fluctuation onset' temperature, indicating that the lifetime of the superconducting fluctuations is finite and large even at $2T_c$, for which there is no direct experimental evidence at present.

The excess conductivity $\Delta\sigma(T) = \sigma_{exp}(T) - \sigma_{calc}(T)$ determined using the relation $\rho(T) = \rho(0) + bT$ for film C1 and equation (2) for films C2 and L was found to diverge sharply as T approaches T_c^{mf}. This is in qualitative agreement with the conventional theory which predicts a divergence of the magnitude of the order parameter fluctuations at T close to T_c^{mf}. The critical temperature region t in which the TDGL theory is not applicable can be estimated using typical values for $YBa_2Cu_3O_7$; $T_c^{mf} = 91$ K, the zero-temperature upper critical field $H_{c2}(0) = 674$ T and the GL parameter $K = 200$ [15], and therefore t is found to be about 2×10^{-2}. For $t \geqslant 2 \times 10^{-2}$, $\Delta\sigma(T)$ can in principle be determined using equation (1) (power-law dependence of $\Delta\sigma$ on t). Although the rate of decay of the fluctuating superconducting pairs is explicitly considered in obtaining equation (1), their effect on the quasi-particle conductivity is not considered. An additional term has been proposed to equation (1) by Maki and Thompson (as quoted by Skocpol and Tinkham [16]) to account for the effect of fluctuations on the quasi-particle conductivity and it was found to be four times equation (1) in the case of 3D conduction and $(e^2/8\hbar d)[(t-\delta)^{-1}\ln(t/\delta)^{-1}]$ for 2D conduction, where δ is the pair-breaking parameter and d the film thickness. The criterion for 2D conduction is $d/\xi(T) \ll 1$ where $\xi(T)$ is the superconducting coherence length. In the present case, even $d/\xi(0)$ for all the three films is much greater than unity and hence 2D conduction can be completely ruled out. The addition of an extra term to equation (1) changes only the magnitude of $\Delta\sigma(T)$, leaving the power-law temperature dependence intact. In the present work, however, $\Delta\sigma(T)$ for all the three films determined from the experimental data does not show a power-law dependence on t as predicted in the range $9 \times 10^{-4} < t < 4 \times 10^{-1}$; this can be clearly seen in figure 2. It has a continuously changing curvature which has been observed earlier. However, the previous reports have inferred changes in the dimensionality of electrical transport on the basis of linear fits to small portions of the curve [2].

The above method of analysis relies on the accurate determination of T_c^{mf}. In the case of oxide superconductors, the fluctuation effects on the conductivity are spread over a large temperature range compared with the conventional superconductors because of their extremely short coherence length ξ and the high value of $T_c(0)$. Hence the accurate determination of T_c^{mf} is difficult. An alternative method of analysing the fluctuation effects which does not depend on T_c^{mf} has been used in the case of Tl–Ba–Ca–Cu–O thin films and single crystals [17, 18]. According to this method, equation (1) can be rewritten as

$$[\Delta\sigma(T)]^{-1/\eta} = D^{-1/\eta}[(T - T_c^{mf})/T_c^{mf}] \tag{3}$$

where the constant D is given by $e^2/32\hbar\xi(0)$ for 3D conduction and $e^2/16\hbar d$ for 2D conduction. Differentiating and rearranging equation (3) gives

$$\ln[-\mathrm{d}(\Delta\sigma)/\mathrm{d}T] = \ln(D^{-1/\eta}/T_c) + (1 + 1/\eta)\ln(\Delta\sigma). \tag{4}$$

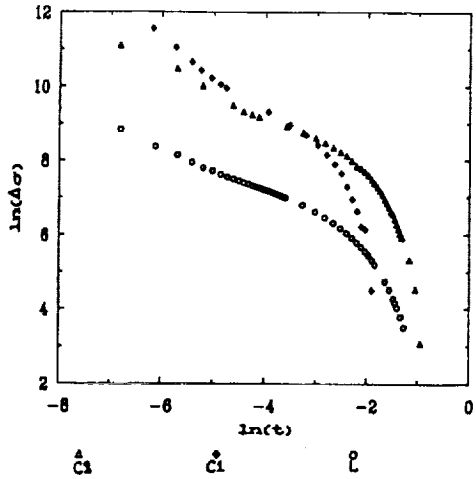

Figure 2. The excess conductivity $\Delta\sigma$ as a function of the reduced temperature $t = \ln(T/T_c^{mf})$ for all three films. It can be seen that a 'power-law' fit is not feasible except in small ranges of t. Δ, C2; ♦, C1; O, L.

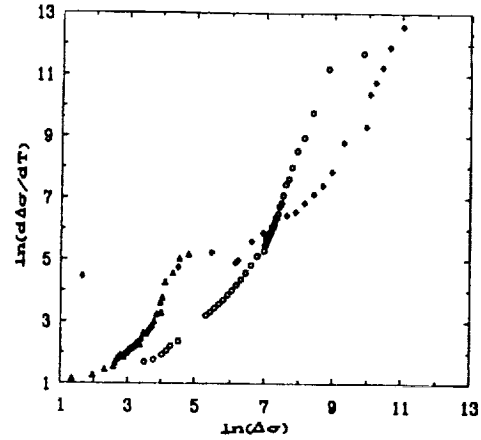

Figure 3. The excess conductivity $\Delta\sigma$ data represented according to equation (4), which is independent of T_c^{mf}. The presence of continuous curvature in the whole temperature range indicates a clear deviation from power-law behaviour.

The dimensionality η can be deduced from the slope of the $\ln[-\mathrm{d}(\Delta\sigma)/\mathrm{d}T]$ versus $\ln(\Delta\sigma)$ plot and using equation (4). Figure 3 shows $\Delta\sigma$ plotted according to this modified scheme. It can be clearly seen that even this alternative methodology which is independent of T_c^{mf} does not give conclusive evidence for the dimensionality of conduction in these films. Even according to this modified scheme of analysis the data exhibit a continuous curvature in the whole range and the dimensionality can be inferred only by fitting small portions of the excess conductivity. The recent electrical transport, mid-infrared phonon spectrum and heat capacity studies have clearly shown that the 'onset' temperature for fluctuations can be as high as about $2T_c$. The onset of fluctuations in the electrical transport behaviour has been attributed to the quasi-2D Maki–Thompson correction factor which has a logarithmic temperature dependence [3, 14]. The $\Delta\sigma$-values in the present work, however, could not be fitted satisfactorily to a logarithmic temperature dependence. The $\Delta\sigma(T)$ data are replotted as shown in figure 4 and it can be clearly seen that $\Delta\sigma(T)$ has an exponential dependence on t: $\Delta\sigma(T) \propto \exp(t^{-\alpha})$ where α is the slope in the range $9 \times 10^{-4} < t < 10^{-1}$ for all the three films. This clearly illustrates two important points.

(i) The TDGL theory underestimates the critical temperature region by at least an order of magnitude.

(ii) The mean-field approximations are not valid in the case of $YBa_2Cu_3O_{7-x}$.

The underestimation of the critical region has been attributed to the large contribution of the higher-order fluctuation corrections [19]. In the critical region, $\Delta\sigma$ is predicted to diverge as t goes to 0 with a temperature dependence similar to that in the mean-field region but with an exponent different from η based on the 3D XY model [20]. The results of the present work, however, cannot be understood even according to these models.

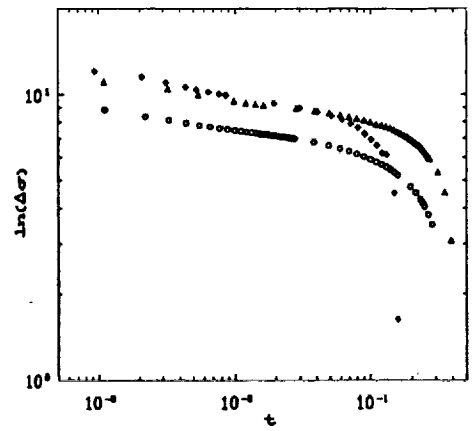

Figure 4. Log-normal plot of $\Delta\sigma$ versus t, showing the exponential temperature dependence of $\Delta\sigma$ for all the films in the range $9 \times 10^{-4} < t < 10^{-1}$.

5. Conclusions

The macroscopic and microscopic properties of the oxide materials in their superconducting state are being extensively studied. Many models have already been proposed to explain these properties. However, the normal-state behaviour remains the least studied to date. The only phenomenological model that has been proposed to explain the normal-state electron transport behaviour is the RVB model. The results of the present work indicate that it is insufficient to explain the transport behaviour above T_c. The linear and hopping coefficients obtained for the two films which obey the RVB expression for conductivity are much lower than the values predicted by the model.

The excess conductivity in the mean-field region of the three films studied does not obey the temperature dependence predicted by the TDGL theory. Even though such a behaviour has been observed before, the results are still fitted to the TDGL theory and the dimensionality of the electrical transport determined. However, we find that the excess conductivity is better represented by an exponential relation and that there is no model at present, macroscopic or microscopic, which can explain this type of behaviour. Hence the dimensionality of electrical transport is still inconclusive. The onset temperature for fluctuations observed in the present work, $t \simeq 0.1$, agrees with that observed by Regan *et al* [4], indicating that the length of the critical region is larger than that predicted by the theory. However, the functional dependence on temperature is found to be different.

Acknowledgments

SV wishes to acknowledge the US National Research Council for an Associateship at Lewis Research Center, NASA, and MAS acknowledges NASA for the support through grant NAG-440751. The authors acknowledge Professor J Scofield for the use of his evaporation system, J D Warner for the laser-ablated film, and T Harris and G Kitchen for their assistance. Critical reading of the manuscript by Dr Padma Satish is gratefully acknowledged.

References

[1] Aslamazov L G and Larkin A I 1968 *Phys. Lett.* **26A** 238

[2] Sudhakar N, Pillai M K, Banerjee A, Bahadur D, Das A, Gupta K P, Sharma S V and Majumdar A K 1991 *Solid State Commun.* **77** 529

Vidal F, Veira J A, Maza J, Ponte J J, Amador J, Cascales C, Casais M T and Rasines I 1988 *Physica* C **156** 165

Freitas P P, Tsuei C C and Plaskett T S 1987 *Phys. Rev.* B **36** 833

Ausloos M and Laurent Ch 1988 *Phys. Rev.* B **37** 611

Oh B, Char K, Kent A D, Naito M, Beasley M R, Geballe T H, Hammond R H, Kapitulnik A and Graybeal J M 1988 *Phys. Rev.* B **37** 1861

Padmanabhan V P N and Shahi K 1991 *Physica* C **172** 427

[3] Ong N P, Wang Z Z, Hagen S, Jing T W, Clayhold J and Horvath J 1988 *Physica* C **153–5** 1072

Hikita M and Suzuki M 1989 *Phys. Rev.* B **39** 4756

Kim J J, Kim J, Shin H J, Lee H J and Ku J K 1990 *Solid State Commun.* **75** 921

[4] Regan S, Lowe A J and Howson M A 1991 *J. Phys.: Condens. Matter* **3** 9245

[5] Vidal F, Torron C, Veira J A, Miguelez F F and Maza J 1991 *J. Phys.: Condens. Matter* **3** 5219

[6] Howson M A, Salamon M B, Freidmann T A, Rice J P and Ginsberg D M 1990 *Phys. Rev.* B **41** 300

[7] Anderson P W and Zou Z 1988 *Phys. Rev. Lett.* **60** 132

[8] Stan M A and Satish Vitta to be published

[9] Veira J A and Vidal F 1989 *Physica* C **159** 468

[10] Maki K and Thompson R S 1989 *Phys. Rev.* B **39** 2767

[11] Pickett W E, Krakauer H, Cohen R J and Singh D J 1992 *Science* **255** 46

[12] Tozer S W, Kleinsasser A W, Penny T, Kaiser D and Holtzberg F 1987 *Phys. Rev. Lett.* **59** 1768

[13] Obhi H S and Salje E K H 1992 *J. Phys.: Condens. Matter* **4** 195

[14] Ausloos M, Gillet F, Laurent Ch and Clippe P 1991 *J. Phys. B: At. Mol. Opt. Phys.* **84** 13

[15] Welp U, Kwok W K, Crabtree G W, Vandervoot K G and Liu J Z 1989 *Phys. Rev. Lett.* **62** 1908

[16] Skocpol W J and Tinkham M 1975 *Rep. Prog. Phys.* **38** 1049

[17] Kim D H, Goldman A M, Kang J H, Gray K E and Kampwirth R T 1989 *Phys. Rev.* B **39** 12 275

[18] Duan H M, Kiehl W, Dong C, Cordes A W, Saeed M J, Viar D L and Hermann A M 1991 *Phys. Rev.* B **43** 12 925

[19] Fisher D S, Fisher M P A and Huse D A 1991 *Phys. Rev.* B **43** 130

[20] Lobb C J 1987 *Phys. Rev.* B **36** 3930

Ellipsometric study of ambient-produced overlayer growth rate on $YBa_2Cu_3O_{7-x}$ films

Robert M. Sieg
Cleveland State University, Cleveland, Ohio 44115

Samuel A. Alterovitz and Joseph D. Warner
NASA Lewis Research Center, Cleveland, Ohio 44135

(Received 28 August 1992; accepted for publication 18 January 1993)

An ellipsometric study of ambient-reaction-produced $BaCO_3$ overlayer growth on laser-ablated $YBa_2Cu_3O_{7-x}$ is presented as a function of time. The effects of the anisotropy of $YBa_2Cu_3O_{7-x}$ on the ellipsometric data inversion process are discussed, and it is concluded that with certain restrictions on the data acquisition method, the anisotropic substrate can be adequately modeled by its isotropic pseudodielectric function for the purpose of overlayer thickness estimation. It is found that after an initial period of rapid growth attributed to the chemical reaction of the exposed surface bonds, the $BaCO_3$ overlayer growth is linear at 1–2 Å per day. This slow growth rate is attributed to the complexity of the $BaCO_3$ forming reaction, together with the need for ambient reactants to diffuse through the overlayer.

I. INTRODUCTION

Previously,[1] we have reported results of ellipsometric measurements of the pseudodielectric function of $YBa_2Cu_3O_{7-x}$ (YBCO) prepared by laser ablation and coevaporation. We also reported observing growth of a transparent overlayer on the laser-ablated films. This overlayer growth has been observed by other experimenters[2] and has been determined to be $BaCO_3$ resulting from interaction between YBCO and CO_2 in humid air,[3–5] a conclusion with which we concurred. In this article we report systematic ellipsometric measurements of the growth rate of this overlayer on laser-ablated films exposed to air. We discuss the effects of the anisotropy of the YBCO substrate on the ellipsometric inversion process and show that by fixing certain ellipsometer settings the effects of the anisotropy can be minimized. We further show that under these restrictions the YBCO substrate can be approximated by its isotropic pseudodielectric function for the purpose of estimating the transparent overlayer thickness. Finally, we present the results of the overlayer growth time dependence measurements and discuss the results in light of the chemical mechanism which is believed to create the overlayer.

II. EXPERIMENT

Samples were prepared by laser ablation[1] using an excimer laser operating at 248 nm, energy density of 1.5 J/cm^2/pulse, with 4 pulses per second. The target was a sintered 25-mm-diam YBCO pellet located 8 cm from the sample at 45° to the laser beam. The beam was rastered up and down 1 cm over the target using an external lens on a translator. The films were deposited on strontium titanate ($SrTiO_3$), zirconium dioxide (ZrO_2), and lanthanum aluminate ($LaAlO_3$) substrates, which were mounted on a stainless-steel plate heated to 775 °C. The oxygen pressure was 170 mTorr throughout the deposition. X-ray diffraction showed the films to be c-axis aligned. Comparison[1] of our measured pseudodielectric functions with published data[6] also indicated our films closely approximated c-axis-aligned YBCO single-crystal material. Critical temperatures for the films were ~86 K. Film thicknesses averaged about 3000 Å.

The rotating analyzer spectroscopic ellipsometer system[7] reflects monochromatic linearly polarized light off the sample and measures the complex reflection ratio ρ:

$$\rho=\frac{E_{p,r}/E_{s,r}}{E_{p,i}/E_{s,i}}=\left(\frac{E_{p,r}}{E_{s,r}}\right)\left(\frac{E_{s,i}}{E_{p,i}}\right)=\frac{E_{p,r}}{E_{s,r}}\tan(\theta), \qquad (1)$$

where $E_{p,r}$ and $E_{s,r}$ are the parallel and perpendicular components (with respect to the plane of incidence) of the reflected electric field intensity, $E_{p,i}$ and $E_{s,i}$ are the corresponding quantities for the incident light, and θ is the incident light polarization azimuth, i.e., $\tan(\theta)=E_{s,i}/E_{p,i}$. The rotating analyzer ellipsometer actually measures the $E_{p,r}/E_{s,r}$ ratio, while the $E_{s,i}/E_{p,i}$ ratio is determined by a fixed polarizer azimuth θ. Two films, identified here as samples A and B, both deposited on strontium titanate, were selected for systematic monitoring of overlayer growth. These samples were cleaned with a bromine etch (1% Br/ethanol solution for 30 s followed by ethanol and blow drying)[5] to remove the overlayer, and were measured less than 10 min after cleaning, and periodically thereafter. Both samples were left mounted throughout the growth monitoring period to maximize precision. The samples were monitored for a period of 4–10 days after cleaning, and were exposed to the air throughout the monitoring period. Each sample was etched two different times to determine repeatability, giving four etches in all. Additionally, sample A was mechanically cleaned and measured periodically over a period of 106 days to examine longer-term overlayer growth. Here the sample was not left mounted continuously but rather mounted periodically for measurements; hence the precision is poorer for this long-term monitoring. Between measurements, the sample was left exposed to air. Overlayer growth measurements were taken at a fixed angle of incidence: 65° for the first etch of

© J. Appl. Phys. 73 (9), 1 May 1993. Reprinted, with permission, from American Institute of Physics.

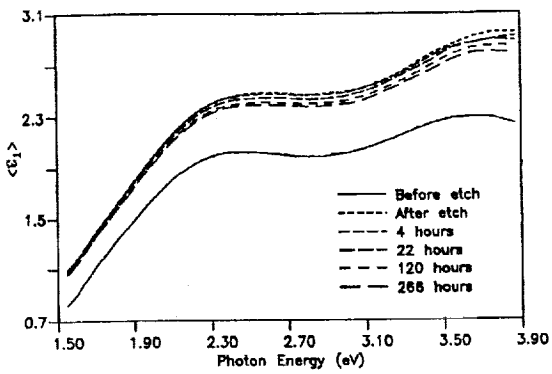

FIG. 1. Experimental $\langle \epsilon_1 \rangle$ for several representative scans of sample A taken before and after the first etch.

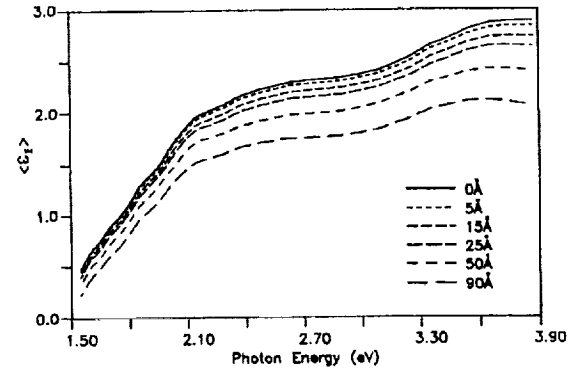

FIG. 2. Computer simulation of overlayer ($n=1.55$, $k=0$) growth on anisotropic substrate. $\langle \epsilon_1 \rangle$ is calculated at angle of incidence 70°. The curve labeled 0 Å corresponds to the actual substrate spectrum, which is taken from Ref. 6.

each sample and 70° for the second etch and also for the long-term monitoring of sample A; the wavelength range varied slightly but was always within the range 3200–8000 Å (1.55–3.87 eV). The polarizer azimuth θ was held constant at 24° for the first etches and also for the long-term monitoring of sample A; 20° was used for the second etch of each sample. These polarizer values have been shown to provide maximum precision, i.e., $|\rho| \approx \tan(\theta)$.[8]

III. RESULTS

Figure 1 shows $\langle \epsilon_1 \rangle$, the real part of the pseudodielectric function, for several representative measurements taken before and after the first etch of sample A. The pseudodielectric function is the apparent dielectric function of the sample, i.e., the dielectric function of an equivalent isotropic bulk material calculated using an isotropic two-phase (ambient/substrate) model.[9] The pseudodielectric function $\langle \epsilon \rangle$ is obtained directly from the ellipsometrically measured complex reflectance ratio ρ, using the formula[9]

$$\langle \epsilon \rangle = \epsilon_a \left[\sin^2(\phi) + \sin^2(\phi)\tan^2(\phi) \left(\frac{1-\rho}{1+\rho} \right)^2 \right] \qquad (2)$$

In the above equation ϵ_a is the dielectric function of the ambient ($\epsilon_a = 1$ for air), ϕ is the experimental angle of incidence, and ρ is the ellipsometrically measured quantity defined previously. For an ideal two-phase system, $\langle \epsilon \rangle = \epsilon_s$, the substrate dielectric function. However, (2) defines the pseudodielectric function $\langle \epsilon \rangle$ for all cases. The lowest curve in Fig. 1 is the measurement taken prior to the bromine etch. The highest curve is the measurement taken immediately after the etch. The curves in between are measurements taken at later times. The magnitude of $\langle \epsilon_1 \rangle$ decreases with increasing time. The measured quantity $\langle \epsilon \rangle$ is expected to be a continuous function of overlayer thickness, and computer simulation using an isotropic substrate whose pseudodielectric function was similar to our measure $\langle \epsilon \rangle$ (Ref. 6) showed that the magnitude of the real part of the pseudodielectric function $\langle \epsilon_1 \rangle$ in our range of measurement decreased with increasing overlayer thickness, as shown in Fig. 2. This is in accordance with our measurements: The large increase in $\langle \epsilon_1 \rangle$ magnitude immediately after etching indicates removal of the overlayer, and the steady decrease in magnitude as time increases indicates overlayer growth. Similar results are seen for the other growth monitoring measurements. Figure 3 shows the same information for the second etch of sample B in a different form. Here the real part of the pseudorefractive index $\langle n \rangle$ ($\langle \epsilon \rangle = \langle n \rangle^2$) at incident light wavelength of 4900 Å is plotted as a function of time. Again, a steady decrease in the magnitude of the real part with increasing time is seen. This effect of a transparent overlayer on the real part of $\langle n \rangle$ was also verified by computer simulation. Both the actual measurement of $\langle \epsilon_1 \rangle$ and the computer simulations of $\langle \epsilon_1 \rangle$ show that the effect of the overlayer is much more pronounced at higher photon energies (lower wavelengths). This is because the low-energy light penetrates deeper into the substrate, making it less sensitive to the overlayer.

IV. DATA ANALYSIS AND DISCUSSION

From the pseudodielectric function of single-crystal YBCO (Ref. 6) we estimate the light penetration depth in the range of measurement to be under 750 Å, making the

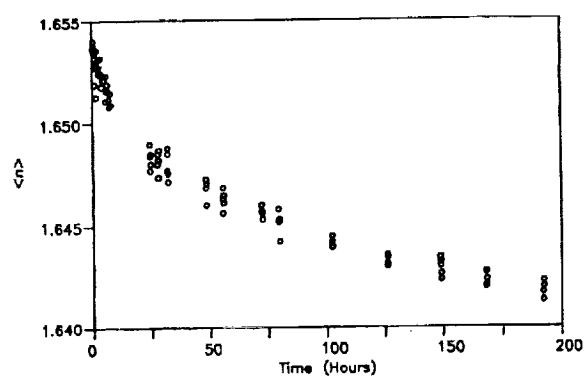

FIG. 3. Measured real part of $\langle n \rangle$ at light wavelength 4900 Å as a function of time for sample B, second etch.

YBCO film the effective substrate for ellipsometric purposes. To obtain estimates of the overlayer thicknesses, it is necessary to invert the ellipsometric data. Because of the mathematical complexity of this inversion process, a least-squares fit is usually performed.[10] A model of the system must be formulated, and appropriate model parameters optimized in the least-squares sense with respect to the measurement. Such a model typically consists of a layered structure atop an optically thick substrate. Abrupt interfaces are assumed, and layers are assumed to be isotropic and homogeneous with regard to thickness and optical properties.[11] For overlayer measurements, the pseudodielectric function of the specific substrate to be studied is typically measured prior to overlayer deposition after sufficient cleaning to approximate the two-phase model. The overlayer is then introduced and the sample remeasured and analyzed with a three-phase (ambient/overlayer/substrate) model, using the pseudodielectric function of the initial uncontaminated surface measurement to model the substrate optical properties. This process provides a built-in correction for imperfections in the substrate which would not be accounted for by the use of standard reference data.[9] Additionally, if the sample is left mounted on the ellipsometer between initial measurement of the substrate pseudodielectric function and subsequent measurement of the three-phase system, as was done in this study, effects of substrate inhomogeneity are also minimized by guaranteeing that the optical constants used to model the substrate are optimum for the specific location at which overlayer measurements are being taken.

In the present case, the above procedure is complicated by the fact that YBCO is a biaxially anisotropic material.[12] The pseudodielectric function is calculated assuming an isotropic two-phase system, and thus it cannot completely describe the optical properties of the anisotropic substrate, which should be described by a dielectric tensor.[12] To investigate the possible effects of this anisotropic substrate on the measurement of a transparent overlayer, we took two approaches: First, we performed computer simulations of untwinned single-crystal YBCO to determine which system parameters are affected by the anisotropy and to what degree. This provided information on how best to set up the overlayer measurement to minimize potential inaccuracies caused by the anisotropy, as well as providing bounds on the anisotropy-induced error. Second, we performed experimental measurements to identify to what degree the anisotropy effects predicted by computer simulation for untwinned single-crystal YBCO were actually seen in the laser-ablated YBCO films. These films are not single crystals but rather consist of microscopic grains of *c*-axis-oriented YBCO crystals with the *a* and *b* crystal directions aligned with the strontium titanate substrate crystal directions.[2,12] There will be a high degree of twinning in the *a-b* plane.[2,12] We expect this type of crystal structure to reduce the observable effects of the anisotropy.

The computer simulations of ellipsometric measurements of untwinned single-crystal YBCO were based upon the biaxial substrate model developed by Graves.[11,13] This model calculates the complex amplitude reflection coefficients for a biaxially anisotropic substrate oriented such that one crystal axis is perpendicular to the sample surface while the a second crystal axis is perpendicular to the plane of incidence of the light. In the present case, the YBCO films are predominantly *c*-axis aligned, so that the *c* axis is perpendicular to the sample surface as required by the Graves model. The dielectric tensor components of YBCO were taken from Kircher *et al.*[12] Simulations were done using the *c* axis perpendicular to the interface and either the *b* axis perpendicular to the plane of incidence (*abc* orientation) or the *a* axis perpendicular to the plane of incidence (*bac* orientation). Physically this corresponds to measurement of an untwinned single crystal of YBCO, for which the maximum observable anisotropy effect would be expected. Comparison of the pseudodielectric function of *abc*-oriented simulations with the pseudodielectric function of *bac*-oriented simulations shows the effect of a 90° rotation on the measurement of such a single crystal. We performed these simulations at an angle of incidence of 65°, and found that the difference between the *abc*-oriented crystal pseudodielectric function and the *bac*-oriented crystal pseudodielectric function is enormous, with differences between the real and imaginary parts of $\langle\epsilon\rangle$ of the two orientations exceeding the absolute magnitude of these quantities. For example, at the wavelength 5500 Å, $\langle\epsilon_1\rangle=3$ for the *abc* orientation, while $\langle\epsilon_1\rangle=1$ for the *bac* orientation. Additionally, the shape of the two spectra differed significantly. In contrast, our measurements of laser-ablated YBCO films as a function of sample azimuth showed variation in $\langle\epsilon_1\rangle$ and $\langle\epsilon_2\rangle$ of less than 0.3 all cases, and the shape of the spectra measured at different sample azimuths was very similar. The dependence of the ellipsometric measurement on sample azimuth has been reduced significantly by the complex crystal structure of the laser-ablated films, but it is still detectable, as shown by these measurements.

We next simulated the pseudodielectric function of untwinned single-crystal YBCO with no overlayer at various angles of incidence. Our simulations showed that the pseudodielectric function is a strong function of the ellipsometer angle of incidence for both the *abc* orientation and the *bac* orientation, with variation in spectral magnitudes greater than 15% for incident angle variation from 65° to 75°. The variation of the pseudodielectric function for each orientation was in opposition: the real part of $\langle n\rangle$ decreased with increasing angle of incidence for the *abc* orientation, whereas it increased with increasing angle of incidence for the *bac* orientation. For comparison, we measured numerous films at various angles of incidence. The measured pseudodielectric function was found to vary by 5% or less. Again, the effect of the anisotropy has been greatly reduced by the complex film structure, but has not been completely eliminated.

In our third simulation, we determined bounds on the error that can be expected in using an isotropic three-phase model to analyze a system with an anisotropic substrate. Using the anisotropic model, we simulated ellipsometric data for various overlayer thicknesses (overlayer $n=1.55$ $k=0$) at an angle of incidence of 70°. This generated data

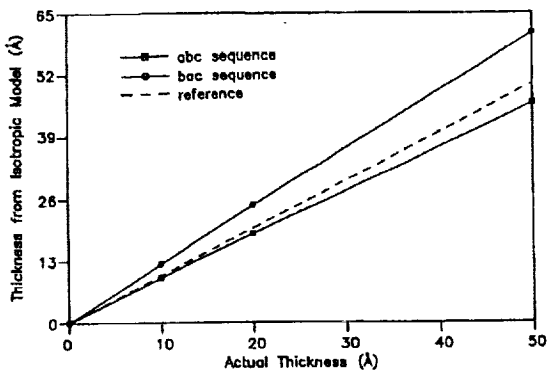

FIG. 4. Computer simulation using a three-phase isotropic model to analyze a system with an anisotropic substrate. *abc*: *c* axis perpendicular to interface, *b* axis perpendicular to plane of incidence; *bac*: *c* axis perpendicular to interface, *a* axis perpendicular to plane of incidence. Reference is calculated isotropic thickness equal actual thickness.

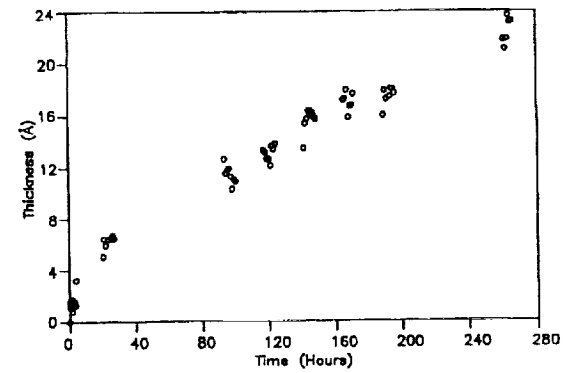

FIG. 5. Results of isotropic three-phase modeling of sample A, first etch growth monitoring. The plotted overlayer thickness is the only model parameter.

was then inverted using the isotropic three-phase model to obtain the overlayer thickness, using the simulated pseudodielectric function of the anisotropic substrate with no overlayer as the effective isotropic substrate. Simulation results are given in Fig. 4. The reference line in this graph is the ideal result, i.e., the overlayer thickness determined by the isotropic model exactly equals the overlayer thickness simulated on the anisotropic substrate. The absolute error is 20% or less, and the calculated thickness is directly proportional to the actual thickness. Thus, use of the isotropic model in this case may result in some error in the absolute growth rate, but the shape of the growth curve will be correct. As with the angle-of-incidence variation, the effects of the two orientations *abc* and *bac* oppose each other, with the *abc*-oriented crystal resulting in an underestimated thickness while the *bac*-oriented crystal results in an overestimate. In view of our previous results showing significant reduction in the observed effect of YBCO anisotropy in the laser-ablated films, the boundaries shown in Fig. 4 are expected to greatly overestimate the actual overlayer measurement error.

One potential effect of substrate anisotropy on ellipsometric measurements that cannot be studied using the Graves model is the effect of off-diagonal components of the reflectance matrix which result when the crystallographic axes are not aligned with the optical axes as required by Graves model. In general, the relationship between the incidence electric-field vector and the reflected electric-field vector is given by[11]

$$\begin{bmatrix} E_{p,r} \\ E_{s,r} \end{bmatrix} = \begin{bmatrix} R_{p,p} & R_{p,s} \\ R_{s,p} & R_{s,s} \end{bmatrix} \begin{bmatrix} E_{p,i} \\ E_{s,i} \end{bmatrix} \tag{3}$$

Equation (3) states that the reflected complex amplitudes are related to the incident complex amplitudes by a 2×2 reflection matrix. This matrix is a property of the sample and is a function only of wavelength and angle of incidence. For either an isotropic system or a biaxially anisotropic system with the axial alignment specified for Graves model $R_{p,s}=R_{s,p}=0$ and the ellipsometrically measured ratio ρ reduces to $\rho=R_{p,p}/R_{s,s}$.[11] Thus, ρ is a function only of the reflection matrix, which is a property of the sample. In the case of a biaxially anisotropic system in which the optical axes and crystallographic axes do not coincide, $R_{s,p}$ and $R_{p,s}$ are not generally zero. The measured ratio ρ can be written as

$$\rho=\left(\frac{E_{p,r}}{E_{s,r}}\right)\left(\frac{E_{s,i}}{E_{p,i}}\right)=\frac{R_{p,p}+R_{p,s}\tan(\theta)}{R_{s,p}+R_{s,s}\tan(\theta)}\tan(\theta). \tag{4}$$

The ellipsometric measurement in this case is a function of both the reflectance matrix and the polarizer azimuth θ. We measured the effect of the polarizer azimuth setting both on a laser-ablated YBCO film and also on an isotropic reference sample. The reference sample was an amorphous carbon film on silicon, similar to samples described in Ref. 7. The film was nearly transparent ($k<0.13$) with thickness $\sim$1950 Å. For such a sample the amplitude and phase of ρ oscillates slowly (one complete cycle in our spectral range), so that we could locate spectral regions where the measured ρ of the YBCO film could be compared with measured ρ values of similar magnitude and phase for an isotropic system. The polarizer azimuth was varied between 20° and 70°. In this range, the variations of ρ for the isotropic sample are within the experimental error. For the YBCO film the variations in $\langle\epsilon_1\rangle$ and $\langle\epsilon_2\rangle$ are less than 8% of the amplitude between polarizer values of 20° and 70°. Between 20° and 45° the changes are less than 4%. Again, a small but observable effect of the anisotropy is seen in the laser-ablated film.

Based upon the above results, we used the measurement and analysis procedure outlined previously for isotropic systems, with the additional constraints of using a fixed angle of incidence and a fixed polarizer azimuth, so as to avoid any measurement variations not directly attributable to surface changes. Also, since each sample was left mounted throughout the overlayer growth measurement, the sample azimuth remained unchanged. The overlayer was modeled as a transparent dielectric material with refractive index of 1.55,[1] and the YBCO substrate was modeled by the pseudodielectric function measured immediately after etching. The resultant overlayer thickness

TABLE I. Results of linear regression analysis applied to growth monitoring results analyzed by an isotropic three-phase model. Only measurements taken after 12 h or longer were included in the fit. R is the correlation coefficient; $R = \pm 1$ is a perfect fit. m denotes mechanically cleaned.

Sample	Etch	Hours	Rate[a]	Intercept[b]	R
A	1	266	1.62	5.03	0.983
A	2	95	2.12	6.62	0.983
A	m	2557	0.95	2.29	0.981
B	1	214	2.01	1.80	0.985
B	2	192	0.87	6.42	0.937

[a]The rate in Å/day.
[b]The intercept in Å.

versus time plot for the first etch of sample A is given in Fig. 5. Two distinct regions are seen. For about the first 5 h the overlayer grows rapidly. When the overlayer reaches ~5 Å the growth slows and becomes linear, with a growth rate of 1.62 Å per day, as determined by linear regression. Results for the other three etches were similar in shape. The four etch results plus the long-term monitoring of sample A after mechanical cleaning were each fitted to a linear model for overlayer measurements taken after 12 h, i.e., in the linear region. The results are shown in Table I. In this table, the intercept is the y intercept of the regression line; this gives an estimate of the thickness reached in the initial rapid growth region. The initial growth period stops at about 2–6 Å, i.e., about one monolayer. In the linear region, the growth rate is in the range 1–2 Å per day, which is below one monolayer per day.

The type of growth curve observed here on YBCO is different from the logarithmic curve typically observed in the oxidation of semiconductors, such as the oxidation rate of silicon and gallium arsenide measured by Lukeš.[14] In the case of oxidation, the ambient reactant O_2 is plentiful, and the overlayer growth rate is controlled by the diffusion rate of oxygen through the growing oxide overlayer. In the present case, the YBCO overlayer is believed to be produced by the following chemical reactions:[3]

$$3H_2O + 2YBa_2Cu_3O_7 \rightarrow Y_2BaCuO_5 + 3Ba(OH)_2 + 5CuO + 0.5O_2, \quad (5)$$

$$Ba(OH)_2 + CO_2 \rightarrow BaCO_3 + H_2O.$$

These reactions are clearly more complicated than a simple oxidation reaction, and also involve two reactants, H_2O and CO_2, which make up a much smaller molar fraction of air than does O_2. The growth curve observed here is quite similar to the growth rate of silver sulfide tarnish on silver exposed to room air,[11] where an initial period of rapid growth is seen up to 2 Å, after which the growth rate slows and becomes linear at ~4 Å per day.

Variations in the ultimate YBCO overlayer thickness reached during the initial rapid growth phase are probably due to two factors: variations in surface quality, and differences in the delay time between etching and the initial measurement of the substrate dielectric function. This latter factor will be particularly significant if the initial growth curve shape is logarithmic; any overlayer growth that occurs prior to the initial measurement will be absorbed into the effective substrate measurement. Variations in the linear region slope may be due to variations in atmospheric conditions such as humidity which would affect the availability of the limiting reagents in Eq. (5). As a final comment, we note that the final measurement at 2557 h for the mechanically cleaned long-term monitoring of sample A gave a thickness of 100 Å as analyzed by the isotropic three-phase model. This measurement is the measurement labeled "Before etch" on Fig. 1; the effect of the removal of this 100 Å overlayer by the bromine etch is seen very clearly in the pseudodielectric function.

V. CONCLUSIONS

We have measured ellipsometrically insulator overlayer growth on laser-ablated YBCO thin films due to exposure to air. After formation of an initial monolayer, the growth proceeds linearly and rather slowly, e.g., 1–2 Å per day. This information should be useful in appraising the effect of air exposure on various sample processing steps, such as making electrical contacts. In the process, we considered the effects of substrate anisotropy on overlayer estimation and have presented a method of estimating overlayer growth on an anisotropic substrate.

ACKNOWLEDGMENTS

The authors would like to thank Jill E. Dunning for help in some of the growth monitoring measurements, and Dr. J. Kircher for supplying a diskette of the YBCO tensor component spectra.

[1] S. A. Alterovitz, R. M. Sieg, J. D. Warner, M. A. Stan, and S. Vitta, in *Proceedings of the 2nd International Conference on Electronic Materials*, edited by T. Sugano, R. P. H. Chang, H. Kamimura, I. Hayashi, and T. Kamiya (Int. MRS, Pittsburgh, PA, 1990), p. 147.
[2] M. P. Petrov, A. I. Grachev, M. V. Krasin'kova, A. A. Nechitailov, V. V. Prokoflev, V. V. Poborchy, S. I. Shagin, and N. F. Kartenko, Solid State Commun. 67, 1197 (1988).
[3] M. F. Yan, R. L. Barns, H. M. O'Bryan, Jr., P. K. Gallagher, R. C. Sherwood, and S. Jin, Appl. Phys. Lett. 51, 532 (1987).
[4] N. P. Bansal and A. L. Sandkuhl, Appl. Phys. Lett. 52, 323 (1988).
[5] R. P. Vasquez, B. D. Hunt, and M. C. Foote, Appl. Phys. Lett. 53, 2692 (1988).
[6] M. K. Kelly, P. Barboux, J. M. Tarascon, D. E. Aspnes, W. A. Bonner, and P. A. Morris, Phys. Rev. B 38, 870 (1988).
[7] S. A. Alterovitz, R. M. Sieg, N. S. Shoemaker, and J. J. Pouch, Mater. Res. Soc. Symp. Proc. 152, 21 (1989).
[8] D. E. Aspnes, J. Opt. Soc. Am. 64, 639 (1974).
[9] D. E. Aspnes and A. A. Studna, Phys. Rev. B 27, 985 (1983).
[10] D. W. Marquardt, J. Soc. Indust. Appl. Math. 11, 431 (1963).
[11] R. M. A. Azzam and N. M. Bashara, *Ellipsometry and Polarized Light* (North-Holland, Amsterdam, 1979).
[12] J. Kircher, M. K. Kelly, S. Rashkeev, M. Alouani, D. Fuchs, and M. Cardona, Phys. Rev. B 44, 217 (1991) and private communication.
[13] R. H. W. Graves, J. Opt. Soc. Am. 59, 1225 (1969).
[14] F. Lukeš, Surf. Sci. 30, 91 (1972).

Magnetic flux relaxation in $YBa_2Cu_3O_{7-x}$ thin film: thermal or athermal*

Satish Vitta,† M. A. Stan,‡ J. D. Warner and S. A. Alterovitz
NASA Lewis Research Center, Cleveland, OH 44135 (USA)

(Received March 15, 1991; revised May 28, 1991)

Abstract

The magnetic flux relaxation behavior of $YBa_2Cu_3O_{7-x}$ thin film on $LaAlO_3$ for $H \parallel c$ was studied in the range 4.2–40 K and 0.2–1.0 T. Both the normalized flux relaxation rate S and the flux pinning energy U_0 exhibit a weak field dependence at low temperatures ($T \leqslant 20$ K). Within this regime S and U_0 are observed to increase continuously from 1.0×10^{-2} to 2.0×10^{-2} and 45 to 130 meV respectively, as the temperature T increases from 4.2 to 20 K. While S is observed to decrease in proportion to kT for $T \leqslant 20$ K, it does not extrapolate to zero at $T = 0$, which is in contradiction to the thermally activated flux creep and vortex glass models. This behavior is discussed in terms of the athermal quantum tunneling of flux lines. The magnetic field dependence of U_0, however, is not completely understood.

1. Introduction

In type II superconductors the pinning of magnetic flux lines is responsible for the lack of dissipation during the flow of high current densities. The pinning is caused by various types of defects, *i.e.* grain boundaries, twins, point defects and inhomogeneities. The observation of a high degree of mobility of these flux lines in the oxide superconductors [1–3] has stimulated many theoretical studies and has led to the proposal of several models. According to the conventional thermal flux motion model [4, 5] the magnetization relaxes logarithmically with time t for $t < t_{cr}$, where t_{cr} is a crossover time given by $t_{cr} = t_{hop} \exp[U/kT]$, t_{hop} is the flux line hopping time (10^{-6}–10^{-12} s), U is the net flux pinning energy, k is the Boltzmann constant and T is temperature. At $t > t_{cr}$, or for high T, the motion of flux lines attains a steady state and the magnetization relaxes exponentially with t [6]. However, the observation of logarithmic decay even at large values of T and the non-linear behavior of the relaxation rate has led to many alternative models for the nature of the pinning energy U [7–9].

An alternative description of dissipation in high temperature superconductors is the vortex glass model [10, 11]. In this model there is a truly superconducting state in the presence of high magnetic fields below the glass transition temperature. Within this regime the sample voltage is predicted to vanish exponentially with decreasing current. Recently, the vortex glass model has been used to explain the apparent temperature independent value of $S = 0.02$–0.035 reported by many researchers [12].

In the present work, the relaxation of screening-current-induced magnetization in a $YBa_2Cu_3O_{7-x}$ thin film has been studied as a function of temperature T and external field H. The magnetization is found to relax logarithmically up to 10^4 s for T as high as $0.45\,T_c$, where T_c is the superconducting transition temperature. S appears to saturate with increasing temperatures for $T > 20$ K. This observation is consistent with the predictions of the vortex glass model; however the $[\ln(t)]^{-1}$ time dependent relaxation appropriate to the model is not observed. For $T \leqslant 20$ K, S is observed to decrease linearly with decreasing T but does not extrapolate to zero at $T = 0$. The linear dependence of S on T in the low-T region is consistent with both the thermally activated creep and vortex glass models. The finite value of S at $T = 0$ obtained by extrapolation cannot be explained by either model and is discussed in terms of "quantum tunneling" or the "athermal flux motion" model [13]. We also observe U_0 to decrease with increasing H for all temperatures and fields used,

*Presented at the 18th International Conference on Metallurgical Coatings and Thin Films, San Diego, CA, USA, April 22–26, 1991. In error, an unrevised version of this paper was published in *Thin Solid Films, 206* (1991) 137–142.

Correspondence should be addressed to: Dr. M. A. Stan, Mail Stop 54-5, NASA Lewis Research Center, Cleveland, OH 44135, USA.

†Present address: Department of Metallurgy, Indian Institute of Technology, Powai, Bombay 400 076, India.

‡Department of Physics, Kent State University, Kent, OH 44242, USA.

© Reprinted with the kind permission of Elsevier Sequoia, Lausanne, Switzerland, publishers of the journal Thin Solid Films, no. 217, pp. 156-160.

PRECEDING PAGE BLANK NOT FILMED

although the $1/H$ dependence suggested by Yeshurun and Malozemoff [1] is not observed.

2. Experimental methods

The $YBa_2Cu_3O_{7-x}$ thin film, approximately 0.3 μm thick, was deposited by the pulsed laser ablation technique onto a heated (100) $LaAlO_3$ substrate. The film texture was determined by the standard $\theta-2\theta$ scan and rocking curve, and shows that the grains are preferentially aligned with their c-axis along the plane normal. The film has a smooth surface and the average grain size, determined by scanning electron microscopy, is approximately 0.25 μm. The superconducting transition temperature $T_c(0)$ determined by the standard four probe d.c. technique is 88.5 K with a transition width of *ca.* 1.0 K.

The magnetization and magnetic flux relaxation was studied using a commercial SQUID magnetometer. Hysteresis loops were made at various temperatures for $H \| c$, from which the critical current J_c was determined. The values at 4.2 K and 77 K were 2.4×10^7 A cm^{-2} and 1.0×10^6 A cm^{-2} respectively. Such values are typical of high quality films. The data collection procedure is described in detail in ref. 3. The diamagnetic transition temperature determined from the field-cooled magnetization of 2 mT applied along the c-axis was found to be 88.5 K and is the same as that determined by the electrical transport method.

3. Results

The relaxation of the screening-current-induced magnetization at $H = 0.2$ T, 0.4 T, 1.0 T and 2.0 T applied perpendicular to the orthorhombic *ab* plane of the crystals was studied in the temperature range $0.05\ T_c < T < 0.45\ T_c$. The magnetization was found to relax logarithmically with t up to 10^4 s at all the temperatures and fields studied. The relaxation rate $dM/d\ln t$ is shown in Figs. 1(a) and 1(b) as a function of T and H respectively. It may be observed in Fig. 1(a) that $dM/d\ln t$ exhibits a maximum at approximately 10 K. Such behavior has been observed in grain aligned powdered $YBa_2Cu_3O_{7-x}$ specimens [2] and attributed to partial flux penetration when $H < H^*$, where H^* is the field at which the magnetization reaches the maximum at a given temperature. In our relaxation measurements, however, $H > 2.5H^*$ for all temperatures and fields used. We therefore believe the films are fully penetrated by the flux and that the films are in the critical state. The relaxation rate $dM/d\ln t$ normalized by the initial magnetization M_0 at t_0 eliminates the uncertainties associated with the determination of the demagnetization

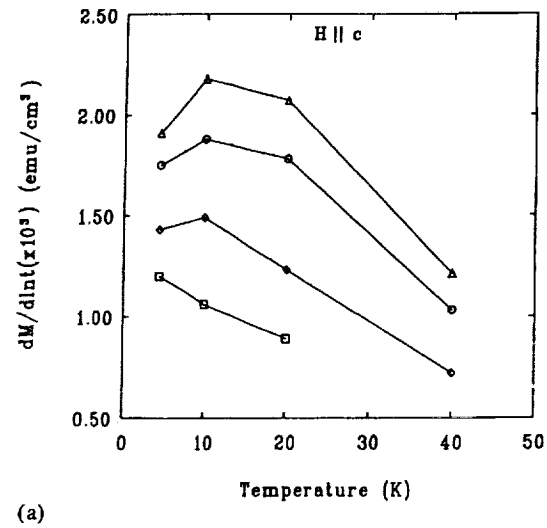

(a)

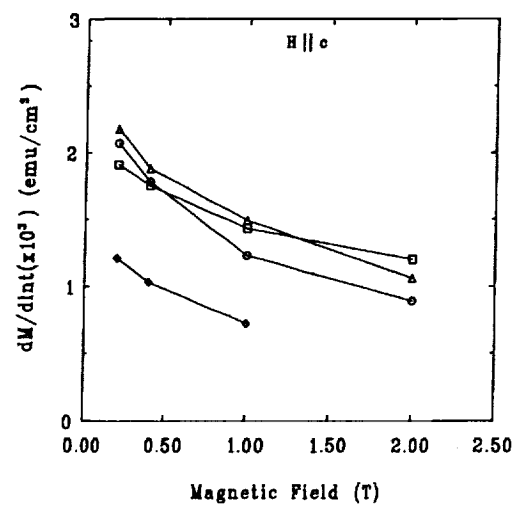

(b)

Fig. 1. The logarithmic relaxation rate $dM/d\ln t$ of the screening current induced magnetization: (a) As a function of temperature T at various fields △, 0.2 T; ○, 0.4 T; ◇, 1.0 T; □, 2.0 T; (b) as a function of external field H at various temperatures □, 4.2 K; △, 10 K; ○, 20 K; ◇, 40 K. The lines connecting the data points are aids to the eye.

factor, and allows the possible determination of the pinning energy U_0. In analyzing the results of the present work, t_0 is taken to be 10^3 s so that the relaxation is in the logarithmic regime. Figures 2(a) and 2(b) show the normalized relaxation rate $1/M_0\, dM/d\ln t \equiv S$ as functions of T and H respectively.

4. Discussion

In a typical relaxation measurement, the net flux pinning energy U is zero at $t = 0$ and increases rapidly with t. The time dependence of U is implicitly contained

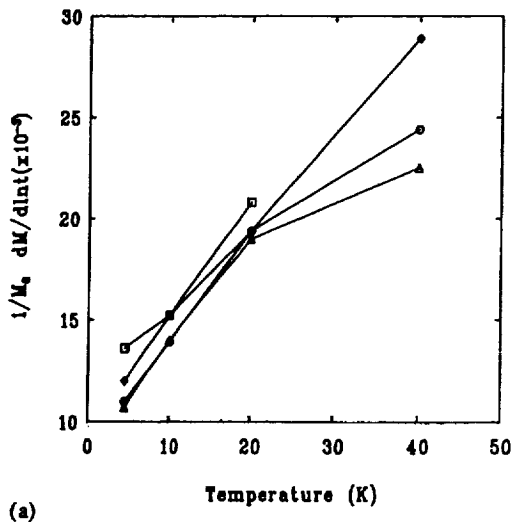

(a)

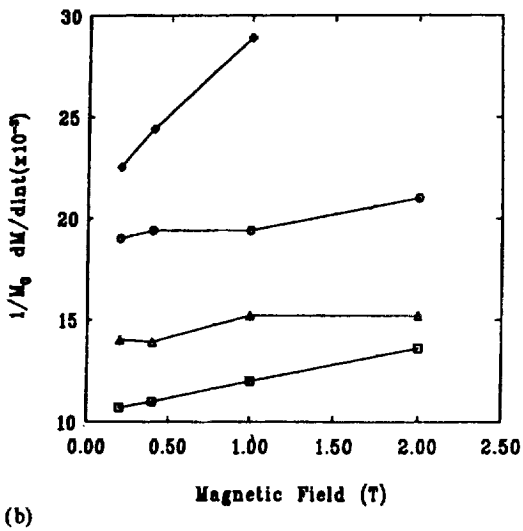

(b)

Fig. 2. The relaxation rate normalized by the initial magnetization M_0: (a) as a function of temperature T; (b) as a function of external field H. See caption of Fig. 1 notation.

within the screening current J which equals J_c at $t = 0$. The driving force for the motion of these flux lines is a combination of flux line interaction, thermal activation and the flux line gradient (Lorentz force). In the conventional thermally activated flux motion model, U is assumed to be a linear function of J and to have a depth U_0 when $J = 0$.

This leads to the classical relation [4, 5, 9] for $t \gg t_{hop}$,

$$M(t) = M(0)[1 - \{kT/U_0\} \ln(t/t_{hop})] \quad (1)$$

The relaxation rate normalized by the initial magnetization can be obtained from the above relation and is given as

$$1/M_0 \, dM/d \ln t \equiv S = -kT/[U_0 - kT \ln(t_0/t_{hop})] \quad (2)$$

According to the above relation, S is a linear function of T when $U_0 \gg kT \ln(t_0/t_{hop})$. Since U_0 must go to zero as $T \longrightarrow T_c$, it also predicts a divergence or an upward curvature for the S curve as T increases. From Fig. 2(a) it can be seen that S is approximately linear in T for $T \leqslant 20$ K, and takes on a weaker temperature dependence for higher temperatures. This type of behavior has been observed before in magnetization studies on single crystals, aligned powders and thin films [1–3]. The flux pinning energy U_0 obtained from eqn. (2) by considering t_{hop} to be typically 10^{-8} s is shown in Fig. 3(a). At every field U_0 is an increasing, convex function of temperature. The observation that U_0 is an increasing function of temperature rather than a decreasing function of temperature has led Hagen and Griessen [14] to propose that a distribution of U_0 values exists in these materials.

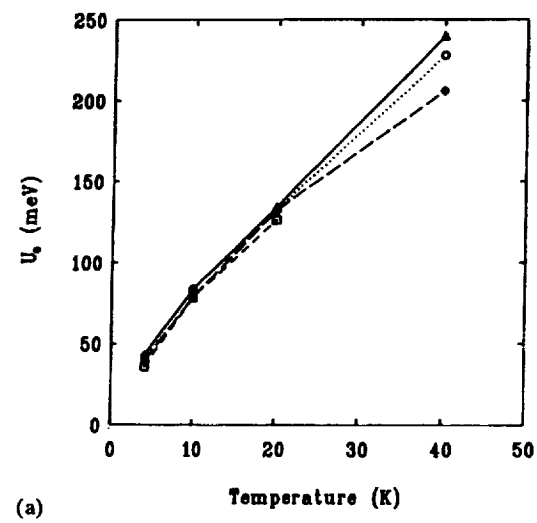

(a)

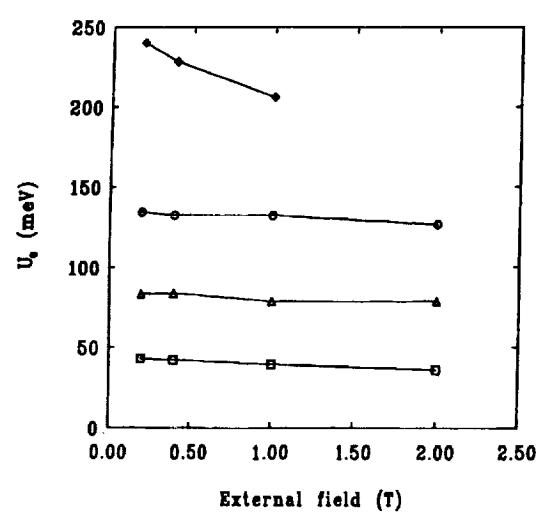

(b)

Fig. 3. The flux pinning energy U_0 obtained using eqn. (2) shown as a function of temperature (a) and external field (b). See caption of Fig. 1 notation.

In the vortex glass state, dissipation from the formation of vortex loops results in a magnetic relaxation of the form [12]

$$M(t) = M(0)[1 + (\mu kT/U_0)\ln(t/t_{hop})]^{-1/\mu} \quad (3)$$

where μ is the glass exponent. For times which are short compared with t_{cr} and where $\mu = 1$, eqn. (3) becomes equivalent to eqn. (1) and the resulting S is given by eqn. (2). In other words, at low temperatures the predictions of the activated flux creep and vortex glass are identical and in qualitative agreement with the data of Fig. 2(a). At times which are long compared with t_{cr} (or equivalently at higher temperatures) the vortex glass model predictes that $M \propto [\ln(t)]^{-1}$ and S takes on a temperature independent value given by $S = -[\ln(t/t_{hop})]$. Malozemoff and Fisher [12] argue that the nearly constant value of S reported in the literature is a consequence of the logarithmic dependence of S on the observation time. The data of Fig. 2(a) show that our values of S fall within the range of values observed by Malozemoff and Fisher, and that S tends to saturate for all fields as the temperature is increased. The latter fact is in qualitative agreement with the vortex glass model. While we have qualitative agreement with the temperature dependence predicted by the vortex glass model we do not observe the concomitant $[\ln(t)]^{-1}$ relaxation. Instead the magnetization decays as $\ln(t)$ at all temperatures used in this study.

Recently, substantial magnetic relaxation has been reported at temperatures as low as 0.1 K in $YBa_2Cu_3O_{7-x}$ grain aligned powder [15] and at 1.6 K in c-axis aligned thin film [16] for H applied along the c-axis. In the present work, however, 4.2 K was the lowest T at which the relaxation behavior was studied. In the low temperature limit both the thermally activated creep and the vortex glass models predict (eqn. (2)) that S vanishes as $T \longrightarrow 0$. Extrapolation of the data (Fig. 2(a)) to $T = 0$ results in a non-zero S, in contradiction to both models. This behavior has also been observed in molybdenum disulfides for $T < 0.2\ T_c$ by Mitin [13]. He has proposed that the observed relaxation results from *quantum tunneling or hopping* of the flux line segments across the potential barrier separating two pinning centers, and is athermal in nature. The hopping time for this process was estimated to be *ca.* 10^{-12} s, which is comparable to t_{hop} used in the present analysis. This phenomenon is similar in principle to the electron transport mechanism in disordered semiconductors [17]—quantum tunneling crossing over to thermal activation as T increases and domination of the highest rate process at any given T. At present there is no single model incorporating both these processes.

The magnetic field H dependence of U_0 is shown in Fig. 3(b). As can be seen from this figure, the H dependence of U_0 changes continuously as T is increased. From this figure we observe that U_0 is weakly field dependent for $T \leqslant 20$ K. At all temperatures however, U_0 is observed to decrease with increasing field. On the other hand Xu *et al.* [2] observed U to increase with increasing fields for the same range of temperatures used in this experiment. Recent studies of the field dependence of U_0 in grain aligned [18] and single crystal [19] $YBa_2Cu_3O_{7-x}$ have shown U_0 to increase with increasing fields at low temperatures and to decrease with increasing H for T near T_{irr}, where T_{irr} is the irreversibility temperature. This has been attributed to the variation of pinning strength, creation of field induced pinning centers and granularity. The disparity of the various field dependencies clearly shows that H dependence of U_0 is also not completely understood at present.

5. Conclusions

The temperature and magnetic field dependence of the flux pinning energy in a c-axis oriented $YBa_2Cu_3O_{7-x}$ thin film have been investigated. The observed linear temperature dependence of S at low temperatures is consistent for both the thermally activated flux creep and the vortex glass models. The observed non-linear temperature dependence of S for $T \geqslant 20$ K is in agreement with the vortex glass model, but we do not observe the expected $[\ln(t)]^{-1}$ decay as predicted in this model. The behavior in the $T = 0$ limit, however, cannot be understood in terms of either model. At present one must resort to considering an athermal flux line tunneling mechanism for motion at $T = 0$. It therefore appears that no single model adequately describes the temperature, time, and field dependence of the magnetic relaxation in $YBa_2Cu_3O_{7-x}$ thin films.

Acknowledgments

S.V. wishes to acknowledge the U.S. National Research Council for an Associateship at NASA Lewis Research Center and M.A.S. acknowledges NASA for support through grant no. NAG-440751.

References

1 Y. Yeshurun and A. P. Malozemoff, *Phys. Rev. Lett.*, *60* (1988) 2202.
2 Y. Xu, M. Suenaga, A. R. Moodenbaugh and D. O. Welch, *Phys. Rev. B*, *40* (1989) 10882.
3 Satish Vitta, M. A. Stan and S. A. Alterovitz, *IEEE Trans. Magn.*, *23* (1991) 1083.
4 P. W. Anderson and Y. B. Kim, *Rev. Mod. Phys.*, *36* (1964) 39.

5 M. R. Beasley, R. Labusch and W. W. Webb, *Phys. Rev.*, *181* (1969) 682.
6 P. H. Kes, J. Aarts, J. van den Berg, C. J. van der Beek and J. A. Mydosh, *Supercond. Sci. Technol.*, *1* (1989) 242.
7 D. O. Welch, *IEEE Trans. Magn.*, *23* (1991) 1133.
8 E. Zeldov, N. M. Amer, G. Koren, A. Gupta, M. W. McElfresh and R. J. Gambino, *Appl. Phys. Lett.*, *56* (1990) 680.
9 R. Griessen, *Physica C*, *172* (1991) 441.
10 M. P. A. Fisher, *Phys. Rev. Lett.*, *62* (1989) 1415.
11 D. S. Fisher, M. P. A. Fisher, and D. Huse, *Phys. Rev. B*, *43* (1991) 103.
12 A. P. Malozemoff and M. P. A. Fisher, *Phys. Rev. B*, *42* (1990) 6784.
13 A. V. Mitin, *Sov. Phys. JETP*, *66* (1987) 335.
14 C. W. Hagen and R. Griessen, *Phys. Rev. Lett.*, *62* (1989) 2857.
15 A. Hamzic, L. Fruchter and I. A. Campbell, *Nature*, *345* (1990) 515.
16 R. Griessen, J. G. Lensink, T. A. M. Schroder, and B. Dam, *Cryogenics*, *30* (1990) 563.
17 N. F. Mott, *Electronic Processes in Non-Crystalline Materials*, Clarendon, Oxford, 1979, p. 7.
18 C. Keller, H. Kupfer, A. Gurevich, R. Meier-Eirmer, T. Wolf, R. Flukiger, V. Selvamanickam and K. Salama. *J. Appl. Phys.*, *68* (1990) 3498.
19 M. Daeumling, J. M. Seuntjens and D. C. Larbalestier, *Nature*, *346* (1990) 332.

BIOGRAPHIES

PRECEDING PAGE BLANK NOT FILMED

Samuel A. Alterovitz

Samuel A. Alterovitz received a Ph.D. degree in Solid State Physics in 1971 from Tel Aviv University, Israel. After a 2-year postdoctoral appointment at the University of Illinois, Urbana, Illinois, he joined the staff of the Physics Department at Tel Aviv University where he achieved the rank of tenured associated professor. In both places he worked on properties of superconducting materials, especially critical currents and critical fields. In 1981 he accepted a position in the Electrical Engineering Department at the University of Nebraska, Lincoln, Nebraska, as senior engineering research scientist. In 1983 he transferred to NASA Lewis Research Center where he is now a senior research scientist. He played an important role in developing new materials (e.g., InGaAs) for high-speed, low-noise, high-efficiency electronic devices. He also developed ellipsometry for novel and multilayer structures. He is now working on epitaxial lift-off technique development, materials and devices for extended temperature electronics applications, and on further applications of the ellipsometric technique. Dr. Alterovitz has authored over 120 papers in referred journals and over 110 meeting presentations and has edited three books. Dr. Alterovitz is a member of the American Physical Society, the Materials Research Society, and the American Vacuum Society.

Christopher M. Chorey

Christopher M. Chorey received his B.S. degree in Electrical Engineering in 1984, and his M.S. degree in Materials Science in 1987 from Case Western Reserve University. With the support of NASA Lewis Research Center, he performed 2 years of additional graduate work at Case Western Reserve University from 1987 to 1988, focusing on fabrication and testing of AlGaAs-based, high-frequency, electro-optic modulators. Mr. Chorey is currently studying microwave properties of high-temperature superconductors.

PRECEDING PAGE BLANK NOT FILMED

Alan N. Downey joined NASA Lewis Research Center in 1977 as a co-op student. He received his B.S.E.E. degree from Cleveland State University in 1979, and his M.S.E.E. degree from the University of Toledo in 1983. In 1979 he joined the Space Communications Division of Lewis. From 1979 to 1985, he was engaged in microwave measurements and solid-state technology research, followed by a 3-year hiatus in the Communications Projects Branch as Experiments Manager for the Applications Technology Satellites Program. Mr. Downey returned to the Solid State Technology Branch in July 1989. His current research interests include the RF characterization of novel High Electron Mobility Transistor (HEMT) structures at cryogenic temperatures, Monolithic Microwave Integrated Circuits (MMIC) applications, and micromachined passive electronic components for submillimeter wave radiometry.

Alan N. Downey

Edward J. Haugland received his B.S. degree in Physics from the University of Minnesota, and M.S. and Ph.D. degrees in Solid State Physics from Case Western Reserve University. He joined NASA Lewis Research Center in 1980 as a member of the Solid State Technology Branch. Since that time, he has been involved with experimental research on electrical properties of III-V semiconductor materials, heterostructures, and SiC. Dr. Haugland was responsible for contracts concerning development of high-power Impact Ionization Avalanche Transit Time (IMPATT) diodes and Monolithic Microwave Integrated Circuits (MMIC) power amplifiers.
Dr. Haugland is a member of the American Physical Society.

Edward J. Haugland

Thomas J. Kascak received a B.S.E.E. degree from Case Western Reserve University in 1959 and joined Union Carbide Corporation where he was concerned with performance and reliability aspects of dry cell and alkaline batteries. Mr. Kascak received an M.S. degree in Physics in 1965 from John Carroll University, Cleveland, Ohio. From 1966 to the present, he has been employed at the Lewis Research Center in Cleveland, Ohio. At NASA he has been involved in several work areas, starting with research on thermonic heat to electric power conversion devices. In 1973 he transferred to the Launch Vehicles Division where he had contract management responsibilities dealing with the guidance equipment for the NASA Atlas/Centaur launch vehicle systems. In 1980 he transferred to the Space Electronics Division where he has been involved in various aspects of microwave and millimeter wave solid-state devices and circuits. He had responsibilities for formulating and managing several NASA sponsored contractual efforts involving MMIC development programs. One of these efforts, a 20-GHz MMIC Transmit Module, resulted in the R&D Magazine IR-100 Award. For the last few years, he had the responsibility for the setup of the Division's in-house solid-state facilities. Recently he has managed a contractual effort involving the pulsed laser deposition of high-Tc superconducting YBCO films on sapphire substrates for use in microwave/millimeter wave applications.

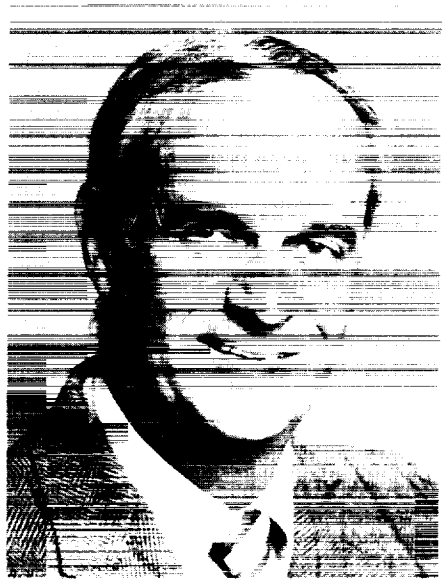

Thomas J. Kascak

Mr. Kascak has authored papers on thermionic direct energy conversion devices, 20- and 30-GHz MMIC devices, and MMIC based phased array antennas. Mr. Kascak is a member of the American Vacuum Society (AVS).

Regis F. Leonard received his Ph.D. degree in Physics from the Carnegie Institute of Technology in 1963 and came to NASA Lewis Research Center that same year. Since that time, he has completed 10 years of basic research concerning the physics of nuclear structures. For 6 years, Dr. Leonard worked toward the development of a unique Lewis facility that uses neutron radiation to treat cancer patients. For the last 11 years, he has helped develop technology in support of NASA's communications programs. This assignment includes work on the ACTS proof-of-concept (POC) technology program and, as head of the RF Systems Section, the development of an in-house communications system test capability for the ACTS POC hardware. For the last 6 years, he has served as Chief of the Solid State Technology Branch. Dr. Leonard is responsible for NASA's MMIC technology development program — an active, in-house, solid-state, research program — and a sizeable university grant program which supports basic research as applicable to solid-state electronics.

Regis F. Leonard

Rafael A. Mena received his B.S. degree in Electrical Engineering in 1988 from the University of Texas at El Paso, and an M.S. degree in Solid State Physics in 1990 from Arizona State University. While at Arizona State University, he made theoretical calculations on the effect of a magnetic field on the optical properties of semiconductor alloys. In 1990 he joined the Solid State Technology Branch at NASA Lewis Research Center as a full-time employee. His current interests lie in both the theoretical and experimental investigation of the electrical properties of novel semiconductor materials.

Rafael A. Mena

Felix A. Miranda received his B.S. degree in Physics from the University of Puerto Rico in 1983, an M.S. degree in Physics from the Rensselaer Polytechnic Institute in 1986, and a Ph.D. degree in Physics from Case Western Reserve University in 1991. He joined NASA Lewis Research Center in March 1991 as a member of the Solid State Technology Branch. Since then he has been involved with experimental research on millimeter and microwave properties of High Transition Temperature Superconducting (HTS) thin films and HTS-based passive microwave devices. Dr. Miranda is a member of the American Physical Society and the Institute of Electrical and Electronics Engineers.

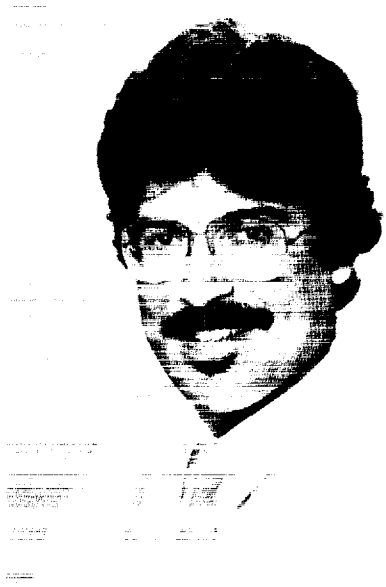

Felix A. Miranda

Carlos R. Morrison received his B.S. degree in Physics with honors, and a minor in Mathematics from Hofstra University in 1986. While attending Hofstra, he was elected to membership in the Sigma-Pi-Sigma National Physics Honor Society, the Kapa-Mu-Epsilon National Mathematics Honor Society, and the Society of Physics Students. He received an M.S. degree in Physics from the Polytechnic Institute of New York in 1989 and, in September of that year, joined NASA Lewis Research Center where he worked briefly in Reliability and Quality Assurance. He then transferred to the Solid State Technology Branch in January 1990. In September 1992, he was awarded a U.S. patent for the "Morrison's Temporal Device," which is a type of headband for use in relieving headaches. Currently, Mr. Morrison is involved with plasma deposition of thin films.

Carlos R. Morrison

George E. Ponchak received his B.E.E. from Cleveland State University in 1983 and his M.S.E.E. from Case Western Reserve University in 1987. He joined NASA Lewis Research Center in July 1983. Since joining NASA, he has been responsible for research and development of microwave/millimeter wave transmission lines and passive elements. Mr. Ponchak has developed many coplanar waveguide (CPW) circuit elements including several novel CPW to rectangular waveguide transitions, CPW pin diode switches, and CPW discontinuity equivalent circuit models. Mr. Ponchak has coauthored 22 papers on these topics. He is currently interested in the development of dielectric waveguides and micromachined waveguides for millimeter and submillimeter wave circuits. In addition, he has been responsible for the management of several MMIC development contracts. Mr. Ponchak is currently pursuing a Ph.D. in Electrical Engineering at the University of Michigan.

George E. Ponchak

John J. Pouch received his Ph.D. from Wayne State University in Detroit, Michigan, in 1981. Since 1983 he has been involved in surface science and plasma processing at the NASA Lewis Research Center.

John J. Pouch

Robert R. Romanofsky received his B.S. degree in Electrical Engineering from Pennsylvania State University and his M.S. degree in Electrical Engineering from the University of Toledo. Mr. Romanofsky has been employed in the Space Electronics Division of NASA Lewis Research Center since 1983. He spent 1 year at NASA Headquarters in Washington, D.C., as the acting program manager for superconductivity and RF communications. His work has involved microwave transmission line research and device characterization and modeling. Recently, he has been investigating microwave applications of high-temperature superconductivity.

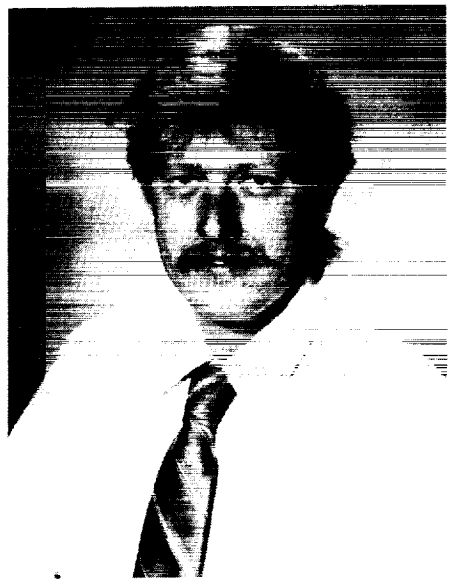

Robert R. Romanofsky

David Rosenfeld received his B.S., M.S., and Ph.D. degrees in Electrical Engineering from the Technion-Israel Institute of Technology in 1983, 1985, and 1989, respectively. In 1989 he joined Kidron Microelectronics Research Center the Technion where he researched the properties of low band-gap materials used for infrared imaging systems, focusing on the connections between the material parameters, the device properties, and the performance of the complete imaging system. Currently, Dr. Rosenfeld holds a National Research Council Fellowship and is researching the properties of SiGe heterostructures.

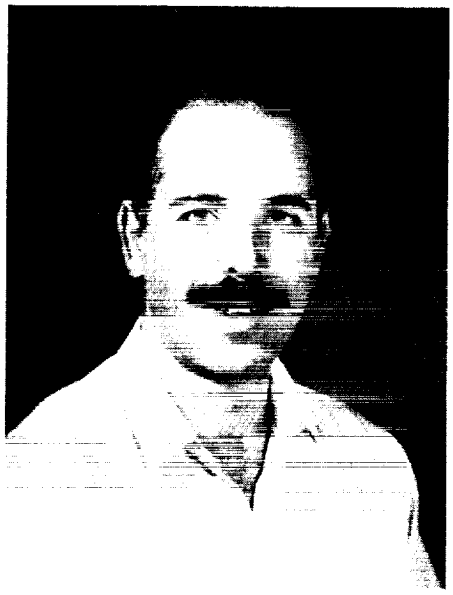

David Rosenfeld

Samuel E. Schacham received his B.S. degree in Mathematics and Physics with honors in 1971, and an M.S. degree in Physics in 1973 from Bar Ilan University, Israel. He performed research work on nonlinear optical effects in liquid crystals at the Weitzmann Institute and Bar Ilan University. He received a Ph.D. degree in Biomedical Engineering in 1978 from Northwestern University working on applications of lasers to microendoscopy. From 1978 to 1981, he was the manager of the optic group at Fibronics, Ltd., Haifa, Israel. From there he joined the Department of Electrical Engineering at the Technion in Haifa. In 1988 he was a visiting scientist at MCNC Research, Triangle Park, North Carolina, working on optical interconnects as part of the packaging group. Presently, he is with NASA Lewis Research Center as a National Research Council Senior Research Associate. His present research interests are in the physical properties of quantum structures and narrow band-gap semiconductors. His list of publications include 54 papers in international scientific journals and referred conferences.

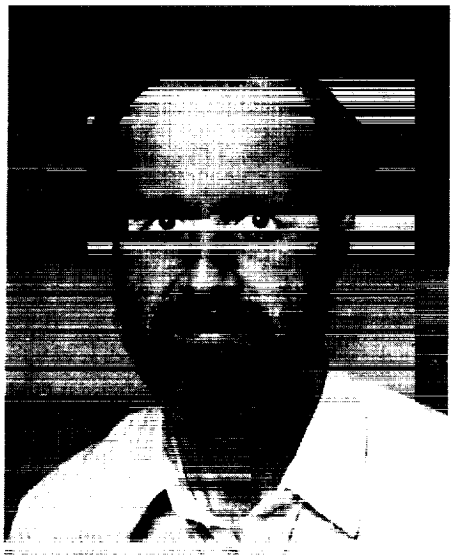

Samuel E. Schacham

Ajit K. Sil received his B.S. degree from Calcutta University, India, and emigrated to the United States where he was employed by Oakwood Downriver Medical Center. He received his second B.S. degree in Electronic Engineering Technology in 1988 from Wayne State University. He joined NASA Lewis Research Center in July of 1989 as a member of the Solid State Technology Branch. Mr. Sil works with microwave integrated circuits and solid-state devices. He is currently working toward his M.S.E.E. degree at Cleveland State University.

Ajit K. Sil

Rainee N. Simons received his B.S. degree in Electronics and Communications Engineering from Mysore University, India, in 1972, and an M. Tech. degree in Electronics and Communications Engineering from the Indian Institute of Technology in 1974. In 1983 he received a Ph.D. degree in Electrical Engineering from the Indian Institute of Technology. He started his career in 1979 as a Senior Scientific Officer at the Indian Institute of Technology. From 1985 to the present, he has been with the Solid State Technology Branch of NASA Lewis Research Center, as a National Research Council Research Associate from 1985 to 1987, as a Case Western Reserve University Research Associate from 1987 to 1990, and as a senior research engineer for Sverdrup Technology, Inc. from 1990 to the present. At NASA, Dr. Simons' research has included microwave and millimeter wave semiconductor devices, circuits and antennas, space terahertz technology, optical control of semiconductor devices, and superconductivity. Dr. Simons is the author of a book entitled "Optical Control of Microwave Devices." He has received the distinguished alumni award from his alma mater and several NASA Tech Brief and Group Achievement awards. Dr. Simons is a senior member of IEEE.

Rainee N. Simons

Mark A. Stan received his B.S.E.E. degree in 1978 from the University of Akron. He was employed by the Allen-Bradley Company as a digital circuit design engineer until 1980 when he returned to graduate school at Case Western Reserve University to study the physics of melting in two-dimensional systems. He completed work for his M.S. degree in 1982 and Ph.D. degree in 1988. In 1987 Dr. Stan began research work at NASA Lewis Research Center in the areas of characterization and growth of high-temperature superconductors. Currently, Dr. Stan is a Resident Research Associate. He is a member of the American Physical Society, the Materials Research Society, and the Institute of Electrical and Electronic Engineers.

Mark A. Stan

Stephan Stecura received his M.S. degree in Physical Chemistry in 1957 from Western Reserve University, and a Ph.D. degree in Solid-State Reaction Kinetics-Thermodynamics in 1965 from Georgetown University. From 1958 to 1965 at College Park Metallurgy Center, he studied the kinetics of crystallographic transformation and the high-temperature properties of oxides by high-temperature, x-ray diffraction techniques. He designed and built high-temperature, x-ray diffraction equipment and was invited to present the high-temperature, x-ray diffraction, arc-image furnace (capable of reaching 3000 °C in air) at the International Crystallographic Society meeting. Since 1965 he has been with NASA Lewis Research Center. Dr. Stecura's work here on heat pipes led him to determine the corrosion mechanism and the true solubilities of containment metals and alloys in alkali metals. He developed thermal barrier systems for the protection of alloy components at very high temperatures, up to 1600 °C, on air-cooled components. Currently, he is studying the properties of superconducting materials and trying to identify substrate materials for superconducting films. Dr. Stecura is recognized as an authority on the thermal barrier system technology that he developed. For his work in this field, he has received two IR-100 awards, one major Space Act award, and three major patents. He has written more than 30 original publications and is a member of the American Ceramic Society.

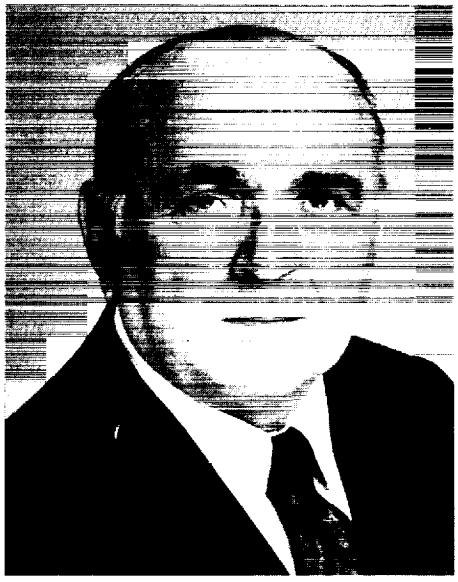

Stephan Stecura

C-4

Susan R. Taub received her B.S. degree in Electrical Engineering Technology in 1988, and an M.S. degree in Electrical Engineering in 1990 from Temple University. In 1988 and 1989, she worked for AT&T Bell Laboratories developing PSPICE compatible models for power Metaloxide Semiconductor Field Effect Transistor (MOSFET's). She joined the Solid State Technology Branch of NASA Lewis Research Center in 1990 and is currently involved in the design and characterization of MMIC's and the investigation of HEMT performance at cryogenic temperatures.
Ms. Taub is a member of IEEE.

Susan R. Taub

Joseph D. Warner received his M.S. degree in Physics from Carnegie-Mellon University in 1977. From 1977 to 1981, he performed research on magnetic phase transition at low temperature. Since that time, he has been with NASA Lewis Research Center where he characterized various insulators on GaAs and was among the first to demonstrate growth of GaAs by laser-assisted Organo-Metallic Chemical Vapor Deposition (OMCVD) at temperatures below 500 °C. Presently, he has set up a laser ablation experiment to grow high-temperature superconducting thin films. In 1989 he received a NASA Achievement Award for his part in establishing a high-temperature superconductor program at NASA Lewis. Mr. Warner has authored papers on magnetic phase transitions, electrical properties of insulation films on III-V compounds, laser-assisted growth of GaAs and AlGaAs, and properties and growth of high-temperature superconductors.
Mr. Warner is a member of the American Physical Society, the American Vacuum Society, and the Materials Research Society.

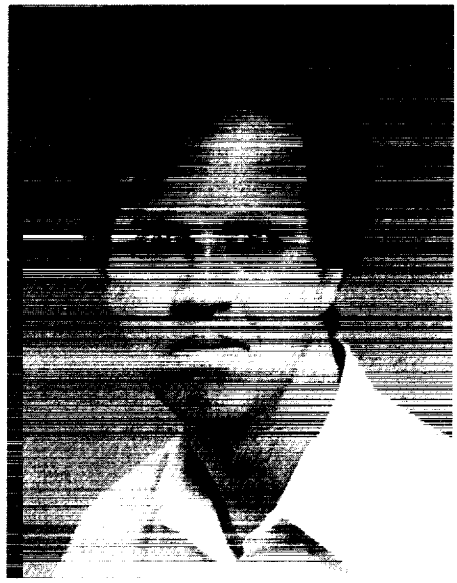

Joseph D. Warner

Paul G. Young earned his Ph.D. in Electrical Engineering in 1993 from the University of Toledo, a M.S. in Electrical Engineering from the University of Cincinnati in 1987, and a B.S.E.E. from the University of Toledo in 1985. From 1987 to 1990, he was employed by Harris/RCA in the Solid State Division as a technical staff member. He has been active in the areas of III-V compound semiconductor process development with an emphasis on InP self-gate aligned MOSFET structures and GaAs MODFET structures. Presently, his research interests are in epitaxial liftoff MODFET devices, SiGe n-MODFET and TBT structures, cryogenic on-wafer measurement of devices, SCC MESFET devices for RF high-power applications, and high-temperature devices.

Paul G. Young

SOLID STATE TECHNOLOGY BRANCH MEMBERS

Address: NASA Lewis Research Center
21000 Brookpark Road
Cleveland, Ohio 44135
FAX: (216) 433-8705

NAME	PHONE	MAIL STOP
*Leonard Regis F., Dr.	(216) 433-3500	54-5
Alterovitz, Samuel A., Dr.	(216) 433-3517	54-5
Bhasin, Kul B., Dr.	(216) 433-3676	77-5
Chorey, Chris	(216) 433-3379	77-5
Cubbage, Crystal D.	(216) 433-3644	77-5
Downey, Alan N.	(216) 433-3508	54-5
Haugland, Edward J., Dr.	(216) 433-3516	54-5
Kascak, Thomas J.	(216) 433-3505	54-5
Mena, Rafael A.	(216) 433-5641	54-5
Miranda, Felix A., Dr.	(216) 433-6589	77-5
Morrison, Carlos R.	(216) 433-8447	54-5
Ponchak, George E.	(216) 433-3504	54-5
Pouch, John J., Dr.	(216) 433-3523	54-5
Romanofsky, Robert R.	(216) 433-3507	54-5
Rosenfeld, David	(216) 433-8539	54-5
Sil, Ajit K.	(216) 433-8610	54-5
Simons, Rainee N., Dr.	(216) 433-3462	54-5
Stan, Mark A., Dr.	(216) 433-8369	54-5
Stecura, Stephan, Dr.	(216) 433-3264	54-5
Taub, Susan R.	(216) 433-6571	54-5
Warner, Joseph D.	(216) 433-3677	77-5
Young, Paul G., Dr.	(216) 433-5641	54-5

Branch Secretary:

Linda Mayes	(216) 433-3514	54-5

*Chief, Solid State Technology Branch

REPORT DOCUMENTATION PAGE

Form Approved
OMB No. 0704-0188

Public reporting burden for this collection of information is estimated to average 1 hour per response, including the time for reviewing instructions, searching existing data sources, gathering and maintaining the data needed, and completing and reviewing the collection of information. Send comments regarding this burden estimate or any other aspect of this collection of information, including suggestions for reducing this burden, to Washington Headquarters Services, Directorate for Information Operations and Reports, 1215 Jefferson Davis Highway, Suite 1204, Arlington, VA 22202-4302, and to the Office of Management and Budget, Paperwork Reduction Project (0704-0188), Washington, DC 20503.

1. AGENCY USE ONLY (*Leave blank*)

2. REPORT DATE
August 1993

3. REPORT TYPE AND DATES COVERED
Technical Memorandum

4. TITLE AND SUBTITLE
Solid State Technology Branch of NASA Lewis Research Center
Fifth Annual Digest
June 1992–June 1993

5. FUNDING NUMBERS
WU-506-72-1B

6. AUTHOR(S)

7. PERFORMING ORGANIZATION NAME(S) AND ADDRESS(ES)
National Aeronautics and Space Administration
Lewis Research Center
Cleveland, Ohio 44135-3191

8. PERFORMING ORGANIZATION REPORT NUMBER
E-8004

9. SPONSORING/MONITORING AGENCY NAME(S) AND ADDRESS(ES)
National Aeronautics and Space Administration
Washington, D.C. 20546-0001

10. SPONSORING/MONITORING AGENCY REPORT NUMBER
NASA TM-106303

11. SUPPLEMENTARY NOTES
Responsible person, Ajit Sil, (216) 433-8610.

12a. DISTRIBUTION/AVAILABILITY STATEMENT
Unclassified - Unlimited
Subject Category 32

12b. DISTRIBUTION CODE

13. ABSTRACT ***(Maximum 200 words)***

The digest is a collection of papers written by the members of the Solid State Technology Branch of NASA Lewis Research Center from June 1992–June 1993. The papers cover a range of topics relating to superconductivity, MMIC's, coplanar waveguide, and material characterization.

14. SUBJECT TERMS
Microwave integrated circuits; Microwave transmission lines; Antennas; Transistors; Superconductors; Semiconductor materials

15. NUMBER OF PAGES
301

16. PRICE CODE
A14

17. SECURITY CLASSIFICATION OF REPORT
Unclassified

18. SECURITY CLASSIFICATION OF THIS PAGE
Unclassified

19. SECURITY CLASSIFICATION OF ABSTRACT
Unclassified

20. LIMITATION OF ABSTRACT